MILLISECOND PULSARS AND PULSAR WIND NEBULAE AS SOURCES OF GAMMA RAYS AND COSMIC RAYS

C Venter MSc

12006653

Thesis submitted for the degree Doctor of Philosophy at the Potchefstroom Campus of the North-West University

Supervisor: Prof OC de Jager

June 2008

Dedication

To my loving heavenly Father, Creator of heaven and earth, in Whom we have everlasting life through Jesus Christ, by the powerful working of His Holy Spirit.

"He counts the number of the stars;
He calls them all by name.
Great is our Lord, and mighty in power;
His understanding is infinite."
(Ps. 147:4,5 NKJV).

"Praise Him, sun and moon;
Praise Him, you stars of light!
Praise Him, you heavens of heavens,
And you waters above the heavens!
Let them praise the name of the LORD,
For He commanded and they were created."
(Ps. 148:3-5 NKJV).

Acknowledgements

- Heartfelt thanks to my parents. Their passion for God and His work is truly inspirational, and their love and support priceless. Mom, thanks for applying your exceptional proof-reading skills!
- A big thank you to prof. De Jager, my supervisor, for his academic leadership, many exceptional ideas, patient ear, enriching presence, hard work, and invaluable help – in good and also bad times.
- Thank you very much to dr. Ingo Buesching and prof. Marius Potgieter for allowing me to refer to our collaborative work in this thesis. It has been a pleasure to be part of the joint research effort, and see your expertise at work.
- Thanks to my friends and family for their support and interest.
- Thank you to all the colleagues of the Physics Department for their friendliness and encouragement. You are my "work family".
- Above all, I would like to thank my Heavenly Father Whose dreams for our lives are bigger than we ourselves can ever envision.

The financial assistance of the Department of Labour (DoL) towards this research is hereby gratefully acknowledged. Opinions expressed and conclusions arrived at, are those of the author and are not necessarily to be attributed to the DoL.

Abstract

MILLISECOND PULSARS AND PULSAR WIND NEBULAE
AS SOURCES OF GAMMA RAYS AND COSMIC RAYS

Our main aim was to implement a fully 3D General Relativistic (GR) frame-dragging polar cap (PC) millisecond pulsar (MSP) model as a numerical code, and constrain it using multiwavelength and cosmic-ray data. We also modelled pulsar wind nebulae (PWN) as sources of gamma rays and cosmic rays. Detailed modelling of the unscreened and screened MSPs PSR J0437-4715 and PSR B1821-24 yielded low curvature radiation (CR) cut-off energies and highlighted the need for 4^{th} generation Cherenkov telescopes and / or space telescopes such as *GLAST* in order to observe CR emission from gamma-ray MSPs. We also constrained their gamma-ray efficiencies using *EGRET* upper limits. We studied the behaviour of the basic MSP model for a mesh of $(P, \dot{P}, \chi, \zeta)$-space, and found that cut-off energies, efficiencies, energy fluxes, and integral fluxes generally decrease with larger P and smaller $\dot{P}$, and that their maxima occur for on-beam radiation. Accurate knowledge of pulsar geometry is therefore crucial when making predictions regarding MSP visibility. In addition, screening complicates the matter. We furthermore found that beaming correction factors may be significantly larger than unity, and that if these factors are unknown, actual trends may be concealed. We numerically confirmed the theoretical expectation that the gamma-ray efficiency is $\approx 7\%$ for MSPs with unscreened PCs. Using a population of 59 MSPs, we found that roughly half of these are expected to be visible for *GLAST*. We performed a population study of MSPs in the globular cluster (GC) 47 Tucanae and obtained "geometry-averaged" results with relatively small uncertainties. The *EGRET* upper limit at 1 GeV constrained the number of visible GC pulsars to $N \approx 27$. Larger values of N imply a reduction in the model-predicted pulsed integral flux, even more severely so in the case of a *GLAST LAT* non-detection of the cumulative flux. We also calculated the unpulsed inverse Compton scattering (ICS) and synchrotron radiation (SR) fluxes due to particles escaping from the ensemble of MSPs and found that the ICS flux will probably not be visible for *H.E.S.S.*, while telescopes such as *Chandra* and *Hubble* should yield upper limits for the SR component of diffuse radiation. We modelled the PWN G0.9+0.1, and found optimal fits for the pulsar's initial spin-down luminosity and injection spectral break energy using multiwavelength data. From these followed predictions for the putative embedded pulsar's present-day spin-down power and PC magnetic field strength. We furthermore participated in ongoing collaborative research involving pulsars and PWN as sources of cosmic rays. We concluded that while PSR J0437-4715 is not expected to make a significant contribution to the local interstellar spectrum (LIS), both Geminga and B0656+14 may make a non-negligible contribution to the local cosmic ray positron spectrum. We predicted an anisotropy in the positron LIS due to the latter two pulsars of up to a few percent, which will probably only be testable by the *PAMELA* mission. We lastly obtained constraints on the birth periods of and diffusion coefficients in the direction of these pulsars. Future work include considering multipolar magnetic fields, including an E_θ-component in the accelerating E-field, reconsidering electrodynamic boundary conditions, and performing magnetospheric particle-in-cell (PIC) simulations.

KEY WORDS: General Relativistic (GR) frame dragging — GR Electrodynamics — Millisecond Pulsar Visibility — Non-thermal Radiation Processes — Pair Production — Pulsar Wind Nebulae — Gamma Rays — Cosmic Rays — *H.E.S.S.* —*GLAST* — Individual Pulsars: PSR J0437-4715, PSR B1821-24.

Opsomming

MILLISEKONDE-PULSARE EN PULSARWINDNEWELS
AS BRONNE VAN GAMMASTRALE EN KOSMIESE STRALE

Ons hoofdoel was die implementering van 'n volledige 3D Algemeen-relativistiese poolkapmodel, wat raamsleuring insluit, vir 'n millisekonde-pulsar (MSP) as numeriese kode, en beperking van hierdie model deur multi-golflengtedata en kosmiesestraaldata te gebruik. Ons het ook pulsarwindnewels (PWN) as bronne van gammastrale en kosmiese strale gemodelleer. Detail modellering van die onafgeskermde en afgeskermde MSP's PSR J0437-4715 en PSR B1821-24 het lae krommingstraling (KS) energie-afsnitte tot gevolg gehad, wat die behoefte aan vierdegenerasie Cherenkov-teleskope en / of ruimteteleskope soos *GLAST* beklemtoon vir die waarneming van KS vanaf gammastraal-MSP's. Ons het die gammastraal-effektiwiteite beperk deur *EGRET*-bogrense te gebruik. Ons het die gedrag van die basiese MSP-model vir 'n rooster van $(P, \dot{P}, \chi, \zeta)$-ruimte bestudeer, en gevind dat afsny-energieë, effektiwiteite, energievloed, en integrale vloed oor die algemeen afneem met groter P en kleiner $\dot{P}$, en dat hul maksima naby die magneet-as voorkom. Akkurate kennis rakende pulsargeometrie is dus van kardinale belang wanneer voorspellings oor MSP-sigbaarheid gemaak word. Hierdie saak word voorts deur afskerming gekompliseer. Ons het ook gevind dat stralingskorreksiefaktore drasties groter as een kan wees, en dat wetmatighede verborge kan bly as hierdie faktore onbekend is. Ons het numeries die teoretiese verwagting bevestig dat die gammastraal-effektiwiteit $\approx 7\%$ is vir MSP's met onafgeskermde poolkappe. Deur van 'n populasie van 59 MSP's gebruik te maak, kon ons aantoon dat ongeveer die helfte van die lede sigbaar behoort te wees vir *GLAST*. Ons het 'n populasiestudie uitgevoer van MSP's in die geslote stertros (GS) 47 Tucanae en "geometrie-gemiddelde" resultate met relatief klein onsekerhede verkry. Die *EGRET*-bogrens by 1 GeV het die aantal sigbare GS-pulsare tot $N \approx 27$ beperk. Groter waardes van N impliseer 'n vermindering in die model-voorspelde integrale vloed, en nog baie meer indien *GLAST LAT* die kumulatiewe vloed nie waarneem nie. Ons het die ongepulseerde inverse Comptonverstrooingskomponent (ICV) en sinkrotronstralingskomponent (SS), afkomstig van deeltjies wat die populasie MSP's verlaat, bereken, en gevind dat die ICV-vloed moontlik nie vir *H.E.S.S.* sigbaar sal wees nie, terwyl teleskope soos *Chandra* en *Hubble* bogrense vir die SS-komponent van diffuse straling mag stel. Ons het die PWN G0.9+0.1 gemodelleer, en beste passings vir die geboorte-afspinhelderheid en spektraal-breekpuntenergie van die MSP-geproduseerde deeltjiespektrum verkry deur multi-golflengtedata te gebruik. Hieruit het voorspellings gevolg vir die steeds onontdekte ingeslote pulsar se huidige afspin-helderheid en poolkap-magneetveldsterkte. Ons het deelgeneem aan voortgaande navorsing rakende pulsare en PWN as bronne van kosmiese strale. Ons het tot die gevolgtrekking gekom dat, hoewel daar nie verwag word dat PSR J0437-4715 'n betekenisvolle bydrae tot die lokale interstellêre spektrum (LIS) sal maak nie, beide Geminga en B0656+14 nie-weglaatbare bydraes kan maak tot die lokale kosmiese-straal positronspektrum. Ons het 'n anisotropie in die positron-LIS a.g.v. lg. twee pulsare voorspel van tot 'n paar persent. Hierdie anisotropie sal moontlik slegs deur die *PAMELA*-sending getoets kan word. Ons het laastens beperkings op die geboorteperiodes van en diffusie-koëffisiënte in die rigting van hierdie pulsare verkry. Toekomstige studie sluit in bestudering van multipolêre magneetvelde, insluiting van 'n E_θ-komponent in die versnellende E-veld, heroorweging van elektrodinamiese randvoorwaardes, asook magnetosferiese deeltjie-in-sel-simulasies (DIS).
SLEUTELWOORDE: Algemeen-relativistiese (AR) Raamsleuring — AR-Elektrodinamika — Millisekonde-pulsarsigbaarheid — Nie-termiese Stralingsprosesse — Paarproduksie — Pulsarwindnewels — Gammastrale — Kosmiese Strale — *H.E.S.S.* — *GLAST* — Individuele Pulsare: PSR J0437-4715, PSR B1821-24.

Nomenclature

AGILE	Astro-rivelatore Gamma a Immagini LEggero
AGN	Active galactic nuclei
ASCA	Advanced Satellite for Cosmology and Astrophysics
AXPs	Anomalous X-ray pulsars
CANGAROO	Collaboration of Australia and Nippon (Japan) for a Gamma-Ray Observatory in the Outback
CANGAROO-II	Collaboration of Australia and Nippon (Japan) for a Gamma-Ray Observatory in the Outback Phase 2
CANGAROO-III	Collaboration of Australia and Nippon (Japan) for a Gamma-Ray Observatory in the Outback Phase 3
CGRO	Compton Gamma-Ray Observatory
CHPC	Centre for High Performance Computing
CAT	Cherenkov Array at Themis
CR	Curvature radiation
CTA	Cherenkov Telescope Array
EXOSAT	European X-ray Observatory Satellite
EBL	Extragalactic background light
EGRET	Energetic Gamma-Ray Experiment Telescope
EHE	Extremely high energy
EOS	Equation of state
EUVE	Extreme Ultraviolet Explorer
FSR	Field sign reversal
GC	Globular cluster
GLAST	Gamma-Ray Large Area Space Telescope (Has since been renamed to *FERMI Gamma-ray Space Telescope*)

GLAST LAT	*GLAST* Large Area Telescope
GR	General Relativity / General Relativistic
GRMHD	General Relativistic MHD
HAWC	High Altitude Water Cherenkov Experiment
HE	High energy
HEAO 1	High Energy Astrophysical Observatory 1
HEAO 2	High Energy Astrophysical Observatory 2
HEAO 3	High Energy Astrophysical Observatory 3
HEASARC	High Energy Astrophysics Science Archive Research Centre
HEGRA	High Energy Gamma Ray Astronomy
H.E.S.S.	High Energy Stereoscopic System
H.E.S.S.-II	High Energy Stereoscopic System Phase 2
HMBPs	High mass binary pulsars
IACTs	Imaging Atmospheric Cherenkov Telescopes
ICS	Inverse Compton Scattering
IMBPs	Intermediate mass binary pulsars
IR	Infra-red
ISM	Interstellar medium
LC	Light cylinder
LIS	Local interstellar spectrum
LMBPs	Low mass binary pulsars
LMC	Large Magellanic Cloud
MAGIC	Major Atmospheric Gamma-Ray Imaging Cherenkov
MAGIC-II	Major Atmospheric Gamma-Ray Imaging Cherenkov Phase 2
MSP	Millisecond pulsar
NS	Neutron star
OG	Outer Gap
PC	Polar cap
PFF	Pair formation front
PMTs	Photo-multiplyer tubes
PWN	Pulsar Wind Nebula(e)
QPO	Quasi-periodic oscillation

ROSAT	Röntgensatellit
RRats	Rotating Radio Transients
RXTE	Rossi X-ray Timing Explorer
SAS-1	Small Astronomy Satellite 1
SAS-2	Small Astronomy Satellite 2
SGR	Soft gamma-ray repeaters
SKA	Square Kilometer Array
SNR	Supernova Remnant
SR	Synchrotron radiation
UHE	Ultra high energy
VERITAS	Very Energetic Radiation Imaging Telescope Array System
VHE	Very high energy
VLA	Very Large Array
XMM-Newton	X-ray Multi-Mirror Mission
1D	one-dimensional
2D	two-dimensional
3D	three-dimensional

Commonly-used Symbols

P	Pulsar period
P	Power
P_0	Pulsar birth period
$\dot{P}$	Pulsar period time-derivative
$\dot{P}_0$	Pulsar period time-derivative at pulsar birth
Ω	Angular frequency
Ω_0	Birth angular frequency
$\dot{\Omega}$	Angular frequency time-derivative
$\dot{\Omega}_0$	Angular frequency time-derivative at pulsar birth
M	Stellar mass
I	Moment of inertia
R	Stellar radius
$R_6 = R/10^6$ cm	Normalised stellar radius
$R_{\rm LC}$	Light cylinder radius
$R_{\rm PC}$	Polar cap (PC) radius
$A_{\rm PC}$	PC area
h	Height above the PC
h	Planck's constant
$\hbar$	$= h/2\pi$
h_c	Normalised height of PFF
z	Normalised height above the PC
z_c	Normalised height of pair formation (PFF) front above PC
η_c	Normalised radial coordinate of PFF above PC
r_s	Pulsar wind shock radius
κ	Compactness parameter
κ'	Curvature

dS	Incremental surface element
ds	Incremental path length
ϵ	$= 2GM/(c^2R)$
ϵ	Geometric parameter
τ	Age
τ	Energy ratio
α^{P}	Pitch angle
α_{fine}	Fine structure constant
α	Gravitational redshift function
α	Inclination angle
ν or f	Frequency
σ	Standard deviation
σ	Magnetisation parameter
σ	Inverse Compton cross section
β	Normalised speed v/c
β'	Impact angle
β^{slice}	Duty cycle
d	Distance
$f(\eta)$	Correction factor for dipole magnetic flux
$H(\eta)$	GR correction factor
$\delta(\eta)$	Simplifying function
γ_i	Simplifying function
$\tilde{\gamma}_i$	Simplifying function
δ	Used in energy bin size ($dE_i \approx \delta E_i$)
Ψ	Magnetic flux
γ	Lorentz factor
γ	Associated with gamma-ray photons
e^-	Electron
e^+	Positron
e	Electron charge
q	Particle charge
q	Telescope sensitivity factor
ϑ_{PC}	PC angle

Θ_0	Magnetic colatitude of last open field line at stellar surface
Θ_0^c	Approximation of magnetic colatitude of last open field line for canonical pulsars at stellar surface
$\Theta(\eta)$	Magnetic colatitude of last open field line
$\Theta^c(\eta)$	Approximation of magnetic colatitude of last open field line for canonical pulsars
ζ_0	Ratio of approximate and full expressions of magnetic colatitude of last open field line at stellar surface
$\zeta(\eta)$	Ratio of approximate and full expressions of magnetic colatitude of last open field line
ζ	Observer angle
c	Speed of light in vacuum
m_e	Electron mass
$\mathbf{\Omega}$	Spin axis
μ	Magnetic moment
μ	Proper motion
$\vec{\mu}$	Magnetic dipole axis
$\mathbf{B}$	Magnetic field
$\mathbf{E}$	Electric field
$E_{\|\|}$	E-field parallel to the magnetic field lines
B_0	Magnetic field strength at the pole
$B_\perp$	Perpendicular magnetic field
$B_{\rm crit}$	Critical magnetic field
χ'	Erber parameter
χ	Inclination angle
$\dot{E}_{\rm rot}$	Spin-down luminosity
$L_{\rm md}$	Magnetic dipole radiation loss rate
$L_{\rm prim}$	Primary particles' luminosity
$L_\gamma^{\rm beam}$	Total beam gamma-ray luminosity
$L_\gamma^{\rm slice}$	Slice gamma-ray luminosity
$\eta_\gamma^{\rm beam}$	Total beam gamma-ray efficiency
$\eta_\gamma^{\rm slice}$	Slice gamma-ray efficiency
$\dot{E}$	Energy loss rate
$I(E, dE)$	Indicator function
$F(>E)$	Integral flux

dN/dE	Photon spectrum (units e.g. ergs/s/cm^2)
p	Spectral index
U	Energy density
E_0	Cut-off energy
Q^i	Single pulsar injection spectrum
$\langle Q^j \rangle_{\rm cum}$	Average cumulative injection spectrum
ϑ	Polar angle (corotating frame)
ξ	Normalised polar coordinate (corotating frame)
r	Radial distance from stellar centre (corotating frame)
η	Normalised radial coordinate (corotating frame)
ϕ	Magnetic azimuthal coordinate (corotating frame)

Contents

1 Introduction **1**

1.1 Pulsar Physics . . . 2

1.1.1 Historical Overview . . . 2

1.1.2 Millisecond Pulsars . . . 6

1.1.3 The Basic Pulsar Model . . . 10

1.1.4 Polar Cap (PC) Models . . . 13

1.1.5 Outer Gap (OG) Models . . . 23

1.1.6 Slot Gap (SG) Models . . . 26

1.1.7 Two-Pole Caustic Model . . . 27

1.1.8 Other Topics . . . 28

1.2 Pulsar Wind Nebulae (PWN) . . . 29

1.2.1 Definition . . . 29

1.2.2 Classification . . . 31

1.2.3 Theoretical interpretation . . . 32

1.2.4 PWN as Probes . . . 34

1.3 Gamma-Ray Astronomy . . . 35

1.3.1 Definition . . . 35

1.3.2 Historical Overview . . . 36

1.3.3 Observed Gamma-ray Pulsars . . . 38

1.3.4 The *High Energy Stereoscopic System (H.E.S.S.)* . . . 39

1.3.5 *GLAST LAT* . . . 44

1.3.6 Future Opportunities . . . 46

1.4 Cosmic Rays . . . 47

1.4.1 Overview . . . 47

1.5 Motivation . . . 51

1.5.1 Context . . . 51
1.5.2 Specific Aims . . . 52
1.5.3 Exploiting Favourable Conditions to Constrain Models . . . 53
1.6 Thesis Outline . . . 55
1.7 Publications . . . 56
1.7.1 Peer-reviewed Papers . . . 56
1.7.2 Conference Proceedings . . . 56

2 Modelling the Pulsar Magnetosphere **58**
2.1 Radiation and other Relevant Processes in the Pulsar Magnetosphere . . . 59
2.1.1 Synchrotron Radiation (SR) . . . 59
2.1.2 Curvature Radiation (CR) . . . 64
2.1.3 Inverse Compton Scattering (ICS) . . . 66
2.1.4 Magnetic Photon Absorption . . . 69
2.1.5 Thermionic Emission of Charges . . . 74
2.2 The Lense-Thirring Effect . . . 75
2.3 GR-corrected Magnetic Field and Electric Potential . . . 76
2.3.1 Basic Equations . . . 77
2.3.2 Equations in Corotating Reference Frame . . . 78
2.3.3 The External Magnetic Field of a Rotating Neutron Star . . . 79
2.3.4 The Electric Potential . . . 84
2.4 $E_{||}$ for Different Scenarios . . . 86
2.4.1 'Classic' Case . . . 86
2.4.2 No Upper PFF – Near Surface Case ($\eta \simeq 1$) . . . 86
2.4.3 No Upper PFF – Distant Case ($\eta \gg 1$) . . . 88
2.4.4 Screened $E_{||}$ – Near Case ($\eta \sim 1$) . . . 89
2.4.5 Screened $E_{||}$ – Distant Case ($\eta \gg 1$) . . . 90
2.4.6 High-altitude $E_{||}$ for MSPs . . . 90
2.5 The Magnetospheric Model for Charged Particle and Photon Transport . . . 91
2.5.1 Coordinates . . . 92
2.5.2 Choice of Electric Field and $\eta_{\rm break}$ . . . 92

2.5.3 Magnetic Field . . . 93
2.5.4 Curvature Radius . . . 94
2.5.5 Surface Area . . . 96
2.5.6 Path Length . . . 96
2.5.7 Calculation of Tangent and Observer Angles Using Spherical Trigonometry . . . 97
2.5.8 Slippage and Aberration . . . 98
2.5.9 Transport Equation . . . 100
2.5.10 Calculating Spectra, Fluxes, and Luminosities involving Beaming Corrections . . . 100
2.5.11 Correction to CR Spectrum Calculations . . . 105
2.5.12 Equation of State (EOS) . . . 108
2.6 Conclusion . . . 109

3 Modelling of Single Millisecond Pulsars **111**
3.1 Introduction . . . 112
3.2 Background . . . 114
3.2.1 PSR J0437-4715 . . . 114
3.2.2 PSR B1824-21 . . . 119
3.3 Model-Independent Pre-Analysis . . . 123
3.3.1 General Pulsar Physics Fundamentals . . . 123
3.3.2 Constraining Gamma-Ray Efficiency Using Upper Limits . . . 124
3.4 Oscillations in the GR Electric Field . . . 127
3.5 Some Theoretical Results . . . 129
3.5.1 Gamma-Ray Luminosity . . . 130
3.5.2 Integration of Spectra . . . 131
3.5.3 CR Cut-Off Energy . . . 133
3.6 Results of the 'GR Model': PSR J0437-4715 (Unscreened Case) . . . 133
3.6.1 Optical Depth . . . 133
3.6.2 CR Cut-Off Energy . . . 135
3.6.3 Electron and Photon Energies vs. Distance . . . 139
3.6.4 Spectra and Fluxes . . . 140
3.6.5 Constraining the Gamma-ray Efficiency . . . 143
3.6.6 Lightcurves . . . 146

3.7 Results of the 'GR Model': PSR B1821-24 (Screened Case) 148
3.7.1 Optical Depth 148
3.7.2 CR Cut-Off Energy 148
3.7.3 Electron and Photon Energies vs. Distance 150
3.7.4 Spectra and Fluxes 151
3.7.5 Constraining the Gamma-ray Efficiency 154
3.8 Conclusion 154

4 Millisecond Pulsar Population Studies **159**
4.1 Introduction 159
4.2 Preliminaries 161
4.2.1 Screening of PC Potentials 161
4.2.2 Proper Motion 163
4.3 The Effects of Geometry and Rotational Characteristics on MSP Visibility: A Parameter Study 163
4.3.1 Method 164
4.3.2 Results and Discussion 167
4.3.3 Summary 185
4.4 Systematic Beaming Effects 185
4.4.1 Method 185
4.4.2 Results and Discussion 188
4.4.3 Summary 196
4.5 MSPs in Globular Clusters 196
4.5.1 Background 197
4.5.2 Pulsed Gamma-Ray Flux from 47 Tucanae 198
4.5.3 Geometry-averaged Spectra and Luminosities 200
4.5.4 Constraints on Number of Visible Members and Average Integral Fluxes 202
4.5.5 Other GCs 204
4.6 Conclusion 204
4.6.1 Population Study Involving Pulsar Parameter Space 205
4.6.2 Population Study Involving a 'Real' Population of Mainly Unscreened MSPs . 205
4.6.3 Population Study Involving a Population of MSPs in a Globular Cluster 206
4.6.4 The Link Between Radio and Gamma-ray Telescopes 207

4.6.5 The Effect of a "New E-Field" 208

5 Beyond the Light Cylinder **209**

5.1 Introduction 209

5.2 Unpulsed Radiation from an Ensemble of MSPs in 47 Tucanae 209

5.2.1 Cumulative Injection Spectrum 209

5.2.2 Escape and Radiation Loss Time Scales 211

5.2.3 Calculation of Unpulsed High-Energy Flux 213

5.2.4 Discussion 214

5.3 Pulsar Parameters Derived from Multiwavelength Observations of G0.9+0.1 215

5.3.1 Background 215

5.3.2 The PWN Model 218

5.3.3 Best-fit Parameters 221

5.3.4 Summary 223

5.4 Contributions from Nearby Pulsars to the Local Cosmic Ray Electron Spectrum . . . 223

5.5 Constraints on the Lepton Content of PWN from the Local Cosmic Ray Positron Spectrum 224

5.6 A Cosmic Ray Positron Anisotropy due to Two Middle-Aged, Nearby Pulsars? 225

5.7 Conclusion 226

6 Model Refinements **228**

6.1 Including a Theta-component in the Accelerating E-field 228

6.2 Implementing the Lorentz Transformation Using Spherical Trigonometry 231

6.3 Parametrization of Φ and ρ 234

6.4 Summary 238

7 Conclusion **240**

7.1 Main Results And Contributions 241

7.2 Detailed Conclusions 244

7.2.1 Implementing a PC GR Frame-Dragging Pulsar Model in a Computer Code . . 245

7.2.2 Predicting Single MSP Visibility for Screened and Unscreened Pulsars 246

7.2.3 Studying the MSP Model Behaviour in Pulsar Parameter Space 249

7.2.4 Obtaining Constraints on the MSP Model by Modelling Single MSP Spectra . 249

7.2.5 Obtaining Constraints on the MSP Model by Modelling MSP Population Cumulative Spectra: Pulsed and Unpulsed Radiation 249
7.2.6 Obtaining Constraints on the MSP Model by Modelling the Contribution of Nearby Pulsars to the Local Cosmic-Ray Spectrum 251
7.2.7 Studying the Typical Beaming Angles of MSPs 252
7.2.8 Investigating Future Model Refinements 252
7.2.9 PWN Modelling 253
7.3 Future Outlook and Recommendations 253

A Various Mathematical Results **256**
A.1 Estimation of the Generalised Gamma-Luminosity as Function of Inclination Angle . . 256
A.2 Integral of Generic Spectral Form 258
A.3 Flat Shape of the Integral Flux at Low Energies 260
A.4 Scaling of Integral Flux 260
A.5 Relating Bolometric and Observer Luminosities 262
A.6 Logarithmic Binning 262
A.7 Logarithmic Integration 264

B Selected Publications **265**
B.1 Contributions from Nearby Pulsars to the Local Cosmic Ray Electron Spectrum . . . 265
B.1.1 Abstract 265
B.1.2 Introduction 266
B.1.3 Steady-State Millisecond Pulsar Model: PSR J0437-4715 268
B.1.4 Impulsive Injection – Canonical Pulsar Model: Geminga 271
B.1.5 Conclusion 277
B.1.6 Acknowledgments 278
B.2 Constraints on the Lepton Content of PWN from the Local Cosmic Ray Positron Spectrum 278
B.2.1 Abstract 279
B.2.2 Introduction 279
B.2.3 The Positron LIS 279
B.2.4 Positrons from PWN 280
B.2.5 Conclusions 284
B.2.6 Acknowledgements 285
B.3 A Cosmic Ray Positron Anisotropy due to Two Middle-Aged, Nearby Pulsars? 285

B.3.1 Abstract 285
B.3.2 Introduction 286
B.3.3 Positrons from PWNe 286
B.3.4 Propagation of Cosmic Ray Positrons and Local Anisotropy 289
B.3.5 Conclusions 291
B.3.6 Acknowledgments 292

List of Figures

1.1 An optical image of the Crab Nebula 3
1.2 Pulsar histograms showing the number of pulsars for certain period ranges 7
1.3 Discovery of GC pulsars as function of time 8
1.4 An artist's impression of an MSP / red giant binary system 10
1.5 PB-diagram showing the spread of pulsars according to their observed periods and derived magnetic fields 11
1.6 $P\dot{P}$-diagram for pulsars in the *Parkes Observatory ATNF Pulsar Catalogue* with $\dot{P} > 0$ 13
1.7 Magnetosphere of a rotator with antiparallel spin and magnetic axes filled with charge-separated plasma 15
1.8 A pulsar magnetosphere according to Goldreich & Julian (1969) 17
1.9 Numeric pair death lines calculated by Harding et al. (2002b) 21
1.10 Schematic view of a non-aligned rotator with PC and OG regions indicated 23
1.11 Structure of the OG 24
1.12 Structure of the 'slot gap' 26
1.13 Schematic diagram of a PWN within an SNR 32
1.14 Skymap of VHE sources 36
1.15 Lightcurves of seven gamma-ray pulsars 39
1.16 Montage of *H.E.S.S.* Telescopes and components, situated in Namibia 40
1.17 Gamma-ray image of the SNR RX J1713.7 − 3946 obtained with the *H.E.S.S.* Telescopes 41
1.18 Integral sensitivity plot of *GLAST LAT* 44
1.19 The "Kifune plot" 46
1.20 The spectrum of cosmic rays 48
1.21 The positron fraction in cosmic rays as function of energy 50

2.1 Graphs of $F(x)$ and $G(x)$ 61

2.2 The spectrum of a source of SR which exhibits the phenomenon of synchrotron self-absorption 63
2.3 Representation of the combined CR and magnetic photon absorption processes 64
2.4 Graphs of $\Psi(\eta)$ and $f(\eta)$ vs. η 80
2.5 The GR and classical magnetic field of an MSP 82
2.6 Graphs of the polar angle vs. altitude for the last closed magnetic field line (Classical and GR cases) 83
2.7 $H(\eta)$ vs. η 85
2.8 $\delta(\eta)$ vs. η 87
2.9 Graphs of the different expressions for $E_{||}$ vs. altitude 91
2.10 The fit for η_{break}, where the near and far approximations of the E-field coincide 93
2.11 GR-corrected electric field used in the model 94
2.12 Definition of various angles with regards to a beam of radiation along a B-line 97
2.13 Schematic illustration of aberration and slippage 99
2.14 Correction of CR spectrum 106
2.15 Comparison of uncorrected and corrected CR spectra 108

3.1 Mean pulse profile and polarisation properties of PSR J0437-4715 at 1512 MHz 116
3.2 X-ray pulse profiles of PSR J0437-4715 118
3.3 Integrated radio and X-ray pulse profiles of PSR B1821-24 121
3.4 The maximum gamma-ray efficiency vs. photon spectral index vs. CR cut-off energy for PSR J0437-4715 125
3.5 The maximum gamma-ray efficiency vs. photon spectral index vs. CR cut-off energy for PSR B1821-24 127
3.6 Parallel GR electric field showing sign reversal 128
3.7 Electric field sign reversal in ϕ-ξ-η-parameter space 129
3.8 Oscillatory particle motion due to sign reversal of E-field 130
3.9 Graph of L_{γ}^{beam} vs. $\dot{E}_{\text{rot}}$ 134
3.10 Contour plot of $\log_{10}$ of the CR cut-off energy vs. observer angle ζ and magnetic inclination angle χ for PSR J0437-4715 137
3.11 Contour plot of the maximum CR energy vs. magnetic azimuthal angle ϕ and scaled polar angle angle ξ for PSR J0437-4715 138

3.12 Gamma-ray energy, electron energy, and fractional gamma-ray luminosity vs. path length along the magnetic field line for PSR J0437-4715 139
3.13 Differential spectra predictions for PSR J0437-4715 141
3.14 Integral flux predictions for PSR J0437-4715 142
3.15 Histogram: Comparison of mean and cut-off energies 144
3.16 Histogram of the beaming correction for PSR J0437-4715 145
3.17 Predicted lightcurve of PSR J0437-4715 147
3.18 Contour plot of $\log_{10}$ of the CR cut-off energy vs. observer angle ζ and magnetic inclination angle χ for PSR B1821-24 149
3.19 Contour plot of the maximum CR energy vs. scaled polar angle angle ξ and magnetic azimuthal angle ϕ for PSR B1821-24 150
3.20 Gamma-ray energy, electron energy, and fractional gamma-ray luminosity vs. path length along the magnetic field line for PSR B1821-24 151
3.21 Differential spectra predictions for PSR B1821-24 152
3.22 Integral flux predictions for PSR B1821-24 153

4.1 Condition for screened PC potentials 162
4.2 Graphs of dN/dE, E^2dN/dE, and integral flux 165
4.3 Determining the CR cut-off energy using the integral flux 166
4.4 Contour graphs of the $\log_{10}$ of CR cut-off energy E_0 (in GeV) vs. $\dot{P}$ and P, for different χ and ζ 168
4.5 Contour graphs of the $\log_{10}$ of the total beam gamma-ray efficiency $\eta_\gamma^{\rm beam}$ (%) vs. $\dot{P}$ and P, for different χ and ζ 169
4.6 Contour graphs of the $\log_{10}$ of the slice gamma-ray efficiency $\eta_\gamma^{\rm slice}$ (%) vs. $\dot{P}$ and P, for different χ and ζ 170
4.7 Contour graphs of the $\log_{10}$ of integral flux above 100 MeV $\overline{F}^{\rm slice}(>100\,{\rm MeV})$ vs. $\dot{P}$ and P, for different χ and ζ 171
4.8 Contour graphs of the $\log_{10}$ of integral flux above 1 GeV $\overline{F}^{\rm slice}(>1\,{\rm GeV})$ vs. $\dot{P}$ and P, for different χ and ζ 172
4.9 Contour graphs of the $\log_{10}$ of integral flux above 10 GeV $\overline{F}^{\rm slice}(>10\,{\rm GeV})$ vs. $\dot{P}$ and P, for different χ and ζ 173
4.10 Contour graphs of the $\log_{10}$ of energy flux $U^{\rm slice}$ vs. $\dot{P}$ and P, for different χ and ζ . . 174
4.11 Contour graphs of the $\log_{10}$ of $\Lambda = \epsilon\overline{\Delta\Omega}^{\rm beam}/\beta^{\rm slice}$ vs. $\dot{P}$ and P, for different χ and ζ . 175

4.12 Contour graphs of the energy ratio $\tau = \overline{E}/E_0$ vs. $\dot{P}$ and P, for different χ and ζ . . . 176
4.13 Contour graphs of various pulsar quantities for the MSP with $\log_{10}(P) = -2.3$ and $\log_{10}(\dot{P}) = -21$ for different χ and ζ. 177
4.14 Contour graphs of various pulsar quantities for the MSP with $\log_{10}(P) = -2.2$ and $\log_{10}(\dot{P}) = -19$ for different χ and ζ. 178
4.15 Contour graphs of various pulsar quantities for the MSP with $\log_{10}(P) = -2.5$ and $\log_{10}(\dot{P}) = -19$ for different χ and ζ. 179
4.16 The $P\dot{P}$-diagram for 59 selected MSPs for which beaming correction factor calculations have been performed. 186
4.17 Graphs of scaled energy flux and $L_\gamma^{\rm beam}$ vs. $\dot{E}_{\rm rot}$ 189
4.18 Distribution of the $\log_{10}$ of the beaming correction factors interpolated for $\sim$ 300 000 random combinations of χ and ζ, as well as one actual realisation for 59 MSPs. 190
4.19 Distributions of integral flux and Λ for PSR J0437-4715; distribution of the $\log_{10}$ of the CR cut-off energy for the population of 59 MSPs 191
4.20 Distribution of the $\log_{10}$ of the integral fluxes interpolated for $\sim$ 300 000 random combinations of χ and ζ, as well as one actual realisation for 59 MSPs. 192
4.21 Graph of $L_\gamma^{\rm beam}$ vs. $0.75\kappa(1-\kappa)\dot{E}_{\rm rot}$. 193
4.22 Graph of $L_\gamma^{\rm beam}$ vs. $L_{\rm prim,max}(\chi)$. 194
4.23 Graph of $L_{\rm prim,max}(0)$ vs. $L_{\rm prim,max}(\chi)$. 195
4.24 Graph indicating the convergence of the mean and standard deviation of the average cumulative values of the $E_\gamma^2 dN_\gamma/dE$ spectrum for a population of MSPs in 47 Tucanae. 201
4.25 Average differential pulsed gamma-ray spectrum with 2σ-error bands for a population of MSPs in 47 Tucanae 203
4.26 *KAT* radio integration time for 2σ detection vs. $L_\gamma^{\rm beam}/d^2$. 207

5.1 Cumulative injection spectrum of relativistic particles originating in the magnetospheres of an ensemble of MSPs in 47 Tucanae 210
5.2 Radiation loss, escape, and effective timescales for radiation from 47 Tucanae 212
5.3 Predicted unpulsed high-energy spectra from 47 Tucanae 214
5.4 G0.9+0.1 best-fit parameter search 219
5.5 SED of G0.9+0.1 for best-fit parameters 222

6.1 Contour graphs of the parallel E-field $-E_{||}$ (with and without a ϑ-component) vs. ξ and ϕ, for different radial heights η above the PC 230

A.1 $\Gamma(1-p)$ vs. p 258

B.1 Electron source spectra for the MSP PSR J0437-4715 at the light cylinder for different source parameters 270

B.2 Propagated spectra at earth from the MSP PSR J0437-4715 272

B.3 Spindown power $L_{\rm sd}(t)$ of Geminga, assuming an initial period of 40 ms 275

B.4 Contribution of Geminga to the local (interstellar) cosmic ray electron spectrum for different diffusion coefficients 276

B.5 Contribution of Geminga to the local (interstellar) cosmic ray electron spectrum for different source distances 277

B.6 Contribution of Geminga to the local (interstellar) cosmic ray electron spectrum for different release times 278

B.7 Positron flux at earth 280

B.8 Expected cosmic ray positron spectra for different diffusion coefficients and birth periods of Geminga 282

B.9 Tolerable magnitude k_0 of the interstellar diffusion coefficient against the pulsar birth period P_0 for different model parameters 284

B.10 Contribution of Geminga to the positron LIS for different diffusion coefficients and birth periods; the expected local anisotropy due to Geminga 289

B.11 Contribution of B0656+14 to the positron LIS for different diffusion coefficients and birth periods; the expected local anisotropy due to B0656+14 291

List of Tables

3.1 Comparing different authors' converging results for peak CR energy $\epsilon_{\rm CR}^{\rm max}$ of PSR J0437-4715 for similar pulsar parameters and an unscreened electric field. 136

3.2 Estimating the gamma-ray luminosity from integral flux curves 144

3.3 Comparing different authors' converging results for peak CR energy $\epsilon_{\rm CR}^{\rm max}$ of PSR B1821-24, for similar pulsar parameters 149

4.1 Definitions of different combinations of (χ, ζ) as used in contour graphs 167

5.1 Values of parameters used for the PWN model of G0.9+0.1 220

5.2 'Best fit' parameters for G0.9+0.1 for individual and collective (multiwavelength) fits, as well as observed values. 221

6.1 Comparison of different expressions for the potential and charge density in PC models. 237

Chapter 1

Introduction

The field of Gamma-ray Astronomy is blossoming. Much has happened since the early days when the field was still in its infant stages. (Someone satirically referred to those days of humble beginnings as an era when there were "two gamma-ray sources and three gamma rays"). Today is an era of unparalleled scientific discovery and interest, a far cry from the few gamma rays observed during the first few decades. Gamma-ray Astronomy has now matured and has taken its place alongside Astronomy in the the other more traditional wavelength regimes of radio, optical, and X-rays as an indispensible harbinger of information at the very highest energies, and thus of the most violent and cataclysmic events known in the universe. No description and understanding of extreme astrophysical sources will be complete without the crucial insight provided by this discipline. This is evidenced by the fact that the prestigious Descartes Science Prize for transnational scientific teams has been awarded to the *High Energy Sterioscopic System (H.E.S.S.)* for opening up a new window on astronomy research by discovering gamma-ray sources at an unprecedented rate.

There is much anticipation and excitement regarding the most recent developments on the experimental side of things. *H.E.S.S.* (e.g. Hinton, 2004) is proving to be a major source of new and cutting-edge discoveries. *H.E.S.S. Phase II* is already under construction, promising even better sensitivity and resolution. This will be the precursor of the *Cherenkov Telescope Array (CTA)*, an envisioned network of gamma-ray Imaging Atmospheric Cherenkov Telescopes (IACTs) which will be the counterpart of the long-awaited *Square Kilometer Array (SKA)* of Radio Astronomy.

The successful *Energetic Gamma-Ray Experiment Telescope (EGRET)* era (e.g. Hartman et al., 1999) of investigation via a gamma-ray space telescope will be vastly improved upon with the launch of the *Gamma-Ray Large Area Space Telescope (GLAST)* in 2008 (e.g. Thompson, 2007). For example, it is expected that the current gamma-ray pulsar population of about 7 pulsars will be significantly

increased to a few hundred, which will provide much needed statistics for population studies (e.g. Ransom, 2007).

There is much to look forward to, and in the wake of all these recent developments, there is a larger impetus toward theoretical and numerical modelling of high-energy gamma-radiation. As computers keep improving, astrophysicists share in the advantages of increasingly greater computational capabilities. Locally, our department is fortunate to be responsible for one of the Flagship Programmes of the *Centre for High Performance Computing*, a National Facility in South Africa providing a cluster of 640 nodes for scientific computation. This is in addition to our valued participation in the *H.E.S.S.* Collaboration.

In this chapter, a broad overview of theory and observations that form the canvas on which the vivid picture of gamma-ray and cosmic-ray sources are painted will be given. As noted by this thesis' title, we consider four main and intertwined themes: millisecond pulsars (MSPs - Section 1.1.2), pulsar wind nebulae (PWN - Section 1.2), gamma rays (Section 1.3), and cosmic rays (Section 1.4). In what follows, each of these will be briefly discussed, before we reach Section 1.5 where we will motivate the work of the rest of the thesis, and give a thesis outline (Section 1.6). In Section 1.7, a list of publications emanating from contributions made by this work will be given.

1.1 Pulsar Physics

This section, which builds on earlier work (Venter, 2004), will form the main part of the present chapter and is intended as a broad overview of various aspects of the discipline of pulsar physics. This background will be necessary for interpreting the model predictions of single pulsars and populations of pulsars, to be presented in Chapters 3 and 4.

1.1.1 Historical Overview

A luminous 'guest star' was observed rising above the eastern horizon just before sunrise on 4 July 1 054 AD by the imperial astronomer to the Chinese court, Yang Wei-T'e. What we observe today as the Crab Nebula (NGC 1952) is the remains of the supernova explosion of 1 054 AD (see Figure 1.1). The debris of the explosion is still moving out at a speed of about 1 800 km/s after nearly one millennium. At a distance of 2 000 pc, this Nebula has a luminosity 75 000 times that of our sun. Relativistic electrons radiate synchrotron emission as they follow curved paths through the nebular magnetic field, causing the Nebula to glow with a characteristic blueish light. Philamentary structures can also be seen in the expanding remnant structure (Misner et al., 1973).

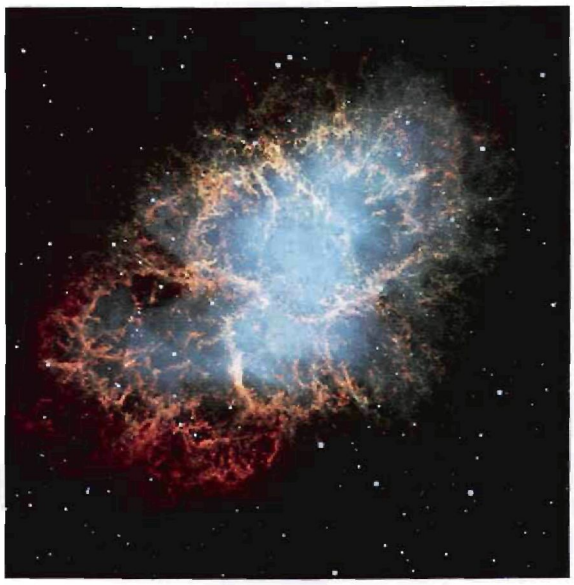

Figure 1.1: An optical image of the Crab Nebula showing expanding philamentary structures and diffuse synchrotron radiation (SR). This object represents the standard candle in Gamma-ray Astronomy. (The FORS Team, *VLT*, European Southern Observatory).

Another artefact of the explosion mentioned above is a neutron star (NS). Shortly after the discovery of the neutron by Chadwick in 1932, Landau was the first to speculate about the possible existence of such an astrophysical object. Using Fermi-Dirac statistics and basic quantum mechanics, he was able to derive an approximate stellar radius of 3×10^5 cm in the very same year (Becker & Pavlov, 2002, and references therein).

Baade & Zwicky (1934) were first to propose that supernovae represent the transition of an ordinary star into a body of considerably smaller mass – a 'neutron star' consisting mainly of neutrons. These stars represent one stellar-evolutionary endpoint and are created by the gravitational collapse of a sufficiently massive star in the absence of radiation pressure provided by thermonuclear reactions to balance the force of gravity. This occurs once the star's core is converted into iron by a long cycle of nuclear fusion reactions, after which no more thermonuclear reactions occur spontaneously, since fusion reactions involving iron absorb rather than release energy. Motivated by the notion of white dwarfs (another evolutionary endpoint) being supported against gravitational collapse by degenerate electron pressure, Baade & Zwicky proposed that NSs would similarly be supported by degenerate neutron pressure, as both electrons and neutrons obey Pauli's exclusion principle (Friedman & Kaufmann, III, 2002).

Oppenheimer & Volkoff (1939) constructed the first detailed models of NS structure using the equa-

tion of state (EOS) of a cold Fermi gas and general relativity (GR), and thereby laid the foundations of the general relativistic (GR) theory of stellar structure (Misner et al., 1973). They calculated that stars more massive than 3 $M_{\odot}$ would collapse into black holes (the so-called Oppenheimer-Volkoff limit for this last stellar-evolutionary terminus). Only when pulsars were actually discovered were these theories taken seriously.

Some years later Duyvendak (1942) and Mayall & Oort (1942) concluded that the Crab Nebula (see Figure 1.1) had to be the remnant of the supernova explosion recorded by the Chinese in 1 054 AD. They put forth arguments involving the estimated distance, position, maximum apparent and absolute magnitudes, rate of decline of naked-eye visibility of the star, as well as modern expansion measures of the Crab Nebula. Baade (1942) acknowledged this identification and added that the nova of 1 054 AD was a supernova of Type I. Minkowski (1942) agreed and suggested that the central star of the Crab Nebula could be the remnant of the exploded star of 1 054 AD.

In 1962 Rossi & Giacconi (whose pioneering contribution to astrophysics was recognised by being awarded the 2002 Physics Nobel Prize) serendipitously detected X-rays from Sco X-1, a source in the constellation Scorpius (Giacconi et al., 1962). Considering the minimum energy needed to penetrate the thin- and thick-window counters, it was estimated that the radiation had to be produced by electrons with energies of the order of tens of keV (or less likely, protons with energies of the order of one MeV). These X-rays were thought to be synchrotron radiation (SR) from cosmic electrons, i.e. it was attributed to a non-thermal process which accelerated the electrons to very high energies. Later on a source in the constellation Taurus coinciding with the Crab Supernova Remnant, Tau X-1, was detected (Bowyer et al., 1964), and among the many theoretical explanations for the origin of this X-radiation was the hypothesis of Chiu & Salpeter (1964) that it is thermal radiation from the surface of a hot NS (Becker & Pavlov, 2002). Since an NS was expected to appear as a point source, and the X-ray emission from the Crab Supernova Remnant had a finite angular size, the claim that an NS had been found was inhibited.

While a Cambridge research group was investigating interplanetary scintillation of compact radio sources, radio pulses arriving with a period of 1.3373011 seconds were observed (Hewish et al., 1968). This serendipitous discovery was made in 1967 by the graduate student Jocelyn Bell, for which the head of the research group, Anthony Hewish, later received the Physics Nobel Prize. The observed pulsations were so rapid and regular that they were at first supposed to have originated from an extraterrestrial civilization, and was hence code-named LGM1 meaning "Little Green Man 1". The LGM-hypothesis was soon abandoned after the discovery of three more pulsating sources at different locations in the sky. It was then concluded that a new natural phenomenon, later to be called *pulsars*,

had been discovered (Kanbach, 2001).

This discovery had a major influence on the international astronomical community, and in 1968 alone more than 100 papers regarding observations or theoretical interpretations of pulsars were published (Manchester & Taylor, 1977). Wheeler (1966) speculated that the energy source of the Crab Nebula could be a rotating NS with its magnetic field well coupled to the surrounding ion clouds, in contrast with earlier ideas of heat or vibrational energy of the NS as energy sources. Pacini (1967, 1968) also discussed conversion of rotational energy of an NS into magnetic-dipole radiation and ultimately into particle motions, his first paper predating the discovery of the first pulsar by the Cambridge group.

Gold (1968, 1969) proposed that pulsars might be rotating NSs spinning at the pulsation frequency, because no other theoretically known astronomical objects would possess the short and accurate periodicities as those observed. His suggestion was subsequently confirmed by observations. He also forwarded the view of a corotating magnetosphere and proposed that a rotation-powered pulsar spins down, since its rotational energy is radiated away by relativistic particles. Cocke et al. (1969) established a link between supernovae, NSs and pulsars with their discovery that the 'remnant star' identified by Baade and Minkowski in 1942 was in fact a pulsar. They observed strong optical pulses in addition to radio pulses (with a period of 33 ms) detected previously by Staelin & Reifenstein (1968). Within a year, X-ray (Fritz et al., 1969) and gamma-ray pulsations (Hillier et al., 1970) were also detected from this object. (Following the discovery of Cocke et al. (1969), Richards & Comella (1969) observed the slowing down of the pulsations from the Crab pulsar, confirming the pulsar's energy loss; also see Gaensler & Slane (2006)). Detection of high-energy radiation provides evidence for particle acceleration mechanisms leading to energy spectra, as opposed to single line detection. Today we can be certain that the Crab Pulsar is the energy source for the magnetic field, particle energy, as well as the accelerated expansion of the Nebula, with the total luminosity required more or less equal to the rotational luminosity of the Crab Pulsar (Lyne & Graham-Smith, 1990).

The first evidence for the gigantic magnetic fields of $\sim 10^{12}$ G expected for canonical pulsars came from spectral observation of Her X-1, a pulsating X-ray source in the constellation Hercules discovered by Tananbaum et al. (1972) using *Uhuru*. It was Trümper who first inferred a magnetic field strength of $B = 5.3 \times 10^{12}$ G from observations of a strong line feature at $\sim$ 58 keV in the pulsed X-ray spectrum of Her X-1, interpreting it as electron cyclotron emission at the basic frequency from the hot plasma of the rotating NS (Trümper et al., 1978). Currently, pulsars are broadly divided into high-B (canonical) and low-B (MSP) classes (Section 1.1.2), with typical B-fields of $\sim 10^{12}$ G and $\sim 10^{8}$ G. This distinction also corresponds to an age division, with the canonical pulsars being 'young', and the

MSPs 'old'.

The observations of Hillier et al. (1970) showed that the Crab Pulsar's high-energy power exceeded that in the optical waveband by more than two orders of magnitude. The need for more sensitive satellite-based X-ray and gamma-ray observatories were therefore highlighted (Becker & Pavlov, 2002). The launch of the satellite missions *SAS-II* and *COS-B* in the mid-seventies presented a major step forward for Galactic Gamma-ray Astronomy (Schönfelder, 2001). Many more important high-energy results regarding isolated NSs were obtained by the subsequent launching of *High Energy Astrophysical Observatories (HEAO 1, HEAO2 ("Einstein") & HEAO 3)* as well as the numerous other missions covering X-rays to gamma rays. Recently, the *Chandra X-ray Observatory* and *XMM-Newton (X-Ray Multi-Mirror Mission)* experiments also provided renewed theoretical interest in modelling pulsar magnetospheres (Rudak, Dyks & Bulik 2002), and prospects of the next generation of gamma-ray experiments, including *AGILE (Astro-rivelatore Gamma a Immagini LEggero)*, *GLAST*, and *H.E.S.S.-II* are all the more exciting (e.g. Baring, 2004). Some of these missions, and Gamma-ray Astronomy in general, are briefly discussed in Section 1.3.

1.1.2 Millisecond Pulsars

Although many different classes of pulsars are known, including (old, low-B) MSPs, (young, high-B) canonical pulsars, (very large B) magnetars, anomalous X-ray pulsars (AXPs), soft gamma-ray repeaters (SGR), and Rotating Radio Transients (RRats - McLaughlin et al. (2006)), the main focus of this thesis is on MSPs, and this section will therefore deal mainly with MSPs. See e.g. Becker & Pavlov (2002) for a review and references pertaining to the other classes of pulsars, and Lorimer (2005) for review of MSPs and binary pulsars.

Shortly after the discovery of the first radio pulsar, the 33 ms pulsar in the Crab Nebula (Staelin & Reifenstein, 1968) and the 89 ms pulsar in the Vela supernova remnant (SNR) (Large et al., 1968) were observed. These might be viewed as the first observations of a new class of pulsars. However, the term *millisecond pulsars* generally implies pulsars with periods less than $\sim$ 10 milliseconds (Carroll & Ostlie, 1996). The first 'real' MSP, PSR B1937+21, was observed in 1981 by Backer and colleagues with the Arecibo radio telescope (Backer et al., 1982). It has a period of 1.56 ms and a magnetic field $\sim 10^4$ times lower than the typical magnetic fields of young pulsars, which is of the order $\sim 10^{12}$ G. (The relatively weak magnetic field is characteristic of MSPs, and has implications regarding the nature of magnetospheric acceleration; see Sections 2.4, 3.6.1, and 3.7.1).

In the following decade, only three more MSPs with periods less than 20 ms were found in the Galactic disk, in contrast to the large number found in globular clusters (GCs). The latter class

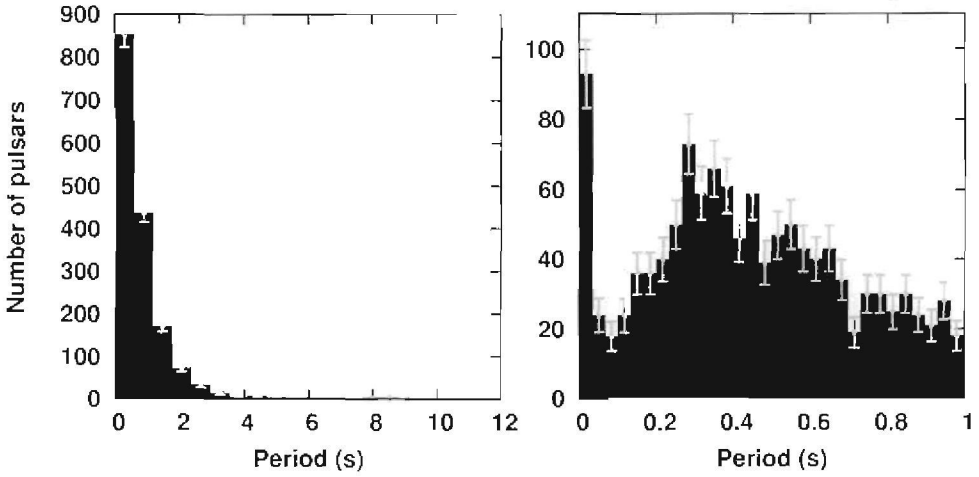

Figure 1.2: Pulsar histograms showing the number of pulsars for certain period ranges. In the right panel, a smaller bin size was used to illustrate the spread of low-period pulsars. Errors were estimated using the square root of the number of pulsars in each bin. Pulsar data with $\dot{P} > 0$ were obtained from `www.atnf.csiro.au/research/pulsar/psrcat` (Manchester et al., 2005).

of pulsars are not suitable for many precision timing applications including detection of gravitational waves, since the gravitational potential of the cluster stars causes large and time-varying perturbations of the pulse arrival times (Blandford et al., 1987). Therefore, the search was on for more MSPs in the Galactic disk, which were expected to be distributed more or less uniformly (Johnston & Bailes, 1991, see Chapter 3 for results involving the energy spectra and visibility of single MSPs). The discovery of PSR B1257+12 confirmed the existence of MSPs at high Galactic latitudes (Wolszczan, 1990; Manchester, 1995). On the other hand, a complete sample of MSPs in GCs may provide interesting possibilities for studies on the nature, formation, and evolution of MSPs. Grindlay et al. (2002) observed MSP samples in the GCs 47 Tuc (NGC 104) and NGC 6397, with the population of MSPs in 47 Tuc estimated to be $\sim 35 - 90$. They derived the X-ray luminosities, spin-down energies, and characteristic ages (Eq. [1.5]) for MSPs in 47 Tuc for the first time, using a common distance of $d = 4.5 \pm 0.3$ kpc. (In Section 4.5 we model the pulsed cumulative gamma-ray flux of a population of MSPs in 47 Tuc; refer to Camilo & Rasio (2005); Bogdanov et al. (2006a); Cameron et al. (2007); Ransom (2008) for more information on GC pulsars, and MSPs in 47 Tuc). Figure 1.3, from Ransom (2008), indicates the discovery of GC pulsars as function of time, with different instruments, as well as the number of pulsars located in various GCs.

Many other novel discoveries have been made, including (Manchester et al., 2001): the first binary pulsar PSR B1913+16 (Hulse & Taylor, 1974) which provided the first (indirect) observational evidence

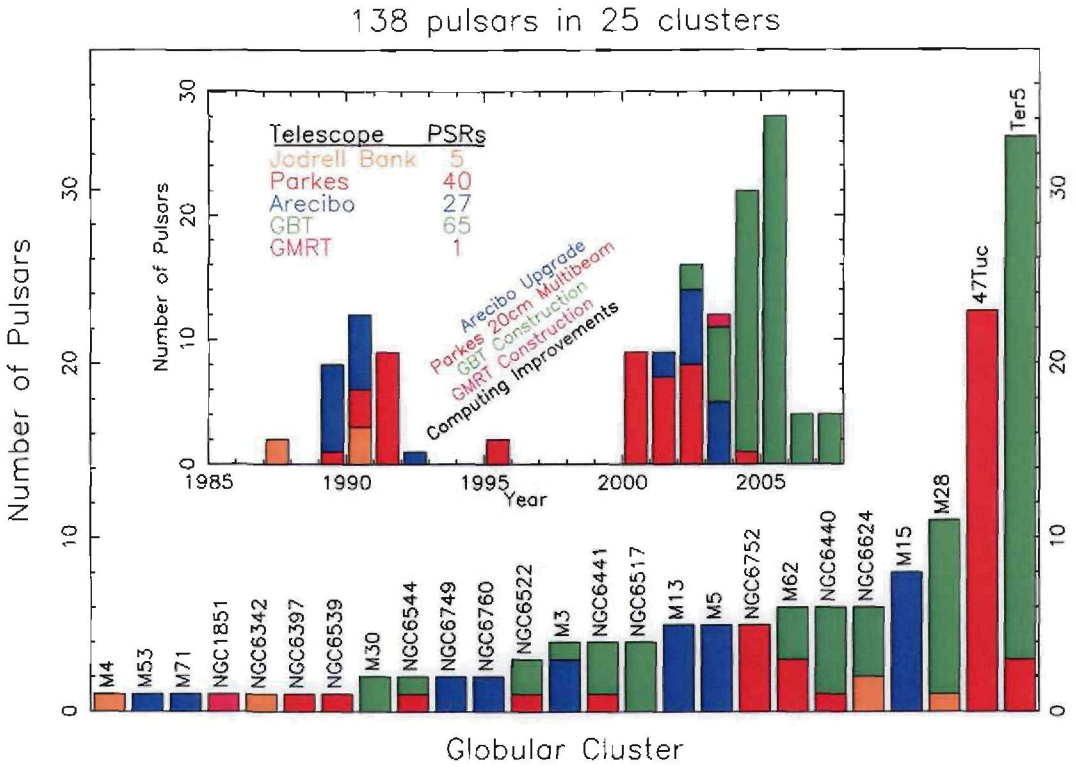

Figure 1.3: Discovery of GC pulsars as function of time, with different instruments, as well as the number of pulsars located in various GCs. Figure from Ransom (2008).

for gravitational waves, thereby confirming GR predictions (this resulted in the award of a Physics Nobel Prize to Taylor & Hulse; also see Taylor & Weisberg (1989)); the first star with planetary-mass companions (Wolszczan & Frail, 1992); the first pulsar with a massive stellar companion (Johnston et al., 1992); and the first eclipsing pulsar (Fruchter et al., 1988).

About 730 pulsars were known by mid-1997. During the *Parkes Southern Pulsar Survey*, 298 pulsars - 101 previously unknown - were detected, with 17 being newly discovered MSPs (Lyne et al., 1998). This includes the discovery of one of the nearest and brightest MSPs known, PSR J0437-4715, which has a period of 5.75 ms (Johnston et al., 1993). The *Parkes Multibeam Pulsar Survey* detected more than 600 new pulsars (Kramer et al., 2003). Currently, the Parkes Observatory's *ATNF Pulsar Catalogue* contains ~2 000 entries, ~ 150 of them being MSPs with periods $\leq$ 10 ms (`www.atnf.csiro.au/research/pulsar/psrcat`; Manchester et al. (2005), see Figure 1.2).

One of the most exciting discoveries of the last few years has been that of the double-pulsar system J0737-3039(A/B), a very compact double NS system consisting of two radio pulsars (Burgay et al., 2003; Lyne et al., 2004). Pulsar A has a period (P = 22.7 ms), magnetic field (6×10^9 G)

and characteristic rotational age ($\tau = 2.10 \times 10^8$ yr) of a typical MSP, while pulsar B has the basic properties of a relatively young, unrecycled pulsar ($P = 2.77$ s, $B = 2 \times 10^{12}$ G, and $\tau = 5 \times 10^7$ yr). The component masses are also accurately known ($M_A = 1.337 M_\odot$, and $M_B = 1.250 M_\odot$). This system is expected to merge in about 8.5×10^7 yr, a time much shorter than for any other known neutron-star binary (Burgay et al., 2003). Lyne et al. (2004) observed a short eclipse of J0737-3039A by J0737-3039B, as well as orbital modulation of J0737-3039B's flux density and pulse shape. This has been attributed to the influence of J0737-3039A's energy flux on J0737-3039B's magnetosphere, allowing the probing of magneto-ionic properties of a pulsar magnetosphere. The binary system has an orbital period of only 2.4 hours, and provides a unique laboratory for relativistic gravitational physics, enabling strong-field tests of GR by using the theory-independent mass ratio of the two member stars (Kramer et al., 2006b). The following post-Keplerian parameters have been measured (see e.g. Lyne (2006); Kramer (2008a) and references therein): relativistic periastron advance (rotation of the line connecting the two pulsars at closest approach), gravitational redshift and time dilation, Shapiro delay, and gravitational radiation and orbital decay (i.e. a decrease in the orbital period due to energy loss in the form of gravitational waves).

'Recycled pulsars' (i.e. MSPs and binary pulsars) are generally divided into two categories based on the likely mass of the companion of the pulsar in a binary system. High mass binary pulsars (HMBPs) have massive companions believed to be NSs with typical masses of ~ 1.4 $M_\odot$, whereas low mass binary pulsars (LMBPs) have low mass white dwarf companions (PSR J0437-4715 falls into this category). A third category may have to be introduced for dealing with intermediate mass binary pulsars (IMBPs) with white dwarf companions of masses > 0.7 $M_\odot$ (Kulkarni, 1995). About 80% of observed MSPs occur in binary systems with magnetic fields of $\sim 8 \times 10^7 - 3 \times 10^9$ G (Padmanabhan, 2001).

It is believed that MSPs are NSs in binary systems that were spun up by mass accretion from their companion stars (Alpar et al., 1982; Bhattacharya & van den Heuvel, 1991). After the pulsar enters the 'graveyard', moving below the so-called 'death line' on a $P\dot{P}$-diagram (as in Figure 1.6), where there is no more discharge in the magnetosphere (see Section 1.1.4), MSP companions evolve and become red giant stars. These giants continue to grow and at some stage they start transferring mass and angular momentum to their companion pulsar, and the pulsar is "born again". The mass transfer occurs via an accretion disk orbiting the NS, which delivers a torque to the pulsar, and an MSP is created (For a detailed discussion, see Kulkarni, 1995, and references therein).

The problem is that not all MSPs are part of binary systems. The case of the 'Black Widow' (PSR 1957+20) might provide a possible solution. This pulsar is seen to evaporate its companion, 'eating it

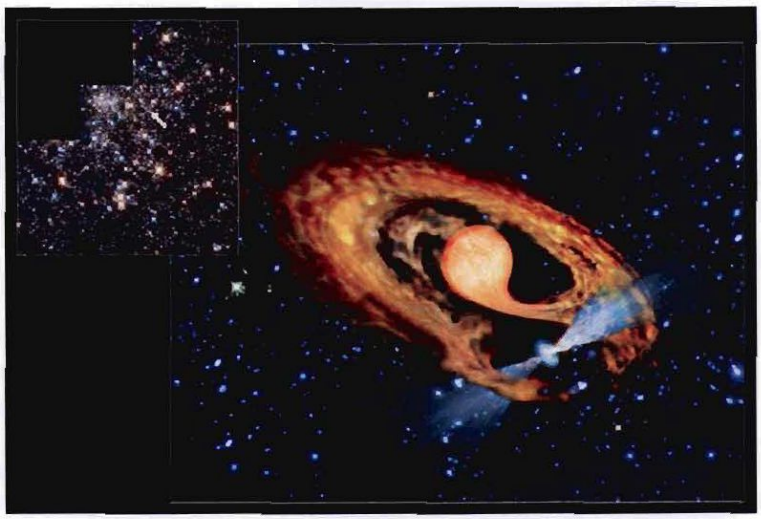

Figure 1.4: An artist's impression of an MSP / red giant binary system. The insert shows the *Hubble Space Telescope* image of the GC NGC 6397 (upper left) with a white arrow indicating the binary system's position. It is believed that the observation of this binary system might be the first experimental validation of the 'recycling' theory of MSP formation, where the pulsar is spun up by accreting mass from its red star companion (Ferraro et al., 2001).

up' as a black widow spider does with its prey (Fruchter et al., 1988). The hypothesis that all single MSPs developed from systems in which the companion was ablated is not popular anymore, since ablation rates seem too low to support such a scenario. Also, the origin of relatively low magnetic field strength for MSPs as inferred from Eq. (1.4) remains to be explained satisfactorily. Exciting new *Hubble* observations of the pulsar-companion system in the GC NGC 6397 revealed that the companion of the pulsar is not a white dwarf as was expected, but a red giant with a radius about 100 times larger than that of a white dwarf (Figure 1.4). This might provide the first experimental evidence supporting the 'recycling scenario' as an explanation for MSP formation (Ferraro et al., 2001; Ransom, 2008).

1.1.3 The Basic Pulsar Model

When radiation pressure due to thermonuclear processes in a star ceases (this occurs when a star's nuclear fuel is exhausted), core contraction accompanied by the release of gravitational binding energy and emission of neutrinos and gravitational waves occur. Depending on the collapsing mass, either a white dwarf, an NS, or a black hole will be formed. A 'hydrodynamic bounce' may occur as the core rebounds, and a shock wave will then propagate outward into the mantle, and may lead to a

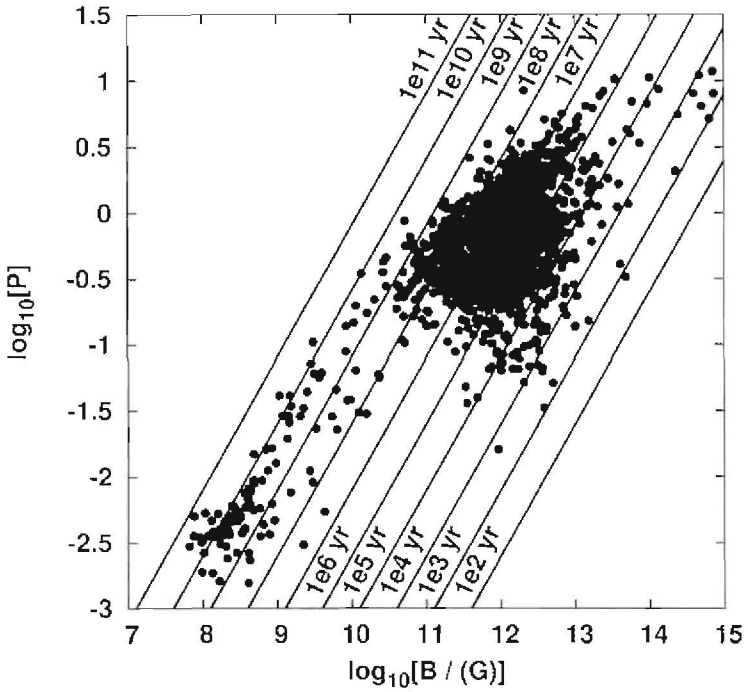

Figure 1.5: A PB-diagram showing the spread of pulsars according to their observed periods and derived magnetic fields (see Eq. [1.4]). Pulsar data with $\dot{P} > 0$ were obtained from `www.atnf.csiro.au/research/pulsar/psrcat` (Manchester et al., 2005).

spectacular supernova explosion (e.g. Bowers & Deeming, 1984; Tayler, 1994).

Nuclei in the stellar core with a central density of $\sim 10^{15}$ g cm^{-3} disintegrate into nucleons and electrons, and protons and electrons recombine via inverse beta-decay to form neutrons. The degenerate neutron gas can support cores of masses up to $\sim 3.6\ M_{\odot}$. For higher core masses, it is believed that a black hole will ensue (Kanbach, 2001).

If the stellar core rotates more or less rigidly, and angular momentum ($J \sim M_i R_i^2 \Omega_i$) is conserved during collapse, with M_i, R_i and Ω_i the initial mass, radius, and angular velocity, the final angular velocity will be

$$\Omega_f \sim \Omega_i \left(\frac{R_i}{R_f} \right)^2 . \tag{1.1}$$

For typical values of $R_i \sim 10^{11}$ cm and $R_f \sim 10^6$ cm, this represents an increase in angular velocity by a factor of $\sim 10^{10}$, yielding rotational periods in the range of milliseconds up to a few seconds. Since the stellar interior is fully conductive, magnetic flux ($\Phi_B \equiv \oint \mathbf{B} \cdot d\mathbf{a} \sim B_i R_i^2$) will also be conserved

during collapse, which implies that

$$B_f \sim B_i \left(\frac{R_i}{R_f}\right)^2. \tag{1.2}$$

This relation yields typical NS magnetic fields of $\sim 10^{12}$ G. Stellar core collapse therefore leads to a rapidly spinning, highly magnetised NS.

As rotational energy is converted into electromagnetic and particle energy, the NS will 'spin down', i.e. rotate slower. This is one of the key predictions of the rotation-powered pulsar model, and subsequent measurement of this slow-down was a dramatic confirmation of the basic idea. The NS may be modelled by a spinning spherical volume with a dipolar magnetic field. An estimate for the polar magnetic field strength may be obtained by equating the rate of slowing down and the dipole radiation loss (Ostriker & Gunn, 1969):

$$\dot{E}_{\rm rot} \equiv \frac{d}{dt}\left(\frac{1}{2}I\Omega^2\right) = I\Omega\dot{\Omega} = L_{\rm md} = -\frac{2}{3c^3}\mu^2 \sin^2\chi\,\Omega^4, \tag{1.3}$$

with $L_{\rm md}$ the dipole radiation loss, $I \sim MR^2$ the moment of inertia, $\mu \equiv B_0R^3/2$ the magnetic moment, B_0 the magnetic field strength at the pole, R the stellar radius, χ the angle between the magnetic and spin axes, and c the speed of light (see however Eq. [1.30]). Solving for B_0 by inserting typical values of $I = 10^{45}$ g cm^2, $R = 10^6$ cm, and $\chi \sim 90°$ gives (in Gaussian units)

$$B_0 \sim 6 \times 10^{19}\sqrt{P\dot{P}}, \tag{1.4}$$

with P the period in seconds and $\dot{P}$ its derivative in s s^{-1}. Estimates of the magnetic fields of pulsars are particularly important for determining whether or not pair production will take place (see the discussion of the Sturrock Model in Section 1.1.4 and the discussion of pair production in Section 2.4, 3.6.1, and 3.7.1).

The characteristic 'rotational age' τ can be derived by assuming that $\mu_\perp \equiv \mu \sin\chi$ stays constant, and noting that $\dot{\Omega} \propto -\Omega^3$ (Eq. [1.3]). By integrating and substituting $\Omega^2 = -\dot{\Omega}/w\Omega$, with w a constant, we arrive at

$$\tau = -\frac{\Omega}{2\dot{\Omega}}\left[1 - \left(\frac{\Omega}{\Omega_0}\right)^2\right] \approx -\frac{\Omega}{2\dot{\Omega}} \equiv \frac{P}{2\dot{P}} \tag{1.5}$$

when $\Omega_0 \gg \Omega$. It is customary to draw a $P\dot{P}$-diagram (Figure 1.6), which is the pulsar physics equivalent of an HR-diagram or periodic table. Alternatively, a PB-diagram is sometimes drawn (Figure 1.5). Two pulsar populations clearly emerge on these figures: the canonical population clustering in the centre, and the MSP population lying in the lower left corner.

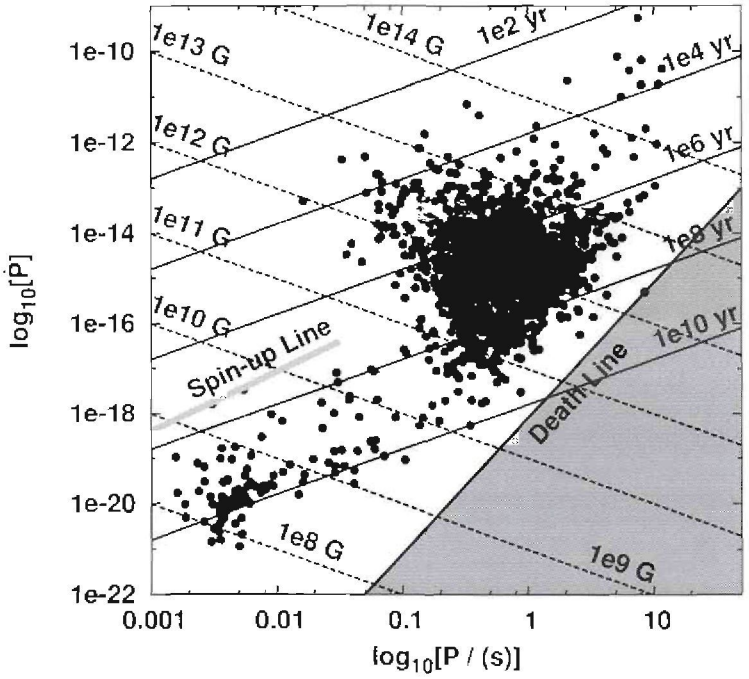

Figure 1.6: The $P\dot{P}$-diagram of pulsars in the *Parkes Observatory ATNF Pulsar Catalogue* with $\dot{P} > 0$ (Manchester et al., 2005), analogous to the HR-diagram in Astrophysics or the periodic table in Chemistry, indicating pulsar population properties and evolution. Lines of constant magnetic field (dashed) and characteristic rotational age (solid) as derived from Eq. (1.4) and Eq. (1.5) are shown. A theoretical death line $\dot{P} = 10^{-18}P^3$ on the border of the so-called 'graveyard area', as well as a spin-up line $\dot{P} = 4 \times 10^{-15}P^{4/3}$ are also shown (see discussion on the Sturrock Model in Section 1.1.4 for details). MSPs lie at the bottom left corner of the diagram, while canonical pulsars lie at the centre. The theoretical death line correspond to the condition that the potential is too low for pair creation and subsequent radio emission to occur, leading to the 'death' of canonical pulsars. These dead pulsars may be spun up, thereby entering the MSP-area, subject to the spin-up upper limit indicated by the spin-up line.

1.1.4 Polar Cap (PC) Models

(i) Aligned Rotator with a Dipolar Magnetic Field in Vacuum

Consider a rotating NS to be an almost perfectly conductive sphere, with a dipolar external magnetic field aligned with the spin axis (i.e. $\vec{\mu} \parallel \Omega$). (The general case of an oblique rotator in vacuum was solved by Deutsch (1955)). Also assume that there are no charges in the surrounding magnetosphere (Mészáros, 1992). Such a star forms a unipolar inductor because there exists a potential difference between points at different latitudes. Assume that the star is a uniformly magnetised sphere with internal magnetic field $\mathbf{B}_{\rm in} = B_0\vec{e}_z \parallel \vec{\mu}$. The non-relativistic (classical) components of the exterior

magnetic dipole field are (Padmanabhan, 2001)

$$B_{r,\mathrm{out}} = \frac{2\mu}{r^3}\cos\vartheta, \tag{1.6}$$

$$B_{\vartheta,\mathrm{out}} = \frac{\mu}{r^3}\sin\vartheta, \tag{1.7}$$

and $\mu = B_0 R^3/2$ as noted in Section 1.1.3. For a magnetic dipole field, the family of magnetic field lines is represented by the expression (see Figure 2.5)

$$r = k\sin^2\vartheta, \tag{1.8}$$

with k a constant labelling the individual field lines. Alignment of the spin and magnetic axes leads to a static external field. The stellar surface rotates with velocity $\mathbf{v} = \boldsymbol{\Omega} \times \mathbf{R}$, and the surface charges will be subjected to a Lorentz force $(q/c)(\mathbf{v} \times \mathbf{B}_{\mathrm{in}})$. Charge redistribution has to take place in order that electric fields, due to charge separation, counterbalance the magnetic forces and no permanent currents flow in the star ($\mathbf{E}_{\mathrm{in}} \cdot \mathbf{B}_{\mathrm{in}} = 0$ for a conductor). This implies that (see Eq. [1.18])

$$\mathbf{E}_{\mathrm{in}} = -\frac{\boldsymbol{\Omega} \times \mathbf{r} \times \mathbf{B}_{\mathrm{in}}}{c} = -\frac{\Omega B_0 r \sin\vartheta}{c}(\sin\vartheta\,\vec{e}_r + \cos\vartheta\,\vec{e}_\vartheta). \tag{1.9}$$

Since the interior electric field satisfies the condition $\nabla \times \mathbf{E}_{\mathrm{in}} = 0$, we can write

$$\mathbf{E}_{\mathrm{in}} = -\nabla\Phi_{\mathrm{in}}(r,\vartheta). \tag{1.10}$$

Upon integration we find

$$\Phi_{\mathrm{in}}(r,\vartheta) = \frac{\Omega B_0 r^2}{2c}\sin^2\vartheta + \Phi_0, \tag{1.11}$$

or in terms of a Legendre polynomial,

$$\Phi_{\mathrm{in}}(r,\vartheta) = -\left(\frac{\Omega B_0 r^2}{3c}\right)[P_2(\cos\vartheta) - 1] + \Phi_0, \tag{1.12}$$

with Φ_0 a constant.

The magnetic field lines are equipotentials since $\mathbf{E}_{\mathrm{in}} \cdot \mathbf{B}_{\mathrm{in}} = 0$. The external electric field can be solved using Laplace's equation $\nabla^2\Phi_{\mathrm{out}}(r,\vartheta) = 0$ based on the assumption of an empty exterior magnetosphere. Taking the general solution of this equation to be of the form

$$\Phi_{\mathrm{out}}(r,\vartheta) = \sum_{l=1}^{\infty}\frac{a_l}{r^{l+1}}P_l(\cos\vartheta) \tag{1.13}$$

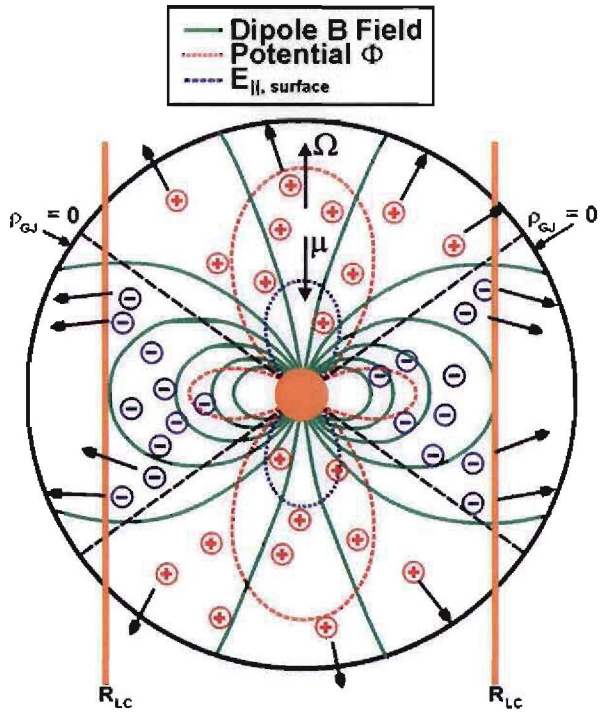

Figure 1.7: Magnetosphere of a rotator with antiparallel spin and magnetic axes. The dipole magnetic field, electric potential and electric field (parallel to the magnetic field) on the stellar surface are shown as indicated in the legend. The light cylinder is also shown. As discussed in Section 1.1.4, the magnetosphere cannot be empty, but must be filled with a charge-separated plasma. Plasma outflow may occur along open field lines crossing the light cylinder. The boundary shown indicates a value of zero for the corotation charge density (or the Goldreich-Julian charge density – see Eq. [1.19]). Adapted from (Kanbach, 2001).

and by requiring continuity for the electric potential at the stellar surface, one finds that the exterior electric potential is

$$\Phi_{\rm out} = -\frac{Q}{r^3}\left(3\cos^2\vartheta - 1\right), \tag{1.14}$$

with $Q \equiv B_0\Omega R^5/6c$ the quadrupole moment and the constant $\Phi_0 = -(\Omega B_0 R^2/3c)$. The corresponding electric field components are

$$E_{r,\rm out} = -\frac{9Q}{r^4}\left(\cos^2\vartheta - \frac{1}{3}\right), \tag{1.15}$$

$$E_{\vartheta,\rm out} = -\frac{6Q}{r^4}\cos\vartheta\sin\vartheta. \tag{1.16}$$

The component of $\mathbf{E}_{\rm out}$ parallel to $\mathbf{B}_{\rm out}$ just outside the pulsar is

$$\frac{\mathbf{E}_{\rm out}\cdot\mathbf{B}_{\rm out}}{|\mathbf{B}_{\rm out}|}\approx -\frac{\Omega R}{c}B_0\cos^3\vartheta\sim 2\times 10^8\,B_{12}P^{-1}\ \text{statvolt/cm}, \tag{1.17}$$

with $B_{12}\equiv B_0/10^{12}$ G. The electric force acting on the surface electrons and ions is thus orders of magnitude stronger than the gravitational binding force ($\sim 10^8$ times for a proton), so that the charges will be pulled out from the stellar surface to fill the surrounding magnetosphere. This shows that a rotating magnetic NS cannot be surrounded by vacuum; the magnetosphere must contain a plasma distribution (Goldreich & Julian, 1969).

Note that the parallel electric field has only one sign, implying that only charge of one sign may be pulled out from the surface. (The sign changes if the spin and magnetic axes are counteraligned; see the following section). This might lead to a non-sustainable charge flow, and ways will have to be found to 'complete the circuit', and therefore have a steady flow of current from the pulsar surface.

(ii) Rotating Pulsar Magnetosphere ('Standard Model')

Following Goldreich & Julian (1969), consider a rotating NS in a plasma-filled magnetosphere which is an excellent electrical conductor and neglect particle inertia. (In what follows, we will be considering exterior electric and magnetic fields and will consequently drop the subscripts). The rotating version of Ohm's law requires (see Eq. [1.9])

$$\mathbf{E}+\frac{\mathbf{\Omega}\times\mathbf{r}\times\mathbf{B}}{c}=0, \tag{1.18}$$

because the charges pulled out from the stellar surface redistribute themselves so that no Lorentz force acts on them, thus forming a corotating (force-free) magnetosphere. The magnetic field lines are very nearly electric equipotentials, so that charges may flow freely along them. This is equivalent to the condition $\mathbf{E}\cdot\mathbf{B}=0$. Solving Gauss' equation for this electric field yields the so-called Goldreich-Julian charge density

$$\rho_{\rm GJ}=\frac{\nabla\cdot\mathbf{E}}{4\pi}\approx -\frac{\mathbf{\Omega}\cdot\mathbf{B}}{2\pi c}. \tag{1.19}$$

This is the charge density of the corotating magnetosphere, and corresponds to an electron number density of

$$n_e\sim 7\times 10^{-2}\frac{B_z}{P}\ \text{cm}^{-3}, \tag{1.20}$$

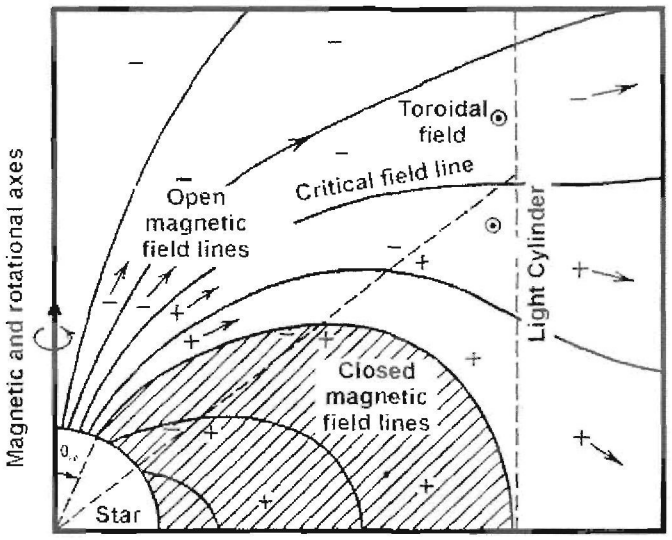

Figure 1.8: A pulsar magnetosphere according to Goldreich & Julian (1969). It is postulated that negative charges flow out near the pole and positive charges flow out near the PC angle, along open magnetic field lines. The critical field line represents the boundary between these two field line regions. (In the Sturrock Model, pair production may ensue in this open field line region – see following section). The dashed line indicates a zero value of the Goldreich-Julian charge density. (This surface plays an important role in the outer gap (OG) models - see Section 1.1.5). The shaded area represents the corotating magnetic field line region. Adapted from Lipunov (1992).

with B_z in Gauss. If the magnetic axis is reflected about a horizontal axis, the sign of the charge density will change. (Regions with $\mathbf{\Omega} \cdot \mathbf{B} > 0$ will have negative $\rho_{\rm GJ}$, and vice versa for regions with $\mathbf{\Omega} \cdot \mathbf{B} < 0$). The dashed line in Figure 1.8 represents the condition $\mathbf{\Omega} \cdot \mathbf{B} = 0$, i.e. zero charge density (see Section 1.1.5). The charges cannot corotate beyond the so-called light cylinder radius $R_{\rm LC}$, where the tangential velocity equals the speed of light:

$$R_{\rm LC} \equiv \frac{c}{\Omega} \approx 5 \times 10^9 P \text{ cm}. \tag{1.21}$$

Nearby the surface, the magnetic field lines corotate. Relativistic effects of retardation and plasma mass loading will distort the magnetosphere near $R_{\rm LC}$ significantly, so that field lines that would have closed beyond $R_{\rm LC}$ become open fields lines. Using Eq. (1.8) and noting that the last closed magnetic field line starts at a PC angle $\vartheta_{\rm PC}$ on the stellar surface and reaches the light cylinder at a polar angle

of $\pi/2$, we may conclude that the PC angle is given by

$$\vartheta_{\rm PC} = \sin^{-1}\left(\sqrt{\frac{\Omega R}{c}}\right) \sim \sqrt{\frac{\Omega R}{c}}. \tag{1.22}$$

The radius of the PC which contains the open field lines is

$$R_{\rm PC} \approx R\sin\vartheta_{\rm PC} \approx R\sqrt{\frac{\Omega R}{c}}. \tag{1.23}$$

The potential difference between the pole and $\vartheta_{\rm PC}$ is

$$-\Delta\Phi = \frac{1}{2}B_0 R\left(\frac{\Omega R}{c}\right)^2 \approx \frac{B_0 R\vartheta_{\rm PC}^4}{2} = \sqrt{\frac{3|L_{\rm md}|}{2c}}, \tag{1.24}$$

assuming $\chi = 90°$ when obtaining the last equality (see Eq. [1.3]). Charged particles escape from the pulsar magnetosphere along the open magnetic field lines as they "slide off" the B-lines due to rotation, which creates a toroidal magnetic field component (Figure 1.8). This escaping current creates a deviation from the Goldreich-Julian charge density, which in turn leads to the creation of an electric field component parallel to the magnetic field lines. (A similar mechanism operates when GR frame dragging is taken into account: the dragging of inertial frames leads to a deviation from the steady-state, corotation charge density, creating a parallel electric field which will try to restore the steady state; see Section 2.3.2). This parallel electric field will rip charges from the stellar surface and accelerate them along the magnetic field lines, thereby continuously replenishing the magnetosphere's charge density.

Since there cannot be a net outflow of charges, the potential at the base of the open field lines close to the spin axis is thought to be negative relative to the exterior, while it should be positive relative to the exterior near the PC angle. This would allow both positive and negative charges to be removed from the surface and to stream out along the magnetic field lines, preserving charge neutrality. The magnetic field line on which the surface and exterior potentials are equal is called the critical line. However, this hypothesis is merely an ad hoc addition to the theory. This 'return current' problem is not solved mathematically, as the problem of a single sign charge density, implying a single sign parallel electric field near the stellar surface, remains (see Eq. [1.19]).

Assuming that a Goldreich-Julian charge density is present and that charges flow out at the speed

of light, the number density of relativistic particles is (see Eq. [1.19] and Eq. [1.20])

$$n_c \sim \frac{\Omega B_0}{2\pi ce}. \tag{1.25}$$

The area of a PC is (see Figure 1.10)

$$A_{\rm PC} \sim \pi R_{\rm PC}^2 \sim \frac{\pi \Omega R^3}{c}. \tag{1.26}$$

Thus the primary particle flux from the pulsar is

$$\dot{N}_{\rm p} \sim 2cA_{\rm PC}n_c \sim \frac{B_0\Omega^2R^3}{ec} \sim 10^{30}B_{12}P^{-2}\ {\rm s}^{-1}. \tag{1.27}$$

The Goldreich-Julian PC current is therefore given by (assuming $\chi = 90°$, and using two PCs)

$$I_{\rm GJ} \approx 2\rho_{\rm GJ}cA = e\dot{N}_{\rm p} = \sqrt{6c|L_{\rm md}|}. \tag{1.28}$$

The particle luminosity then follows

$$L_{\rm prim} \sim -\Delta\Phi I_{\rm GJ} = 3|L_{\rm md}|. \tag{1.29}$$

Therefore, the particle luminosity has the same functional dependence on Ω as the dipolar loss term, i.e. $L_{\rm prim} \propto \Omega^{n+1}$, with $n = \Omega\ddot{\Omega}/\dot{\Omega}^2 = 3$ the braking index, and these terms are also of the same order, so that the observed spin-down of pulsars may thus be explained (Ostriker & Gunn, 1969; Manchester & Taylor, 1977). Note that the above is an approximate derivation. For a general inclination angle χ, we should write

$$\dot{E}_{\rm rot} = I\Omega\dot{\Omega} = L_{\rm prim} + L_{\rm md}, \tag{1.30}$$

so that the pulsar spins down due to both particle acceleration and radiation losses. Observations have furthermore shown that the braking index $n < 3$, confirming that part of the torque on the pulsar is due to outflow of particles (Lyne & Graham-Smith, 1990). (This deviation may even be an indication of multipolar magnetic field components being present in the pulsar magnetosphere).

Despite giving a successful description of a pulsar, this standard model suffers some problems, including:

- The return current problem (Where does the circuit which uses the potential difference close?);
- Charges of one sign are to flow through regions containing charges of the opposite sign;

- The parallel electric field which is responsible for pulling charges from the stellar surface equals zero for a magnetosphere with the Goldreich-Julian charge density, since $\mathbf{E} \cdot \mathbf{B} = 0$. One needs a deviation from the Goldreich-Julian charge density in order to create an accelerating electric field;

- The equilibrium charge density $\rho_{\rm GJ}$ cannot exist everywhere with particles streaming out at relativistic speeds (Michel, 1982);

- Inherent instability of this pulsar model (Thacker et al., 1998), implying that it may be a non-unique model solution (Smith et al., 2001).

However, the standard model is thought to provide a very good picture of a pulsar, one which is likely to be incorporated into more sophisticated models dealing with oblique rotators with self-consistent charged magnetospheres. Moreover, recent measurements by Kramer et al. (2006a) involving PSR B1931+24 might be interpreted as dramatic experimental confirmation of the magnitude of the Goldreich-Julian charge density. This pulsar was found to act as an ordinary radio pulsar during active phases, but abruptly switching off to become undetectable for about a month before switching on again. The pulsar's rotation furthermore slows down 50% faster during the 'on' stage as compared to the 'off' stage. These measurements have allowed the authors to estimate the magnetospheric currents in a pulsar magnetosphere for the first time, and they found a value for the charge density which corresponds to the predicted Goldreich-Julian value within a few percent.

(iii) Sturrock Model

Sturrock (1971) extended the standard model by considering particle outflow along the open field lines. Using $\rho_{\rm GJ} \sim (\Omega B_0/2\pi c) = (1/4\pi)\nabla^2\Phi \sim (1/4\pi)\Phi/h^2$, with h a typical acceleration height, and assuming $h \sim R_{\rm PC}$, we find

$$\Phi \sim \frac{2\Omega B_0}{c} h^2 \sim \frac{2\Omega^2 R^3 B_0}{c^2}. \tag{1.31}$$

The typical height is estimated as follows. Since particles are flowing out at relativistic speeds along the open magnetic field lines, there can be no steady state in this region. This implies that $\mathbf{E} \cdot \mathbf{B} \neq 0$ up to a certain height h above the stellar surface. At this typical height, the primary electrons will have gained sufficient energy from acceleration by the parallel electric field for pair production to occur (more details in next paragraph), and a 'pair formation front' will be created (see Section (v) on the Arons et al. model). This typical height may be taken more or less equal to the PC radius. Utilising the above estimates leads to a potential drop of $\Delta V \sim 3 \times 10^{13} B_{12} P^{-2}$ V. If this potential

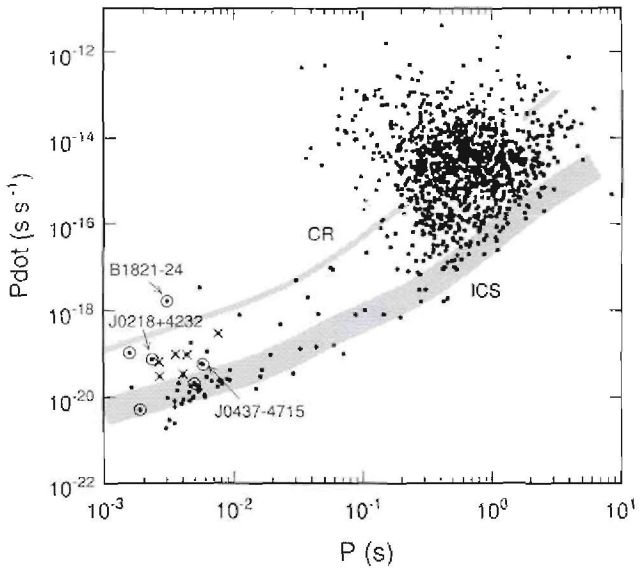

Figure 1.9: Numeric pair death lines for curvature radiation (CR) and inverse Compton scattering (ICS) for different EOSs (see text), for the fixed $\xi \equiv \vartheta/\vartheta_{PC}$ which indicates the normalised magnetic colatitude of the magnetic field line along which primary electrons are accelerated (Harding et al., 2002b). The width of the death lines indicates the uncertainties in surface temperature, mass, radius, and moment of inertia. This updated figure is from Harding et al. (2005b).

is available to accelerate particles, electrons will reach Lorentz factors of $\sim 10^7$ or larger. SR will dissipate perpendicular energy, but longitudinal energy due to acceleration will be lost via curvature radiation (CR) as the particles move along curved field lines (see Section 2.1.2). Estimating the typical curvature radius of the magnetic field lines, curvature photon energy, and magnetic field strength, one finds that the curvature photons will be subject to pair production (magnetic photon absorption) in young pulsars. This process will be discussed at some length in Section 2.1.4.

A condition for the occurrence of pair production is that the product of the magnetic field component perpendicular to the photon propagation direction and the photon energy has to be large enough. Sturrock envisaged that the secondary electron-positron pairs formed during pair production would also be accelerated and create gamma rays, which in turn may again form pairs, leading to a pair cascade.

Observed gamma rays will thus originate because of CR, while radio emission occurs due to bunching and coherent radiation from the electron-positron pairs. A pulsar will stop radiating when the potential difference $\Delta V \propto BP^{-2} \sim \dot{P}^{1/2}P^{-3/2}$ decreases due to spin-down to a level where pair creation is no longer possible. This corresponds to a theoretical death line $\dot{P} \propto P^3$, as indicated on

$P\dot{P}$-diagrams (e.g. Figure 1.6). Recently, numerical death lines were calculated by Harding et al. (2002b) for different models of the EOS, corresponding to a no PFF formation condition (see Figure 1.9). (A spin-up line of the form $\dot{P} \propto P^{4/3}$ is usually also indicated and represents a limit to the spin-up of MSPs corresponding to the Eddington limit accretion rate - Taylor & Stinebring (1986)). Some problems with this model include:

- Impossibility of charges to move at light speed everywhere, since charges have finite inertia (e.g. Michel, 1974);
- Existence of potential variations across the PC (an improvent of the 1D treatment by Sturrock) which will reduce the potential (Tademaru, 1974).

It is still assumed that equal amounts of positive and negative charges leave the stellar surface, as was the case with the standard model.

(iv) Ruderman-Sutherland Model

Ruderman & Sutherland (1975) investigated the loss of electrons from the surface while ions are retained because of their larger binding energy. They modelled an axisymmetric, counteraligned rotator. They deduced that formation of vacuum gaps would take place where positive charges would have been ejected (see Figure 1.10). Field lines in these regions wouldn't be forced to corotate, as $\mathbf{E} \cdot \mathbf{B} \neq 0$ in these vacuum gaps. More or less the same potential difference is available as in the Sturrock Model, with the gap height assumed $h \sim R_{\rm PC}$ or less. Electron-positron pairs are produced in the vacuum gaps when a spark discharge occurs as a result of a potential of $\Delta V \sim 10^{12}$ V. These pairs are accelerated by the parallel electric field, reaching sufficient energies to lead to a pair cascade themselves.

As the particles move beyond a height h, the parallel electric field vanishes and they stream outward. The plasma is more or less neutral, so that the charges of one sign don't have to move through regions of opposite sign anymore (as was the case in the standard model). This model depends heavily on the fact that the binding energy of (mainly Fe) ions exceeds the available potential. The gamma-ray radiation is again due to CR, but the radio radiation originates above the vacuum gaps where bunching by plasma instabilities will lead to coherent radio emission. The vacuum gap regions are expected to move around the PC, possibly explaining nomadic subpulses (Mészáros, 1992).

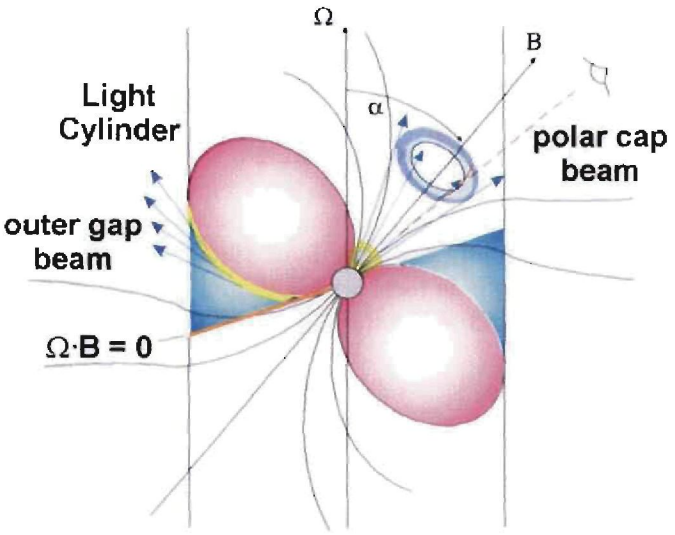

Figure 1.10: Schematic view of a non-aligned rotator with PC and OG regions indicated as discussed in the sections on the various pulsar models. These regions represent two possible locations where the observed radiation is believed to originate. Adapted from Kanbach (2001).

1.1.5 Outer Gap (OG) Models

Large outer magnetospheric gaps may develop (see Figure 1.10) with radiation originating in regions near the light cylinder (Cheng et al., 1986a,b). In this model an oblique rotator with charge density similar to the Goldreich-Julian charge density is considered. It is postulated that the return current flows through a neutral sheet defined by $\mathbf{\Omega} \cdot \mathbf{B} = 0$, and that negative charges on open field lines farther from the magnetic axis than the neutral surface will then flow past the light cylinder. The remaining region is net positive and will prevent further outflow of positive charges. By this mechanism a gap, with a potential drop similar to the one in the Sturrock Model (when effects of pair formation are ignored) is created. Since $\mathbf{E} \cdot \mathbf{B} \neq 0$ in the gaps, primary particle acceleration will occur. Gamma-ray emission from these particles will lead to formation of electron-positron pairs which will screen the electric field, ensuring that $\mathbf{E} \cdot \mathbf{B} = 0$ in regions other than the OGs. Secondary and tertiary radiation from the plasma-filled regions are required in order that primary pairs may be produced in the OG.

It is believed that the outer magnetosphere consists of three regions (see Figure 1.11). In the gap, region I, primary electrons and positrons are accelerated in opposite directions due to the non-vanishing parallel electric field. This acceleration is limited by CR losses or inverse Compton scattering (ICS) on infra-red (IR) photons present in the surrounding magnetosphere. Some gamma rays undergo pair production in the gap, but the majority spill over into region II where only a small parallel electric field

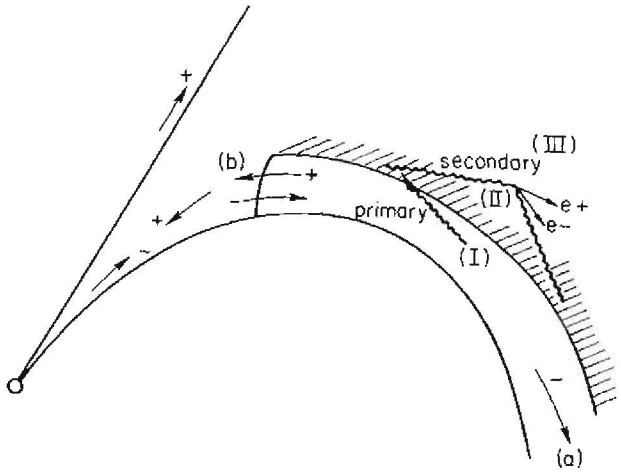

Figure 1.11: Structure of the OG showing region I (the OG where primary particle acceleration and pair production may occur), region II (where a small parallel electric field exists and secondary pair production as well as SR may occur) and region III (filled with tertiary electron-positron pairs responsible for softer radiation). From Cheng et al. (1986b).

is present. Secondary electron-positron pairs are created in this region, radiating secondary gamma rays and X-rays via SR. Tertiary electron-positron pairs may be created and will fill region III, which is quite distant from the gap. These pairs may be responsible for softer radiation. It is this radiation that produces gamma rays by the ICS-mechanism involving the primary pairs. This radiation also interacts with the primary gamma rays, producing pairs in region II. In this model, the secondary photons are largely responsible for the high-energy spectrum, since the primary spectrum is believed to be expended in the creation of particles. The gap energetics may be of the Crab or Vela type, subject to certain conditions (Ho, 1990).

Chiang & Romani (1992) computed lightcurves for various magnetosphere geometries, and constructed models for specific viewing angles. This work was followed by the paper of Chiang & Romani (1994) which represented an improvement of the basic OG model (Cheng et al., 1986a,b). Cheng et al. (2000) next studied the 3D structure of the OG and its local properties, and calculated phase-resolved gamma-ray pulsar spectra.

Hirotani and others reconsidered the traditional OG model and extended it to a non-vacuum situation, i.e. the case where the gaps are no longer vacuum (Hirotani & Shibata, 1999a,b,c, 2001a,b; Hirotani et al., 2003). This refinement led them to solve the set of Maxwell and Boltzmann equations for particles and gamma rays self-consistently. As a first step, they considered the 1D case, and concluded that external charged particle injection at nearly the Goldreich-Julian rate doesn't quench

the gap, but rather shifts its position. They also found that the particle energy distribution cannot be described by a power law, and that particles escaping from the gap contribute significantly to the gamma-ray luminosity for young pulsars (explaining the phase-averaged soft gamma-ray spectrum of the Vela pulsar observed by *EGRET*). The gamma-ray luminosity emitted by escaping particles was furthermore found to follow the relation $L_\gamma \sim \dot{E}_{\rm rot}^{1/2}$ naturally, and the authors foresaw the possibility of co-existence of PC and OG accelerators (also see Hirotani, 2005, for a brief review).

Zhang et al. (2004) reconsidered the OG gap size assuming a dipolar B-field, and obtained relations for the gamma-ray luminosity in terms of the spin-down luminosity. Dyks et al. (2004a) considered polarisation of pulsar radiation in the context of OG models, and compared their results with those of Romani & Yadigaroglu (1995) who used a 3D geometrical OG model. Dyks et al. (2004b) generalised these results by considering the impact of the Special Relativistic effects of aberration and light-travel time delay on high-energy lightcurves and polarisation characteristics in the context of PC, OG, and caustic models (see Section 1.1.7).

Takata et al. (2004) considered a trans-field structure when self-consistently calculating the E-field of an aligned rotator, showing that the critical value of the electron-positron charge density above which the electrodynamical solution disappears, is significantly enhanced in this case. Takata et al. (2006) next generalised the 1D calculations of Hirotani et al. (2003) and studied a 2D OG model, noting that the current through the gap as well as the magnetic inclination angle may be constrained in this case, as the gap width and thickness are linked with the gamma-ray flux and spectral cut-off energy. Hirotani (2007) obtained a new 2D solution, extending the work of Takata et al. (2004, 2006), and demonstrated that the created charge density may become super-Goldreich-Julian if the trans-field thickness of the gap is large enough. In the new solution, which extends from the NS surface to the outer magnetosphere (thus combining PC and OG accelerators), ions may be extracted from the stellar surface as space-charge-limited flow. Using a 3D particle simulation for a global, axisymmetric magnetosphere, Wada & Shibata (2007) showed that loss of particles from the system may form a relativistic wind of electron-positron plasma, maintaining the charge deficiency in the OG, and therefore pair creation, the mechanism by which new particles are supplied to maintain a steady state. Takata et al. (2008) lastly used a 2D OG model to study the particle acceleration and non-thermal radiation in the optical through gamma-ray bands via CR, SR, and ICS, from both outgoing and ingoing particles.

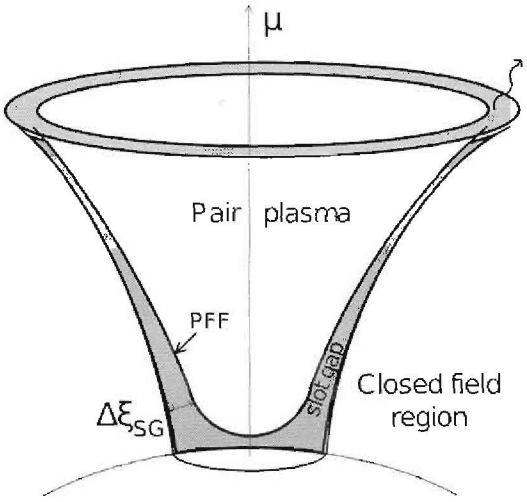

Figure 1.12: Structure of the 'slot gap', between the pair formation front (PFF) and last closed magnetic field line. From Harding & Muslimov (2005).

1.1.6 Slot Gap (SG) Models

In the context of young pulsars, where screening of the E-field occurs due to pair production, so-called SGs may develop (see Figure 1.12): pair-free regions of slower acceleration close to the last closed magnetic field lines, in which the parallel electric field is unscreened (Muslimov & Harding, 2004a). The origins of the SG model may be traced to the work of Arons and colleagues, who concentrated on oblique rotators with a charge density differing from the usual Goldreich-Julian charge density (Fawley et al., 1977; Scharlemann et al., 1978; Arons & Scharlemann, 1979; Arons, 1981, 1983). These authors expected auroral currents to flow along the boundary of the last closed field line surface, providing a possible solution to the return current problem. When considering an oblique rotator, the concepts of favourably vs. unfavourably curved field lines emerge. Near unfavourably bent lines (those bending away from the spin axis) space charge will build up and will eventually halt outflow. At the favourably curved field lines, a "starvation" electric field is created which is not shorted out. This field will accelerate particles which will radiate gamma rays via the CR mechanism and may lead to pair cascades. A pair formation front (PFF) will then be formed where the parallel electric field is shorted out by the electron-positron pairs. If the area near the side boundaries of the favourably curved tube is a good conductor with a small starvation parallel electric field, pair formation may not occur there and an SG may form: the height of the PFF is smallest in the middle of the flow tube, and increases as the edge of the flow tube is approached. Arons (1983) incorporated both electron and ion emission in his SG model, and found particle acceleration power of the order of a few tenths of a percent of the

spin-down power for short-period pulsars, but close to the spin-down power for long-period pulsars with complex surface magnetic fields. Further developments followed in Arons (1996), who did not consider the SG as a viable high-energy emission region (Muslimov & Harding, 2004a).

Muslimov & Harding (2003) revived the SG model in a GR context, and showed that although the E-field in the SG is boosted by the frame-dragging effect, it is reduced due to the SG geometry by a factor proportional to the square of the SG width. The frame-dragging effect furthermore operates over the entire PC, not just at favourably curved B-lines. This model provided the possibility of acceleration at smaller magnetic inclination angles, as well as a larger emission beam. Both these features are necessary in order to fit observed wide, double-peaked pulse profiles. The combination of a small solid angle and wide emission beam furthermore yields significantly larger predictions for the gamma-ray flux than in the case of PC models (Harding & Muslimov, 2005). Muslimov & Harding (2004a) extended the regime of SG acceleration to much higher altitudes by matching the high-altitude SG solution to that of Muslimov & Harding (2003), which was obtained for lower altitudes. Hirotani (2007) however pointed out that the assumption of Muslimov & Harding (2004a) that the sign of the plasma flowing in the gap consisted of only one sign, leads to an E-field which induces an electric current which in turn contradicts global current patterns, if the gap is close to the last open B-field line. Harding & Muslimov (2005) applied the GR SG model to unidentified *EGRET* sources, and found that many of the positional coincidences of radio pulsars with *EGRET* sources may plausibly be real, since the SG model reproduces the observed flux of many of these *EGRET* sources. Harding & Muslimov (2005) lastly discussed the probability of observing radio-quiet gamma-ray pulsars in the context of an SG pulsar model. A review of PC and SG models is given in Harding (2007a). Harding et al. (2008) recently applied a 3D model of optical through gamma-ray radiation from an SG accelerator to the Crab pulsar, and found reasonably good fits to the spectrum and pulse profiles.

1.1.7 Two-Pole Caustic Model

Dyks & Rudak (2003) presented a new model of high-energy lightcurves from rotation-powered pulsars. They noted that the PC model does predict the characteristic double-peak light curve (from a hollow-cone beam), but that long high-energy duty cycles and narrow opening angles for gamma-ray emission imply nearly aligned rotators (where $\chi \sim \vartheta_{\rm PC}$: Daugherty & Harding, 1994). On the other hand, the OG model prefers highly inclined rotators, and is unable to account for outer wings in the double-peak lightcurves, or a substantial level of the off-pulse emission in the Crab pulsar. The above considerations led Dyks & Rudak (2003) to consider a new model of where a gap region, satisfying the following, forms the essential ingredient (see Dyks et al., 2004b, for a comparison of the effects of aberration

and light-travel time delay on high-energy lightcurves and polarisation characteristics in the context of the two-pole caustic model, the OG model, and the PC model):

1. The gap region extends from each PC to the light cylinder;
2. The gap is thin and confined to the surface of last open magnetic-field lines;
3. Photon emissivity is uniform within the gap region.

The object of the caustic model is to find a geometric explanation (including relativistic effects) for lightcurves, rather than going into the details of the fundamental electric field and particle acceleration within the magnetosphere. By postulating an extended accelerator along the last closed field line (where the tangential high-energy emission is reminiscent of a *caustic* in optics: a curve to which light rays are tangent), a caustic nature of high-energy peaks result. The Special Relativistic effects of aberration and time-of-flight delays cause photons emitted at different altitudes to be piled up at the same phase of a pulse, producing prominent peaks.

The caustic model lightcurves are dominated by strong peaks (either double or single) of caustic origin, and the double peaks arise from a crossing of two caustics associated with different magnetic poles. Some generic features of the lightcurves emerge which are consistent with the observed characteristics of pulsar lightcurves:

1. The most natural (probable) shape consists of two peaks;
2. The peaks possess well-developed wings;
3. A bridge (interpeak) emission component is present;
4. There is a non-vanishing off-pulse emission level;
5. The radio pulse occurs before the leading high-energy peak.

1.1.8 Other Topics

The field of pulsar physics is broad and encompasses a host of subtopics. These include, amongst others, force-free relativistic MHD simulations (e.g. Spitkovsky, 2006), thermal emission from NSs (e.g. Zavlin, 2007), NS cooling and interior structure (e.g. Yakovlev et al., 2005), NS atmospheres (e.g. Zavlin & Pavlov, 2002), (strong-field) tests of GR using pulsars (e.g. Kramer, 2008b), glitches (e.g. Janssen & Stappers, 2006), etc. These topics will not be pursued any further.

1.2 Pulsar Wind Nebulae (PWN)

This section is aimed at giving a brief introduction to the topic of pulsar wind nebulae (PWN). It should therefore be seen as a prelude to Section 5.3 of Chapter 5, where we model the PWN G0.9+0.1. Following the single pulsar and population studies to be presented in Chapters 3 and 4, Section 5.3 will serve as another application of pulsar physics, but with a broader view: the acceleration and radiation of particles beyond the light cylinder will be considered. Other applications in Chapter 5 include studying cosmic rays originating in PWN.

1.2.1 Definition

PWN are pulsars displaying a prominent nebular emission (De Angelis et al., 2007). This happens when the particle wind from a fast moving isolated NS interacts with the surrounding interstellar medium (ISM) or surrounding SNR, and complex structures arise, where $0.001 - 0.1\%$ of the NS spin-down energy is converted into electromagnetic radiation (Caraveo, 2006). In order to differentiate PWN (Crab-like SNRs) from normal shell-type SNRs, the term "filled-centre" or "plerionic" nebulae (derived from the ancient Greek word *pleres*, meaning "full") was coined by Weiler & Panagia (1978). (The term "composite" is however reserved for PWN surrounded by a shell-like SNR – Gaensler & Slane (2006)). The original definition of "plerions" included sources characterised by the following properties (Weiler & Panagia, 1978; de Jager, 2005):

1. Filled centre or blob-like form, brightest in the centre, and decreasing in all directions toward the edges;
2. Flat radio spectrum, with the spectral index between -0.1 (later: 0) and -0.3;
3. Well organized internal magnetic field structure;
4. A high degree of linear polarisation at high radio frequencies.

As technological advances were made in the field of X-ray Astronomy, and sensitive instruments like *Chandra* and *XMM-Newton* made important contributions, the definition has been broadened by de Jager & Venter (2005); de Jager & Djannati-Ataï (2008) to include the following:

5. A jet / torus geometry in the vicinity of the pulsar, with the jet pointing in the same direction as the pulsar spin axis, and the torus showing an underluminous region inside a characteristic scale radius $r_s \sim 10^{17} - 10^{18}$ cm, believed to be the pulsar wind shock radius;

6. Evidence for reacceleration of particles somewhere between the pulsar light cylinder $R_{\rm LC}$ and r_s, responsible for a hard X-ray spectrum with a photon index $\sim 1.5 - 2.0$ near r_s;

7. Observed spectral steepening at $r > r_s$ (synchrotron cooling), with the size of the PWN decreasing with increasing energies, as observed for the Crab and several other PWN. The photon indices of the cooled spectra range between $2.0 - 2.5$.

Recent advances in the Gamma-ray Astronomy field (see Section 1.3) have allowed the observation of a population of evolved very high energy (VHE) gamma-ray emitting PWN for the first time (Aharonian et al., 2005a, 2006f; de Jager & Djannati-Ataï, 2008). PWN emitting VHE gamma rays with relatively high efficiency should generally have the following properties (de Jager & Venter, 2005; de Jager & Djannati-Ataï, 2008):

1. A particle-dominated wind, such that the overall (total) wind magnetisation parameter of the PWN $\sigma_{\rm tot} \ll 1$;

2. Rapid expansion of the PWN during its early phases of high power input from the pulsar, resulting in a low B-field in the PWN, and hence in the survival of the majority of VHE emitting electrons since early epochs. (This condition, together with the former, imply that synchrotron losses are much less important relative to IC losses);

3. Ideally, in addition to the previous two conditions, the lifetime of VHE radiating particles should be comparable to, or longer than, the age of the system. The particles will then survive the earlier epochs characterised by a stronger field, so that the total amount of energy in electrons in the PWN is a significant fraction of the maximal rotational kinetic energy of the NS at birth $(I\dot{\Omega}_0^2/2)$. In this case, adiabatic losses are the main source of losses, so that the VHE PWN-size is not expected to be energy-dependent.

4. A much larger birth spin-down power than present spin-down power $(I\Omega_0\dot{\Omega}_0 \gg I\Omega\dot{\Omega})$. This, together with the previous conditions, will result in the contribution of relic VHE-emitting electrons, stored in the reservoir since birth, to the present VHE gamma-ray flux. In this case the integrated spin-down power over a timescale into the past, which collects electrons from the epoch of a much higher spin-down power, is observed.

There are currently 9 firm identifications of galactic PWN at VHE energies (although there are more candidates): the Crab Nebula, plerions in the composite SNRs G0.9+0.1 and MSH 15-52, Vela X nebula, two new sources in the Kookaburra complex, the association of HESS J1825-137

with PSR B1823-13, G21.5-0.9, and Kes 75 (Gallant, 2007; Djannati-Atai et al., 2007; Gallant et al., 2008). Association of the VHE *H.E.S.S.* sources with PWN is usually supported by a combination of positional and morphological evidence, multi-wavelength observations, and plausible PWN model parameters. This means that PWN constitutes the most populated class of identified galactic VHE sources (De Angelis et al., 2007). The Crab Nebula is considered to be the most important prototype PWN (with no trace of an associated SNR – Slane (2008)), serving as a calibration source for hard X-rays to TeV gamma rays (de Jager & Venter, 2005). It was also the first source to be seen at TeV energies (Weekes et al., 1989, see Section 1.3.2).

1.2.2 Classification

PWN may be classified according to the external pressure which confines the NS wind. Young NSs form static PWN, as the surrounding supernova ejecta exert an effective confining pressure (see Chevalier (2004) for a list of probable young PWN, including their estimated ages). Older NSs escape from the faded SNR, move through the unperturbed ISM, and the wind is confined by ram pressure. This forms a bow-shock PWN (Caraveo, 2006; Gaensler & Slane, 2006; Gaensler, 2005). (As mentioned above, the term "composite" PWN is also sometimes used to describe PWN which are surrounded by shell-like SNRs – Gaensler & Slane (2006)).

For static PWN, axial symmetry, typically with tori and / or jet structure in many of these cases, is interpreted as an indication of the rotation axis of the central NS. Alignment between spin axis and space velocity is also assumed to be a standard property (Caraveo, 2006), and is now being found in a multitude of PWN (Slane, 2008). (Ng & Romani (2004) recently fitted 3D torus models to X-ray PWN and from this obtained orientations, shock scales, and postshock wind speeds). Interestingly, an astrophysical jet has been resolved in the gamma-ray waveband for the first time when the PWN of PSR 1509-58 (HESS J1514-591) was detected by *H.E.S.S.* (Aharonian et al., 2005b; de Jager, 2005).

Bow-shocks (which are typically fainter than static PWN), are frequently seen in H_α as arc-shaped structures tracing the forward shock, corresponding to sudden excitation of the neutral ISM. Otherwise, X-ray emission (and / or radio on larger scales) are observed, where a cometary shape, elongated behind the NS, is due to SR from the NS shocked downstream particles (Caraveo, 2006). The bow-shock nebulae are thus formed where pulsars with high space velocities move through the ISM at supersonic speeds. The number of this class of PWN is growing, especially due to high spatial resolution X-ray observations (Gaensler & Slane, 2006).

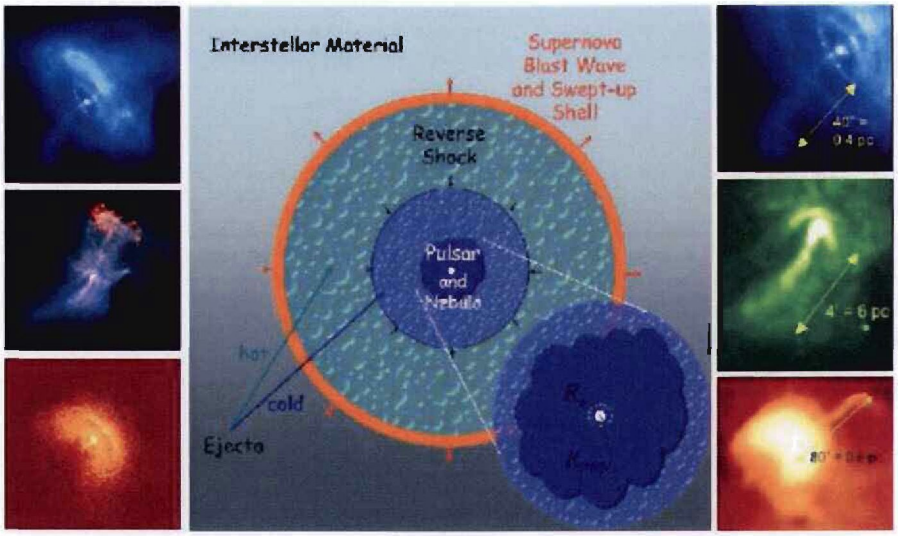

Figure 1.13: Schematic diagram of a PWN within an SNR. On the left are *Chandra* images of the Crab Nebula, PSR B1509-58, and Vela. On the right, the jets of these nebulae are shown (where north is up, and east is to the left). Figure taken from Slane (2008).

1.2.3 Theoretical interpretation

A very small part of the spin-down luminosity is usually seen in the pulsations from pulsars. It is assumed that most of the pulsar's rotational energy is converted into a relativistic wind, so that the PWN acts as an energy reservoir collecting the rotational energy lost by its embedded pulsar (Amato, 2003). (Typically only pulsars with $\dot{E}_{\rm rot} \gtrsim 4 \times 10^{36}$ ergs/s produce prominent PWN – Gotthelf (2004)). At some distance from the pulsar, a balance between the wind and confining pressures occurs, producing a shock at which relativistic wind particles are accelerated (and obtain randomised pitch angles). The latter particles radiate synchrotron emission, leading to a pulsar-powered nebula (Gaensler, 2001).

In Figure 1.13, the most basic picture of a PWN is illustrated (from Slane, 2008). The cold, highly relativistic stellar wind flows away from the NS in an inner zone with Lorentz factor $\Gamma \sim 10^6$. At a distance r_s, the wind passes through a termination shock, and flow is decelerated, while particle energies are boosted by another factor of $\geq 10^3$. The termination shock radius r_s may be estimated by equating the bulk wind pressure to the ambient pressure $P_{\rm amb}$ (Kargaltsev & Pavlov, 2008):

$$r_s \sim \left(\frac{\dot{E}_{\rm rot}}{4\pi c P_{\rm amb}} \right)^{1/2} . \tag{1.32}$$

Beyond the shock radius r_s, a bubble of relativistic, hot, magnetised fluid is created, where energetic electrons in the wind radiate non-thermally via synchrotron emission in the wound-up toroidal magnetic field, forming the PWN. The PWN is confined at a radius $r_{\rm PWN}$ by either the inertia of the supernova ejecta, or the pressure of the interior of a surrounding SNR (Slane, 2008). The structure of the PWN is therefore regulated by the input power from the pulsar, as well as the density of the ambient medium (Slane, 2005). The confining SNR may partly penetrate the outer bubble due to Rayleigh-Taylor instabilities, leading to filaments within the synchrotron nebula (Amato, 2003).

All pulsars are expected to be associated with PWN, as any active pulsar must posses a stellar wind (Kargaltsev & Pavlov, 2008). Detailed theoretical models, which incorporate particle injection and diffusion, magnetic field evolution, and radiative and adiabatic losses, have allowed successful predictions and interpretations of some basic PWN properties (see e.g. the seminal papers of Reynolds & Chevalier (1984); Kennel & Coroniti (1984) which followed the first attempts of Rees & Gunn (1974)). Recent advances in computational capability have allowed detailed studies of the interaction and evolution of a PWN-SNR system (e.g. Blondin et al., 2001; van der Swaluw et al., 2001; Bucciantini et al., 2003; van der Swaluw et al., 2004; Bucciantini, 2008a). Development of 3D time-dependent shock-capturing General Relativistic MHD (GRMHD) codes furthermore led to the possibility of testing theories about jet-torus structure of PWN (see e.g. Del Zanna et al., 2003, 2007) and modelling synchrotron emission from PWN (Del Zanna et al., 2006), in addition to the detailed modelling of many other astrophysical applications.

It is expected that the stellar wind must mainly consist of electron-positron pairs formed in the pulsar magnetosphere, as well as of a minor fraction of ions (protons or highly ionised iron nuclei) which may still be energetically dominant in the wind (Amato, 2003). Radio through X-ray radiation is believed to be synchrotron emission resulting from pulsar injected electrons. X-rays result from young (freshly injected) electrons, while radio emission come mainly from relic electrons (de Jager, 2005). High-energy X-rays are thus emitted by particles having short synchrotron lifetimes, compared to the much longer lifetimes of radio-producing particles. This means that a PWN should typically increase in size at lower frequencies, as observed for the Crab Nebula (Bucciantini, 2008b). The VHE emission of PWN is likely of leptonic origin. VHE spectra typically become steeper with increasing distance from the pulsar, supporting the interpretation that energetic electrons efficiently lose energy via SR, and age progressively rapidly as they move away from the acceleration site. VHE gamma rays are produced via ICS (De Angelis et al., 2007).

The total energy injected into the PWN is typically two orders of magnitude lower than the energy in the SNR. This means that the evolution of the SNR can have important implications for the PWN,

but not vice versa (unless the birth period P_0 is of the order of 1 ms – van der Swaluw & Wu (2001)). Three main phases of the evolution of a PWN inside an SNR can be identified (Chevalier, 2004; Gaensler & Slane, 2006; Bucciantini, 2008a):

1. In the free expansion phase, the supernova ejecta are in free expansion, and the PWN is expanding inside these cold ejecta. The spin-down energy is high in this case, and almost constant, so that the PWN should be easily observable (The Crab Nebula is thought to be in this phase currently).

2. The PWN next reaches the reverse shock in the SNR shell, and the SNR ejecta compress the PWN, so that its pressure increases, and it pushes back the inner edge of the SNR (a PWN may be displaced from its position over the pulsar, or even be crushed). This phase is called the reverberation phase.

3. The so-called 'Sedov-phase' represents a phase when the PWN expands adiabatically inside the heated SNR. It is believed that the PWN will only be observable as a faint, extended radio source during this stage. It is also expected to be an HE and VHE gamma-ray active phase (de Jager & Venter, 2005; de Jager, 2008).

One outstanding problem is the so-called sigma-paradox. The value of the ratio between the Poynting flux and kinetic energy flux in the unshocked pulsar wind ($\sigma \equiv B^2/4\pi\rho\Gamma c^2$, with Γ the wind Lorentz factor) is expected to be much greater than unity by current pulsar theories (typically $\sigma > 10^4$ – Amato (2003)). However, very low values of σ have been found by MHD modellers (e.g. $\sigma \lesssim 10^{-2}$) if flow and pressure boundary conditions are to be met at the outer edge of the PWN (Gaensler & Slane, 2006). The nature of the stellar wind must therefore change dramatically between the pulsar light cylinder and the termination shock, but it is not clear how such a transition occurs.

1.2.4 PWN as Probes

PWN can serve as powerful probes of a pulsar's interaction with its surroundings. In addition to possibly giving clues regarding the configuration of the NS magnetosphere and particle acceleration mechanisms therein, as well as the geometry, energetics, and composition of the particle wind, PWN may yield valuable information regarding the space velocity of the pulsar itself, as well as the density and ionisation state of the ambient medium (Gaensler, 2001; Caraveo, 2006).

Furthermore, an interesting class of offset PWN is also expected to be observed. Since most star formation is taking place in inhomogeneous molecular clouds, a reverse shock on the PWN from an

SNR expansion into an inhomogeneous ISM should lead to these asymmetric structures (de Jager, 2005). Such observations can also give more information regarding the composition and density of the ISM.

High-energy groups such as *H.E.S.S.* (de Jager & Djannati-Ataï, 2008), *VERITAS* (Konopelko, 2007), and *GLAST* (Funk, 2007) are expected to continue to actively observe PWN in the near future at gamma-ray energies, providing insight into the particle populations within PWN, in addition to the wealth of X-ray and radio data available which show signatures of the nebular magnetic field. Recently, de Jager (2008) has also shown how *GLAST* observations may lead to measurements of pulsar birth periods.

1.3 Gamma-Ray Astronomy

During this study, we will mainly be interested in high-energy radiation as harbingers of information from the acceleration sites of particles in pulsars and PWN. In contrast with cosmic rays (Section 1.4), these high-energy photons are not deflected by magnetic fields present in the space which lies between the source and detector, so that directional information is preserved. High-energy gamma-ray sources may thus be uniquely identified, and the morphology may be studied when these are resolved by the powerful new gamma-ray telescopes. Some basics of Gamma-Ray Astronomy are therefore briefly reviewed below.

1.3.1 Definition

About 0.1% to 1% of the total radiation classified as cosmic rays (see Section 1.4) consists of photons with energy higher than 1 MeV; for historical reasons these are called *gamma rays* (De Angelis et al., 2007). As gamma radiation represents the most energetic part of the electromagnetic spectrum, it therefore provides information about the most energetic processes and phenomena in the Universe (Schönfelder, 2001).

De Angelis et al. (2007) define the energy ranges associated with high energy (HE), very high energy (VHE), ultra high energy (UHE), and extremely high energy (EHE) gamma rays as follows:

HE	20 MeV	–	100 GeV
VHE	100 GeV	–	30 TeV
UHE	30 TeV	–	30 PeV
EHE	30 PeV	–	no limit.

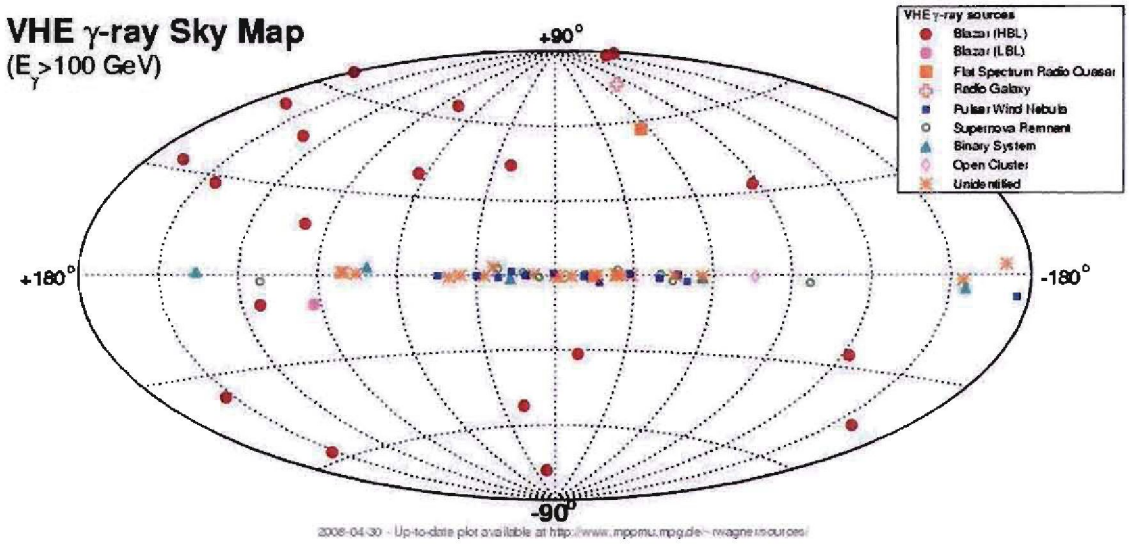

Figure 1.14: Skymap of VHE sources form the website maintained by R. Wagner (`http://www.mppmu.mpg.de/~rwagner/sources/`).

The above is somewhat arbitrary. Schönfelder (2001) notes that Gamma-ray Astronomy may be defined as extending from $\sim$ 500 keV to more than 1 TeV (i.e. more than six orders of magnitude in energy). This definition may be subdivided into Spaceborne Gamma-ray Astronomy, operating in the band $\sim$ 500 keV$-$100 GeV, as well as Ground-based Gamma-ray Astronomy, which operates at energies above $\sim$ 100 GeV (although the newest Cherenkov telescopes are hoping to push this threshold down to tens of GeV; see Section 1.3.4).

Many sources contribute to the (continuously changing) gamma-ray flux we detect on earth, including NSs, stellar and massive black holes, supernova explosions and remnants, quasars, gamma-ray bursts, and cosmic rays (via interaction with matter and fields) (Schönfelder, 2001). Over 70 VHE sources have been detected (Figure 1.14), in addition to the 271 sources detected by *EGRET* above 100 MeV, which include 5 pulsars, 1 solar flare, 66 high-confidence blazar identifications, 27 possible blazar identifications, 1 likely radio galaxy (Cen A), 1 normal galaxy (LMC), and 170 unidentified sources (Hartman et al., 1999).

1.3.2 Historical Overview

Early predictions in the 1950s raised hopes of detecting gamma rays from processes such as π^0-meson decay from cosmic-ray interstellar matter intercations, or cosmic-ray bremsstrahlung. However, early instruments suffered from limited statistics or systematic uncertainties, and many spurious detections

followed. The first reliable cosmic gamma-ray detections from space and from earth's atmosphere were made by *Explorer 11* and *OSO-III* in the 60s. In 1967, gamma-ray bursts were also first detected by the Vela satellites of the U.S. Department of Defense, which was only publisised in 1973 (see Schönfelder, 2001, and references therein).

The *Small Astronomy Satellite 1 (SAS-1)* launched in 1970 and later dubbed *'Uhuru'*, detected 339 new X-ray sources (Forman et al., 1978). The majority of the sources detected were accretion-powered pulsars, i.e. binary systems in which NSs accrete matter from the companion star. *SAS-2* was launched in 1972 and represented the first satellite devoted to Gamma-ray Astronomy (Fichtel et al., 1975) operating at an energy range of 35 MeV−1 GeV (Becker & Pavlov, 2002). This experiment followed pioneering satellite experiments such as *COSMOS-208, COSMOS-264, OSO-3*, and *OGO-5*, which were operated in the early seventies (see references in Fichtel et al., 1975). *SAS-2* detected gamma-ray pulses from the Crab (Kniffen et al., 1974) and Vela (Thompson et al., 1975) pulsars, as well as some unidentified gamma-ray sources, including Geminga, which was only identified some twenty years later (Halpern & Holt, 1992). The *COS-B* mission was the first to complete a detailed gamma-ray map of the Galaxy in 1975 (Mayer-Hasselwander et al., 1982), following the gamma-ray map of *SAS-2* by (Fichtel et al. (1975); see e.g. Kanbach (2002)). Using *COS-B*, Kanbach et al. (1980) found that Vela's spectrum could be represented by a power law $dN/dE \propto E^{-\Gamma}$ with $\Gamma = 1.89 \pm 0.06$ for the phase-averaged spectrum, providing clear evidence for the existence of non-thermal accelerating processes.

The X-ray *High Energy Astrophysical Observatories (HEAO 1, HEAO 2 ("Einstein")*, and *HEAO 3)* and *EXOSAT (European X-ray Observatory Satellite)*, launched in the late seventies / early eighties, studied the high-energy sky (Becker & Pavlov, 2002). Ground-based Gamma-ray Astronomy (using atmospheric Cherenkov imaging) was boosted in the late 80s after Hillas (1985) developed a technique to discriminate between gamma-ray initiated showers and proton-initiated showers, and a few TeV-sources have subsequently been established (Schönfelder, 2001). The first credible detection of a TeV source was that of the Crab Nebula (Weekes et al., 1989).

The French telescope *SIGMA* was launched in December 1989, and detected about 30 sources close to the Galactic Centre, most of them highly variable (Vargas et al., 1997). During the 90s, the higher sensitivity of *ROSAT (Röntgensatellit)*, a factor of ∼1 000 better than *Uhuru*, provided information on fluxes for all known radio pulsars, and also discovered pulsed emission from Geminga[1]. Its complementary instrument *ASCA (Advanced Satellite for Cosmology and Astrophysics)* made observations

[1] `http://heasarc.gsfc.nasa.gov`

in the harder X-ray band, and was the first satellite to use CCD detectors for X-ray Astronomy. *EUVE (Extreme Ultraviolet Explorer)* observed several NSs at very soft X-rays, whereas *BeppoSAX* and *RXTE (Rossi X-ray Timing Explorer)* also studied X-ray binaries (Becker & Pavlov, 2002), in addition to the observation of X-ray afterglows from a few gamma-ray burst sources by *BeppoSAX* (Schönfelder, 2001). The *Compton Gamma-Ray Observatory (CGRO)* studied the gamma-ray sky in the range 50 keV−30 GeV during 1991−2000 (Kniffen, 1990), while *EGRET* detected five new gamma-ray pulsars (Thompson, 2001), in addition to the well-known Crab and Vela pulsars. For more information, NASA's High Energy Astrophysics Science Archive Research Centre (HEASARC) website may be consulted (`http://heasarc.gsfc.nasa.gov/`). This website gives an overview of past and current observatories, including their capabilities, and main discoveries.

1.3.3 Observed Gamma-ray Pulsars

The largest fraction of energy loss from pulsars is converted into high-energy gamma rays, even though such a small number of them are detected relative to the number of radio pulsars (Caraveo, 2006). However, only seven identifications of gamma-ray pulsars based on *EGRET* data have been made: Crab, Vela, PSR B1706-44, PSR B1951+32, PSR B1055-52, PSR B1509-58 (seen only up to 10 MeV), and the radio-quiet Geminga (Thompson, 2001, see Figure 1.15). (One should also probably keep in mind that there is also the marginal detection of the MSP J0218+4232; see Kuiper et al. (2000)). The following general characteristics emerge (Kanbach, 2002):

1. The lightcurves are usually double-peaked with the pulsed emission covering more than 50% of the rotation (wide beam of emission);

2. The gamma-ray spectra are hard, with the luminosity typically achieving a maximum around 1 GeV (i.e. all the spectra show evidence of a high-energy turnover);

3. Different sites of emission are implied by the fact that the spectra vary with rotational phase;

4. The gamma-ray luminosity scales with the particle flux (Goldreich-Julian current $\sim \dot{E}_{\rm rot}^{1/2}$) from the open regions of the magnetosphere.

Unless a new pulsed component appears at higher energies, progress will therefore be the greatest in the $1 - 20$ GeV range, where important measurements of the spectral cut-offs may be obtained (Thompson, 2001, also see Section 1.3.5). If TeV gamma rays are detected from pulsars, OG pulsar models would be favoured over PC models, since pair creation which occurs in the latter class of

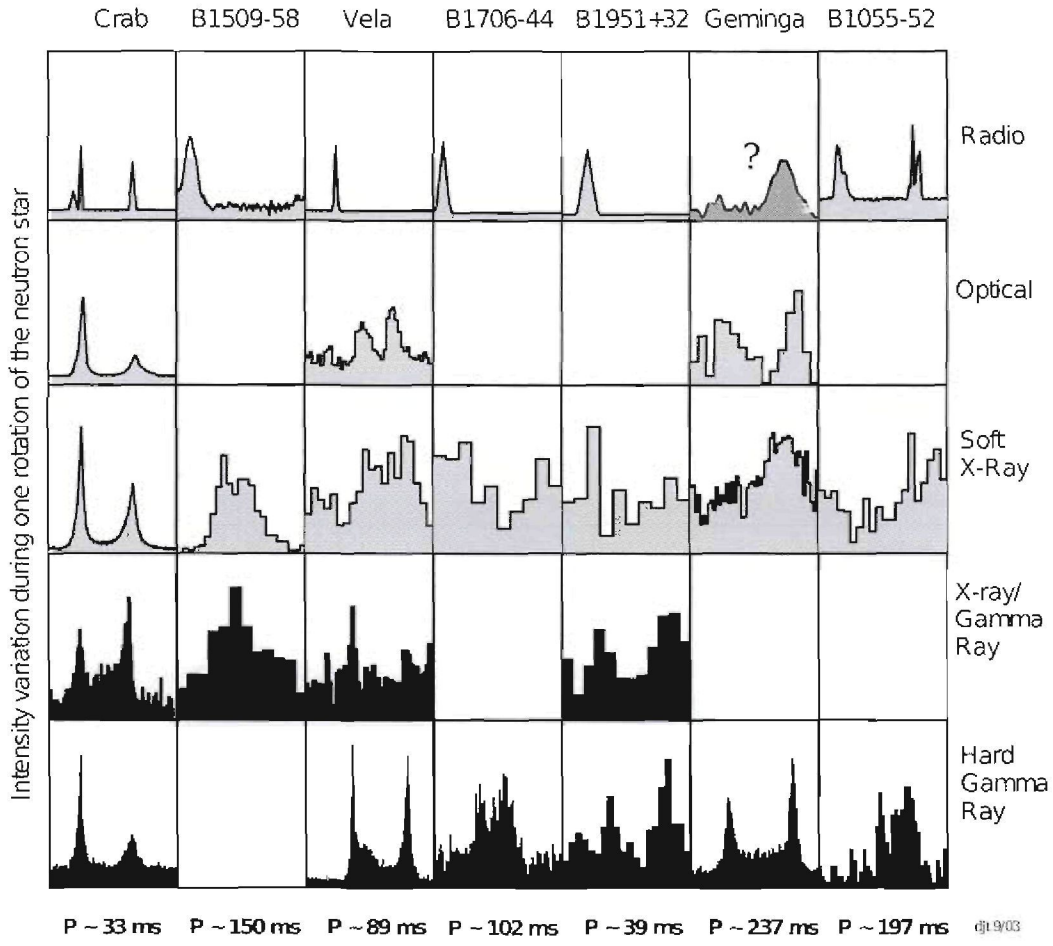

Figure 1.15: Lightcurves of seven gamma-ray pulsars, shown for the radio through hard gamma-ray bands. From Thompson (2004a).

models will attenuate this VHE emission (Catanese & Weekes, 1999). Interestingly, the efficiency of gamma-ray radiation increases for the older objects (Caraveo, 2006).

1.3.4 The *High Energy Stereoscopic System (H.E.S.S.)*

This section will give a brief introduction to *H.E.S.S. Phase I*. More information may be obtained at the official *H.E.S.S.* website (`http://www.mpi-hd.mpg.de/hfm/HESS/HESS.html`). Phase 2 will be mentioned in Section 1.3.6.

(i) Introduction

First ideas in 1995 of a *H.E.S.S.*-type experiment which would succeed previous generation experiments *Cherenkov Array at Themis (CAT)* and *High Energy Gamma Ray Astronomy (HEGRA)* were

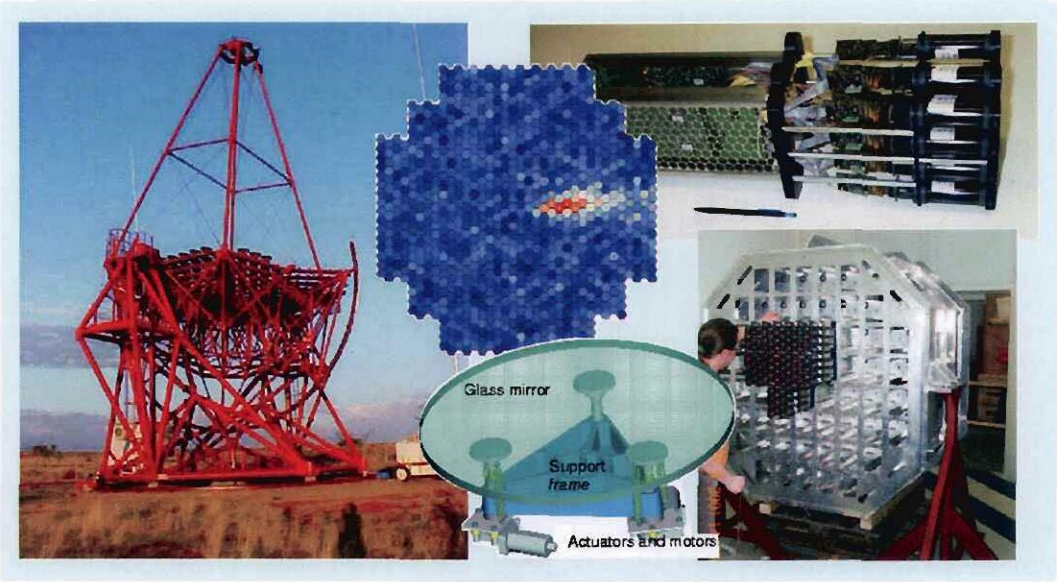

Figure 1.16: Montage of *H.E.S.S.* Telescopes and components, situated in Namibia (`http://www.mpi-hd.mpg.de/hfm/HESS/HESS.html`). Clockwise: One of the four *H.E.S.S.* Telescopes; image of an air shower as seen by a *H.E.S.S.* camera; a single camera drawer; camera body with some of the 960 drawers inserted; a *H.E.S.S.* mirror facet.

followed by an official Letter of Intent in 1997, which summarises the intention of constructing a large stereoscopic system of Imaging Atmospheric Cherenkov Telescopes (IACTs) for VHE gamma-ray Astronomy from the ground. The name *H.E.S.S. (High Energy Stereoscopic System)* captures the two main features of the telescopes, namely the simultaneous observation of air showers with several telescopes, and the combined use of individual telescopes to increase the effective gamma-ray detection area. The name was also chosen in honour of the Physics Nobel Prize laureate of 1936, Victor Hess, the discoverer of cosmic rays. The *H.E.S.S.* Telescopes are situated in the Khomas highlands of Namibia (23°16'18" S, 16°30'00" E, 1 800 m above sea level) known for its excellent optical quality (Hofmann, 2001). The Project went into operation in June 2002 (Hofmann, 2002) and the first phase consisting of four IACTs went into operation on 10 December 2003. *H.E.S.S.* was recently awarded the 2006 Descartes Science Prize for Research of the European Commission, as it has played an enormous role to revolutionise Astronomy at the very highest energies. This is evidenced by the huge number of VHE sources observed and discovered by *H.E.S.S.* The list[2] of exciting discoveries includes (Hofmann, 2005):

[2] `http://www.mpi-hd.mpg.de/hfm/HESS/HESS.html`

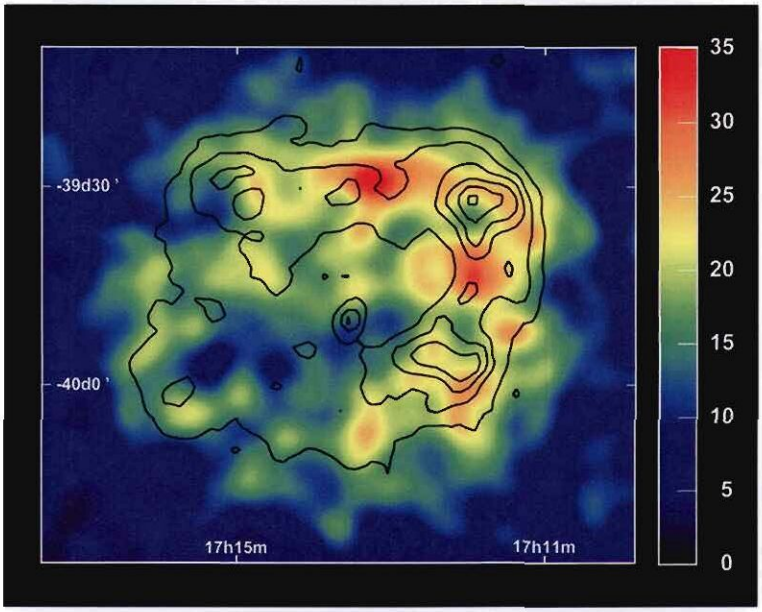

Figure 1.17: Gamma-ray image of the SNR RX J1713.7 – 3946 obtained with the *H.E.S.S.* Telescopes (Aharonian et al., 2004a).

- The first image of a supernova shell (SNR RX J1713.7-3946, see Figure 1.17) in TeV gamma rays, giving unequivocal proof that supernovae are capable of producing large quantities of galactic cosmic rays (Aharonian et al., 2004a);

- A sensitive survey of the Galactic plane revealing a new population of TeV gamma-ray sources, with typical sizes of the order of a tenth of a degree, some of which have no known radio or X-ray counterpart (so-called "dark" nucleonic cosmic-ray sources; Aharonian et al., 2005a, 2006f). A large fraction of these sources are believed to be PWN (see Section 1.2);

- The first evidence for gamma-ray emission > 100 GeV from a candidate microquasar, LS 5039 (de Naurois et al., 2005), and subsequently, the first observation of periodic VHE gamma-ray emission (orbital modulation) from this high mass X-ray binary (Aharonian et al., 2006a);

- Detection of the gamma-ray afterglow from Galactic Centre gas clouds (the emission, due to cosmic-ray interaction with interstellar gas, being correlated spatially with giant molecular clouds in the central 200 parsecs of the Milky Way), indicative a of pre-historic particle accelerator (e.g. a single supernova explosion around 10^4 years ago) (Aharonian et al., 2006c; Buesching et al., 2007b);

- Observations of the Galactic Centre Region in VHE gamma rays (Hinton et al., 2005);

- Measurements of two distant blazars (H 2356 – 309 and 1ES 1101 – 232), revealing that intergalactic space is more transparent to gamma rays than previously thought, since the newly derived upper limit on the diffuse extragalactic background light (EBL) at optical / near infrared wavelengths is very close to the lower limit given by the integrated light of resolved galaxies (Aharonian et al., 2006b);

- The discovery of drastic variations (on timescales of days) of VHE gamma rays from the central engine of the radio galaxy M87, implying a very compact emission region with a dimension similar to the Schwarzschild radius of the central black hole (Aharonian et al., 2006e);

- Detection of VHE gamma-ray emission towards the young stellar cluster Westerlund 2 (Reimer et al., 2007).

(ii) Physics Goals and Performance

The goals for the *H.E.S.S.* Experiment include (Hofmann, 1997, 1999):

- To study non-thermal phenomena in the Universe comprehensively;

- To provide high sensitivity in the TeV regime with an energy threshold of about 100 GeV;

- To lower the minimal detectable flux to a level better than 10^{-12} photons/cm^2/s, thereby improving the sensitivity by an order of magnitude compared to the *HEGRA* System that operated on the Canary Island of La Palma (Daum, 2001), a precursor of the *H.E.S.S.* Telescope;

- To study the shape of extended sources;

- To measure energy spectra and cut-off energies;

- To provide sensitivity for distant extragalactic sources.

A single *H.E.S.S.* Telescope would not be a significant improvement over an experiment such as *Whipple IACT* (precursor of *VERITAS*). The stereoscopic observation technique however allows enhanced background rejection, unique determination of the shower direction, and accurate measurement of the energy of a gamma-ray shower. The *EGRET* detector aboard *CGRO* (follow-up of the earlier *SAS-2* and *COS-B* satellites) was effectively used to study energy ranges of $\sim$ 100 MeV$-$10 GeV. The relatively small effective area and low flux of gamma rays limit the energy range of space missions such as *EGRET* and *GLAST*. *H.E.S.S.* therefore fills the gap in the energy range $>$ 100 GeV, as

ground-based detectors have a much larger effective detection area, which compensates for the larger background encountered by them.

H.E.S.S. is characterised by a low energy threshold (the energy of peak detection rate for typical source spectra) of about 100 GeV near zenith, increasing with zenith angle to 250 GeV at 45° and 700 GeV at 60°(Hinton, 2004; Hofmann, 2005). In addition, the System has a 1% Crab flux sensitivity, which results from the good angular resolution and background rejection obtained by the stereoscopic technique (Hinton, 2004). An angular resolution of 0.1° is provided for individual gamma rays, while gamma-ray sources can typically be located with a precision of 1′ or better, limited for intense sources by systematic errors at the 20″ level. This means that the sensitivity of *H.E.S.S.* is about one order of magnitude better than previous instruments, allowing the detection of sources with a flux of 1% of the Crab Nebula in 25 hours (Hofmann, 2005).

(iii) Some Technical Details of *H.E.S.S. Phase I*

In Phase I, four identical telescopes were placed on the corners of a 120 m × 120 m square region. Each has a steel mount and dish weighing about 60 tonnes. The camera is placed at a focal length of 15 m and is supported by four masts connected to the four corners of the dish. The dish has an altitude-azimuth mount which rotates on a 15 m diameter circular rail. The 4 kW drive motors accelerate the telescope to its peak slewing speed of 100°/min in less than 1 s. Encoders on both axes provide 10″ digital resolution, which is improved by another factor of 2 or 3 by additional analogue encoder outputs (Hofmann, 2001, 2003).

The *H.E.S.S.* telescopes have a mirror area of about 100 m^2 per telescope. Each telescope's mirror is comprised of 380 round segments with diameters of 60 cm. These facets are made of ground glass which have been aluminised and quartz coated, and they have reflectivities of about 80%. They are arranged on a spherical surface following the Davis-Cotton design. Each facet may be moved using remote control and can be aligned with a precision of up to a few micrometres. The notion of using these facets was conceived because a single mirror would be very heavy and costly. Long-term scrutiny has shown that no significant degradation took place over the period of one year (Hofmann, 2001, 2003).

The cameras serve to record the short and faint light flashes generated by air showers. Their exposure time is about one million times shorter than modern digital cameras. They have a field of view of 5° owing to their large focal length and their pixel size of 0.16° (3 mrd) is well matched to the typical image sizes. Each camera is contained in a cylindrical box of 1.4 m diameter and 1 m depth which contains 960 photo-multiplyer tubes (PMTs) as well as all the electronics for signal

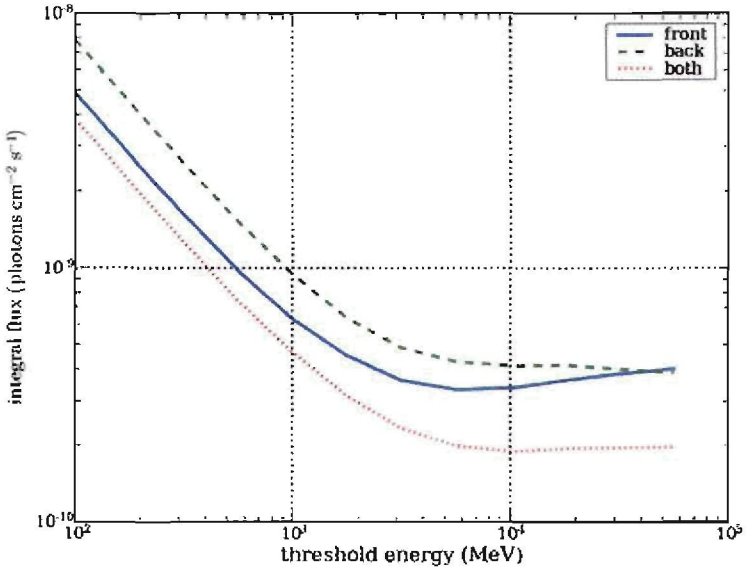

Figure 1.18: Integral sensitivity plot (5σ sensitivity for $E > E_0$) of *GLAST LAT*, assuming an E^{-2}-spectrum source at high latitude (From `http://www-glast.slac.stanford.edu`).

processing, triggering and digitisation, and weighs about 820 kg. In order to simplify construction and maintenance, the 960 PMTs were grouped into 60 drawers of 16 pixels each. Communication with the cameras is accomplished via optical fibres. The camera circuitry dissipates almost 5 kW of electrical power and nearly 100 fans provide adequate air flow inside the camera (Hofmann, 2001, 2003).

1.3.5 *GLAST LAT*

The *Gamma-ray Large Area Space Telescope (GLAST)*[3] is a space-based observatory (Smith, 2008) which has recently been launched (June 2008), and will operate for $5 - 10$ years in a low-earth orbit. Unlike its predecessor, the *Compton Gamma-ray Observatory (CGRO)*, *GLAST* will operate primarily as an all-sky monitor, continuously scanning the sky, instead of making pointed observations. It will carry two instruments: the *GLAST Burst Monitor (GBM)*, sensitive to photon energies between 8 keV and 25 MeV and optimised to detect gamma-ray bursts, and the *Large Area Telescope (LAT)*, sensitive to gamma rays between 20 MeV and 300 GeV and designed to survey the gamma-ray sky with unprecedented sensitivity (Carson, 2006; Ritz, 2007, also see Figure 1.18).

LAT will have a field of view of 2.4 sr, enabling it to observe 20% of the sky at any instant, and to

[3] *GLAST* has been renamed to *FERMI Gamma-ray Space Telescope* since the time of writing.

scan the entire sky once every three hours. The predicted one-year sensitivity is $F(E > 100 \text{ MeV}) > 3 \times 10^{-9}$ cm^{-2}s^{-1} for a point source with a differential photon spectrum proportional to E^{-2} observed at high latitude. The brightest point sources will be localised to $\sim 0.4'$ and the weakest sources to several arcminutes. The *LAT* will be much more sensitive than its predecessor, the *EGRET* instrument aboard *CGRO*; in one day, it will detect (at 5σ) the weakest sources that *EGRET* detected during the entire *CGRO* mission (1991 – 2000). The *LAT* is projected to detect thousands of gamma-ray sources over the lifetime of the *GLAST* mission (Carson, 2006; McEnery, 2006).

It is expected that *GLAST LAT* will bring insight to the whole range of high-energy gamma-ray phenomena (Thompson, 2004b), including bursts, AGN, pulsars, SNRs, diffuse emission, and unidentified sources (and new source classes Torres, 2007). Coordinated multiwavelength observations will prove invaluable to this campaign (e.g. Smith, 2008). The exciting possibility of combined studies of astrophysical sources by *GLAST* and existing ground-based VHE gamma-ray experiments such as *H.E.S.S.*, *VERITAS*, and *MAGIC* in the range 20 MeV−50 TeV is furthermore noted by Funk et al. (2007).

The *GLAST* mission objectives[4] are to

1. Explore the most extreme environments in the Universe, where nature harnesses energies far beyond anything possible on earth;
2. Search for signs of new laws of physics and what composes the mysterious Dark Matter (e.g. Atwood, 2006);
3. Explain how black holes accelerate immense jets of material to nearly light speed;
4. Help crack the mysteries of the stupendously powerful explosions known as gamma-ray bursts;
5. Answer long-standing questions across a broad range of topics, including solar flares, pulsars, and the origin of cosmic rays.

In the context of this study, it is interesting to note that *GLAST* will allow detailed investigation of SNR and PWN (Funk et al., 2006). According to estimates of de Jager (2008), ~ 50 PWN will be detected by *GLAST LAT* if the ratio of birth period to current period is < 0.5. Most importantly, however, is that *GLAST LAT* should detect tens to hundreds of new gamma-ray pulsars (although using a scanning instead of a pointing mode may impact negatively on this number – Ransom (2007)), and measure luminosities, lightcurves, and phase-resolved spectra with unprecedented resolution, in

[4] http://glast.gsfc.nasa.gov/

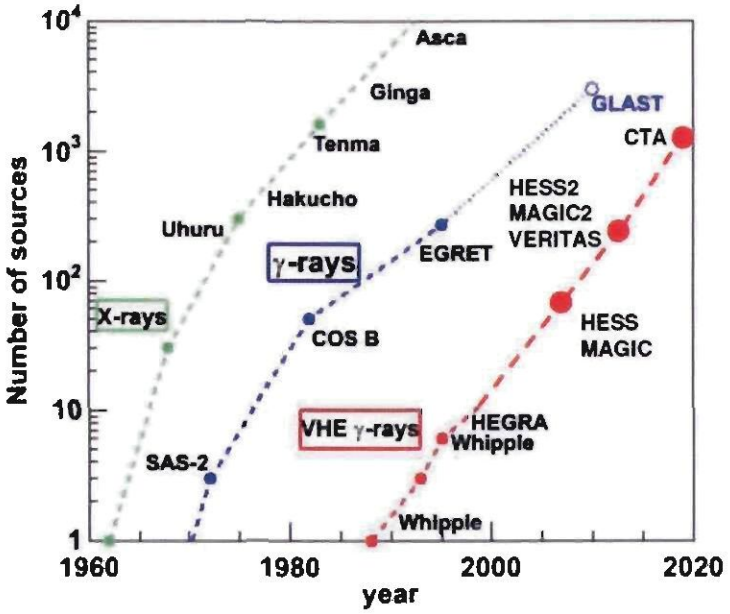

Figure 1.19: The "Kifune plot" shows how the amount of detected X-ray, gamma-ray, and VHE-gamma-ray sources varied and will vary with time from year 1960 to year 2020; the contribution from the different observatories is highlighted. Figure from De Angelis et al. (2007).

addition to possibly detecting radio-quiet pulsars like Geminga (Thompson, 2007). Hopefully, *GLAST LAT* will be able to measure spectral cut-offs well enough to distinguish PC from OG model shapes, thereby placing strong limits on the altitude of high-energy emission from pulsars. If sharp cut-offs are measured in a number of pulsar spectra, it will also be possible to test the predicted correlation between cut-off energy and surface field strength (Harding, 2007b).

1.3.6 Future Opportunities

Following the launch of the Italian satellite *AGILE* in April 2007, the *GLAST* satellite (with an effective area of about one order of magnitude larger than that of *AGILE*) is in orbit as of June 2008 (as mentioned in Section 1.3.5). These developments give ample motivation for ground-based telescopes to try and lower their energy threshold (e.g. Punch, 2005), so that concurrent observations may be performed in overlapping energy space. A second *MAGIC* Telescope, at a distance of 80 m from the first one, is expected to be inaugurated in September 2008 (*MAGIC II*), thereby substantially increasing the sensitivity and improving the angular resolution to about 0.07 degrees. The second phase of the *H.E.S.S.* Telescope, consisting of the addition of a single large telescope (with a diameter of 28 m) to the current four smaller telescopes, is expected to be inaugurated in 2009, making this the

largest Cherenkov telescope in the world, with an expected energy threshold of $\sim 20 - 50$ GeV (De Angelis et al., 2007, also see Punch (2005); Vincent (2005)). De Angelis et al. (2007) draw attention to the fact that space instruments beyond *GLAST* will probably be postponed for some 30 years due to the cost of space technology. This means that ground-based IACTs will therefore play an increasingly important role in the future. The most ambitious plans are to build an array of IACTs called the *Cherenkov Telescope Array (CTA)*[5] (construction will commence around 2012) which will be a factor of ten more sensitive than current experiments (Konopelko, 2005; Hermann et al., 2007). For full sky coverage, both a northern and southern hemisphere station are forseen.

Contributions from the different observatories in terms of discovering new sources are usually summarised in a "Kifune plot", which plots the amount of detected X-ray, gamma-ray, and VHE-gamma-ray sources as functions of time (see Figure 1.19). It is clear that the advent of the IACTs like *MAGIC* and *H.E.S.S.* increased the known VHE-gamma-ray source population by a factor of 10, and a factor of 10 improvement in the GeV range is expected for 2008–2010 from observations by *AGILE* and *GLAST*. A factor 2–3 improvement in the TeV range will be reached by *H.E.S.S.-II*, *MAGIC-II*, and *VERITAS*. Beyond TeV energies, the combination of *CTA* and the *High Altitude Water Cherenkov Experiment (HAWC)* will be required (De Angelis et al., 2007). See `http://heasarc.gsfc.nasa.gov/` for more information on future high-energy space missions. A list of all cosmic-ray, gamma-ray, neutrino, and similar experiments (ground-based, airborne, or underground) may be found at `http://www.mpi-hd.mpg.de/hfm/CosmicRay/CosmicRaySites.html`

1.4 Cosmic Rays

This is the last Section in the current chapter which has a background nature. Subsequent to our modelling of single pulsars (Chapter 3) and populations of pulsars (Chapter 4), we also investigate in which sense the underlying pulsar model may be constrained by considering the high-energy particles escaping from pulsars in the form of leptonic cosmic rays. Our results on this topic will be presented in Chapter 5.

1.4.1 Overview

The study of Cosmic-ray Astrophysics had its origins in the quest of understanding high-energy radiation (or rather particles) bombarding earth almost isotropically from outer space (Simpson, 2001). Nearly one century ago, two pioneering works by Hess in 1912 (who was awarded the Nobel Prize

[5] `http://www.mpi-hd.mpg.de/hfm/CTA/`

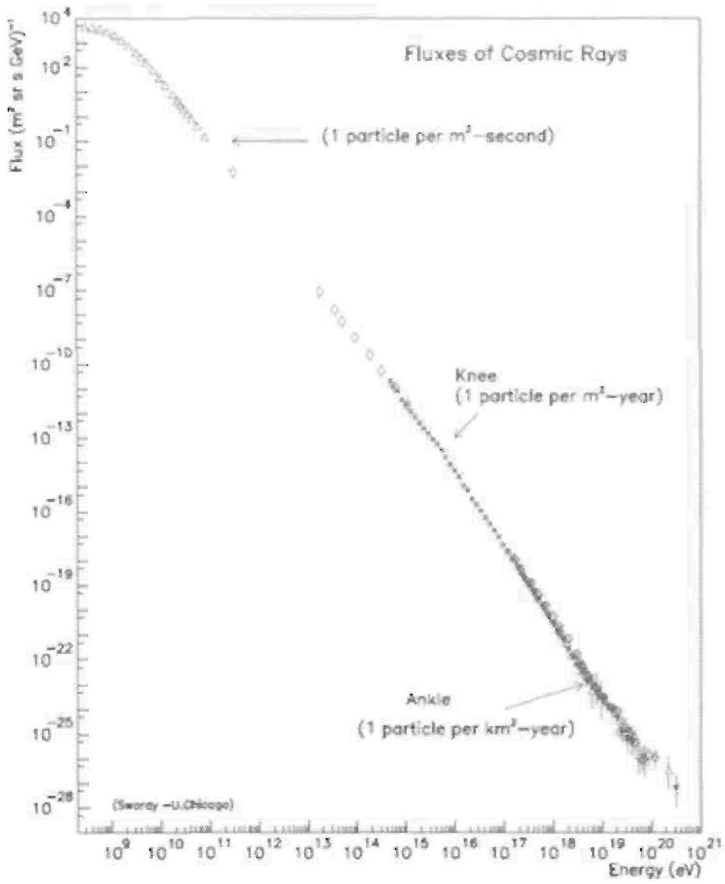

Figure 1.20: The spectrum of cosmic rays. From De Angelis et al. (2007).

for Physics in 1936), and Pacini, demonstrated that such particles are of extraterrestrial origin (De Angelis et al., 2007), as their intensity increases with altitude. These particles were subsequently called *cosmic rays* by Millikan in the mid-1920s. The question of whether cosmic rays were charged or not were settled by Clay and Compton by 1933, who showed that cosmic-ray intensities depend on geomagnetic latitude. Later work by Forbush in the late 1930s proved that the cosmic-ray intensity in the earth's atmosphere varied with time. Particle and high-energy physics, radiocarbon dating, and magnetic fields and plasmas of astrophysical origin are just some of the research fields which were born from cosmic-ray research, which nowadays falls under the topic of astroparticle physics (Simpson, 2001).

Since the energy of cosmic rays by far exceeds the temperatures of astronomical objects, they provide valuable information regarding the non-thermal part of the Universe. Excluding neutrinos, cosmic rays mainly consist of charged particles, such as protons (about 90%), helium nuclei (less than

10%), ionised heavier elements (less than 1%), and electrons (less than 1%), while only 0.1% to 1% of the total radiation consists of photons (gamma rays) with energy higher than 1 MeV (see Section 1.3.1; De Angelis et al., 2007).

The energy of cosmic rays covers more than 10 orders of magnitude, from tens of MeV to 10^{20} eV and higher. The dependence of the flux on the energy E of the particles can be approximated by a power law, with spectral index which varies between 2.5 and 3.5 (see Figure 1.20). Cosmic rays below the "knee" ($\sim 10^{15}$ eV) are believed to have a galactic origin, having been confined inside our Galaxy for at least 10^7 years. Particles above 10^{17} eV are believed to be mostly of extragalactic origin, possibly produced in violent outbursts in e.g. AGN, since the galactic magnetic field is not able to trap them in our Galaxy (Tayler, 1994; De Angelis et al., 2007). Infalling primary cosmic rays reaching earth undergo high-energy inelastic collisions in the upper atmosphere with atmospheric atoms and molecules, producing cascades of lighter (secondary) particles. The secondary particles are subject to further interaction, and may lead to a shower of particles. Pions and kaons are produced, which decay to produce muons. Muons make up more than half of the cosmic radiation at sea level, the remainder being mostly electrons, positrons, and photons from cascade events[6] (Schlickeiser, 2002).

From measurements, we may infer that (i) the solar wind disturbs the determination of particle fluxes below kinetic energies of $\sim$ 500 MeV/nucleon for nuclei, and below 5 GeV for electrons; this is referred to as solar modulation; (ii) the sun, and some of the planets, produce cosmic radiation, distinct from galactic and extragalactic components (Schlickeiser, 2002). Cosmic rays may therefore generally be categorised as follows (Langer, 2004):

1. Galactic cosmic rays, originating far outside the solar system, and being accelerated during supernova explosions;

2. Solar energetic particles originating from solar flares;

3. Anomalous cosmic rays consisting of interstellar neutral atoms which are singly ionised close to the sun.

4. Jovian electrons, released by Jupiter's magnetosphere.

The exact origin of cosmic rays is difficult to determine, as these charged particles are deflected by the Galactic magnetic field before reaching earth, and this has been a long-standing problem, now nearly 100 years old. SNRs have traditionally been suspected to be the accelerators of galactic cosmic

[6] http://hyperphysics.phy-astr.gsu.edu/hbase/hph.html

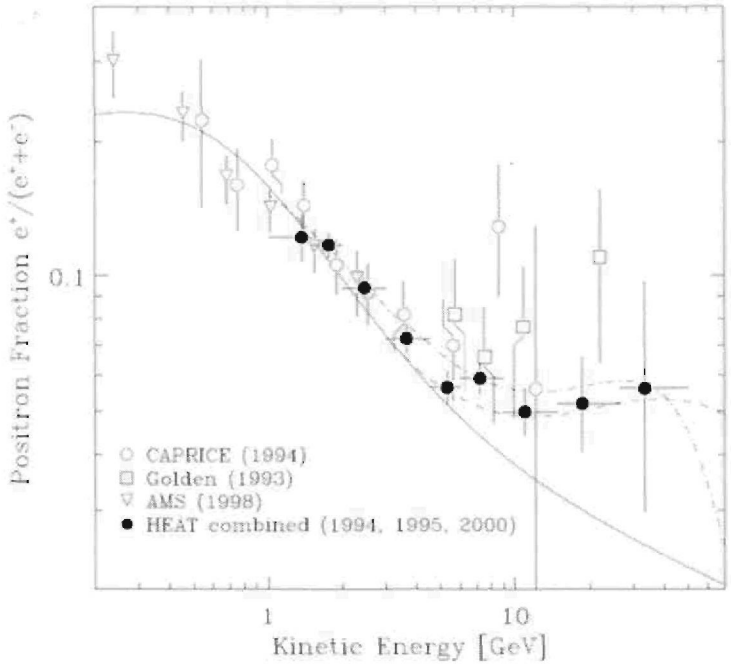

Figure 1.21: The positron fraction in cosmic rays as function of energy. From Beatty et al. (2004).

rays, although many uncertainties pertaining to the mass and type of the progenitor stars, the specific nature of the circumstellar environment, and the galactic origin of the accelerated material exist (e.g. Baring, 2000). Recently, *H.E.S.S.* produced the first image of a supernova shell (SNR RX J1713.7-3946, see Figure 1.17) in TeV gamma rays, and inferred that supernovae are capable of producing large quantities of galactic cosmic rays (Aharonian et al., 2004a, see Section 1.3.4). Subsequent detection of VHE gamma-ray emission towards the young stellar cluster Westerlund 2 provided ample evidence that particle acceleration to extreme energies is associated with this region (Reimer et al., 2007). *Chandra* observations of Galactic SNR Cassiopeia A furthermore found locations where particles seem to be accelerated nearly as fast as is theoretically possible (the Bohm limit), indicating efficient electron acceleration to cosmic-ray energies (Stage et al., 2006).

In Chapter 5, we will be interested in studying pulsars as sources of leptonic cosmic rays. Since electron (lepton) SR and ICS losses are very high, finding high-energy electrons will imply that they come from nearby sources. At high energies (above a few GeV), positrons and electrons are furthermore not expected to be modulated by the solar wind, so that transport calculations will be simplified. At these energies, the flux of the positron component is $\sim$ 10% of that of the electron component (e.g. Beatty et al., 2004, see Figure 1.21), so that if pulsars are sources of cosmic-ray positrons, one should

expect a clear signal in the positron local interstellar spectrum (LIS), in the form of an anisotropy. Detailed results will be presented in Sections 5.4 through 5.6, and Appendix B.

A fuller treatment of cosmic rays may be found by referring to e.g. Berezinskii et al. (1990) and Schlickeiser (2002).

1.5 Motivation

1.5.1 Context

During the recent 363rd Heraeus Seminar entitled *"Neutron Stars and Pulsars – About 40 Years After the Discovery"*, one speaker summed up the state of the field of pulsar physics quite succinctly when he said that he hoped that in another forty years' time we won't still be arguing whether the PC or OG model is the correct one! This tugs at the heart of one of the pulsar community's frustrations: the paradox that although experimental high-energy physics has improved astronomically over the past decades, even higher-sensitivity observations are required in order to rule out one of the two main competing pulsar models (discussed in Section 1.1; also see Baring (2004)). De Angelis et al. (2007) points out that one clear goal of VHE Astrophysics is to discriminate between different processes of pulsar magnetospheric emission (e.g. PC vs. OG models), and adds that no test of these models has been achieved in the range $10 - 100$ GeV yet. The launch of *GLAST* and construction of second phases of successful ground-based gamma-ray telescopes such as *H.E.S.S.* and *MAGIC* certainly fuel the hope of astrophysicists to finally lay this burning issue to bed.

When applying for a Ph.D. in the topic of pulsar physics, one has to decide what the scope and motivation of such a study will be. Apart from the vague, personal aspirations to produce a work of good quality, one which will contribute to the body of knowledge of the field, one has to set specific goals (an ongoing process). The trade-offs to be considered are how deep one will go into a specific part of the problem, given the fixed duration of the study, as finding answers to some questions usually leads to many more unanswered questions. The criteria then is whether the study provides a connected, logical unit, containing enough original research to warrant peers' approval.

Following these basic guidelines, the first question to be settled is whether the thesis will be on development and use of experimental equipment, data accumulation and analysis, numeric simulation, or theoretical modelling. Fortunately, these divisions are not rigid or clear-cut, and the lines may be blurred: computational skills are required to implement complex theoretical models in order to obtain testable results; these results should be compared with the newest available experimental data; sophisticated experiments however need a firm theoretical understanding to keep producing state-of-

the-art, usable observations. And of course, there are always the serendipitous discoveries that open up unexpected new avenues of research and improvement.

Secondly, it should be stated clearly that it will be unreasonable to expect that one could come up with a brand new pulsar model during the course of study which lasts only about 10% of the age of the field. It is unlikely that the wheel will be successfully reinvented in such a short space of time. The second best option then is to choose to implement and scrutinise one of the two main pulsar models, possibly leading to verification or improvement of the chosen model, or even new ideas in that specific context. Lastly, data are essential in order to draw conclusions about the applicability and maturity of the model.

In this thesis we opted to work with one of the most sophisticated models in the PC category, which includes the effect of GR frame dragging, enhancing the predicted accelerating electric field in the pulsar magnetosphere. We wanted to test this model in a variety of ways, by implementing it in a numerical code and performing various applications. Finally, we wanted to try and constrain the fundamental electromagnetic pulsar-related quantities by using multiwavelength and cosmic-ray data. The possibility of using 'fortuitous circumstances' to constrain the pulsar model, and subsequent PWN models, is considered in Section 1.5.3.

The details of the theoretical background and model implementation are described in Chapter 2. Next, three applications follow: (i) a case study of the gamma-radiation of the MSPs PSR J0437-4715 and PSR B1821-24 (Chapter 3), (ii) a study of the average behaviour and visibility of a population of MSPs (Chapter 4), and (iii) the study of the particle output of pulsars and their possible contribution to the local interstellar electron / positron spectrum. The latter application links the pulsar studies with the related topic of PWN, which is applied to G0.9+0.1 in Chapter 5. The scope of this work is thereby broadened to include two archetypes of the high-energy family of gamma-ray sources, being sources of gamma rays and cosmic rays. In Chapter 6, the effect of an alternative E-field will be considered, after which will follow the conclusions in Chapter 7.

1.5.2 Specific Aims

Specifically, the aims of this study have been to:

1. Implement a PC GR frame-dragging pulsar model in a computer code, and using a single computer / a cluster of computers to solve problems as detailed below.

2. Predict single MSP visibility, for examples of both screened and unscreened pulsars.

3. Study the MSP model behaviour in pulsar parameter space.

4. Obtain constraints on the MSP model by modelling: i) Single MSP spectra, ii) MSP population cumulative spectra, and iii) The contribution of nearby pulsars to the local cosmic-ray spectrum.

5. Study the typical beaming angles of MSPs using the basic MSP model, in order to facilitate the deriving of sensible future constraints on gamma-ray efficiency using e.g. *GLAST* data.

6. Investigate model refinements, e.g. the contribution of a ϑ-component to the accelerating electric field.

7. PWN modelling, and limiting e.g. the age and birth period in the case of G0.9+0.1.

In Section 1.6, each following chapter is briefly described to give a bird's eye view of the thesis. Section 1.7 furthermore lists publications following from the work presented in this thesis.

1.5.3 Exploiting Favourable Conditions to Constrain Models

In order to reach the goals set in Section 1.5.2, we noted that the following favourable circumstances provide unique opportunities for deriving model constraints:

1. Rigorous derivation of a PC *General Relativistic* pulsar model was available for testing (e.g Muslimov & Harding, 1997; Harding & Muslimov, 1998), saving a lot of time and energy. We could therefore focus our attention on the implementation and constraining of the model, rather than deriving a new model. Also, this model was hoped to better account for available data, following earlier attempts by other authors using *classical* electrodynamics (e.g. Arons, 1983; Bulik et al., 2000). The frame-dragging effect leads to a purely GR E-field component, and this new E-field may be a factor of $\gtrsim 100$ larger than its flat spacetime counterpart (Muslimov & Tsygan, 1992). The possibility exists to obtain significantly different results when modelling e.g. MSP visibility using this new E-field.

2. Being in the fortunate position of being part of the *H.E.S.S.* Collaboration, direct theoretical contributions could be made to observational papers involving gamma-ray MSPs.

3. Membership of a Flagship Project of the *Centre for High Performance Computing (CHPC)*[7] guaranteed access to a 640-CPU computing facility. This facilitated population studies of MSPs.

4. From the GR model, we have the analytical prediction of $L_\gamma \approx 0.75\kappa(1-\kappa)\dot{E}_{\rm rot}$ (Harding et al., 2002b, see Section A.1 for the general derivation), against which our code could be tested (see Figures 4.21 through 4.23 in Section 4.3).

[7] `www.chpc.ac.za`

5. Similar work have been done on spectra and lightcurves (e.g. Frąckowiak & Rudak, 2005a; Harding et al., 2005b), so that calibration of model results was possible (see Chapter 3).

6. Previously (Venter, 2004), we modelled the MSP PSR J0437-4715. *This pulsar was an obvious choice*, for the following reasons: (i) Several important parameters, most notably the mass and distance (van Straten et al., 2001), are known to a high degree of accuracy. (ii) PSR J0437-4715 is one of the closest pulsars to earth, lying at a distance of 139 ± 3 pc (van Straten et al., 2001). PSR J0437-4715 may therefore be expected to be much brighter and easier observable than other MSPs. (iii) Observations show that the radio and X-ray beams virtually coincide (Zavlin et al., 2002), implying that the observer's line of site cuts the PC near the magnetic axis, providing certainty about geometric constraints, and the possibility of on-beam radiation (also see Manchester & Johnston, 1995). These conditions still hold, and PSR J0437-4715 was furthermore selected as a *H.E.S.S.* target for these reasons. We wanted to model PSR J0437-4715's visibility using a new, refined model. Furthermore, since the E-field of PSR J0437-4715 is believed to be largely unscreened (Section 3.6.1), PSR J0437-4715 presented a *unique laboratory* where the naked electric potential may be probed without the complicating effect of pair cascades.

7. In addition to modelling PSR J0437-4715 as an example of an unscreened MSP, we selected PSR B1821-24 as an example of a screened pulsar, since (i) it has a very large $\dot{E}_{\rm rot}$, promising to be a bright source, and (ii) approximate values of the screened E-field were readily available for easy numeric implementation (Dyks & Rudak, 2000). (While the MSP J0218+4232 is the only MSP for which a detection of HE pulsed radiation has been claimed (Kuiper et al., 2000), the significance was quite low – 3.2σ with the H-test – and the 'ranking parameter' $\dot{E}/d^2$ is much smaller than for PSR J0437-4715 and PSR B1821-24. We therefore did not model this pulsar; see e.g. Frąckowiak & Rudak (2005a,b) for modelling).

8. Fortunately, effects such as Lorentz transformation from the corotating to the observer frame mainly impact on the phase of the radiation, and by using phase-averaged results, we could largely side-step this issue. These effects are furthermore more pronounced for high-altitude emission, where the electric field has dropped significantly enough to result in the less important low-energy component of the spectrum.

9. Population studies of MSPs allowed the possibility of circumventing the severely hampering problem of unknown pulsar geometry. Geometry-averaged results allowed significant constraints to be derived (Section 4.5).

10. Using multiwavelength data allowed us to constrain the age and birth period of the PWN G0.9+0.1 (Section 5.3).

11. Collaboration with cosmic-ray transport experts facilitated the constraining of pulsar parameters (e.g. Section 5.5).

1.6 Thesis Outline

Chapter 1: Introduction

Background on pulsars, PWN, Gamma-ray Astronomy, and cosmic rays, as well as a motivation for the current study are presented.

Chapter 2: Modelling the Pulsar Magnetosphere

We highlight the underpinnings of GR frame dragging, and follow the derivation of the GR-corrected electrodynamical equations, and specifically the derivation of an $E_{||}$-field valid for MSPs.

Chapter 3: Modelling of Single Millisecond Pulsars

Several results are represented obtained from numerical modelling. The MSPs PSR J0437-4715 and PSR B1821-24 are used as case studies for the unscreened and screened E-field cases.

Chapter 4: Millisecond Pulsar Population Studies

The model behaviour for a portion of parameter space is investigated. A population of MSPs is used to show that beaming correction factors may be significantly larger than unity. The cumulative gamma-ray output from a population of MSPs in the GC 47 Tucanae is modelled.

Chapter 5: Beyond the Light Cylinder

Modelling PWN, as well as pulsar contributions to the LIS.

Chapter 6: Model Refinements

Briefly evaluating the influence of e.g. adding a theta-component to the parallel electric field.

Chapter 7: Conclusion

Providing a summary and outlook.

Appendix A: Various Mathematical Results

Some mathematical details are presented.

Appendix B: Selected Publications

Inclusion of three papers dealing with the origin and transport of cosmic rays in the context of pulsars and PWN, which are not extensively discussed in the main thesis.

Bibliography

1.7 Publications

The following publications were produced during the time of Ph.D. study (Publications on cosmic rays are included in Appendix B):

1.7.1 Peer-reviewed Papers

1. Venter, C. & de Jager, O.C. 2008, *Constraining A General-Relativistic Frame-Dragging Model for Pulsed Radiation from a Population of Millisecond Pulsars in 47 Tucanae using GLAST LAT*, Astrophys. J. Lett., 680, L125-L128.

2. Buesching, I., de Jager, O.C., Potgieter, M.S., & Venter, C., 2008, *A Cosmic Ray Positron Anisotropy due to Two Middle-Aged, Nearby Pulsars?*, Astrophys. J. Lett., 678, L39-L42.

3. Buesching, I., Venter, C., & de Jager, O.C., 2008, *Contributions from Nearby Pulsars to the Local Cosmic Ray Electron Spectrum*, Adv. Space Res., 42, 497-503.

4. Venter, C. & de Jager, O.C., 2005, *Empirical Constraints on the General Relativistic Electric Field Associated with PSR J0437-4715*, Astrophys. J. Lett., 619, L167-L170.

5. Venter, C. & de Jager, O.C. 2005, *Spectral Constraints for Millisecond Pulsars due to General Relativistic Frame Dragging*, in *The Multiwavelength Approach to Unidentified Gamma-Ray Sources*, Astrophys. & Space Science, 297, 399-407.

1.7.2 Conference Proceedings

1. Buesching, I., de Jager, O.C., Potgieter, M.S., & Venter, C., 2007, *Constraints on the Lepton Content of PWN from the Local CR Positron Spectrum*, Conf. Proc. of the 30^{th} ICRC Conference in Mérida, Mexico (in press).

2. Fuessling, M., Schlenker, S., Venter, C., Eifert, T., Manchester, R., & Schmidt, S. 2007, *Search for Pulsed VHE Gamma-Ray Emission from Young Pulsars with H.E.S.S.*, Conf. Proc. of the 30^{th} ICRC Conference in Mérida, Mexico (in press).

3. Venter, C. & de Jager, O.C., 2006, *Constraints on the Parameters of the Unseen Pulsar in the PWN G0.9+0.1 from Radio, X-Ray, and VHE Gamma-Ray Observations*, Proc. of the 363 WE-Heraeus Seminar on: Neutron Stars and Pulsars (Posters and contributed talks), ed. W. Becker & H.H. Huang, MPE Report 291, 801, 40-43 (astro-ph/0612652).

4. de Jager, O.C. & Venter, C., 2005, *Ground-based Gamma-Ray Observations of Pulsars and their Nebulae: Towards a New Order*, in Towards a Network of Atmospheric Cherenkov Detectors VII, ed. B. Degrange & G. Fontaine (astro-ph/0511098).

5. Venter, C., de Jager, O.C., & Tiplady, A., 2005, *Gamma-Ray Pulsar Visibility*, in Astrophysical Sources of High Energy Particles and Radiation, ed. T. Bulik, B. Rudak, B., & G. Madejski, AIP Conf. Series, 801, 278-281.

Chapter 2

Modelling the Pulsar Magnetosphere

The basic picture of the pulsar magnetosphere in the polar cap (PC) models, although incomplete, is that of Goldreich & Julian (1969). The vacuum electric field induced by the fast rotating, highly magnetised neutron star, greatly exceeds the gravitational force at the stellar surface and rips charges from the star, creating a force-free, corotating magnetosphere characterised by the Goldreich-Julian charge density $\rho_{\rm GJ}$ (see Eq. [1.19] and [2.99]). (Thermionic emission (see Section 2.1.5) from a hot PC also plays a role in ejecting charges from the stellar surface (Luo et al., 2000)). Deviations from the $\rho_{\rm GJ}$ cause a departure from the $\mathbf{E} \cdot \mathbf{B} = 0$ condition, and leads to an accelerating E-field parallel to the magnetic field lines, $E_{||}$. In fact, particle acceleration and subsequent gamma-ray emission can only take place when there is a local departure from $\rho_{\rm GJ}$, i.e. when the force-free conditions aren't met (e.g. Harding, 1995). This departure may be caused in a number of ways, but in this chapter we will focus on the effect of GR frame dragging (Section 2.2) causing departures from $\rho_{\rm GJ}$ which enhances $E_{||}$.

Primary particles, once ejected from the stellar surface, are accelerated and radiate via the curvature radiation (CR) mechanism (see Section 2.1.2). Gamma-ray emission may also be the result of inverse Compton scattering (ICS; see Section 2.1.3). CR and ICS photons will then, under the right circumstances, form electron-positron pairs via magnetic photon absorption (pair production – see Section 2.1.4), and a cascade process may ensue, creating a pair formation front (PFF) where the electric field will be screened (Sturrock, 1971). Synchrotron radiation (SR) may furthermore provide a mechanism for converting the perpendicular energy of these pairs into high-energy radiation (see Section 2.1.1). The origin of the radio emission, however, still remains somewhat of a mystery (Sakai & Shibata, 2003).

In this chapter (updated from a previous work – Venter (2004)), we will discuss some background

providing context for the implementation of the MSP model that will be used throughout the thesis. We will start by reviewing relevant radiation and transport processes that occur in the pulsar magnetosphere (Section 2.1), including SR, CR, ICS, magnetic photon absorption, and thermionic emission of charges. Next, we will briefly discuss GR frame dragging (Section 2.2), after which we will outline the GR electrodynamical approach of Harding and Muslimov which forms the basis of the 'GR pulsar model' to be applied in later chapters (Section 2.3). Next, we will summarise the expressions of the accelerating E-field valid for different scenarios (Section 2.4), and conclude the chapter by discussing how this model has been implemented in a computer code (Section 2.5).

2.1 Radiation and other Relevant Processes in the Pulsar Magnetosphere

The most important results are summarised in the sections below. The reader is referred to the paper of Blumenthal & Gould (1970) for more details.

2.1.1 Synchrotron Radiation (SR)

When charged particles are accelerated by a magnetic field, they will radiate. Cyclotron radiation occurs when the particles have non-relativistic speeds (Rybicki & Lightman, 1979). SR (or magneto-bremsstrahlung) operates when a charged particle gyrates relativistically about a magnetic field line and radiates a spectrum of harmonics which extends to frequencies of order γ^3 times the gyrofrequency (Lyne & Graham-Smith, 1990), with γ the Lorentz factor of the particles. A transition from cyclotron radiation to SR takes place as the speeds of the charged particles increase from being non-relativistic to being ultra-relativistic.

SR was originally observed in early betatron experiments in which electrons were first accelerated to ultra-relativistic energies (Longair, 1994). A detailed analysis was given by Schott in 1912. For a more recent discussion, see Ginzburg & Syrovatskii (1965, 1969).

A relativistic particle's equations of motion reveal that it will follow a helical path as it gyrates about the magnetic field when the velocity component parallel to the magnetic field is non-zero. The gyration (rotation) frequency is (Rybicki & Lightman, 1979)

$$\omega_B = \frac{qB}{\gamma mc}, \tag{2.1}$$

with q the particle charge, m the particle mass, and B the magnitude of the magnetic field. When

$\mathbf{v} \cdot \mathbf{B} = 0$, the particle follows a circular path with radius (Padmanabhan, 2000)

$$r_B = \frac{v}{\omega_B} = \frac{mcv}{qB}\gamma, \tag{2.2}$$

and v is the particle's speed.

In the classical, non-relativistic case, a single accelerated charge radiates with power given by the Larmor formula:

$$P = \frac{2q^2a^2}{3c^3}, \tag{2.3}$$

where a is the acceleration. When considering the relativistic case, a frame K' which is instantaneously at rest, i.e. one in which the particle has a zero velocity for an instant in time, is utilised, as well as a frame K moving with velocity $-v$. It can be shown that the power is equal for these two frames and that

$$a'_{||} = \gamma^3 a_{||} \tag{2.4}$$

$$a'_{\perp} = \gamma^2 a_{\perp}. \tag{2.5}$$

Note that $a_\perp = \omega_B v_\perp$ for the gyrating component. Using the above expressions together with Eq. (2.3), we get

$$P = \frac{2q^2}{3c^3}\mathbf{a}' \cdot \mathbf{a}' = \frac{2q^2}{3c^3}\left((a'_\perp)^2 + (a'_{||})^2\right) = \frac{2q^2}{3c^3}\gamma^4\left(a_\perp^2 + \gamma^2 a_{||}^2\right) = \frac{2q^2}{3c^3}\gamma^4\left(\omega_B^2 v_\perp^2 + \gamma^2 a_{||}^2\right). \tag{2.6}$$

If $d\mathbf{v}_{||}/dt = 0$, the total emitted radiation is

$$P = \frac{2q^2}{3c^3}\gamma^4\left(\frac{qB}{\gamma mc}\right)^2 v_\perp^2. \tag{2.7}$$

When this formula is averaged over all angles for a given speed $\beta = v/c$ and for an isotropic distribution of velocities, one obtains (Padmanabhan, 2000)

$$P_{\text{Synchrotron}} = \frac{4}{3}\sigma_T(c\beta^2\gamma^2)U_B \propto E^2B^2, \tag{2.8}$$

with $\sigma_T \equiv 8\pi r_0^2/3$ the Thomson cross section, $r_0 \equiv e^2/mc^2$, E the particle energy, and $U_B = B^2/8\pi$ the magnetic energy density. Because of beaming effects, emitted radiation appear concentrated around the velocity direction. A cone of emission with angular width of $\sim 1/\gamma$ is encountered in the relativistic case. The observed pulses are much smaller than the gyration period, by a factor of γ^3. Defining a

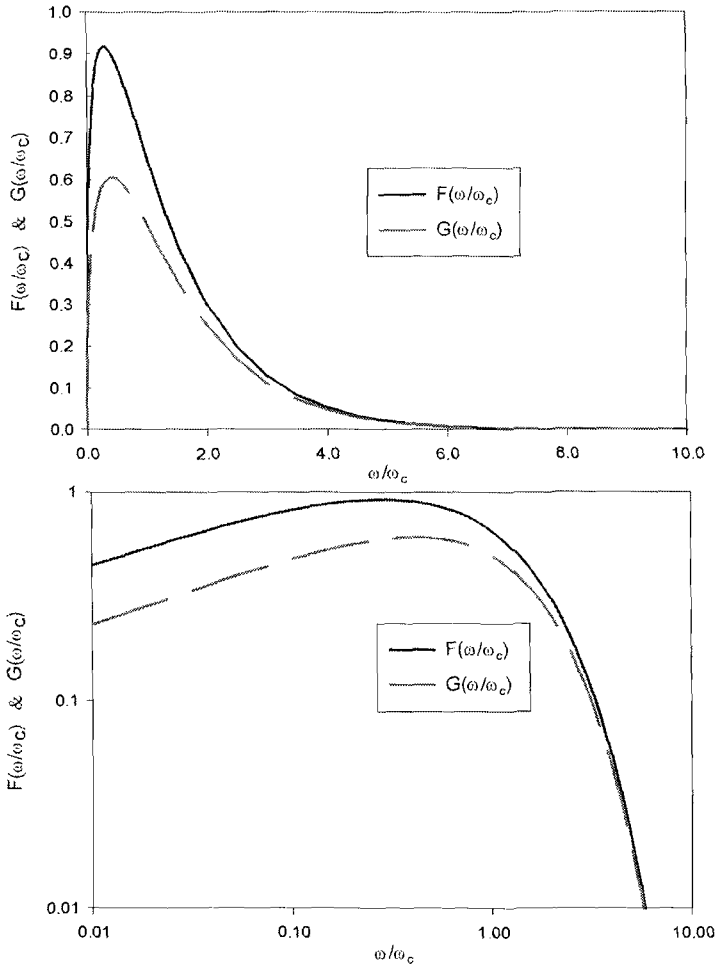

Figure 2.1: Graphs of $F(x)$ and $G(x)$ as in Eq. (2.11) and (2.18). (Numerical data for $F(x)$ and $G(x)$ were obtained from Rohlfs (2000)).

critical frequency

$$\omega_c \equiv \frac{3}{2}\gamma^3 \omega_B \sin\alpha^{\mathrm{p}}, \tag{2.9}$$

with α^{p} the pitch angle, it can be shown (Rybicki & Lightman, 1979) that the power per unit frequency emitted by a single electron is

$$P(\omega) = \frac{\sqrt{3}}{2\pi}\frac{q^3 B \sin\alpha^{\mathrm{p}}}{mc^2} F\left(\frac{\omega}{\omega_c}\right), \tag{2.10}$$

with (see Figure 2.1)

$$F(x) \equiv x\int_x^\infty K_{\frac{5}{3}}(\xi)d\xi, \tag{2.11}$$

and $K_{5/3}$ the modified Bessel function of order 5/3. This function has the following asymptotic forms

$$F(x) \sim \frac{4\pi}{\sqrt{3}\Gamma(\frac{1}{3})}\left(\frac{x}{2}\right)^{1/3}, \qquad x \ll 1 \tag{2.12}$$

$$F(x) \sim \left(\frac{\pi}{2}\right)^{1/2} e^{-x} x^{1/2}, \qquad x \gg 1. \tag{2.13}$$

Assuming that the number density $N(E)$ of particles with energies $\in (E, E+dE)$ may be expressed as a power law

$$N(E)dE = CE^{-p}dE, \quad E_1 < E < E_2, \tag{2.14}$$

with C a function of source parameters, the total power radiated per unit volume per unit frequency is given (using Eq. (2.10)) by

$$P_{\rm tot}(\omega) = \int_{E_1}^{E_2} P(\omega)N(E)dE \propto \int_{\gamma_1}^{\gamma_2} P(\omega)\gamma^{-p}d\gamma \propto \int_{\gamma_1}^{\gamma_2} F\left(\frac{\omega}{\omega_c}\right)\gamma^{-p}d\gamma. \tag{2.15}$$

Changing variables to $x \equiv \omega/\omega_c$, and using $\omega_c \propto \gamma^2$ (see Eq. [2.1] and [2.9]), we find

$$P_{\rm tot}(\omega) \propto \omega^{-(p-1)/2} \int_{x_1}^{x_2} F(x)x^{(p-3)/2}dx, \tag{2.16}$$

where the limits x_1 and x_2 correspond to γ_1 and γ_2. When the integration interval is sufficiently large so that we may write $x_1 \approx 0$ and $x_2 \approx \infty$, the integral is approximately constant and we find

$$P_{\rm tot}(\omega) \propto \omega^{-(p-1)/2} \propto \omega^{-s}, \tag{2.17}$$

with $s = (p-1)/2$ the index of the energy spectrum. (Exact calculations of SR transition rates and spectra of electrons in strong B-fields were carried out by Harding & Preece (1987)).

Defining (see Figure 2.1)

$$G(x) \equiv xK_{\frac{2}{3}}(x), \tag{2.18}$$

with $K_{2/3}$ the modified Bessel function of order 2/3, it can be shown that

$$P_{\perp}(\omega) = \frac{\sqrt{3}q^3 B \sin\alpha^{\rm p}}{4\pi mc^2}[F(x)+G(x)] \tag{2.19}$$

$$P_{||}(\omega) = \frac{\sqrt{3}q^3 B \sin\alpha^{\rm p}}{4\pi mc^2}[F(x)-G(x)], \tag{2.20}$$

and the sum of these reduces back to Eq. (2.10). The radiation from a single particle will be elliptically

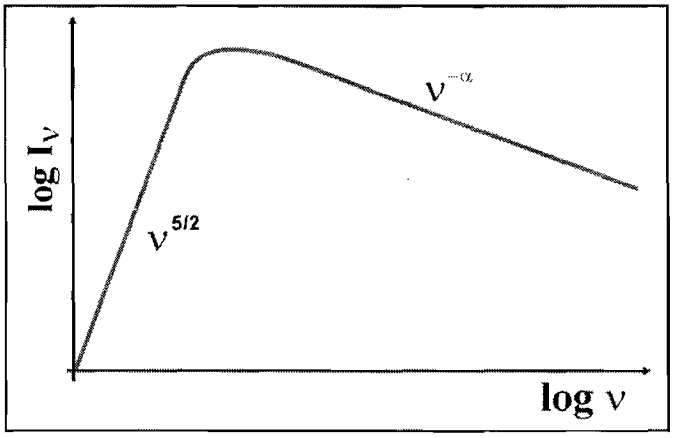

Figure 2.2: The spectrum of a source of SR which exhibits the phenomenon of synchrotron self-absorption. The second spectral index $\alpha = (p-1)/2$ (See text for details; adapted from Longair (1994)).

polarised, but the radiation of a reasonable distribution will be partially linearly polarised and the degree of linear polarisation for particles with an energy γ is given by

$$\Pi(\omega) = \frac{P_\perp(\omega) - P_{||}(\omega)}{P_\perp(\omega) + P_{||}(\omega)} = \frac{G(x)}{F(x)}. \tag{2.21}$$

The polarisation of the frequency-integrated radiation can be shown to be 75%.
The following are therefore characteristic of SR (Rybicki & Lightman, 1979):

- Radiation from a single particle lies within a cone of angular width $\sim 1/\gamma$;
- The single particle spectrum extends up to $\omega \sim \omega_c$ and is a function of ω/ω_c alone;
- For a power-law distribution of particles with index p over a sufficiently broad energy range, the spectral index of the radiation is $s = (p-1)/2$;
- High linear polarisation of radiation due to a distribution of particles at energy γ.

Synchrotron self-absorption may occur when a photon is absorbed by a charge in a magnetic field, or when stimulated emission takes place and a particle will emit more strongly into a direction and at a frequency where photons are already present. It can be shown that for optically thick SR, the intensity $I_\nu \propto \nu^{5/2}$, while for optically thin SR, $I_\nu \propto \nu^{-(p-1)/2}$ when assuming a power-law particle distribution (see Figure 2.2).

SR is an important process in pulsar physics, and features in canonical pulsar PC models, where CR (see Section 2.1.2) and ICS (see Section 2.1.3) are also taken into account (Zhang & Harding,

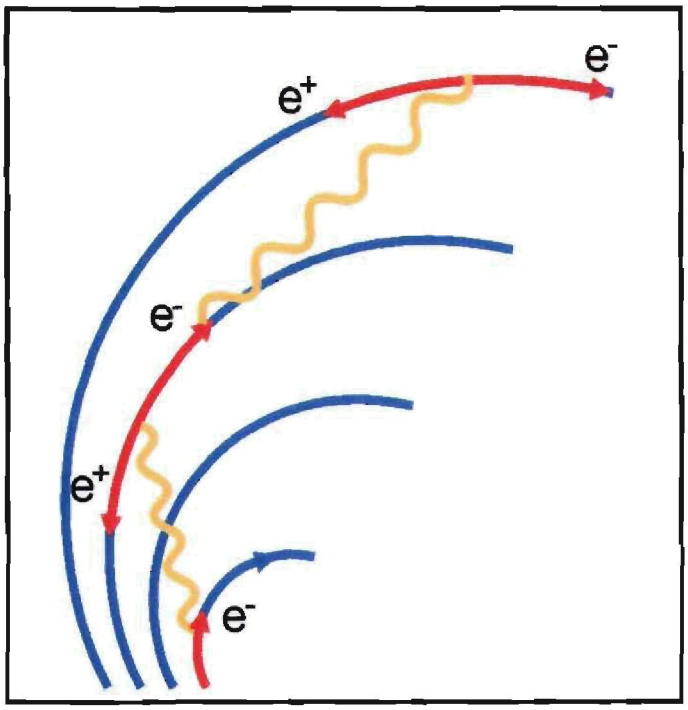

Figure 2.3: Representation of the combined CR and magnetic photon absorption processes (see Section 2.1.4). Adapted from Padmanabhan (2001).

2000). When magnetic photon absorption occurs (see Section 2.1.4), electron-positron pairs with relativistic momenta perpendicular to the local magnetic field are created from photons, and the perpendicular energy of these pairs (i.e. secondary particles) is converted to high-energy radiation via the SR mechanism during a very short time (Sturrock et al., 1989; Malov & Machabeli, 2001). In addition, we will also calculate SR spectra from relativistic leptons in PWN in Chapter 5.

2.1.2 Curvature Radiation (CR)

Curvature radiation (CR) may occur whenever a charged particle follows a curved path (see Figure 2.3). Under certain circumstances, this process may operate in conjuction with pair production (see Section 2.1.4). CR may furthermore occur even when SR or cyclotron radiation does not (when the particles are in their ground Landau level). When particles are in higher Landau levels, all these modes of radiation may occur (Mészáros, 1992).

CR is connected with a change in longitudinal energy with respect to $\mathbf{B}$ as opposed to SR (which is connected with a change in transverse energy). Since primary particles accelerated from the stellar surface move along the open field lines, their kinetic energy transverse to the magnetic field will be much smaller than their longitudinal kinetic energy. CR will therefore be a much more important

radiation process than SR with regard to the primary particles (Sturrock, 1971).

Assuming that the radius of curvature is large enough to justify the use of classical radiation formulae (Mészáros, 1992), the instantaneous CR power spectrum is given by (Jackson, 1975)

$$\left(\frac{dP}{dE}\right)_{\rm CR} = \sqrt{3}\alpha_{\rm fine}\gamma\left(\frac{c}{2\pi\rho_c}\right)F\left(\frac{\omega}{\omega_0}\right), \tag{2.22}$$

(see Eq. [2.10]), with

$$\omega_0 = \frac{3}{2}\frac{c\gamma^3}{\rho_{\rm c}} \tag{2.23}$$

the typical frequency obtained for a curvature radius $\rho_{\rm c}$, and (as defined in Eq. [2.11])

$$F(x) \equiv x\int_x^\infty K_{5/3}(x')dx' = \begin{cases} 2.149x^{1/3} & x \ll 1 \\ 1.253x^{1/2}e^{-x} & x \gg 1, \end{cases} \tag{2.24}$$

with e the electron charge, c the speed of light in vacuum, and γ the particle's Lorentz factor. This spectrum is the same as that of classical SR for equal $\rho_{\rm c}$. The frequency-integrated power is given by (e.g. Jackson (1975); Bulik et al. (2000); Luo et al. (2000); Story et al. (2007); see Eq. [2.7])

$$P = \frac{2}{3}\frac{e^2c}{\rho_c^2}\beta^4\gamma^4\,{\rm ergs/s}, \tag{2.25}$$

with $\beta \equiv v/c$, implying $\dot{\gamma}_{\rm CR} \propto \gamma^4/\rho_c^2$. In the above formulas, we may use the following approximation for the curvature radius (also see Section 2.5.4) of the magnetic field lines associated with a spinning dipole (Harding, 1981; Luo et al., 2000):

$$\rho_{\rm c} \approx \frac{4}{3}\left(\frac{cr\sin^2\vartheta_{\rm PC}}{\Omega\sin^2\vartheta_*}\right)^{1/2} = \frac{4}{3}\left(\frac{r}{\sin\vartheta}\right) \approx \frac{4}{3}\left(\frac{r}{\vartheta}\right), \tag{2.26}$$

with ϑ_* the polar angle of the magnetic field line at the stellar surface, and $\vartheta_{\rm PC}$ the PC angle. For typical pulsar parameters $R \sim 10^6$ cm and $B \sim 10^{12}$ G and electron-positron energies of $10^{12} - 10^{13}$ eV, CR photons have energies in the GeV range and an electron-positron cascade may occur (see Section 2.1.4). Since CR by relativistic electrons is confined to a narrow emission cone ($\Delta\vartheta \sim 1/\gamma$), the emission of CR photons may be modelled as originating tangential to the magnetic field lines in the rotating frame of reference (Manchester & Taylor, 1977; Harding et al., 1978).

The characteristic CR photon energy (in units of m_ec^2 – see Eq. [2.23]) is (e.g. Luo et al., 2000)

$$E_\gamma^{\rm c} = \frac{3}{2}\left(\frac{\lambda_c}{\rho_{\rm c}}\right)\gamma^3, \tag{2.27}$$

where $\lambda_c = \hbar/m_e c \approx 3.86 \times 10^{-11}$ cm is the Compton wavelength. The CR spectrum has a maximum at E_γ^c and falls off exponentially for $E_\gamma > E_\gamma^c$. For a mono-energetic beam of particles, the CR photon spectrum $dN/dE \propto E_\gamma^{-5/3}$ towards lower energies ($E_\gamma < E_\gamma^c$), up to an energy $E_{\gamma,\mathrm{break}} = 9\hbar c/4r_0 \approx$ 150 MeV (with r_0 the classical electron radius, $\hbar \equiv h/2\pi$, and h Planck's constant), below which the CR tail becomes $\propto E_\gamma^{-2/3}$ (Rudak & Dyks, 1999). This corresponds to particles having a high initial energy, after which cooling via CR takes place (see Model A in Bulik et al. (2000)). When there is continuous acceleration of primary particles above the stellar surface due to a parallel electric field in addition to CR losses, the CR photon spectrum changes to $\propto E_\gamma^{-2/3}$ (see Section 3.5.2) below the cut-off energy (Harding et al., 2002b). For canonical pulsars, energy cut-off is due to magnetic pair production, but in the case of MSPs near or below the CR death line (see Section 3.6.1), there is a natural CR cut-off at E_γ^c (see Eq. [2.27]).

It is important to take CR into account when modelling pulsar radiation mechanisms (see e.g. Harding et al., 1978). CR photons provide the means for SR to take place, because the CR photons decay into electron-positron pairs in the case of pulsars with large spin-down values. (ICS may also provide high energy photons which may decay into electron-positron pairs). SR then represents the mechanism for conversion of the perpendicular lepton energies into high-energy radiation (Zhang & Harding, 2000), as discussed in the previous section.

CR is the dominant process for canonical pulsars with spin-down energies $\dot{E}_{\mathrm{rot}} \lesssim 10^{34}$ erg s^{-1} and for the older pulsars (MSPs) with spin-down energies $\dot{E}_{\mathrm{rot}} \lesssim 10^{35}$ erg s^{-1}. These MSPs lie below this CR death line (see Harding et al., 2002b), implying that pair production does not take place, so that SR will not ensue. It seems that this scenario is also applicable to PSR J0437-4715 (see Section 3.6.1).

2.1.3 Inverse Compton Scattering (ICS)

In 1923, Compton's experiment (the results of which earned him the 1927 Nobel Prize in Physics) involving the scattering of X-rays off a target provided proof of Einstein's notion that both momentum and energy are transferred via photons (Halliday et al., 1997). From the conservation of energy and momentum, when treating the photon as a particle with momentum $p = hf/c = h/\lambda$, with h Planck's constant and f the frequency, one may obtain an expression for the Compton shift

$$\Delta\lambda \equiv \lambda' - \lambda = \frac{h}{mc}(1 - \cos\phi), \tag{2.28}$$

with λ the initial wavelength, λ' the wavelength of the scattered photon, and ϕ the scattering angle of the photon. In this process, called Compton scattering, a high-energy photon transfers energy and

momentum to a low-energy electron, leading to an increase of the photon's wavelength.

ICS involves the inverse situation of Compton scattering: collisions of high-energy electrons (or other particles) with low-energy photons resulting in higher photon energies (i.e. "boosting" of photon energies). This process may also be viewed as SR by high-energy electrons as they move in an electromagnetic radiation field (Lyne & Graham-Smith, 1990). ICS is likely to be important for relativistic electrons propagating through regions of large energy densities of radiation (Longair, 1994). A relativistic electron with Lorentz factor γ may up-scatter a low-energy photon (with energy $hf \ll m_e c^2$ – classical Thomson scattering limit) to a high-energy photon by a factor of order γ^2. The energy of the Compton-boosted photon (having an initial energy ϵ) is (Ramanamurthy & Wolfendale, 1986)

$$E_\gamma \sim \epsilon\gamma^2, \quad \gamma\epsilon \ll m_e c^2 \quad - \quad \text{"Thomson" limit} \tag{2.29}$$

$$E_\gamma \sim \gamma m_e c^2, \quad \gamma\epsilon \gg m_e c^2 \quad - \quad \text{"Extreme Klein-Nishina" limit.} \tag{2.30}$$

The net power lost by an electron in an isotropic radiation field and converted into increased radiation (for a low-energy photon – in the Thomson limit), is

$$P_{\text{Compton}} = \frac{4}{3}\sigma_{\text{T}}(c\beta^2\gamma^2)U_{\text{rad}}, \tag{2.31}$$

with U_{rad} the initial photon energy density, and σ_{T} the classical Thomson scattering cross section. Using Eq. (2.8), it follows that

$$\frac{P_{\text{Synchrotron}}}{P_{\text{Compton}}} = \frac{U_B}{U_{\text{rad}}}, \tag{2.32}$$

implying that losses due to SR and ICS are in the same ratio as the magnetic field energy density and the photon energy density. (This is valid for arbitrary electron speeds, but for target photon energies $\gamma hf \ll m_e c^2$ – Thomson limit).

To understand the transition between the Thomson and extreme Klein-Nishina regimes given by Eq. (2.29) and (2.30), consider the following. When the initial photon energy becomes high, quantum effects become important, and σ_T (see definition following Eq. [2.8]) should be replaced by the Klein-Nishina cross section (Rybicki & Lightman, 1979)

$$\sigma = \sigma_T \frac{3}{4}\left[\frac{1+x}{x^3}\left\{\frac{2x(1+x)}{1+2x} - \ln(1+2x)\right\} + \frac{1}{2x}\ln(1+2x) - \frac{1+3x}{(1+2x)^2}\right], \tag{2.33}$$

where $x \equiv \gamma hf/m_e c^2$. The main effect is the reduction of the classical value of the cross section as

the photon energy increases. In the non-relativistic case of the Thomson limit (see Eq. [2.29])

$$\sigma \approx \sigma_T \left(1 - 2x + \frac{26x^2}{5} + \ldots\right), \quad x \ll 1, \tag{2.34}$$

and for the ultra-relativistic case (corresponding to Eq. [2.30])

$$\sigma = \frac{3}{8}\sigma_T \frac{1}{x}\left(\ln 2x + \frac{1}{2}\right), \quad x \gg 1. \tag{2.35}$$

The total Compton spectrum may be computed by integrating the production rate $dN'(\epsilon,\gamma)/dE_\gamma$, with γ the electron Lorentz factor, over soft photon energy ϵ and γ (Blumenthal & Gould, 1970):

$$\left(\frac{dN}{dE_\gamma}\right)_{\text{tot}} = \iint dN_e \left(\frac{dN'(\epsilon,\gamma)}{dE_\gamma}\right) d\gamma d\epsilon, \tag{2.36}$$

with $dN_e = N_e(\gamma)d\gamma$ the differential number of electrons. If we assume that the electron energy distribution is a power law, $N_e \propto \gamma^{-p}$, and a black body soft photon distribution, it follows that

$$\left(\frac{dN}{dE_\gamma}\right)_{\text{tot}} \propto E_\gamma^{-(p+1)/2} \quad - \text{ Thomson limit,} \tag{2.37}$$

$$\left(\frac{dN}{dE_\gamma}\right)_{\text{tot}} \propto E_\gamma^{-(p+1)} \quad - \text{ Extreme Klein-Nishina limit.} \tag{2.38}$$

We therefore see that the first expression has the same form as in the case of SR (for which the energy spectrum is given in Eq. [2.17]), given a power-law distribution of electrons, while the spectrum is much steeper in the extreme Klein-Nishina regime.

ICS is important for pulsars and PWN in general (see e.g. de Jager et al., 1996), and also in the case of PSR J0437-4715, from which thermal as well as non-thermal X-ray radiation have been detected (Zavlin et al., 2002, although Bogdanov et al. (2006b) argues for thermal origin only; see Section 3.2.1.). The presence of a photon field of X-rays means that electrons (or positrons) accelerated in the open field line region along the magnetic field lines will tend to scatter the thermal X-rays originating at the stellar surface, upscattering them to gamma-ray energies. Assuming classical electrodynamics, Bulik et al. (2000) have shown that the ICS component of PSR J0437-4715's energy spectrum is small compared to the CR component, but important for TeV gamma-ray observations. It is important to redo these calculations for an injection of a thermalised pool of electrons into a GR field. This is however beyond the scope of the present study.

2.1.4 Magnetic Photon Absorption

Due to the presence of high-energy particles, efficient radiation processes, and a pair production mechanism in the pulsar magnetosphere, particle-photon cascades are likely to occur in pulsar magnetospheres where strong magnetic and electric fields exist (Daugherty & Harding, 1982). CR photons whose energies are large enough, have a high probability of producing electron-positron pairs. The members of the pairs are likely to radiate SR photons, which in turn may be able to produce other electron-positron pairs. This process may continue until the SR photon energies are too low for further pair production, so that these photons may escape for detection. The lowest energy pairs may provide a mechanism for the production of radio and optical emission. The pair cascading scenario was originally introduced by (Sturrock, 1971) and has since been studied extensively (e.g. Daugherty & Harding, 1983; Burns & Harding, 1984; Sturrock et al., 1989; Baring & Harding, 2001; Arendt & Eilek, 2002; Levinson et al., 2005).

(i) No Electric Field

Since a magnetic field may absorb momentum, there exists a probability for photons with high enough energy to convert into electron-positron pairs. This probability is expressed as a photon attenuation coefficient $\alpha(\chi')$ which determines the number of pairs created ($n_{\rm pairs}$) when a certain photon path length d is traversed in a magnetic field B (Erber, 1966):

$$n_{\rm pairs} = n_{\rm photons}(1 - \exp\left[-\alpha(\chi')d\right]) \simeq n_{\rm photons}\alpha(\chi')d, \tag{2.39}$$

the approximation being valid when the optical depth is small enough. The photon attenuation coefficient / photon absorption per unit length (when considering a perpendicular, unbounded, uniform magnetic field $B_\perp \ll B_{\rm crit}$) is given by (Erber, 1966)

$$\alpha(\chi') = \frac{1}{2}\left(\frac{\alpha_{\rm fine}}{\lambda_{\rm c}}\right)\left(\frac{B_\perp}{B_{\rm crit}}\right)T(\chi'), \tag{2.40}$$

with $\alpha_{\rm fine} = e^2/\hbar c \approx 1/137$ the fine structure constant, $\lambda_{\rm c}$ the Compton wavelength (see definition following Eq. [2.27]), $\chi' \equiv \frac{1}{2}(hf/m_e c^2)(B_\perp/B_{\rm crit})$ the Erber parameter, and $B_{\rm crit} = m_e^2 c^3/e\hbar = 4.414 \times 10^{13}$ G the critical magnetic field corresponding to the equality of the cyclotron energy with the electron rest energy ($\hbar\Omega_e = m_e c^2$). The dimensionless function $T(\chi')$ is given by (Erber, 1966)

$$T(\chi') = \frac{4}{3\pi^2(\chi')^2}\int_0^\infty\int_0^\infty du\,dw\left\{\left[2\cosh^2 w\cosh^5 u - \sinh^2 u\cosh^3 u\right]K_{1/3}^2\delta' +\right.$$

$$\left[2\cosh^2 w - 1\right]\cosh^5 u\, K_{2/3}^2\delta'\Big\}, \tag{2.41}$$

with

$$\delta' = \left(\frac{2}{3\chi'}\cosh^2 w \cosh^3 u\right). \tag{2.42}$$

Using the asymptotic properties of the modified Bessel functions, the following limiting cases of $T(\chi')$ may be derived

$$T(\chi') = \begin{cases} 0.46\exp[-4/(3\chi')] & \chi' \ll 1 \\ 0.60(\chi')^{-1/3} & \chi' \gg 1. \end{cases} \tag{2.43}$$

Using the approximation for $T(\chi')$ where $\chi' \ll 1$, Eq. (2.40) becomes (Luo et al., 2000)

$$\alpha(\chi') = 0.46\left(\frac{\alpha_{\rm fine}}{\lambda_c}\right)\left(\frac{\chi'}{\epsilon_\gamma}\right)\exp\left(-\frac{4}{3\chi'}\right), \tag{2.44}$$

with $\chi' = 0.5\epsilon_\gamma\epsilon_B\sin\vartheta_{\gamma B}$, where $\epsilon_B = B/B_{\rm crit}$, ϵ_γ the photon energy in units of $m_e c^2$, and $\vartheta_{\gamma B}$ the photon propagation angle relative to the local magnetic field line direction. It is therefore clear that the opacity increases exponentially with increasing χ'.

As a general rule of thumb, one may use the approximation due to Sturrock (1971) for the condition for pair production (Harding et al., 1978)

$$\epsilon_\gamma B_\perp \gtrsim 10^{11.9}, \tag{2.45}$$

with ϵ_γ the photon energy in units of $m_e c^2$, and $B_\perp$ measured in Gauss.

The relatively lower magnetic fields of MSPs imply that higher photon energies or larger photon propagation angles (longer photon propagation paths) are required in order that pair production may occur. Higher photon energies will lead to a PFF closer to the PC if pair formation indeed occurs. For typical MSP parameters, Luo et al. (2000) finds that the maximum value of χ' is too small to reach an opacity of unity. They find a typical optical depth of $\sim 10^{-13}$, indicating that pair production will most probably not occur for the typical MSP parameters they assumed. We came to similar conclusions in Section 3.6.1 for the case of PSR J0437-4715.

(ii) Non-zero Electric Field

In 1975, Daugherty & Lerche suggested that the pair production rate in a strong magnetic field may be drastically altered in the presence of an electric field. (The validity of this suggestion will be discussed

in the following section). These authors generalised the results of Erber (1966) under the conditions

$$\mathbf{E}\cdot\mathbf{B}=0,\quad \mathbf{E}^2-\mathbf{B}^2\leq 0. \tag{2.46}$$

Without loss of generality, they considered an inertial frame with static electric and magnetic fields directed along the positive y- and z-axes, and considered a photon of energy E_γ with direction cosines η_x, η_y, and η_z. By performing a Lorentz transformation to a frame containing only a magnetic field, evaluating the expression valid where only a magnetic field is present (see Eq. [2.44]) and transforming back to the original reference frame, they obtained the rate $\zeta' \equiv c\alpha(\chi')$ of pair production (Daugherty & Lerche, 1975)

$$\begin{aligned}\zeta' &= 0.23c\left(\frac{\alpha_{\rm fine}}{\lambda_c}\right)\left(\frac{B}{B_{\rm crit}}\right)\left(1-\frac{E^2}{B^2}\right)\left(1-\frac{E\eta_x}{B}\right)^{-1}\left[\left(\eta_x-\frac{E}{B}\right)^2+\eta_y^2\left(1-\frac{E^2}{B^2}\right)\right]^{1/2}\times \\ &\exp\left\{-\frac{8}{3}\left(\frac{m_ec^2}{E_\gamma}\right)\left(\frac{B_{\rm crit}}{B}\right)\left[\left(\eta_x-\frac{E}{B}\right)^2+\eta_y^2\left(1-\frac{E^2}{B^2}\right)\right]^{-1/2}\right\}\ {\rm s}^{-1}.\end{aligned} \tag{2.47}$$

This expression holds as long as

$$\chi_2'\equiv\frac{1}{2}\left(\frac{E_\gamma}{m_ec^2}\right)\left(\frac{B}{B_{\rm crit}}\right)\left[\left(\eta_x-\frac{E}{B}\right)^2+\eta_y^2\left(1-\frac{E^2}{B^2}\right)\right]^{1/2}\ll 1. \tag{2.48}$$

Using $B_\perp = B(\eta_x^2+\eta_y^2)^{1/2}$, it is easy to show that Eq. (2.47) reduces back to Eq. (2.44) for the case when $\mathbf{E}=0$. One important result is that the 'free propagation direction', i.e. one in which the pair production rate is zero, is given by

$$(\eta_x,\eta_y,\eta_z)_{\rm FP}=\left(\frac{E}{B},0,\pm\left(1-\frac{E^2}{B^2}\right)^{1/2}\right). \tag{2.49}$$

Also, for the case where $(\eta_x,\eta_y,\eta_z)=(0,0,1)$, i.e. photon propagation parallel to the magnetic field,

$$\zeta'=0.23c\left(\frac{\alpha_{\rm fine}}{\lambda_c}\right)\frac{E}{B_{\rm crit}}\left(1-\frac{E^2}{B^2}\right)\exp\left[-\frac{8}{3}\left(\frac{m_ec^2}{E_\gamma}\right)\frac{B_{\rm crit}}{E}\right]. \tag{2.50}$$

Daugherty & Lerche (1976) generalised these results for the case when $\mathbf{E}\cdot\mathbf{B}\neq 0$. Their discussion involved the quantum-mechanical complication that the electric field may spontaneously break down into electron-positron pairs, as well as questions regarding the self-consistency of their approach. They concluded that the pair production rate is highly sensitive to the photon's propagation angle and to both the parallel and perpendicular components of the electric field, making the determination of

the pair production rate and radiation due to particle acceleration very model-dependent. However, Harding et al. (1978) found that the presence of an electric field parallel to the magnetic field had a very small effect on the optical depths, on average several parts in 1 000. The effect of $\mathbf{E}_{||}$ became larger as the emission angle as measured from the dipole axis increased.

(iii) Importance of an Electric Field

A useful argument by Zheng et al. (1998) enables one to ignore the electric field when calculating the pair production rate as a first order approximation. Their argument runs as follows.

The usual Goldreich-Julian force-free condition requires a perpendicular induced electric field $\mathbf{E} = -(\mathbf{v}/c) \times \mathbf{B}$, with $\mathbf{v}$ the corotating velocity (see Eq. [1.18]). This field is much smaller than $\mathbf{B}$, since $v \ll c$, and the application of Eq. (2.50) seems justified. However, the use of Eq. (2.50) leads to unnatural conclusions.

(a) Firstly, when considering a magnetic field configuration consisting of straight, corotating field lines in the frame where the electric field vanishes (this approximation holds close to the stellar surface), a photon will be emitted parallel to these lines, but cannot be absorbed, since there is no perpendicular magnetic field component. Observing the same process in the laboratory frame, severe pair production will take place, since the rotationally-induced electric field is quite strong. Thus, we see contradicting pictures in different observer frames.

(b) Secondly, a gamma ray travels a certain distance before $B_\perp$ becomes sufficiently strong to absorb it. But, according to Eq. (2.50), the photon may be absorbed immediately, at the same position where it was emitted. Thus, it would be nearly impossible for high energy photons to be formed in a rapidly rotating magnetosphere. The use of (0,0,1) as the photon propagation direction is only valid in the frame where there is no perpendicular electric field or in the corotating frame of an aligned pulsar, and not necessarily in the laboratory frame.

Since there exists an electric field in the laboratory frame, a drift velocity $\mathbf{v}_d = c\mathbf{E} \times \mathbf{B}/B^2$ will be introduced in addition to the velocity component of the electrons along the magnetic field. For an aligned rotator, where $\mathbf{v}, \mathbf{E}$, and $\mathbf{B}$ are mutually perpendicular, Zheng et al. (1998) find the photon's propagation direction in the laboratory frame to be $(\eta_x, \eta_y, \eta_z) = (\sin\delta, 0, \cos\delta) = (v/c, 0, [1-(v/c)^2]^{1/2})$, with δ the angle between the gamma ray and the magnetic field line, rather than (0,0,1). This is however equivalent to the free propagation direction $(\eta_x, \eta_y, \eta_z) = (E/B, 0, [1-(E/B)^2]^{1/2})$, where $\zeta' = 0$, which means that *the electric field plays no role in the pair production process in this case.* The two contradictions disappear, since firstly, the photon will not be absorbed (immediately) in the laboratory frame anymore, because it is emitted in the free propagation direction, and secondly,

the photon is now allowed to move a certain distance until $B_\perp$ is strong enough for absorption to take place. The role of the induced electric field for pair production furthermore *remains negligible* as the photon travels a certain distance. Zheng et al. (1998) find that, for their straight magnetic field line approximation, with the magnetic field strength decreasing as r^{-3}, the attenuation coefficient is at least two orders of magnitude smaller than for the case when the photon propagation is in the direction of (0,0,1).

For the oblique rotator case where the magnetic and spin axes are non-aligned, the photon direction will deviate from $(v/c, 0, [1-(v/c)^2]^{1/2})$. But the attenuation coefficient is very small in the region around this direction. (Also, the steady state electric field generally falls off as r^{-4}. This implies that when the photon direction eventually deviates significantly from the region around the free propagation direction, so that it may be necessary to include the effect of the electric field, the field may again be considered negligible due to its small magnitude). *This means that the validity of the conclusion that the electric field is not so important for pair production, may be generalised to hold also for the oblique rotator case.* In any case, Eq. (2.50) only strictly holds for the aligned rotator case, since a parallel electric component remains in the corotating frame of an oblique rotator.

The above-mentioned approximation for electrons accelerated along B-field lines while experiencing a negligible drift, resulting in the emission of photons tangentially to the **B**-direction, will be employed in our magnetospheric simulation, with results on pair production for PSR J0437-4715 presented in Section 3.6.1.

(iv) Superstrong Magnetic Fields and High Photon Energies

Pair production in magnetic fields $\gtrsim 10^{12}$ G and with photon energies near the energy threshold ($\hbar\omega \gtrsim 2m_ec^2$) has been investigated by Daugherty & Harding (1983). The attenuation coefficient exhibits "sawtooth" behaviour near threshold, because of the onset of quantum effects due to the discreteness of the electron and positron energies in the magnetic field. For $\epsilon_\gamma \sin\vartheta_{\gamma B} > 2m_ec^2$, the absorption per unit length is given by

$$\alpha(\chi') \approx 0.46 \left(\frac{\alpha_{\rm fine}}{\lambda_c}\right) \left(\frac{\chi'}{\epsilon_\gamma}\right) \exp\left[-\frac{4}{3\chi'}(1+\delta)\right], \tag{2.51}$$

and $\delta \approx 0.42(\chi'/\epsilon_B)^{-2.7}\epsilon_B^{-0.0038}$, describing the near-threshold effect. For a high energy and low magnetic field, $\delta \ll 1$ and Eq. (2.51) reduces back to Eq. (2.44). While this regime may exist for canonical pulsars, it may be ignored for MSPs which generally have comparatively low magnetic fields (also see Luo, 1996).

2.1.5 Thermionic Emission of Charges

PC models may be classified according to the vacuum gap model (where charges are assumed to be tightly bound), the space-charge limited flow (SCLF) model (where free emission of charges is assumed), and a model where the PC can only supply some charges (Luo et al., 2000). The space-charge-limited approximation was used when deriving the GR-corrected electric and magnetic fields (Section 2.3).

For an MSP PC with $\mathbf{\Omega} \cdot \mathbf{B} > 0$, the threshold temperature for thermionic emission of electrons is (Flowers et al., 1977; Usov & Melrose, 1996; Luo et al., 2000):

$$T_e \approx (2.3 \times 10^4\,\mathrm{K}) \left(\frac{Z}{26}\right)^{4/5} B_9^{2/5}, \tag{2.52}$$

with $Z = 26$ the charge per nucleon (i.e. the iron crust of the neutron star) and $B_{12} = B_0/10^{12}$ G the surface magnetic field strength. When the temperature exceeds T_e, the thermal energy is greater than the work function and thermionic emission will take place. For ions from a positive PC with $\mathbf{\Omega} \cdot \mathbf{B} < 0$ (Usov & Melrose, 1996)

$$T_i \approx (2.3 \times 10^3\,\mathrm{K}) B_9^{0.73}. \tag{2.53}$$

In the case of PSR J0437-4715, Zavlin et al. (2002) inferred a PC temperature decreasing outward from 2×10^6 K at the core to 5×10^5 K at the rim using X-ray observations of this pulsar obtained by the *Chandra X-Ray Observatory*. It is thus clear that the detected X-ray energies corresponding to the PC region of PSR J0437-4715 are well above the threshold temperatures ($T_e \sim 10^4$ K, given $B_0 \sim 10^9$ G). This supports the use of the SCLF approximation where there is a free supply of charges from the PC due to thermionic emission. (The condition that the PC temperature should be greater than this threshold temperature is a necessary one, but may however not be sufficient to garuantee SCLF conditions, as the SCLF solution is unstable to perturbations – Dyks 2008, personal communication).

From Eq. (2.53), it is clear that there will also be a supply of ions from the surface, ensuring charge neutrality. However, the ions are much heavier, and they are therefore considered to be significantly less efficient radiators than electrons. In Chapter 3, we will only consider the dominant radiation component for PSR J0437-4715 (in the GeV-range), which is CR due to primary electrons accelerated by an unscreened E-field (Sections 2.4.2 and 2.4.3), in the absence of pair creation. For the case of PSR B1821-24, screening will occur, and we will use the modified electric field which is screened out at the height of the PFF (Section 2.4.4). Again, our main focus will be on the CR component of the

primary electrons.

2.2 The Lense-Thirring Effect

The effect of a massive rotating body on its surrounding spacetime was first described by Lense & Thirring in 1918, shortly after Einstein published his theory of General Relativity. As a massive body rotates, it "drags" inertial frames with it. An analogy may be drawn between such a massive rotating body and a rotating sphere immersed in a viscous fluid. The sphere will drag the fluid along as it rotates. Furthermore, the angular velocities of the local inertial frames are parallel to the angular momentum of the rotating body near the poles, but antiparallel near the equator (where the local inertial frames rotate in a direction opposite to that of the rotating body). This can be made plausible by the viscous fluid analogy. Imagine little rods being set down at various points in the fluid, and observe their rotation as the fluid flows. Near the poles, the rods will rotate in the same direction as the rotating body, but near the equator, the ends of rods closest to the body will be dragged more rapidly by the fluid than the opposite ends. This is because the fluid is dragged more slowly at larger distances from the body. Thus, the rods will rotate in the direction opposite to that of the sphere near the equator. This analogy can be made mathematically rigorous (Misner et al., 1973).

The orbital plane of a test particle orbiting a rotating object, having a tilted orbit with respect to the object's equatorial plane, will experience a torque due to the GR effect described by Lense and Thirring (Armitage & Natarajan, 1999). This will cause the plane of orbit to precess around the angular momentum axis of the rotating object. The nodal precession frequency, first calculated by Lense and Thirring in the weak field limit, is given by (see Eq. 2.62)

$$\nu_{\rm LT} = \frac{GJ}{\pi c^2 r^3}, \tag{2.54}$$

with G the gravitational constant, J the angular momentum of the rotating object, c the speed of light, and r the radius of the test particle's circular orbit (Stella & Vietri, 1998). The general formula is given by (Hartle, 2003)

$$\mathbf{\Omega}_{\rm LT} = \frac{G}{c^2 r^3}\left[3\left(\mathbf{J}\cdot\vec{e}_r\right)\vec{e}_r - \mathbf{J}\right], \tag{2.55}$$

which reduces to Eq. (2.54) when $\mathbf{r}$ points along $\mathbf{J}$. This is a characteristic dipole pattern, with $\mathbf{J}$ playing the role of the dipole moment.

The Lense-Thirring effect serves several theoretical and experimental 'uses'. It plays an important role in e.g. the definition of the angular momentum of a gravitating body as well as in black-hole

physics (Misner et al., 1973). The Lense-Thirring effect is the only known GR effect which depends strongly enough on the angular momentum of a rotating body in order to be used in the experimental determination of this quantity for certain bodies. Haas & Ross (1975) therefore proposed to put gyroscopes in close Jovian and solar orbits for measuring the angular momentum of Jupiter and the sun via this effect. Stella & Vietri (1998) proposed that Lense-Thirring precession may be directly observable in the form of quasi-periodic oscillations (QPOs) in the X-ray lightcurves of low-mass X-ray binaries (LMXRBs). They interpreted peaks in the power spectra as due to precession of the innermost part of the accretion disk, which is dominated by this effect. If their suggestion is validated, it will provide constraints on the NS equation of state (Armitage & Natarajan, 1999).

The Lense-Thirring effect is encountered when deriving the basic Maxwell equations in the GR regime (see Section 2.3.1), showing up as a non-diagonal component in the metric of Eq. (2.61). It is this effect that leads to "dragging of inertial frames". The incorporation of GR-effects into an electrodynamic model of a pulsar holds the promise of solving some problems of flat spacetime models. *Harding & Muslimov (1998) found that the electric field component parallel to the exterior magnetic field, $E_{||}$, is typically* $50 - 100$ *times larger (for a 1 s pulsar) than the flat spacetime counterpart due to GR frame dragging that takes place.* This implies that charged particles may be accelerated to much higher energies above the PC, leading to more energetic radiation. This may better explain observations of pulsar gamma rays as mentioned in the problem statement (see Section 1.5.3). It is therefore necessary to give a broad introduction to the GR framework in which an MSP model may be developed, which is done in the following paragraphs.

2.3 GR-corrected Magnetic Field and Electric Potential

In this section, we summarise the work of Muslimov, Tsygan and Harding (Muslimov & Tsygan, 1992; Muslimov & Harding, 1997; Harding & Muslimov, 1998). The aim in doing this is to give a broad introduction to the basic framework of GR electrodynamics as applied to pulsars, emphasising the fundamental quantities as they appear in the GR regime. We state the GR form of the Maxwell equations for a certain metric (Section 2.3.1) and also their rewritten form as they apply to a frame of reference corotating with the NS (Section 2.3.2). Muslimov & Tsygan (1992) assume a certain structure for the exterior magnetic field (Section 2.3.3), after which they solve for the charge density and electric potential (Section 2.3.4). From the potential, they derive the electric field component parallel to the magnetic field (Section 2.4) for several cases (Muslimov & Harding, 1997; Harding & Muslimov, 1998).

2.3.1 Basic Equations

The classical Maxwell Equations of electrodynamics are well-known (see e.g. Griffiths, 1999):

$$\nabla \cdot \mathbf{E} = 4\pi\rho \tag{2.56}$$

$$\nabla \times \mathbf{E} = -\frac{1}{c}\frac{\partial \mathbf{B}}{\partial t} \tag{2.57}$$

$$\nabla \cdot \mathbf{B} = 0 \tag{2.58}$$

$$\nabla \times \mathbf{B} = \frac{1}{c}\frac{\partial \mathbf{E}}{\partial t} + \frac{4\pi}{c}\mathbf{j} \tag{2.59}$$

from which follows the charge continuity equation

$$\nabla \cdot \mathbf{j} = -\frac{\partial \rho}{\partial t}. \tag{2.60}$$

These equations are written in cgs units. The symbols have their normal meaning: $\mathbf{E} \equiv$ electric field, $\rho \equiv$ charge density, $c \equiv$ speed of light in vacuum, $\mathbf{B} \equiv$ magnetic field, $\mathbf{j} \equiv$ current density, $t \equiv$ time, $\nabla \equiv (\partial/\partial x, \partial/\partial y, \partial/\partial z)$ in Cartesian coordinates.

The Maxwell equations in a GR scenario describing the electrodynamics around a rotating NS may be derived in different ways. Muslimov & Harding (1997) use the geometrical point of view, considering a metric of an asymptotically flat, stationary, axially symmetric spacetime around a rotating gravitating body (e.g. Landau & Lifshitz, 1975) in spherical polar coordinates $x^0 = ct$, $x^1 = r$, $x^2 = \vartheta$ and $x^3 = \phi$:

$$ds^2 = \alpha^2(cdt)^2 - \alpha^{-2}(dr)^2 - r^2(d\vartheta)^2 - (r\sin\vartheta)^2(d\phi - \omega dt)^2, \tag{2.61}$$

with $\alpha = (1 - r_g/r)^{1/2}$ the gravitational redshift function, $\omega = 2GJ/c^2r^3$, and $r_g = 2GM/c^2$ the gravitational radius of the NS with mass M and angular momentum $\mathbf{J}$. This metric (2.61) is the approximation of the Kerr metric when the ratio J/Mcr_g is small. The presence of the non-diagonal component in this metric leads to the dragging of inertial frames (Lense-Thirring effect, see Section 2.2) with angular velocity (see Eq. [2.54] and [2.55])

$$\vec{\omega} = \frac{2G\mathbf{J}}{c^2r^3}. \tag{2.62}$$

Muslimov & Harding (1997) then derive the Maxwell equations, where all the electrodynamic quantities $\mathbf{E}$, $\mathbf{B}$, $\mathbf{j}$, and ρ are measured by the Zero Angular Momentum Observer (ZAMO) in a local orthonormal

basis in spherical geometry:

$$\nabla \cdot \mathbf{E} = 4\pi\rho \tag{2.63}$$

$$\nabla \times (\alpha \mathbf{E}) = -\frac{1}{c}\left(\frac{\partial \mathbf{B}}{\partial t} + \mathcal{L}_{\omega \mathbf{m}}\mathbf{B}\right) \tag{2.64}$$

$$\nabla \cdot \mathbf{B} = 0 \tag{2.65}$$

$$\nabla \times (\alpha \mathbf{B}) = \frac{1}{c}\left(\frac{\partial \mathbf{E}}{\partial t} + \mathcal{L}_{\omega \mathbf{m}}\mathbf{E}\right) + \frac{4\pi}{c}\alpha \mathbf{j}, \tag{2.66}$$

with $\mathcal{L}_{\omega \mathbf{m}}$ the Lie derivative along the vector $\mathbf{w} \equiv \omega \mathbf{m}$, $\mathbf{m} \equiv r \sin\vartheta\, \mathbf{e}_{\hat{\phi}}$ the Killing vector corresponding to the axial symmetry, and $\mathbf{e}_{\hat{\phi}}$ the local unit azimuthal basis vector. The action of the Lie derivative on the fields $\mathbf{E}$ and $\mathbf{B}$ is given by

$$\mathcal{L}_{\omega \mathbf{m}}\mathbf{B} = -\nabla \times (\mathbf{w} \times \mathbf{B}), \tag{2.67}$$

$$\mathcal{L}_{\omega \mathbf{m}}\mathbf{E} = -[\nabla \times (\mathbf{w} \times \mathbf{E}) - \mathbf{w}(\nabla \cdot \mathbf{E})]. \tag{2.68}$$

Finally, the charge continuity equation becomes

$$\nabla \cdot (\alpha \mathbf{j}) = -\frac{\partial \rho}{\partial t} - \omega \mathbf{m} \cdot \nabla \rho. \tag{2.69}$$

2.3.2 Equations in Corotating Reference Frame

In what follows, we consider a reference frame corotating with the NS. If the angular velocity of a NS relative to a distant observer is $\mathbf{\Omega}$, then Eq. (2.64) and (2.67) become (Muslimov & Harding, 1997)

$$\nabla \times \left[\alpha \mathbf{E} - \frac{1}{c}(\mathbf{w} - \mathbf{u}) \times \mathbf{B}\right] = -\frac{1}{c}\frac{\partial \mathbf{B}}{\partial t} \tag{2.70}$$

in the corotating frame, and $\mathbf{u} = \Omega r \sin\vartheta\, \mathbf{e}_{\hat{\phi}}$. Assuming that the magnetic field is stationary in the corotating frame, Muslimov & Harding (1997) set $\partial \mathbf{B}/\partial t = 0$. It then follows that

$$\alpha \mathbf{E} - \frac{1}{c}(\mathbf{w} - \mathbf{u}) \times \mathbf{B} = -\nabla \Phi, \tag{2.71}$$

with Φ a scalar electric potential. Taking the divergence of Eq. (2.71) and using Eq. (2.63) leads to

$$\nabla \cdot \left[\frac{1}{\alpha}\nabla \Phi + \frac{1}{\alpha c}(\mathbf{u} - \mathbf{w}) \times \mathbf{B}\right] = -4\pi\rho. \tag{2.72}$$

To complete the system of equations, one must include the GR equation of motion of a particle of

charge q

$$\frac{1}{\alpha}\frac{d\mathbf{p}}{dt} = \mu\gamma\mathbf{g} + q\left(\mathbf{E} + \frac{\mathbf{v}}{c} \times \mathbf{B}\right) + \mathbf{f}, \tag{2.73}$$

with $d/dt \equiv \partial/\partial t + \omega\mathbf{m} \cdot \nabla + \alpha\mathbf{v} \cdot \nabla$, and $\partial/\partial t + \omega\mathbf{m} \cdot \nabla$ is the global time derivative along ZAMO trajectories, $\mathbf{p} = \gamma\mu\mathbf{v}$ is the particle momentum, $\gamma = \left(1 - v^2/c^2\right)^{-1/2}$ is the Lorentz factor, μ the rest mass of a particle, $\mathbf{f}$ an external force other than electromagnetic, and $\mathbf{g}$ the gravitational acceleration. Muslimov & Harding (1997) ignores acceleration due to gravity in this problem.

In the following section, we state the assumed external magnetic field. This magnetic field structure should obey Eq. (2.65) and Eq. (2.66). Using Eq. (2.72), one may then solve for the electric potential (Section 2.3.4) and derive the electric field component parallel to the magnetic field lines for different cases (Section 2.4) subject to certain boundary conditions.

It should be noted that a more recent derivation of GR electrodynamics applicable to pulsar physics due to Sakai & Shibata (2003) includes the effect of gravity on the particle dynamics. They solve the electric field and particle equation of motion for the region just above the stellar surface and conclude that gravity affects particle dynamics and may not be ignored. They also argue that the assumption of Muslimov & Tsygan (1992) of constancy of particle speed is violated for oscillatory motion of particles, which indeed occurs. Furthermore, the small angle approximation used in the following sections to obtain analytical solutions may not be applicable to MSPs. A numerical approach for solving the modified Maxwell equations may therefore be preferable. These points will be taken into account in future studies. For our present purposes, however, we ignore these refinements and use the results of Muslimov, Tsygan, and Harding as mentioned previously.

2.3.3 The External Magnetic Field of a Rotating Neutron Star

Under the assumption that the effects of the magnetospheric currents on the external magnetic configuration of the star are negligibly small in the inner magnetosphere, so that the temporal and spatial derivatives of $\mathbf{E}$ are negligible in this region, Eq. (2.66) may be rewritten as

$$\nabla \times (\alpha\mathbf{B}) = 0, \tag{2.74}$$

since the terms on the right-hand side of Eq. (2.66) are of order $\lesssim R^{-1}(\Omega R/c)^2 B$ within the light cylinder, and can be neglected (Muslimov & Harding, 1997). (For a 1 s canonical pulsar, $R^{-1}(\Omega R/c)^2 B \sim 0.05$, but for an MSP with a period of 5 ms, $R^{-1}(\Omega R/c)^2 B \sim 2$). Muslimov & Harding (1997) assume that the external magnetic field is a static dipole GR-corrected magnetic field. Written in magnetic

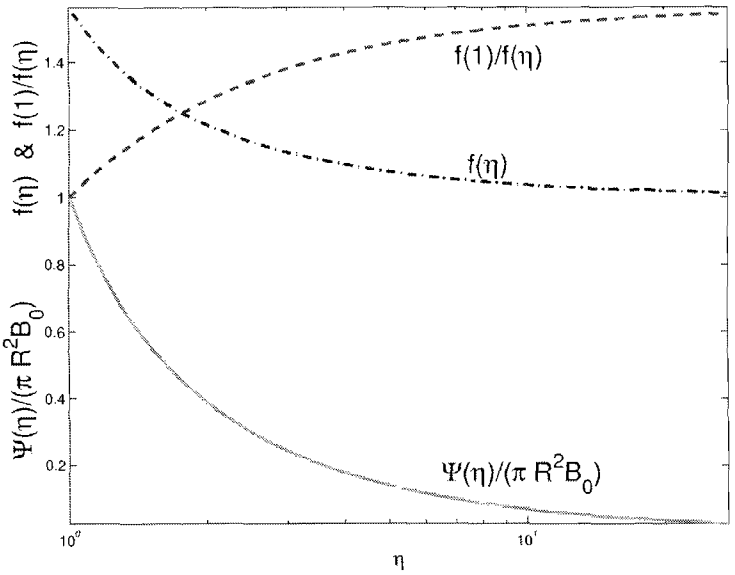

Figure 2.4: The graphs of $\Psi(\eta)$ and $f(\eta)$ vs. η as in Eq. (2.77) and (2.78). The graph of $f(1)/f(\eta)$ vs. η is also shown.

polar components (r, ϑ and ϕ), it is given by the expression:

$$\mathbf{B^d} = -\frac{1}{2\pi r \sin\vartheta}\mathbf{e}_{\hat{\phi}} \times \nabla \left[\Psi(r)\sin^2\vartheta\right], \tag{2.75}$$

with

$$\Psi(r) \equiv \int \mathbf{B}\cdot\mathbf{d\Sigma} = \int_0^{\pi}\int_0^{2\pi} B_{\hat{r}} r^2 \sin\vartheta d\vartheta d\phi \tag{2.76}$$

the magnetic flux through the magnetic hemisphere of radius r, and the circumflex indicates base vectors of an orthonormal basis. Muslimov & Harding (1997) now state that the following functional form for Ψ is required by Eq. (2.74) (see Figure 2.4)

$$\Psi(\eta) = \pi R^2 B_0 \frac{f(\eta)}{f(1)}\frac{1}{\eta} \tag{2.77}$$

$$f(\eta) = -3\left(\frac{\eta}{\epsilon}\right)^3\left[\ln\left(1-\frac{\epsilon}{\eta}\right)+\frac{\epsilon}{\eta}\left(1+\frac{\epsilon}{2\eta}\right)\right], \tag{2.78}$$

with B_0 the magnetic field strength at the stellar surface, $\epsilon \equiv r_g/R$, $\eta \equiv r/R$ a dimensionless radial coordinate, and R the NS radius. The function $f(\eta)$ is the correction factor for the dipole component of the magnetic flux through the magnetic hemisphere of radius r in a Schwarzchild metric (Harding

& Muslimov, 1998). By setting $x = \epsilon/\eta$ and using the expansion

$$\ln(1-x) = -\sum_{k=1}^{\infty} \frac{x^k}{k}, \tag{2.79}$$

we may write

$$f(x) = 3\sum_{k=0}^{\infty} \frac{x^k}{k+3}, \quad 0 < x < 1. \tag{2.80}$$

When $x \ll 1$, i.e. far from the stellar surface where $\epsilon \ll \eta$,

$$f(\eta) \approx 1 + \left(\frac{3}{4}\right)\left(\frac{\epsilon}{\eta}\right) + \left(\frac{3}{5}\right)\left(\frac{\epsilon}{\eta}\right)^2, \tag{2.81}$$

so that the correction tends to unity far from the surface (Muslimov & Harding, 1997, see Figure 2.4). The axially symmetric components of the magnetic field are (Muslimov & Tsygan, 1992; Muslimov & Harding, 1997)

$$B^d_{\hat{r}} \equiv \frac{1}{\pi}\frac{\Psi}{r^2}\cos\vartheta = B_0 \frac{f(\eta)}{f(1)}\frac{1}{\eta^3}\cos\vartheta \tag{2.82}$$

$$B^d_{\hat{\vartheta}} \equiv -\frac{\alpha}{2\pi r}\frac{\partial\Psi}{\partial r}\sin\vartheta = \frac{1}{2}B_0\alpha\left[-2\frac{f(\eta)}{f(1)} + \frac{3}{f(1)(1-\epsilon/\eta)}\right]\frac{1}{\eta^3}\sin\vartheta. \tag{2.83}$$

It is now easy to see that these generalised expressions reduce back to the classical dipolar B-field expressions (Eq. [1.6] and [1.7]) when the mass $M \to 0$ ($\epsilon \to 0$, $\alpha \to 1$, and $f(\eta) \to 1$):

$$B_r^{\text{classic}} = \frac{B_0}{\eta^3}\cos\vartheta \tag{2.84}$$

$$B_\vartheta^{\text{classic}} = \frac{B_0}{2\eta^3}\sin\vartheta. \tag{2.85}$$

Together with the scaled radial coordinate η, the scaled polar angle (magnetic colatitude)

$$\xi \equiv \frac{\vartheta}{\Theta} \tag{2.86}$$

will be used, with Θ the magnetic colatitude of a radius vector moving along the last open magnetic field line. Note that $\xi \in [0,1]$. The family of magnetic field lines is described by

$$\Psi(r)\sin^2\vartheta = \Psi(R)\sin^2\vartheta_0 \tag{2.87}$$

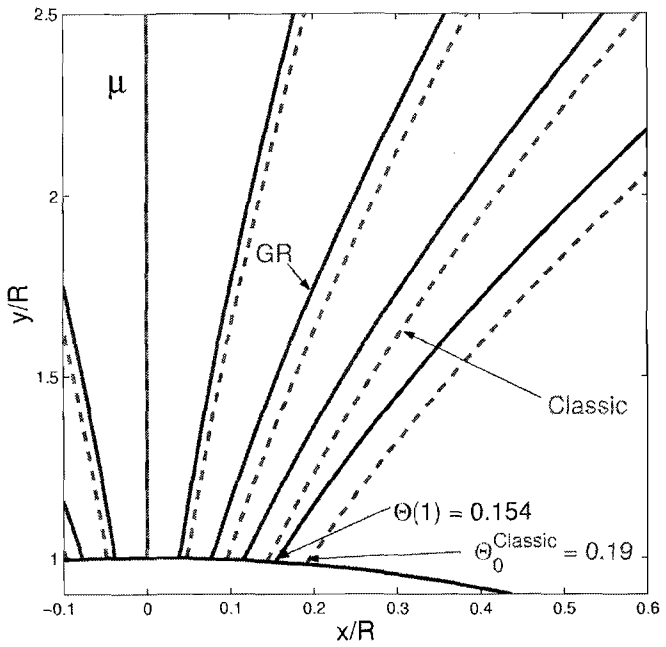

Figure 2.5: The GR and classical magnetic field for PSR J0437-4715 (see Eq. [2.89] and [2.132]). The $\xi = 0$ lines coincide for the two cases. The PC angles are also indicated: $\Theta(1)$ for GR and $\Theta_0^{\text{classic}}$ for the classical case.

(see Figure 2.5 and Eq. [1.8]), with ϑ_0 the magnetic colatitude of a magnetic field line at the stellar surface ($\eta = 1$). From this follows the GR formula for an open magnetic field line

$$\vartheta = \sin^{-1}\left\{\left[\frac{\Psi(R)}{\Psi(r)}\sin^2\vartheta_0\right]^{1/2}\right\} \tag{2.88}$$

$$= \sin^{-1}\left\{\left[\eta\frac{f(1)}{f(\eta)}\right]^{1/2}\sin(\xi\Theta_0)\right\}, \tag{2.89}$$

with Θ_0 the magnetic colatitude of the last open field line ($\xi = 1$) at the stellar surface. Because $\vartheta = \pi/2$ for this line at the light cylinder radius, we can write

$$\Theta_0 \equiv \sin^{-1}\left\{\left[\frac{\Psi(R_{\rm LC})}{\Psi(R)}\right]^{1/2}\right\} \tag{2.90}$$

$$= \sin^{-1}\left\{\left[\frac{f(R_{\rm LC}/R)R}{f(1)R_{\rm LC}}\right]^{1/2}\right\} \tag{2.91}$$

$$= \sin^{-1}\left\{\left[\frac{\Omega R}{c}\frac{f(c/(\Omega R))}{f(1)}\right]^{1/2}\right\}. \tag{2.92}$$

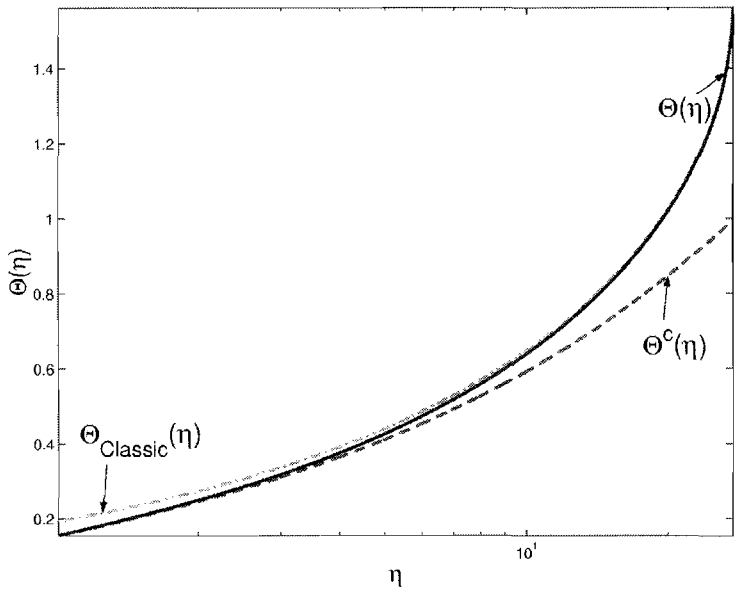

Figure 2.6: Graphs of the polar angle vs. altitude for the last closed magnetic field line (for typical parameters of PSR J0437-4715): $\Theta(\eta)$ and $\Theta^{\rm c}(\eta)$ as in Eq. (2.94) and (2.95) for the GR case, and $\Theta_{\rm classic}(\eta) = \sin^{-1}\left(\sqrt{\eta\Omega R/c}\right)$ for the classic case. Note that the GR approximation is close to the true value close to the star, while it deviates when η becomes large. Also, the GR and classical values coincide far from the star as expected, since the GR effects are greatest at distances close to the star.

In the case of canonical pulsars, we may use an approximate value for Θ_0 (Harding & Muslimov, 1998):

$$\Theta_0^{\rm c} \equiv \left[\frac{\Omega R}{cf(1)}\right]^{\frac{1}{2}}, \tag{2.93}$$

where the superscript "c" refers to the approximation for canonical pulsars. For shorter period pulsars (such as MSPs) one should rather use

$$\Theta(\eta) = \sin^{-1}\left\{\left[\frac{\Omega R}{c}\frac{\eta f(c/(\Omega R))}{f(\eta)}\right]^{1/2}\right\} \tag{2.94}$$

for the magnetic colatitude of the last open field line instead of the approximation for canonical pulsars (Harding & Muslimov, 1998):

$$\Theta^{\rm c}(\eta) \equiv \Theta_0^{\rm c}\left[\eta\frac{f(1)}{f(\eta)}\right]^{1/2} = \left[\frac{\Omega R}{c}\frac{\eta}{f(\eta)}\right]^{1/2}. \tag{2.95}$$

From Figure 2.6 it is evident that the GR expression for $\Theta(\eta)$ is close to the classical value $\Theta_{\rm classic}(\eta) = \sin^{-1}\left(\sqrt{\eta\Omega R/c}\right)$ when $\eta \gg 1$, but deviates increasingly from this value as $\eta \to 1$. This is expected, since the GR effect becomes more important close to the stellar surface.

For later use, define

$$\zeta_0 \equiv \frac{\Theta_0^c}{\Theta_0}, \tag{2.96}$$

$$\zeta(\eta) \equiv \frac{\Theta^c(\eta)}{\Theta(\eta)}. \tag{2.97}$$

These factors are typically corrections of order unity. (The function $\zeta(\eta)$ goes down from 1 to $\sim$ 0.65 as the radial coordinate increases from R to $R_{\rm LC}$ in the case of PSR J0437-4715). Note that by definition $\Theta^c(1) = \Theta_0^c$ and $\Theta(1) = \Theta_0$, implying that $\zeta(1) = \zeta_0$.

2.3.4 The Electric Potential

Equation (2.72) may be written as (Muslimov & Tsygan, 1992)

$$\nabla \cdot \left(\frac{1}{\alpha}\nabla\Phi\right) = -4\pi\left(\rho - \rho_{\rm GJ}\right), \tag{2.98}$$

with

$$\rho_{\rm GJ} \equiv -\frac{1}{4\pi c}\nabla \cdot \left[\frac{1}{\alpha}(\mathbf{u}-\mathbf{w}) \times \mathbf{B}\right] = -\frac{1}{4\pi c}\nabla \cdot \left[\frac{1}{\alpha}\left(1 - \frac{\kappa}{\eta^3}\right)\mathbf{u} \times \mathbf{B}\right] \tag{2.99}$$

the GR version of the Goldreich-Julian charge density (see Eq. [1.19]), and $\kappa \equiv \epsilon I/I_0$, I the moment of inertia of the star, $I_0 \equiv MR^2$, and M the mass of the star. Muslimov & Harding (1997) next use the small-angle approximation $\vartheta \ll 1$. (This approximation may need to be revised when dealing with MSPs, as their PC angles are typically much larger than those of canonical pulsars, since $\vartheta_{\rm PC} = \sin^{-1}\left(\sqrt{2\pi R/cP}\right) \sim P^{-1/2}$). In this approximation, Eq. (2.99) becomes

$$\rho_{\rm GJ} \simeq -\frac{\Omega B_0}{2\pi c\alpha\eta^3}\frac{f(\eta)}{f(1)}\left[\left(1 - \frac{\kappa}{\eta^3}\right)\cos\chi + \frac{3}{2}H(\eta)\zeta(\eta)\Theta(\eta)\xi\sin\chi\cos\phi\right], \tag{2.100}$$

with

$$H(\eta) = \frac{\epsilon}{\eta} - \frac{\kappa}{\eta^3} + \left(1 - \frac{3\epsilon}{2\eta} + \frac{\kappa}{2\eta^3}\right)\left[f(\eta)\left(1 - \frac{\epsilon}{\eta}\right)\right]^{-1} \tag{2.101}$$

(see Figure 2.7), and χ the angle between the magnetic and spin axes, ϕ the magnetic azimuthal angle, and $\zeta(\eta)$ as defined in Eq. (2.97). Both $H(\eta)$ and $f(\eta)$ defined in Eq. (2.101) and Eq. (2.78) are numerical factors that account for the static part of the curved spacetime metric (Harding &

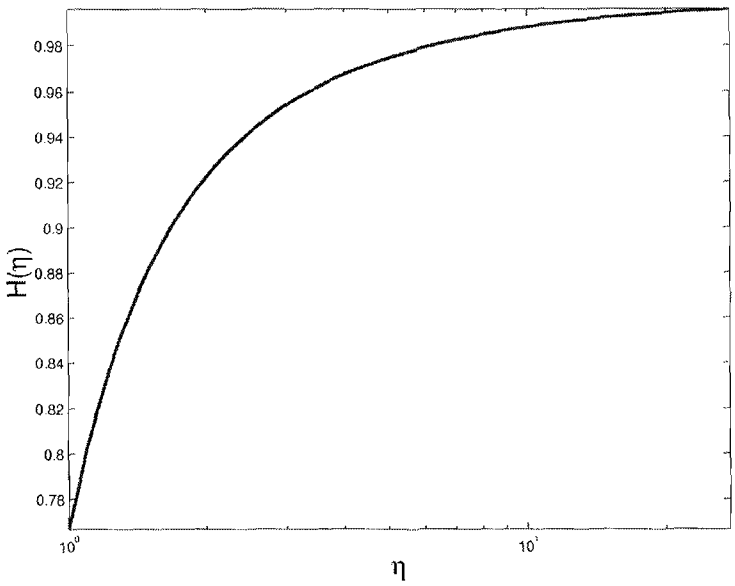

Figure 2.7: $H(\eta)$ vs. η as in Eq. (2.101).

Muslimov, 1998) and are equal to 1 in flat space.

When solving for the electric potential Φ, Muslimov & Harding (1997) use the space-charge-limited approximation. Ejection of charges from the stellar surface takes place, and the charges flow along the open field lines. These currents increase until the volume charge in the open magnetosphere is sufficient to shield an electric field component parallel to the magnetic field. This approximation implies the following boundary conditions (Muslimov & Tsygan, 1992):

- There exists a closed magnetosphere filled with plasma sufficiently dense so that the condition $\mathbf{E} \cdot \mathbf{B} = 0$ applies (i.e. strict corotation of the magnetosphere with the star);
- $E_{||} = \mathbf{E} \cdot \mathbf{B}/|B| = 0$ at the stellar surface where $\eta = 1$ (shielding by the ejected charges takes place);
- $\Phi = 0$ on the last closed magnetic field line $\xi = 1$ (boundary between the open and closed magnetosphere) as well as at the stellar surface. The stellar surface and last closed field lines therefore form an equipotential surface.

Furthermore, the charged particle motions are treated as being relativistic ($v = c$), but this assumption was questioned by Sakai & Shibata (2003). Muslimov & Tsygan (1992) give the general solution of Eq. (2.69):

$$\rho = \frac{\Omega B_0}{2\pi c \alpha \eta^3} \frac{f(\eta)}{f(1)} \left[A(\xi) \cos\chi + \frac{3}{2} D(\xi) \sin\chi \cos\phi \right], \tag{2.102}$$

with $A(\xi)$ and $D(\xi)$ functions whose forms are determined by solving the Poisson equation (2.98), using Eq. (2.100). From this follows the electric potential Φ and accelerating E-field $E_{||}$. In the next section, we list expressions for Φ and $E_{||}$, valid for different scenarios.

2.4 $E_{||}$ for Different Scenarios

See Figure 2.9 for graphs of the different cases.

2.4.1 'Classic' Case

For purposes of comparison, we include the 'classic' function for $E_{||}$ as used by Bulik et al. (2000). In this model, they assume that $E_{||}$ falls off exponentially with height above the PC:

$$E_{||} = E_0' \exp\left(-\frac{h}{R_{\rm PC}}\right), \tag{2.103}$$

with E_0' a constant, h the height above the PC, and $R_{\rm PC}$ the PC radius.

2.4.2 No Upper PFF – Near Surface Case ($\eta \simeq 1$)

First define (see Figure 2.8)

$$\delta(\eta) \equiv \frac{\partial}{\partial \eta} \ln[\zeta(\eta)\Theta(\eta)H(\eta)] \tag{2.104}$$

in order to write

$$\frac{\partial[\zeta(\eta)\Theta(\eta)H(\eta)]}{\partial \eta} = \zeta(\eta)\Theta(\eta)H(\eta)\delta(\eta). \tag{2.105}$$

We will use this function later when taking the derivative of the electric potential in order to find the electric field components. Muslimov & Tsygan (1992) give the explicit expression for $\delta(\eta)$:

$$\begin{aligned} \delta(\eta) &= \frac{1}{H(\eta)}\left\{-\frac{2\epsilon}{\eta^2}+\frac{4\kappa}{\eta^4}+\frac{3}{(\eta-\epsilon)f(\eta)}\left[\frac{\epsilon}{\eta}-\frac{\kappa}{\eta^3}\right.\right. \\ &- \left.\left.\left(1-\frac{3\epsilon}{2\eta}+\frac{\kappa}{2\eta^3}\right)\left(\frac{4}{3}-\frac{\epsilon}{\eta}-\frac{3}{2f(\eta)}\right)\left(1-\frac{\epsilon}{\eta}\right)^{-1}\right]\right\}. \end{aligned} \tag{2.106}$$

Using Eq. (2.98), Eq. (2.102), and considering the limit $z \equiv \eta - 1 \ll 1$ (close to the stellar surface) in the small-angle approximation, and also incorporating the boundary conditions, Muslimov & Tsygan (1992) obtain the following expression for the electric potential Φ:

$$\Phi = 12\Phi_0\sqrt{1-\epsilon}(\zeta_0\Theta_0)^3\cos\chi\left\{\kappa\sum_{i=1}^{\infty}\left[\left(e^{-\gamma_i(1)(\eta-1)}-1+\gamma_i(1)(\eta-1)\right)\frac{J_0(k_i\xi)}{k_i^4 J_1(k_i)}\right]\right.$$

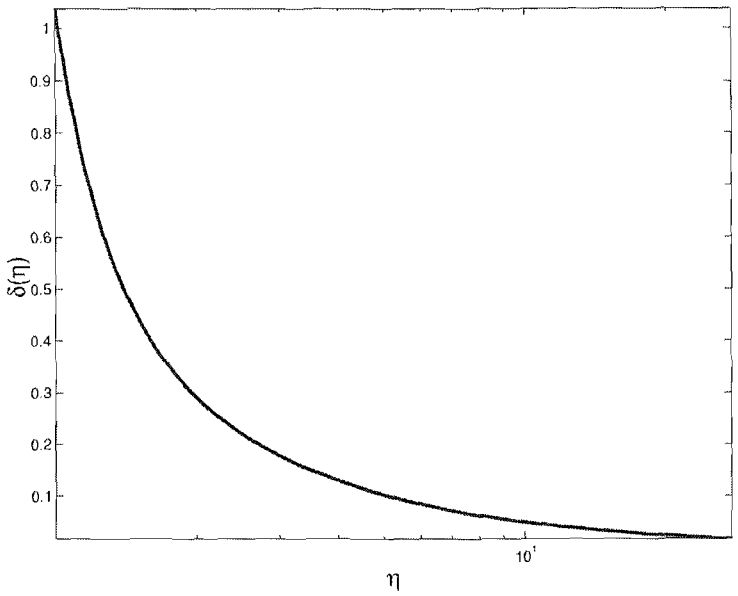

Figure 2.8: $\delta(\eta)$ vs. η as in Eq. (2.104) and (2.106), with $\epsilon = 0.4660$ and $\kappa = 0.1482$.

$$+ \quad \frac{1}{2}\zeta_0\Theta_0 H(1)\delta(1)\sin\chi\cos\phi\sum_{i=1}^{\infty}\left[\left(e^{-\tilde{\gamma}_i(1)(\eta-1)} - 1 + \tilde{\gamma}_i(1)(\eta-1)\right)\frac{J_1(\tilde{k}_i\xi)}{\tilde{k}_i^4 J_2(\tilde{k}_i)}\right]\Bigg\}, \quad (2.107)$$

with

$$\gamma_i(\eta) = \frac{k_i}{\eta\zeta(\eta)\Theta(\eta)\sqrt{1-\epsilon/\eta}} \quad (2.108)$$

$$\tilde{\gamma}_i(\eta) = \frac{\tilde{k}_i}{\eta\zeta(\eta)\Theta(\eta)\sqrt{1-\epsilon/\eta}} \quad (2.109)$$

$$\Phi_0 \equiv \frac{B_0\Omega R^2}{c}, \quad (2.110)$$

and k_i and $\tilde{k}_i$ are the positive roots of the Bessel functions J_0 and J_1. To a very good approximation, $k_{i+1} \approx k_i + \pi$, $i = 1, 2, 3, \ldots$ with $k_1 = 2.40482556\ldots$ and $\tilde{k}_{i+1} \approx \tilde{k}_i + \pi$, $i = 1, 2, 3, \ldots$ with $\tilde{k}_1 = 3.83170597\ldots$ The approximation becomes even better when it is implemented for $i > 2$ or higher (e.g. when the true values of k_1 and k_2 are first used to calculate k_3, and not the recursive relation above). Using Eq. (2.107) and the fact that $E_{||} \approx E_r$ in this region, Muslimov & Tsygan (1992) and Muslimov & Harding (1997) obtain:

$$E_{||} = -\frac{\Phi_0}{R}\left\{12\kappa(\zeta_0\Theta_0)^2 s_1\cos\chi + 6s_2(\zeta_0\Theta_0)^3 H(1)\delta(1)\sin\chi\cos\phi\right\}, \quad (2.111)$$

with

$$s_1 = \sum_{i=1}^{\infty} \frac{J_0(k_i\xi)}{k_i^3 J_1(k_i)} \mathcal{F}_1(\gamma_i(1), \eta) \tag{2.112}$$

$$s_2 = \sum_{i=1}^{\infty} \frac{J_1(\tilde{k}_i\xi)}{\tilde{k}_i^3 J_2(\tilde{k}_i)} \mathcal{F}_1(\tilde{\gamma}_i(1), \eta) \tag{2.113}$$

$$\mathcal{F}_1(\gamma, \eta) = 1 - e^{-\gamma(1)(\eta-1)}, \tag{2.114}$$

and $\gamma(1)$ may be $\gamma_i(1)$ or $\tilde{\gamma}_i(1)$ in the last expression (see Eq. [2.108] and [2.109]). Note that the parallel E-field $E_{||}(\eta = 1) = 0$ as required by the boundary conditions.

Muslimov & Tsygan (1992) give an additional factor η^{-1} in Eq. (2.107), i.e. Φ_0/η instead of Φ_0, the inclusion of which introduces the problem that Eq. (2.111) does not follow from Eq. (2.107). We will ignore this factor and use Eq. (2.111) as derived by Muslimov & Harding (1997).

2.4.3 No Upper PFF – Distant Case ($\eta \gg 1$)

This is the case of no upper PFF and for height $R_{\rm PC} < h < R_{\rm LC}$. Harding & Muslimov (1998) give the expression for ρ valid for any radius (see Eq. [2.102])

$$\rho = -\frac{\Omega B_0}{2\pi c \alpha \eta^3} \frac{f(\eta)}{f(1)} \left[(1-\kappa)\cos\chi + \frac{3}{2}\zeta_0\Theta_0 H(1)\xi \sin\chi\cos\phi \right], \tag{2.115}$$

from which implies an electric potential (Muslimov & Tsygan, 1992; Harding & Muslimov, 1998)

$$\Phi = \frac{1}{2}\Phi_0 (\zeta_0\Theta_0)^2 \left\{ \kappa \left(1 - \frac{1}{\eta^3}\right)\cos\chi + \frac{3}{4}\left[\zeta(\eta)\Theta(\eta)H(\eta) - \zeta_0\Theta_0 H(1)\right]\xi\sin\chi\cos\phi \right\} \left(1-\xi^2\right). \tag{2.116}$$

It should be noted that Eq. (2.116) satisfies the boundary conditions $\Phi_{|\xi=1} = 0$ and $\Phi_{|\eta=1} = 0$. Since the radial component of the electric field more or less coincides with $E_{||}$ in the region of the PC, where the magnetic field is close to being radial, one may write

$$\begin{aligned} E_{||} &\simeq -\frac{\partial\Phi}{\partial r} \\ &= -\frac{\partial\Phi}{\partial\eta}\frac{d\eta}{dr} \\ &= -E_0 (\zeta_0\Theta_0)^2 \left\{ \frac{3}{2}\frac{\kappa}{\eta^4}\cos\chi + \frac{3}{8}\zeta(\eta)\Theta(\eta)H(\eta)\delta(\eta)\xi\sin\chi\cos\phi \right\} \left(1-\xi^2\right), \end{aligned} \tag{2.117}$$

with $E_0 \equiv \Phi_0/R$.

2.4.4 Screened $E_{||}$ – Near Case ($\eta \sim 1$)

Let $z \equiv \eta - 1$ be the normalised height above the stellar surface. Let $\eta = \eta_c > 1$ represent the height of the PFF, where the electric field is screened by the electron-positron pairs formed via pair production (the normalised height of the PFF is given by $z_c \equiv \eta_c - 1$). The solution of Poisson's equation with upper boundary condition $E_{||}(\eta = \eta_c) = 0$ in the limit where $z_c \ll 1$ (i.e. close to the stellar surface) and $z \leq z_c$ yields the following expression for the accelerating component of the electric field (Harding & Muslimov, 1998):

$$E_{||} \simeq -E_0(\zeta_0\Theta_0)^3\sqrt{1-\epsilon}\left\{\frac{3}{2}\kappa S_1\cos\chi + \frac{3}{8}\zeta_0\Theta_0 H(1)\delta(1)S_2\sin\chi\cos\phi\right\}, \tag{2.118}$$

with

$$\begin{aligned}
S_1 &= \sum_{i=1}^{\infty}\frac{8J_0(k_i\xi)}{k_i^4 J_1(k_i)}\mathcal{F}(z, z_c, \gamma_i(\eta)) && (2.119)\\
S_2 &= \sum_{i=1}^{\infty}\frac{16J_1(\tilde{k}_i\xi)}{\tilde{k}_i^4 J_2(\tilde{k}_i)}\mathcal{F}(z, z_c, \tilde{\gamma}_i(\eta)) && (2.120)\\
\mathcal{F}(z, z_c, \gamma) &= -[a_1(\gamma\eta - 1)e^{\gamma z} + a_2(\gamma\eta + 1)e^{-\gamma z} + \\
&\quad a_1(1-\gamma) - a_2(1+\gamma)]/(a_1 + a_2) && (2.121)\\
a_1 &= (\gamma\eta_c + 1)e^{-\gamma z_c} - \gamma - 1 && (2.122)\\
a_2 &= \gamma - 1 - (\gamma\eta_c - 1)e^{\gamma z_c}, && (2.123)
\end{aligned}$$

with $\gamma_i(\eta)$ and $\tilde{\gamma}_i(\eta)$ defined in Eq. (2.108) and (2.109). (The argument γ of function $\mathcal{F}$ in Eq. (2.121) may be one of these two). Many simple approximations valid for different regions above the stellar surface may be derived for Eq. (2.118). One such approximation which may be useful was derived by Dyks & Rudak (2000) for a star with $M = 1.4M_\odot$ and $R = 10^6$ cm, and is valid when the PFF height h_c approaches $R_{\rm PC}$:

$$E_{||} \simeq 1.46\frac{B_{12}}{P^{3/2}}h\left(1 - \frac{h}{h_c}\right)f_1(\xi)\cos\chi \text{ Gauss}, \tag{2.124}$$

with $B_{12} = B_0/10^{12}$ G, P the rotation period in seconds, h the height above the stellar surface in cm, and

$$f_1(\xi) = \sum_{i=1}^{\infty}\frac{4J_0(k_i\xi)}{k_i^2 J_1(k_i)}. \tag{2.125}$$

(Dyks (2008, personal communication) points out that the non-GR term has been neglected in their approximation, since it was forseen that this expression would only be used for nearly-aligned pulsars. For general inclination angles, an azimuthal dependence has to be taken into account as well,

possibly impacting the results described in Section 3.7.2).

2.4.5 Screened $E_{||}$ – Distant Case ($\eta \gg 1$)

In the limit $z \equiv \eta - 1 \gg \zeta_0\Theta_0$ and $z_c \equiv \eta_c - 1 \gg \zeta_0\Theta_0$, Harding & Muslimov (1998) give the following expression for $E_{||}$:

$$E_{||} \simeq -E_0(\zeta_0\Theta_0)^2 \left\{ \frac{3\kappa}{2\eta^4} S_1' \cos\chi + \frac{3}{8}\zeta(\eta)\Theta(\eta)H(\eta)\delta(\eta)S_2' \sin\chi\cos\phi \right\}, \tag{2.126}$$

with

$$S_1' = \left(1-\xi^2\right) - \left(\frac{\eta}{\eta_c}\right)^3 \sum_{i=1}^{\infty} \frac{8J_0(k_i\xi)}{k_i^3 J_1(k_i)} \mathcal{F}_2(\gamma_i(\eta_c), \eta_c, \eta) \tag{2.127}$$

$$S_2' = \xi\left(1-\xi^2\right) - \frac{\eta_c}{\eta}\frac{\zeta(\eta_c)\Theta(\eta_c)H(\eta_c)\delta(\eta_c)}{\zeta(\eta)\Theta(\eta)H(\eta)\delta(\eta)} \sum_{i=1}^{\infty} \frac{16J_1(\tilde{k}_i\xi)}{\tilde{k}_i^3 J_2(\tilde{k}_i)} \mathcal{F}_2(\tilde{\gamma}_i(\eta_c), \eta_c, \eta) \tag{2.128}$$

and in this case

$$\gamma_i(\eta_c) = \frac{k_i}{\zeta(\eta_c)\Theta(\eta_c)\eta_c\sqrt{1-\epsilon/\eta_c}} \tag{2.129}$$

$$\tilde{\gamma}_i(\eta_c) = \frac{\tilde{k}_i}{\zeta(\eta_c)\Theta(\eta_c)\eta_c\sqrt{1-\epsilon/\eta_c}}, \tag{2.130}$$

and lastly,

$$\mathcal{F}_2(\gamma_i(\eta_c), \eta_c, \eta) = e^{-\gamma_i(\eta_c)(\eta_c-\eta)}. \tag{2.131}$$

2.4.6 High-altitude $E_{||}$ for MSPs

New expressions for the E-field of pair-starved pulsars for very high altitudes have been obtained by Muslimov & Harding (2004b). This E-field is dependent on a best-fit radial parameter η_c which is a function of χ, ϕ, and P. Since the E-field drops as η^4, the E-field is very small at these altitudes, and makes less of a contribution to the high-energy part of the CR spectrum. Also, this expression reduces back to Eq. (2.117) for lower altitudes. The parameter η_c further complicates matters. We therefore opt to keep using the above expressions in subsequent work, where the most important part of the gamma-ray spectrum is expected to be produced closer to the NS surface (i.e. excluding the highest altitudes which lead to off-beam radiation), where the E-field is still large (Muslimov & Harding, 2004b). In Chapter 6, we will briefly consider some model refinements which may be implemented in future, e.g. including a E_ϑ-component in the definition of the accelerating E-field (Section 6.1).

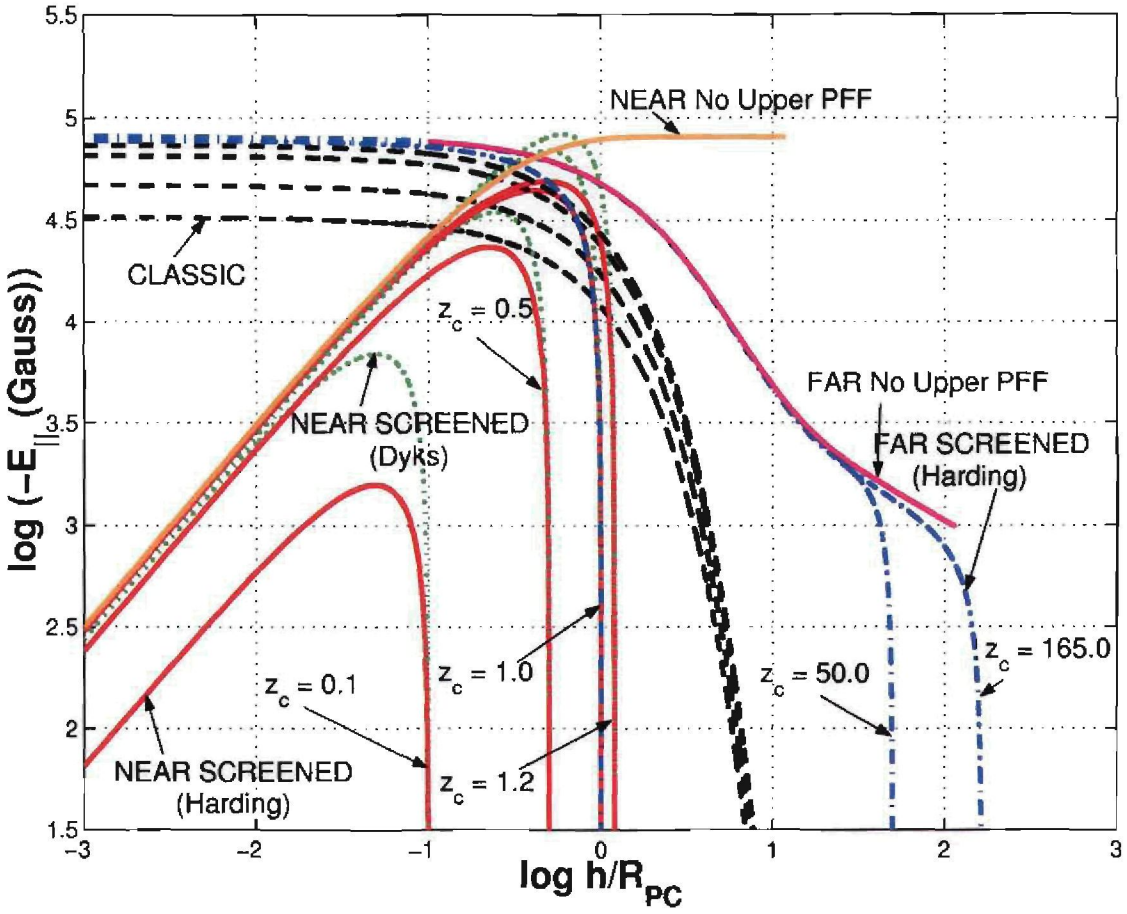

Figure 2.9: Graphs of the different expressions for $E_{||}$ as functions of height above the stellar surface scaled with the PC radius. In this graph, z_c is given in units of R_{PC}/R. 'CLASSIC' (the black dashed curves) correspond to Eq. (2.103), 'NEAR SCREENED (Dyks)' (the green dotted curves) to Eq. (2.124), 'NEAR SCREENED (Harding)' (solid red curves coinciding with the 'NEAR SCREENED (Dyks)' at cut-off) to Eq. (2.118), 'FAR SCREENED (Harding)' (blue dash-dotted curves) to Eq. (2.126), 'NEAR No Upper PFF' (solid orange curve rising to a constant value) to Eq. (2.111), and 'FAR No Upper PFF' (solid magenta curve with no cut-off) to Eq. (2.117). Note that the 'NEAR SCREENED (Dyks)' approximation to the 'NEAR SCREENED (Harding)' case is best when $h \sim R_{PC}$. For the screened cases, $E_{||}$ increases linearly in h, after which it is screened at a height h_c (normalised height z_c) and goes to zero. As the PFF height h_c (or z_c) is increased, the graphs for the 'FAR SCREENED (Harding)' case converge smoothly to the 'FAR No Upper PFF' case. One can also see that the 'NEAR No Upper PFF' case intersects the 'FAR No Upper PFF' case at $h \lesssim R_{PC}$ (this point is called η_{break} in Section 2.5.2).

2.5 The Magnetospheric Model for Charged Particle and Photon Transport

In this section we will describe various aspects of the implementation of a numerical code to simulate the magnetosphere of a typical MSP. This includes the description of the coordinate system (Sec-

tion 2.5.1), **E**- and **B**-fields (Sections 2.5.2 and 2.5.3), curvature radius (Section 2.5.4), calculation of surface patches (Section 2.5.5) and path length along the B-lines (Section 2.5.6), and of various angles describing the emission direction (Section 2.5.7), the effect of slippage and aberration (Section 2.5.8), and electron acceleration and losses, as well as photon energies (Section 2.5.9). Lastly, we will also discuss the calculation of spectra, fluxes, and luminosities involving beaming corrections (Section 2.5.10). Detailed results for PSR J0437-4715 and PSR B1821-24 are presented in Chapter 3, while this model is applied to a population study in Chapter 4, as well as the study of cosmic rays leaving the magnetosphere in Chapter 5.

2.5.1 Coordinates

The dipole magnetic field is axially symmetric, while other expressions e.g. the E-field and charge density depend on the azimuthal angle ϕ. We chose to work in the 3D spherical coordinate system where the polar angle ϑ is measured from the B-axis $\vec{\mu}$ (i.e. $\vec{\mu}$ corresponds to $\vartheta = 0$, and ϑ goes up to $\pi/2$ radians for the last closed magnetic field line ($\xi = 1$) at $r = R_{\rm LC}$). The distance r is measured from the origin at the centre of the star, while the magnetic azimuthal angle $\phi = 0$ corresponds to the direction of the rotation axis. Particles are labelled by (scaled) spherical coordinates $(\eta = r/R, \xi = \vartheta/\Theta(\eta), \phi)$ as they move along the B-lines, and radiate CR due to the fact that their motion is constrained along the curved field lines. The ranges for these coordinates are $1 \leq \eta \lesssim c/(\Omega R)$, $0 \leq \xi \leq 1$, and $0 \leq \phi \leq 2\pi$. For constant ϕ, we may transform to a 2D xy-plane using $x = r\sin\vartheta$ and $y = r\cos\vartheta$.

2.5.2 Choice of Electric Field and $\eta_{\rm break}$

The optical depth for pair creation (see Section 2.1.4) is insignificantly small for PSR J0437-4715, as will be shown in Section 3.6.1. Generally, we will use the expressions of Eq. (2.111) and (2.117) for pair-starved (millisecond) pulsars, derived for the near surface ($\eta \simeq 1$) and far ($\eta \gg 1$) unscreened cases, because no PFF will be created. By equating these equations, one may find the position where the two graphs of the nearby and far E-fields coincide. This position was found numerically and it became evident that the radial coordinate where the graphs coincide, $\eta_{\rm break}$, depends mainly on the value of P, and is furthermore quite insensitive to the values of ϕ, ξ, M, R, χ, and $\dot{P}$. Previously (Venter, 2004), we therefore used the approximation $\eta_{\rm break} = 1.065$ (which is exact for $\xi = 0.7$ and $\phi = 60°$ – see Figure 2.11) for PSR J0437-4715, resulting in errors of $\sim 0.3\%$. However, when modelling a population of pulsars, we realised that we should also take different P and $\dot{P}$ into account. We obtained an excellent fit of $\eta_{\rm break} = 1 + 0.0123P^{-0.333}$ as shown in Figure 2.10, and subsequently used this in our code to have a practical way of deciding which E-field approximation to use at different heights above the

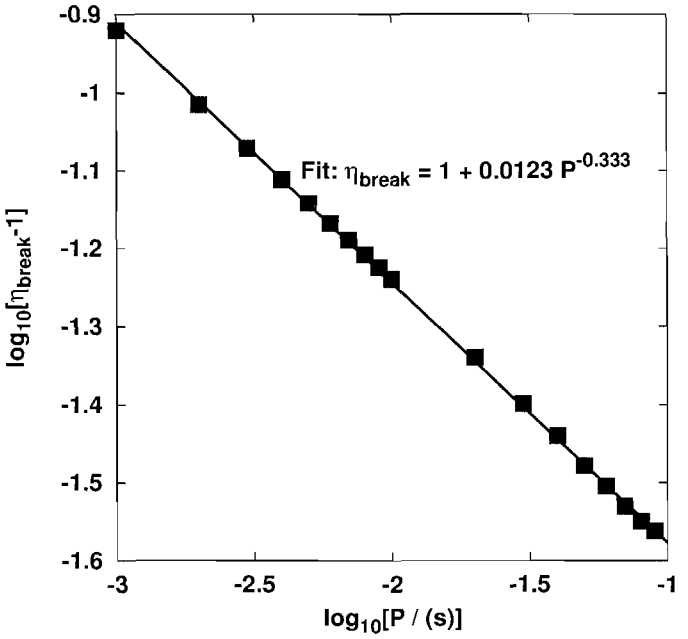

Figure 2.10: The fit for $\eta_{\rm break}$, where the near and far approximations of the E-field coincide (see text for details).

stellar surface.

For pulsars with screened magnetospheres, such as PSR B1821-24 (Section 3.7.1), we use Eq. (2.124) when calculating particle acceleration. We furthermore use $h_c = R_{\rm PC}$ as the PFF height in our calculations.

2.5.3 Magnetic Field

The classical expression for the magnetic field lines is given by

$$r = k \sin^2 \vartheta \tag{2.132}$$

(see Eq. [1.8]), with k a constant labelling the field lines. The corresponding GR-corrected formula was given in Eq. (2.87)

$$\Psi(r) \sin^2 \vartheta = \Psi(R) \sin^2 \vartheta_0, \tag{2.133}$$

which reduces to

$$\vartheta = \sin^{-1} \left\{ [\eta f(1)/f(\eta)]^{1/2} \sin(\xi_* \Theta_0) \right\}, \tag{2.134}$$

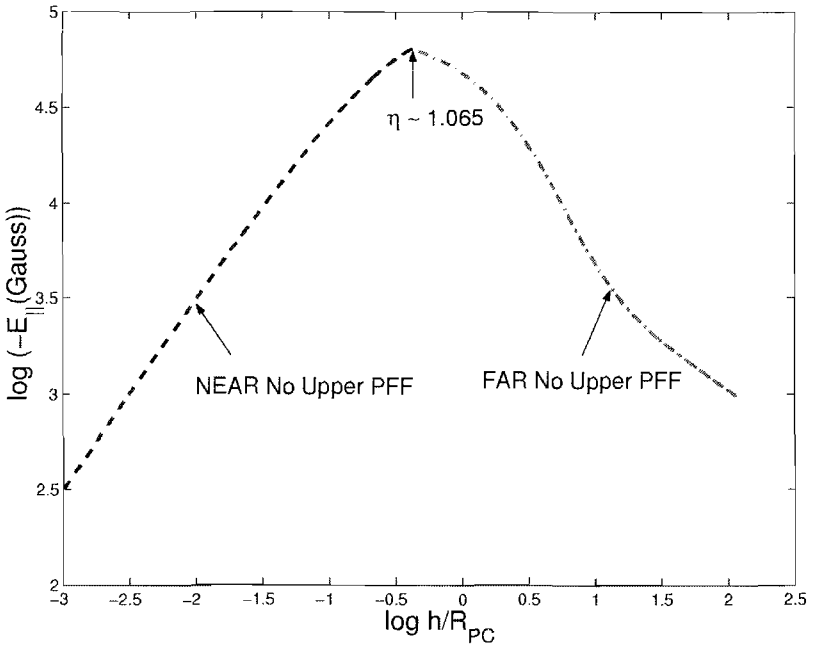

Figure 2.11: The GR-corrected electric field used in the model for PSR J0437-4715 (with $\xi = 0.7$ and $\phi = 60°$ in this figure), assuming that nearly no pair production takes place (see Section 2.5.2). All unscreened MSPs will have similar E-fields, depending on their pulsar parameters, e.g. equation of state (M, R, and I), P, and $\dot{P}$.

with Θ_0 the magnetic colatitude of the last open field line ($\xi = 1$) at the stellar surface (see Figure 2.5). It should be noted that in order to label magnetic field lines uniquely, the values of $\xi(R) = \xi_*$ at the surface (field line footprints) were used. Therefore, when η and ξ_* are specified, the corresponding polar angle $\vartheta(\eta, \xi_*)$ may be calculated using Θ_0 as given by Eq. (2.92). Next, the scaled polar angle, ranging from 0 to 1, is calculated using

$$\xi(\eta) \equiv \vartheta / \Theta(\eta), \tag{2.135}$$

with $\Theta(\eta)$ given by Eq. (2.94).

2.5.4 Curvature Radius

It is important to know the curvature radius ρ_c of the path a particle follows as it radiates, since CR depends on this radius: the characteristic CR energy scales with ρ_c^{-1}, and the CR power with ρ_c^{-2} (see Section 2.1.2).

Generally, the curvature of a curve C defined by the vector function $\mathbf{r}$ at a given point is defined

by (Stewart, 1999a)

$$\kappa' = \left| \frac{d\mathbf{T}}{ds} \right|, \tag{2.136}$$

with $\mathbf{T} = \mathbf{r}'/|\mathbf{r}'|$ the tangent vector, and $\mathbf{r}'(t)$ the derivative of $\mathbf{r}$ with respect to the parameter t according to which the curve C is parametrised. Also, s is the arc length or path length along the curve C. For a 2D case, we may write (Stewart, 1999b)

$$\kappa'(s) = \left| \frac{d\phi'(s)}{ds} \right|, \tag{2.137}$$

where $\phi'(s)$ is the counter-clockwise angle of the tangent at that point as measured from the positive x-axis. If a smooth curve C has parametric equations $x(\vartheta)$ and $y(\vartheta)$, then (Stewart, 1999b)

$$\kappa'(s) = \frac{|\dot{x}\ddot{y} - \ddot{x}\dot{y}|}{[\dot{x}^2 + \dot{y}^2]^{3/2}}, \tag{2.138}$$

with $\dot{x} = dx/d\vartheta$ and $\ddot{x} = d^2x/d\vartheta^2$ and similarly for $\dot{y}$ and $\ddot{y}$. The curvature on each point of a circle of radius R is simply $\kappa' = 1/R$. Generally, the curvature radius of any curve C at a given point is then defined as

$$\rho_{\rm c}(s) = 1/\kappa'(s). \tag{2.139}$$

The classical radius of curvature for a dipolar magnetic field is therefore given by (Daugherty & Harding, 1982)

$$\rho_{\rm c}^{\rm classic}(k,\vartheta) = \frac{k \sin\vartheta (1 + 3\cos^2\vartheta)^{3/2}}{3(1+\cos^2\vartheta)}. \tag{2.140}$$

For the GR case, the geometry is different (see Section 2.3.3). Harding & Muslimov (1998) find that the GR curvature radius is about $\sim 25 - 30\%$ larger than the flat space counterpart for typical pulsar parameters (although we find only a few percent difference). For the GR-corrected $\rho_{\rm c}$, we find

$$\rho_{\rm c} = \left| \frac{T}{N} \right| \tag{2.141}$$

$$T = 2R(a\eta)^{3/2} \left[\frac{K^2}{4} + \frac{(1+PL)^2}{P} \right]^{3/2} \tag{2.142}$$

$$N = aK(Pf(\eta))^{1/2} \left[L \left\{ 2 + P\left(1 + L + \frac{f(\eta)(K-3)}{a\eta} \right) \right\} + K \left[1 - \frac{K(1-f(\eta)/3)}{2} \right] - \left(L + \frac{1}{P} \right) \left\{ K \left(\frac{3}{2} - \frac{f(\eta)}{3} \right) - 3 \right\} \right] \tag{2.143}$$

$$a = f(1)\sin^2(\xi_* \Theta_0) \tag{2.144}$$

$$K = \frac{3\eta}{f(\eta)(\eta - \epsilon)} \tag{2.145}$$

$$L = 1 - \frac{K}{2} \tag{2.146}$$

$$P = \frac{a\eta}{f(\eta) - a\eta}, \tag{2.147}$$

and $f(\eta)$ is defined by Eq. (2.78). Also $\epsilon = 2GM/c^2R$.

2.5.5 Surface Area

Generally, if a smooth parametric surface A is described by a position vector $\mathbf{r}(\vartheta, \phi)$, and A is only covered once as (ϑ, ϕ) ranges throughout the parameter domain D, the surface area of A is given by (Stewart, 1999a)

$$S = \int\int_D |\mathbf{r}_\vartheta \times \mathbf{r}_\phi| \, d\vartheta d\phi. \tag{2.148}$$

We approximate the surface of a NS by a sphere of radius R. A surface patch centred at (R, ξ_*, ϕ), and created by letting ξ_* vary by $\Delta\xi_*$, and ϕ by $\Delta\phi$, is calculated using

$$dS = \int_0^{\Delta\phi} \int_{(\xi_* - d\xi_*/2)\Theta_0}^{(\xi_* + d\xi_*/2)\Theta_0} R^2 \sin\vartheta d\vartheta d\phi \tag{2.149}$$

$$= R^2 \left[\cos\left((\xi_* - d\xi_*/2)\Theta_0\right) - \cos\left((\xi_* + d\xi_*/2)\Theta_0\right)\right]. \tag{2.150}$$

2.5.6 Path Length

The length of a curve C described parametrically by $x = f(\vartheta)$ and $y = g(\vartheta)$, with $\vartheta_1 \leq \vartheta \leq \vartheta_2$, and f' and g' continuous on $[\vartheta_1, \vartheta_2]$, and C traversed only once as ϑ ranges from ϑ_1 to ϑ_2, is given by (Stewart, 1999a)

$$ds = \int_{\vartheta_1}^{\vartheta_2} \sqrt{\left(\frac{dx}{d\vartheta}\right)^2 + \left(\frac{dy}{d\vartheta}\right)^2} \, d\vartheta. \tag{2.151}$$

For electrons moving along a classical dipolar B-field line, $x = k\sin^3\vartheta, y = k\sin^2\vartheta\cos\vartheta$, so that Eq. (2.151) becomes

$$ds = -\frac{k}{2} \int_{p_1}^{p_2} \sqrt{\frac{1}{p} + 3} \, dp, \tag{2.152}$$

with $p = \cos^2\vartheta$. Solving Eq. (2.152) leads to

$$ds = -\left(\frac{k}{2}\right) \left[\left(p + 3p^2\right)^{1/2} + \frac{\sqrt{3}}{6} \ln\left(\sqrt{3}\left(p + \frac{1}{6}\right) + \left(p + 3p^2\right)^{1/2}\right)\right]_{p_1}^{p_2}. \tag{2.153}$$

In the GR case, we find

$$ds = R \int_{\eta_1}^{\eta_2} \sqrt{1 + PL^2} \, d\eta, \tag{2.154}$$

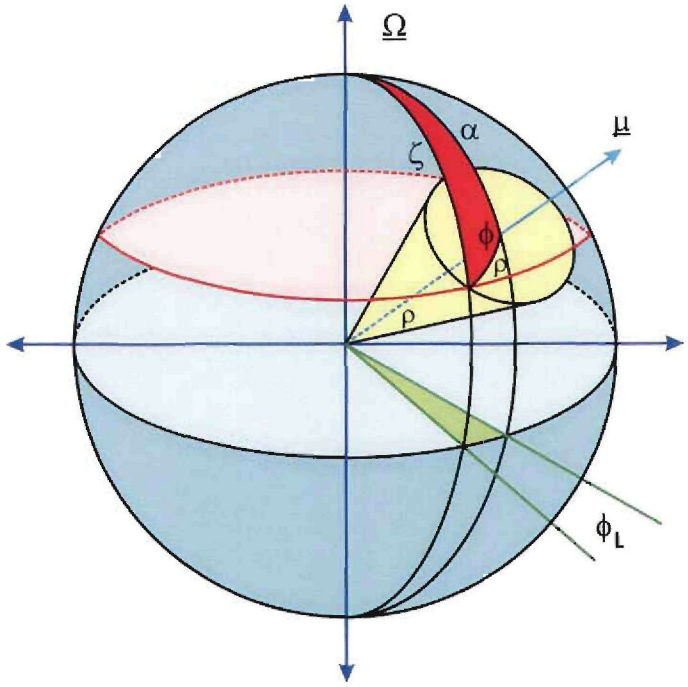

Figure 2.12: Definition of various angles with regards to a beam of radiation along a B-line (also see Figure 1 of Lyne & Manchester, 1988). Shown are the inclination angle $\alpha \equiv \chi$, observer angle ζ, beam opening angle (angle tangent to B-line) ρ, magnetic azimuthal angle ϕ, and phase $\phi_{\rm L}$.

with L and P given by Eq. (2.146) and (2.147). Equation (2.154) was integrated numerically to obtain the distance an electron has travelled along a GR-corrected B-line between coordinates η_1 and η_2.

2.5.7 Calculation of Tangent and Observer Angles Using Spherical Trigonometry

For a given magnetic azimuthal angle ϕ, inclination angle $\chi \equiv \alpha$, and opening angle ρ (see Figure 2.12), we may solve for observer angle ζ using the spherical trigonometric cosine rule (also see Lyne & Manchester, 1988; Story et al., 2007):

$$\zeta = \cos^{-1}\left\{\cos\chi\cos\rho + \sin\chi\sin\chi\cos\phi\right\}. \tag{2.155}$$

Using ζ, we may next solve for the phase angle $\phi_{\rm L}$:

$$\phi_{\rm L} = \cos^{-1}\left\{\frac{\cos\rho - \cos\zeta\cos\chi}{\sin\zeta\sin\chi}\right\}. \tag{2.156}$$

(One may normalise this angle to correspond to the range (0,1) using $0.5 + \phi_{\rm L}/(2\pi)$). For the beam opening angle, we use the angle tangent to the B-field line at the emission point, measured from the spin axis. The classic expression for the B-line slope is given by

$$\frac{dy}{dx} = \frac{1}{3}\left(2\cot\vartheta - \tan\vartheta\right), \tag{2.157}$$

with $x = r\sin\vartheta$ and $y = r\cos\vartheta$. This expression reduces to the well-known approximation $\rho \approx 3\vartheta/2$ when ϑ is small; see e.g. Luo et al. (2000). For the GR dipolar B-field, we find

$$\rho = \tan^{-1}\left\{\frac{\sin\vartheta - \cos\vartheta P^{1/2}L}{\cos\vartheta + \sin\vartheta P^{1/2}L}\right\}, \tag{2.158}$$

where L and P have been defined in Eq. (2.146) and (2.147). When the denominator in the above was negative, we added π to the value of ρ. These angles for the emission direction of the gamma rays should be corrected for Special Relativistic effects when η becomes large, as noted in Section 2.5.8.

2.5.8 Slippage and Aberration

We assume that the curvature photons propagate tangentially to the magnetic field lines at the points of emission. In the observer's frame, there is an aberration effect proportional to the local velocity of rotation. It appears as though the photon is emitted at an angle to the field line, and it follows a curved path (Harding et al., 1978). The corotating observer will however observe the non-aberrated photon travel direction (see Figure 2.13).

Aberration causes the lightcurve to appear asymmetric and furthermore leads to different values for the optical depths of the leading and trailing sides of the PC. As the relative angles between the photon propagation directions and local magnetic field lines of one side of the PC increase, exceeding those of the other side, the optical depths of the side with the greater relative angles will be correspondingly greater due to the enhancement of the perpendicular magnetic field components $B_\perp$ (see Eq. [2.40]). This leads to asymmetrical pulse shapes. Dyks & Rudak (2002) have argued that rotationally-induced propagation effects may lead to asymmetric photon pair production, which may in turn lead to asymmetric gamma-ray pulse profiles if pair production is important.

Slippage takes place when the magnetic pole rotates past a photon ray path, causing the photons to 'see' a time-dependent magnetic field. This will also cause a variation in the optical depth, leading to different pair production rates in different regions of the magnetosphere if the circumstances for pair production are favourable.

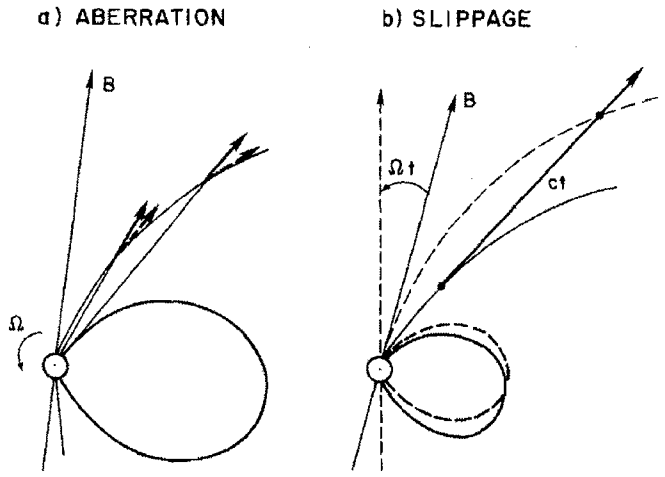

Figure 2.13: Schematic illustration of aberration, which changes the apparent direction of emission from dashed to solid arrow directions, and slippage which causes the photon to experience a time-dependent magnetic field. From Harding et al. (1978).

When considering either low-$\dot{E}_{\rm rot}$ pulsars, where screening will not take place, or only the radiation coming from electron primaries in screened pulsars, we may largely ignore the effects of slippage (although slippage may in some cases lead to significantly lower spectral cut-offs for the leading spectrum as compared to the trailing spectrum, having implications for screened pulsar visibility – Dyks 2008, personal communication). The Special Relativistic effects of aberration and time-of-flight delays, due to a corotation speed of $\beta_{\rm rot} = \Omega r_{\rm em} \sin\zeta/c$, with $r_{\rm em}$ the emission radius, lead to phase shifts of the radiation of (Dyks et al., 2004b; Harding, 2005)

$$\Delta\phi_{\rm ab} \approx \Delta\phi_{\rm tof} \approx -\frac{\Omega r_{\rm em}}{c}, \tag{2.159}$$

so that the non-rotating observer will see radiation arriving at an earlier phase. These effects become large when r becomes a significant fraction of the light cylinder radius (i.e. at large values of $\beta_{\rm rot}$). However, in what follows we will be mainly considering phase-averaged results (except in the case of Section 3.6.6), so that these effects may generally be ignored. The effect of Special Relativity on the observer angle ζ is of order $(\Omega r_{\rm em}/c)^{3/2}$ to $(\Omega r_{\rm em}/c)^2$ (Dyks 2008, personal communication), and will be ignored.

2.5.9 Transport Equation

The change in the energy E_e of a primary electron as it moves along B-lines in the pulsar magnetosphere, is given by

$$\frac{dE_e}{dt} = \left(\frac{dE_e}{dt}\right)_{\text{acceleration}} + \left(\frac{dE_e}{dt}\right)_{\text{losses}}. \tag{2.160}$$

In the MSP model, we only considered CR, neglecting SR and ICS (in Chapter 5, we will also study SR and ICS from PWN). Assuming that the electrons propagate at ultra-relativistic speeds, Eq. (2.160) becomes (see Eq. [2.25])

$$\frac{dE_e}{dt} = e\beta c E_{||} - \frac{2}{3}\left(\frac{e^2 c}{\rho_c^2}\right)\gamma^4, \tag{2.161}$$

with $E_{||}$ the component of the electric field parallel to the magnetic field. The derivation of electrodynamic pulsar expressions were done subject to the boundary condition that the initial speed of an electron is

$$v_0 = c \tag{2.162}$$

at the stellar surface (e.g. Muslimov & Tsygan, 1992). This is justified, since the electrons will become relativistic within a few cm above the surface. For practical implementation, we assumed $v_0 = 0.9999c$. When computing spectra, we assumed that each photon acquired the characteristic CR energy (see Eq. [2.27])

$$E_\gamma = E_\gamma^c = \frac{3}{2}\left(\frac{\lambda_c}{\rho_c}\right)\gamma^3. \tag{2.163}$$

The incremental change in the Lorentz factor γ of the electron during a time interval $\Delta t = ds/v$ is then given by

$$\Delta\gamma = \left[\frac{1}{m_e c^2}\left(e\beta c E_{||} - \frac{2}{3}\left(\frac{e^2 c}{\rho_c^2}\right)\beta^4\gamma^4\right)\right]\frac{ds}{v}, \tag{2.164}$$

with $v = c(1 - 1/\gamma^2)^{1/2}$, and β, $E_{||}$, ρ_c, γ, ds, and v are functions of (r, ϑ, ϕ). This expression is used in the numerical simulation program to solve for γ, and calculate spectra and photon energies. In order to increase computation speeds, we used exponential step lengths in some cases (Section A.7), instead of linear ones.

2.5.10 Calculating Spectra, Fluxes, and Luminosities involving Beaming Corrections

In subsequent chapters, we will be interested in predicting the gamma-ray spectra, fluxes, and luminosities expected from MSPs, and whether the MSPs will be visible for a given telescope or not. Furthermore, a key geometrical issue in pulsar physics is that of correctly relating the observed (slice)

flux / luminosity to the beam-integrated flux / luminosity. This transformation is characterised by a geometrical factor involving the beaming solid angle by which the observed energy flux has to be multiplied in order to obtain the beam-integrated flux. Some have taken this multiplicative correction factor to be unity in the absence of a better value. This geometric correction may however be calculated from first principles using a pulsar model. Below, we will derive this correction, and present other details of our spectra and luminosity calculations.

The observed photon spectrum (for a specific observer angle ζ) is calculated by (e.g. Venter & de Jager, 2005a)

$$\left(\frac{dN}{dE}\right)^{\rm slice}(E,\chi,\zeta) = \frac{1}{\Delta\Omega^{\rm slice} d^2 dE}\iiint_{\zeta-d\zeta/2}^{\zeta+d\zeta/2}\left[\frac{dL}{d\phi_L\, dE\, d\zeta}\right]\frac{I(E,dE)}{E_\gamma^{\rm c}}\, d\phi_L\, dE\, d\zeta \quad (2.165)$$

$$= \frac{\beta^{\rm slice}}{\Delta\Omega^{\rm patch} d^2 dE}\iiint_{\zeta-d\zeta/2}^{\zeta+d\zeta/2}\left[\frac{dL}{d\phi_L\, dE\, d\zeta}\right]\frac{I(E,dE)}{E_\gamma^{\rm c}}\, d\phi_L\, dE\, d\zeta \quad (2.166)$$

$$= \frac{\beta^{\rm slice}}{\Delta\Omega^{\rm patch} d^2}\frac{dL(E)}{EdE}. \quad (2.167)$$

The incremental gamma-ray luminosity dL is calculated for each time-step as the primary electrons are accelerated along the B-field lines and radiate CR. Primary electrons leave a stellar surface patch dS relativistically ($\beta_0 = v_0/c \sim 1$) at a rate of $d\dot{N}_e = \rho_e dS\beta_0 c/e$, where ρ_e is the charge density. They radiate CR at a characteristic energy of $E_\gamma^{\rm c} = 1.5\lambda_c\gamma^3 m_e c^2 \rho_c^{-1}$ (Eq. [2.27]). The CR is associated with an incremental gamma-ray luminosity of $dL = d\dot{N}_e \dot{E}_{\rm CR} dt$, which is radiated in a time dt. The CR loss rate is given by $\dot{E}_{\rm CR} \approx 2e^2 c\gamma^4/(3\rho_c^2)$ (Eq. [2.25]). Therefore, dL is associated with phase angle $\phi_{\rm L}$ and observer angle ζ, giving the direction of the emission, as well as the energy of the radiation. We accumulate the values of dL as we follow primary electrons moving along B-lines above the PC, after which we bin them according to the photon energy. We use the dimensionless indicator function $I(E,dE)$ to pick out radiation in the energy range $(E, E+dE)$: $I(E,dE)$ is unity when the characteristic CR energy is in the particular bin with energy range $(E, E+dE)$, and zero otherwise. (This is shorthand for indicating a binning procedure, where dL/E is sorted according to energy, and then the sorted values of each bin are added to give the total dL/E per energy bin). The resulting spectrum / rate dL/E is next divided by the energy bin size dE, as well as the area of an azimuthal slice projected from the pulsar to a distance d to earth: $\overline{\Delta\Omega}^{\rm slice} = \overline{\Delta\Omega}^{\rm patch}/\beta^{\rm slice} = 2\pi\sin\zeta d\zeta$, since $\overline{\Delta\Omega}^{\rm patch} = \sin\zeta d\zeta \Delta\phi_L$ and the $\beta^{\rm slice} = \Delta\phi_L/2\pi$. The normalised pulse width (duty cycle) $\beta^{\rm slice}$ is thus used to calculate the phase-averaged spectrum. (See Section A.6 in the Appendix for more information on the binning procedure; here the bar indicates the solid angle averaged over all energies).

The photon spectrum calculated over the whole beam of the PC is given by

$$\left(\frac{dN}{dE}\right)^{\rm beam}(E,\chi) = \frac{1}{\overline{\Delta\Omega}^{\rm beam} d^2 dE} \iiint \left[\frac{dL}{d\phi_L\, dE d\zeta}\right] \frac{I(E,dE)}{E_\gamma^c}\, d\phi_L\, dE\, d\zeta. \tag{2.168}$$

The superscript 'slice' is intended to distinguish the (phase-averaged) observed quantity, which is calculated as a function of observer angle ζ, from the total value of the same quantity calculated for the total beam from the PC (integrated over ζ), indicated by superscript 'beam'. Typically, $\sim 10^6$ values of $dL/(d\phi_L\, dE\, d\zeta)$ were used when calculating $(dN/dE)^{\rm slice}$, compared to the $\sim 5 \times 10^7$ values that were generated for the case of the full beam. The luminosity for the beam from one PC is straightforwardly defined as

$$L_\gamma^{\rm beam} = \iiint \left[\frac{dL}{d\phi_L\, dE\, d\zeta}\right] d\phi_L\, dE\, d\zeta, \tag{2.169}$$

while the observer's luminosity $L_\gamma^{\rm slice}$, i.e. that part of the beam-integrated luminosity which is radiated into a slice defined by ζ and $d\zeta$, is calculated by

$$L_\gamma^{\rm slice} = \iiint_{\zeta-d\zeta/2}^{\zeta+d\zeta/2} \left[\frac{dL}{d\phi_L\, dE\, d\zeta}\right] d\phi_L\, dE\, d\zeta. \tag{2.170}$$

These luminosities may also be recovered using the photon spectra:

$$L_\gamma^{\rm beam} = \overline{\Delta\Omega}^{\rm beam} d^2 \int E \left(\frac{dN}{dE}\right)^{\rm beam} dE \tag{2.171}$$

$$L_\gamma^{\rm slice} = \overline{\Delta\Omega}^{\rm slice} d^2 \int E \left(\frac{dN}{dE}\right)^{\rm slice} dE. \tag{2.172}$$

The phase-averaged observer integral flux is calculated by

$$\overline{F}^{\rm slice}(>E_1) = \int_{E_1}^{\infty} \left(\frac{dN}{dE}\right)^{\rm slice} dE \tag{2.173}$$

$$= \int_{E_1}^{\infty} \left\{ \frac{1}{2\pi d^2 \sin\zeta\, d\zeta dE} \iiint_{\zeta-d\zeta/2}^{\zeta+d\zeta/2} \left[\frac{dL}{d\phi_L\, dE\, d\zeta}\right] \frac{I(E,dE)}{E_\gamma^c}\, d\phi_L\, dE\, d\zeta \right\} dE. \tag{2.174}$$

The phase-averaged energy flux firstly has to be scaled up using the pulse width (see Figure 3.17). This is because the observer sees an average value, but the pulsar is actually radiating a higher value equal to the pulse peak over the full azimuthal range. Correction for this effect is done by dividing the observed energy flux by the normalised pulse width $\beta^{\rm slice}$. Secondly, the observed energy flux is a function of ζ. Since the radiation beam is not uniform nor symmetrical, one has to apply a correction for each ζ-slice. Typically, the larger the impact angle $\beta' = \zeta - \chi$, the lower the energy flux. In order

to scale up to the correct beam-integrated luminosity, one needs a factor $\epsilon(\chi,\zeta)$ which will be defined using Eq. (2.171) and (2.172). We therefore scale the observed energy flux up to the beam-integrated energy flux using two correction factors:

$$\int E\left(\frac{dN}{dE}\right)^{\rm beam} dE = \left(\frac{\epsilon}{\beta^{\rm slice}}\right)\int E\left(\frac{dN}{dE}\right)^{\rm slice} dE. \tag{2.175}$$

This becomes

$$\begin{aligned} L_\gamma^{\rm beam} &= \overline{\Delta\Omega}^{\rm beam} d^2 \int E\left(\frac{dN}{dE}\right)^{\rm beam} dE && (2.176)\\ &= \overline{\Delta\Omega}^{\rm beam} d^2 \left(\frac{\epsilon}{\beta^{\rm slice}}\right)\int E\left(\frac{dN}{dE}\right)^{\rm slice} dE && (2.177)\\ &= \left(\frac{\overline{\Delta\Omega}^{\rm beam}\epsilon}{\overline{\Delta\Omega}^{\rm slice}\beta^{\rm slice}}\right) L_\gamma^{\rm slice} && (2.178)\\ &= \left(\frac{\overline{\Delta\Omega}^{\rm beam}}{\overline{\Delta\Omega}^{\rm patch}}\right)\epsilon L_\gamma^{\rm slice} = \alpha_{\rm L} L_\gamma^{\rm slice}. && (2.179) \end{aligned}$$

The physical interpretation of $\alpha_{\rm L}$ is therefore that the scaling of the luminosity from the slice to the total beam luminosity involves two parameters: (i) it is firstly scaled by the ratio of the beaming angles for the beam and the patch, and (ii) it is scaled to be equal to a luminosity which is averaged over the beam. The second scaling will lower the beam luminosity if the impact angle is small, implying a slice luminosity larger than the beam average (so as not to overestimate the beam luminosity), and will scale up the slice luminosity in the case of off-beam radiation. The definition of the parameter ϵ follows from Eq. (2.179):

$$\epsilon \equiv \frac{\beta^{\rm slice}\int E\,(dN/dE)^{\rm beam}\,dE}{\int E\,(dN/dE)^{\rm slice}\,dE}. \tag{2.180}$$

Finally, define the geometrical beaming correction factor Λ:

$$\Lambda \equiv \frac{\epsilon\overline{\Delta\Omega}^{\rm beam}}{\beta^{\rm slice}} = 2\pi\sin\zeta d\zeta\left(\frac{L_\gamma^{\rm beam}}{L_\gamma^{\rm slice}}\right). \tag{2.181}$$

One may then lastly formally obtain an expression for the beam luminosity:

$$\begin{aligned} L_\gamma^{\rm beam} &= \alpha_{\rm L} L_\gamma^{\rm slice}\\ &= \left(\frac{\Lambda}{\overline{\Delta\Omega}^{\rm slice}}\right)\overline{\Delta\Omega}^{\rm slice} d^2\int_0^\infty E\left(\frac{dN}{dE}\right)^{\rm slice} dE\\ &= \Lambda d^2 U^{\rm slice}, && (2.182) \end{aligned}$$

using the definition of the energy flux

$$U^{\rm slice} \equiv \int_0^\infty E \left(\frac{dN}{dE}\right)^{\rm slice} dE. \tag{2.183}$$

Alternatively, we may write

$$\begin{aligned} L_\gamma^{\rm beam} &= \Lambda d^2 \overline{E} \int_0^\infty \left(\frac{dN}{dE}\right)^{\rm slice} dE \\ &= \Lambda d^2 \overline{E} F^{\rm slice}, \end{aligned} \tag{2.184}$$

where

$$\overline{E} \equiv \frac{\int_0^\infty E(dN/dE)^{\rm slice}\, dE}{\int_0^\infty (dN/dE)^{\rm slice}\, dE}, \tag{2.185}$$

and

$$F^{\rm slice} \equiv \int_0^\infty \left(\frac{dN}{dE}\right)^{\rm slice} dE. \tag{2.186}$$

If the photon spectrum is measured, one may immediately obtain $\overline{E}$ via (numerical) integration, and then estimate the gamma-ray efficiency η_γ using (2.184). However, if the spectrum is not available, one may constrain η_γ as follows. Let us define

$$\tau \equiv \frac{\overline{E}}{E_0} \tag{2.187}$$

to obtain

$$L_\gamma^{\rm beam} = \Lambda d^2 \tau E_0 F^{\rm slice}, \tag{2.188}$$

where E_0 is the CR cut-off energy, and it turns out that typically $\tau \sim 1$ (see Figure 4.12). Model integral flux curves may be fitted to upper limits, implying an upper limit for the beam luminosity, and thus η_γ. This has been done for PSR J0437-4715 in Section 3.6.5, and for PSR B1821-24 in Section 3.7.5. In general, it therefore follows that the beam luminosity implied by an integral flux curve is roughly proportional to the area under the curve, times a geometrical correction factor accounting for pulsar beaming. This geometric factor Λ may be quite large in the case of off-beam radiation (see Figures 4.11 and 4.18).

Note that Eq. (2.181) cannot be used to solve for $\overline{\Delta\Omega}^{\rm beam}$, since it implicitly assumes that the latter is known when ϵ is calculated via the photon spectrum $(dN/dE)^{\rm beam}$ (Eq. [2.180]). The beaming factor Λ may thus be viewed as an irreducible factor. Trying to disentangle the various terms would require a model-dependent approach. To obtain values for $\overline{\Delta\Omega}^{\rm beam}$ and $\beta^{\rm slice}$, one may bin the incremental

luminosity according to the half-width ρ and magnetic colatitude ϕ, and calculate the integral

$$\overline{\Delta\Omega}^{\rm beam} = \int_0^{\overline{\rho}_{90}} \int_0^{2\pi} \sin\rho \, d\rho \, d\phi \tag{2.189}$$

for the beam of radiation, defined e.g. as the region which contains 90% of the total luminosity $L_\gamma^{\rm beam}$. This corresponds to an average beam angle $\overline{\rho}_{90}$, so that

$$\overline{\Delta\Omega}^{\rm beam} \approx \pi \overline{\rho}_{90}^2 \quad (\text{small } \overline{\rho}_{90}). \tag{2.190}$$

The average beam half angle $\overline{\rho}_{90}$ is obtained from the cumulative graph of $[dL_\gamma/(d\rho\, d\phi)](>\rho)$ vs. ρ. The duty cycle $\beta^{\rm slice}$ may next be estimated as the normalised half-width of the observer lightcurves. Finally, $\overline{\Delta\Omega}^{\rm beam}$ and $\beta^{\rm slice}$ may be used to obtain ϵ. The main quantity of importance however remains the scaling factor $\alpha_{\rm L} = \Lambda/\overline{\Delta\Omega}^{\rm slice}$ between the observer (slice) and total beam luminosities, so the matter of disentangling the various factors which constitute Λ will not be pursued any further.

2.5.11 Correction to CR Spectrum Calculations

To save computational time when computing CR gamma-ray spectra (Section 2.5.10), we have calculated the incremental photon luminosity dL, radiated in an incremental time dt, using the total radiated CR power per electron primary $\dot{E}_{\rm CR} \propto \gamma^4/\rho_c^2$ (obtained when integrating the instantaneous CR power spectrum over energy):

$$dL = \dot{N} dt \dot{E}_{\rm CR}, \tag{2.191}$$

with $\dot{N}$ the number of electron primaries coming from a stellar surface patch per second. We then binned $dL/E_\gamma^{\rm c}$ according to $E_\gamma^{\rm c}$ (see Eq. [2.165]), with $E_\gamma^{\rm c} \propto \gamma^3/\rho_c$ the characteristic CR spectral energy (Section 2.1.2). One may view this technique as a method approximating single primary CR spectra by 'Dirac delta functions' positioned at $E_\gamma^{\rm c}$ (in an energy bin of size dE), and with integrated values (areas) $\propto dL/E_\gamma^{\rm c}/dE$. This approximation indeed saves time, as a single particle CR spectrum (over many photon energies) is approximated by only one point (at one photon energy), and yields values that are reasonably close to more complicated and time-consuming calculations of CR gamma-ray integral fluxes and photon spectra. This is especially true for population studies, where the computation time may become very long for large regions of parameter space and large numbers of population members. Also, the correct value of the total CR gamma-ray power (integrated over the whole PC) is implicitly present in the resulting gamma-ray spectra (and may be recovered as the first energy moment of the photon spectrum – see Eq.[2.172]). An example of spectral results obtained

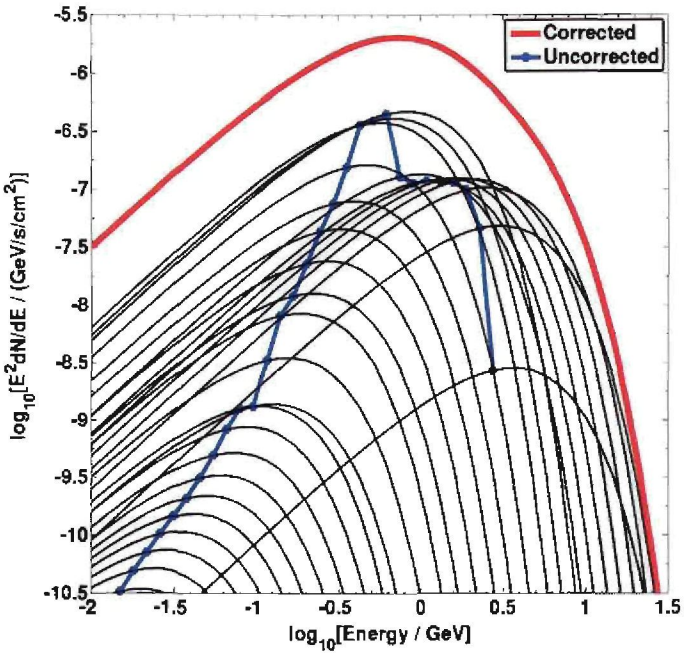

Figure 2.14: Correction of CR spectrum. The blue line represents the old E^2dN/dE-spectrum Y_i. The black lines are the approximate spectra $K_iE^{4/3}\exp(-E/E_i)$ of each bin i, fitted through the point Y_i of the blue spectrum at the energy E_i. The red line represents the corrected spectrum Y_i' (not normalised), which is the sum of all black spectra.

using this method may be seen in Figure 2 of Venter & de Jager (2005a) as well as in Figure 2 of Venter & de Jager (2008a).

It has however been pointed out (Dyks 2008, personal communication) that this method of calculating CR spectra is a bit crude. Firstly, one loses the 'spread' of the radiation over many photon energies when one ignores both the low- and high-energy tails of these single particle spectra. This method therefore leads to very hard low-energy spectral tails, as well as very abrupt high-energy cut-offs. Both of these features imply that the resulting spectra do not compare very well to similar calculations (e.g. Frąckowiak & Rudak, 2005a; Harding et al., 2005b). Addition of low-energy tails should lead to a cumulative E^2dN/dE-spectrum with a low-energy slope of 4/3 (Rudak & Dyks, 1999), while addition of high-energy tails should lead to a broader cumulative spectral cut-off.

To solve this problem, we propose the following correction to transform the values of $E^2dN/dE(E_i) \equiv Y_i$ (as calculated in Section 2.5.10), where $i = 1, 2, ..., N$ signifies the i^{th} energy bin, and E_i the average energy associated with bin i, to Y_i'. Firstly, we approximate the instantaneous CR power spectrum

(see Eq. [2.22]), which gives dN/dE when divided by photon energy, and integrates to $\dot{E}_{\rm CR}$, by

$$\frac{dP_{\rm CR}}{dE} = KE^{-2/3}\exp\left(-\frac{E}{E_\gamma^{\rm c}}\right), \tag{2.192}$$

as motivated by the approximate forms of the integral $y\int_y^\infty K_{5/3}(x)dx$ (see Eq. [2.11] and [2.24]; also note that Story et al. (2007) consider the low-energy approximation, without exponential cut-off, as suitable for their pulsar population study). We note that each point of the spectrum Y_i represents the addition of many single CR (delta) spectra, where only the total power has been used, as explained above. Full CR should however been used. It is reasonable to argue that the sum of full CR spectra at bin i may be approximated by one full (cumulative) CR spectrum with characteristic energy E_i. This leads to the following expression for each (relative) normalisation constant K_i:

$$K_i = \frac{Y_i}{E_i^{4/3}\exp(-1)}. \tag{2.193}$$

To rectify our neglect of full CR spectra, we now calculate the final CR spectrum Y_i' by adding all the cumulative CR spectra fitted through each Y_i (see Figure 2.14):

$$Y_i' = \sum_{j=1}^{N} K_j E_i^{4/3}\exp\left(-\frac{E_i}{E_j}\right). \tag{2.194}$$

When $i = j$, we recover Y_i using the definition of K_i. This calculation leads to the red line in Figure 2.14.

We lastly normalise Y_i' using the total luminosity represented by the νF_ν-spectra (see Section A.7)

$$L_1 = \int_0^\infty E^2\left(\frac{dN}{dE}\right)dE \approx \sum_{i=0}^{N}\frac{Y_i}{E_i}dE_i = \sum_{i=0}^{N} Y_i\delta, \tag{2.195}$$

$$L_2 \approx \sum_{i=0}^{N} Y_i'\delta, \tag{2.196}$$

and multiplying Y_i' by the factor L_1/L_2.

Our correction may lastly be compared to a full calculation of the CR spectrum, using $dP_{\rm CR}/dE$ at each step (i.e. no approximations). We have compared the corrected and full calculation results for the case of PSR J0437-4715, and found that the resulting spectra are very similar. We therefore deemed the corrected CR spectra (requiring less computational time) calibrated and reasonable approximations to the true values (see Figure 2.15, where we also show the integral flux $F(>E) = \int_0^\infty (dN/dE)dE$).

The inclusion of exponential cut-offs in the correction described above leads to broader high-energy

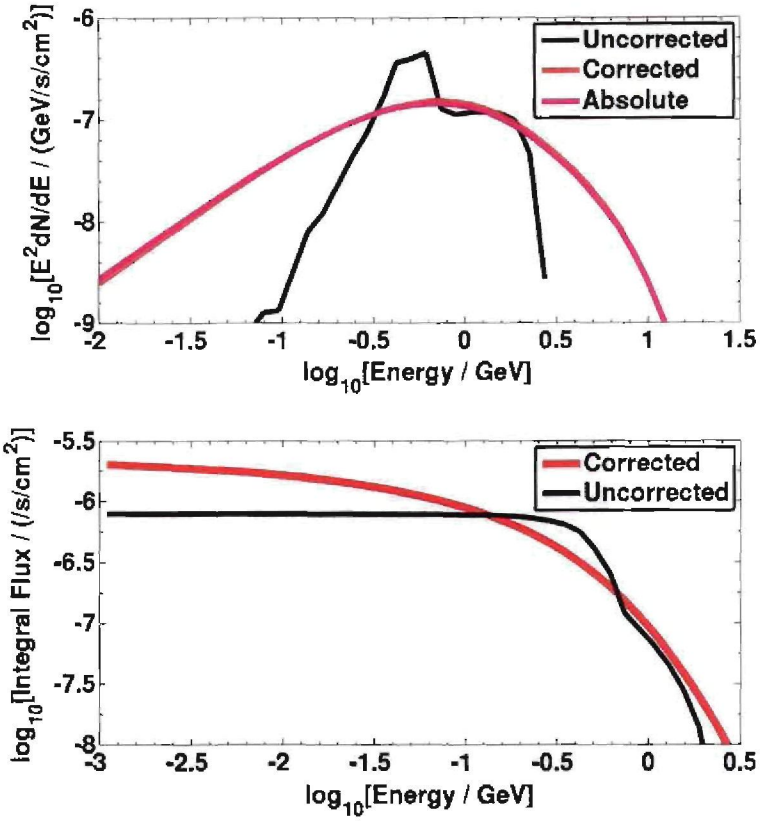

Figure 2.15: Comparison of uncorrected (black line), corrected (red dashed line), and correctly calculated ('absolute'; magenta line) CR spectra for the case of PSR J0437-4715 with $R = 1.5 \times 10^6$ cm, $\chi = 35°$, and $\zeta = 40°$.

tails of the CR spectra. This is an important improvement of our high-energy CR flux predictions, as future ground-based telescopes such as H.E.S.S.-II will probe the tails of CR spectra from pulsar candidates. We have therefore applied the correction described in this section to the results in Sections 3.6.4, 3.7.4, and 4.5.4.

2.5.12 Equation of State (EOS)

Pulsar masses are estimated to range from $1 - 2.5 M_\odot$, depending on the EOS model (Yakovlev et al., 2005), while stellar radii are typically estimated to be a few times 10^6 cm. This leads to typical moments of inertia of $I \sim 10^{45}$ g cm^2. Harding et al. (2002b) performed numerical death line calculations, where they employed NS models standardly used in thermal evolution calculations, plus a strange star model. These NS models correspond to a star with the baryon mass of $1.4 M_\odot$, and different radii and moments of inertia $(R_6, I_{45}) = (1.6, 2.2)$, $(1.1, 1.2)$, $(0.8, 0.6)$, and $(0.7, 0.7)$. Other examples include $(M/M_\odot, R_6, I_{45}) = (1.26, 1.59, 2.28)$, $(1.97, 1.59, 3.9)$, and $(2.64, 1.47, 5.18)$

(see references in Harding et al. (2002b)).

We decided to include the effect of varying the EOS in our model calculations. We however did not to prescribe to any specific EOS model, but used canonical values of $M = 1.4M_{\odot}$ (or $M = 1.58_{\odot}$ in the case of PSR J0437-4715), $R_6 = 1.3 - 1.7$, and $I = 0.4MR^2$. By varying R, and thus I, we could obtain variation in our predicted gamma-ray spectra (see e.g. Figure 3.13).

2.6 Conclusion

This chapter was meant to give an overview of the relevant processes, quantities, and other elements needed for constructing a successful MSP model, as well as to describe the synthesis of all the different concepts when implementing the model in a computer code. Radiation processes relevant to the pulsar magnetosphere were firstly considered: SR (Section 2.1.1), CR (Section 2.1.2), and ICS (Section 2.1.3). When high-energy photons traverse a very strong magnetic field, pair production is expected to ensue. We discussed pair production in Section 2.1.4, distinguishing between the cases where there is no E-field, an E-field is present, or the B-field is superstrong. We also discussed the importance of the presence of an E-field for the pair production rate. In Section 2.1.5, we noted that high-temperature PCs are likely to have a free supply of charge, as the binding energies of both electrons and ions may be exceeded.

Turning to the GR effect of frame dragging, we touched on the Lense-Thirring effect, which describes the precession of intertial frames close to a rotating mass (Section 2.2). In the case of a fast-rotating pulsar, this GR effect enhances the induced E-field over that of the classical value. We described the GR framework of Harding, Muslimov, and Tsygan for the pulsar model described in this Chapter (Section 2.3), mentioning the basic equations (Section 2.3.1), rewriting them in the corotating frame (Section 2.3.2), and obtaining expressions for the GR-corrected B-field (Section 2.3.3), electric potential (Section 2.3.4), and parallel electric field for different scenarios (Section 2.4).

With the basics in place, we next described some details of our implementation of the pulsar model in a computer code. We reported on the coordinate system we used (Section 2.5.1), choices of the **E**- and **B**-fields (Sections 2.5.2 and 2.5.3), the calculation of the curvature radius of B-field lines as a function of position in the pulsar magnetosphere (Section 2.5.4), surface patches (Section 2.5.5), and path length traversed by primary electrons moving along the B-lines (Section 2.5.6). Next, we wanted to calculate high-energy radiation spectra for different observers, and therefore needed various angles describing photon emission directions (Section 2.5.7). We discussed the Special Relativistic effects of slippage and aberration (Section 2.5.8), and justified why these were not explicitly included

in our calculations. We set up and outlined the solution of the transport equation accounting for electron acceleration and losses in Section 2.5.9. From this, the radiation properties of the CR gamma rays may be calculated. Lastly, we discussed the calculation of spectra, fluxes, and luminosities involving beaming corrections (Section 2.5.10), as well as a correction to the calculation of CR spectra (Section 2.5.11), and some comments on the EOS (Section 2.5.12).

The basic pulsar model and its implementation have thus been presented in this chapter, which may be viewed as being in a similar category as Chapter 1, providing background and context for the rest of the thesis. (Some model refinements are considered in Chapter 6, while some mathematical details were relegated to Appendix A). Next, our main aim was to scrutinise this model (Section 1.5) using different applications. We wanted to obtain model predictions for single MSPs, a population of MSPs, and for cosmic rays leaving MSP magnetospheres, and test these against available data in order to derive model constraints. Results on the various applications are presented in Chapters 3 through 5. In addition to studying MSPs as sources of gamma rays and cosmic rays, we also studied PWN using a different model in Chapter 5. In Chapter 7, we will discuss how the basic model fared against the data, and propose model changes that could be taken into account in future.

Chapter 3

Modelling of Single Millisecond Pulsars

Chapter 1 emphasised that millisecond pulsars (MSPs) are cosmic lighthouses which convert rotational energy into radiation and particle energy. These are extreme astrophysical objects: a solar mass packed into a sphere with a radius of about 10 km yields an exceedingly dense, stable, hot stellar remnant, spinning lightning fast, and possessing a magnetic field one billion times that of the earth. It is this (typically assumed dipolar) field which induces the quadrupolar electric field responsible for accelerating electric charges, ripped from the stellar surface, to relativistic energies. The charges' constrained motion along the magnetic field lines in the corotating MSP magnetosphere enables us in principle to validate an MSP's existence in, and investigate its properties at, high-energy wavelengths. However, geometry plays a major role in MSP visibility, and has to be duly taken into account. MSPs thus truly represent invaluable laboratories for testing the laws of nature under utmost conditions.

In Chapter 2, the conceptual basis and resulting theoretical models of isolated MSPs, as well as their implementation as computer code, have been discussed in great detail. The cases of both screened and unscreened electric potentials (Section 2.3.4) have been considered within the context of a General Relativistic (GR) framework. Model implementation included the consideration of the GR effects on the magnetic field and its corresponding curvature radius, as well as on the induced GR electric field which accelerates primary electrons and therefore indirectly imparts energy to the eventually escaping gamma rays. What is yet to be done is to include effects such as light bending, gravitational (Shapiro) time delays, aberration, and redshift, as well as the effect of gravity on the escaping charges.

This chapter presents a first application of the pulsar models developed in Chapter 2, namely results following from the modelling of single, isolated pulsars. We selected the nearby MSP PSR J0437-4715 as an example of a pulsar with an unscreened electric field since it lies below the curvature radiation (CR) death line on a $P\dot{P}$-diagram. (In truth, PSR J0437-4715 has a white dwarf companion, but to

simplify our modelling, we regard it as 'single' for our purposes, neglecting small effects on the gamma rays, e.g. Shapiro delays and light bending, as they traverse the dynamic curved spacetime in the intra-binary region). Also, PSR B1821-24 is currently the MSP (with $P < 10$ ms) with the highest spin-down power $\dot{E}_{\rm rot}$ (Manchester et al., 2005), and we will take it as an example of an MSP with a screened E-field. PSR J0437-4715 and PSR B1821-24 are arguably the best candidates for observation by current gamma-ray telescopes (the first due to its proximity, and the latter due to its high spin-down power), and the study of these two MSPs are therefore justified from an observational point of view, in addition to being archetypes of different classes of MSPs from a theoretical perspective (see Section 1.5 for a fuller motivation).

This chapter is organised as follows. After a brief introduction (Section 3.1), a summary of observations is given in Section 3.2.1 and 3.2.2 for PSR J0437-4715 and PSR B1821-24. We then offer a preliminary 'first look' analysis involving the constraining of the gamma-ray efficiency $\eta_\gamma^{\rm beam}$ of each of these pulsars in Section 3.3. In this Section, we follow a model-independent approach which will provide benchmark values for this important parameter. We furthermore confirmed oscillations in the accelerating GR electric field, as described in Section 3.4. Next, some useful theoretical results are presented (Section 3.5). This is followed by detailed results obtained from numerical modelling using the Harding-Muslimov-Tsygan GR model, including pair production optical depth (Sections 3.6.1 and 3.7.1), CR spectral cut-off energies (Sections 3.6.2 and 3.7.2), electron and photon energies as functions of altitude above the stellar surface (Sections 3.6.3 and 3.7.3), predicted gamma-ray fluxes and visibility (Sections 3.6.4 and 3.7.4), constraints on gamma-ray efficiency (Sections 3.6.5 and 3.7.5), and lightcurves (Section 3.6.6). The culmination of the modelling will be conclusions regarding the visibility of these pulsars for the *High Energy Stereoscopic System Phase I (H.E.S.S.-I)* and future telescopes (Section 3.8). Much of this chapter has been published previously (Venter & de Jager, 2005a; de Jager & Venter, 2005; Venter & de Jager, 2005b; Venter et al., 2005), and also builds on initial efforts of an earlier work (Venter, 2004).

3.1 Introduction

Since the discovery of the first pulsar (Hewish et al., 1968), much theoretical work has been done both in a classical (e.g. Goldreich & Julian, 1969; Sturrock, 1971; Cheng et al., 1986a; Arons, 1983; Beskin & Malyshkin, 1998; Thomas & Gangadhara, 2007) and GR (e.g. Beskin, 1990; Muslimov & Tsygan, 1992; Gonthier & Harding, 1994; Sengupta, 1995; Sakai & Shibata, 2003) framework. In the polar cap (PC) scenario (e.g. Daugherty & Harding, 1996; Rudak et al., 2002; Baring, 2004; Harding,

2007a), a number of papers have been written concerning the development and investigation of a self-consistent GR pulsar model (e.g. Muslimov & Harding, 1997; Harding & Muslimov, 1998; Harding et al., 2002b), along with its observational implications (e.g. Venter & de Jager, 2005a; Harding et al., 2005b; Frąckowiak & Rudak, 2005a,b), since it has been noted (see e.g. Muslimov & Harding, 1997; Dyks et al., 2001) that GR frame dragging in rotating neutron stars is a first order effect which has to be included in a self-consistent model of pulsar magnetospheric structure and associated radiation and transport processes.

Usov (1983) was the first to suggest that the low magnetic field strengths of MSPs allow gamma rays of up to at least 100 GeV to escape pair production. Most MSPs have (largely) unscreened electric fields due to the low optical depths of primary curvature gamma rays for pair production in such low-B pulsar magnetospheres (Harding et al., 2002b). Radiation reaction limited curvature gamma rays up to about 100 GeV from MSPs have been predicted (Harding et al., 2002b; Bulik et al., 2000), making nearby MSPs such as PSR J0437-4715 (Johnston et al., 1993) attractive targets for ground-based gamma-ray groups (Bulik et al., 2000; Venter, 2004). The unscreened case offers a unique opportunity to test fundamental GR quantities (as there are less free parameters in this case), without having to invoke additional modifications such as pair formation fronts (Harding & Muslimov, 1998), with associated slot gaps (Muslimov & Harding, 2003), needed to explain most observations of canonical (high-B) pulsars. The assumption that (nearly) no screening takes place in PSR J0437-4715's magnetosphere was indeed validated *a posteriori* and is also supported by the fact that PSR J0437-4715 has a relatively low spin-down power, inhibiting magnetic pair production (Harding et al., 2002b). This means that the value of the GR derived parallel electric field may be used with confidence in the (more optimal) case of PSR J0437-4715 (see Section 3.6.1). However, PSR B1821-24 has a much larger spin-down power, and we will treat its E-field as screened, modified by the existence of numerous electron-positron pairs (see Section 3.7.1). (See Sections 3.2.1 and 3.2.2 for a background on these MSPs involving multiwavelength observations).

A central question to answer when modelling single MSPs is that of visibility in a particular wave-band for a particular telescope. Two factors determine the visibility of pulsars: spectral cut-off energy and observable flux (de Jager & Venter, 2005). If the cut-off energy is $\gtrsim$ the threshold energy of the telescope, and the flux sensitivity is $\lesssim 0.05\dot{E}/d^2$, with d the distance, VHE gamma rays from a pulsar should be visible. One of the main uncertainties when modelling pulsars, however, is the geometry (i.e. magnetic inclination angle χ between the magnetic and spin axes, and the angle ζ of the observer's line of sight with respect to the spin axis) of the pulsar, which significantly influences predictions of cut-off energy and flux (Sections 3.6.2 and 3.7.2). That these two characteristics determine an MSP's

visibility is most clearly seen in predicted gamma-ray spectra, with telescope sensitivities overlaid (Sections 3.6.4 and 3.7.4). For small CR energy cut-offs, it will be extremely challenging to obtain a pulsed signal from low-energy data when the telescope threshold is not low enough (Section 3.8).

A quantitative numerical MSP model provides the means of constraining fundamental electrodynamic quantities using observations. The effect of GR on MSP spectral cut-offs, pulse profiles, integral flux, and conversion efficiency of spin-down power to gamma-ray luminosity is investigated in this chapter by simulating radiative and transport processes which occur in a pulsar magnetosphere (using a finite-element approach).

Lastly, and quite importantly, the detailed study of single MSPs provides the first step toward a population study (Chapter 4). No adequate population study can be performed which would provide a window on the ensemble averages of quantities as well as trends and general pulsar characteristics, without a clear understanding of the population's building blocks, i.e. single, isolated MSPs.

3.2 Background

3.2.1 PSR J0437-4715

PSR J0437-4715 was discovered in 1993 during a survey of the southern sky for MSPs (Johnston et al., 1993). PSR J0437-4715 is in a 5.7-day period, circular orbit binary system with a low mass companion. It is currently the closest MSP to earth (Manchester et al., 2005), and second closest neutron star (NS), after PSR J0108-1431 (Tauris et al., 1994). Its proximity made detailed study possible, as is evidenced by the large number of papers generated since its discovery (there are currently references to PSR J0437-4715 in over 340 papers).

Shortly after the reported discovery in radio, Becker & Trümper (1993) discovered pulsed X-ray emission believed to be of thermal origin, which may e.g. be caused by a PC heated by particles streaming downward from the magnetosphere. In the same year, Bell et al. (1993) detected an optical companion star, a cool white dwarf, and thereby gathered circumstantial evidence that MSPs' magnetic fields do not decay. Bailyn (1993) argued that his observations revealed an optical companion to PSR J0437-4715, the colour and magnitude of which are consistent with a $0.2M_{\odot}$ helium white dwarf, confirming some earlier indications found by Becker et al. (1993). Both Bailyn (1993) and Danziger et al. (1993) place the companion's temperature at $\sim$ 4000 K, and indicate a cooling time of $\sim 10^9$ yr (which at that time was larger than the MSP's spin-down timescale of $\tau_c = P/2\dot{P}$, prior to the correction of $\dot{P}$).

Using the temperature and magnitude of the companion, Hansen & Phinney (1998) were able to

derive constraints on its mass ($M_c = 0.22M_\odot - 0.375M_\odot$), cooling age ($2.5 - 5.3$ Gyr), and the pulsar initial period ($P_0 < 5.3$ ms; also see Huang & Wu (2003) who estimate $P_0 < 1.05$ ms, and Fernández & Reisenegger (2005) who obtain $P_0 < 5.33$ ms). The cooling age is smaller than the kinematically corrected spin-down age of PSR J0437-4715 of $4 - 50$ Gyr (Hansen & Phinney, 1998). Bell et al. (1995) give a cooling age of $\sim 1 - 4$ Gyr and a pulsar characteristic age of ~ 5 Gyr. This follows from proper motion measurements (agreeing with that of the optical companion, thereby confirming the association) which enabled corrections to $\dot{P}$, influencing spin-down age, luminosity, and magnetic field estimates (also see Camilo et al., 1994; Toscano et al., 1999). Sandhu et al. (1997) furthermore used proper motion results in conjunction with results from Hansen & Phinney (1998) to obtain an upper limit of ~ 180 pc for the pulsar distance, 30% farther than the distance derived from the dispersion measure. Gothoskar & Gupta (2000) found that the scintillation speed for this MSP is nearly double its proper motion speed, and attributes it to scattering from the Local Bubble. Further measurements by Bell et al. (1997) allowed constraints on the orbital inclination angle ($i < 50°$), and companion mass ($M_c > 0.19M_\odot$). Using Shapiro delays, van Straten et al. (2001) determined the MSP and companion masses to be $(1.58 \pm 0.18)M_\odot$ and $(0.236 \pm 0.017)M_\odot$ (see Jacoby et al., 2005, for a similar study involving PSR J1909-3744). In the same paper, extremely accurate values of distance ($d = 139 \pm 3$ pc) and proper motion ($\mu = 140.892 \pm 0.006$ mas/yr) were obtained. Using these, the intrinsic spin period derivative $\dot{P}_{\rm int}$ of $(1.86 \pm 0.08) \times 10^{-20}$ was obtained, which implied an improved characteristic MSP age of 4.9 Gyr. These authors furthermore inferred a value of $i = 42.75°$ for the orbital inclination angle.

Pavlov & Zavlin (1997) obtained pulsar mass and radius constraints of $M < 1.6M_\odot(R/10\ \text{km})$ and $R > 8.8(M/1.4M_\odot)$ km using X-ray spectra and lightcurves. When using a geometry of $\chi = 35°$ and $\zeta = 40°$ (Manchester & Johnston, 1995), they obtained $1.4 < M/R_{10} < 1.6$, and $8.8 < R < 10$ km for $M = 1.4M_\odot$, while extremely low values of $M/R_{10} < 0.3$ (with $R_{10} = R/10$ km), implying $M < 0.5M_\odot$, follows for $\chi = 20°$ and $\zeta = 24°$, as obtained from (Gil & Krawczyk, 1997). (Notice however that Gil & Krawczyk (1997) give $\chi = 20°$ and $\beta' = -4°$, implying $\zeta = 16°$, not $\zeta = 24°$). Accordingly, Sandhu et al. (1997) obtained $0.22M_\odot \leq M_c \leq 0.32M_\odot$ when the MSP mass is assumed to be $1.4M_\odot$. Pavlov & Zavlin (2000) furthermore showed that observed X-ray polarisation is sensitive to the NS mass-to-radius ratio which is needed to constrain the equation of state (EOS) of the superdense matter in NS interiors. Recently, Bogdanov et al. (2007) presented a model for thermal X-ray emission from PSR J0437-4715 and obtained constraints on the radius for a mass of $M = 1.4M_\odot$ ($R = 6.8 - 13.8$ km with 90% confidence, and $R > 6.7$ km with 99.9% confidence).

Bell et al. (1995) confirmed the existence of an Hα nebula (generated by the interaction of the

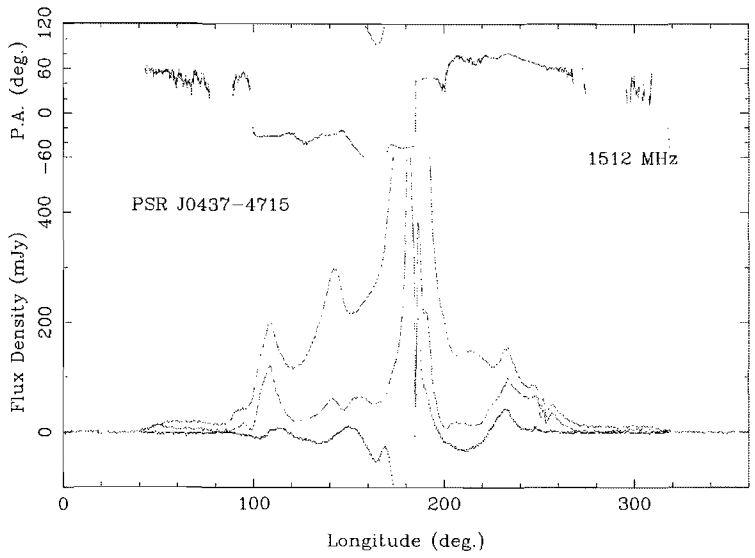

Figure 3.1: Mean pulse profile and polarisation properties of PSR J0437-4715 at 1512 MHz (Navarro et al., 1997). The upper graph shows the position angle of the linearly polarised component (Manchester, 2001). In the lower graph, the top solid line indicates the total intensity (Stokes I), the lower solid line the linearly polarised intensity (Stokes L), and the dotted line is the circularly polarised component (Stokes V). The "double notch" feature may be seen close to 255° longitude.

relativistic pulsar wind with the interstellar medium (ISM)) assosicated with PSR J0437-4715. Because of this MSP's supersonic motion through the ISM, the nebula has the form of a bow shock (earlier seen by Bell et al., 1993). This makes PSR J0437-4715 one of only five pulsar wind bow-shock nebulae observed in Hα (Bucciantini & Bandiera, 2001; Bucciantini, 2002a,b; Bucciantini et al., 2005, also refer to these papers for MHD modelling of bow-shock nebulae). Becker & Trümper (1999) however found no X-ray emission from the side wings of the bow-shock nebula (also see Zavlin et al., 2002).

Mean pulse shape and polarisation parameters obtained for PSR J0437-4715 at 438, 660, and 1512 MHz (Navarro et al., 1997) revealed a very wide and complex pulse profile, covering more than 80% of the period (see Hibschman & Arons, 2001, for modelling). The profile has at least 12 identifiable pulse components and high polarisation (Kramer et al., 1998), both linear and circular (Manchester, 2001). The position angle does not follow the simple rotating-vector model, implying departures from a dipole field configuration in the emission region (Manchester & Johnston, 1995; Navarro & Manchester, 1996; Navarro et al., 1997; Bogdanov et al., 2007). Also, an unusual "double notch" (W-shape) appears close to longitude 255° (see Figure 3.1), and evolves strongly with frequency. This has been modelled in the context of aberration and retardation of the radiation within a pulsar magnetosphere (Wright,

2004), a pulsar absorbing inward radio radiation (Dyks et al., 2005), as well as free electron maser models (Dyks et al., 2007). PSR J0437-4715's pulse width and shape furthermore varies with radiation frequency (McConnell et al., 1996; Kramer et al., 1999). Jenet et al. (1998) investigated single pulse properties of PSR J0437-4715 at 20 cm, and their results include that individual pulses exhibit a wide variety of morphologies, "giant pulses", as have e.g. been observed for the Crab pulsar, are ruled out (also see Li et al., 2003), a significant inverse correlation exists between pulse peak and width, and that overall, the single-pulse properties of PSR J0437-4715 are similar to those of the normal slow-rotating pulsars. Vivekanand et al. (1998) found slow variation of the integrated profile, but no pulse nulling or systematic drifting. Vivekanand (2000) found that radio emission occurs over both short ($\sim$ 0.03 periods) and long (tens to hundreds of periods) timescales, with the short timescale emission occasionally taking the form of intense spikes. Vivekanand (2001) furthermore showed that slow integrated-profile variations seen in one of the components of PSR J0437-4715 are correlated with variations of the spiky emission in that component.

Manchester & Johnston (1995) presented mean pulse polarisation properties of PSR J0437-4715, and inferred that the central strong pulse component is most likely emitted in a direction close to that of the magnetic axis. A least squares-fit of the rotating-vector (dipolar) model to the observed position angle variation did not converge. Parameters providing a reasonable fit were then found ($\chi = 35°$, $\zeta = 40°$). Gil & Krawczyk (1996, 1997) found fits ($\chi = 20°$, $\zeta = 16°$) using a relativistic rotating-vector model, and argued for coherent CR as the radio emission mechanism (see Qiao et al., 2002, for a profile model involving inverse Compton Scattering (ICS)), as well as for a purely dipolar magnetic field. Chen et al. (1998) and Ruderman (2003) furthermore favour alignment of PSR J0437-4715's magnetic and spin axes on theoretical grounds.

After the *Röntgensatellit (ROSAT)* detection of pulsed X-rays from PSR J0437-4715 (Becker & Trümper, 1993), Barret et al. (1994) obtained the first X-ray / soft gamma-ray upper limits for PSR J0437-4715, limiting the hard X-ray conversion efficiency to less than 7×10^{-2}. Subsequently, Edelstein et al. (1995) reported the first detection of extreme UV radiation (100 Å) from an MSP using the *Extreme Ultraviolet Explorer (EUVE)* (also see Korpela & Bowyer, 1998). A very high surface temperature of $\sim 10^5$ K may be responsible for this radiation, requiring surface reheating in view of PSR J0437-4715's old age (according to standard NS cooling models). *EUVE* claimed pulsed emission when Halpern et al. (1996) obtained a light curve for PSR J0437-4715 in the 65 – 120 Å range and presented a combined analysis of the *EUVE* and *ROSAT* data (Becker & Trümper, 1993), reiterating the necessity of a reheating mechanism. Kargaltsev et al. (2004) detected emission in the optical-UV range (1 150 – 1 700 Å), for the first time from an MSP. This radiation is interpreted as

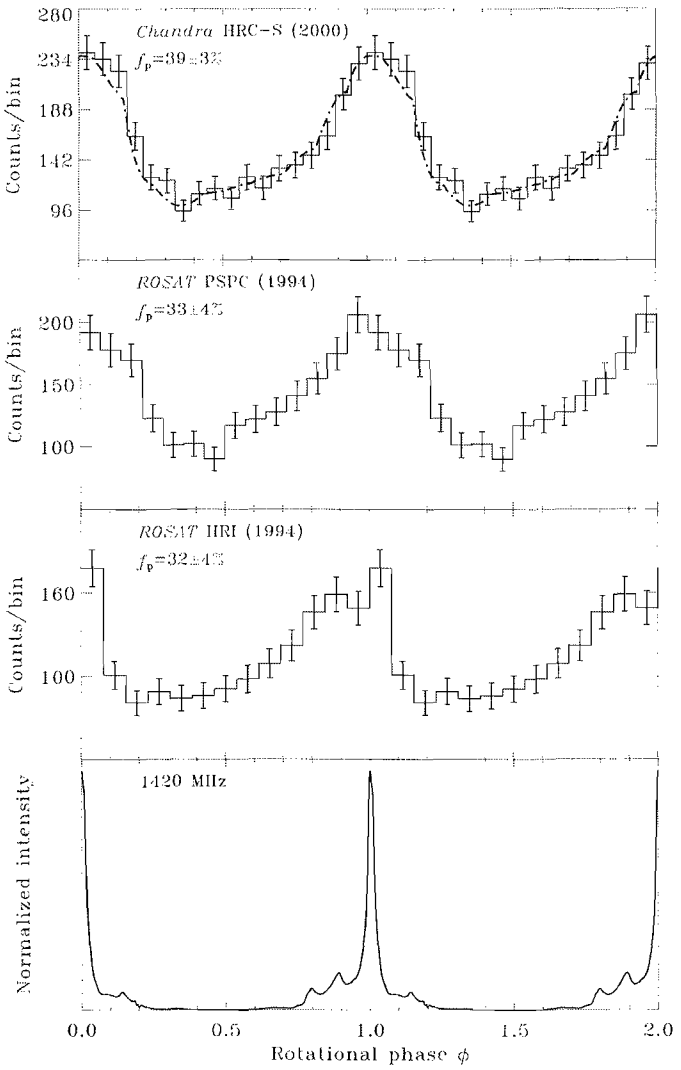

Figure 3.2: X-ray pulse profiles of PSR J0437-4715 from *Chandra*, *ROSAT*, and radio observations. *ROSAT* curves were aligned with that of *Chandra*. The radio and *Chandra* curves are however in phase. Figure from Zavlin et al. (2002).

thermal radiation from an NS surface of $\sim 10^5$ K, also implying the operation of a heating mechanism. No pulsations have however been detected. Circumstantial evidence suggests a magnetic field of $B \sim 7 \times 10^8$ G.

The *Advanced Satellite for Cosmology and Astrophysics (ASCA)* observed PSR J0437-4715 in X-rays, but this observation suffered from significant contamination of the nearby AGN RX J0437-4711 in the same field of view (Kawai et al., 1998). There is marginal evidence for periodic X-ray emission, and a thermal interpretation is preferred. Becker & Trümper (1997) noted that the spectrum of PSR J0437-4715 can be fitted with a power law with a photon index of ≈ -2.4, and an X-ray conversion efficiency

of $\sim 4 \times 10^{-3}$ was found (Becker & Trümper, 1999). Zavlin & Pavlov (1998) regarded this fit, which is an indication of non-thermal soft X-rays, as implausible, and proposed that the observed X-ray radiation originates from two hot PCs with emitting layers comprised of hydrogen (also see Rajagopal & Romani, 1996; Bogdanov et al., 2007). Either a uniform temperature, or a two-component (core & rim) temperature, close to $\sim 10^6$ K, was put forward. Zavlin et al. (2002) attempted to resolve this controversy by using *Chandra X-ray Observatory* data at energies above *ROSAT* and *EUVE* bands. From analysis of combined *ROSAT* and *Chandra* data, they concluded that the pulsar spectrum consists of two components: (i) a non-thermal power-law spectrum, originating within the pulsar magnetosphere, with a photon index of ≈ 2, and (ii) a thermal spectrum emitted by heated PCs, corresponding to a temperature of 2×10^6 K at the centre, and decreasing outwards to 5×10^5 K at the rim. Recently, Bogdanov et al. (2006b) proposed that all soft X-rays are indeed of purely thermal origin, and that the additional faint power-law tail is due to weak Comptonisation of the thermal (blackbody or hydrogen atmosphere) PC emission by energetic electrons / positrons.

Whereas the relative phase between the radio and X-ray pulses of PSR J0437-4715 could not be constrained due to limits of the *ROSAT* clock (Becker & Trümper, 1999), Zavlin et al. (2002) inferred that the phases of the X-ray and radio pulses are virtually the same (within the *Chandra* absolute time; see Figure 3.2). The *X-ray Multi-Mirror Mission* (XMM-Newton) data confirmed conclusions from previous observations that the pulsar spectrum is best fitted by a two-temperature PC model with hydrogen atmosphere, together with a non-thermal power-law component. The pulse phase and pulsed fraction were furthermore found to depend on energy (Zavlin, 2006).

Although no gamma rays have been observed from PSR J0437-4715 yet, Eifert (2005) provided a preliminary analysis of *H.E.S.S.* observations of this MSP, resulting in high-energy upper limits, in addition to the lower-energy *Energetic Gamma-Ray Experiment Telescope (EGRET)* limits given by Fierro et al. (1995). A paper is underway (Aharonian et al., 2008) which will discuss high-energy MSP observations with *H.E.S.S.* This is complementary to an earlier paper giving VHE pulsed upper limits for young pulsars (Aharonian et al., 2007).

3.2.2 PSR B1824-21

Following the discovery of the first MSP (Backer et al., 1982), Alpar et al. (1982) noted that neutron stars with sufficiently low magnetic fields which accrete for long times from a surrounding keplerian disk can be spun up to millisecond periods (also see Backus et al., 1982). Motivated by the suggestion of Alpar et al. (1982) that MSP progenitors are identified with low-mass X-ray binaries (LMXBs), and the fact that there is a great concentration of LMXBs in the cores of globular clusters (GCs), Hamilton

et al. (1985) found a source with an anomalously steep radio spectrum in M28 using the *Very Large Array (VLA)*. Mahoney & Erickson (1985) subsequently observed this source with the *Clark Lake TPT Synthesis Telescope* and inferred a spectral index of -2.44. These authors furthermore noted that only pulsars have well-documented spectra which are as steep as this. Two years later, Lyne et al. (1987) reported the discovery of the isolated MSP PSR B1821-24 (with period $P = 3$ ms) in the core of the GC M28 (also see Middleditch et al., 1987; Kulkarni et al., 1987), following the determination of its spectrum and polarisation properties (Erickson et al., 1987). In the following months, a number of theoretical papers appeared speculating on the origin of MSPs (Romani et al., 1987; Michel, 1987; Verbunt et al., 1987; White & Stella, 1988). For a review of pulsars in GCs, see Camilo & Rasio (2005); Ransom (2008) and references therein.

Foster et al. (1988) next measured a period derivative of $\dot{P} = 1.6 \times 10^{-18}$ ss^{-1}, and concluded that it is intrinsic to the recycled MSP PSR B1821-24, following the pre-discovery suggestion by Blandford et al. (1987) that the pulsar-candidate in M28 may be used to probe the gravitational potential of the cluster core (the effect of which would be detectable as an anomalous period second derivative $\ddot{P}$). Foster et al. (1991) measured the spectral indices of the two main radio pulse components of PSR B1821-24, but their observational sensitivity prohibited their doing the same for the third broad component.

Cognard et al. (1995) measured an apparent second period derivative of $\ddot{P} = 1.6 \times 10^{-30}$ s/s^2 using the *Nançay Radio Telescope*, and found that it was not consistent with the theoretical value implied by a braking index $n = 3$ for a dipolar field, when spin-down is attributed to magnetic coupling. The high value of $\dot{P}$ is probably due to rotation irregularities, rather than processes of gravitational acceleration, unless $\ddot{P}$ is a jerk induced during a close encounter in the GC M28 (Cognard et al., 1996). A contradiction between the optical and radio proper motions was furthermore found. Follow-up observations allowed the determination of secular variations in the dispersion measure, as well as the demonstration that the index of the power-law spatial spectrum of electron density fluctuations in the direction of PSR B1821-24 is consistent with a Kolmogorov turbulent medium (Cognard & Lestrade, 1997). Cognard & Backer (2004) lastly detected a microglitch from PSR B1821-24, the first time from an MSP.

Backer & Sallmen (1997) measured two narrow radio components of the average pulse profiles of PSR B1821-24, 108° apart, with the leading component's spectral index being steeper than that of the second component (indicated by (1) and (2) in Figure 3.3). The third broad component shares the steeper index of component 1. Since components 1 and 3 are $\sim$ 175° apart, Backer & Sallmen (1997) assumed that these originate from different PCs, and fitted a Radhakrishnan-Cooke model

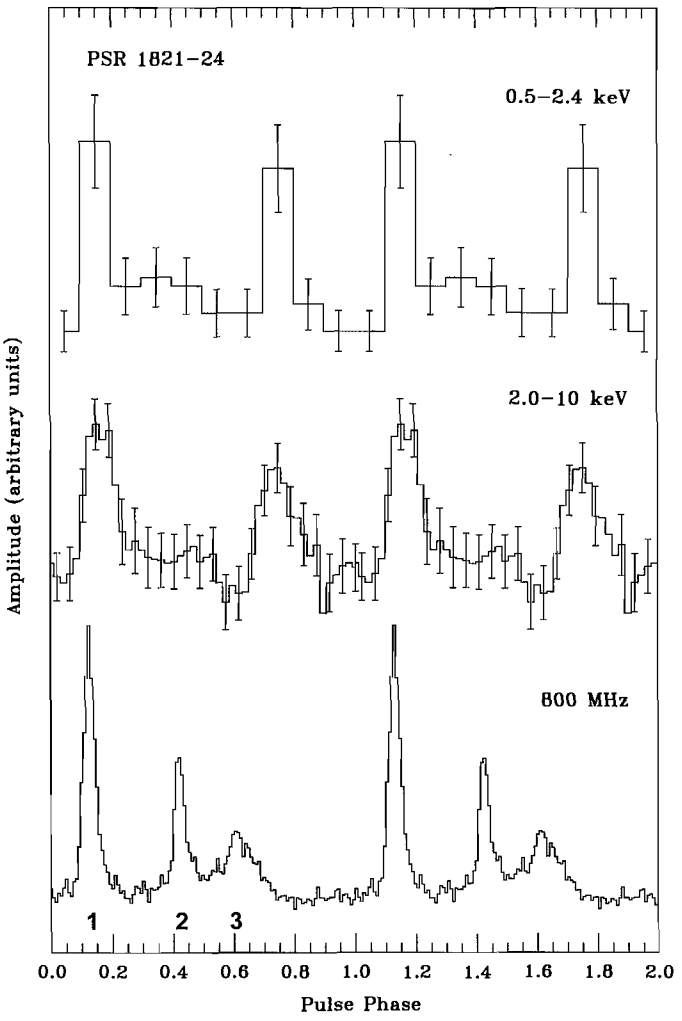

Figure 3.3: Integrated radio and X-ray pulse profiles of PSR B1821-24 as seen by *ROSAT*, *ASCA*, and the *NRAO*. Figure from Becker & Trümper (1999).

with inclination angle $\chi = 50°$ and oberver angle $\zeta = 90°$. The flux of component 2 was furthermore found to be unstable on long timescales at 1 395 MHz, but not at 800 MHz. Absolute alignment of the X-ray and radio intensity profiles was prohibited by inaccurate absolute timing of the *ASCA* data (Saito et al., 1997).

The measured $\dot{P}$ implies a very high spin-down luminosity for an MSP, making PSR B1821-24 a very likely candidate for rotation-powered non-thermal X-ray emission (Backer & Sallmen, 1997). Indeed, Danner et al. (1994) found a faint X-ray source coincident with PSR B1821-24's position, as well as marginal evidence for X-ray pulsations at the radio period, using *ROSAT* (later argued to be spurious by Verbunt (2001)). X-ray pulsations were subsequently confirmed by Saito et al. (1997) and Danner et al. (1997), following upper limits given by Schroeder et al. (1995) in the $70 - 160$ keV band.

Saito et al. (1997) observed a non-thermal double-peak X-ray pulse having a hard power-law spectrum with phase-averaged photon index of ~ 1.9 using *ASCA*. Spectral indices for each of the individual pulses have also been obtained (~ 1.5 and ~ 2.9 respectively). Kawai et al. (1998) confirmed a $\sim 160°$ separation of the two X-ray peaks, similar to the 108° separation obtained for the main radio peaks by Backer & Sallmen (1997), as well as a spectral index of ~ 1.9. Rots et al. (1998) investigated the phase lag between PSR B1821-24's X-ray and radio pulses using the *Rossi X-ray Timing Explorer (RXTE)* and showed that the radio peak precedes the X-ray pulse by 0.02 pulsar periods, while the wide X-ray pulse lags the last of the two wider radio components by 0.08 periods. This was confirmed by Saito et al. (2001) who observed PSR B1821-24 with *RXTE* and found no apparent variation of the pulse profile from 1.6 to 20 keV. The X-ray pulse components have furthermore been extracted, and their energy spectra were both shown to be compatible with a power-law index of 1.1. Becker et al. (2003) measured the unconfused phase-averaged X-ray spectrum of PSR B1821-24 for the first time, and found a best-fit power-law index of ~ 1.2 (also see Testa et al., 2004; Weisskopf et al., 2004). The marginal detection of an emission line at 3.3 keV may provide evidence that the magnetic field is different from a centered dipole. An X-ray efficiency of 5.8×10^{-4} was also inferred.

Rutledge et al. (2004) performed microsecond timing of PSR B1821-24 with *Chandra* and detected two X-ray pulses as well as significant persistent non-pulsed emission (comprising $\sim 15\%$ of the total flux), and emission trailing the main components. They furthermore found that the phases in X-ray wander with respect to the radio ephemeris, likely due to a variable dispersion measure which impacts on the radio arrival times. Concerning the non-pulsed emission, Cheng et al. (2006) recently argued that stellar interactions with the relativistic wind from PSR B1821-24 would likely significantly affect the establishment of a PWN, and that the low level of non-thermal non-pulsed X-ray emission from PSR B1821-24 may therefore rather represent the contribution from the pulsar's magnetosphere. This is because some unpulsed X-ray emission (in the form of nearly isotropic SR) is expected if the distribution of the (large) pitch angles of charged particles in the magnetosphere is uniform.

Using *RXTE*, *BeppoSAX*, and *Chandra* data, Mineo et al. (2004) measured two narrow X-ray peaks separated by a phase distance of 0.45, and obtained a spectral index of 1.3 for the pulsed emission over the range 1.6−20 keV. This index differs only marginally when fitted separately for each of the X-ray peaks. Lastly, a search for X-ray emission that behaves similar to radio giant pulses (concentrated in a narrow window coincident with the X-ray pulse – Romani & Johnston, 2001) yielded a negative result.

From the previous paragraphs on the X-ray emission of PSR B1821-24, it follows that PSR B1821-24 belongs to a group of X-ray MSPs with high spin-down luminosities, exhibiting non-thermal X-ray

emission described by pure power-law spectra of photon index 1.5 to 2, as well as pulsed profiles with strong narrow peaks and large pulsed fractions. This is in contrast with PSR J0437-4715 (see Section 3.2.1) which belongs to a group of MSPs with lower spin-down luminosities, having a thermal X-ray component, with smoother pulsations and lower pulsed fractions (Zavlin, 2006).

Golden et al. (2001) searched for an optical counterpart for PSR B1821-24 using *HST* archive images, but none of the candidates in the radio error circle exhibited emission expected from an MSP which is magnetospherically active. This followed a 4σ upper limit of $0.3L_{\odot}$ for optical pulsed emission from PSR B1821-24, for frequencies up to 500 Hz, limiting the optical efficiency to $< 5\times10^{-4}$, obtained by Middleditch et al. (1988).

Using *EGRET*, Fierro et al. (1995) provided 3σ upper limits to unpulsed gamma-ray emission from PSR B1821-24 above 100 MeV and 1 GeV, updating previous limits by Nel et al. (1992). Results from the *H.E.S.S.* telescope regarding PSR B1821-24 should appear soon (Aharonian et al., 2008).

3.3 Model-Independent Pre-Analysis

This section is meant as prelude, where we consider what may be learned from gamma-ray data alone, with the minimum assumptions involved. Using the most general model, it will be shown that the gamma-ray efficiency $\eta_{\gamma}^{\rm beam}$ of PSR J0437-4715 and PSR B1821-24 may be constrained to a few percent (depending on the geometry) when only a few upper limits are available. Also, the impact of future missions is discussed.

Since this section is only a very basic "first look", PSR B1821-24 is treated as having an unscreened potential in this section only. In later sections (e.g. Section 3.7.4), a screened potential is assumed so as to compare the results with that obtained for the unscreened potential of PSR J0437-4715 (e.g. Section 3.6.4). The efficiencies $\eta_{\gamma}^{\rm beam}$ of PSR J0437-4715 and PSR B1821-24 are constrained in Sections 3.6.5 and 3.7.5 using the GR model.

3.3.1 General Pulsar Physics Fundamentals

For low-spin-down pulsars ($\dot{E}_{\rm rot} < \dot{E}_{\rm rot,break}$ – Section 3.6.1), we have simpler physics, because there is no screening of the accelerating electric field for both PC and outer gap (OG) pulsar models. For this case,

$$I_{\rm PC} \propto \dot{E}_{\rm rot}^{1/2} \tag{3.1}$$

$$V_{\rm PC} \propto \dot{E}_{\rm rot}^{1/2} \tag{3.2}$$

$$E_{||} = \frac{V_{\rm PC}}{h}, \tag{3.3}$$

with $I_{\rm PC}$ the outflowing current, $V_{\rm PC}$ the accelerating potential, $E_{||}$ the component of the electric field parallel to the magnetic field lines, and h the typical acceleration height. From this follows that

$$L_{\rm prim,\,unscreened} \propto V_{\rm PC} I_{\rm PC} \propto \dot{E}_{\rm rot}, \tag{3.4}$$

with $L_{\rm prim,\,unscreened}$ the primary particle luminosity for the unscreened case, and $\dot{E}_{\rm rot} = I\Omega\dot{\Omega}$ the spin-down power. However, for the screened case (see Figure 3.9),

$$L_{\rm prim,\,screened} \propto \dot{E}_{\rm rot}^{1/2}. \tag{3.5}$$

The following relation holds for the maximum gamma-ray energy for all models (see Section 3.5.3):

$$E_\gamma^{\rm max} \propto E_{||}^{3/4} \rho_c^{1/2}. \tag{3.6}$$

For CR-dominated acceleration (unscreened case),

$$L_\gamma^{\rm beam} \sim L_{\rm prim} = \eta_\gamma^{\rm beam} \dot{E}_{\rm rot}, \tag{3.7}$$

with $L_\gamma^{\rm beam}$ the gamma-ray luminosity. The OG models predict $\eta_\gamma^{\rm beam} \sim 0.01$, whereas the GR PC model predicts $\eta_\gamma^{\rm beam} \sim 0.75\kappa(1-\kappa) \sim 0.1$ for consistency with the gamma-ray pulsar population luminosities (Harding et al., 2002b).

For PSR J0437-4715-type parameters (with small curvature radius ρ_c), we have CR radiation reaction limited acceleration (we restict our attention to the CR radiation mechanism only, as it is the dominant one in this case). We expect the PC current $I_{\rm PC}$ to be close to the Goldreich-Julian value. High-energy upper limits however restrict the spectral cut-off energy and thus the maximum energy available for particle acceleration. Therefore, $V_{\rm PC}$ is constrained. A combination of low-energy and high-energy upper limits constrain the gamma-ray luminosity (which is roughly proportional to the area under the integral flux graph), or equivalently the gamma-ray efficiency $\eta_\gamma^{\rm beam}$.

3.3.2 Constraining Gamma-Ray Efficiency Using Upper Limits

In the previous section, it was noted that one expects the gamma-ray efficiency to be $\sim 1 - 10\%$ for unscreened pulsars, depending on the model one uses. In this section, we now consider the constraints

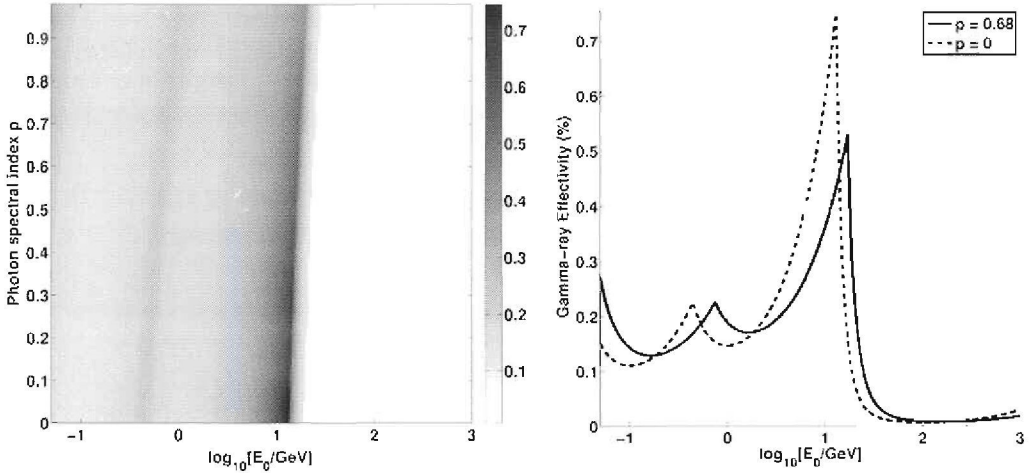

Figure 3.4: Left panel: The maximum gamma-ray efficiency (%) vs. photon spectral index vs. CR cut-off energy for PSR J0437-4715. The following constraints were assumed: $F(>100$ MeV$) = 15.1 \times 10^{-8}$ cm^{-2}s^{-1} and $F(>1$ GeV$) = 2 \times 10^{-8}$ cm^{-2}s^{-1} (*EGRET* – Fierro et al. (1995)), and $F(>100$ GeV$) = 10^{-11}$ cm^{-2}s^{-1} (*H.E.S.S.* – Hinton (2004)). Also, $M = 1.58 M_{\odot}$, $R = 1.5 \times 10^6$ cm, moment of inertia $I = 0.4MR^2$, $d = 139$ pc, and $\Lambda = 1$ have been used. For different values of Λ and d, $\eta_{\gamma}^{\rm beam}$ should be scaled by Λd^2. (In Chapter 4 we show that the beaming factor may be $\gtrsim 10$). Right panel: Same as left, but for two fixed values of p.

obtained from the data alone, independent of any particular pulsar model. We will however have to make the minimum assumption of a certain functional form for the photon spectrum (with typical units of erg^{-1}cm^{-2}s^{-1}; see Eq. [3.20]):

$$\left(\frac{dN}{dE}\right)^{\rm slice} = KE^{-p} \exp\left(-\frac{E}{E_0}\right). \tag{3.8}$$

The spectral index of the photon spectrum dN/dE due to a single electron primary (or mono-energetic beam of particles) radiating CR is -2/3 (Rudak & Dyks, 1999). However, if one includes the effect of an observer's restricted view by making slices through the PC and sampling radiation from electrons with various energies (i.e. not use beam-averaged values), it is possible that this index might deviate somewhat from -2/3. In what follows, we keep the spectral index p a free parameter. The energy E_0 is the cut-off energy of the CR spectrum which is accumulated over all visible magnetic field lines.

Given N upper limits for the integral flux, say $F(>E_i)$, with $i = 1, 2, \cdots, N$, one may constrain the gamma-ray efficiency. The upper limits yield N independent relations (see Section 3.5.2):

$$F(>E_i)^{\rm slice} \geq \int_{E_i}^{\infty} \left(\frac{dN}{dE}\right)^{\rm slice} dE = KE_0^{1-p}\Gamma(1-p,\, E_i/E_0), \quad i = 1, 2, \cdots, N, \tag{3.9}$$

with $\Gamma(1-p,\, E_i/E_0)$ indicating the upper incomplete Γ-function in this case. There are therefore N constraints on the normalisation 'constant' $K(E_0, p)$ when the upper limits are treated independently (since the integral flux spectrum do not necessarily go through all upper limits):

$$K \leq \frac{F(>E_i)^{\text{slice}}}{E_0^{1-p}\Gamma(1-p,\, E_i/E_0)}, \quad i = 1, 2, \cdots, N. \tag{3.10}$$

Different upper limits will constrain K the most for different combinations of E_0 and p. (It may be viewed as each upper limit having a 'sphere of influence' – see Figure 3.5 where each independent upper limit creates a 'valley', constraining $\eta_\gamma^{\text{beam}}$ the most when E_0 is closest to E_i). As noted previously, the combination of low-energy and high-energy upper limits constrain the gamma-ray efficiency.

The gamma-ray efficiency is defined by

$$\eta_\gamma^{\text{beam}} = \frac{1}{\dot{E}_{\text{rot}}}\left(\frac{\epsilon\overline{\Delta\Omega}^{\text{beam}} d^2}{\beta^{\text{slice}}}\right)\int_0^\infty E\left(\frac{dN}{dE}\right)^{\text{slice}} dE = \frac{1}{\dot{E}_{\text{rot}}}\Lambda d^2 K E_0^{2-p}\,\Gamma(2-p), \tag{3.11}$$

with $\Gamma(2-p)$ indicating the normal Γ-function. Here $\overline{\Delta\Omega}^{\text{beam}}$ indicates the solid angle subtended by the beam of radiation from the PC, d the pulsar distance, and β^{slice} the normalised pulse width (duty cycle) of the particular slice which will be visible to the observer. The quantity $\Lambda = \epsilon\overline{\Delta\Omega}^{\text{beam}}/\beta^{\text{slice}}$ may be viewed as a geometrical correction (beaming) factor which scales the flux in the observer's slice up to the total beam-averaged flux (see Section 2.5.10).

One may next use the smallest (most constrained) value of K for each value of E_0 and p, denoted by $K_{\text{min}}(E_0, p)$, to obtain a constraint on the gamma-ray efficiency $\eta_\gamma^{\text{beam}}$:

$$\eta_\gamma^{\text{beam}} \leq \frac{1}{\dot{E}_{\text{rot}}}\Lambda d^2 K_{\text{min}}(E_0, p) E_0^{2-p}\,\Gamma(2-p). \tag{3.12}$$

Thus,

$$\eta_\gamma^{\text{beam}}(E_0, p) \leq \min\left\{\frac{\Lambda d^2 F(>E_i)^{\text{slice}} E_0\,\Gamma(2-p)}{\dot{E}_{\text{rot}}\Gamma(1-p,\, E_i/E_0)}\right\}, \quad i = 1, 2, \cdots, N. \tag{3.13}$$

One may finally infer the minimum $\eta_\gamma^{\text{beam}}$ over all E_0 and p. This is shown in Figures 3.4 and 3.5. It should be evident that the pulsar viewing geometry directly determines the tightness of the constraint on $\eta_\gamma^{\text{beam}}$ in the sense that the choice of Λ occurs as a linear term in Eq. (3.12). An increase in this geometric factor will worsen the upper limit on $\eta_\gamma^{\text{beam}}$ by the same factor. (In Chapter 4 we show that the beaming factor may be $\gtrsim 10$). This constraint is also proportional to the square of the distance.

From Figures 3.4 and 3.5, we therefore note that the maximum expected gamma-ray efficiencies for PSR J0437-4715 and PSR B1821-24 are $\lesssim 0.7\Lambda$ % and $\lesssim 1.3\Lambda$ %, assuming the functional form

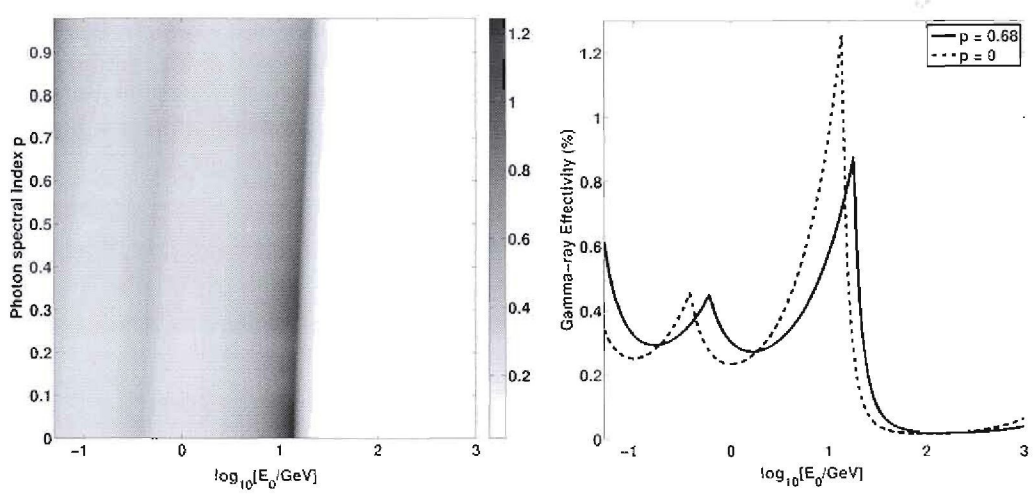

Figure 3.5: Left panel: The maximum gamma-ray efficiency (%) vs. photon spectral index vs. CR cut-off energy for PSR B1821-24. The following constraints were assumed: $F(>100\ \mathrm{MeV}) = 16.1 \times 10^{-8}\ \mathrm{cm^{-2}s^{-1}}$ and $F(>1\ \mathrm{GeV}) = 1.5 \times 10^{-8}\ \mathrm{cm^{-2}s^{-1}}$ (*EGRET* – Fierro et al. (1995)), and $F(>100\ \mathrm{GeV}) = 10^{-11}\ \mathrm{cm^{-2}s^{-1}}$ (*H.E.S.S.* – Hinton (2004)). Also, $M = 1.58 M_{\odot}$, $R = 1.5 \times 10^{6}$ cm, $I = 0.4MR^2$, $d = 4900$ pc, and $\Lambda = 1$ have been used. For different values of Λ and d, $\eta_{\gamma}^{\mathrm{beam}}$ should be scaled by Λd^2. (In Chapter 4 we show that the beaming factor may be $\gtrsim 10$). Right panel: Same as left, but for two fixed values of p.

of dN/dE as in Eq. (3.8). It should however be noted that these upper limits are not so tight, since the value of the geometrical beaming factor Λ may be quite large, in some cases well over 100 (see Section 4.3). When the sensitivities of the *Gamma Ray Large Area Space Telescope (GLAST)* and the *Cherenkov Telescope Array (CTA)* are used, assuming non-detection, one can constrain the gamma-ray efficiencies much more severely. Assuming $F(>100\ \mathrm{MeV}) = 2 \times 10^{-9}\ \mathrm{cm^{-2}s^{-1}}$ for *GLAST* (Thompson (2007) mentions an improvement of *GLAST LAT (Large Area Telescope)* sensitivity over that of *EGRET* by a factor > 30) and $F(>30\ \mathrm{GeV}) = 1 \times 10^{-11}\ \mathrm{cm^{-2}s^{-1}}$ for *CTA* (Hermann et al., 2007), we obtain $\eta_{\gamma}^{\mathrm{beam}} \lesssim 0.04\Lambda$ % and $\eta_{\gamma}^{\mathrm{beam}} \lesssim 0.07\Lambda$ % for PSR J0437-4715 and PSR B1821-24.

3.4 Oscillations in the GR Electric Field

When plotting the unscreened GR electric field (Figure 3.6), it is obvious that sign reversals take place for certain parameters and at certain heights above the PC (Venter & de Jager, 2005b). In the case of PSR J0437-4715, the fundamental unscreened expression for $E_{||}$ (Eq. [2.117]) changes sign along $\sim 40\%$ of the magnetic field lines originating at the PC. This field reversal is most pronounced when the magnetic azimuthal angle $\phi \sim \pi$, whereas no field reversals occur for $\phi \sim 0$. Figure 3.7 denotes

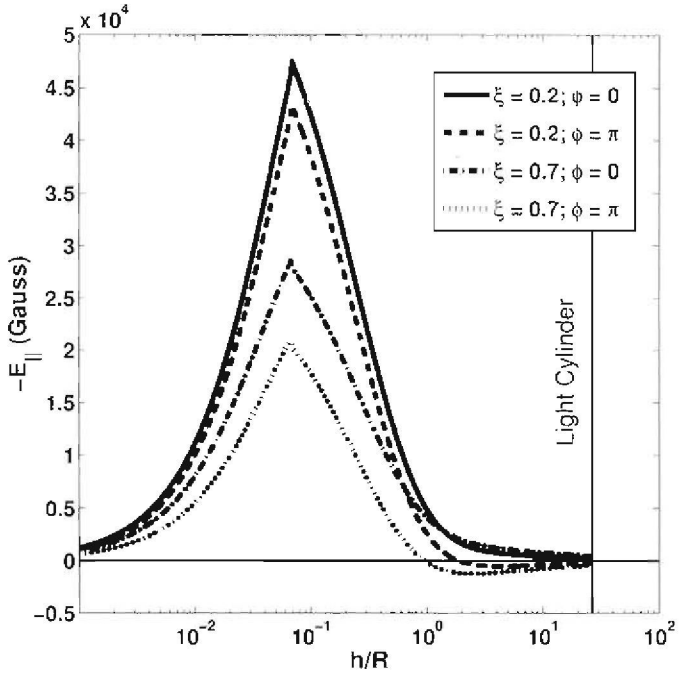

Figure 3.6: Electric field component parallel to the magnetic field vs. scaled height above the stellar surface for a polar magnetic field strength $B_0 = 4 \times 10^8$ G, $R = 10^6$ cm, and $I = 10^{45}$ g.cm^2. Note the sign reversal for $\phi = \pi$ above $h \sim R$, which leads to oscillatory motion of charged particles in the pulsar magnetosphere. From Venter & de Jager (2005b).

electric field sign reversal in ϕ-ξ-η-parameter space (with $\xi = \vartheta/\Theta$ the normalised polar coordinate, and $\eta = r/R$ the normalised radial coordinate). The contours indicate where the sum of the two terms in curly brackets in Eq. (2.117) is zero. Sign reversal takes place when a contour line is crossed along the rightward horizontal direction on the graph (i.e. as the electron's altitude is increased while moving along a magnetic field line). On the other hand, there is no sign reversal for certain ranges of ϕ, e.g. $\phi/2\pi < 0.25$ and $\phi/2\pi > 0.75$. Also, for a fixed value of ϕ, the distance beyond which the E-field's sign reverses, increases as ξ decreases and vice versa. This implies that field sign reversals occur increasingly sooner (in terms of altitude) the closer a particle is to the last closed magnetic field line.

When the electric field's sign reverses, charges which have previously been accelerated, are now slowed down. This generally leads to oscillation of particles between certain radii above the stellar surface. Figure 3.8 indicates the Lorentz factor as a function of radius (panel a), as well as a particle's radial coordinate η as a function of time (panel (b)). From the decay in amplitude of the latter graph, one can deduce that the particle will eventually reach a steady-state position. Trapping of

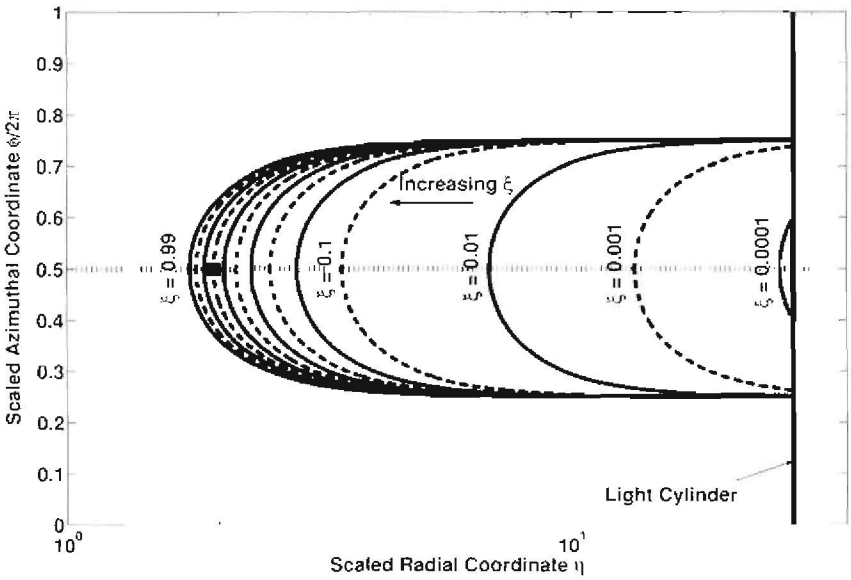

Figure 3.7: Electric field sign reversal in ϕ-ξ-η-parameter space. The values of ξ increases from small values (near the magnetic axis – right hand side of the figure) to values close to one (near the last closed field line – left side of the figure). The contours indicate the range of ϕ and η (for fixed values of ξ) for which the sum of the two terms in curly brackets in Eq. (2.117) is zero. Sign reversal takes place when a line is crossed along the rightward horizontal direction. Note that for certain ϕ-values, e.g. $\phi/2\pi < 0.25$ and $\phi/2\pi > 0.75$, there is no sign reversal. Furthermore, for a fixed value of ϕ, the distance beyond which the sign reverses increases as ξ decreases and vice versa. The contours correspond to different scaled colatitudes ξ of the footpoints of magnetic field lines: $\xi = 0.0001$, 0.001, 0.01, 0.1, 0.2, 0.3, 0.4, 0.5, 0.6, 0.7, 0.8, 0.9, and 0.99. The square indicates the parameter choice of the panel (a) of Figure 3.8.

electrons may ensue at magnetic field lines along which the electric field reverses. The system is expected to reach a steady state as a result of the redistribution of charges along these B-field lines. These B-lines may become equipotential lines, or a reduced current may develop, resulting in the suppression of particle acceleration along them. This justifies our neglect of those B-field lines (for which E-field reversals occur) when performing model calculations (Oscillations due to the existence of the $\cos\phi$-term may be traced back to the work of Arons & Scharlemann (1979); Arons (1983)).

3.5 Some Theoretical Results

This section discusses some useful theoretical derivations. More details, as well as other results, are given in Appendix A.

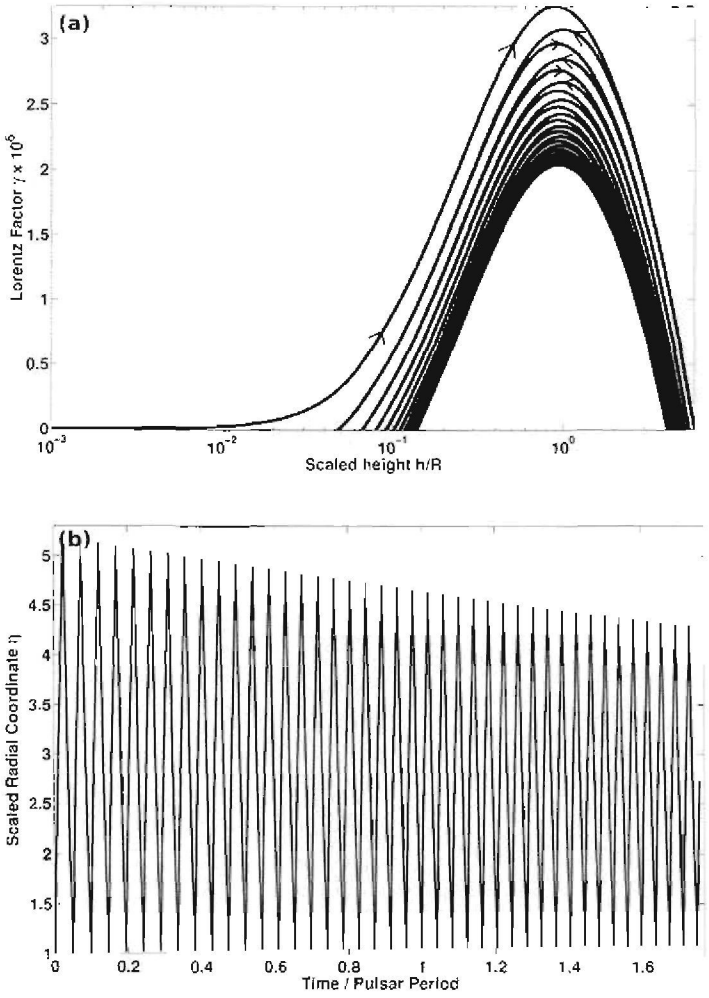

Figure 3.8: Panel (a): The graph of Lorentz factor of an electron vs. scaled height ($\phi = \pi$; $\xi = 0.7$). Panel (b): The graph of the scaled radial distance of a particle as a function of time (in pulsar period units; $\phi = \pi$; $\xi = 0.9$). From the decay in amplitude, one can deduce that the particle will eventually reach a steady-state position.

3.5.1 Gamma-Ray Luminosity

One of the most interesting predictions of Muslimov & Harding (1997) is that the unscreened primary electron luminosity is predicted to be equal to a quadratic function of the compactness parameter κ of the NS, times the spin-down power (see derivation in Section A.1 of Appendix A):

$$L^{|\chi=0}_{\rm prim,max} = \frac{3}{4}\kappa(1-\kappa)\dot{E}_{\rm rot}, \tag{3.14}$$

where

$$\dot{E}_{\rm rot} = I\Omega\dot{\Omega} \approx \frac{B_0^2\Omega^4 R^6}{6c^3 f^2(1)}, \tag{3.15}$$

and $f(\eta)$ is defined in Eq. (2.78). Here B_0 refers to the magnetic field strength at the pole.

A more detailed analysis (using $\int_0^{2\pi}\cos\phi d\phi = 0$ and $\int_0^{2\pi}\cos^2\phi d\phi = \pi$; see Section A.1) yields the general result for an oblique rotator (Venter & de Jager, 2005b):

$$\begin{aligned} L_{\rm prim} &= \frac{3}{4}\left(1-\frac{1}{\eta^3}\right)\kappa(1-\kappa)\cos^2\chi\dot{E}_{\rm rot} \\ &+ \frac{9}{64}\Theta_0^c H(1)\sin^2\chi\left[\Theta^c(\eta)H(\eta) - \Theta_0^c H(1)\right]\dot{E}_{\rm rot} \qquad (3.16) \\ &= L_{\rm prim}^{|\chi=0}\left\{\cos^2\chi + \frac{3}{16}\frac{\Theta_0^c H(1)\sin^2\chi\left[\Theta^c(\eta)H(\eta) - \Theta_0^c H(1)\right]}{(1-1/\eta^3)\,\kappa(1-\kappa)}\right\}. \qquad (3.17) \end{aligned}$$

However, $\Theta^c(\eta)$'s definition is only valid inside the light cylinder. Adopting a value of $\Theta^c(\eta) = \pi/2$ for distances $\eta > c/(\Omega R)$, and letting $\eta \to \infty$, we obtain (with $H(\eta) \to 1$ as $\eta \to \infty$)

$$L_{\rm prim,max} = L_{\rm prim,max}^{|\chi=0}\left\{\cos^2\chi + C\sin^2\chi\right\} \tag{3.18}$$

with

$$C = \frac{3\Theta_0^c H(1)\left[\pi/2 - \Theta_0^c H(1)\right]}{16\kappa(1-\kappa)}, \tag{3.19}$$

which reduces back to Eq. (3.14) when $\chi = 0$.

Evaluation of Eq. (3.14) and (3.18) leads to the conclusion that the maximum efficiency $\eta_\gamma^{\rm max}$ of conversion of pulsar spin-down power into gamma-ray luminosity $L_\gamma^{\rm beam}$ is about 10% for typical pulsar parameters (with $\kappa \sim 0.15$) when assuming that $L_\gamma^{\rm beam} \sim L_{\rm prim,max}$ (see Eq. [3.24]; Harding et al. (2002b)).

In Chapter 4, Eq. (3.18) is applied to a population of MSPs, and generally leads to lower and more accurate predictions for the gamma-ray luminosity than Eq. (3.14). Refer to Figure 4.23 in Section 4.4.

3.5.2 Integration of Spectra

CR photon spectra have the form of a power law with a spectral index of -2/3 when a single electron primary is continuously accelerated by a parallel electric field (Harding et al., 2002b), with an exponential cut-off occurring at energies greater than E_0 (see Section 2.1.2). In Appendix A (Section A.2), it is shown that integration of a spectrum of the form

$$\left(\frac{dN}{dE}\right)^{\rm slice} = KE^{-p}\exp\left(-\frac{E}{E_0}\right), \tag{3.20}$$

with K, E_0, and p constants, may be cast in the form of a Γ-function if the limits of integration are 0 and ∞:

$$\int_0^\infty KE^{-p}\exp\left(-\frac{E}{E_0}\right)dE = KE_0^{1-p}\,\Gamma(1-p). \tag{3.21}$$

Eq. (3.21) is an improvement over the approximation

$$\int_0^\infty KE^{-p}\exp\left(-\frac{E}{E_0}\right)dE \approx \int_0^{E_0} KE^{-p}dE = KE_0^{1-p}(1-p)^{-1}. \tag{3.22}$$

It is furthermore shown that the total gamma-ray luminosity of a beam of radiation coming from the pulsar may be written as (see Eq. [2.177], [2.181], and [A.30])

$$L_\gamma^{\rm beam} \equiv \Lambda d^2 \int_0^\infty E\left(\frac{dN}{dE}\right)^{\rm slice} dE = \Lambda d^2 K E_0^{2-p}\,\Gamma(2-p). \tag{3.23}$$

Making the approximation (Harding et al., 2002b)

$$L_\gamma \approx 0.5 L_{\rm prim,max}^{|\chi=0}, \tag{3.24}$$

the normalisation constant may be written as (using Eq. [3.14])

$$K^{|\chi=0}(E_0, p, \kappa, \dot{E}_{\rm rot}, \Lambda, d) = \frac{3\kappa(1-\kappa)\dot{E}_{\rm rot}}{8\Lambda d^2 E_0^{2-p}\Gamma(2-p)}. \tag{3.25}$$

Using Eq. (3.18) instead of Eq. (3.14) leads to the more general result

$$K(\chi, E_0, p, \kappa, \dot{E}_{\rm rot}, \Lambda, d) = K^{|\chi=0}\left(\cos^2\chi + C\sin^2\right), \tag{3.26}$$

and C is defined in Eq. (3.19).

Lastly, the integral flux may be written as (see Eq. [2.186] and [A.27])

$$\overline{F}^{\rm slice}(>E_1) = \int_{E_1}^\infty \left(\frac{dN}{dE}\right)^{\rm slice} dE = KE_0^{1-p}\,\Gamma(1-p, E_1/E_0), \tag{3.27}$$

where $\Gamma(1-p, E_1/E_0)$ signifies the upper incomplete Γ-function.

3.5.3 CR Cut-Off Energy

By setting $(dE_e/dt)_{\rm CR} = 0$ in the equation for the change in electron energy as it moves above the PC (Eq. [2.161])

$$\frac{dE_e}{dt} = e\beta c E_{||} + \left(\frac{dE_e}{dt}\right)_{\rm CR} \tag{3.28}$$

and using the characteristic CR photon energy of (Eq. [2.27])

$$E_\gamma = \frac{3}{2}\left(\frac{\lambda_c}{\rho_c}\right)\gamma^3 m_e c^2, \tag{3.29}$$

we obtain a maximum photon energy (for all PC models) of

$$E_\gamma^{\rm max} = \left(\frac{3}{2}\right)^{7/4} \lambda_c \left(\frac{\beta E_{||}}{e}\right)^{3/4} \rho_c^{1/2} m_e c^2, \tag{3.30}$$

with $(dE/dt)_{\rm CR} = 2/3(e^2 c/\rho_c^2)\gamma^4$, E_e the electron energy, λ_c the Compton wavelength, m_e and e the electron mass and charge, β the normalised electron speed, ρ_c the curvature radius, and γ the electron's Lorentz factor. Numerical evaluation of this equation for the GR case gave unexpectedly low typical CR spectral cut-offs compared to the 'classical' notion that these should be around 100 GeV (Venter, 2004, also see Section 3.6.2).

3.6 Results of the 'GR Model': PSR J0437-4715 (Unscreened Case)

In this section, we give some results obtained by running a numerical code developed to simulate an MSP magnetosphere (as discussed in Chapter 2). This section, together with its parallel version for PSR B1821-24 (Section 3.7), constitute the main part of the current chapter. PSR J0437-4715 will serve as an example of the class of pulsars with unscreened electric potentials, while PSR B1821-24 will be used to exemplify the effects of screening via electron-positron pairs in the magnetosphere.

3.6.1 Optical Depth

In the GR MSP model under consideration, there exists a spin-down luminosity $\dot{E}_{\rm rot,\,break}$ below which no screening of the accelerating E-field will take place due to the production of electron-positron pairs from CR gamma-ray photons (Harding et al., 2002b):

$$\dot{E}_{\rm rot,break} \approx 1.4 \times 10^{34} \left(\frac{P}{B_{12}^2}\right)^{1/7} \quad {\rm ergs/s}. \tag{3.31}$$

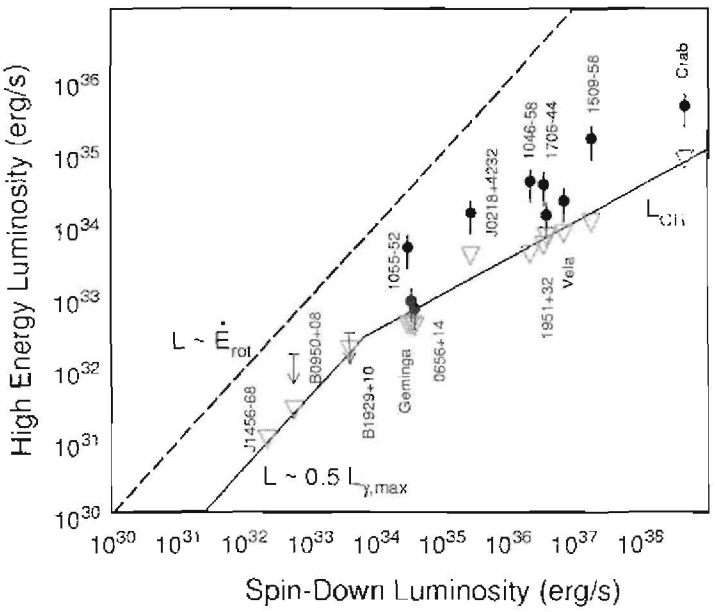

Figure 3.9: Graph of $L_\gamma^{\rm beam}$ vs. $\dot{E}_{\rm rot}$ indicating two regions: young pulsars (top right) following the relation $L_\gamma^{\rm beam} \sim \dot{E}_{\rm rot}^{1/2}$, and older pulsars (bottom left) below the CR death line at $\dot{E}_{\rm rot} \lesssim 10^{34}$ erg s^{-1} where no screening due to pair production is expected, following the relation $L_\gamma^{\rm beam} \sim \dot{E}_{\rm rot}$ (see Section 3.3). Figure from Harding et al. (2002b).

Here, $B_{12} = B_0/10^{12}$ G, and P is the pulsar period in seconds. (Note the positive sign of the power of P). According to this equation, the CR death line is at $\dot{E}_{\rm rot} \lesssim 10^{34}$ erg s^{-1} for canonical pulsars (see Figure 3.9), and at $\dot{E}_{\rm rot} \lesssim 10^{35}$ erg s^{-1} for MSPs.

Most MSPs do not have completely screened E-fields (Harding et al., 2005b) (as 'canonical' pulsars do), allowing particles streaming from the PC to be accelerated up to high altitudes (Muslimov & Harding, 2004b). This implies high pair production attenuation spectral cut-offs (Harding et al., 2005b), and therefore photons escaping with relatively large CR energies, which promises favourable conditions for observation depending on the gamma-ray flux.

Evaluating PSR J0437-4715's spin-down luminosity, using $I = 1 \times 10^{45}$ g.cm^2, yields $\dot{E}_{\rm rot} \sim 10^{34}$ erg.s^{-1}. This is less than $\dot{E}_{\rm rot,break}$ which is $\sim 6 \times 10^{34}$ ergs/s for PSR J0437-4715, indicating that pair production should not take place. Detailed modelling results in typical values of $\chi' \sim 10^{-5} - 10^{-11}$ of the Erber parameter (Erber, 1966), implying zero optical depth. (Note that the optical depth is zero along the magnetic axis $\vec{\mu}$ where $B_\perp = 0$). This confirms that pair production will not take place, as an optical depth of unity is required for this to happen. We also observe the expected asymmetry

of the optical depths for different PC 'sides', i.e. the leading and trailing parts of the magnetosphere (Dyks & Rudak, 2002).

In addition, Bulik et al. (2000) gave the energy condition for pair production for a photon with momentum parallel to the local magnetic field at a height h above the stellar surface. Pair production will take place when the photon energy satisfies

$$E_\gamma \geq 10^2 \left(\frac{P}{10^{-3}\,\mathrm{s}}\right)^{1/2} \left(\frac{B_0}{10^9\,\mathrm{G}}\right)^{-1} \left(\frac{R}{10^6\,\mathrm{cm}}\right)^{-1/2} \left(1+\frac{h}{R}\right)^{5/2} \mathrm{GeV}. \tag{3.32}$$

Evaluating this equation for PSR J0437-4715 further supports an unscreened scenario. Therefore, the CR spectral cut-offs (see Section 3.6.2) may be regarded as the 'final' values for cut-off energy, not impacted by reprocessing of high-energy photons into pairs, lowering the spectral cut-off in screened pulsar magnetospheres.

Presumably, a small number of CR electron-positron pairs are required to account for the observed radio radiation. However, this should have a negligible impact on the CR gamma-ray radiation. PSR J0437-4715 therefore provides an exceedingly fortunate environment for the investigation of the GR-Maxwell laws, because the number of free parameters are limited in the unscreened case (see Section 1.5). However, a low intensity of IC-scattered UV photons / soft X-rays into the TeV range may contribute to a weak pair production component.

3.6.2 CR Cut-Off Energy

Studies involving spectral cut-offs of MSP gamma-ray spectra are important for two reasons. First and foremost, in addition to flux predictions, the spectral cut-off of a given pulsar gamma-ray spectrum determines whether the pulsar will be visible for a particular gamma-ray telescope. As noted previously, if the cut-off energy is $\gtrsim$ the threshold energy of the telescope, and the flux sensitivity is $\lesssim 0.05\dot{E}_{\mathrm{rot}}/d^2$, VHE gamma rays from a pulsar should be visible (de Jager & Venter, 2005). Secondly, the nature of the spectral cut-offs may be a discriminator between the rival PC and OG models. The first class of models predicts a super-exponential cut-off, while the latter predicts an exponential cut-off (Thompson, 2007).

For PSR J0437-4715, we find a maximum CR cut-off energy of $1 - 20$ GeV, depending on the assumed geometry (magnetic inclination angle χ between the magnetic and spin axes, and the angle ζ of the observer's line of sight with respect to the spin axis) and EOS (i.e. radius R, moment of inertia I, and mass M). This compares favourably with a value of $\sim$ 10 GeV obtained by Harding et al. (2005b) and Frąckowiak & Rudak (2005a,b). Table 3.1 compares different authors' converging results

for CR cut-off energies of PSR J0437-4715. In Chapter 4, this result generalises as a function of P, $\dot{P}$, χ, and ζ; see Figure 4.4.

One of the main uncertainties when modelling pulsars, is the geometry (i.e. χ and ζ) of the pulsar, which significantly influences predictions of cut-off energy. Because our model takes the observer and inclination angles into account, it is possible to find the CR cut-off energy as a function of χ and ζ. The result of this calculation for PSR J0437-4715 is shown in Figure 3.10. The CR cut-off energies were estimated from $E^2(dN/dE)$-spectra which we calculated for different combinations of χ and ζ in the range [10°, 85°] (de Jager & Venter, 2005). Maximum CR cut-off energies $\lesssim 10$ GeV (for the parameters listed in the caption of Figure 3.10) are obtained when $\chi \sim \zeta$. This should be expected, since the observer sweeping close to the magnetic axis will sample radiation due to particle acceleration by the highest values of the electric potential. Equality does not hold exactly, as these maxima are below the $y = x$ line. This is due to the asymmetric character of the E-field with respect to the magnetic azimuthal angle ϕ. The energy maxima occuring at small values of χ also agrees with the fact that the E-field has a $\cos\chi$-term dominating at low altitudes, with a $\sin\chi$-term coming into play at larger altitudes.

Venter & de Jager (2005a) found that for the parameter ranges $R_6 \equiv R/10^6$ cm $= 1.3 - 1.7$ (e.g. Kargaltsev et al., 2004), $I_{45} \equiv I/10^{45}$ g.cm$^2 = 1 - 3$ (e.g. Harding et al., 2002b), and $(\chi,\zeta) = (35°, 40°)$ (Manchester & Johnston, 1995), $(\chi,\zeta) = (20°, 25°)$ (Pavlov & Zavlin, 1997) and $(\chi,\zeta) = (20°, 16°)$ (Gil & Krawczyk, 1997), the maximum CR cut-off energy of ~ 17 GeV is obtained for $R_6 = 1.3$, $I_{45} = 3$, and $\chi = 20°$. A pulsar mass of $M = 1.58M_\odot$ was used, as derived from Shapiro delays (van Straten

Reference	χ (°)	$\epsilon_{\rm CR}^{\rm max}$ (GeV)
Venter & de Jager (2005a)	all	$\lesssim 17$
Venter & de Jager (2005a)	20; 35	$\sim 1 - 10$
Venter et al. (2005)	all	$\sim 1 - 20$
Venter et al. (2005)	10	$\lesssim 10$
Harding et al. (2005b)	10	~ 5
Frąckowiak & Rudak (2005a)	20; 35	~ 10
Frąckowiak & Rudak (2005b)	35	~ 10
de Jager & Venter (2005)	10; 20	$\lesssim 10$
de Jager & Venter (2005)	35	$\lesssim 1$

Table 3.1: Comparing different authors' converging results for peak CR energy $\epsilon_{\rm CR}^{\rm max}$ of PSR J0437-4715 for similar pulsar parameters and an unscreened electric field. This is markedly smaller than the range $\sim 50 - 100$ GeV expected prior to these newer calculations. Taken from de Jager & Venter (2005).

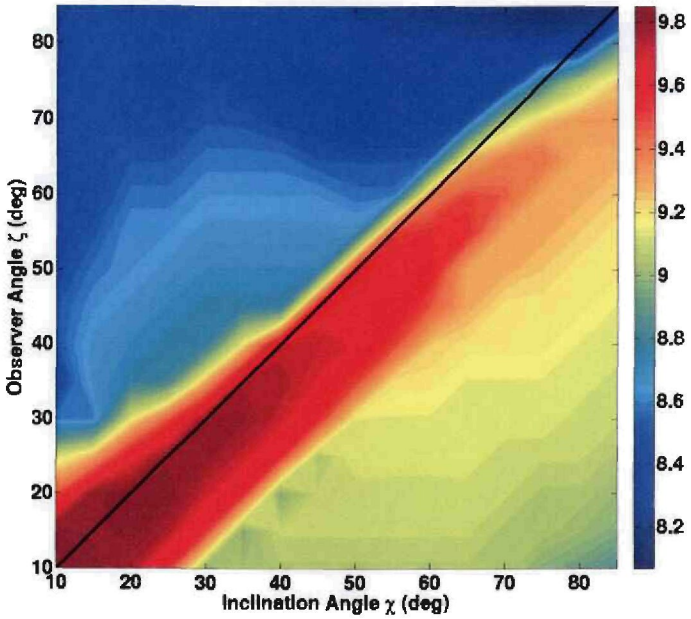

Figure 3.10: Contour plot of $\log_{10}$ of the CR cut-off energy in units of eV vs. observer angle ζ and magnetic inclination angle χ for PSR J0437-4715, representing the "unscreened case". A pulsar radius $R = 10^6$ cm, moment of inertia $I = 3 \times 10^{45}$ g.cm^2, and mass $M = 1.58 M_\odot$ were used. Figure from de Jager & Venter (2005).

et al., 2001). This corresponds to a compactness parameter $\kappa \sim 0.2$ and surface magnetic field strength $B_8 \equiv B_0/10^8$ G ~ 7.2 (see Eq. [1.4]). The relative altitude for maximum CR energy is obtained as $\eta \sim 1.47$, corresponding to a normalised field line colatitude of $\xi \sim 0.1$ and $\rho_c \sim 10^8$ cm, while the magnetic azimuth $\phi = 0$ results in a maximum GR potential (also see Figures 3.11 and 3.12). For this result, I was treated as an independent parameter. However, it was later realised that I is a function of M and R, so in what follows, it was assumed that $I = 0.4MR^2$.

In Figure 3.11, the maximum CR energy is shown as a function of magnetic azimuthal angle ϕ and normalised polar angle ξ. For the parameters used (see figure caption), a maximum energy is found close to $\xi \sim 0.1 - 0.2$. It decreases toward $\xi = 1$, as there is a $(1 - \xi^2)$-term in the expression for the E-field (Eq. [2.117]). The 'valley' in ϕ is also visible where field reversals occur (see Figure 3.7; the CR energy has been set to 0.01 GeV when the Lorentz factor $\gamma < 1$). This part of the PC is ignored when computing e.g. spectra and luminosities, as explained in Section 3.4.

Historically it appeared as if MSPs would provide suitable laboratories for current (then future) 3$^{\text{rd}}$ generation ground-based gamma-ray telescopes. CR cut-off energies for MSPs such as PSR J0437-4715 were predicted to be in the range 50−100 GeV by Harding et al. (2002b) and Bulik et al. (2000), making

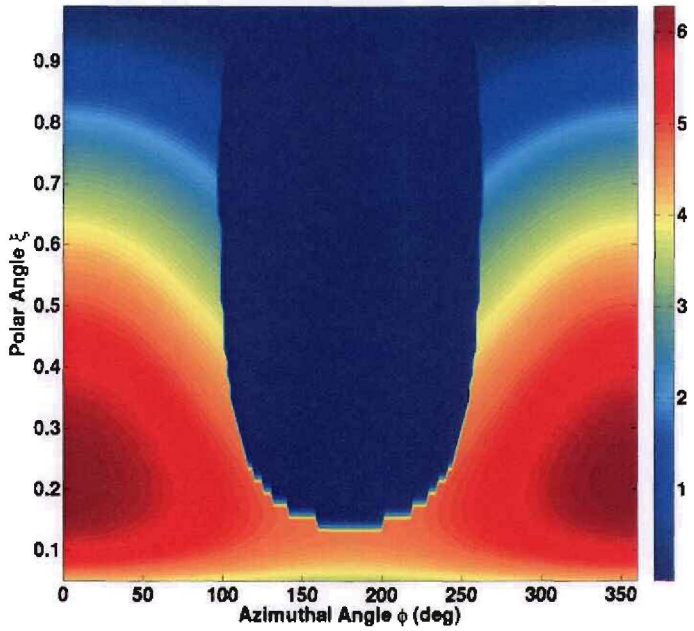

Figure 3.11: Contour plot of the maximum CR energy (GeV) vs. magnetic azimuthal angle ϕ and scaled polar angle angle ξ for PSR J0437-4715. A pulsar radius $R = 1.5 \times 10^6$ cm, moment of inertia $I = 0.4MR^2$, mass $M = 1.58M_\odot$, and $\chi = 35°$ were used. The CR energy has been set to 0.01 GeV where the Lorentz factor γ becomes less than 1, typically around $\phi = 180°$.

proposals for ground-based telescopes with imaging thresholds near 100 GeV (e.g. *H.E.S.S.* (Hofmann, 2001) and the *Collaboration of Australia and Nippon (Japan) for a Gamma-Ray Observatory in the Outback (CANGAROO)* (Enomoto et al., 2002)) attractive. From the present GR theory it appears as though these telescopes may not be able to see the spectral tail corresponding to the intense primary CR component, since the hard primary CR spectrum does not extend to energies above $\sim$ 20 GeV, as verified by both analytical and numerical (finite-element) approaches. New calculations and final calibration of 3$^{\rm rd}$ generation telescopes indicate that 4$^{\rm th}$ generation Cherenkov telescopes (see e.g. Konopelko, 2005; Konopelko et al., 2007) and *GLAST* (Funk et al., 2007) are generally needed in order to observe gamma-ray MSPs, due to the relatively low cut-off energies (Bulik & Rudak, 1999; Bulik et al., 2000; Harding et al., 2005a,b). A detection will make PSR J0437-4715 only the second gamma-ray MSP, after the probable detection of PSR 0218+4232 (Kuiper et al., 2000).

An inverse Compton component resulting from TeV electrons upscattering the UV / soft X-rays from the surface of PSR J0437-4715 may however still be detectable, although this prediction by Bulik et al. (2000) should be re-evaluated within a GR electrodynamical framework.

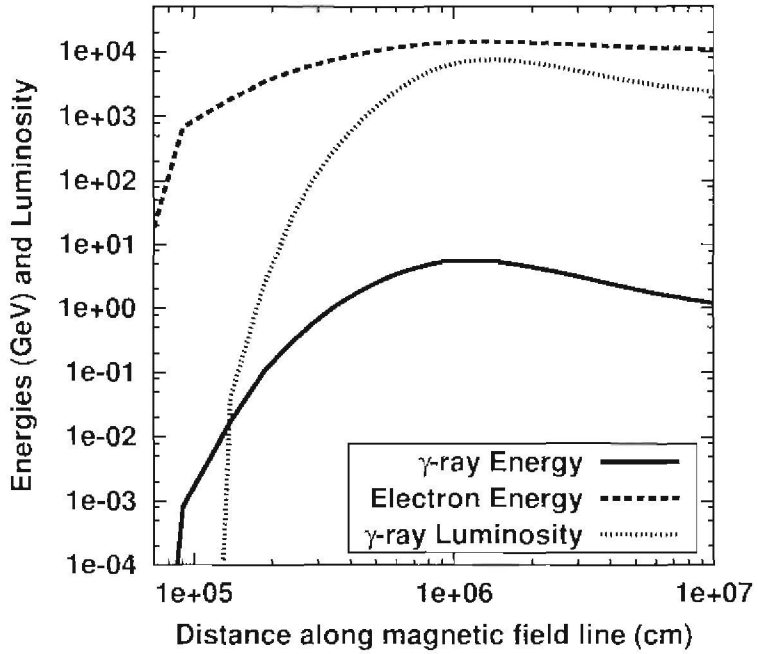

Figure 3.12: Gamma-ray energy (GeV), electron energy (GeV), and fractional gamma-ray luminosity (relative units) vs. path length along the magnetic field line (cm) for PSR J0437-4715. Note the maximum gamma-ray energy in the range $\sim$ 10 GeV, and maximum electron energy of $\sim$ 10 TeV. Also note that the positions of the maxima of the energies correspond quite well to the position where the maximum of the fractional gamma-ray luminosity occurs. The graph was obtained for $\chi = 35°$, $\phi = 0$, $\xi = 0.1$, $R = 1.5 \times 10^6$ cm, and $M = 1.58 M_\odot$. The light cylinder for PSR J0437-4715 is at $r = 27.5 \times 10^6$ cm.

3.6.3 Electron and Photon Energies vs. Distance

In Figure 3.12 gamma-ray and electron energies are presented as functions of path length along a B-line. Also shown is the fractional gamma-ray luminosity (the incremental luminosity dL radiated in a time step dt). The graph was obtained for $\chi = 35°$, $\phi = 0$, $\xi = 0.1$, $R = 1.5 \times 10^6$ cm, and $M = 1.58 M_\odot$. On this graph, the maximum gamma-ray energy is in the range $\sim$ 10 GeV as mentioned in Section 3.6.2, while the maximum electron energy is $\sim$ 10 TeV. These are typical values for these quantities for the case of PSR J0437-4715.

It should furthermore be noted that the position above the PC where the maxima of the energies occur correspond reasonably well to the position of the maximum of the fractional gamma-ray luminosity. This means that photons of the maximum CR energy (and electrons having energies close to the maximum energy) are produced abundantly. If there were a mismatch between the energy and luminosity maxima, it would have implied that high-energy photons would be rare, and that e.g.

lower energy photons would dominate the gamma-ray photon spectrum. Since this is not the case, the maximum CR photon energies quoted in Section 3.6.2 may be taken with confidence. The spectral cut-off energy is typically a bit lower than the maximum CR energy (see e.g. Figures 3.13 and 3.14).

3.6.4 Spectra and Fluxes

This section is basically an update of the work which appeared in Venter & de Jager (2005a), where we simulated the magnetosphere of the nearby MSP PSR J0437-4715, but now including the correction discussed in Section 2.5.11. From the GR model, we obtained predicted gamma-ray differential and integral fluxes, and compared these with data as well as other theoretical predictions.

In Figure 3.13, differential (νF_ν) spectra of PSR J0437-4715 are shown. The thick solid lines indicate the band of possible spectra predicted by this work for $R_6 = (1.3, 1.5, 1.7)$, $\chi = (10°, 20°, 35°)$, and $\zeta = (10°, 16°, 20°, 30°, 40°)$. This prediction highlights the importance of an accurate knowledge of a pulsar's geometry and EOS. Also indicated are differential spectra from Frąckowiak & Rudak (2005a) for $\chi = 20°$, $\zeta = 16°$, Frąckowiak & Rudak (2005b) for $\chi = 35°$, $\zeta = 40°$, as well as single particle spectra from Harding et al. (2005b) for $\chi \sim 10°$ and $\xi = 0.5$. Also shown are the *H.E.S.S.* (Hinton, 2004) and *GLAST LAT* (Harding et al., 2005b) sensitivities.

Harding et al. (2005b) fixed their scaled magnetic colatitude $\xi = 0.5$ (i.e. they simulated radiation from one B-line only), whereas we sampled over a range of ξ-values. Furthermore, Harding et al. (2005b) only calculated a single electron spectrum and normalised it, whereas we accelerated primary electrons leaving the stellar surface at a rate of $\sim 10^{31}$ s^{-1} and selected radiation which fell into the range $(\zeta - d\zeta/2, \zeta + d\zeta/2)$, which enabled us to calculate absolute fluxes. Our range of spectra more or less includes the predictions of Frąckowiak & Rudak (2005a,b) and Harding et al. (2005b), and the spectral shapes are similar.

We found that the *EGRET* upper limits constrained the gamma-ray flux of the model, and we used the 1 GeV upper limit to constrain the gamma-ray efficiency of PSR J0437-4715 (see Section 3.6.5). Since the *EGRET* upper limits (Fierro et al., 1995) are also violated by the prediction of Harding et al. (2005b), these authors argued that the emission may be off-beam, and calculated the spectrum of radiation from a particle with emission altitude above 2 stellar radii. This lowers the flux, and may salvage the problem. Frąckowiak & Rudak (2005b) similarly found fluxes exceeding the *EGRET* observations, but argued that this contradiction may be alleviated easily by introducing small-scale perturbations to the dipolar magnetic field (also see Navarro et al. (1997)).

Figure 3.14 shows the complementary integral flux curves. The thick solid lines, curves (a) and (b), indicate the band of possible spectra predicted by this work for $R_6 = (1.3, 1.5, 1.7)$, $\chi = (10°, 20°, 35°)$,

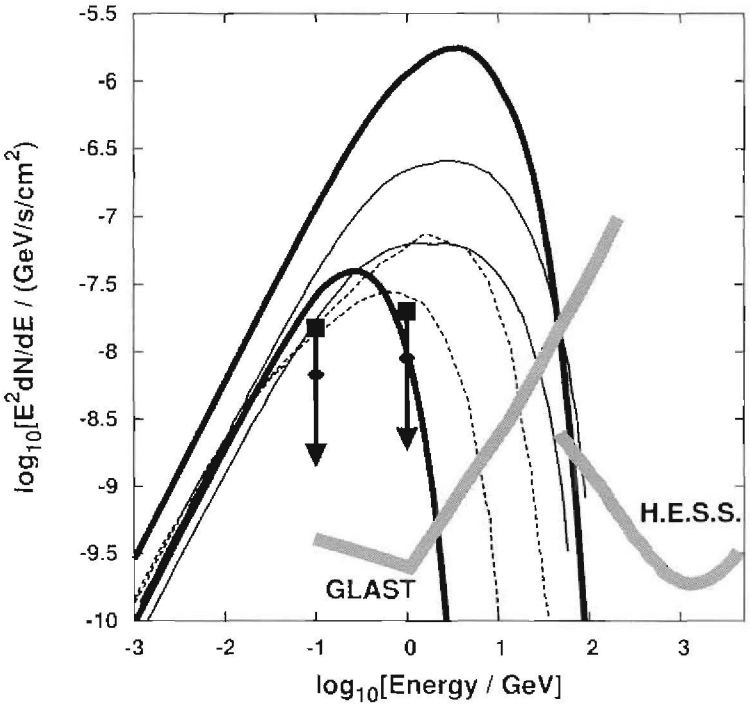

Figure 3.13: Differential spectra of PSR J0437-4715. The top thin solid line is from Frąckowiak & Rudak (2005a) for $\chi = 20°$, $\zeta = 16°$, while the bottom thin solid line is from Frąckowiak & Rudak (2005b) for $\chi = 35°$, $\zeta = 40°$. The two dashed lines are from Harding et al. (2005b) for $\chi \sim 10°$ and $\xi = 0.5$; the top dashed line represents emission along the total B-line, while the bottom dashed line shows only emission above $\eta = 2$. The thick solid lines indicate the band of possible spectra predicted by this work for $R_6 = (1.3, 1.5, 1.7)$, $\chi = (10°, 20°, 35°)$, and $\zeta = (10°, 16°, 20°, 30°, 40°)$. Also shown are the *EGRET* upper limits (squares – Fierro et al., 1995) and *H.E.S.S.* (Hinton, 2004) sensitivity, both converted to differential values assuming an E^{-2} spectrum. The diamonds are the *EGRET* upper limits divided by $\sqrt{5}$ (see text for details). The differential *GLAST LAT* sensitivity is from Harding et al. (2005b). For the corresponding integral fluxes, see Figure 3.14.

and $\zeta = (10°, 16°, 20°, 30°, 40°)$. Curve (c), the dot-dashed line, for which $R_6 = 1.5$, $\chi = 35°$, $M = 1.58 M_\odot$, $I = 0.4 M R^2$, and $\zeta = 40°$, represents an intermediate curve. The top thin solid line was obtained by integrating the differential spectrum of Frąckowiak & Rudak (2005a) for $\chi = 20°$, $\zeta = 16°$. The bottom thin solid line is similarly the integrated differential spectrum given by Frąckowiak & Rudak (2005b) for $\chi = 35°$, $\zeta = 40°$. The two dashed lines are the integrated differential spectra from Harding et al. (2005b) for $\chi \sim 10°$ and $\xi = 0.5$; the top dashed line represents emission along the total B-line, while the bottom dashed line shows only emission above $\eta = 2$. The squares represent *EGRET* integral flux upper limits (Fierro et al., 1995), while the diamonds represent these upper

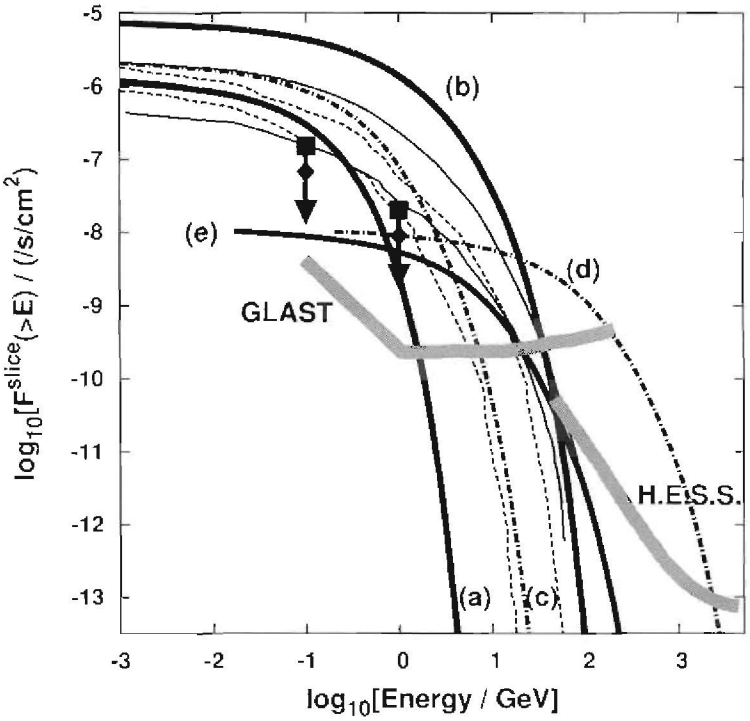

Figure 3.14: Observer time-averaged integral flux vs. energy. The top thin solid line was obtained by integrating the differential spectrum of Frąckowiak & Rudak (2005a) for $\chi = 20°$, $\zeta = 16°$. The bottom thin solid line is similarly the integrated differential spectrum given by Frąckowiak & Rudak (2005b) for $\chi = 35°$, $\zeta = 40°$. The two dashed lines are the integrated differential spectra from Harding et al. (2005b) for $\chi \sim 10°$ and $\xi = 0.5$; the top dashed line represents emission along the total B-line, while the bottom dashed line shows only emission above $\eta = 2$. The thick solid lines, curves (a) and (b), indicate the band of possible spectra predicted by this work for $R_6 = (1.3, 1.5, 1.7)$, $\chi = (10°, 20°, 35°)$, and $\zeta = (10°, 16°, 20°, 30°, 40°)$. Curve (c), the dot-dashed line, for which $R_6 = 1.5$, $\chi = 35°$, $M = 1.58 M_\odot$, $I = 0.4MR^2$, and $\zeta = 40°$, represents an intermediate curve. Curve (d) (dot-dashed line) is curve (c) scaled by a factor $\lambda \sim 200$, while curve (e) (thick solid line) is curve (d) shifted to the left by a factor ~ 12 (see text for details). The squares represent *EGRET* integral flux upper limits (Fierro et al., 1995), while the diamonds represent these upper limits reduced by a factor $\sqrt{5}$, appropriate for a beam with main pulse width of ~ 0.2. Also indicated are the *H.E.S.S.* sensitivity for 50 hours (Hinton, 2004), and the *GLAST LAT* sensitivity (Harding et al., 2005b) converted to integral values assuming an E^{-2} spectrum. See corresponding differential fluxes of Figure 3.13. Using curve (e), the gamma-ray efficiency may be constrained, as shown in Section 3.6.5.

limits reduced by a factor $\sqrt{5}$, appropriate for a beam with main pulse width of ~ 0.2. Also indicated are the *H.E.S.S.* sensitivity for 50 hours (Hinton, 2004), and the *GLAST LAT* sensitivity (Harding et al., 2005b) converted to integral values assuming an E^{-2} spectrum.

The 100 MeV and 1 GeV *EGRET* flux upper limits from Fierro et al. (1995), indicated by the squares on Figure 3.14, clearly constrain the flux band defined by (a) and (b). If we define an *a priori* phase interval of $\beta^{\rm slice} \sim 0.2$, centered on the radio pulse, and recalculate the *EGRET* flux upper limits from the factor five ($= 1/\beta^{\rm slice}$) reduced skymap background, we should get the even more constraining upper limits given by the diamonds in Figure 3.14. We therefore have to revise the predicted fluxes for PSR J0437-4715 and we do so based on the following scaling argument (also see Section A.4 in Appendix A): If we assume that the particle and hence gamma-ray luminosity only scales with the spin-down power and neutron star compactness, as in Eq. (3.14) and Eq. (3.18), i.e. the product of the current and voltage for a pair-starved pulsar is a constant as predicted by Eq. (3.14), we may scale the set of curves (a) through (c) (according to this condition of a constant photon luminosity $L_\gamma^{\rm slice}$) in terms of the limiting voltage and hence the cut-off energy to give $\overline{F}_{\gamma,1}^{\rm slice}(>E_1) \times E_{\rm cutoff,1} \sim \overline{F}_{\gamma,2}^{\rm slice}(> E_2) \times E_{\rm cutoff,2}$ (for constant $\beta^{\rm slice}$ and $\overline{\Delta\Omega}^{\rm slice}$, and energies $E_1 < E_2$; $E_{\rm cutoff,1} < E_{\rm cutoff,2}$). In particular, when curve (c) is scaled according to $E_{\rm cutoff,2} = \lambda E_{\rm cutoff,1}$, implying $\overline{F}_{\gamma,2}^{\rm slice}(>E_2) \sim \overline{F}_{\gamma,1}^{\rm slice}(>E_1)/\lambda$, with $\lambda \sim 200$, curve (d) is obtained, which no longer violates the revised *EGRET* upper limit at 1 GeV, but the cut-off energy then exceeds the *H.E.S.S.* threshold energy of $\sim$ 100 GeV. If curve (d) is now translated to the left (by a factor ~ 12) so that the energy cut-off also falls below the *H.E.S.S.* sensitivity curves, curve (e) is obtained, which would be consistent with both *EGRET* and *H.E.S.S.* (if the latter instrument does not detect this pulsar). Using curve (e), we constrain the gamma-ray efficiency of PSR J0437-4715 in Section 3.6.5.

3.6.5 Constraining the Gamma-ray Efficiency

When evaluating Eq. (3.18) for PSR J0437-4715, we obtained efficiencies of $2 - 11\%$ for converting spin-down power into particle luminosity (Venter & de Jager, 2005a). The total gamma-ray luminosity $L_\gamma^{\rm beam}$ is calculated by integrating the fractional luminosity dL emitted at a position (r, ϑ, ϕ) in a time-step dt over the whole volume of the magnetosphere. Since we could not start with initial particle velocities of c (i.e. infinite Lorentz factor), we assumed values close to c and found, via numerical calculation, convergent photon luminosities of $2 - 9\%$ of the spin-down power (depending on R, I, χ and ζ), i.e. $L_\gamma^{\rm beam}/L_{\rm prim,max} \sim 1$. This means that almost all particle luminosity is converted into photon luminosity as expected for strong radiation reaction. Radiation reaction, combined with further (weak) acceleration towards the light cylinder, result in a total residual electron power of $\sim 1 - 2.5\%$ of the spin-down power at the light cylinder.

However, since the *EGRET* limits impose constraints on the model, the value of $\eta_\gamma^{\rm beam}$ needs to be carefully treated in order to obtain sensible constraints on this parameter. When the predicted flux

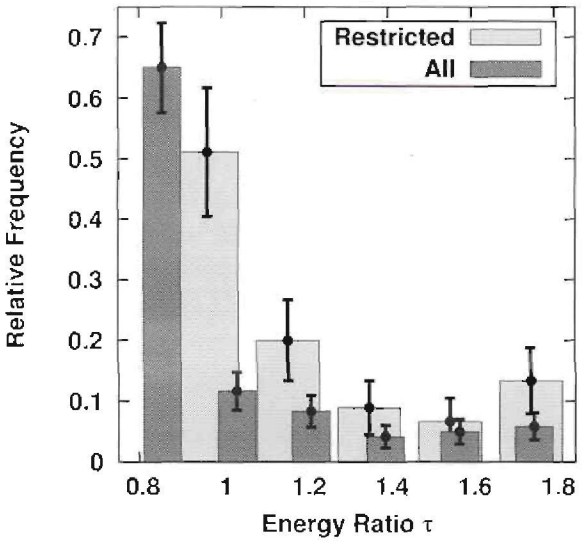

Figure 3.15: Comparison of mean and cut-off energies, with their ratio typically being close to unity. In the legend, 'All' refers to the parameter range $R_6 = (1.3, 1.5, 1.7)$, $\chi = (10°, 20°, 35°, 45°)$, and $\zeta = (10°, 16°, 20°, 30°, 40°, 45°, 50°, 60°, 70°, 80°, 90°)$, while 'Restricted' refers to the range $R_6 = (1.3, 1.5, 1.7)$, $\chi = (10°, 20°, 35°)$, and $\zeta = (10°, 16°, 20°, 30°, 40°)$. Errors shown are $\sqrt{n_i}/\sum_i n_i$, where n_i is the number of values in each bin i. Also, $M = 1.58M_\odot$ and $I = 0.4MR^2$ were used (and τ was calculated for 'uncorrected' CR spectra – see Section 2.5.11).

exceeds the experimental limits, the value of $\eta_\gamma^{\rm beam}$ cannot be taken as a firm prediction, and an upper limit of this parameter must be found. We do this by scaling the integral flux curve until it obeys the experimental limits, and then derive constraints on $\eta_\gamma^{\rm beam}$, as explained below.

The theoretical details are dealt with in Section 2.5.10. This section presents a fuller treatment of

Curve (c)						
Λ	λ	τ	E_0	$\overline{F}^{\rm slice}$	$\dot{E}_{\rm dot}$	$\eta_\gamma^{\rm beam}$
~ 6	–	~ 1.6	$10^{-1.0}$ GeV	$10^{-5.7}$ /cm^2/s	1.1×10^{34} ergs/s	$\sim 6\%$
Curve (d)						
Λ	λ	τ	E_0	$\overline{F}^{\rm slice}$	$\dot{E}_{\rm dot}$	$\eta_\gamma^{\rm beam}$
~ 6	~ 200	~ 1.6	$10^{1.4}$ GeV	$10^{-8.0}$ /cm^2/s	1.1×10^{34} ergs/s	$\sim 6\%$
Curve (e)						
Λ	λ	τ	E_0	$\overline{F}^{\rm slice}$	$\dot{E}_{\rm dot}$	$\eta_\gamma^{\rm beam}$
~ 6	~ 200	~ 1.6	$10^{0.4}$ GeV	$10^{-8.0}$ /cm^2/s	1.1×10^{34} ergs/s	$\sim 0.6\%$

Table 3.2: Estimating the gamma-ray luminosity from integral flux curves: the values of E_0 and $\overline{F}^{\rm slice}(>E)$ are read from Figure 3.14.

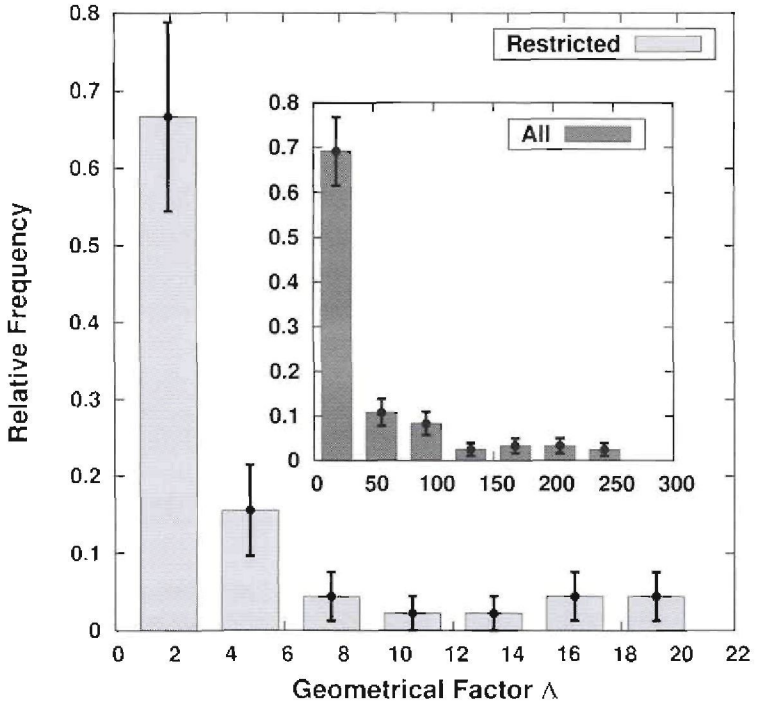

Figure 3.16: Histogram of the beaming correction for PSR J0437-4715. For the main graph, 'Restricted' refers to the range $R_6 = (1.3, 1.5, 1.7)$, $\chi = (10°, 20°, 35°)$, and $\zeta = (10°, 16°, 20°, 30°, 40°)$, while in the inset, 'All' refers to the parameter range $R_6 = (1.3, 1.5, 1.7)$, $\chi = (10°, 20°, 35°, 45°)$, and $\zeta = (10°, 16°, 20°, 30°, 40°, 45°, 50°, 60°, 70°, 80°, 90°)$. Errors shown are $\sqrt{n_i}/\sum_i n_i$, where n_i is the number of values in each bin i. From this figure, we infer that for 'favourable' (on-beam) radiation, the correction factor is typically small, while it becomes very large for off-beam geometries (shown in the inset). Also, $M = 1.58 M_\odot$ and $I = 0.4 M R^2$ were used.

the preliminary analysis presented in Section 3.3. Using the formula below (see Eq. [2.188])

$$L_\gamma^{\rm beam} = \Lambda d^2 \tau E_0 \overline{F}^{\rm slice}(>E), \tag{3.33}$$

(assuming $E \ll E_0$) and assuming that the geometric factor Λ as well as τ stay constant while scaling the flux graph, the implied $\eta_\gamma^{\rm beam}$ may be estimated directly from Figure 3.14, as shown in Table 3.2.

More detailed calculation gives $\Lambda = 5.72$, $\lambda = 200$, $E_0 = 10^{-0.886}$ GeV $= 0.130$ GeV, $\overline{E} = 10^{-0.682}$ GeV $= 0.208$ GeV, and $\tau = \overline{E}/E_0 = 1.60$ for curve (c). After scaling to curve (e) in Figure 3.14, $E_0 = 10^{0.336}$ GeV $= 2.17$ GeV, and $\overline{F}^{\rm slice}(>E_1) = 10^{-7.99}/{\rm cm}^2/{\rm s} = 1.02 \times 10^{-8}/{\rm cm}^2/{\rm s}$,

with $E_1 \ll E_0$. This yields the constraint

$$\eta_\gamma^{\rm beam} \leq 0.55\%. \tag{3.34}$$

This is slightly larger than the constraint $\eta_\gamma^{\rm beam} \leq 0.3\%$ quoted in Venter & de Jager (2005a). There, we used a wrong reduced *EGRET* upper limit, and thus the scaled value of $\overline{F}^{\rm slice}(>1$ GeV) was too small. Also, we now have a different geometry (χ and ζ), and we furthermore use $I = 0.4MR^2$ instead of using I as a free parameter. This changes the spin-down luminosity $\dot{E}_{\rm rot}$. The uncorrected CR spectrum gives a constraint of $\eta_\gamma^{\rm beam} \leq 1.5\%$. The difference between this (uncorrected) result and the one quoted in Venter & de Jager (2005a) can be understood as follows:

$$\eta_{\rm new} = \eta_{\rm old}\left(\frac{\dot{E}_{\rm old}}{\dot{E}_{\rm new}}\right)\left(\frac{\sin\zeta_{\rm new}}{\sin\zeta_{\rm old}}\right)\left(\frac{\overline{F}^{\rm slice}_{\rm new}}{\overline{F}^{\rm slice}_{\rm old}}\right) \sim 5\eta_{\rm old}. \tag{3.35}$$

However, using the corrected CR spectrum now leads to the constraint of $\eta_\gamma^{\rm beam} \leq 0.55\%$. Forthcoming *GLAST* observations will possibly be able to directly measure the value of $\eta_\gamma^{\rm beam}$.

A non-detection by *H.E.S.S.*, as implied by curve (e), therefore leads to a gamma-ray luminosity of $L_\gamma^{\rm beam} \lesssim 0.0055\dot{E}_{\rm rot}$. This value should be compared with the model-independent pre-analysis value of $L_\gamma^{\rm beam} \lesssim 0.007\Lambda\dot{E}_{\rm rot} \sim 0.04\dot{E}_{\rm rot}$ (Section 3.3), $L_\gamma^{\rm beam} \lesssim 0.014\dot{E}_{\rm rot}$ predicted by Eq. (45) of Muslimov & Harding (2004b) for pair-starved pulsars with off-beam geometry (using $P \approx 5.76$ ms and $\dot{E}_{\rm rot} \sim 1.1 \times 10^{34}$ erg.s^{-1}), and with the prediction of $L_\gamma^{\rm beam} \sim 3 \times 10^{-5}\dot{E}_{\rm rot}$ given by Rudak & Dyks (1999) for a pulsar with $P = 1$ ms, and $B_0 = 10^9$ G.

Note that the geometric factor Λ varies quite a lot, but is relatively small for on-beam radiation. Furthermore, the value of $\tau = \overline{E}/E_0$ is reasonably close to unity ($\overline{E} = \int_0^\infty E(dN/dE)^{\rm slice}\,dE \div \int_0^\infty (dN/dE)^{\rm slice}\,dE$). See Figures 3.15 and 3.16, where histograms of τ and Λ are shown. More details are given in Section 4.3 where a pulsar population study is conducted.

3.6.6 Lightcurves

This section briefly deals with some preliminary results involving lightcurve calculations for PSR J0437-4715 (there is no parallel section for PSR B1821-24). A full treatment will only be available when the correct Lorentz transformation is done from the corotating to the observer frame (which is beyond the scope of this work). Since fluxes and differential spectra are phase-averaged quantities, this transformation is not expected to impact the results given above significantly. See e.g. Dyks et al. (2004b); Frąckowiak & Rudak (2005a,b) for more advanced calculations involving corrections for aberration

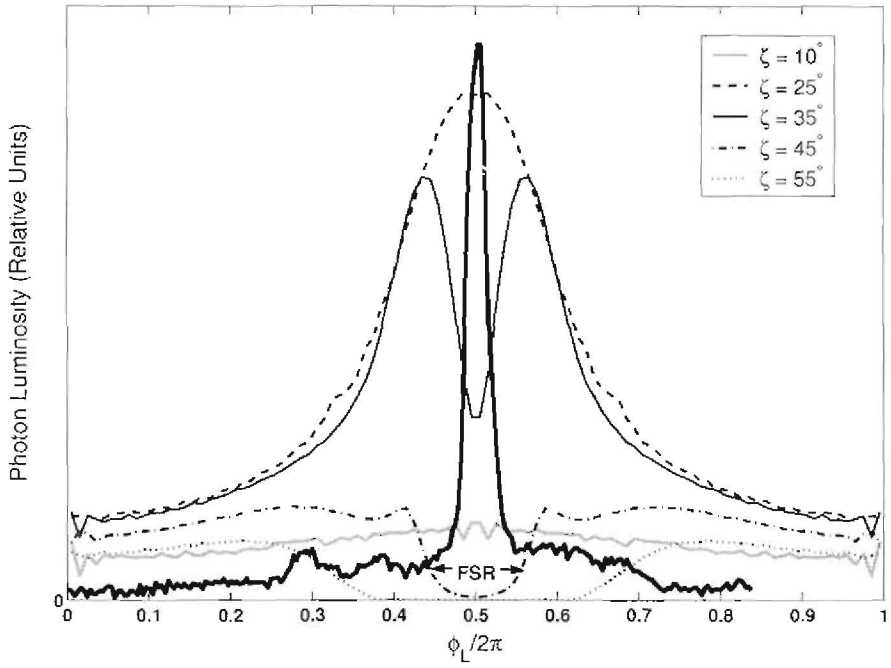

Figure 3.17: Photon luminosity (in relative units) vs. observer pulse phase (with phase 0.5 corresponding either to $\phi = 0$ or $\phi = \pi$, depending on ζ) for PSR J0437-4715 for different ζ (see legend). The following parameters were assumed: $P \approx 5.76$ ms (period), $R_6 = 1.3$, $I_{45} = 1$, $M = 1.58\,M_\odot$ and $\chi = 35°$. The radio pulse at 4.6 GHz (thick solid line – Manchester & Johnston (1995)) is superimposed for reference (see `www.atnf.csiro.au/research/pulsar/psrcat`). The "valleys" at observer phase ~ 0.5 of the lightcurves with $\zeta \geq \chi$ are probably due to electric field sign reversal (FSR), since the magnetic field lines where these reversals occur, were ignored (see Section 3.4). (The photon energy range more or less corresponds to that used in Figure 3.14). Figure from Venter & de Jager (2005a).

and photon-travel-time delays.

From our calculations, we infer that GR theory predicts a relatively narrow pulse ($\beta^{\rm slice} \sim 0.2$ phase width) centered on the magnetic axis. Assuming that most of the power is radiated into a cone with half emission angle ϑ_B (the polar tangential angle at the emission point), one may estimate the beaming solid angle as $\overline{\Delta\Omega}^{\rm beam}(>E) \sim 2\pi(1-\cos\vartheta_B) \sim 0.5$ sr per PC when selecting radiation with energy $\gtrsim 100$ MeV (for $\chi = 35°$). This value is quite insensitive to the EOS, and differs only by $\sim 20\%$ when other reasonable values of R and M are used (Venter & de Jager, 2005b). We expect that *GLAST LAT* should measure lightcurves of PSR J0437-4715 around a few GeV.

Lightcurves for PSR J0437-4715, for different observer angles ζ, are shown in Figure 3.17. Maximal heights are obtained when $\zeta \sim \chi$. However, the pulse heights decrease rapidly as the radiation becomes

off-beam (i.e. when the impact angle $\beta' = \zeta - \chi$ becomes large). The 'dips' in lightcurves with $\zeta \geq \chi$ near phase $\phi_L/2\pi \sim 0.5$ (where $\phi \sim \pi$) are most probably due to the sign reversal of the electric field, because the magnetic field lines where this sign reversal occurs, were ignored in all calculations (Venter & de Jager, 2005a). Zavlin et al. (2002) showed that the radio and X-ray pulses are in phase. If these pulses are produced by accelerated particles in the magnetosphere (as e.g. indicated by the fact that the X-ray pulse has a non-thermal component) close to the magnetic axis, they should be in phase with a (as yet undetected) gamma-ray pulse produced by CR radiation.

3.7 Results of the 'GR Model': PSR B1821-24 (Screened Case)

This section is parallel to the previous one (Section 3.6), and will accordingly be shorter. We chose PSR B1821-24 as an example of an MSP with a screened electric potential.

3.7.1 Optical Depth

PSR B1821-24 has a very large spin-down luminosity ($\sim 2 \times 10^{36}$ ergs/s) for an MSP. When evaluating Eq. (3.31) for the case of PSR B1821-24, we obtain $\dot{E}_{\rm rot,break} \sim 4 \times 10^{34}$ ergs/s. PSR B1821-24 therefore clearly lies beyond this spin-down break, and is subsequently treated as having a screened potential (see Section 2.4.4). In what follows, the approximation of Dyks & Rudak (2000) is used, with a pair formation front height of $h = R_{\rm PC} \sim (\Omega R^3/c)^{1/2}$. PSR B1821-24 may therefore be viewed as an example of a screened pulsar, in contrast to PSR J0437-4715 which is believed to be an unscreened pulsar (Section 3.6.1).

3.7.2 CR Cut-Off Energy

CR energies up to $\sim$ 150 GeV were found for PSR B1821-24 when $\zeta \sim \chi$ (de Jager & Venter, 2005). This is compatible with results of Harding et al. (2005b) and Frąckowiak & Rudak (2005b) (see Table 3.3). The CR cut-off energy decreases rapidly when the impact angle becomes large (also see Section 3.7.4). Figure 3.18 shows CR cut-off energy as a function of χ and ζ. This case is more symmetrical with respect to the $y = x$ line than that of PSR J0437-4715 (see Figure 3.10). The largest energies are furthermore obtained for small χ since the electric field scales with the factor $\cos\chi$ (Dyks & Rudak, 2000).

PSR B1821-24 is expected to have a large impact angle (Backer & Sallmen, 1997). This is unfortunate from an observer's point of view, since low spectral cut-offs are expected. Unless the observer sweeps through the magnetic axis, with a small impact angle (and with $\chi \ll 45°$), PSR B1821-24 is

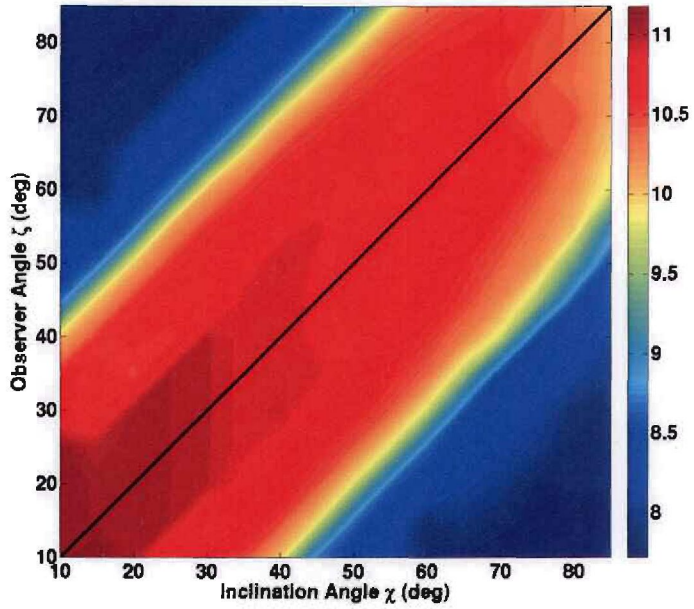

Figure 3.18: Contour plot of $\log_{10}$ of the CR cut-off energy in units of eV vs. observer angle ζ and magnetic inclination angle χ for PSR B1821-24, representing the "screened case". A pulsar radius $R = 10^6$ cm, moment of inertia $I = 3 \times 10^{45}$ g.cm^2, and mass $M = 1.58 M_\odot$ were used. Figure from de Jager & Venter (2005).

not expected to be visible for current 3$^{\text{rd}}$ generation telescopes which have threshold energies around ~ 100 GeV (e.g. Hinton, 2004).

Figure 3.19 shows the maximum CR energy as a function of magnetic azimuthal angle ϕ and normalised polar angle ξ. A maximum energy is found at $\xi = 0$, since that is where the E-field approximation attains a maximum. There is no exclusion region where field reversals occur, as in Figure 3.7, as this E-field doesn't change sign above the PC. Furthermore, the photon energy is independent of ϕ, since the E-field approximation we use is also independent of this coordinate (this may change for more general cases – see Section 2.4.5).

Reference	χ (°)	$\epsilon_{\text{CR}}^{\text{max}}$ (GeV)	Screened
Harding et al. (2005b)	50	~ 43	yes
Frąckowiak & Rudak (2005b)	50	$\gtrsim 100$	no
de Jager & Venter (2005)	50	$\lesssim 70$	yes
de Jager & Venter (2005)	all	$\sim 0.1 - 150$	yes

Table 3.3: Comparing different authors' converging results for peak CR energy $\epsilon_{\text{CR}}^{\text{max}}$, for similar pulsar parameters. From de Jager & Venter (2005).

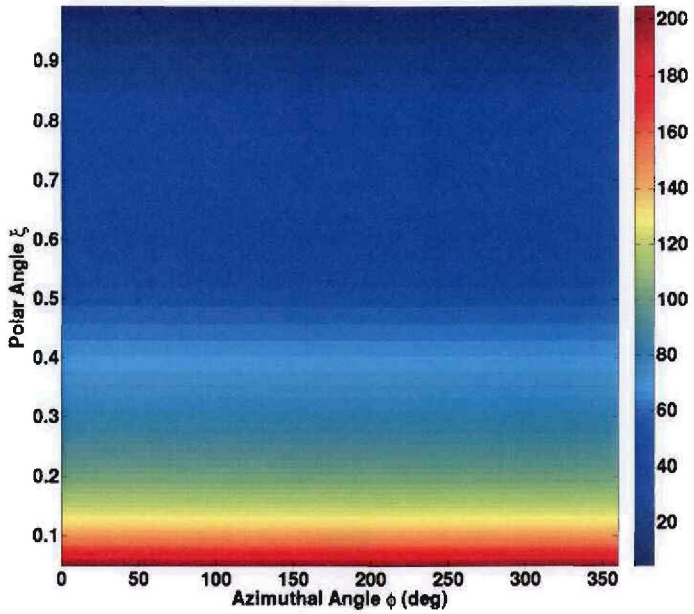

Figure 3.19: Contour plot of the maximum CR energy (GeV) vs. scaled polar angle angle ξ and magnetic azimuthal angle ϕ for PSR B1821-24. A pulsar radius $R = 1.5 \times 10^6$ cm, moment of inertia $I = 0.4MR^2$, mass $M = 1.4M_\odot$, and $\chi = 50°$ were used.

3.7.3 Electron and Photon Energies vs. Distance

As in Section 3.6.3, Figure 3.20 shows the gamma-ray energy, electron energy, and fractional gamma-ray luminosity (in relative units) vs. path length along the magnetic field line s (cm) for PSR B1821-24. The maximum gamma-ray energy is in the range $\sim$ 150 GeV, while the maximum electron energy is $\sim$ 50 TeV. These values are much higher than for PSR J0437-4715, owing to the fact that PSR B1821-24's E-field reaches much higher values (roughly a factor $\sim$ 85 for the parameters given in the figure captions of Figures 3.12 and 3.20). Using (see Eq. [3.6])

$$\left(\frac{E_\gamma^{\rm B1821}}{E_\gamma^{\rm J0437}}\right) \sim \left(\frac{E_{||}^{\rm B1821}}{E_{||}^{\rm J0437}}\right)^{3/4}, \tag{3.36}$$

one may roughly scale the maximum CR energy given in Section 3.6.3 by $\sim 85^{3/4}$, giving $E_\gamma^{\rm B1821} \sim$ 160 GeV (ignoring differences in e.g. χ, ρ_c, and M for the moment), which is quite close to 150 GeV. The maximum electron energy is similarly higher.

As previously, the position of the maxima of the energies correspond quite well to the position where the maximum of the fractional gamma-ray luminosity occurs. In contrast to the unscreened case of Section 3.6.3, these graphs have more well-defined peaks, corresponding to the peak of the

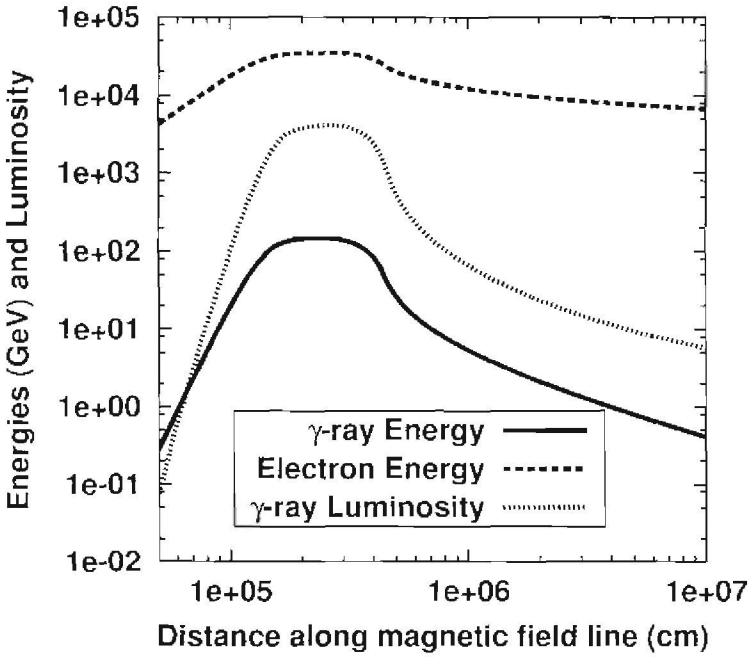

Figure 3.20: Gamma-ray energy (GeV), electron energy (GeV), and fractional gamma-ray luminosity (relative units) vs. path length along the magnetic field line (cm) for PSR B1821-24. Note the maximum gamma-ray energy in the range $\sim$ 150 GeV, and maximum electron energy of $\sim$ 50 TeV. Also note that the positions of the maxima of the energies correspond quite well to the position where the maximum of the fractional gamma-ray luminosity occurs. The graph was obtained for $\chi = 50°$, $\phi = 0$, $\xi = 0.1$, $R = 1.5 \times 10^6$ cm, and $M = 1.4 M_\odot$. (The light cylinder for PSR B1821-24 is at $r = 14.6 \times 10^6$ cm).

screened parallel electric field at an altitude of $s \sim 2 \times 10^5$ cm (measured along the B-field line). This is because the E-field drops to zero just after it has reached a maximum, becoming zero for the rest of the particle's journey to the light cylinder radius. There is thus no more particle acceleration after the E-field drops to zero, and CR losses cause the particle and photon energies to decrease more rapidly than in the case of PSR J0437-4715, where the particles are accelerated by the far-field which falls as r^{-4}. For PSR J0437-4715, this leads to broader peaks for the electron and photon energies. The graph was obtained for $\chi = 50°$, $\phi = 0$, $\xi = 0.1$, $R = 1.5 \times 10^6$ cm, $M = 1.4 M_\odot$, and $I = 0.4 M R^2$.

3.7.4 Spectra and Fluxes

Backer & Sallmen (1997) found a rotating vector solution for $\chi = 50°$ and $\zeta = 90°$ from radio polarimetric data. This implies off-beam radiation with a very small spectral cut-off, and some components from a second PC might be visible. However, only one PC was modelled when considering gamma-ray

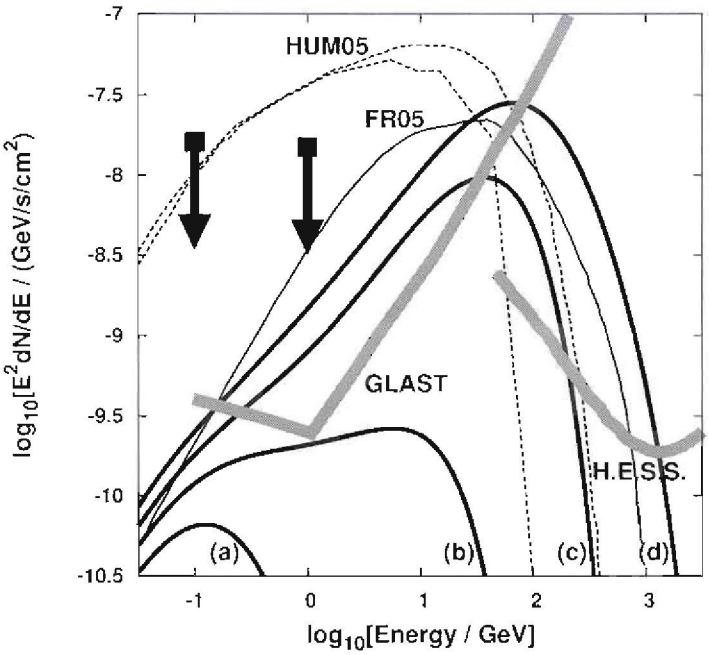

Figure 3.21: Differential spectra of PSR B1821-24. The top dashed lines (labelled 'HUM05') are from Harding et al. (2005b) for $\chi \sim 50°$ and $\xi = 0.7$ for a screened potential. The thin solid line (labelled 'FR05') is from Frąckowiak & Rudak (2005b) for $\chi = 50°$, $\zeta = 48°$. Curves (a) to (d) represent predictions from this work for $\zeta = (90°, 80°, 70°, 50°)$ respectively (thick solid lines). Values of $\chi = 50°$, $R_6 = 1.5$, $M = 1.4M_\odot$, and $I = 0.4MR^2$ have been used for all four curves. Also shown are the *EGRET* upper limits (squares – Fierro et al., 1995) and *H.E.S.S.* (Hinton, 2004) sensitivity, both converted to differential values assuming an E^{-2} spectrum. The differential *GLAST LAT* sensitivity (minimum at $\sim$ 1 GeV) is from Harding et al. (2005b). For the corresponding integral fluxes, see Figure 3.22.

radiation.

Figure 3.21 shows the predicted differential spectra for various geometries. The top dashed lines (labelled 'HUM05') are from Harding et al. (2005b) for $\chi \sim 50°$ and $\xi = 0.7$ for a screened potential (above the *EGRET* upper limit at 1 GeV – Fierro et al. (1995)). The thin solid line (labelled 'FR05') is from Frąckowiak & Rudak (2005b) for $\chi = 50°$, $\zeta = 48°$. Curves (a) to (d) represent predictions from this work for $\zeta = (90°, 80°, 70°, 50°)$ respectively (thick solid lines). The impact of geometry becomes very clear, since the spectral cut-off diminishes rapidly when the impact angle $\beta' = \zeta - \chi$ becomes large. Values of $\chi = 50°$, $R_6 = 1.5$, $M = 1.4M_\odot$, and $I = 0.4MR^2$ have been used for all four curves. Also shown are the *EGRET* upper limits (squares – Fierro et al., 1995) and *H.E.S.S.* (Hinton, 2004) sensitivity, both converted to differential values assuming an E^{-2} spectrum. The differential *GLAST LAT* sensitivity (minimum at $\sim$ 1 GeV) is from Harding et al. (2005b).

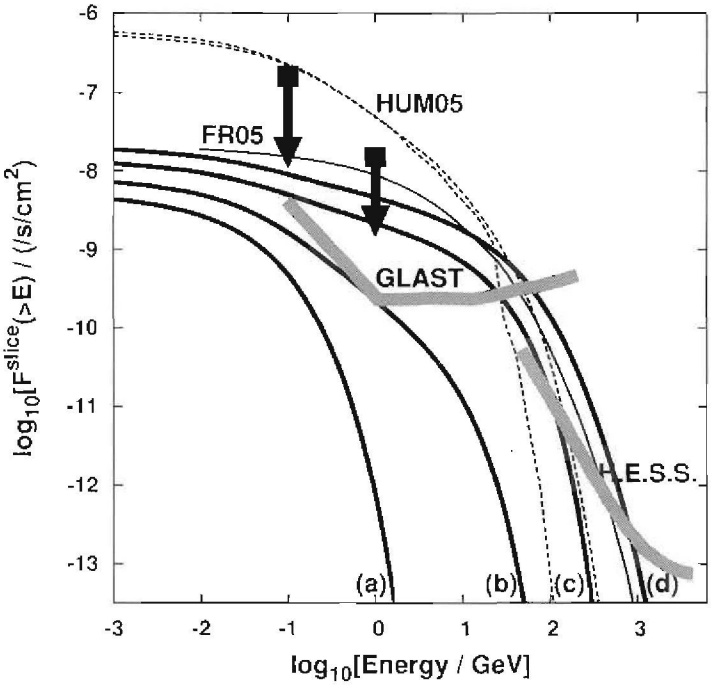

Figure 3.22: Observer time-averaged integral flux vs. energy. The top dashed lines (labelled 'HUM05') are the integrated differential spectra from Harding et al. (2005b), for $\chi \sim 50°$ and $\xi = 0.7$ for a screened potential. The thin solid line (labelled 'FR05') is the integrated differential spectrum from Frąckowiak & Rudak (2005b) for $\chi = 50°$, $\zeta = 48°$. Curves (a) to (d) represent predictions from this work for $\zeta = (90°, 80°, 70°, 50°)$ respectively (thick solid lines). Values of $\chi = 50°$, $R_6 = 1.5$, $M = 1.4M_\odot$, and $I = 0.4MR^2$ have been used for all four curves. Also shown are the *EGRET* upper limits (Fierro et al., 1995) and *H.E.S.S.* (Hinton, 2004) sensitivity. The differential *GLAST LAT* sensitivity Harding et al. (2005b) was converted to integral values assuming an E^{-2} spectrum. See corresponding differential fluxes of Figure 3.21. Using curve (a), the gamma-ray efficiency may be constrained, as shown in Section 3.7.5.

Figure 3.22 shows the observer time-averaged integral flux vs. energy. The top dashed lines (labelled 'HUM05') are the integrated differential spectra from Harding et al. (2005b), for $\chi \sim 50°$ and $\xi = 0.7$ for a screened potential. The thin solid line (labelled 'FR05') is the integrated differential spectrum from Frąckowiak & Rudak (2005b) for $\chi = 50°$, $\zeta = 48°$. Curves (a) to (d) represent predictions from this work for $\zeta = (90°, 80°, 70°, 50°)$ respectively (thick solid lines). Values of $\chi = 50°$, $R_6 = 1.5$, $M = 1.4M_\odot$, and $I = 0.4MR^2$ have been used for all four curves. Also shown are the *EGRET* upper limits (squares – Fierro et al., 1995) and *H.E.S.S.* (Hinton, 2004) sensitivity. The differential *GLAST LAT* sensitivity Harding et al. (2005b) was converted to integral values assuming an E^{-2} spectrum. Curves (a) through (d) are below the *EGRET* upper limits. Curve (d) (and maybe even

curve [c]) should have been visible for *H.E.S.S.*, were the geometry favourable. However, the gamma-ray emission from PSR B1821-24 is expected to be off-beam, so that this pulsar is not expected to be visible for *H.E.S.S.* Assuming that the inferred angles χ and ζ are correct, this MSP might not even be visible for *GLAST LAT*, despite its large spin-down luminosity.

3.7.5 Constraining the Gamma-ray Efficiency

For the geometry $\chi = 50°$ and $\zeta = 90°$ (curve (a) in Figures 3.21 and 3.22), we find that $\Lambda = 1.51 \times 10^3$ (indicative of off-beam radiation), $\overline{E} = 0.0409$ GeV, $E_0 = 0.0287$ GeV, and $\tau = 1.427$ (using the formalism of Section 3.6.5). This gives a value of $\eta_\gamma^{\rm beam} = 1.6\%$. Curve (a) does not contradict the available *EGRET* upper limits, so no scaling is necessary as was done in Section 3.6.5. If curve (a) is indeed scaled to give the largest possible $\eta_\gamma^{\rm beam}$, i.e. so as not to violate the *EGRET* 1 GeV upper limit and *H.E.S.S.* threshold sensitivity, the resulting graph gives an excessively large $\eta_\gamma^{\rm beam}$ of $\sim 714\%$ $\gg 100\%$.

3.8 Conclusion

In this chapter, we presented various results from the GR model of single, isolated pulsars (described in detail in Chapter 2). To make definite predictions, we chose PSR J0437-4715 and PSR B1821-24 as examples of pulsars with unscreened and screened E-fields for detailed modelling. These two MSPs are furthermore probably the best candidates for observation by current gamma-ray telescopes, the first due to its proximity, and the latter due to its high spin-down power.

The implementation of a quantitative numerical MSP model provided the means of comparing e.g. gamma-ray flux predictions and observations, and thereby enabled us to constrain the gamma-ray efficiency, which is roughly proportional to the spin-down luminosity in the unscreened case, and the square root of the spin-down luminosity in the screened case. The effect of GR on MSP spectral cut-offs, pulse profiles, integral flux, and conversion efficiency of spin-down power to gamma-ray luminosity has been investigated by simulating radiative and transport processes which occur in a pulsar magnetosphere (using a finite-element approach). The detailed study of single MSPs also provided the first step toward a population study (Chapter 4).

Following the introduction (Section 3.1), we summarised observations of PSR J0437-4715 and PSR B1821-24 in Sections 3.2.1 and 3.2.2. Next, we offered a preliminary 'first look' analysis, and obtained model-independent constraints on the gamma-ray efficiency $\eta_\gamma^{\rm beam}$ of PSR J0437-4715 and PSR B1821-24 in Section 3.3. In particular, we noted that the maximum expected gamma-ray effi-

ciencies for PSR J0437-4715 and PSR B1821-24 were $\lesssim 0.7\Lambda$ % and $\lesssim 1.3\Lambda$ %, assuming the functional form of $(dN/dE)^{\rm slice}$ as in Eq. (3.8). The effect of beaming is already seen in this result, and more detailed studies involving Λ will follow in Sections 4.3 and 4.4. Assuming non-detection by *GLAST LAT* and *CTA*, we showed that $\eta_\gamma^{\rm beam}$ may be much more severely constrained: $\eta_\gamma^{\rm beam} \lesssim 0.04\Lambda$ % and $\eta_\gamma^{\rm beam} \lesssim 0.07\Lambda$ % for PSR J0437-4715 and PSR B1821-24 respectively.

In Section 3.4 we confirmed the existence of oscillations in the unscreened accelerating GR electric field due to the reversal of the E-field's sign at certain locations above the PC (a well-known effect due to the $\cos\phi$-term in the E-field). It is expected that electrons may be trapped at magnetic field lines along which the electric field reverses. If a steady state is reached, these B-lines may become equipotential lines, or a reduced current may develop, resulting in the suppression of particle acceleration along them. We therefore neglected B-field lines along which E-field reversals occur when performing our model calculations.

In Section 3.5, we presented some useful theoretical results, including the derivation of a general formula for the particle luminosity as a function of inclination angle χ, an elegant form of the integral of certain spectra, and a formula showing that the maximum CR energy is proportional to the product of maximum value of the E-field to the power 0.75, and the square root of the curvature radius at that position.

The main sections of this chapter dealt with detailed results obtained from numerical modelling using the Harding-Muslimov-Tsygan GR model, applied to PSR J0437-4715 (Section 3.6) and PSR B1821-24 (Section 3.7).

We motivated the unscreened E-field of PSR J0437-4715 in Section 3.6.1 by showing that its spin-down luminosity is below the critical luminosity above which screening takes place as predicted by the MSP model. We furthermore evaluated the energy condition for screening given by Bulik et al. (2000), and again concluded that PSR J0437-4715's E-field must be largely unscreened, providing an exceedingly fortunate environment for the investigation of the GR-Maxwell laws because of the limited number of free parameters in this case. In contrast, PSR B1821-24 has a very large spin-down luminosity for an MSP, much larger than the critical spin-down luminosity given in Eq. (3.31). We therefore took PSR B1821-24 as an example of a screened MSP and studied the impact of the screened potential on various model outputs.

In addition to flux predictions, the spectral cut-off of a given pulsar gamma-ray spectrum determines whether the pulsar will be visible for a particular gamma-ray telescope (see e.g. de Jager et al., 2001). Also, the nature of the spectral cut-offs may be a discriminator between the rival PC and OG models. For these reasons, we studied the spectral cut-off energy predictions of PSR J0437-4715 and

PSR B1821-24 in Sections 3.6.2 and 3.7.2.

For PSR J0437-4715, we found a maximum CR cut-off energy of $1 - 20$ GeV, depending on the assumed geometry (χ and ζ) and EOS (i.e. radius R, moment of inertia I, and mass M). This result was in agreement with the findings of similar studies. This is in contrast with earlier studies which predicted PSR J0437-4715's CR cut-off energy to be in the range $50 - 100$ GeV (Harding et al., 2002b; Bulik et al., 2000), making proposals for ground-based telescopes with imaging thresholds near 100 GeV attractive. We furthermore studied the effect of geometry on the spectral cut-off by obtaining a contour plot of the CR energy vs. χ and ζ, indicating that maximum energy values are obtained when $\chi \sim \zeta$. Another contour plot of CR energy vs. scaled polar angle ξ and magnetic azimuthal angle ϕ showed that the maximum photon energy is produced close to the magnetic axis, for large values of $\cos\phi$, while the oscillation of particle trajectories takes place along B-field lines with $\phi \sim 180°$. Unfortunately, the low predictions of the maximum CR energy leads to the conclusion that 4^{th} generation Cherenkov telescopes are generally needed in order to observe CR emission from unscreened gamma-ray MSPs. While an IC component resulting from TeV electrons upscattering the UV / soft X-rays from the surface of PSR J0437-4715 may still be detectable, this prediction by Bulik et al. (2000) should also be re-evaluated within a GR electrodynamical framework.

When evaluating the screened case, we found CR energies of up to ~ 150 GeV for PSR B1821-24, compatible with similar predictions. We demonstrated that the CR cut-off energy decreases rapidly when the impact angle becomes large. The contour plot of CR cut-off energy as a function of χ and ζ was more symmetrical with respect to the $y = x$ line for the screened case, and we confirmed that the largest energies are obtained for small χ since the electric field scales with the factor $\cos\chi$. The contour plot of the maximum CR energy as a function of normalised polar angle ξ and magnetic azimuthal angle ϕ showed that a maximum energy is found at $\xi = 0$ (where the E-field approximation attains a maximum), and that there is no exclusion region where field reversals occur, because the screened E-field doesn't change sign above the PC. (The fact that the unscreened E-field has only one sign, may cause charge accumulation above the PC, changing the electrodynamics of a steady-state solution). The photon energy is furthermore independent of ϕ, since the E-field approximation we used is also independent of this coordinate (this may change for a more detailed treatment). It is unfortunate that PSR B1821-24 is expected to have a large impact angle (from radio polarimetric observations), since low spectral cut-offs are then expected, implying that PSR B1821-24 may also not be visible for current gamma-ray telescopes. Given the low spectral cut-offs for both pulsars, even *CTA* may have a hard time probing the CR tails of the gamma-ray integral fluxes.

Section 3.6.3 and 3.7.3 dealt with the behaviour of electron and photon energies as functions of

altitude above the stellar surface. PSR J0437-4715's maximum gamma-ray energy was shown to be $\sim$ 10 GeV as mentioned previously, while the maximum electron energy was $\sim$ 10 TeV. The position above the PC where the maxima of the energies occurred corresponded reasonably well to the position of the maximum of the fractional gamma-ray luminosity, meaning that photons of the maximum CR energy (and electrons having energies close to the maximum energy) were produced abundantly. For PSR B1821-24, the maximum gamma-ray energy was $\sim$ 150 GeV, while the maximum electron energy was $\sim$ 50 TeV. These values are much higher than for PSR J0437-4715, since PSR B1821-24's E-field reaches much higher values (due to its larger spin-down luminosity). In this case, the position of the maxima of the energies also correspond quite well to the position where the maximum of the fractional gamma-ray luminosity occurs. PSR B1821-24's graphs of photon and electron energy vs. distance have more well-defined peaks than those of PSR J0437-4715, corresponding to the peak of the screened parallel electric field. The E-field drops to zero just after it has reached a maximum, so that there is no further particle acceleration, and CR losses cause the particle and photon energies to decrease more rapidly than in the unscreened case.

Differential and integral fluxes were calculated in Section 3.6.4 and 3.7.4. We produced a band of possible spectra for PSR J0437-4715, with the uncertainty stemming from unknown geometry and EOS parameters. Our range of spectra more or less included the predictions of Frąckowiak & Rudak (2005a,b) and Harding et al. (2005b), and the spectral shapes were similar. We found that the 1 GeV *EGRET* upper limit constrained the integral flux of the GR model (as corroborated by Frąckowiak & Rudak (2005a,b); Harding et al. (2005b)), and we used this upper limit to constrain the gamma-ray efficiency of PSR J0437-4715 by scaling the flux curves so as not to violate the *EGRET* upper limits and *H.E.S.S.* threshold energy. One may try to explain this overprediction in terms of geometry uncertainties, but in Chapter 4 we will show that for an ensemble of the MSPs in the GC 47 Tucanae, the average flux also overshoots the *EGRET* upper limits for that object. Therefore, more serious attempts will have to follow in order to solve this problem. In Section 6.3, we discuss the possibility of using a parametrised potential and charge density, and using data to constrain these fundamental quantities. In addition, more sensitive observations at energies of a few GeV will help to probe the CR spectral tail, and thus limit the accelerating potential.

We furthermore modelled the gamma-ray flux expected from PSR B1821-24. We found that this pulsar is not expected to be visible for *H.E.S.S.* unless the geometry is favourable. Assuming that the inferred angles χ and ζ are correct, this MSP will probably not even be visible for *GLAST LAT*, despite its large spin-down luminosity.

When calculating the particle and gamma-ray efficiencies of PSR J0437-4715, we found that

$L_\gamma^{\rm beam}/L_{\rm prim,max} \sim 1$ (Section 3.6.5). This means that almost all particle luminosity is converted into photon luminosity as expected for strong radiation reaction. Radiation reaction, combined with further (weak) acceleration towards the light cylinder, result in a total residual electron power of $\sim 1 - 2.5\%$ of the spin-down power at the light cylinder. However, since the *EGRET* limits imposed constraints on the GR model, we had to scale the integral flux curve, and found that $\eta_\gamma^{\rm beam} \leq 0.55\%$, although it must be borne in mind that the geometrical beaming factor Λ might alter this constraint significantly. Forthcoming *GLAST* observations will possibly be able to directly measure the value of $\eta_\gamma^{\rm beam}$. For the case of PSR B1821-24, we found that $\Lambda \sim 1\ 500$ (indicative of off-beam radiation), corresponding to a value of $\eta_\gamma^{\rm beam} = 1.6\%$. No scaling of integral flux graphs was necessary, as the predicted curve did not violate experimental limits.

Lastly, the lightcurves of PSR J0437-4715 were briefly studied in Section 3.6.6. We noted that a full treatment would require the correct Lorentz transformation from the corotating to the observer frame (see Section 6.2). We concluded that GR theory predicts a relatively narrow pulse ($\beta^{\rm slice} \sim 0.2$ phase width) centered on the magnetic axis, and found an estimate for the beaming solid angle of ~ 0.5 sr per PC when selecting radiation with energy $\gtrsim 100$ MeV (for $\chi = 35°$). We furthermore calculated lightcurves for PSR J0437-4715 for different observer angles ζ. Maximal heights were obtained when $\zeta \sim \chi$. However, the pulse heights decreased rapidly as the radiation became off-beam. The 'dips' in lightcurves with $\zeta \geq \chi$ near phase $\phi_L/2\pi \sim 0.5$ (where $\phi \sim \pi$) were most probably due to the sign reversal of the electric field. Since the radio and X-ray pulses are in phase, one would expect that the gamma-ray pulse will also be in phase with these, provided all pulses are produced by accelerated particles close to the magnetic axis. We expect that *GLAST LAT* might measure lightcurves of PSR J0437-4715 around a few GeV.

Future model refinements include the transformation from the corotating to the observer frame, including GR effects such as light bending, redshift, aberration, and charge pile-up, as well as investigating multipoles instead of a dipolar magnetic field (Navarro et al., 1997), making more appropriate assumptions concerning the primary electrons' initial velocities (Sakai & Shibata, 2003), and treating the field reversals properly. We furthermore note that inclusion of the E_ϑ-component in the expression of the accelerating E-field promises to change the electrodynamical picture significantly (see Section 6.1). The question remains whether this refinement may provide the means to extract protons from the stellar surface, effectively solving the return current by providing charge neutrality.

Chapter 4

Millisecond Pulsar Population Studies

4.1 Introduction

In order to gain understanding of a certain natural phenomenon, the physicist follows the (cyclic) scientific method of formulating a hypothesis (subject to his / her thought framework and experience), applying known physical laws in constructing and implementing a model (usually subject to simplifying assumptions), obtaining definite predicted outcomes, and comparing his / her results with experimental measurements. Comparison of theory and experiment may lead to refinement of the model, or the need for a new hypothesis. One may focus one's attention on a particular example of a certain natural phenomena, and this will serve as a case study for probing the inner workings or mechanisms of the type of object or process in question. However, one such object is usually a prototype of a larger class of objects which have similar qualities and modes of operation. Applying the model to specific examples may in some cases give limited possibility of making definite progress if, for example, the particular specimen under consideration has some ill-determined parameters, or exhibit atypical behaviour. In order to gain a holistic picture and discover universal trends, it is sometimes advantageous to consider a population of similar objects and to simulate their average / gross characteristics. Alternatively, one might be interested in the operation of a whole system consisting of basic units, rather than that of the individual units. Such an approach may also simplify model calculations. This principle is used in many branches of Physics, e.g. Statistical Thermodynamics, Materials Science, and Particle Physics, where larger "wholes" are made up of more fundamental units.

Two major advantages of this global approach are the ability to overcome the potentially staggering number of individual elements making up a compound system, as well as the smoothing out of individual "eccentricities" (anomalies) to obtain an indication of typical behaviour by considering

system-averaged properties. This may also be applied to the case of Pulsar Physics. When modelling the radiation and particle output of a pulsar, the most obvious test of such a model comes when applying it to a single (isolated) pulsar. This was done in Chapter 3, involving the detailed simulation of the millisecond pulsars (MSPs) PSR J0437-4715 and PSR B1821-24. The next step which naturally presents itself is that of a population study: applying the same model of a single pulsar iteratively for different sets of pulsar parameters. From such a study, one may gain insight into the visibility of a particular group of pulsars, e.g. galactic pulsars, or pulsars in a globular cluster (GC), where relative errors on e.g. average flux are typically smaller than those on the flux of a single pulsar. Also, one would gain more information regarding the behaviour of the single pulsar model for the vast ranges of pulsar parameters involved in a population study.

Unfortunately, the statistics (experimental observations) for gamma-ray pulsar studies are sparse, owing to the fact that only seven gamma-ray pulsars have been observed so far, and of these, only six are high-energy pulsars observed above 100 MeV (Thompson, 2001). The launch of *GLAST* in mid-2008 is expected to change this situation completely, as it is expected to detect many hundreds of new gamma-ray pulsars (Ransom, 2007), possibly with a sizable fraction being pair-starved. When *H.E.S.S.-II* comes online in 2009 / 2010 (in addition to *MAGIC-II* by the end of 2008), one might optimistically expect some pulsar detections from the ground-based Cherenkov telescope community, complementing the work of space missions. Such new discoveries will open up a new window of opportunity for refining high-energy pulsar models, since more rigorous testing will be possible.

In light of the anticipated discovery of many new gamma-ray pulsars, pulsar population studies, such as those discussed in this chapter, will provide valuable means of dialogue between the theory and data, on a broader level than the complementary single-pulsar studies. Therefore, although lack of data may (temporarily) limit comparison of theory and data as well as deriving model constraints, the waiting period leading up to much more new data should be fruitfully used to obtain good theoretical predictions.

Recently, Michel (2004) severely criticised both the Goldreich-Julian-type PC model, as well as outer gap models with gaps of arbitrary sizes and locations. The key to obtaining more certainty as to how pulsars really work must lie in the combination of theory and observation, so that the field may hopefully converge and settle on one model of preference. It may however be useful to focus one's attention on the simplest pulsar population first. By using unscreened MSPs, we opt to select a "clean sample" of pulsars where the basic B- and E-fields may be fundamentally tested observationally. The "pair-starved" (low spin-down) pulsar population facilitates investigation of pulsar physics in its simplest form, without the complicating effect of E-field screening evident in younger pulsars. Having

said this, it is equally important to study the young pulsars, as they represent the bulk of the pulsar population, and therefore should account for the largest part of the new pulsar discoveries by upcoming experiments.

A number of pulsar population studies have been done (e.g. Large, 1971; Bailes & Lorimer, 1995; Romani, 1996; Possenti et al., 1998; Verbunt et al., 1999; McLaughlin & Cordes, 2000; Harding et al., 2002a; Gonthier et al., 2002; Willems & Kolb, 2002; Gonthier et al., 2004; Wang, 2006; Gonthier et al., 2007; Story et al., 2007; Bednarek & Sitarek, 2007). Our approach is unique in the following ways: First, we do not study radio properties of the pulsars, but focus on high-energy gamma-ray radiation. Next, we direct our attention to the pulsed radiation expected from MSPs, and do not model young pulsars. We furthermore tried to do studies which would be complementary to those mentioned above, e.g. involving MSPs in GCs, and beaming effects, as described in the paragraph below.

This chapter is divided into three main parts, corresponding to three major applications of MSP population studies we have performed. After some preliminary remarks (Section 4.2), we investigate the behaviour of the single pulsar model, which was developed and described previously (Chapter 2), in parameter space when considering ranges of parameters appropriate for MSPs (Section 4.3). Secondly, we study the systematic beaming effects of pulsars (Section 4.4). We will show that the beaming correction factors may in some cases be significantly larger than unity, in contrast to the usual assumptions made when analysing pulsar data. As one last application, we study the visibility of the nearby GC 47 Tucanae using the same basic tools, but for a population of GC MSPs with corrected values of their period derivatives (Section 4.5). These results may easily be scaled so that they may be applied to other GCs. Conclusions are presented in Section 4.6.

4.2 Preliminaries

4.2.1 Screening of PC Potentials

When dealing with a population of pulsars, it is important to distinguish between those pulsars which will have screened magnetospheres with copious pair production, and those which will have inhibited screening (see e.g. Section 2.1.4, as well as Sections 3.6.1 and 3.7.1). A useful condition may be found in the context of the frame-dragging pulsar model we are using. Screening will occur when (Harding et al., 2002b)

$$\dot{E}_{\rm rot,break} < \dot{E}_{\rm rot} \tag{4.1}$$

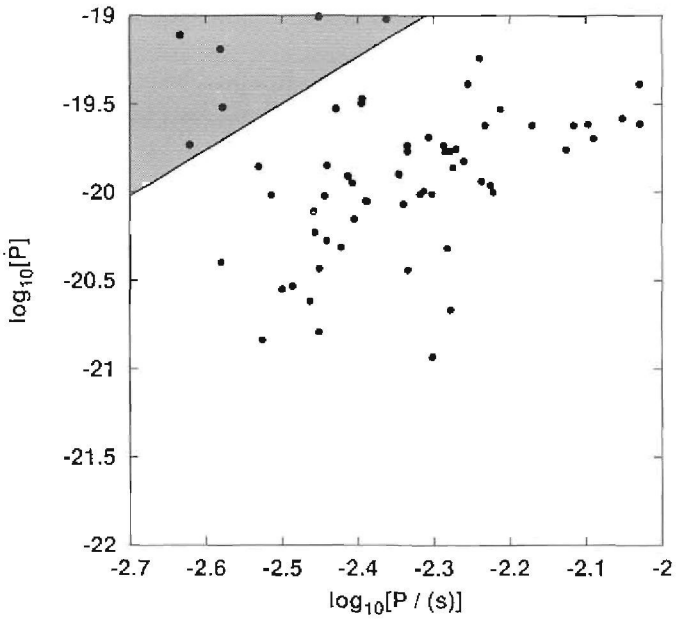

Figure 4.1: Condition for screened PC potentials. The shaded part at the top left of the diagram indicates the region where screening by pair creation occurs, according the Eq. (4.4). Also shown are MSPs from the *ATNF Pulsar Catalogue* (Manchester et al., 2005). This indicates that most MSPs are expected to have unscreened magnetospheric electric fields, as found by Harding et al. (2005b).

$$1.4 \times 10^{34} \left(\frac{P}{B_{12}^2} \right)^{1/7} \quad < \quad \frac{4\pi^2 I \dot{P}}{P^3}. \tag{4.2}$$

The condition for a screened potential may be rewritten in terms of P and $\dot{P}$:

$$\dot{P} > (1.4 \times 10^{262/8})(2\pi)^{-3/2} I^{-1} \left(\frac{R^6}{6c^3 f^2(1)} \right)^{1/8} P^{21/8}. \tag{4.3}$$

When $I = 0.4MR^2$, $R = 10^6$ cm, and $M = 1.4M_\odot$, so that $f(1) \sim 1.5$, this becomes (Venter & de Jager, 2008a)

$$\log \dot{P} > 2.625 \log P - 12.934. \tag{4.4}$$

This condition defines an upper left corner on a $P\dot{P}$-diagram where screened pulsars are found (see Figure 4.1). The boundary line roughly coincides with coordinates (-2.7,-20) and (-2.3,-19). Eq. (4.4) therefore indicates that most MSPs are expected to have unscreened magnetospheric electric fields, as found by Harding et al. (2005b). In subsequent paragraphs, we will use Eq. (4.4) to decide whether to use a screened or unscreened E-field when calculating a particular MSP's properties.

4.2.2 Proper Motion

When a pulsar has a large (transverse) velocity, there will be an apparent transverse quadratic Doppler effect (Shklovskii effect) on $\dot{P}$ (e.g. van Straten et al., 2001; Camilo et al., 1994):

$$\dot{P}_{\rm obs} = \dot{P}_{\rm int} + \beta^m P, \tag{4.5}$$

with $\dot{P}_{\rm obs}$ the observed value of the time-derivative of P, $\dot{P}_{\rm int}$ the intrinsic value, and

$$\beta^m = \frac{\mu^2 d}{c}. \tag{4.6}$$

Here d represents the pulsar distance. The proper motion $\mu = |\vec{\mu}|$ is usually measured in arcseconds per year, and the vector quantity might have right ascension and declination components, i.e. $\mu = \sqrt{\mu_\alpha^2 + \mu_\delta^2}$. To estimate the effect of a pulsar's proper motion on its period-derivative, let us calculate the following quantity

$$\frac{\dot{P}_{\rm obs} - \dot{P}_{\rm int}}{\dot{P}_{\rm int}} = x. \tag{4.7}$$

Using $\tau_{\rm obs} = P/2\dot{P}_{\rm obs}$, and the definition of β_m, one finds

$$\mu\ ({\rm mas/yr}) \approx 2.5 \times 10^6 \left(\frac{x}{1+x}\right)^{1/2} \tau_{\rm yr}^{-1/2} d_{\rm kpc}^{-1/2} \sim (d.\tau_{\rm obs})^{-1/2}. \tag{4.8}$$

The $\dot{P}$-values need to be corrected for this effect, and this is possible when the pulsar's proper motion as well as distance are known (i.e. solving for x from the above expression). The *ATNF Pulsar Catalogue* (Manchester et al., 2005) gives intrinsic $\dot{P}$-values when μ and d are available. This effect is most pronounced for pulsars having a large proper motion and small distance.

4.3 The Effects of Geometry and Rotational Characteristics on MSP Visibility: A Parameter Study

Recent pulsar models confirm the conclusion of the basic pulsar models which have been proposed decades ago: enough energy may be derived from the pulsar's rotation to generate the large potential drops needed for gamma-ray production. Establishing the energy budget (and basic radiative processes) is only one side of the coin. The other vital effect which has to be taken into account when studying pulsar visibility is the geometry of the system. Even if a system has a large energy output, radiation may potentially be dissipated / scattered / converted before it reaches the observer, or it

may never reach the observer due to the geometry and beaming properties of the emission regions in the pulsar PC. Also, the electric potential determining the energy properties of the pulsar radiation is expected to depend on the basic pulsar parameters P and $\dot{P}$, and pulsar models typically predict $\Phi \sim \dot{P}^{1/2} P^{-3/2}$. It is therefore important to consider the role played by different pulsar parameters when considering the question of pulsar visibility. In this section, we will study the effects of varying $(P, \dot{P}, \chi, \zeta)$ on various pulsar characteristics in the framework of the GR frame-dragging model: CR cut-off energy, beam and slice gamma-ray efficiencies, integral flux, energy flux, beaming correction factor, and average energy. This section therefore investigates pulsar properties for a mesh of pulsar parameter space, while Section 4.4 deals with population properties of 'real' pulsars, taken from the *ATNF Pulsar Catalogue* (Manchester et al., 2005).

4.3.1 Method

We have made several runs with the same basic MSP program, for the pulsar period P, period time-derivative $\dot{P}$, inclination angle χ and observer angle ζ (for the definition of χ, and ζ, see Section 2.5.7) in the following ranges: $\log_{10}(P) = -2.7, -2.6, ..., -2.0$; $\log_{10}(\dot{P}) = -22, -21, ..., -19$; $\chi = 10°, 20°, ..., 80°$, and $\zeta = 10°, 20°, ..., 80°$ (i.e. we consider $8 \times 4 \times 8 \times 8 = 2\,048$ MSPs. The values $\chi = 0°$ and $\chi = 90°$ have not been considered, since the first gives problems when calculating the phase angle (Eq. [2.156]), while the latter leads to a surface charge density $\propto \cos\phi$ (see Eq. [2.115]) which reverses sign over half of the PC and therefore needs careful treatment when considering electron primaries). The ranges for P and $\dot{P}$ were chosen bearing in mind that Muslimov & Harding (1997) used the small angle approximation when deriving the MSP model. This means that the expression for the parallel electric field $E_{||}$ becomes less realistic for high altitudes and large polar angles. In addition, oscillations in $E_{||}$ may give rise to unphysical values of the electron Lorentz factor γ for certain regions of the PC (around $\phi \sim \pi$) as explained previously (Section 3.4). We ignore the radiation from these regions of the PC. For some combinations of P and $\dot{P}$, an increasingly larger part of the PC has to be ignored (sometimes as much as $\sim 90\%$), leading to strange and unreasonable spectra (see e.g. the spikes obtained in the left panel of Figure 4.2, which may be due to a combination of violating the small angle approximation, and sign reversals of $E_{||}$). We therefore limit the range of P and $\dot{P}$ in this section, so that we may still obtain reasonable conclusions. One solution would be to redo the calculations with newer high-altitude derivations of $E_{||}$, which should lead to less problems with regards to E-field oscillation (Harding 2007, personal communication; also see Section 2.4.6). This matter will be further considered in Chapter 6. For this limited range of P and $\dot{P}$, we find that only 16% of the MSPs we consider have screened PCs according to Eq. (4.4), for which we use the screened

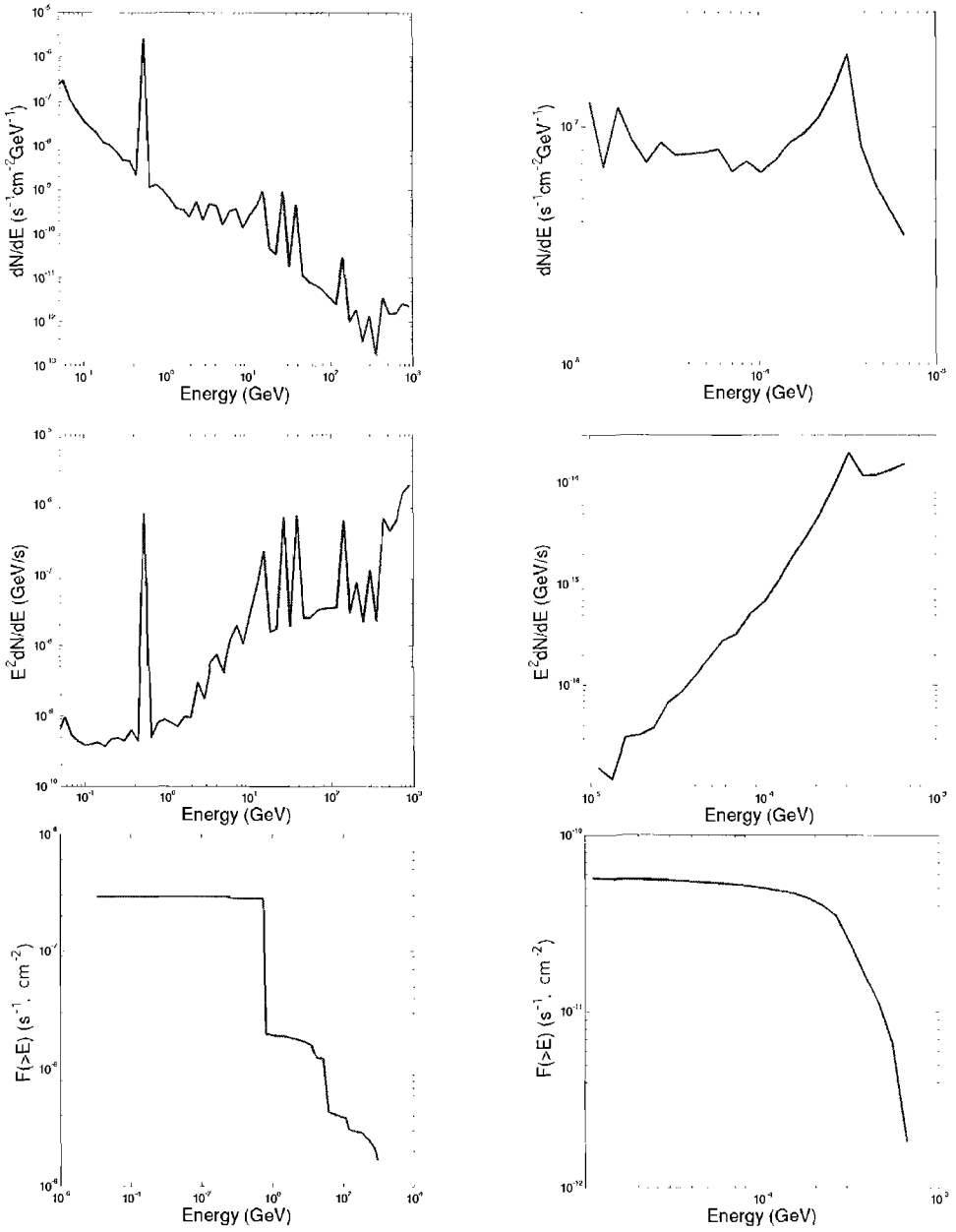

Figure 4.2: Graphs of $(dN/dE)^{\text{slice}}$, $E^2(dN/dE)^{\text{slice}}$, and integral flux $F^{\text{slice}}(>E)$. The left column is for $P = 0.001$ s, $\dot{P} = 10^{-17}$, $\chi = 60°$, and $\zeta = 60°$. The right column is for $P = 0.01$ s, $\dot{P} = 10^{-22}$, $\chi = 10°$, and $\zeta = 30°$. Only runs in the ranges $\log_{10}(P) \in [-2.7, -2.6, ..., -2.0]$, $\log_{10}(\dot{P}) \in [-22, -21, -20, -19]$, $\chi \in [10°, 20°, ..., 80°]$, and $\zeta \in [10°, 20°, ..., 80°]$ were included in the population study of this section, as explained in the text.

electric field (Eq. [2.124]). For the other cases, we use Eq. (2.111) and (2.117).

Firstly, we calculate the incremental luminosity radiated by a primary electron above the PC at

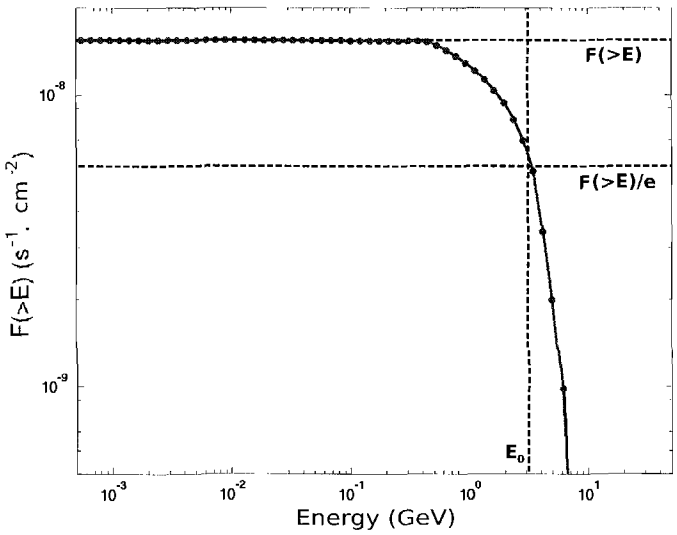

Figure 4.3: Determining the CR cut-off energy using the integral flux. The cut-off energy E_0 is read from the graph where the integral flux has decreased by a factor $\exp(-1)$.

a position (r, ϑ, ϕ). The angle of the tangent to the local magnetic field line with respect to the spin axis is taken as the half beam width ρ of this incremental radation. As previously, for the given χ (inclination angle), ϕ, (magnetic colatitude) and ρ, we calculate ζ (observer angle with respect to the spin axis) and ϕ_L (phase), with (ζ, ϕ_L) defining the beam direction (Section 2.5.7). The characteristic CR energy of this incremental radiation spectrum is taken as $E_\gamma^c = 1.5(\lambda_c/\rho_c)\gamma^3 m_e c^2$ (Section 2.5.9). The total incremental luminosity radiated in a time interval $dt = ds/(\beta_r c)$ (along a magnetic field line segment of distance ds by electrons moving at a speed of β_r) may thus be represented by $dL/(d\phi_L d\zeta dE) = d\dot{N}_e \dot{\gamma}_{\rm CR} m_e c^2\, dt$ (Section 2.5.10). The number of particles which move past the position (r, ϑ, ϕ) per second is given by $d\dot{N}_e(R, \vartheta_0, \phi_0) = \beta_0 c \rho_e dS/e$ (the suscript '0' evaluated at the stellar surface), and is assumed to stay constant along a particular magnetic field line. The initial (surface) speed of the electrons is set to $\beta_0 c = 0.9999c$, dS is the area of the surface patch from which the electrons come, ρ_e the actual charge density, and e the electron charge. We take $\dot{\gamma}_{\rm CR} \approx 2e^2 c\gamma^4/(3\rho_c^2 m_e c^2)$ to be constant over the short time interval $dt \ll P$.

We calculate the differential flux $(dN/dE)^{\rm slice}$, integral flux $F^{\rm slice}(>E)$, energy flux $U^{\rm slice}$, and luminosities $L_\gamma^{\rm slice}$ and $L_\gamma^{\rm beam}$ as explained in Section 2.5.10 (see Eq. [2.165], [2.174], [2.183], [2.169] and [2.170]). It is not straightforward to assign a spectral index α_s to the νF_ν-spectrum by e.g. assuming a functional form of $KE^{-\alpha_s}\exp(-E/E_0)$. In contrast, the integral flux is much smoother and easier to work with.

We estimate the CR cut-off energy E_0 in the following way. We divide the energy range into logarithmic energy bins, and calculate an 'average' energy $E_{\mathrm{avg},i} = 0.5(E_{i-1} + E_i)$ for the i^{th} energy bin spanning $[E_{i-1}, E_i]$, $i = 1, 2, ..., N$. We then plot the integral flux as a function of $E_{\mathrm{avg},i}$ and locate the first value of $\overline{F}^{\mathrm{slice}}(>E)$ smaller than $e^{-1} \times \overline{F}^{\mathrm{slice}}(>E_{\mathrm{avg},1})$, say $\overline{F}^{\mathrm{slice}}(>E_{\mathrm{avg},k})$. Finally, we set the cut-off energy $E_0 = 0.5(E_{\mathrm{avg}\,k-1} + E_{\mathrm{avg},k})$. This method is demonstrated in Figure 4.3. The beam and slice gamma-ray efficiencies are defined by $\eta_\gamma^{\mathrm{beam}} \equiv L_\gamma^{\mathrm{beam}}/\dot{E}_{\mathrm{rot}}$ and $\eta_\gamma^{\mathrm{slice}} \equiv L_\gamma^{\mathrm{slice}}/\dot{E}_{\mathrm{rot}}$. The beaming correction Λ as well as energy ratio τ are calculated using Eq. (2.181), (2.185) and (2.187). The quantities E_0, $\eta_\gamma^{\mathrm{beam}}$, $\eta_\gamma^{\mathrm{slice}}$, $\overline{F}^{\mathrm{slice}}(>100$ MeV), $\overline{F}^{\mathrm{slice}}(>1$ GeV), $\overline{F}^{\mathrm{slice}}(>10$ GeV), U^{slice}, $\Lambda = \epsilon\overline{\Delta\Omega}^{\mathrm{beam}}/\beta^{\mathrm{slice}}$, and τ may therefore be calculated numerically as functions of $(P, \dot{P}, \chi, \zeta)$.

We made contour plots of these quantities for different P and $\dot{P}$, for 'best', 'good', 'average', 'random', 'medium', 'intermediate', 'bad', and 'worst' combinations of χ and ζ, as defined in Table 4.1. The results are presented in Figures 4.4 through 4.12. The canonical values of $M = 1.4M_\odot$, $R = 10^6$ cm, $I = 0.4MR^2$, and $d = 1000$ pc were used in all cases. In addition, we present graphs of the above quantities as functions of geometry χ and ζ, choosing the MSPs with $(\log_{10}[P], \log_{10}[\dot{P}])$ = (-2.3,-21), (-2.2,-19), and (-2.5,-19). These results appear in Figures 4.13 through 4.15, illustrating how these quantities differ for the unscreened and screened cases.

4.3.2 Results and Discussion

(i) CR Cut-Off Energy

It is expected that the CR cut-off energy E_0 should scale with maximum electric potential Φ_{max}. In turn, Φ_{max} typically scales as $\dot{P}^{1/2}P^{-3/2}$, so that E_0 should attain a maximum at small values of P and large values of $\dot{P}$ (for constant geometry). The geometry also plays a role in the sense that on-beam radiation is expected to be much more energetic than off-beam radiation (when there is a

Combination	Description
Maximum (Best)	Maximum over the whole range of chosen χ and ζ
Good	$\chi = \zeta = 10°$
Average	Average over the whole range of chosen χ and ζ
Random	Random χ and ζ in the range (10°, 20°, ..., 80°) for each $(P, \dot{P})$
Medium	$\chi = 40°$, $\zeta = 50°$
Intermediate	$\chi = 30°$, $\zeta = 50°$
Bad	$\chi = 20°$, $\zeta = 70°$
Minimum (Worst)	Minimum over the whole range of chosen χ and ζ

Table 4.1: Definitions of different combinations of (χ, ζ) as used in contour graphs, e.g. Figures 4.4 and 4.5.

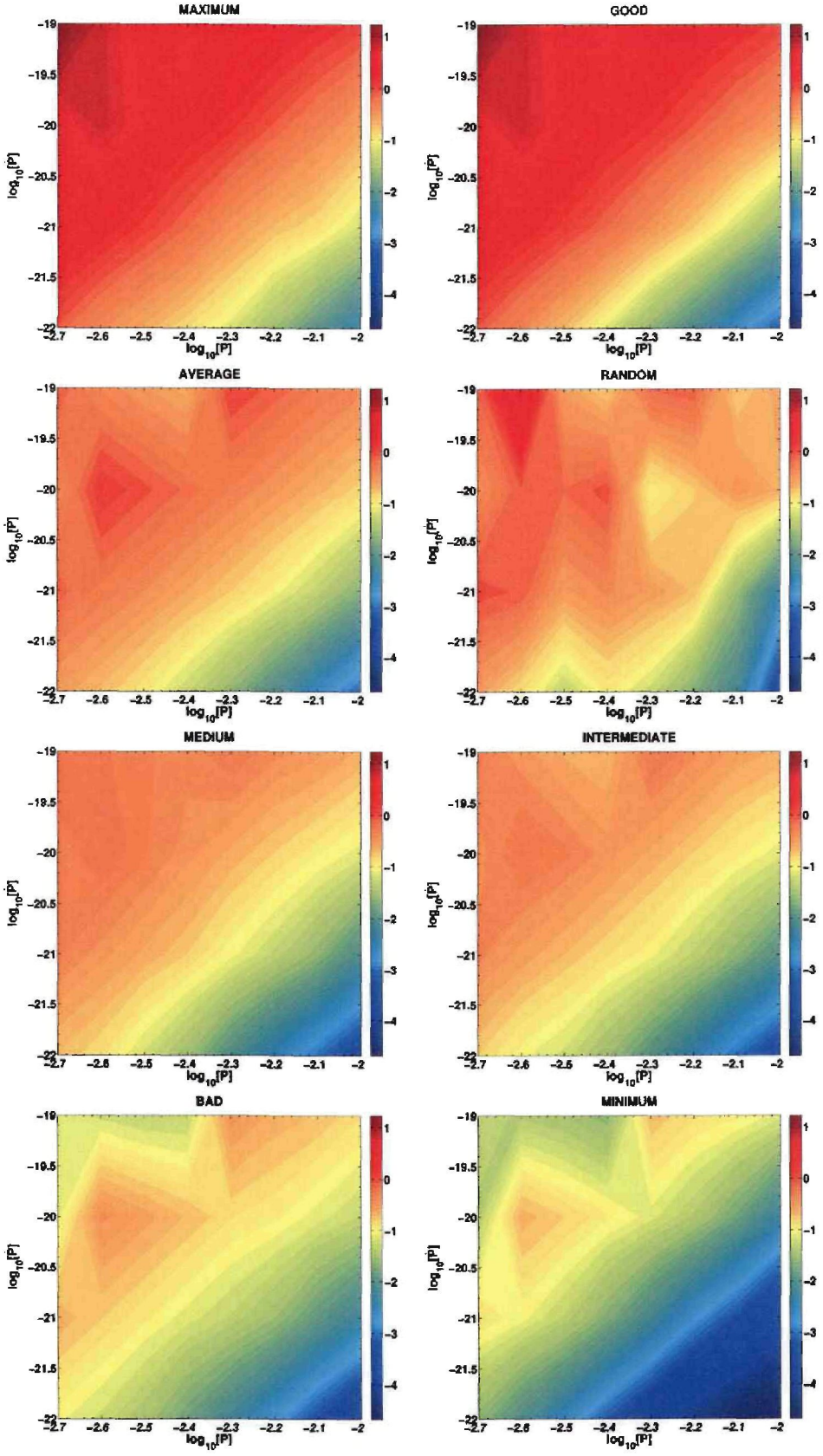

Figure 4.4: Contour graphs of the $\log_{10}$ of CR cut-off energy E_0 (in GeV) vs. $\dot{P}$ and P, for different χ and ζ. Identical (colour) scales for the CR cut-off energy facilitate comparison. This is also the case for the contour graphs to follow. See Table 4.1 for explanation of headings.

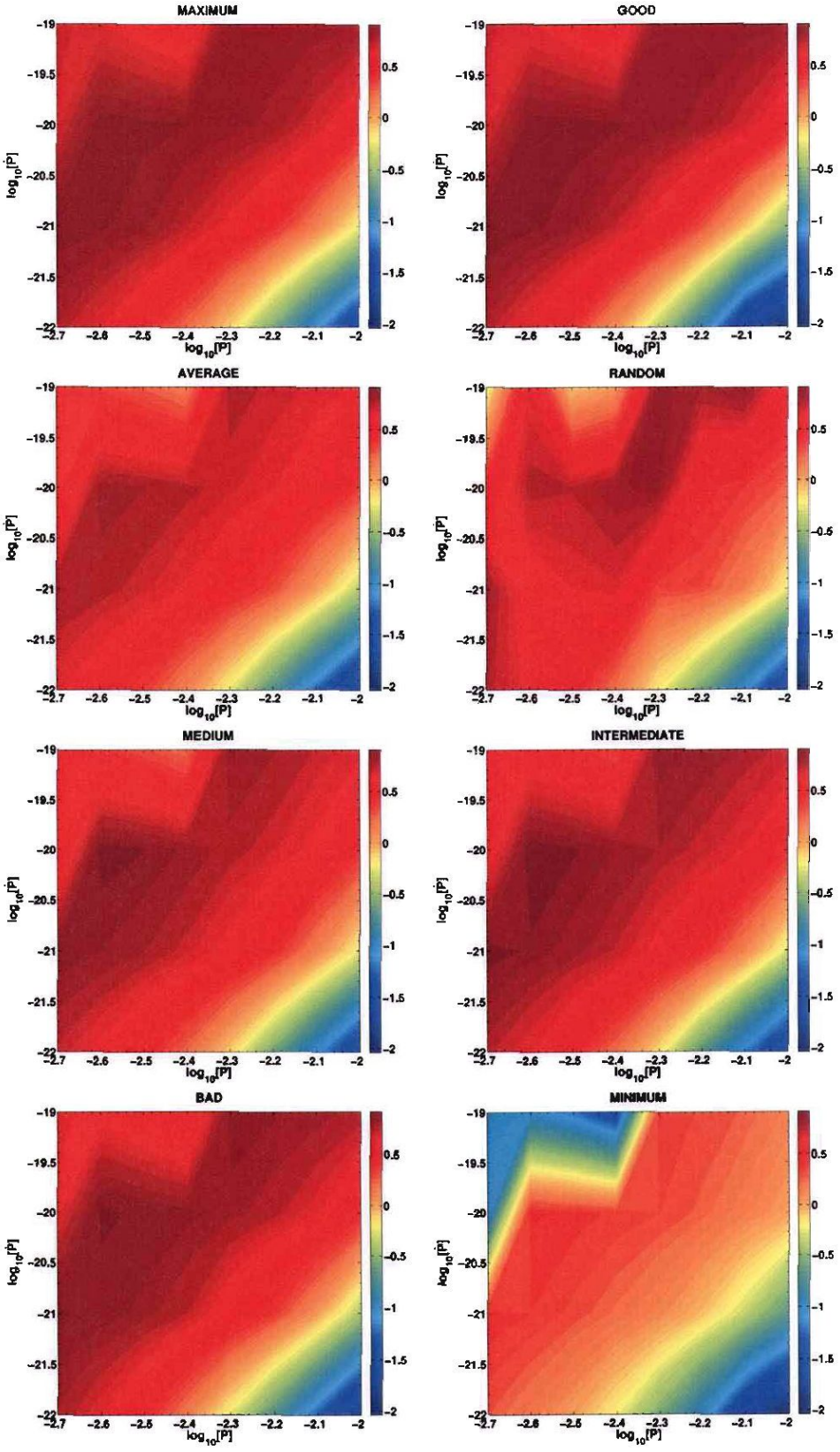

Figure 4.5: Contour graphs of the $\log_{10}$ of the total beam gamma-ray efficiency $\eta_\gamma^{\rm beam}$ (%) vs. $\dot{P}$ and P, for different χ and ζ. See Table 4.1 for explanation of headings.

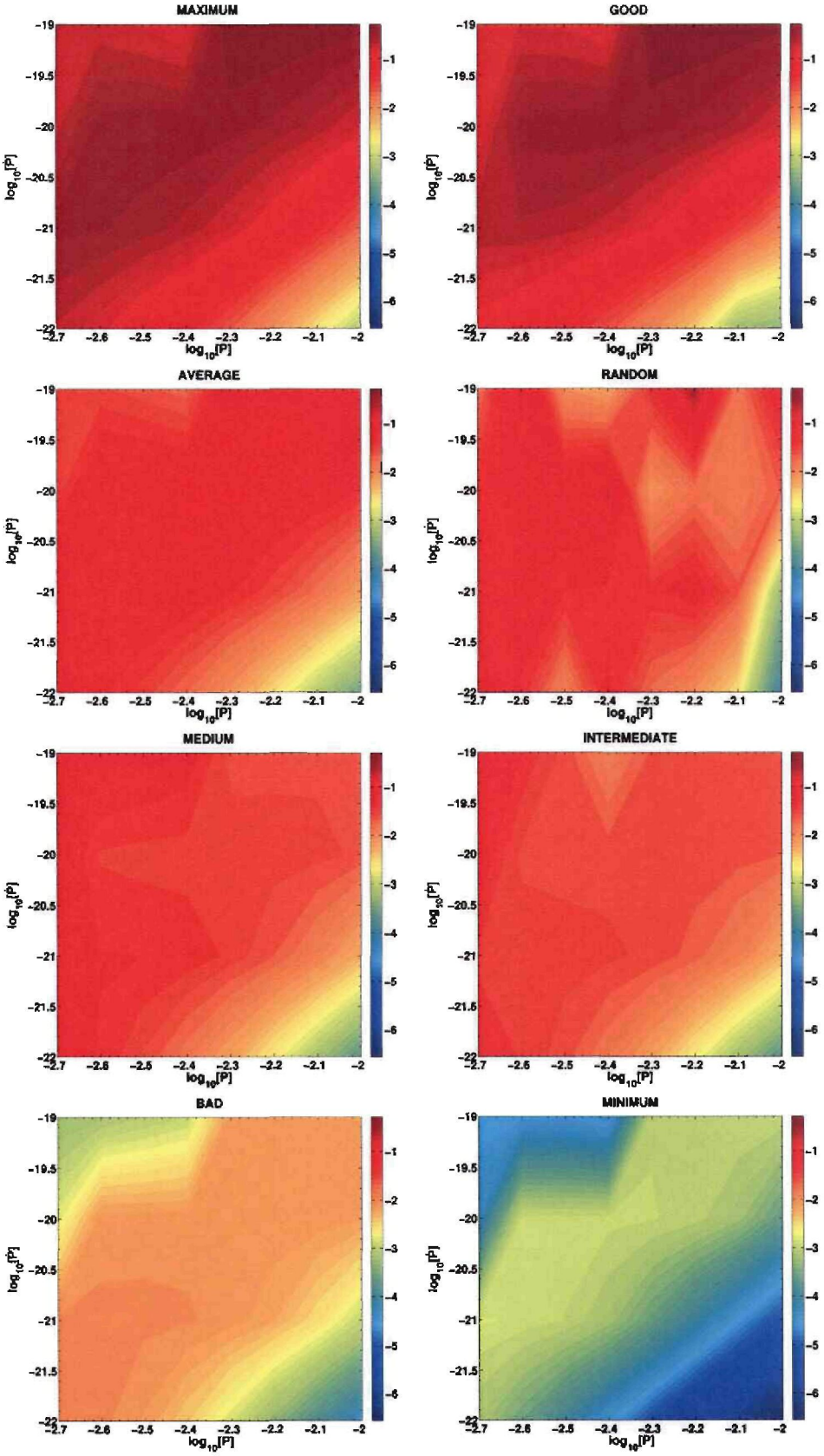

Figure 4.6: Contour graphs of the $\log_{10}$ of the slice gamma-ray efficiency $\eta_\gamma^{\text{slice}}$ (%) vs. $\dot{P}$ and P, for different χ and ζ. See Table 4.1 for explanation of headings.

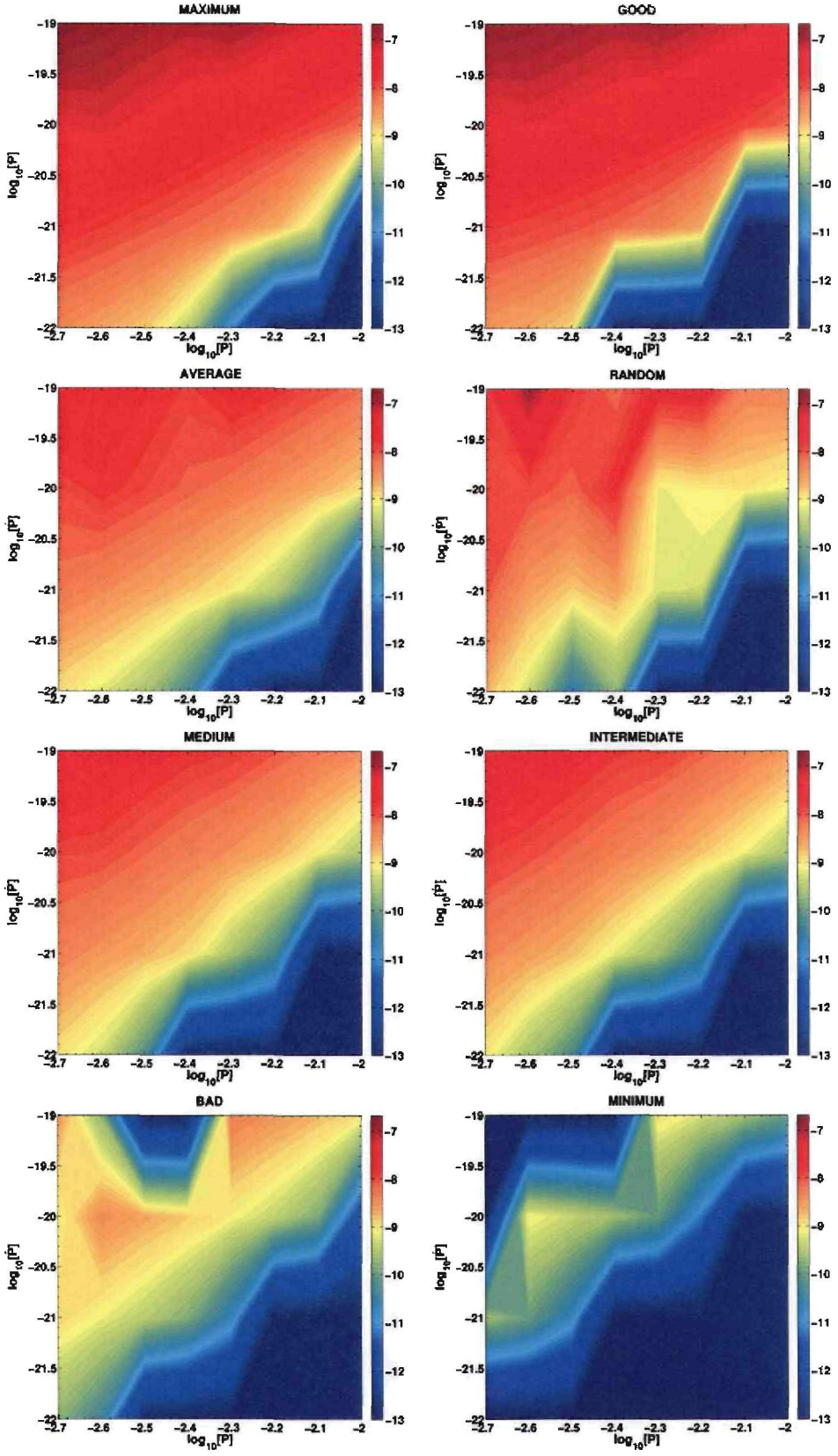

Figure 4.7: Contour graphs of the $\log_{10}$ of integral flux above 100 MeV, $\overline{F}^{\rm slice}(>100\,{\rm MeV})$, in units of $\rm cm^{-2}s^{-1}$ (for $d = 1$ kpc) vs. $\dot{P}$ and P, for different χ and ζ. Zero integral fluxes above 100 MeV (due to small CR energy cut-offs) are indicated by the blue colour, since a value of 10^{-13} $\rm cm^{-2}s^{-1}$ has been assigned to these cases for representational purposes. See Table 4.1 for explanation of headings.

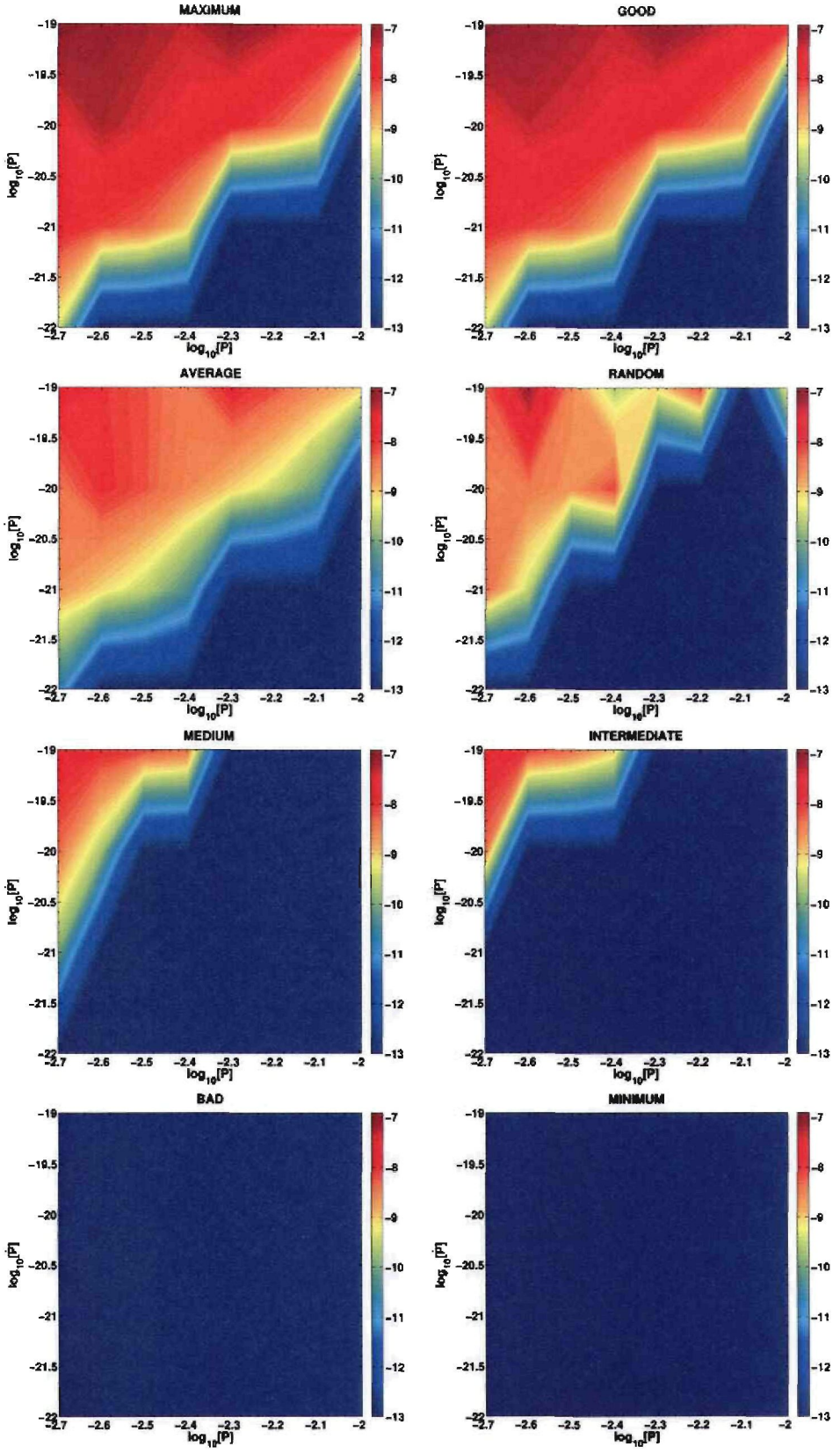

Figure 4.8: Contour graphs of the $\log_{10}$ of integral flux above 1 GeV, $\overline{F}^{\rm slice}(>1\,{\rm GeV})$, in units of $\rm cm^{-2}s^{-1}$ (for $d = 1$ kpc) vs. $\dot{P}$ and P, for different χ and ζ. Zero integral fluxes above 10 GeV (due to small CR energy cut-offs) are indicated by the blue colour, since a value of 10^{-13} $\rm cm^{-2}s^{-1}$ has been assigned to these cases for representational purposes. See Table 4.1 for explanation of headings.

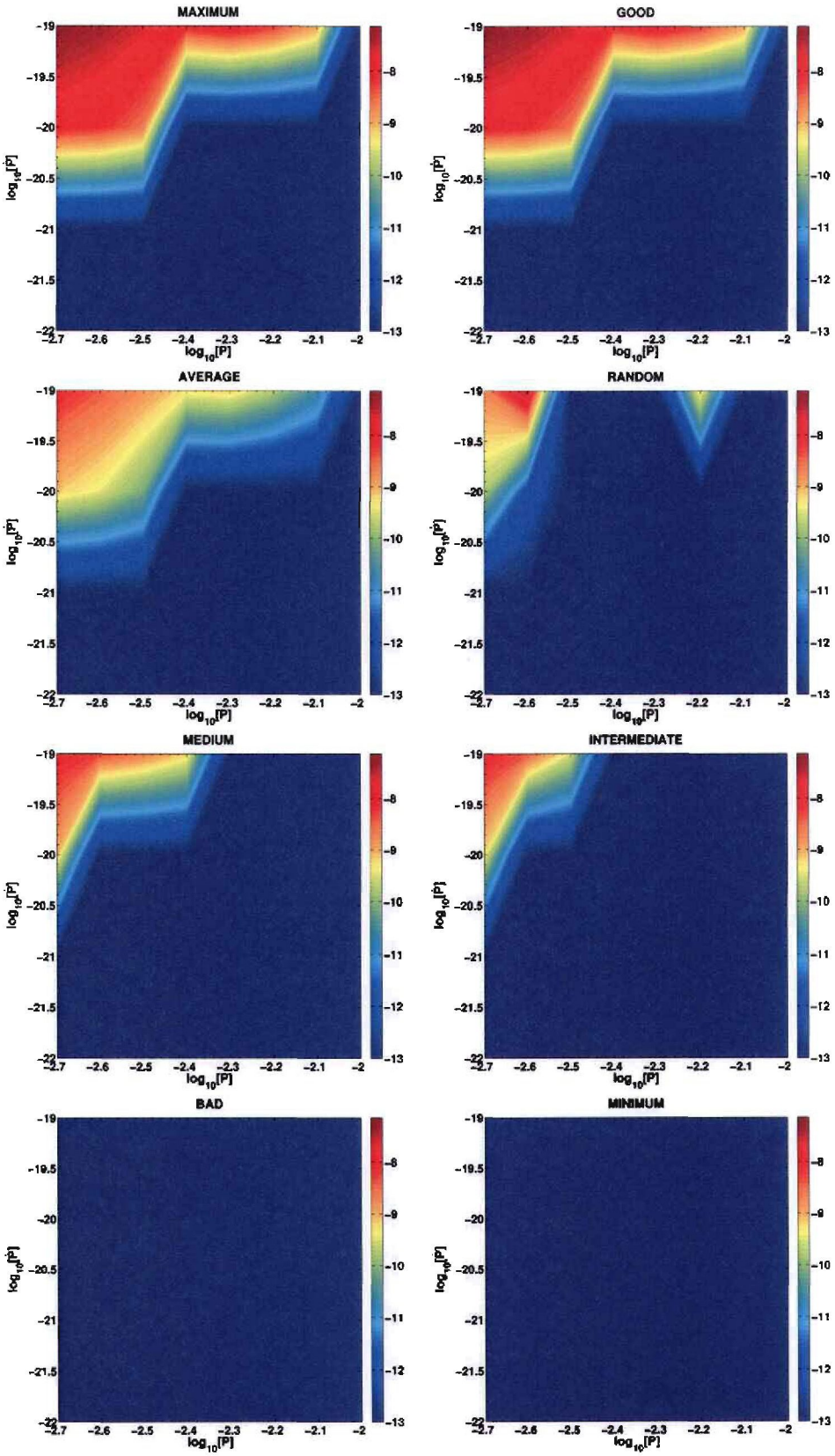

Figure 4.9: Contour graphs of the $\log_{10}$ of integral flux above 10 GeV, $\overline{F}^{\rm slice}(>10\,{\rm GeV})$, in units of $\rm cm^{-2}s^{-1}$ (for $d = 1$ kpc) vs. $\dot{P}$ and P, for different χ and ζ. Zero integral fluxes above 10 GeV (due to small CR energy cut-offs) are indicated by the blue colour, since a value of 10^{-13} $\rm cm^{-2}s^{-1}$ has been assigned to these cases for representational purposes. See Table 4.1 for explanation of headings.

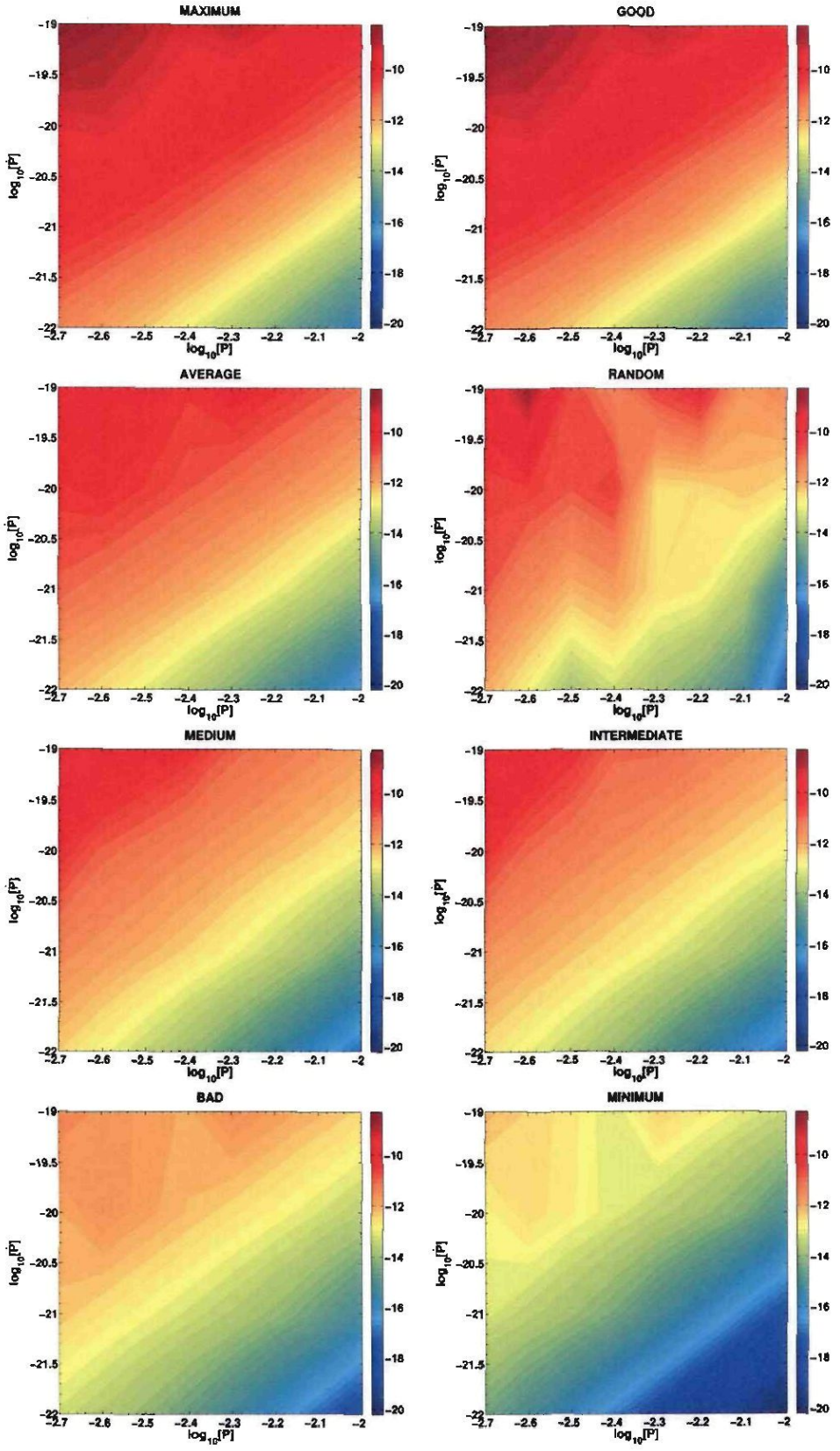

Figure 4.10: Contour graphs of the $\log_{10}$ of energy flux U^{slice} in units of ergs.cm^{-2}s^{-1} (for $d = 1$ kpc) vs. $\dot{P}$ and P, for different χ and ζ. See Table 4.1 for explanation of headings.

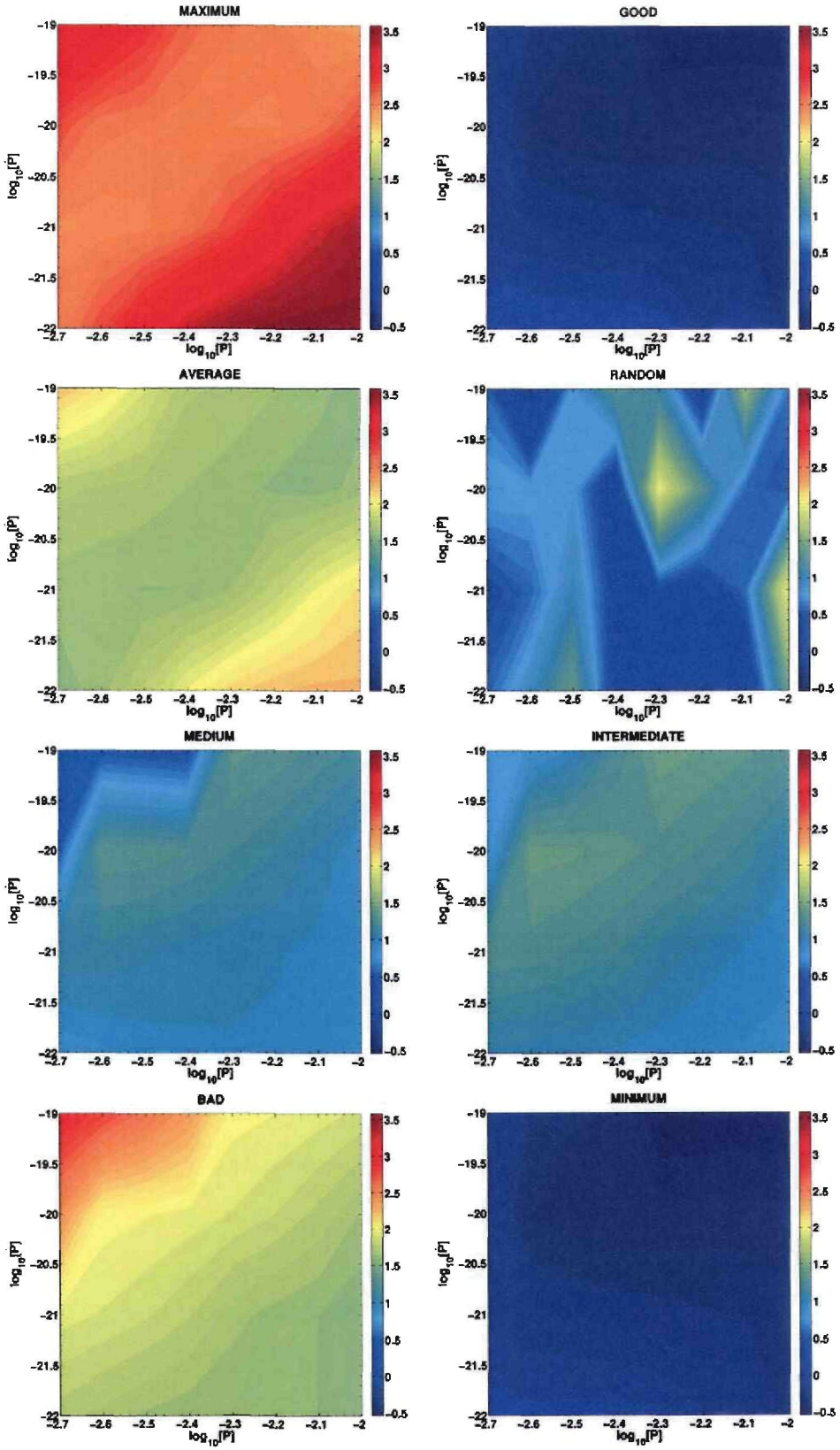

Figure 4.11: Contour graphs of the $\log_{10}$ of $\Lambda = \epsilon\overline{\Delta\Omega}^{\text{beam}}/\beta^{\text{slice}}$ vs. $\dot{P}$ and P, for different χ and ζ. *The sequence of graphs was kept the same as previously; however, 'maximum' and 'bad' now indicate big correction factors, while 'minimum' and 'good' indicate almost no correction when the observer is sweeping close to the magnetic axis.* See Table 4.1 for explanation of headings.

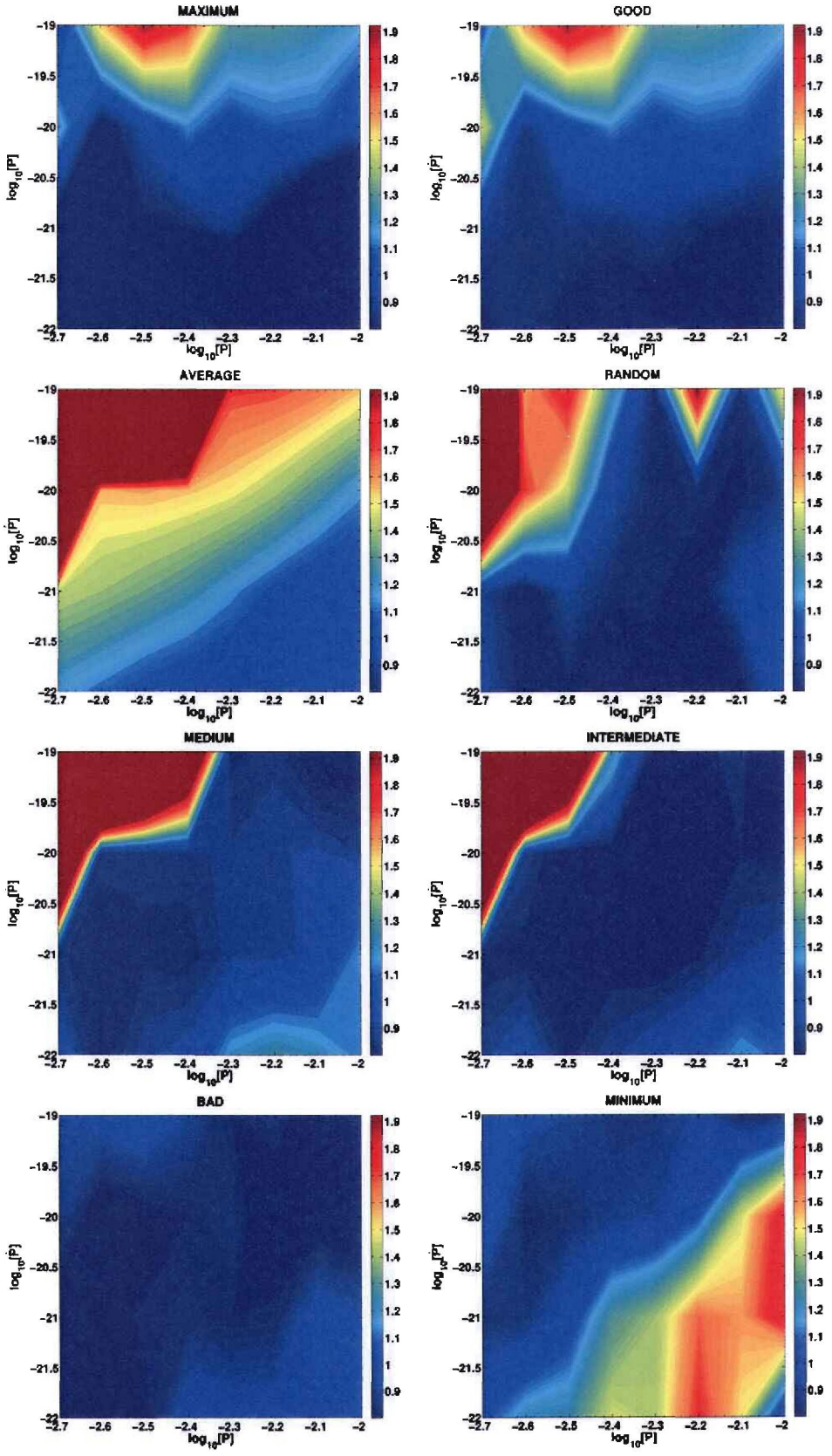

Figure 4.12: Contour graphs of the energy ratio $\tau = \overline{E}/E_0$ vs. $\dot{P}$ and P, for different χ and ζ. See Table 4.1 for explanation of headings.

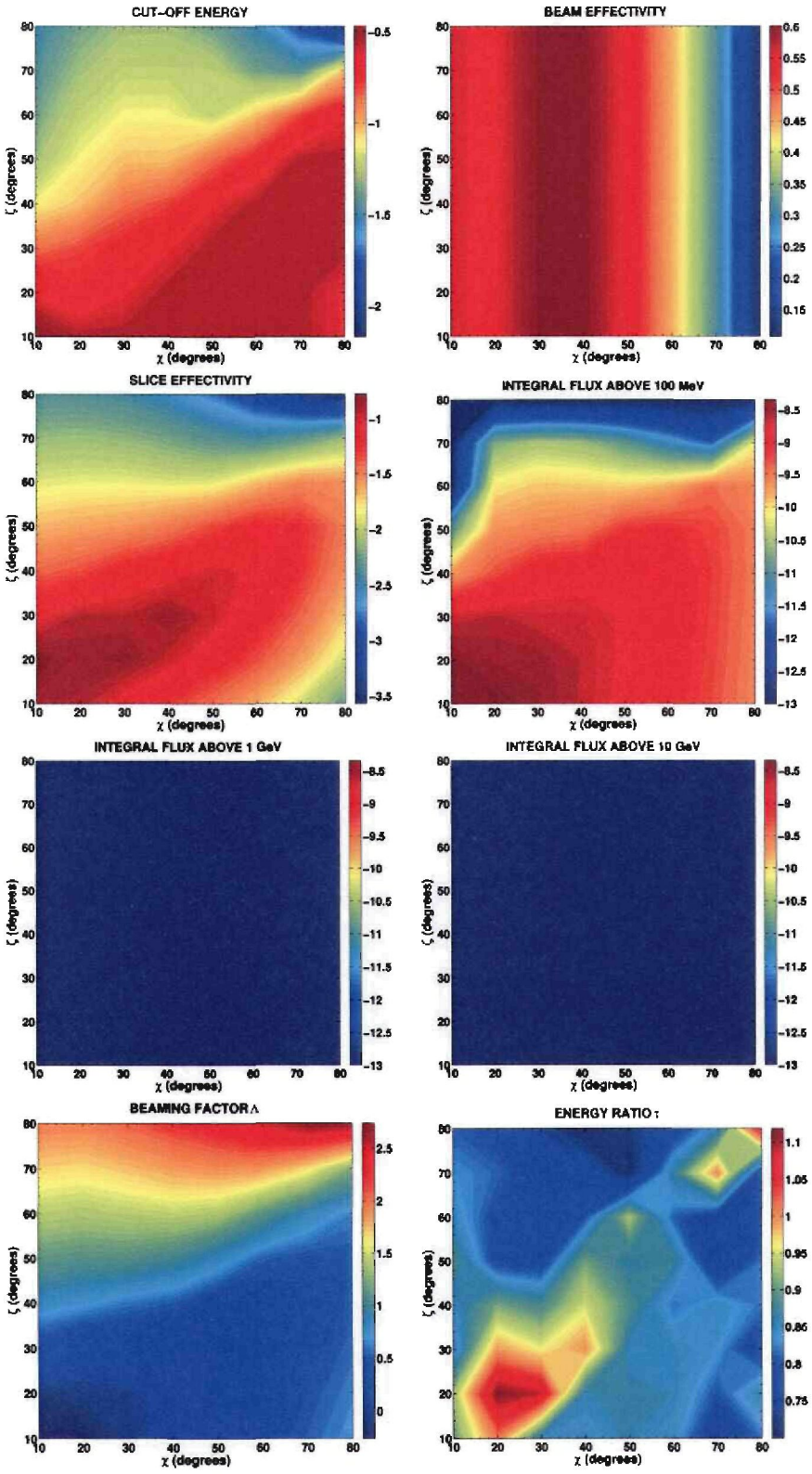

Figure 4.13: Contour graphs for the MSP with $\log_{10}(P) = -2.3$ and $\log_{10}(\dot{P}) = -21$ for different χ and ζ of $\log_{10}$ of the following: E_0 (GeV), $\eta_\gamma^{\rm beam}$ (%), $\eta_\gamma^{\rm slice}$ (%), integral fluxes $F^{\rm slice}(>100$ MeV), $F^{\rm slice}(>1$ GeV), and $F^{\rm slice}(>10$ GeV) in units of cm^{-2}.s^{-1}, and geometrical beaming correction factor. Last panel is for the energy ratio τ. This MSP has an unscreened PC potential.

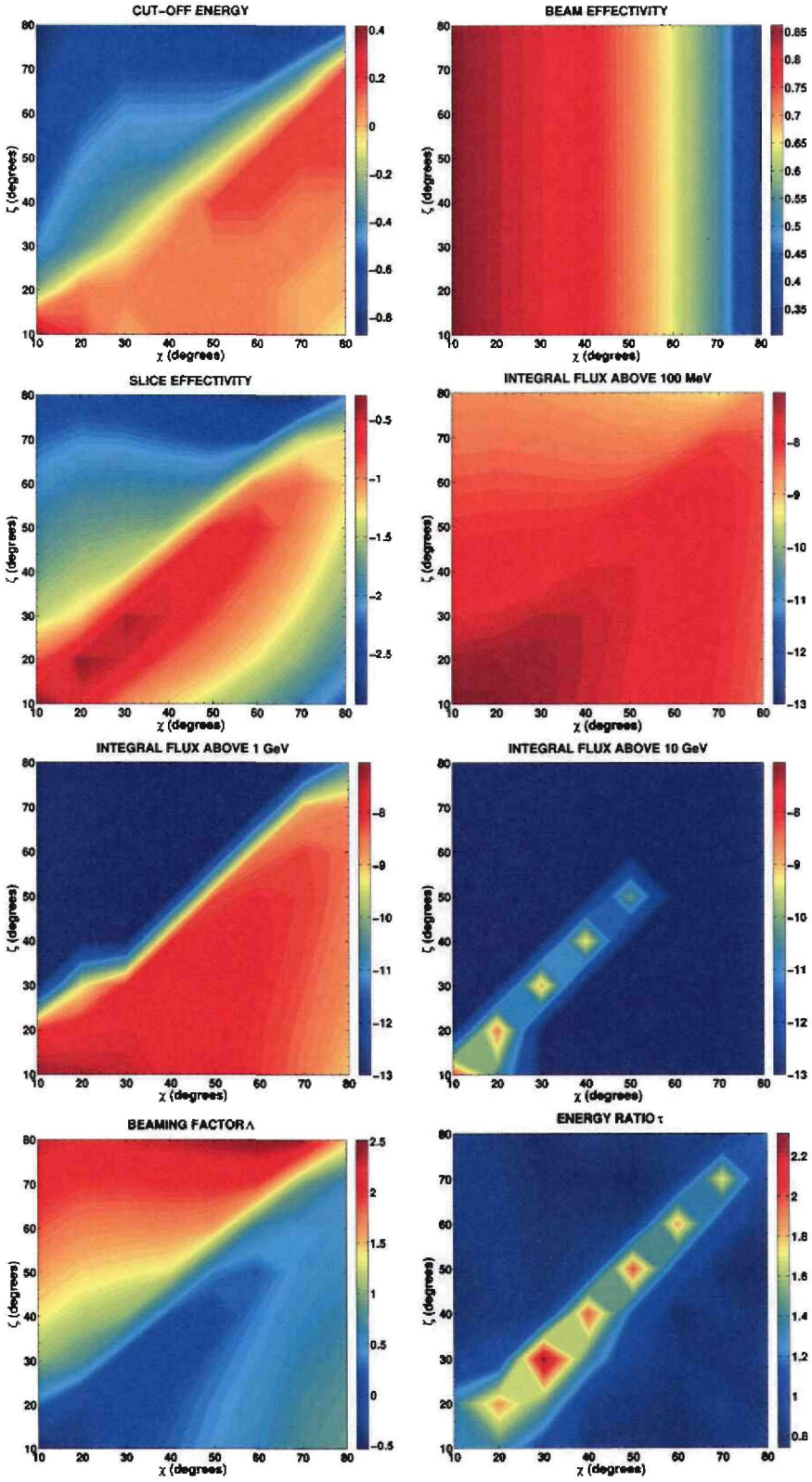

Figure 4.14: Contour graphs for the MSP with $\log_{10}(P) = -2.2$ and $\log_{10}(\dot{P}) = -19$ for different χ and ζ of $\log_{10}$ of the following: E_0 (GeV), $\eta_\gamma^{\rm beam}$ (%), $\eta_\gamma^{\rm slice}$ (%), integral fluxes $F^{\rm slice}(>100$ MeV), $F^{\rm slice}(>1$ GeV), and $F^{\rm slice}(>10$ GeV) in units of $\rm cm^{-2}.s^{-1}$, and geometrical beaming correction factor. Last panel is for the energy ratio τ. This unscreened MSP lies close, but below, the 'screening' line / condition defined by Eq. (4.4).

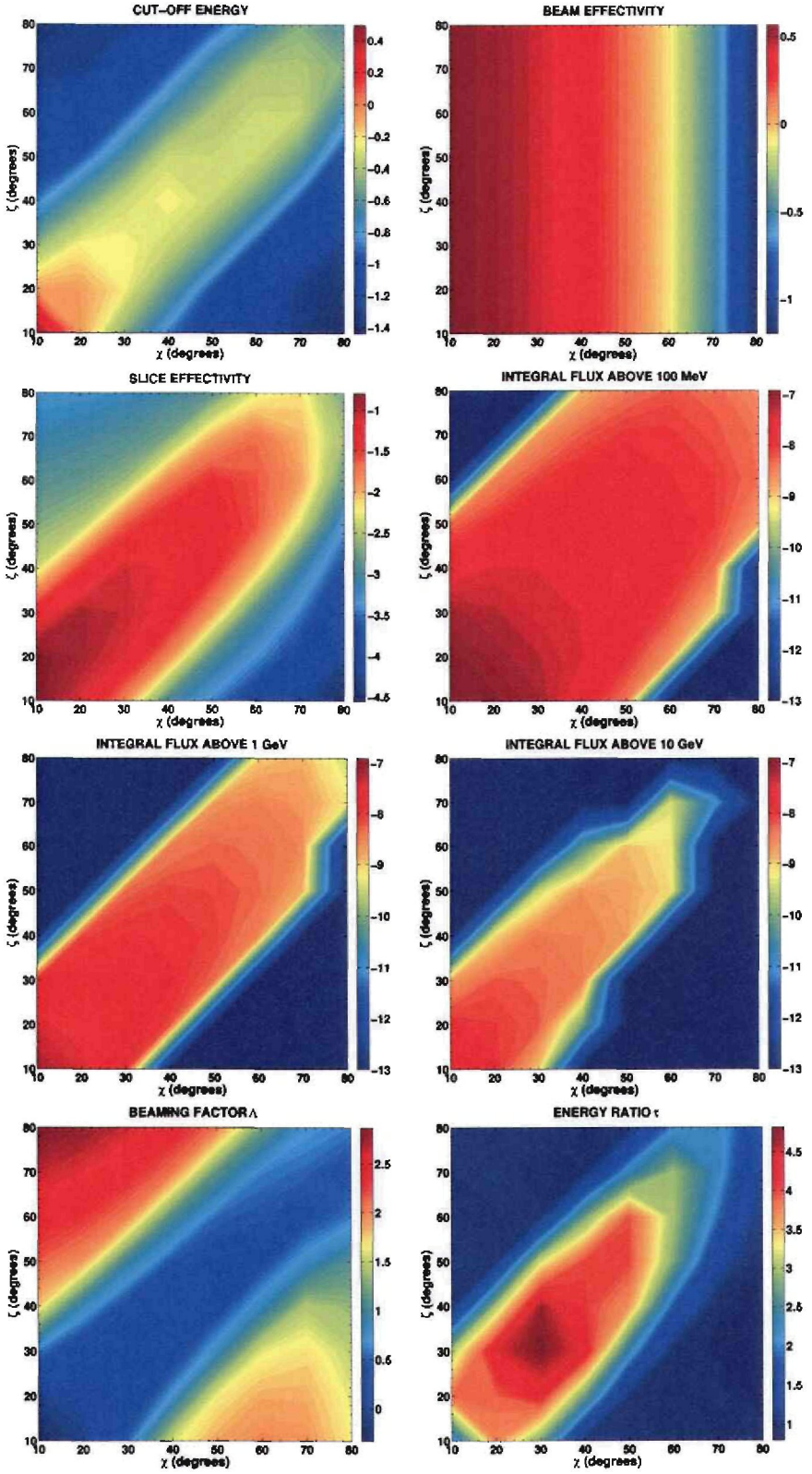

Figure 4.15: Contour graphs for the MSP with $\log_{10}(P) = -2.5$ and $\log_{10}(\dot{P}) = -19$ for different χ and ζ of $\log_{10}$ of the following: E_0 (GeV), $\eta_\gamma^{\rm beam}$ (%), $\eta_\gamma^{\rm slice}$ (%), integral fluxes $F^{\rm slice}(>100$ MeV), $F^{\rm slice}(>1$ GeV), and $F^{\rm slice}(>10$ GeV) in units of cm^{-2}.s^{-1}, and geometrical beaming correction factor. Last panel is for the energy ratio τ. This MSP has a screened PC potential.

large difference between χ and ζ). Figure 4.4 confirms these expectations. When the panels are read from top left to bottom right, the radiation changes from being on-beam to being off-beam.

The largest values of $E_0 \sim 10$ GeV (for the choice of equation of state [EOS] parameters $M = 1.4M_\odot$, $R = 10^6$ cm, and $I = 0.4MR^2$) occur for the case of on-beam radiation, for the largest $\dot{P}$ and smallest P (top left corner in the first panel). This value drops to $E_0 \sim 5 \times 10^{-3}$ GeV for low $\dot{P}$ and large P, even for the on-beam radiation. For the off-beam radiation, E_0 drops to even lower values of $\sim 5 \times 10^{-5}$ GeV for large P and small $\dot{P}$ (bottom right corner of the last panel). The effect of screening is most evident in the last two panels of Figure 4.4: their top left corners, where screening occur, have lower values of E_0 than those in the unscreened part with largest $\dot{P}$ and lowest P (also refer to Figure 4.1). This is because pair creation shorts out the E-field at a height $h_{\rm PFF} \sim R_{\rm PC}$, so that there is no further acceleration beyond this pair formation front (PFF) height, as opposed to the case of MSPs with unscreened PCs (no PFF). The cut-off energy is crucial for determining MSP visibility. If E_0 is below a certain telescope's energy threshold, the CR spectrum will not be visible. From our results, it is evident that we don't expect any MSPs in this $(P, \dot{P})$-range to be visible for current telescopes. Changing the EOS might boost E_0, but typically not enough to make the MSPs visible when assuming reasonable values for M and R. Furthermore, off-beam radiation with low E_0 is also not expected to be visible. If this model is deemed reliable, we will therefore have to wait for *GLAST*, (and possibly *H.E.S.S.-II* and / or *MAGIC-II*) for the discovery of the first gamma-ray MSP (de Jager & Venter, 2005, also see Section 3.8).

(ii) Gamma-Ray Slice and Beam Efficiencies

The first part of the above discussion also applies for the expected values of the beam and slice efficiencies, since $L_\gamma \sim \Phi I_{\rm PC}$, with $I_{\rm PC}$ the PC current which should be close to the GR-corrected 'steady-state' solution of Goldreich and Julian (Eq. [2.99]). It is also important to note that the efficiencies are normalised using $\dot{E}_{\rm rot}$, which changes with $\dot{P}$ and P, so that the values of $\eta_\gamma^{\rm beam}$ and $\eta_\gamma^{\rm slice}$ should be viewed as relative values, and not absolute values. For a fixed geometry, the largest values for $\eta_\gamma^{\rm beam}$ of $\sim 10\%$ occur just below the top left corner of each panel, and then decreases to smaller values in the bottom right corner (as low as $\sim 0.01\%$ for the last panel; see Figure 4.5). The typical value of $\sim 7\%$ occurs over a large range of $\dot{P}$ and P. The effect of screening is again evident, as the values of the efficiencies are suppressed in the screened region (top left corners of panels). Furthermore, the on-beam efficiencies are much larger than the off-beam efficiencies. Similar conclusions hold for the slice efficiency $\eta_\gamma^{\rm slice}$ (Figure 4.6). The value of $\eta_\gamma^{\rm slice}$ decreases from $\sim 0.3\%$ for the most favourable cases to $\sim 5 \times 10^{-7}\%$ for the worst cases. One marked difference is that $\eta_\gamma^{\rm slice}$ has

approximately the same value for a larger range of $\dot{P}$ and P than $\eta_\gamma^{\rm beam}$, so that $\eta_\gamma^{\rm slice}$ is much more sensitive to a change in the geometry, rather to a change in $\dot{P}$ and P. The fact that $\eta_\gamma^{\rm slice}$ decreases much more rapidly than $\eta_\gamma^{\rm beam}$ as the geometry becomes off-beam is to be expected, as the definition of $\eta_\gamma^{\rm slice}$ involves ζ explicitly, while $\eta_\gamma^{\rm beam}$ is the efficiency averaged over the whole PC, and therefore independent of ζ. Of course, both these quantities do depend on χ. We may again observe the effect of screening which lowers the value of both $\eta_\gamma^{\rm beam}$ and $\eta_\gamma^{\rm slice}$ in the top left corners of the panels of Figures 4.5 and 4.6. For $\eta_\gamma^{\rm slice}$, this is seen most clearly in the last two panels of the latter figure.

(iii) Observer Integral Fluxes

Figures 4.7 through 4.9 represent phase-averaged observer integral flux $F^{\rm slice}(>E)$ for $E = 100$ MeV, $E = 1$ GeV, and $E = 10$ GeV, calculated for an assumed distance of $d = 1$ kpc. These should be read in sequence: as the minimum energy E is increased from 100 MeV to 10 GeV, we see quite dramatically that less and less of the MSPs in the $\dot{P}$ and P range are visible (zero fluxes have been assigned a value of 10^{-13} cm^{-2}s^{-1} for representational purposes). This is because the CR cut-off energies are below these energy minima ($E_0 < E$) for the invisible MSPs, increasingly so when the minimum energy increases to 10 GeV. As with the beam efficiencies, the maximum integral flux is found just below the top left corners (where the flux is decreased due to screening, especially visible in the last two panels of Figures 4.7), and the flux decreases when P becomes large and $\dot{P}$ small. As previously, the flux drops rapidly for off-beam radiation, emphasising how crucial a favourable geometry is for an MSP to be visible. The integral flux therefore decreases along three 'dimensions': energy, geometry, and for large P / small $\dot{P}$. The combination of these factors determine whether an MSP will be visible for a particular telescope, i.e. whether the integral flux lies above the telescope's sensitivity. As in the case of Figure 4.4, we conclude that MSPs will probably not be visible for current gamma-ray telescopes.

It should be noted that the 'uncorrected' CR spectra have been used in this section (see Section 2.5.11), leading to more abrupt spectral cut-offs above a few GeV. Corrected CR spectra would give a more reliable assessment of MSP visibility in the super-GeV range of the spectrum (Dyks 2008, personal communication), and their implementation in this context should be strongly considered in future.

(iv) Energy Flux

Figure 4.10 indicates the behaviour of the energy flux $U^{\rm slice} = \int E(dN/dE)^{\rm slice} dE$ for different values of $(P, \dot{P}, \chi, \zeta)$, for $d = 1$ kpc. We make similar conclusions regarding the dependence of $U^{\rm slice}$ on these pulsar parameters as for the efficiencies $\eta_\gamma^{\rm beam}$ and $\eta_\gamma^{\rm slice}$ (since $d^2 U^{\rm slice}$ differs from luminosity

only by a beaming correction factor Λ). Thus $U^{\rm slice}$ gradually tapers off when the geometry becomes unfavourable, or when P becomes large and $\dot{P}$ small. The effect of screening is not so pronounced in this case.

(v) Geometrical Beaming Factor

Figure 4.11 represents the contour graphs of the $\log_{10}$ of $\Lambda = \epsilon \overline{\Delta\Omega}^{\rm beam}/\beta^{\rm slice}$ vs. $\dot{P}$ and P, for different χ and ζ. *Note that the sequence of graphs was kept the same as previously, so that 'maximum' and 'bad' now indicate large correction factors (i.e. unfavourable visibility conditions), while 'minimum' and 'good' indicate almost no correction when the observer is sweeping close to the magnetic axis (i.e. favourable visibility conditions).* As discussed in Section 2.5.10, Λ is needed when scaling the slice energy flux to obtain the total beam luminosity, as it corrects for two effects: (i) The factor ϵ corrects for off-beam geometry effects, so that a small slice energy flux obtained for unfavourable geometry conditions will be scaled up significantly; (ii) The ratio of the beaming angle $\overline{\Delta\Omega}^{\rm beam}$ and pulse width of the observed light curve $\beta^{\rm slice}$ corrects for the beam area as well as the fact that the observer only sees the pulse (peak intensity) for a part of the rotation period, averaged over 2π. The latter ratio has been set to constant values of $0.1 - 1$ sr in the absence of more accurately known values (e.g. Story et al., 2007; Harding et al., 2005b; Fierro et al., 1995). Figure 4.11 however indicates that the correction may be quite significant in the case of off-beam radiation (where ϵ sensitively depends on the assumed pulsar E-field). In the worst cases, $\Lambda \sim 3000$, while the correction is small when the geometry is favourable ($\Lambda \sim 1$). For on-beam radiation, it may even happen that $\Lambda < 1$, since the observed spectrum implies a higher energy flux than the beam-averaged value (e.g. second panel of Figure 4.11). Average values of Λ of $\sim 30 - 150$ are found.

(vi) Energy Ratio

In Figure 4.12, we present graphs of the energy ratio $\tau = \overline{E}/E_0$ vs. $\dot{P}$ and P, for different χ and ζ. From this figure, it is evident that $\tau \sim 1 - 2$, so that the average energy $\overline{E} \equiv \int_0^\infty E(dN/dE)^{\rm slice}\, dE \div \int_0^\infty (dN/dE)^{\rm slice}\, dE$ is usually similar to the cut-off energy E_0, but never less than $\sim 80\%$ of E_0. The value of τ enters into Eq. (2.188) used to estimate the beam luminosity from an integral flux graph (see Section 3.6.5). The reason why 'minimum' doesn't represent the lowest values of τ, is that τ is calculated using the minimum values of $U^{\rm slice}$, $\int (dN/dE)^{\rm slice}$, and E_0, and the resulting value does not necessarily represent the minimum value for τ.

(vii) Single Pulsar Results: Screened and Unscreened Cases

When fixing $\dot{P}$ and P, one may obtain contour graphs of the various pulsar quantities as functions of geometry for a specific MSP. In Figures 4.13 through 4.15, we chose $(\log_{10}[P], \log_{10}[\dot{P}]) = (-2.3, -21)$; $(-2.2, -19)$, and $(-2.5, -19)$. These 'pulsars' have the following ratios for their spin-down power to their critical screening spin-down power (see Section 4.2.1): $\dot{E}_{\rm rot}/\dot{E}_{\rm rot,break} \approx 5 \times 10^{-3}$, 0.5, and 4 respectively. We therefore wanted to see how the pulsar properties would change when moving from the unscreened to the screened case. The first MSP is unscreened, the second still unscreened, but closer to the screened case, and the last one is screened. Their respective spin-down powers are $\dot{E}_{\rm rot} \approx 3.5 \times 10^{31}$ ergs/s, 1.8×10^{34} ergs/s, and 1.4×10^{35} ergs/s. In what follows, we refer to the pulsars as the 'first', 'second', and 'third' pulsar, and count the panels of each figure from top left to bottom right.

The first panels of Figures 4.13 through 4.15 represent the $\log_{10}$ of the CR cut-off energy E_0 in GeV. For the unscreened MSPs, we find similar behaviour than for PSR J0437-4715 (see Figure 3.10, which represents a higher resolution calculation): the largest cut-off energies cluster around the $\chi = \zeta$ line (representing on-beam radiation), although not exactly. This is because the E-field is not a symmetric function of the magnetic azimuthal angle ϕ, and ignoring of B-lines along which particle oscillation occur (Section 3.4) also plays a role. Typical cut-off energies of a few GeV are found, and the energy of the second pulsar (first panel of Figure 4.14) is higher than that of the first (first panel of Figure 4.13), since the latter has a larger spin-down power. The lower halves ($\chi > \zeta$) of the first panels of the unscreened pulsars have higher energies than the top halves ($\chi < \zeta$). This is because there is a $\cos\phi$-term in the E-field, so that the lower half of the PC (large values of ϕ where more particle oscillation typically occur), which is sampled when $\zeta > \chi$, will have less acceleration due to a smaller E-field, and thus smaller values of E_0. (Also see Section 6.1 where the E-field above the PC is plotted as function of (η, ϑ, ϕ)). The first panel of Figure 4.15 is symmetrical with respect to the $\chi = \zeta$ line (i.e. the same for the same impact angle $|\beta'| = |\zeta - \chi|$), since the screened E-field is symmetrical with respect to (independent of) ϕ. The latter pulsar have a similar cut-off energy range than the previous one, indicating the effect of screening: despite having a larger spin-down luminosity, the E-field stops accelerating the electron primaries close to the PC, and E_0 is therefore lower than would have been the case if the PC was unscreened.

The second panels of Figures 4.13 through 4.15 represent the beam efficiency. This efficiency is not a function of ζ, and generally decreases with χ (according to Eq. [A.15] it goes like $\cos^2\chi + C\sin^2\chi$ for the unscreened case, and typically $C \sim 0.3$). Therefore, we have lines of constant values for constant

χ, and generally decreasing values for constant ζ. We also infer typical unscreened values of a few percent ($\sim 4\% - 7\%$) for small values of χ, dropping to $\sim 1\% - 2\%$ for larger values of χ. In the case when screening occurs, we obtain similar behaviour, but much more rapid decrease when χ becomes large. Values range from $\sim 0.05\% - 4\%$ in this case.

It is clear that the slice efficiency (third panels of Figures 4.13 through 4.15) is a function of both χ and ζ. Again, we find asymmetrical clustering of the maxima around $\chi \approx \zeta$ for the unscreened pulsars, similar to the case for E_0. The difference is that the maxima occur in a smaller range of χ and ζ; also for large χ and small ζ, we see small similar values for the slice efficiency than for large ζ and small χ (which is not the case for E_0). The screened case again seems more symmetric with respect to the $\chi = \zeta$ line. It should be noted that the slice efficiencies are significantly smaller than the beam efficiencies as expected. Values range from $\sim 0.4\%$ to values as low as $\sim 3 \times 10^{-4}\%$ for the off-beam radiation in the unscreened case, and $\sim 3 \times 10^{-5}\%$ for the screened case. The slice efficiency therefore decreases much faster in the screened case when χ (or ζ) becomes large.

The next three panels (4, 5 and 6) of Figures 4.13 through 4.15 represent the observer integral fluxes above 100 MeV, 1 GeV, and 10 GeV. For all the pulsars, the integral flux roughly corresponds to the cut-off energy, and the maxima cluster around small $\chi \approx \zeta$. For the first pulsar, the integral flux drops rapidly when ζ becomes large, and becomes invisible above 1 GeV, and 10 GeV (as $E_0 < 1$ GeV). For the second pulsar, non-zero flux is predicted above 1 GeV as well as 10 GeV, although the maximum $E_0 < 10$ GeV. This is because the definition of E_0 only implies that the flux is dropping rapidly beyond E_0 (a high-energy tail), not that there is no flux. Indeed, the flux above 10 GeV is only visible for $\chi = \zeta = 10°, 20°, 30°, 40°, 50°$ (i.e on-beam radiation). For the third pulsar, the flux distribution is again much more symmetrical about $\chi = \zeta$ due to the symmetrical E-field in this case. The flux is of similar magnitude for all cases, although a bit larger for the pulsar with the largest spin-down luminosity (screened case). Note that we assumed a distance of $d = 1$ kpc when computing the flux.

It is encouraging that the beaming factor Λ is generally of order unity for on-beam radiation, and that it rapidly increases for off-beam radiation as expected (panel 7 of Figures 4.13 through 4.15). We want to emphasise the extreme sensitivity of this parameter on the assumed geometry, and also the large values it acquires for off-beam radiation: up to ~ 500! We will have more to say about this beaming correction factor in Section 4.4, where we will compute it for a population of 'real' pulsars, not just grid points in parameter space.

The energy ratio $\tau = \overline{E}/E_0$ is typically unity for the first pulsar, varying by a factor of ~ 2 for the second pulsar, and at most by ~ 5 for the screened pulsar (for a limited range of χ and ζ). Thus, we may estimate the average energy of the unscreened pulsars using the value of the cut-off energy E_0 of

a few GeV with reasonable accuracy, especially for unscreened pulsars.

4.3.3 Summary

In this section we applied the same MSP model for a mesh of $(P, \dot{P}, \chi, \zeta)$-space. We therefore did not deal with 'real pulsars' (as in Section 4.4), but rather wanted to evaluate the behaviour of the pulsar model in parameter space. Generally speaking, cut-off energies, efficiencies, energy fluxes, and integral fluxes decrease with larger P and smaller $\dot{P}$. Also, more and more MSPs become invisible as the minimum energy of the integral flux is increased. The effect of geometry is furthermore evident, where maxima of above-mentioned quantities occur for on-beam radiation (with asymmetrical distributions about the $\chi = \zeta$ line for the unscreened pulsars), while the beaming correction is a minimum in this case. The energy ratio is typically $\sim 1 - 2$, so that the cut-off energy is a good approximation for the average energy of the photon spectrum.

From the detailed discussion in the previous section, it emerges that all the pulsar properties are sensitive functions of the assumed geometry (as well as $\dot{P}$ and P), so that accurate knowledge of pulsar geometry is crucial when making predictions regarding their visibility. In addition, screening complicates the matter for high-$\dot{E}_{\rm rot}$ pulsars, where pair-creation leads to suppression of the E-field.

4.4 Systematic Beaming Effects

Now that the basic pulsar model behaviour has been tested for a grid of values in parameter space, we redo the calculations using pulsars which appear in the *ATNF Pulsar Catalogue* (Manchester et al., 2005), for the parameter range used previously ($-2.7 \leq \log_{10}[P] \leq -2.0$ and $-22 \leq \log_{10}[\dot{P}] \leq -19$). Whe found 59 pulsars in this range (see Figure 4.16). We are specifically interested in the range of values for Λ, $F^{\rm slice}(>100$ MeV), and E_0 for this population, as well as Λ and $F^{\rm slice}(>100$ MeV) for PSR J0437-4715. In addition, we test the accuracy of the generalised prediction of the beam luminosity derived in Section A.1, as opposed to the approximation $L_\gamma \approx 0.75\kappa(1-\kappa)\dot{E}_{\rm rot}$ (Harding et al., 2002b). Proper motion might be important for some of these MSPs (Section 4.2.2), leading to corrected values of $\dot{P}$, and should be taken into account for future studies.

4.4.1 Method

Our selected population (see Figure 4.16) of 59 MSPs has an average distance of $\langle d \rangle = 2.4$ kpc, and average spin-down power of $\left\langle \dot{E}_{\rm rot} \right\rangle = 1.5 \times 10^{34}$ ergs/s. Upon comparison of Figures 4.1 and 4.16, we see that 5 MSPs have screened PCs ($\sim 8\%$ of the population). Due to oscillatory motion (Section 3.4), on

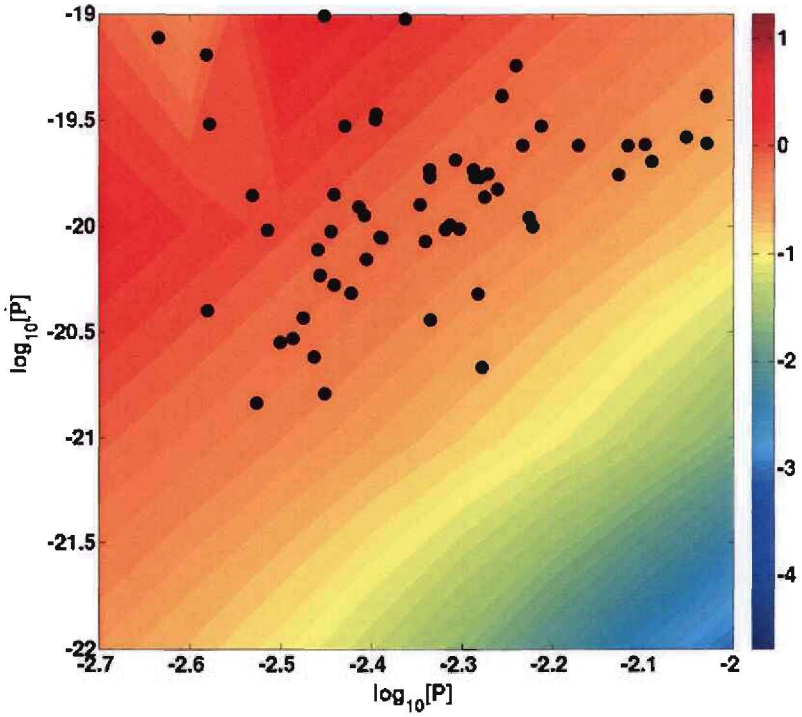

Figure 4.16: The $P\dot{P}$-diagram for the selected 59 MSPs for which beaming correction factor calculations have been performed. Also shown is the $\log_{10}$ of the average CR cut-off energy E_0 in GeV for χ and ζ in the range $(10°, 20°, ..., 80°)$, interpolated along a $P\dot{P}$-grid. (see panel 3 of Figure 4.4).

average $\sim 40\%$ of the PC area has been ignored for each MSP. We once again assume that $M = 1.4M_{\odot}$, $R = 10^6$ cm, and $I = 0.4MR^2$. However, in this section we use each pulsar's measured distance when computing integral fluxes and photon spectra, while we normalised our results in Section 4.3.1 assuming $d = 1$ kpc. We perform two parallel calculations: (i) assuming a random geometry; (ii) interpolating. These will subsequently be discussed.

(i) Random Geometry

For each of the 59 MSPs, we generate a random value of χ and ζ in the range $10°, 20°, \cdots, 80°$. Therefore, the results presented later on is for one realisation of the population, linking a unique combination of $(P, \dot{P}, \chi, \zeta)$ with each of the 59 MSPs. As before (Section 4.3.1), we calculate the incremental luminosity $dL/(d\phi_L d\zeta dE)$ for regions above the PC of each pulsar. From $dL/(d\phi_L d\zeta dE)$, we calculate the slice and beam luminosities $L_\gamma^{\rm slice}$ and $L_\gamma^{\rm beam}$, the photon spectra $(dN/dE)^{\rm slice}$, the integral fluxes $F^{\rm slice}(>E)$, cut-off energies E_0, energy fluxes $U^{\rm slice}$, and beaming correction factors Λ (more details given in Sections 2.5.10 and 4.3.1). Results from this section will be referred to as

the 'random geometry case' in Section 4.4.2 (labelled by an 'R' in the figures), where distributions of various pulsar parameters will be presented for this one realisation of the population consisting of 59 MSPs.

(ii) Interpolation

By using the results for the luminosities, integral fluxes, beaming correction factors, and energy fluxes calculated for a grid of parameter space spanning $(P, \dot{P}, \chi, \zeta)$ in Section 4.3, it is possible to interpolate to find predictions for the population of 59 MSPs under consideration. We iteratively generate random values of χ and ζ in the range $10°, 20°, \cdots, 80°$, and use the measured values of $\dot{P}$ and P to estimate (interpolate) the various pulsar quantities mentioned above.

By way of example, consider the interpolation of the beam luminosity. For a given MSP with measured $\dot{P}$ and P, we first obtain random values for χ and ζ. Next, we obtain four corners of the patch enclosing $\dot{P}$ and P (for the generated values of χ and ζ), say $(P_1, P_2, \dot{P}_1, \dot{P}_2)$. We then calculate the factors

$$t = \frac{P - P_1}{P_2 - P_1}, \tag{4.9}$$

$$u = \frac{\dot{P} - \dot{P}_1}{\dot{P}_2 - \dot{P}_1}. \tag{4.10}$$

Next, we search for the 'corner' values of the luminosity, at the chosen χ and ζ values, in the results from Section 4.3, using

$$L_1 = L_\gamma^{\rm beam}(P_1, \dot{P}_1), \tag{4.11}$$

$$L_2 = L_\gamma^{\rm beam}(P_2, \dot{P}_1), \tag{4.12}$$

$$L_3 = L_\gamma^{\rm beam}(P_2, \dot{P}_2), \tag{4.13}$$

$$L_4 = L_\gamma^{\rm beam}(P_1, \dot{P}_2). \tag{4.14}$$

Finally, we obtain the interpolated value for $L_\gamma^{\rm beam}$ via

$$L_{\rm interp}^{\rm beam} = (1-t)(1-u)L_1 + t(1-u)L_2 + tuL_3 + (1-t)uL_4. \tag{4.15}$$

For the correction factor Λ, the interpolation scheme is not that accurate, so we rather use

$$\Lambda_{\rm interp} = 2\pi \sin(\zeta + d\zeta/2) d\zeta \frac{L_{\rm interp}^{\rm beam}}{L_{\rm interp}^{\rm slice}}. \tag{4.16}$$

We will subsequently refer to the results of this section as the 'interpolation case' (labelled by an 'I' in the figures).

(iii) Calibration

For one choice of random χ and ζ, the results from the above two sections should correspond. We do find good agreement when comparing these two cases, except when interpolating Λ directly. As noted above, the agreement becomes much better when Λ is calculated using the interpolated values for the beam and slice luminosities. It is furthermore found that the agreement is best for the bulk of the MSPs which have unscreened PCs.

4.4.2 Results and Discussion

Figure 4.17 represents the graph of $L_\gamma^{\rm beam}$ vs. $\dot{E}_{\rm rot}$. In the top panel, we assumed $\Lambda = 1$, so that $L_\gamma^{\rm beam} = d^2 U^{\rm slice}$ (see Eq. [2.182]). We used the *GLAST* sensitivity of $F^{\rm GLAST}(>100\,{\rm MeV}) \approx 2 \times 10^{-9}$ cm^{-2}.s^{-1} to dinstinguish between 'visible' and 'invisible' MSPs (28 of the 54 unscreened MSPs are visible). The blue diamonds represent visible MSPs ($F^{\rm slice}(>100\,{\rm MeV}) > F^{\rm GLAST}(>100\,{\rm MeV})$), and magenta circles invisible MSPs ($F^{\rm slice}(>100\,{\rm MeV}) < F^{\rm GLAST}(>100\,{\rm MeV})$). In the bottom panel, the black squares represent the calculated total beam luminosity $L_\gamma^{\rm beam}$ for the 'random geometry' case, for MSPs with an unscreened PC. When the correct beaming factor $\Lambda \neq 1$ is employed, the values $\Lambda d^2 U^{\rm slice}$ coincide with the calculated beam luminosities $L_\gamma^{\rm beam}$. The solid green line is a fit of $\log_{10}[L_\gamma^{\rm beam}] = 1.1358 \log_{10}[\dot{E}_{\rm rot}] - 5.8123$. As the model predicts $L_\gamma^{\rm beam} \propto \dot{E}_{\rm rot}$, we also plotted the solid magenta line representing $L_\gamma^{\rm beam} = 0.07 \dot{E}_{\rm rot}$ (see Eq. [4.17]). This figure strikingly shows that actual trends may be concealed when correction factors Λ are unknown. Furthermore, we will see in the next paragraph that Λ may be significantly larger than unity. It is clear that the observed energy flux usually has to be scaled up to obtain the beam luminosity, but there are some cases when $\Lambda < 1$, and the energy flux has to be scaled down.

From plots of the distribution of the $\log_{10}$ of the beaming correction factors Λ in Figure 4.18, we may infer that Λ may be significantly larger than unity, as noted above. The top three panels are for $\sim 300\,000$ interpolated values, involving random combinations of χ and ζ (marked with 'I'), while the bottom three panels are for one actual realisation for 59 MSPs (i.e. one random choice of χ and ζ for each MSP, marked with 'R'). 'ALL (I)' refers to $59 \times 5\,000 = 295\,000$ values, 'VISIBLE (I)' to all the MSPs with interpolated fluxes $F^{\rm slice}(>100\,{\rm MeV}) > 2 \times 10^{-9}$ cm^{-2}.s^{-1}, and 'INVISIBLE (I)' to all the MSPs with interpolated fluxes $F^{\rm slice}(>100\,{\rm MeV}) < 2 \times 10^{-9}$ cm^{-2}.s^{-1} (Roughly 150 000 values in each case). It is evident that the errors are very small in the interpolated case due to the large

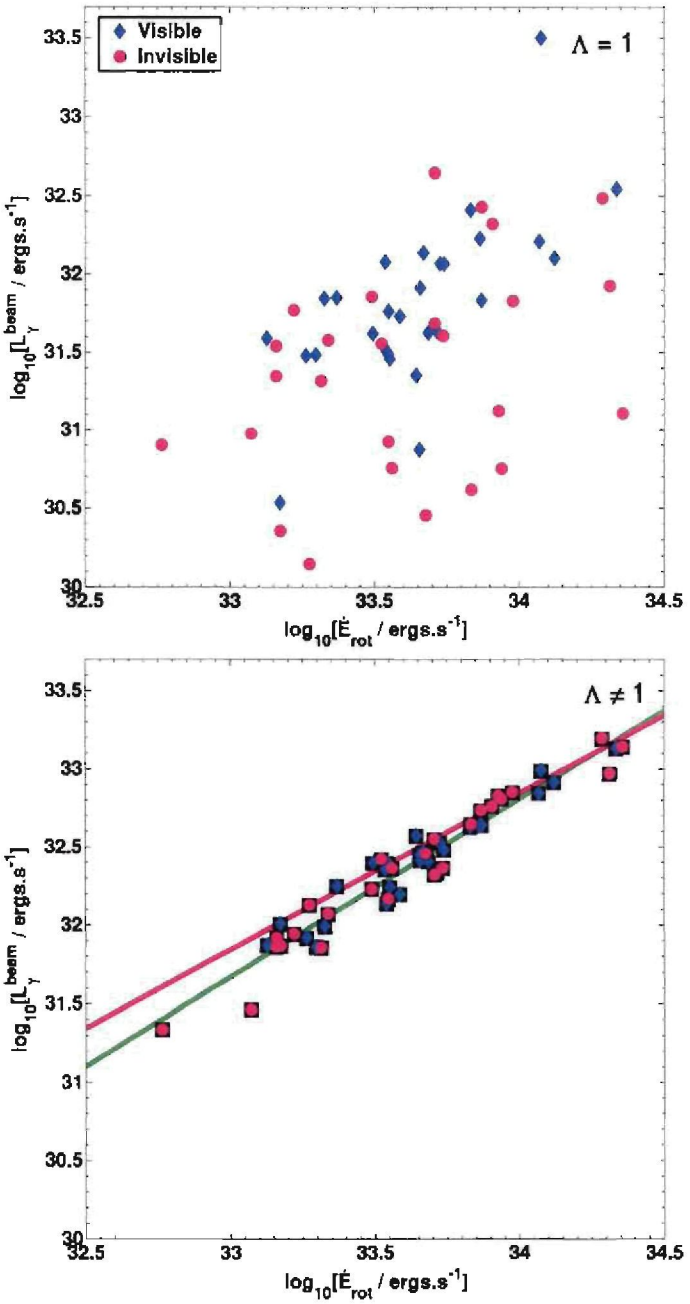

Figure 4.17: Top panel: Predicted beam luminosity $L_\gamma^{\rm beam}$ vs. spin-down power $\dot{E}_{\rm rot}$, assuming that the beaming correction factor $\Lambda = 1$ (i.e. $L_\gamma^{\rm beam} = d^2 U^{\rm slice}$). We used the *GLAST* sensitivity of $F^{\rm GLAST}(>100\,{\rm MeV}) \approx 2 \times 10^{-9}$ cm^{-2}.s^{-1} to dinstinguish between visible and invisible MSPs. The blue diamonds represent visible MSPs ($F^{\rm slice}(>100\,{\rm MeV}) > F^{\rm GLAST}(>100\,{\rm MeV})$), while the magenta circles represent invisible MSPs ($F^{\rm slice}(>100\,{\rm MeV}) < F^{\rm GLAST}(>100\,{\rm MeV})$). We used a sample of 59 pulsars with $\dot{E}_{\rm rot} < 10^{36}$ erg/s (Figure 4.16). Of these, 54 were unscreened (shown in these graphs), 28 visible, and 26 invisible. Bottom panel: Same as left panel, but with $\Lambda \neq 1$, so that $L_\gamma^{\rm beam} = \Lambda d^2 U^{\rm slice}$. The black squares represent the calculated total beam luminosity $L_\gamma^{\rm beam}$. When the correct beaming factors $\Lambda \neq 1$ are employed, the values of $\Lambda d^2 U^{\rm slice}$ coincide with the calculated beam luminosities $L_\gamma^{\rm beam}$. The solid green line is a fit of $\log_{10}[L_\gamma^{\rm beam}] = 1.1358 \log_{10}[\dot{E}_{\rm rot}] - 5.8123$. As the model predicts $L_\gamma^{\rm beam} \propto \dot{E}_{\rm rot}$, we plotted the solid magenta line representing $L_\gamma^{\rm beam} = 0.07 \dot{E}_{\rm rot}$ (see Eq. [4.17]). It is clear that the observed energy flux usually has to be scaled up to obtain the beam luminosity, but there are some cases when $\Lambda < 1$, and the energy flux has to be scaled down.

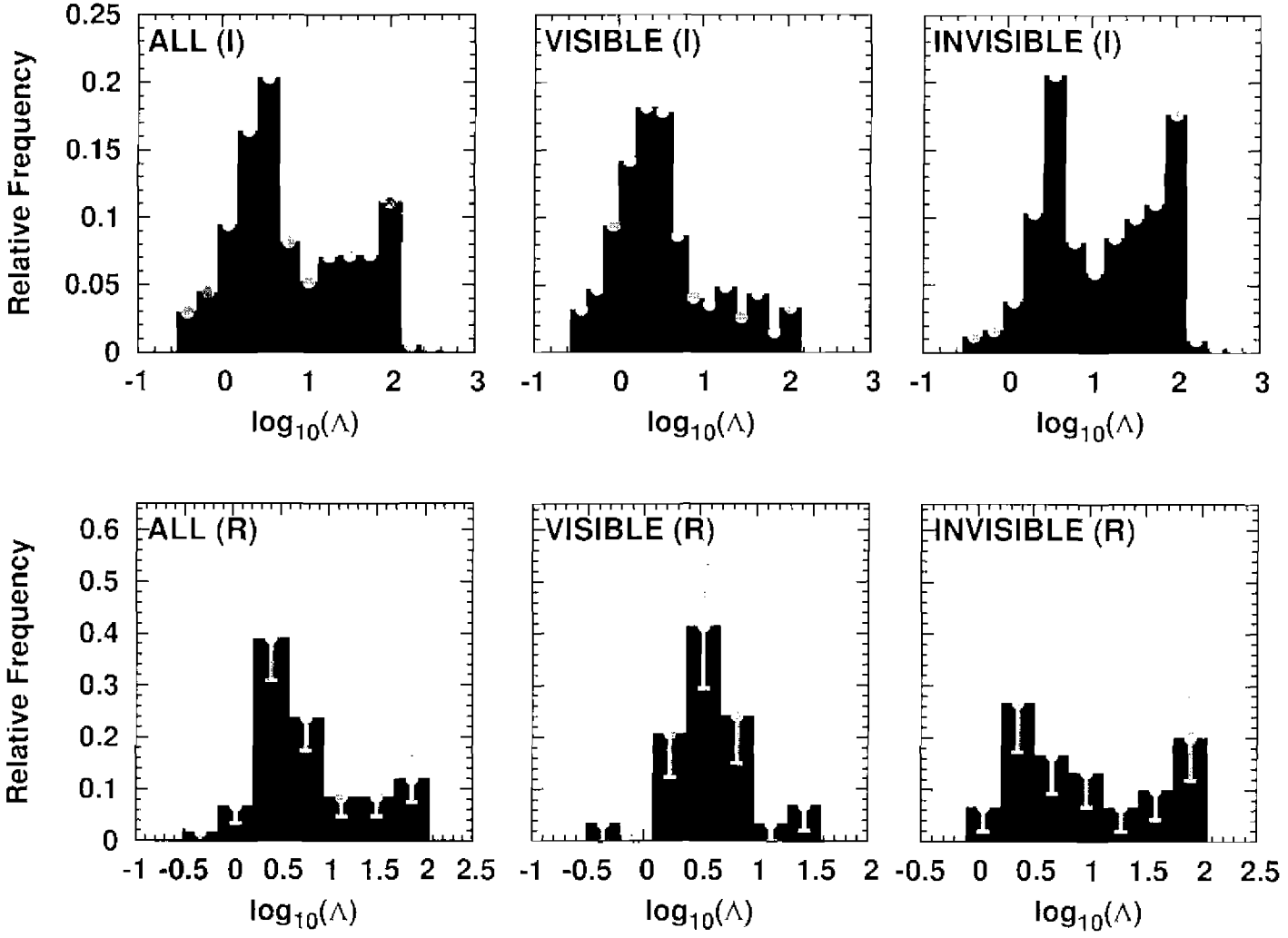

Figure 4.18: Distribution of the $\log_{10}$ of the beaming correction factors Λ interpolated for $\sim$ 300 000 random combinations of χ and ζ (top three panels, marked with 'I'), as well as one actual realisation for 59 MSPs (bottom three panels, marked with 'R'). 'ALL (I)' refers to $59 \times 5\,000 = 295\,000$ values, 'VISIBLE (I)' to all the MSPs with interpolated fluxes $F^{\rm slice}(>100\,{\rm MeV}) > 2 \times 10^{-9}$ cm^{-2}.s^{-1}, and 'INVISIBLE (I)' to all the MSPs with interpolated fluxes $F^{\rm slice}(>100\,{\rm MeV}) < 2 \times 10^{-9}$ cm^{-2}.s^{-1} (Roughly 150 000 values in each case). 'ALL (R)' refers to 59 values for one random combination of χ and ζ, 'VISIBLE (R)' to 29 MSPs with fluxes $F^{\rm slice}(> 100\,{\rm MeV}) > 2 \times 10^{-9}$ cm^{-2}.s^{-1}, and 'INVISIBLE (R)' to 30 the MSPs with fluxes $F^{\rm slice}(> 100\,{\rm MeV}) < 2 \times 10^{-9}$ cm^{-2}.s^{-1}. The averages for all six panels are as follows: $\sim$ 23, $\sim$ 11, $\sim$ 35, $\sim$ 17, $\sim$ 6, and $\sim$ 28 when reading the panels from top left to bottom right. Errors shown are $\sqrt{n_i}/\sum_i n_i$, where n_i is the number of values in each bin i.

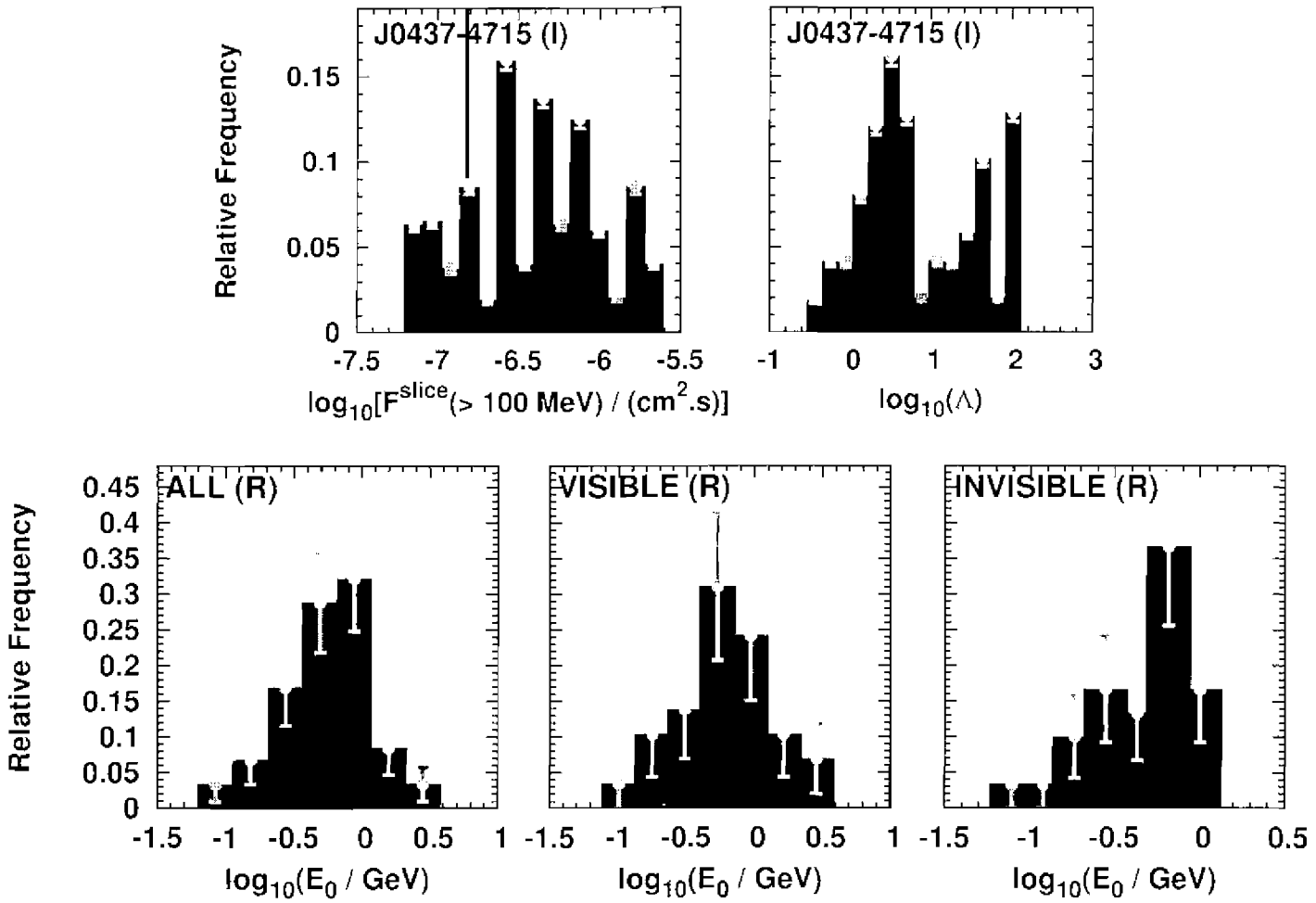

Figure 4.19: Top panel: Distributions of interpolated integral flux and beaming correction factor for PSR J0437-4715 involving 5 000 combinations of χ and ζ. The average integral flux is $\sim 6 \times 10^{-7}$ cm^{-2}.s^{-1}, while the average beaming correction is ~ 25. The shaded region is where the *EGRET* flux upper limit for this pulsar is obeyed. Bottom panel: Distribution of the $\log_{10}$ of the CR cut-off energy E_0 for the 'random geometry case' of the population of 59 MSPs (labelled using 'R'). The three lower panels show distributions for all 59 MSPs, the 29 visible MSPs, and the 30 invisible MSPs. The averages for these cases are ~ 0.7 GeV, ~ 0.9 GeV, and ~ 0.5 GeV respectively. Errors shown are $\sqrt{n_i}/\sum_i n_i$, where n_i is the number of values in each bin i.

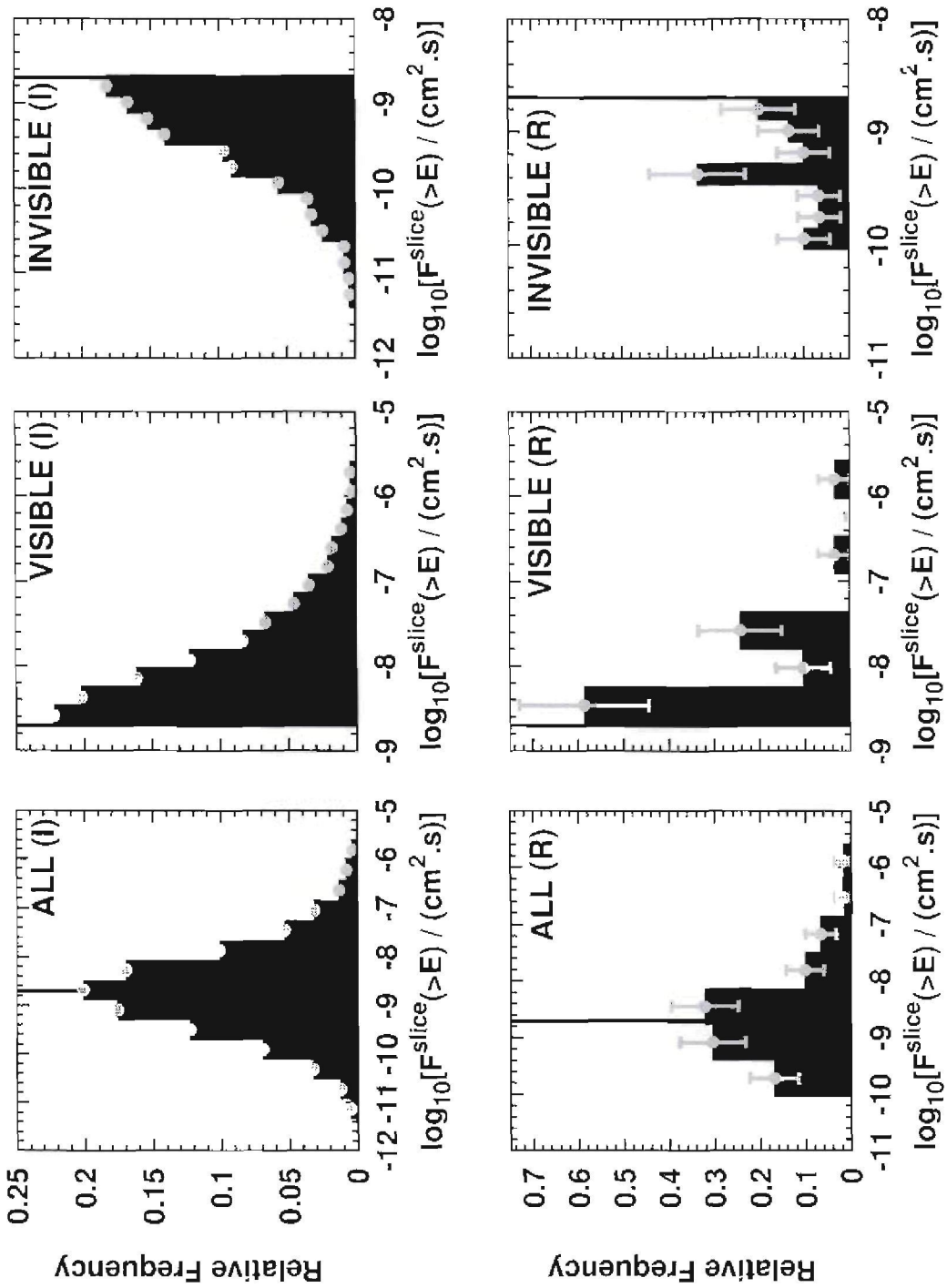

Figure 4.20: Distribution of the $\log_{10}$ of the integral fluxes $F^{\rm slice}(>100\,{\rm MeV})$ interpolated for $\sim 300\,000$ random combinations of χ and ζ (top three panels, marked with 'I'), as well as one actual realisation for 59 MSPs (bottom three panels, marked with 'R'). 'ALL (I)' refers to $59 \times 5\,000 = 295\,000$ values, 'VISIBLE (I)' to all the MSPs with interpolated fluxes $F^{\rm slice}(>100\,{\rm MeV}) > 2 \times 10^{-9}$ cm^{-2}.s^{-1}, and 'INVISIBLE (I)' to all the MSPs with interpolated fluxes $F^{\rm slice}(>100\,{\rm MeV}) < 2 \times 10^{-9}$ cm^{-2}.s^{-1} (Roughly 150 000 values in each case). 'ALL (R)' refers to 59 values for one random combination of χ and ζ, 'VISIBLE (R)' to 29 MSPs with fluxes $F^{\rm slice}(> 100\,{\rm MeV}) > 2 \times 10^{-9}$ cm^{-2}.s^{-1}, and 'INVISIBLE (R)' to 30 of the MSPs with fluxes $F^{\rm slice}(> 100\,{\rm MeV}) < 2 \times 10^{-9}$ cm^{-2}.s^{-1}. The averages for all six panels are as follows (in units of 10^{-8} cm^{-2}.s^{-1}): ~ 2, ~ 4, ~ 0.07, ~ 5, ~ 11, and ~ 0.07 when reading the panels from top left to bottom right. Errors shown are $\sqrt{n_i}/\sum_i n_i$, where n_i is the number of values in each bin i. The shaded regions indicate when MSPs will be invisible for *GLAST*.

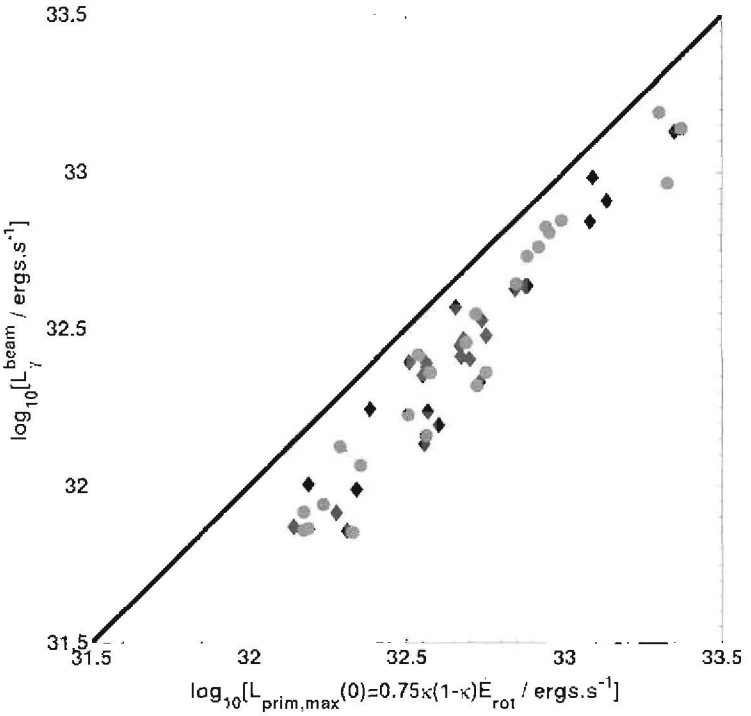

Figure 4.21: Graph of $L_\gamma^{\rm beam}$ vs. $0.75\kappa(1-\kappa)\dot{E}_{\rm rot}$ (i.e. for one PC) for 54 unscreened MSPs. Diamonds indicate visible MSPs, while circles indicate invisible MSPs. The solid black line indicates equality of the quantities represented on the x- and y-axis.

number of calculations (invisible in the top three panels). 'ALL (R)' refers to 59 values for one random combination of χ and ζ, 'VISIBLE (R)' to 29 MSPs with fluxes $F^{\rm slice}(>100\,{\rm MeV}) > 2\times10^{-9}$ cm^{-2}.s^{-1}, and 'INVISIBLE (R)' to 30 of the MSPs with fluxes $F^{\rm slice}(>100\,{\rm MeV}) < 2\times10^{-9}$ cm^{-2}.s^{-1}. The averages for Λ for all six panels are as follows: ~ 23, ~ 11, ~ 35, ~ 17, ~ 6, and ~ 28 when reading the panels from top left to bottom right. The relative spread on the average Λ is up to $\sim 170\%$. We estimated the errors using $\sqrt{n_i}/\sum_i n_i$, where n_i is the number of values in each bin i.

The top two panels of Figure 4.19 show the distributions of the $\log_{10}$ of interpolated integral flux and beaming correction factor for PSR J0437-4715 involving 5 000 combinations of χ and ζ. The average integral flux is $\sim 6\times10^{-7}$ cm^{-2}.s^{-1}, while the average beaming correction is ~ 25. The relative spread on the average values of $F^{\rm slice}(>100\,{\rm MeV})$ and Λ are $\sim 95\%$ and $\sim 150\%$ respectively. The shaded region is where the *EGRET* flux upper limit for this pulsar (Fierro et al., 1995) is obeyed. The bottom three panels of Figure 4.19 indicate the distribution of the $\log_{10}$ of the CR cut-off energy E_0 for the 'random geometry case' of the population of 59 MSPs (labelled using 'R'). The three lower panels show distributions for all 59 MSPs, the 29 visible MSPs, and the 30 invisible MSPs.

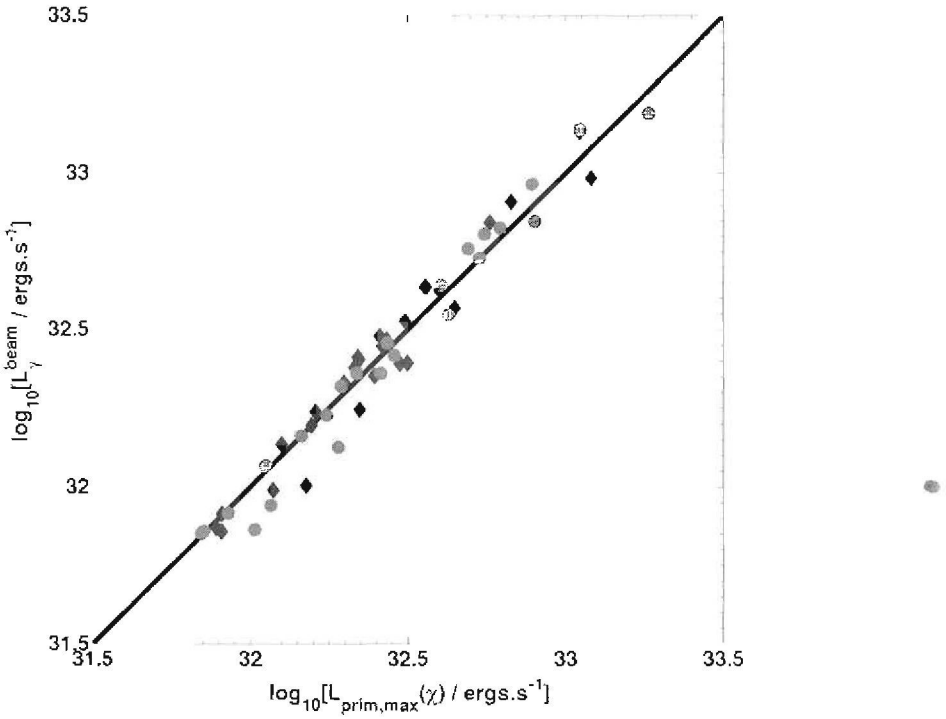

Figure 4.22: Graph of $L_{\gamma}^{\rm beam}$ vs. $L_{\rm prim,max}(\chi)$ (i.e. for one PC) for 54 unscreened MSPs. Diamonds indicate visible MSPs, while circles indicate invisible MSPs. The solid black line indicates equality of the quantities represented on the x- and y-axis.

The averages of E_0 for these cases are ~ 0.7 GeV, ~ 0.9 GeV, and ~ 0.5 GeV respectively (with a significant spread in these values of average E_0 of up to $\sim 93\%$). As expected, the average of E_0 for the invisible MSPs is lower than for the visible MSPs. Errors are calculated as in the previous paragraphs.

Figure 4.20 indicates the distribution of the $\log_{10}$ of the integral fluxes $F^{\rm slice}(>100\,{\rm MeV})$ interpolated for $\sim$ 300 000 random combinations of χ and ζ (top three panels, marked with 'I'), as well as one actual realisation for 59 MSPs (bottom three panels, marked with 'R'). The notation is the same as that used in Figure 4.18. The averages for all six panels are as follows (in units of 10^{-8} cm^{-2}.s^{-1}): ~ 2, ~ 4, ~ 0.07, ~ 5, ~ 11, and ~ 0.07 when reading the panels from top left to bottom right. There is a big relative spread of values of average $F^{\rm slice}(>100\,{\rm MeV})$ of up to $\sim 600\%$. Errors are calculated as for the case of Λ and E_0. The shaded regions indicate when MSPs will be invisible for *GLAST*.

We were lastly interested in evaluating the accuracy of the expressions (A.12) and (A.15) when estimating the gamma-ray beam luminosity, where we assumed that (for MSPs where radiation reaction occurs) $L_{\gamma}^{\rm beam} \approx L_{\rm prim,max}$, the latter quantity being the primary electron luminosity. For the

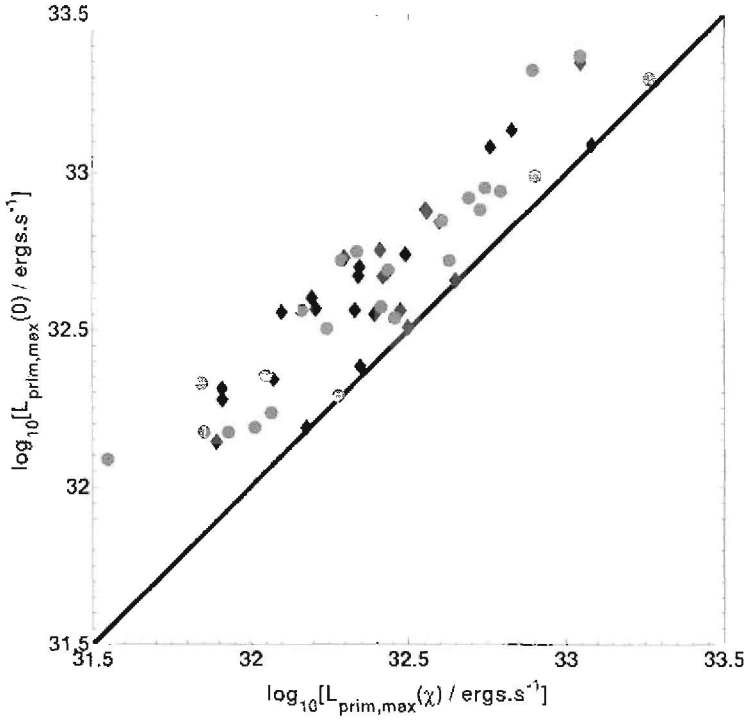

Figure 4.23: Graph of $L_{\rm prim,max}(0)$ vs. $L_{\rm prim,max}(\chi)$ (i.e. for one PC) for 54 unscreened MSPs. Diamonds indicate visible MSPs, while circles indicate invisible MSPs. The solid black line indicates equality of the quantities represented on the x- and y-axis. It is clear that the simple formula for $L_{\rm prim,max}(0)$ overestimates the gamma-ray luminosity.

unscreened case, we expected that $L_\gamma^{\rm beam} \propto \dot{E}_{\rm rot}$ (Harding et al., 2002b). Figure 4.21 indicates that the approximation $L_\gamma^{\rm beam}(0) = 0.75\kappa(1-\kappa)\dot{E}_{\rm rot}$ overpredicts $L_\gamma^{\rm beam}$. When using the more general expression $L_\gamma^{\rm beam}(\chi) = L_\gamma^{\rm beam}(0)[\cos^2\chi + C\sin^2\chi]$, with C a constant (Venter & de Jager, 2005a), the predictions for the numerically calculated beam luminosity become better, so that $L_\gamma^{\rm beam} \approx L_\gamma^{\rm beam}(\chi)$ (see Figure 4.22). This means that generally $L_\gamma^{\rm beam}(0) > L_\gamma^{\rm beam}(\chi)$ (Figure 4.23). As before, diamonds indicate visible MSPs, while circles indicate invisible MSPs in these figures. When we used $C \approx 1/3$, and $\langle \cos^2\chi + C\sin^2\chi \rangle \approx 2/3$ for $0 \leq \chi \leq 90°$, we obtained

$$L_\gamma^{\rm beam}(\chi) = 0.5\kappa(1-\kappa)\dot{E}_{\rm rot} \approx 0.07\dot{E}_{\rm rot}. \tag{4.17}$$

This is the formula we used in Figure 4.17 (magenta solid line), indicating that $\eta_\gamma^{\rm beam} \approx 7\%$.

4.4.3 Summary

One fundamental question which emerges when dealing with pulsar observations, is how to estimate the total luminosity using the measured energy flux. Figures 4.17 and 4.18 show that, in the context of the GR frame-dragging pulsar model, beaming correction factors Λ may be significantly larger than unity. Also, we see that actual trends may be concealed when Λ is unknown. It is encouraging to see that the theoretical expectation $L_\gamma^{\rm beam} \approx 0.07\dot{E}_{\rm rot}$ for MSPs with unscreened PCs is borne out by the numerical calculations presented in Figure 4.17 (where the average numerically-calculated gamma-ray efficiency is $\sim 5\%$, instead of $\sim 7\%$).

From the calculated integral fluxes (Figure 4.20), we see that roughly half of the population of 59 MSPs are expected to be visible for *GLAST*, with fluxes $\sim 10^{-8}$ cm^{-2}.s^{-1}. For this population, we found average CR cut-off energies of ~ 1 GeV, with E_0 being larger for the visible MSPs than for the invisible MSPs, as expected (Figure 4.19).

As the MSP PSR J0437-4715 is part of the population of 59 members, we had the opportunity to obtain distributions of the integral flux and beaming correction factor in this chapter, and compared these with results from Chapter 3, although we had to bear in mind that the EOSs and geometries are different for the two cases. In Section 4.4.2, we found an average integral flux of $\sim 6 \times 10^{-7}$ cm^{-2}.s^{-1}, while the average beaming correction was ~ 25 (for both on-beam and off-beam radiation). From Figure 3.14 in Chapter 3, we found an average value of $F^{\rm slice}(>100\,{\rm MeV}) \sim 10^{-6}$ cm^{-2}.s^{-1}, and from Table 3.2 in Chapter 3, we found $\Lambda \sim 6$ (for on-beam radiation). Given the differences in EOS, and pulsar geometry (which sensitively influences Λ), the agreements are encouraging. We furthermore found that while the *EGRET* flux upper limit at 100 MeV (Fierro et al., 1995) is violated for the on-beam geometries assumed in Figure 3.14, this upper limit is obeyed when the geometry becomes significantly off-beam (see the first panel of Figure 4.19).

Lastly, we found that, assuming $L_\gamma^{\rm beam} \approx L_{\rm prim,max}$, the approximation $L_\gamma^{\rm beam}(0) = 0.75\kappa(1-\kappa)\dot{E}_{\rm rot}$ overpredicts $L_\gamma^{\rm beam}$, and that better results followed when using the more general expression $L_\gamma^{\rm beam}(\chi) = L_\gamma^{\rm beam}(0)[\cos^2\chi + C\sin^2\chi]$. If we use $C \approx 1/3$, the latter equation may be approximated by $L_\gamma^{\rm beam}(\chi) = 0.5\kappa(1-\kappa)\dot{E}_{\rm rot} \approx 0.07\dot{E}_{\rm rot}$, indicating that $\eta_\gamma^{\rm beam} \approx 7\%$ for unscreened MSPs in the context of this model.

4.5 MSPs in Globular Clusters

After exploration of parameter space as well as investigation of the influence of geometry on various measured quantities calculated for a population of MSPs, including beaming correction factors (Sec-

tion 4.3 and 4.4), it is a short step to model the total pulsed gamma-ray output expected from an ensemble of MSPs in the nearby globular cluster (GC) 47 Tucanae. This involves the summation of spectra of a population of MSPs with random geometries. One important point to make is that a population study of this nature allows one to draw conclusions independent of (or averaged over) geometry. This means that if the model output, including errors, violate some experimental upper limits, this violation cannot be attributed to geometry, and salvaged by, for example, invoking "off-beam" radiation to lower fluxes or cut-off energies. No quantity or effect which averages out over a population may be used in this way (including the effect of Lorentz transformations on the observed spectra). It is therefore clear that a population study of this nature provides a way to test a model systematically, smoothing out pathological cases. The results described in this section have been reported in Venter & de Jager (2008a). In Section 5.2 of Chapter 5, we report on the complementary calculations of unpulsed high-energy radiation expected from 47 Tucanae.

4.5.1 Background

MSPs have been detected in several GCs, including the nearby 47 Tucanae (Camilo et al., 2000; Freire et al., 2003). Although only 22 MSPs are currently known to exist in 47 Tucanae (for a recent review, see Lorimer et al., 2003), it is expected that this cluster may harbour $30-60$ MSPs (Camilo & Rasio, 2005; Heinke et al., 2005), or even up to ~ 200 (Ivanova et al., 2005).

In this section, we model the pulsed CR gamma-ray flux expected from a population of MSPs in 47 Tucanae (Section 4.5.2), and compare it with the *GLAST LAT* sensitivity and *EGRET* upper limits. Our approach differs from similar recent studies (Cheng & Taam, 2003; Harding et al., 2005b; Bednarek & Sitarek, 2007) in a number of respects. First, we used a fully 3D General Relativistic (GR) PC pulsar model (see e.g. Venter & de Jager, 2005a), sampling non-thermal gamma-ray radiation from a range of magnetic field lines above the PC. Next, our study involved a population of MSPs, and we sampled randomly from this ensemble. We were therefore able to calculate absolute cumulative fluxes expected from the MSPs in 47 Tucanae, without needing to use approximate spectra, or scale up single MSP predictions or single particle spectra. We were also specifically interested in the range of pulsed spectra expected due to the uncertain geometries and spread in values of the period P and its derivative $\dot{P}$ of these pulsars.

X-rays from the MSPs in 47 Tucanae are believed to be of thermal origin, and are likely produced by a return current heating the pulsars' PCs (Harding & Muslimov, 2002; Cheng & Taam, 2003; Bogdanov et al., 2006a). These X-rays may be Compton upscattered to high-energy gamma rays. However, this inverse Compton scattering (ICS) component is believed to be dominated by the CR

component (see e.g. Figure 3 of Bulik et al., 2000) if telescope thresholds are indeed low enough to reach the CR component, and we therefore omitted it from our calculations below.

We lastly made some conclusions regarding the possibility of constraining a model of gamma-ray radiation from GCs (Section 4.5.4), since an ensemble of MSPs in a GC cluster provides a unique opportunity for specifically constraining the CR frame-dragging pulsar model (e.g. Harding & Muslimov, 1998) in a geometry-independent way (Section 4.5.3).

4.5.2 Pulsed Gamma-Ray Flux from 47 Tucanae

The measured values of $\dot{P}$ for GC pulsars are affected by their acceleration in the gravitational potential of the GC, and therefore need to be corrected to obtain intrinsic period derivatives $\dot{P}_{\rm int}$. This was done for 47 Tucanae by Bogdanov et al. (2006a) who derived spin-down luminosities $\dot{E}_{\rm rot}$ assuming a King model. From their Table 4, we selected 13 MSPs and calculated their corresponding $\dot{P}_{\rm int}$ using their periods P as given by Freire et al. (2003), and the expression $\dot{E}_{\rm rot} = 4\pi^2 I \dot{P}_{\rm int}/P^3$, with I the moment of inertia.

The details of the implementation of our isolated MSP model, using the GR-framework of Harding, Muslimov, & Tsygan (e.g. Harding & Muslimov, 1998), may be found in Venter & de Jager (2005a), where we discussed the essential link between pulsar visibility and the assumed geometry, i.e. magnetic inclination angle χ and observer angle ζ (both measured with respect to the spin axis $\mathbf{\Omega}$).

Harding et al. (2005b) found that most MSPs are inefficiently screened by CR and ICS pairs. Screening caused by electron-positron pairs will lower the accelerating potential, leading to a lower pulsed CR spectral cut-off. Higher numbers of energetic electrons may however boost the unpulsed gamma-ray spectrum. The vast majority of MSPs in our population lie below the critical spin-down luminosity above which screening is expected to occur (Harding et al., 2002b)

$$\dot{E}_{\rm rot,break} \approx 1.4 \times 10^{34} \left(\frac{P}{B_{12}^2}\right)^{1/7} \quad \text{ergs/s.} \tag{4.18}$$

Here, $B_{12} = B/10^{12}$ G and P is the pulsar period in seconds. (Note the positive sign of the power of P). This condition may be rewritten so that screening occurs when (see Eq. [4.4])

$$\log_{10}\dot{P} > 2.625\log_{10}P - 12.934, \tag{4.19}$$

assuming $I = 0.4MR^2$, stellar radius $R = 10^6$ cm, and pulsar mass $M = 1.4M_\odot$. We used an unscreened electrical potential for the bulk of the population, and used the approximation of a screened

electric field given by Dyks & Rudak (2000) for MSPs with spin-down powers greater than this critical spin-down power (which was only the case for 47 Tuc U).

For each pulsar i in our population, we calculated phase-averaged CR spectra via (also see Eq. [12] of Venter & de Jager (2005a), as well as Section 2.5.10)

$$\frac{dN_\gamma^i}{dE}(E_\gamma,\chi,\zeta) = \frac{1}{2\pi d^2 \sin\zeta d\zeta dE_\gamma} \times \int\int_\zeta^{\zeta+d\zeta}\int_0^{2\pi} \frac{I(E_\gamma, E_\gamma+dE_\gamma)}{E_\gamma^c}\left[\frac{dL^i(\phi_L,\chi,\zeta,E_\gamma)}{d\phi_L d\zeta dE_\gamma}\right] d\phi_L d\zeta dE_\gamma, \quad (4.20)$$

where ϕ_L is the phase angle, and $I(E_\gamma, E_\gamma + dE_\gamma)$ picks out the gamma-ray energies in the range $(E_\gamma, E_\gamma + dE_\gamma)$. Primary electrons leave a stellar surface patch dS relativistically ($\beta_0 = v_0/c \sim 1$) at a rate of $d\dot{N}_e = \rho_e dS\beta_0 c/e$, where ρ_e is the charge density. These primaries radiate CR at a position (r,ϑ,ϕ) above the PC with a characteristic energy of $E_\gamma^c = 1.5\lambda_c\gamma^3 m_e c^2 \rho_c^{-1}$, where $\lambda_c = \hbar/(m_e c)$ is the Compton wavelength, and $\rho_c(r,\vartheta,\phi)$ is the curvature radius of the GR-corrected dipolar magnetic field. The CR is associated with an incremental gamma-ray luminosity of $dL = d\dot{N}_e \dot{E}_{\rm CR} dt$, which is radiated in a time dt. The CR loss rate is given by $\dot{E}_{\rm CR} \approx 2e^2 c\gamma^4/(3\rho_c^2)$, where $\gamma(r,\vartheta,\phi)$ is the Lorentz factor of the electron primaries. We calculated CR photon spectra $dN_\gamma^i/dE(E_\gamma,\chi,\zeta)$ for $\chi = \zeta = 10°, 20°, \cdots, 80°$, and $i = 1, 2, ..., 13$, assuming $R = 10^6$ cm, $M = 1.4M_\odot$, and $I = 0.4MR^2$. All spectra ($13 \times 8 \times 8 = 832$) were scaled to a distance of $d = 5$ kpc (Gratton et al., 2003).

We next randomly chose $N = 100$ visible MSPs (with random χ and ζ), and summed their pulsed spectra to obtain a million cumulative spectra from the Monte Carlo process:

$$\left(\frac{dN_\gamma}{dE}\right)_{\rm cum}^j = \sum_{k=1}^{N=100} \frac{dN_\gamma^k}{dE}(E_\gamma,\chi,\zeta), \quad (4.21)$$

where for each index $j = 1, 2, ..., N_t = 10^6$, a total of $N = 100$ spectra (randomly sampled from the abovementioned 832 spectra) were summed. Therefore, j corresponds to a specific choice of χ, ζ, and k-values when oversampling from 13 to 100 pulsar spectra. This procedure was repeated for 1 MSP instead of 100, i.e. setting $N = 1$. Upon comparison of these results, one would expect that the mean values of the single MSP differential spectra would scale with N, and the standard deviations with $\sqrt{N}$. In panel (a) of Figure 4.24, the mean values of $E_\gamma^2 dN_\gamma/dE$ at three different photon energies E_γ are shown as a function of the number N_t of values used to calculate the mean (with a maximum of $N_t = 10^6$). The thick lines indicate results when $N = 100$, while the thin lines indicate results for $N = 1$, scaled by a factor 100. Similarly, panel (b) of Figure 4.24 indicates the standard deviation of $E_\gamma^2 dN_\gamma/dE$ at three different photon energies versus N_t. The thick lines again indicate results when

$N = 100$, while the thin lines indicate results for $N = 1$ scaled by a factor 10. It is clear that the mean and σ-values converged beyond $N_t \sim 10^4$, for both $N = 1$ and $N = 100$. The $N = 1$ results were more erratic at small N_t-values. The relative error on the mean values were therefore a factor 10 lower when using a population of 100 MSPs, as opposed to the much larger error obtained for single pulsars.

Figure 4.25 depicts average cumulative pulsed differential spectra $\left\langle E_\gamma^2 dN_\gamma/dE \right\rangle_{\rm cum}$ for $N = 100$ and $N_t = 10^6$, as well as 2σ-bands (corrected as explained in Section 2.5.11). Also shown are the *GLAST LAT* sensitivity curve (Harding et al., 2005b) and *EGRET* upper limits (Fierro et al., 1995), as well as other predictions of pulsed gamma-ray radiation from 47 Tucanae (Harding et al., 2005b).

4.5.3 Geometry-averaged Spectra and Luminosities

The gamma-ray visibility of an isolated MSP depends extremely sensitively on the assumed pulsar geometry. Inclination and observer angles χ and ζ are usually estimated from radio polarisation measurements (e.g. Manchester & Johnston (1995)), involving the rotating vector model. In our MSP model, the electric potential boundary condition of $\Phi(\xi = 1) = 0$ is used (Muslimov & Harding, 1997) as the last open magnetic field lines ($\xi = 1$) are treated as equipotentials. In addition, the space-charge-limited nature of this model requires that the accelerating electric field parallel to the magnetic field ($E_{||}$) should be zero at the stellar surface ($r = R$). This means that on-beam radiation (when $\chi \sim \zeta$) will have a spectral cut-off which roughly scales with the maximum potential $\Phi_{\rm max}$. Off-beam radiation will however rapidly decrease as the impact angle $\beta' = \zeta - \chi$ increases, because this radiation is produced along field lines where the electric potential Φ, and hence $E_{||}$, has dropped significantly.

An ensemble of MSPs provides the unique opportunity to sidestep the issue of pulsar geometry (which is crucial when modelling a single MSP) by averaging over numerous spectra and geometries, which results in a "geometry-averaged" spectrum with relatively small uncertainty. We also exploited this scenario in the sense that we used results from the corotating frames of the MSPs, since we expected that the effect of Lorentz transformations to the observer frame will average out over the ensemble. *We found that the relative spread of ensemble values for the bolometric gamma-ray and electron luminosities as well as the spin-down power and average gamma-ray spectra were typically one order smaller than for the same quantities averaged as single MSP quantities (i.e. they scale with* $N^{-1/2}$*).* This illustrates the importance of testing pulsar models by observing GCs. (This conclusion follows when using a constant EOS. Variations in the EOS have a much smaller effect than that of differing pulsar geometries, and are therefore not included in this discussion; see Section 4.5.4).

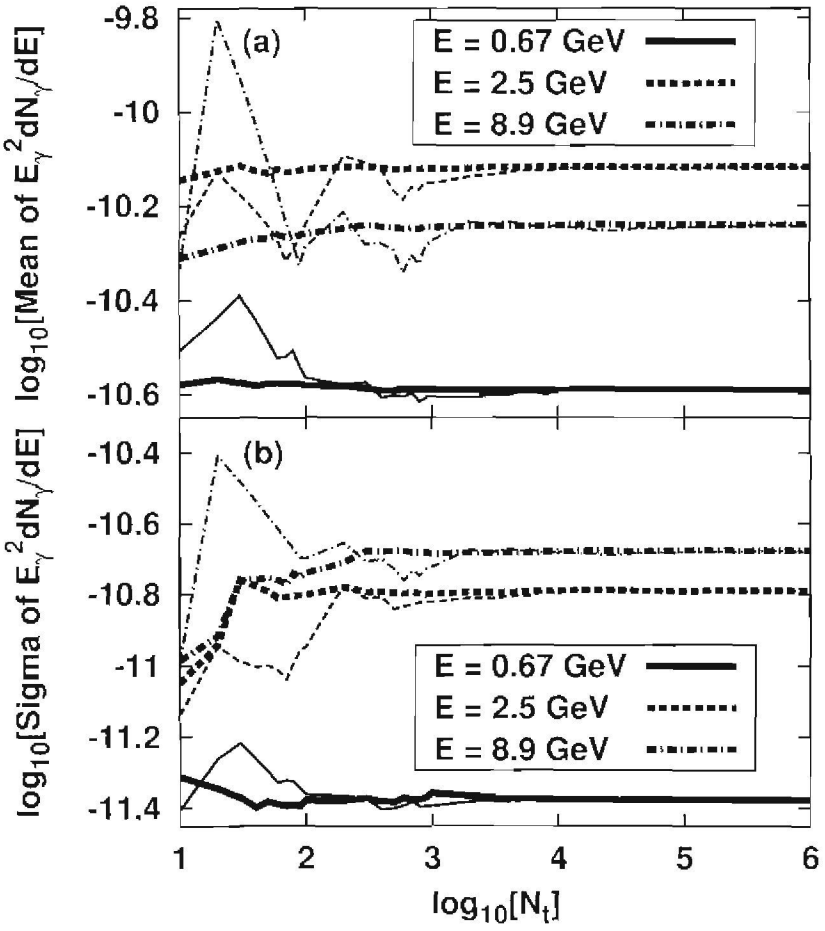

Figure 4.24: The mean and standard deviation σ of $E_\gamma^2 dN_\gamma/dE$ (in units of ergs/s/cm^2) vs. N_t as shown in panel (a) and panel (b), with N_t the number of values of $E_\gamma^2 dN_\gamma/dE$ used to calculate the mean and σ-values. Line types correspond to different energies as shown in the legend. Thick lines are for values of $E_\gamma^2 dN_\gamma/dE$ summed over $N = 100$ randomly chosen visible pulsars, while thin lines are for values of $E_\gamma^2 dN_\gamma/dE$ for single ($N = 1$) randomly chosen pulsars. The latter values were scaled by a factor 100 in panel (a), and a factor $\sqrt{100} = 10$ in panel (b). Results converge beyond $N_t \sim 10^4$. (Figure from Venter & de Jager (2008a); calculations have been done for 'uncorrected' CR spectra – see Section 2.5.11).

Due to the lower relative ensemble errors, one should therefore expect to be able to constrain average pulsar parameters using average spectra and their errors shown in Figure 4.25. This would not be the case if ensemble values did not converge (Figure 4.24) and had relatively small errors. Furthermore, the fact that the ratios of average cumulative luminosities and spin-down powers to their single MSP counterparts are very close to $N = 100$ gives us confidence in our sampling algorithm.

In our model, the predicted average single pulsar efficiencies for electron and gamma-ray production

are typically $\sim 2\%$ and $\sim 7\%$, depending on the population of MSPs used. For our 47 Tucanae MSP population (with $\left\langle \dot{E}_{\rm rot} \right\rangle = 2.2 \times 10^{34}$ ergs/s), we found 0.74% and 6.1%, respectively. This should be compared to the estimate of Bednarek & Sitarek (2007) of 1% for the first value, and to that of Harding et al. (2002b) of $\sim 10\%$ for the latter quantity. Venter & de Jager (2005a) quoted values of $1 - 2.5\%$ and $2 - 9\%$ for these quantities for the case of the pulsar PSR J0437-4715.

In Figure 4.25, we converted integral *EGRET* upper limits (Fierro et al., 1995) and model predictions of Harding et al. (2005b) to differential values assuming a E^{-2} spectrum. Our predicted pulsed gamma-ray flux at 100 MeV is below the differential *EGRET* upper limit, much lower than that of Harding et al. (2005b). Their prediction of the integral flux above 100 MeV exceeds the *EGRET* upper limit by a factor $f \sim 19$ for 15 MSPs, and $f \sim 125$ for 100 MSPs. (This seemingly overprediction of integral flux was also found in the case of PSR J0437-4715 (Venter & de Jager, 2005a). The prediction of Harding et al. (2005b) is a factor $f \sim 35$ above the *EGRET* upper limit for this MSP). However, our summed pulsed spectra violate the *EGRET* upper limit at 1 GeV (Fierro et al., 1995), providing constraints on the low-energy tail of the average pulsed spectrum. *GLAST LAT* observations will however constrain the predicted spectrum at all energies of relevance, which should provide a meaningful constraint on the product of visible pulsars N, and the average integral flux above 1 GeV per pulsar.

4.5.4 Constraints on Number of Visible Members and Average Integral Fluxes

We calculated the pulsed gamma-ray flux expected from a population of MSPs in 47 Tucanae for $N = 100$ visible members, but the spectra can easily be (linearly) scaled to any other reasonable number. We were especially interested in obtaining errors on the pulsed gamma-ray spectrum which would reflect the uncertainty in the geometries, as well as the spread in $\dot{P}$ and P, of the individual pulsars. In this way, we wanted to see whether it would be possible to constrain the underlying pulsar model independently of the assumed pulsar geometry. It remains to be shown whether the spread of the 13 selected pulsars represent the true inherent spread of MSPs in 47 Tucanae.

For the sake of completeness, we furthermore investigated the effect of varying the EOS (M, R, and I). By choosing $I = 0.4MR^2$, and letting M and R vary between $M/M_\odot = 1.4, 1.5, 1.6$ and $R_6 = R/10^6\,{\rm cm} = 1.0, 1.2, 1.4, 1.6$, we found that the maximum integral flux did not vary by more than $\sim 4\%$ (although it increases with both M and R; the spectral cut-off energy furthermore did not vary by more than $\sim 13\%$). Since this variation will not significantly influence our constraints derived below, we used fixed values of $M = 1.4M_\odot$ and $R_6 = 1$ throughout.

Our average pulsed spectrum, including errors, exceeded the *EGRET* upper limit at 1 GeV (for the

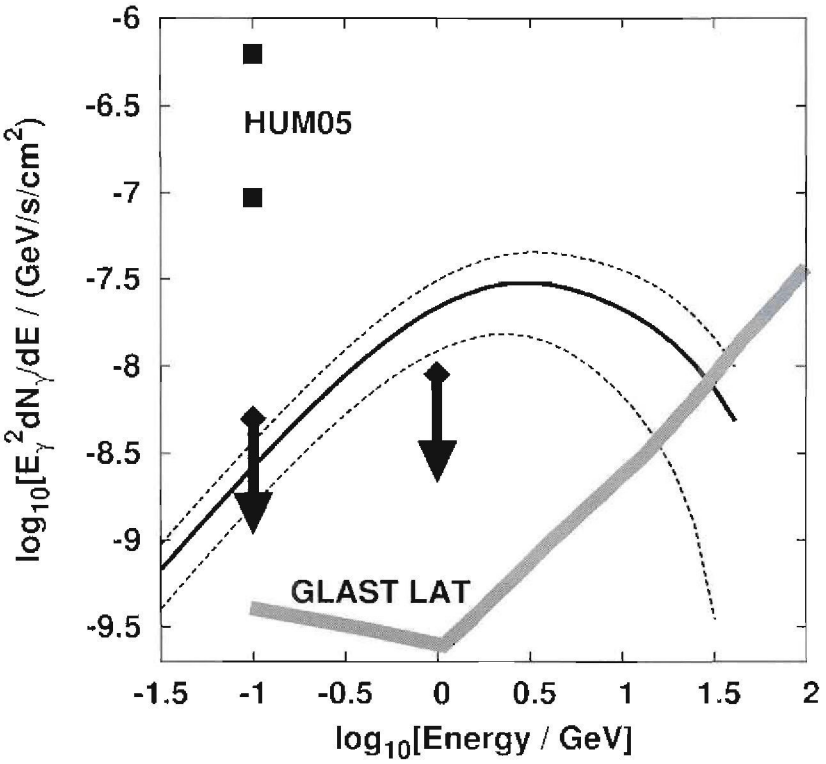

Figure 4.25: Average differential pulsed gamma-ray spectrum (solid line) with 2σ-error bands (shaded band between dashed lines) for $N = 100$ and $N_t = 10^6$, with smoothed high-energy tails. Furthermore we indicate predictions of Harding et al. (2005b): lower square for 15 MSPs, upper square scaled to 100 MSPs, labelled by 'HUM05'. The predictions from Harding et al. (2005b) involves estimates of single-particle spectra scaled using the Goldreich-Julian PC current (Goldreich & Julian, 1969) and arbitrary beaming angles. Our spectra include variations across the PC (sampling different magnetic field lines) as well as variations due to various inclination angles and observer geometries (with beaming angles calculated implicitly). The *GLAST LAT* sensitivity (Harding et al., 2005b) as well as *EGRET* upper limits (diamonds – Fierro et al., 1995) are also shown (the *EGRET* upper limits and results of Harding et al. (2005b) were converted to differential values assuming an E^{-2}-spectrum). This figure is an updated version of Figure 2 in Venter & de Jager (2008a), as 'corrected' CR spectra have now been used – see Section 2.5.11.

average integral flux spectrum, by a factor of ~ 3.76). Assuming that this model predicts the gamma-ray flux correctly, this *EGRET* upper limit constrains the number of GC pulsars to $100/3.76 \approx 27$. Generally, the constraints derived may be summarised as follows:

$$\frac{N\,\langle F_{\rm obs}\rangle}{\langle F_{\rm model}\rangle} \leq \frac{27}{q}, \tag{4.22}$$

with $\langle F_{\rm obs} \rangle$ and $\langle F_{\rm model} \rangle$ the average observed and predicted integral flux above 1 GeV per pulsar, and q a factor indicating telescope sensitivity. For *EGRET*, $q = 1$, while $q = 40$ for *GLAST LAT*. For example, setting $N = 22, 100$, and 200, we found that $\langle F_{\rm obs} \rangle / \langle F_{\rm model} \rangle \leq 1.3, 0.27, 0.14$ for *EGRET*. This indicated that the *EGRET* limit is obeyed for $N = 22$, but that larger values of N imply a reduction in the model-predicted integral flux (by, e.g., factors of 3.7 and 7.4 for $N = 100$ and 200). In the case of a *GLAST LAT* non-detection, we found $\langle F_{\rm obs} \rangle / \langle F_{\rm model} \rangle \leq 0.03, 0.007, 0.003$ for $N = 22, 100$, and 200. *GLAST LAT* might lastly even constrain the maximum average electric potential per pulsar $\langle \Phi_{\rm max} \rangle$ via the CR cut-off energy. It should also in principle be possible to look for the radio periods corresponding to the 22 known MSPs in 47 Tucanae in the gamma-ray data (or detect new gamma-ray periods if beaming properties are different), should *GLAST LAT* detect the cumulative pulsed CR spectrum.

4.5.5 Other GCs

The above results may be easily scaled for other GCs (using the number of MSPs N and distance d), assuming all other input parameters and model conditions are equal, via

$$F^{\rm new} = F^{\rm 47Tuc} \left(\frac{N}{100} \right) \left(\frac{d_{\rm 47Tuc}}{d} \right)^2 , \tag{4.23}$$

with F the differential or integral flux. We plan to do this when presenting future work on the pulsed and unpulsed radiation expected from nearby GCs (Venter & de Jager, 2008b,c).

4.6 Conclusion

In Section 4.1, we noted that a population study generally has two major advantages: the ability to overcome the potentially staggering number of individual elements making up a compound system, as well as the smoothing out of individual "eccentricities" to obtain an indication of typical behaviour by considering system-averaged properties. In contrast to the single (isolated) pulsar studies we performed in Chapter 3, we performed pulsar population studies in the current chapter, applying the same model of a single pulsar iteratively for different sets of pulsar parameters.

We performed three main applications in this chapter: (i) We investigated the behaviour of the single pulsar model in parameter space when considering ranges of parameters appropriate for MSPs (Section 4.3); (ii) We studied the systematic beaming effects of pulsars (Section 4.4); (iii) We studied the visibility of the nearby GC 47 Tucanae for a population of GC MSPs with corrected values of their

period derivatives (Section 4.5).

4.6.1 Population Study Involving Pulsar Parameter Space

We applied the basic MSP model for a mesh of $(P, \dot{P}, \chi, \zeta)$-space and found that cut-off energies, efficiencies, energy fluxes, and integral fluxes generally decrease with larger P and smaller $\dot{P}$. This is expected, since the spin-down power, PC current, and PC electric potential scale with a positive power of $\dot{P}$ and with a negative power of P. The effect of increasing the energy threshold when calculating the integral flux was also apparent, as more and more MSPs became invisible as the minimum energy was increased. The effect of geometry was furthermore evident: maxima of above-mentioned quantities occured for on-beam radiation (with asymmetrical distributions about the $\chi = \zeta$ line for the unscreened pulsars), while the beaming correction Λ was a minimum in this case. We lastly found that the energy ratio τ was typically $\sim 1 - 2$, so that the CR cut-off energy E_0 is a good approximation for the average energy $\overline{E}$ of the photon spectrum. Summarising, we found that pulsar properties are sensitive functions of the assumed geometry (as well as $\dot{P}$ and P), so that accurate knowledge of pulsar geometry is crucial when making predictions regarding their visibility. In addition, screening complicates the matter for high-$\dot{E}_{\rm rot}$ pulsars, where pair-creation leads to suppression of the E-field. The effect of screening was seen by comparing results for various pulsar quantities using 3 MSPs: one unscreened, the second also unscreened, but close to the screened / unscreened border on the $P\dot{P}$-diagram, and the last screened.

4.6.2 Population Study Involving a 'Real' Population of Mainly Unscreened MSPs

We noted that it is of particular interest to estimate the total beam luminosity using the measured energy flux. Our calculations showed that beaming correction factors Λ may be significantly larger than unity, and that actual trends may be concealed when Λ is unknown. From the calculated integral fluxes we inferred that roughly half of the population of 59 MSPs were expected to be visible for *GLAST*, with predicted fluxes of $\sim 10^{-8}$ cm^{-2}.s^{-1}. We furthermore found average CR cut-off energies of ~ 1 GeV for the canonical EOS assumed. With PSR J0437-4715 being part of the population of 59 members, we had the opportunity to compare results with those of Chapter 3. Given the differences in EOS, and pulsar geometry (which sensitively influences Λ), we found agreement for the predicted integral fluxes and beaming correction factors for this MSP. Also, we saw that the *EGRET* flux upper limit at 100 MeV for PSR J0437-4715 (Fierro et al., 1995) is obeyed when the geometry becomes significantly off-beam, in contrast with the conclusion reached for on-beam geometry in Chapter 3. We lastly found that the approximation $L_\gamma^{\rm beam}(0) = 0.75\kappa(1-\kappa)\dot{E}_{\rm rot}$ overpredicts $L_\gamma^{\rm beam}$, and that

better results follow when using the more general expression $L_\gamma^{\rm beam}(\chi) = L_\gamma^{\rm beam}(0)[\cos^2\chi + C\sin^2\chi]$. Assuming $C \approx 1/3$, this becomes $L_\gamma^{\rm beam}(\chi) = 0.5\kappa(1-\kappa)\dot{E}_{\rm rot} \approx 0.07\dot{E}_{\rm rot}$, indicating that $\eta_\gamma^{\rm beam} \approx 7\%$ for unscreened MSPs in the context of this model.

4.6.3 Population Study Involving a Population of MSPs in a Globular Cluster

When considering an ensemble of MSPs, we found that such a population provides the unique opportunity to sidestep the issue of pulsar geometry (which is crucial when modelling a single MSP) by averaging over numerous spectra and geometries, which results in a "geometry-averaged" spectrum with relatively small uncertainty (Venter & de Jager, 2008a). The relative spread of ensemble values for the bolometric gamma-ray and electron luminosities as well as the spin-down power and average gamma-ray spectra are typically one order smaller than for the same quantities averaged as single MSP quantities (for ~ 100 members). This illustrates the importance of testing pulsar models by observing GCs. (We furthermore found that varying the EOS did not alter conclusions significantly, so that the geometry, along with the values of $\dot{P}$ and P, are the main factors determining MSP visibility).

We calculated the pulsed gamma-ray flux expected from a population of MSPs in 47 Tucanae for $N = 100$ visible members, but the spectra can easily be (linearly) scaled to any other reasonable number (we plan to do this when presenting future work on the pulsed and unpulsed radiation expected from nearby GCs – Venter & de Jager (2008b,c)). We were especially interested in obtaining errors on the pulsed gamma-ray spectrum which would reflect the uncertainty in the geometries, as well as the spread in $\dot{P}$ and P, of the individual pulsars. In this way, we wanted to see whether it would be possible to constrain the underlying pulsar model independently of the assumed pulsar geometry. It remains to be shown whether the spread of the 13 selected pulsars represents the true inherent spread of MSPs in 47 Tucanae.

We found good agreement for the average single pulsar efficiencies for electron and gamma-ray production between our results and those of other authors. However, our average pulsed spectrum, including errors, exceeded the *EGRET* upper limit at 1 GeV (for the average integral flux spectrum, by a factor of ~ 3.76). Assuming that this model predicts the gamma-ray flux correctly, this *EGRET* upper limit constrains the number of GC pulsars to $100/3.76 \approx 27$. Generally, setting $N = 22, 100$, and 200, we found that $\langle F_{\rm obs}\rangle \,/\, \langle F_{\rm model}\rangle \leq 1.3, 0.27, 0.14$ for *EGRET*. This indicates that the *EGRET* limit is obeyed for $N = 22$, but that larger values of N imply a reduction in the model-predicted integral flux (by, e.g., factors of 4 and 8 for $N = 100$ and 200). In the case of a *GLAST LAT* non-detection, we found $\langle F_{\rm obs}\rangle \,/\, \langle F_{\rm model}\rangle \leq 0.03, 0.007, 0.003$ for $N = 22, 100$, and 200. We lastly noted that *GLAST LAT* might even constrain the maximum average electric potential per pulsar $\langle \Phi_{\rm max}\rangle$

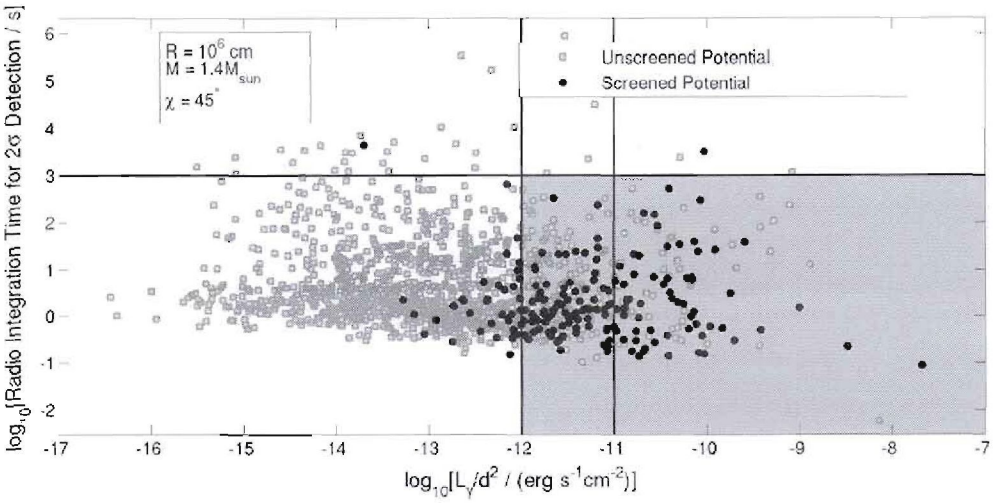

Figure 4.26: *KAT* radio integration time for 2σ-detection vs. $L_\gamma^{\rm beam}/d^2$. The region in the lower right corner will be visible to both *KAT* and *GLAST* after 1 000 seconds of radio integration time. The dark circles indicate MSPs with screened PCs, while the grey squares indicate MSPs with unscreened PCs. For the next phase, *meerKAT*, which will be much more sensitive than *KAT*, the pulsars (dots) will move down as a 2σ detection will be attained much quicker, so that more pulsars will be visible for the combination of *GLAST* and *meerKAT* (Fanaroff 2008, personal communication). Figure taken from Venter et al. (2005).

via the CR cut-off energy.

4.6.4 The Link Between Radio and Gamma-ray Telescopes

As an aside, we now briefly describe the role a radio telescope will play in the identification of gamma-ray pulsars to be observed by *GLAST LAT* (Venter et al., 2005). The proposed *Square Kilometre Array (SKA)* radio telescope is an international 2 billion dollar project. Only South Africa and Australia are still in the run for acting as the host country for this biggest radio astronomy project ever. South Africa is planning the construction of a 10% prototype named *meerKAT*, the extention of the original 1% demonstrator called *KAT (Karoo Array Telescope)*.

Since existing radio telescopes will not be able to monitor all pulsars on a regular basis, *most faint gamma-ray pulsars discovered by GLAST LAT will remain unidentified in the absence of contemporary radio parameters* (also see Ransom, 2007). Figure 4.26 shows the radio integration time vs. L_γ/d^2 (see Harding et al. (2002b) for expressions for L_γ), which is an indication of the expected gamma-flux (Venter et al., 2005). We differentiated between the pulsars expected to have screened and unscreened electric potentials. Also shown are 1 000 seconds of *KAT* observation (for 2σ-detection) and the

GLAST LAT sensitivity ($10^{-12} - 10^{-11}$ erg s^{-1} cm^{-2}), *boxing the fraction of the pulsar population which will be visible to both KAT and GLAST LAT, and underlining the importance of concurrent radio and gamma-ray observations of pulsars.* (Note that *KAT* integration times of some pulsars may deviate depending on the interstellar medium). For the next phase, *meerKAT*, which will be much more sensitive than *KAT*, the pulsars (dots) in Figure 4.26 will move down as a 2σ detection will be attained much quicker, so that more pulsars will be visible for the combination of *GLAST* and *meerKAT* (Fanaroff 2008, personal communication).

4.6.5 The Effect of a "New E-Field"

In this chapter (and the previous), the results of Muslimov & Harding (1997) and Harding & Muslimov (1998) were used when implementing the unscreened parallel E-field into the pulsar model. However, a newer derivation has been done Muslimov & Harding (2004b, see Section 2.4.6). At low altitudes, the two E-fields are essentially the same, and at high altitudes the latter goes to zero, while the first falls off as η^4. It should therefore be expected that the results when using either of these will be close. One important consideration is that the new field leads to less oscillation problems as described earlier, and is therefore more desirable (Harding 2007, personal communication). The effect of including a new E-field on the results of a population study, as well as that of including a ϑ-component in $E_{||}$, is beyond the scope of this study. However, some preliminary investigation has been done in Chapter 6. Future projects may include redoing the work of this chapter with newer formulas for the electric field, or even studying the effect of totally different expressions for $E_{||}$ (and associated charge density).

Chapter 5

Beyond the Light Cylinder

5.1 Introduction

This chapter collects results involving relativistic particles escaping from the magnetospheres of pulsars. Our first application (Section 5.2) focuses on inverse Compton (IC) and synchrotron radiation (SR) due to particles escaping from an ensemble of millisecond pulsars (MSPs) in the globular cluster (GC) 47 Tucanae, giving rise to unpulsed high-energy radiation. It is therefore complementary to the calculations involving the pulsed high-energy radiation from this GC reported in Section 4.5. Next, we present model calculations for the Galactic Centre composite supernova remnant (SNR) G0.9+0.1, enabling us to derive constraints on pulsar parameters using multiwavelength data (Section 5.3). In Section 5.4 through 5.6, we summarise results from ongoing collaborative research on the contribution of nearby pulsars to the local interstellar cosmic ray lepton spectrum. Relevant papers on this subject are included in Appendix B. Lastly, the conclusion follows in Section 5.7.

5.2 Unpulsed Radiation from an Ensemble of MSPs in 47 Tucanae

We will elaborate on the work presented in this section in Venter & de Jager (2008b,c).

5.2.1 Cumulative Injection Spectrum

In Section 4.5, we calculated the expected curvature radiation (CR) gamma-ray spectra for several MSPs in a GC, for several pulsar parameters, and obtained a prediction for the expected cumulative pulsed high-energy gamma-ray flux, with 2σ error bands. The 2σ-spread about the average was due to the different values of P and $\dot{P}$, as well as different angles describing the geometry, χ (inclination angle) and ζ (observer angle), used. Similar to Eq. (4.20), where we calculated the gamma-ray photon

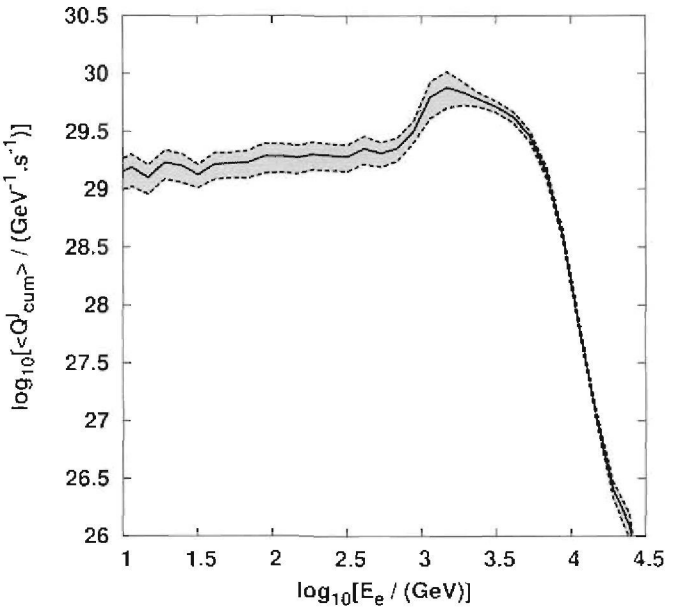

Figure 5.1: Cumulative injection spectrum of relativistic particles originating in the magnetospheres of an ensemble of MSPs in 47 Tucanae. The shaded band between the dotted lines indicate the 2σ-spread about the average cumulative particle spectrum $\langle Q^{j}_{\rm cum} \rangle$.

spectrum, we now use

$$Q^{i} \equiv \frac{d\dot{N}^{i}_{\rm e}}{dE_{\rm e}}(E_{\rm e},\chi) = \frac{1}{dE_{\rm e}} \iiint \left(\frac{d\dot{N}_{\rm e}}{dE^{\rm LC}_{\rm e} d\xi\, d\phi} \right) I(E^{\rm LC}_{\rm e}, dE^{\rm LC}_{\rm e})\, dE^{\rm LC}_{\rm e} d\xi\, d\phi, \tag{5.1}$$

with

$$d\dot{N}_{e} = \frac{\rho_{e} dS \beta_{0} c}{e} \tag{5.2}$$

the number of primary electrons leaving a surface patch $dS(\xi_0, \phi_0)$ and moving along a B-line (assumed to stay constant along the line; ρ_e is the charge density; $\beta_0 \approx 1$ the initial electron speed),

$$E^{\rm LC}_{\rm e} \equiv \gamma(\eta_{\rm LC}) m_{e} c^{2} \tag{5.3}$$

the electron energy at the light cylinder ($\eta = \eta_{\rm LC}$), and γ the electron Lorentz factor, to calculate the spectrum of particles leaving the magnetosphere of each MSP i, with $i = 1, \cdots, 13$. We use the same population of 13 MSPs with corrected period-derivative values as in Section 4.5. The indicator function $I(E^{\rm LC}_{\rm e}, dE^{\rm LC}_{\rm e})$ bins the quantity $d\dot{N}_{\rm e}/dE^{\rm LC}_{\rm e}$ according to the residual electron energy $E_{\rm e}$ at the light cylinder.

As before, we next randomly choose $N = 100$ MSPs (with random χ), and sum their particle spectra to obtain a million cumulative spectra from the Monte Carlo process:

$$Q^j_{\rm cum} = \sum_{k=1}^{N=100} \frac{d\dot{N}^k_{\rm e}}{dE_{\rm e}}(E_{\rm e}, \chi), \tag{5.4}$$

where for each index $j = 1, 2, ..., N_t = 10^6$, a total of $N = 100$ spectra (randomly sampled from 104 spectra: 13 MSPs $\times$ 8 values of χ, $\chi = 10°, 20°, \cdots 80°$) were summed. We therefore oversampled from 13 to 100 pulsar particle spectra, to obtain the cumulative injection spectrum for $N = 100$ MSPs into the GC 47 Tucanae. Note that the single MSP particle spectra Q^i are not functions of ζ, so that the relative error of the average cumulative particle spectrum $\langle Q^j_{\rm cum} \rangle$ is expected to be smaller than for the average cumulative gamma-ray spectrum $\langle (dN_\gamma/dE)^j_{\rm cum} \rangle$ at earth (compare Figure 4.25 in Section 4.5 with Figure 5.1, indicating the cumulative particle spectrum with 2σ-errors). From Figure 5.1, it is clear that there is an accumulation of TeV-particles (characteristic of radiation reaction, where losses limit particle acceleration), causing a bump in the spectrum. The slope of the low-energy part is set by acceleration and radiation processes in the pulsar magnetosphere, with the E-field differing along different B-lines.

5.2.2 Escape and Radiation Loss Time Scales

For soft photons with energy ϵ, we obtain the ICS loss rate by integrating the production rate over (initial) soft photon energy as well as (resulting) gamma-ray energy E_γ (see Blumenthal & Gould (1970) for more details):

$$\left(\frac{dE_{\rm e}}{dt}\right)_{\rm ICS} = \iint \left[\frac{dE_{\rm e}}{dt\, d\epsilon\, dE_\gamma}\right] d\epsilon\, dE_\gamma, \tag{5.5}$$

with $E_{\rm e}$ the electron energy. We used two photon components in this calculation: a bright starlight component with temperature $T_1 = 4\ 500$ K and energy density $u_1 = 40$ eV/cm^3, and the cosmic microwave background radiation (CMBR) component with $T_{\rm CMBR} = 2.76$ K and $u_{\rm CMBR} = 0.265$ eV/cm^3.

The SR loss rate is given by

$$\left(\frac{dE_{\rm e}}{dt}\right)_{\rm SR} = \frac{2}{3}\left(\frac{B^2_{\rm n} E^2_{\rm e}}{422}\right) \quad \text{erg/s}, \tag{5.6}$$

with $B_{\rm n}$ the magnetic field and $E_{\rm e}$ the radiating electron's energy.

The radiation loss and escape timescales are given by

$$\tau_{\rm ICS} = \frac{E_{\rm e}}{(dE_{\rm e}/dt)_{\rm ICS}}, \tag{5.7}$$

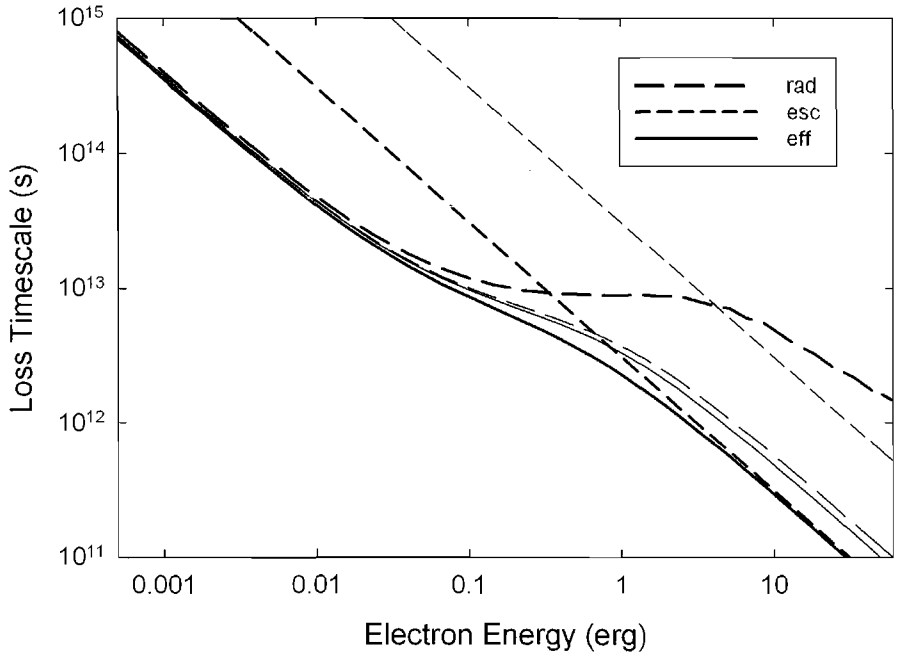

Figure 5.2: Radiation loss, escape, and effective timescales for radiation from 47 Tucanae. Thick lines indicate a B-field strength of 1μG, while thin lines indicate a B-field strength of 10μG.

$$\tau_{\rm SR} = \frac{E_{\rm e}}{(dE_{\rm e}/dt)_{\rm SR}} \propto B_{\rm n}^{-2} E_{\rm e}^{-1}, \tag{5.8}$$

$$\tau_{\rm rad} = \frac{E_{\rm e}}{(dE_{\rm e}/dt)_{\rm SR} + (dE_{\rm e}/dt)_{\rm ICS}}, \tag{5.9}$$

$$\tau_{\rm esc} = \frac{r_{\rm h}^2}{2\kappa_{\rm Bohm}} \propto B_{\rm n} E_{\rm e}^{-1} r_h^2, \tag{5.10}$$

with the escape timescale evaluated in the Bohm limit, where

$$\kappa_{\rm Bohm} = \frac{1}{3} r_{\rm L} v = \frac{1}{3} \left(\frac{E_{\rm e}}{q B_{\rm n}} \right) c, \tag{5.11}$$

$r_{\rm L}$ the Larmor radius, and $r_{\rm h} = 3.67$ pc the half-mass radius of 47 Tucanae. We next obtain the effective loss timescale through (Zhang et al., 2008)

$$\tau_{\rm eff}^{-1} \approx \tau_{\rm esc}^{-1} + \tau_{\rm rad}^{-1}. \tag{5.12}$$

Figure 5.2 indicates these different timescales, where the short-dashed lines are the escape timescales, the long-dashed lines the radiation loss timescales, and the solid lines the effective loss timescales.

Thick lines indicate cases when $B_{\rm n} = 1\mu$G, and thin lines cases when $B_{\rm n} = 10\mu$G. Since $\tau_{\rm esc} \propto B_{\rm n}$, the escape timescale for $B_{\rm n} = 10\mu$G is one order of magnitude larger than the escape timescale for $B_{\rm n} = 1\mu$G. The bright starlight component dominates the radiation timescale at low energies for all B-field strengths, while the CMBR component dominates for $B_{\rm n} = 1\mu$G at high energies. Also, the escape and radiation timescales for $B_{\rm n} = 1\mu$G are equal at $E_{\rm e} \sim 0.3$ erg. When $B_{\rm n} = 10\mu$G, the SR loss rate increases by a factor of 100, and $\tau_{\rm rad}$ is ~ 10 times lower than for the case of $B_{\rm n} = 1\mu$G at high energies. Finally, the effective timescales reflect the behaviour of their component escape and radiation timescales (see Eq. [5.12]). When $B_{\rm n} = 1\mu$G and $B_{\rm n} = 10\mu$G, $\tau_{\rm rad} \ll \tau_{\rm esc}$ at small electron energies, while $\tau_{\rm rad} \gg \tau_{\rm esc}$ at large electron energies for $B_{\rm n} = 1\mu$G. This means that $\tau_{\rm eff} \approx \tau_{\rm rad}$ at small electron energies for all field strengths, while $\tau_{\rm eff} \approx \tau_{\rm esc}$ at large electron energies for $B_{\rm n} = 1\mu$G, but $\tau_{\rm eff} \approx \tau_{\rm rad}$ for $B_{\rm n} = 10\mu$G.

5.2.3 Calculation of Unpulsed High-Energy Flux

We calculate the gamma-ray ICS flux using (see also Blumenthal & Gould (1970); Zhang et al. (2008))

$$\left(\frac{dN_\gamma}{dE}\right)_{\rm ICS} = \frac{1}{E_\gamma 4\pi d^2} \iint \left[\frac{dE_{\rm e}}{dt\, d\epsilon\, dE_\gamma}\right] \left(\frac{dN}{dE_{\rm e}}\right) d\epsilon\, dE_{\rm e}, \tag{5.13}$$

with the steady-state electron spectrum given by

$$\frac{dN}{dE_{\rm e}} = \left\langle Q^j_{\rm cum} \right\rangle \tau_{\rm eff}, \tag{5.14}$$

and $[dE_{\rm e}/(dt\, d\epsilon\, dE_\gamma)]$ the production rate per target photon energy ϵ per gamma-ray energy E_γ. We use $d \approx 5$ kpc (Gratton et al., 2003). The SR component is computed using

$$\left(\frac{dN_\gamma}{dE}\right)_{\rm SR} = \frac{1}{hE_\gamma 4\pi d^2} \int P_\nu \left(\frac{dN}{dE_{\rm e}}\right) dE_{\rm e}, \tag{5.15}$$

with

$$P_\nu(z) = \frac{\sqrt{3} e^3 B_{\rm n} F(z)}{mc^2} \tag{5.16}$$

the power per unit frequency emitted by a single electron, and

$$F(z) = z \int_z^\infty K_{5/3}(\xi) d\xi. \tag{5.17}$$

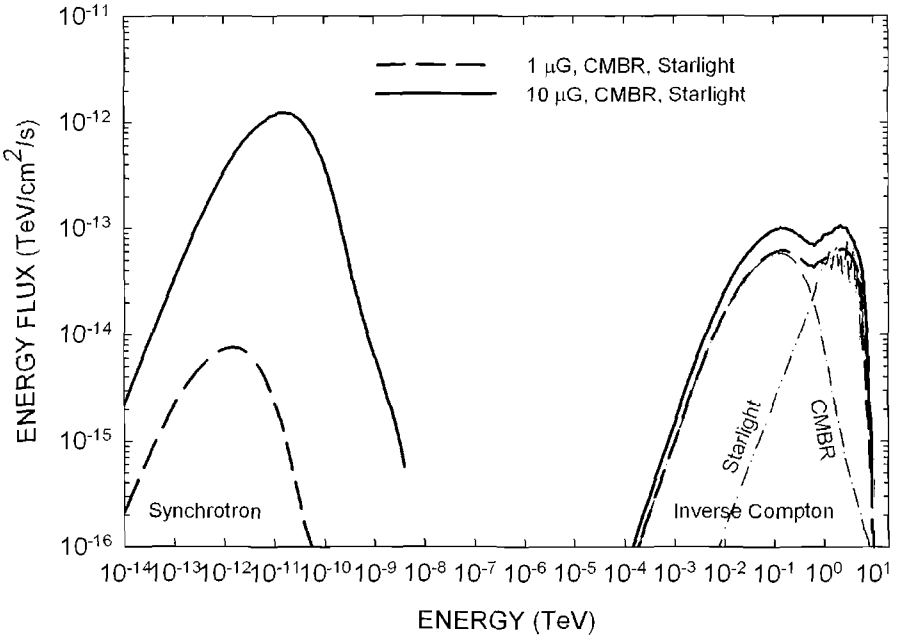

Figure 5.3: Predicted unpulsed high-energy spectra from 47 Tucanae. To the left are the SR components, with the top component for $B_{\rm n} = 10\mu$G dominating, as the SR loss rate $(dE_{\rm e}/dt)_{\rm SR} \propto B_{\rm n}^2$. The IC components occur2 at higher energies, and are nearly the same for $B_{\rm n} = 1\mu$G and $B_{\rm n} = 10\mu$G, although it is a bit larger for $B_{\rm n} = 10\mu$G. Also shown are the starlight (dash-double-dotted line) and CMBR (dash-dotted line) components contributing to the total IC component.

Here $K_{5/3}$ is the modified Bessel function of order 5/3, $z = \nu/\nu_c$, and ν_c the critical frequency defined by (also see Section 2.1.1)

$$\nu_{\rm c} \approx 16.08 \times 10^{12} B_{\rm n} \left(\frac{E_{\rm e}}{1\,{\rm GeV}}\right)^2, \tag{5.18}$$

for $B_{\rm n}$ measured in Gauss.

5.2.4 Discussion

For Crab-like pulsars, the magnetisation parameter decreases from $\sigma \sim 10^5$ at the light cylinder, to $\sigma \sim 3{\times}10^{-3}$ at the PWN shock radius (Kennel & Coroniti, 1984; Bednarek & Sitarek, 2007), indicating efficient conversion of Poynting energy to particle energy. We have however used the particle spectrum, originating at the light cylinder, in regions well beyond the light cylinder. We have thereby not allowed for Poynting flux to be converted into particle energy, leaving the particle spectrum unchanged. This is the most conservative approach. In future, reacceleration of particles may be taken into account, impacting the injection spectrum, and eventual predicted gamma-ray flux.

The predicted unpulsed flux is shown in Figure 5.3. Whereas the ICS fluxes are similar when $B_{\rm n} = 1\mu$G and $B_{\rm n} = 10\mu$G, the SR flux is 100 times larger when $B_{\rm n} = 10\mu$G, as the loss rate $(dE_{\rm e}/dt)_{\rm SR} \propto B_{\rm n}^2$. The SR component occurs in the optical / X-ray waveband, and the ICS, as a result of scattering the starlight and CMBR components, in the gamma-ray waveband. We suspect that the ICS from 47 Tucanae will not be visible for *H.E.S.S.*, while telescopes such as *Chandra* and *Hubble* may find it difficult to test the SR component prediction of diffuse radiation if there are many unresolved sources in the field of view. Upper limits may however be derived for the SR component.

5.3 Pulsar Parameters Derived from Multiwavelength Observations of G0.9+0.1

Results from this section have been reported in Venter & de Jager (2006).

5.3.1 Background

(i) Multiwavelength Observations of SNR G0.9+0.1

While searching for further examples of composite objects, Helfand & Becker (1987) observed G0.9+0.1 in 1984 at 20 cm and 6 cm with the *VLA*, despite its omission from Green's first catalogue (Green, 1984). They could clearly distinguish between a flat radio core component, corresponding to the pulsar wind nebula (PWN), and a steeper shell component, and thus discovered the composite nature of this bright, extended source near the Galactic Centre in the radio band. Using various previous observations, Helfand & Becker (1987) assigned spectral indices of $\alpha_{\rm c} \approx 0.1$ (typical of Crab-like remnants) and $\alpha_{\rm s} \approx 0.6$ to the core and shell components, and also constructed a broad band (radio - X-ray) spectrum of this source. LaRosa et al. (2000) obtained similar indices of 0.12 and 0.77 for the core and shell components from more recent *VLA* measurements at 90 cm, confirming this SNR's composite classification (Weiler & Panagia, 1978).

Helfand & Becker (1987) furthermore indicated a radio core-to-shell diameter ratio of ~ 0.25. Assuming a distance of 10 kpc, they obtained radio luminosities of $L_{\rm R,c} = 7.0 \times 10^{34}$ ergs/s and $L_{\rm R,s} = 2.8 \times 10^{34}$ ergs/s for the core and shell components, and an X-ray luminosity ($0.5 - 4.5$ keV) of $\sim (1-5) \times 10^{34}$ ergs/s for this remnant, setting the X-ray-to-radio flux ratio for the core to $\lesssim 0.6$. Other cited luminosity ratios are $L_{\rm R,c}/L_{\rm R,s} \sim 2.5$ and $L_{\rm X,c}/L_{\rm X,s} \sim 0.5$. Newer results from Sidoli et al. (2000) are $L_{\rm X,c}/L_{\rm R,c} = 1.4$ and $L_{\rm X,c}/L_{\rm X,s} > 1.2$.

BeppoSAX serendipitously detected G0.9+0.1 during a survey of the Galactic Centre (Mereghetti

et al., 1998), obtaining the first firm evidence of X-ray emission from G0.9+0.1, in addition to an earlier marginal detection by the *Einstein Observatory* (Helfand & Becker, 1987) and a non-detection by *ROSAT* (Mereghetti et al., 1998; Sidoli et al., 2001). The *ASCA* Galactic Centre survey also detected significant X-ray emission from an unresolved, compact region in accordance with the radio core in the $3 - 10$ keV band, but no significant emission in the softer energy band (Sakano et al., 1999). Similar updated results for the $0.7 - 10$ keV band, as well as an upper limit of $1.5'$ for the apparent X-ray size, are given in Sakano et al. (2002). Follow-up observations of the Galactic Centre and on-axis observations by *BeppoSAX* (Sidoli et al., 1998, 1999b,a, 2000) confirmed the non-thermal nature of X-rays from its radio core (and thus the composite nature of this remnant), and also found marginal indications of a diffuse character. Only an upper limit for X-ray emission from the SNR shell could be given, probably due to line-of-sight absorption (Sakano et al., 2003).

A higher resolution observation of this source with *Chandra X-Ray Observatory* (Gaensler et al., 2001) revealed a clear axial symmetry for the PWN, which matched the morphology of the radio nebula, as well as a faint X-ray point source along the symmetry axis, and a bright elliptical $5'' \times 8''$ clump to the north of this point source.

SNR G0.9+0.1 was also easily identified in the hard energy band during a wide-angle *XMM-Newton* survey of the CG Region (Sakano et al., 2003, 2004). On-axis observations (Porquet et al., 2003) revealed a large scale X-ray morphology in good correspondence with the 20 cm *VLA* radio contours (Helfand & Becker, 1987), with the X-ray core matching the eastern radio peak, and the western side of the X-ray arc-like feature corresponding to the western radio peak. For the first time, diffuse emission from the radio shell was detected in X-rays (of either thermal or non-thermal origin), in good agreement with the previous upper limit of Sidoli et al. (2000). The data in the region of the PWN are fitted well by both an absorbed power-law and a thermal bremsstrahlung model. Evidence for spectral steepening with increasing radius (which is stronger in this case than in other PWN, e.g. 3C58 & G21.5-0.9) supports a scenario where high-energy electrons undergo SR losses as they diffuse through the nebula. The eastern part of the arc-like feature exhibited harder X-ray emission than the western part, which may be explained in terms of relativistic beaming or Doppler boosting effects. The X-ray point source seen by *Chandra* was visible above 6 keV, and magnetospheric emission seems to be preferred over a black-body model, implying a luminosity of $\sim 10^{33} d_{10}^2$ ergs/s for this source (where $d_{10} = d/10$ kpc is the normalised distance). The deepest X-ray observation ever performed on this SNR (Sidoli et al., 2004) confirmed the spectral softening at larger radial distances from the PWN peak as well as X-ray emission from a region spatially coincident with the radio shell.

INTEGRAL observed the Galactic Centre in the $20 - 100$ keV energy range during $2003 - 2004$

for an effective exposure time of 4.7×10^6 sec (Bélanger et al., 2006). Revnivtsev et al. (2004) clearly observed emission from a region with centroid label IGR J17475-2822. The northern extension of this source (associated with Sgr B2) was tentatively associated with G0.9+0.1 and interpreted as a detection of VHE SR radiation.

Recently, the *H.E.S.S.* Collaboration reported the detection of the composite supernova remnant SNR G0.9+0.1 in very high energy (VHE) gamma rays (Aharonian et al., 2005c) with a significance of $\approx 13\sigma$, after 50 hours of observations of the Galactic Centre region with the full telescope system (also see Aharonian et al., 2006f). The unresolved gamma-ray radiation, which appears to be associated with the plerionic remnant core, corresponds to a photon flux above 200 GeV of $(5.7 \pm 0.7_{\rm stat} \pm 1.2_{\rm sys}) \times 10^{-12}/{\rm cm}^2/{\rm s}$ and luminosity of $\sim 2 \times 10^{34}$ ergs/s, making this one of the faintest VHE gamma-ray sources. For a radially symmetric Gaussian emission region, a 95% confidence limit of $1.3' \sim 3.2$ pc on the source radius is obtained, and similarly for emission from a uniform thin shell, with extension $< 2.2' \sim 5.4$ pc. This is the first time that SNR G0.9+0.1 has been detected at gamma-ray energies (de Jager, 2005), subsequent to the earlier unconstraining upper limit given by *HEGRA* (Aharonian et al., 2002), and *H.E.S.S.* observations in 2003 (resulting in a 4σ detection, Aharonian et al., 2004b). Subsequently, *MAGIC* also detected a small excess from G0.9+0.1 (Albert et al., 2006), but it is however not statistically significant yet due to limited observation time. (See de Jager & Venter (2005) for a recent review of conditions for maximal VHE pulsar and PWN visibility).

(ii) Indications of an Embedded Pulsar

It is widely accepted that the radiation of a PWN is powered by an embedded pulsar which creates a magnetised wind of ultrarelativistic particles, and that the latter are responsible for the observed multiwavelength SR and IC emission (see e.g. Gaensler & Slane, 2006). It is therefore plausible that this is also the case for G0.9+0.1, even though no pulsed emission has been detected yet (Aharonian et al., 2005c).

Helfand & Becker (1987) inferred a current pulsar spin-down luminosity of $L > 5 \times 10^{34}$ ergs/s owing to the fact that X-ray particle lifetimes are less than 100 years. This implies a pulsar period $P < 125$ ms for a typical pulsar magnetic field of $B_{\rm s} \sim 10^{12}$ G. Helfand & Becker (1987) also inferred a total energy in particles and fields of $(0.7 - 5) \times 10^{47}$ ergs, which points to an initial period $P_0 \lesssim 10$ ms, provided that this energy has been derived from the pulsar's rotational energy. Further *VLA* observations at 6 cm and 20 cm however did not reveal any point source above 6σ (0.45 mJy, Frail & Moffett, 1993).

Gray (1994) argued that G0.9+0.1 is a likely pulsar host since its structure is similar to that of SNR 0540-693 (in the Large Magellanic Cloud) which contains a pulsar, but noted that high dispersion measures and interstellar scattering may inhibit detection of pulsed emission from the purported central pulsar.

Despite the fact that no flux variations or pulsations were found in *BeppoSAX* data, Sidoli et al. (2000) argued for the existence of a young central neutron star based on the broad band (radio & X-ray) properties of the SNR. For a free expansion age of 1 100 yr, they obtained a pulsar period $P = 0.19$ s, period-derivative $\dot{P} = 2.8 \times 10^{-12}$ s s^{-1}, and surface magnetic field of $B_{\rm s} \sim 23 \times 10^{12}$ G, whereas for an adiabatic age of 6 800 yr, they obtained $P = 0.078$ s, $\dot{P} = 1.8 \times 10^{-13}$ s s^{-1}, and $B_{\rm s} \sim 3.8 \times 10^{12}$ G.

Observations by *Chandra X-Ray Observatory* revealed a faint X-ray point source along the symmetry axis (CXOU J174722.8-280915) which is considered to be the best candidate for emission from a central pulsar (Gaensler et al., 2001). Another less likely pulsar candidate is a bright elliptical clump, which may be an unresolved intermediate-latitude feature in the pulsar wind or some statistical fluctuation. The data are naturally explained by an equatorial torus and axial jet morphology, implying that this type of morphology might be a common one within the pulsar population.

The central pulsar candidate CXOU J174722.8-280915 was seen by *XMM-Newton* above 6 keV, and magnetospheric emission seems to be preferred over a black-body model, implying a luminosity of $\sim 10^{33} d_{10}^2$ ergs/s for this source (Porquet et al., 2003).

In this section we used radio, X-ray, and gamma-ray data to constrain both a time-dependent injection model (Section 5.3.2) of the downstream electron spectrum (responsible for the total multiwavelength spectrum), and the evolutionary history of the spin-down power. We obtained best fit values for the PWN birth spin-down power L_0, as well as for the injection spectrum break energy $E_{\rm b}$ in Section 5.3.3 and will discuss these results in Section 5.3.4.

5.3.2 The PWN Model

We assumed that the central pulsar's spin-down power has the following functional form:

$$L = I\Omega\dot{\Omega} = -K\Omega^{n+1}, \tag{5.19}$$

with I the moment of inertia, Ω the angular frequency, $\dot{\Omega}$ its time-derivative, and $n = \Omega\ddot{\Omega}/\dot{\Omega}^2$ the braking index. We next assumed that n is a constant (see, however, Chen & Li (2006)) and that the

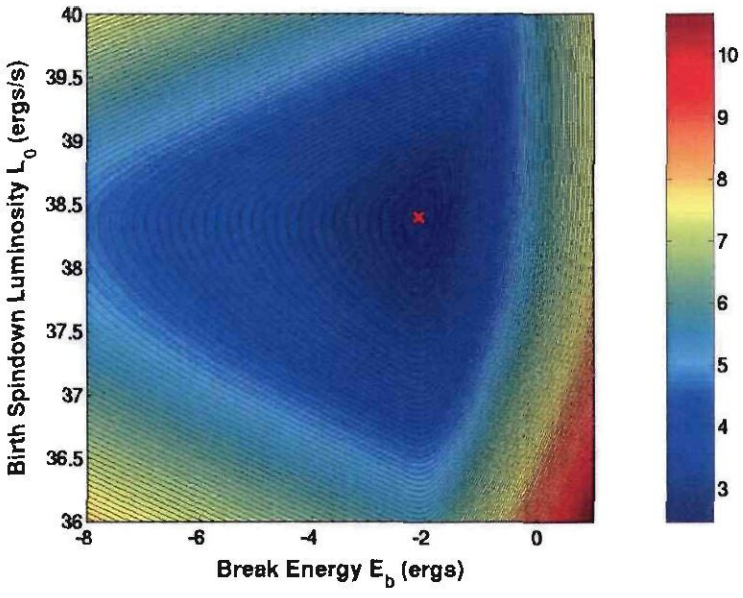

Figure 5.4: Plot of $-\log_{10}\chi_{\rm tot}$ (with $\chi_{\rm tot}$ the rms-total of the individual test statistics $\chi_{\rm s}$ for fits to the radio, X-ray and gamma-ray data) vs. $\log_{10}$ of initial spin-down luminosity L_0 and $\log_{10}$ of injection spectrum break energy $E_{\rm b}$, in order to find the 'best fit' (indicated by an 'X') for L_0 and $E_{\rm b}$ (at a fixed age $T =$ 6 500 yr and birth period $P_0 = 0.043$ s). Figure from Venter & de Jager (2006).

neutron star's crustal magnetic field does not decay. This led to the condition

$$\dot{P}P^{n-2} = \dot{P}_0 P_0^{n-2} \tag{5.20}$$

with $P = 2\pi/\Omega$ the pulsar period, $\dot{P}$ its time-derivative, and the subscript '0' indicating quantities at pulsar birth. Upon integration of $\dot{\Omega}$ from Eq. (5.19), and using Eq. (5.20), one finds the following general expression for the evolution of $L(t)$ (also see Reynolds & Chevalier, 1984):

$$L(t) = L_0 \left[1 + \frac{(n-1)P_0^2 L_0 t}{4\pi^2 I}\right]^{-\frac{n+1}{n-1}}. \tag{5.21}$$

In what follows, we assumed $P_0 = 0.043$ s, as inferred by van der Swaluw & Wu (2001) using the ratio of the PWN and shell radii. We modelled the effect of a time-changing nebular field by

$$B_{\rm n}(t) = \frac{B_0}{1 + (t/\tau_0)^{\alpha}} \tag{5.22}$$

(See Table 5.1 for parameter values). For the electron injection spectrum $Q(E,t)$ (number of electrons per second per energy at the shock radius r_s), we assumed a broken power law with indices α_1 and α_2, and break energy E_b:

$$Q(E,t) = \begin{cases} Q_0(t)\,(E/E_\mathrm{b})^{\alpha_1} & E < E_\mathrm{b} \\ Q_0(t)\,(E/E_\mathrm{b})^{\alpha_2} & E \geq E_\mathrm{b} \end{cases}.$$

We normalised Q by requiring that

$$\int Q(E,t)EdE = \epsilon L(t), \tag{5.23}$$

with $\epsilon \sim 0.1$ a conversion efficiency of spin-down power into particle luminosity. This led to

$$Q_0(t) = \frac{\epsilon L(t)}{E_\mathrm{b}^2}\left[\frac{(\alpha_1+2)\,(\alpha_2+2)}{(\alpha_2-\alpha_1)}\right], \tag{5.24}$$

for $\alpha_2 < -2$.

We next imposed two boundary conditions. The first is that $r_L \lesssim 0.5 r_s$, with r_L the electron's Larmor radius (de Jager & Djannati-Ataï, 2008). This ensures particle confinement within the PWN, and led to a condition on the particle energy:

$$E(t) < \frac{e}{2}\sqrt{\frac{\sigma L(t)}{(1+\sigma)c}}, \tag{5.25}$$

Model Parameter	Symbol	Value / Range
Braking index	n	3
B-field parameter	α	0.5
Present-day B-field	$B_\mathrm{n}(T)$	6 μG
Conversion efficiency	ϵ	0.1
Age	T	6 500 yr
Characteristic timescale	τ_0	500 yr
Distance	d	8.5 kpc
Magnetisation parameter	σ	0.2
Moment of inertia	I	10^{45} g.cm^2
Q break energy	E_b	10^{-8} – 10 ergs
Q index 1	α_1	-1.0
Q index 2	α_2	-2.2
Initial spin-down power	L_0	10^{36} – 10^{40} ergs/s
Birth period	P_0	43 ms

Table 5.1: Values of parameters used for the PWN model of G0.9+0.1.

with $\sigma \equiv L_{\rm EB}/L_{\rm E}$ the ratio of the electromagnetic energy flux to the particle energy flux. The second energy condition was required to ensure that the particles radiating SR emission will survive until time $t = T$ (with T the PWN's age, and $\langle B_{\rm n} \rangle \sim (B_{\rm n}(t)B_{\rm n}(T))^{1/2}$ the average field strength between time t and the current epoch at time T):

$$E(t) < \frac{422}{B_{\rm n}(t)B_{\rm n}(T)(T-t)} \quad \text{ergs.} \tag{5.26}$$

We lastly calculated the particle number density $dN/dE_{\rm e}$ subject to Eq. (5.25) and Eq. (5.26):

$$\frac{dN}{dE_{\rm e}}(E) = \int_0^T Q(E,t)\,dt. \tag{5.27}$$

5.3.3 Best-fit Parameters

Using this time-dependent model for the nebular-averaged particle spectrum, we added the contributions from all epochs which have survived to the present-day to give the net present-day photon spectra as calculated for SR and IC emission (The calculations are similar to those described in Section 5.2.3). In the latter case the target photon fields are the CMBR, as well as galactic target photon fields from the 25 K dust and starlight photon fields, assuming associated densities of ~ 1 eV/cm^3 for each component.

In Table 5.2, we indicate best-fit parameters when performing a collective fit (Model 1, using all multiwavelength data) as well as individual fits (Model 2 corresponds to a fit involving only gamma-ray data, Model 3 only X-ray data, and Model 4 only radio data). We also show the corresponding total energy output $E_{\rm tot} = \int L(t)dt$, integral X-ray flux $F_{\rm X}$ $(2-10$ keV) in ergs/cm^2/s, and integral gamma-ray flux above 0.2 TeV, $F_\gamma(>0.2)$, in /cm^2/s. A distance of $d = 8.5$ kpc was assumed

Data	$E_{\rm b}$	L_0	$F_\gamma(>0.2)$	$F_{\rm X}$	$E_{\rm tot}$	$\chi_{\rm s}$
Model 1: Multiwavelength fit	-2.1	38.4	-11.9	-12.4	48.9	2.4
Model 2: γ-ray-only fit	0.5	38.0	-11.4	—	48.8	-1.0
Model 3: X-ray-only fit	1.0	37.7	—	-11.6	48.7	-0.35
Model 4: Radio-only fit	-2.1	39.8	—	—	49.0	2.2
Observations	—	—	-11.2	-11.2	—	—

Table 5.2: 'Best fit' parameters for G0.9+0.1 for individual and collective (multiwavelength) fits, as well as observed values in last row (Aharonian et al., 2002; Porquet et al., 2003). Column units are $\log_{10}$ of ergs, ergs/s, /cm^2/s, ergs/cm^2/s, ergs, and $\log_{10}$ of a dimensionless test statistic (see text for details, and Figure 5.5 for the SEDs of the corresponding fits).

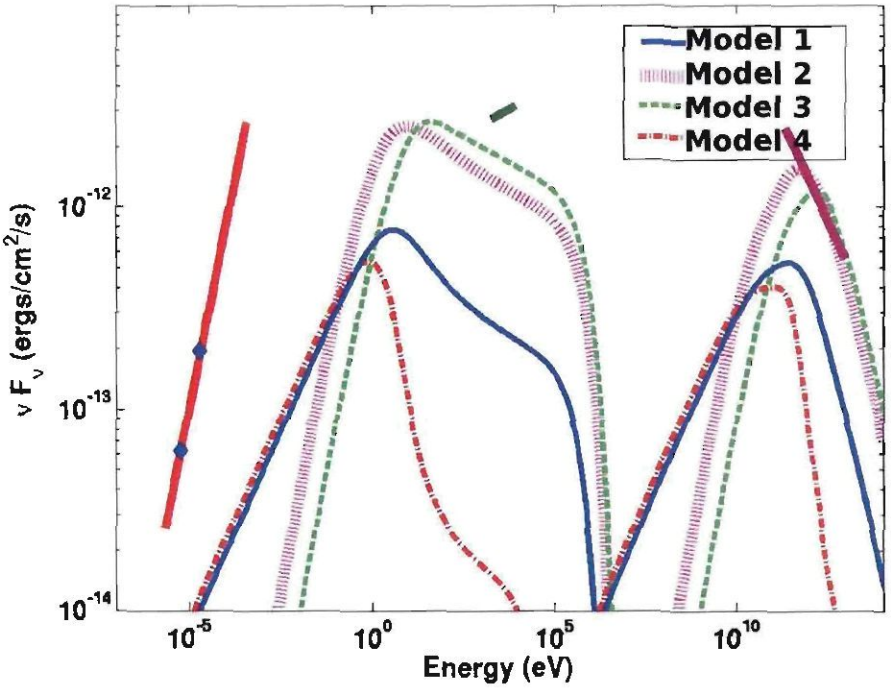

Figure 5.5: Plots of best fits of the spectral energy distribution (SED) of G0.9+0.1, with the different fits corresponding to Table 5.2, i.e. for individual and collective fits of the multiwavelength data (at a fixed age T = 6 500 yr and birth period P_0 = 0.043 s). Also shown are radio data points (blue diamonds) and radio spectrum (red line) taken from Helfand & Becker (1987), X-ray spectrum (dark green line) from Sidoli et al. (2004), and gamma-ray spectrum (magenta line) from Aharonian et al. (2005c).

(Aharonian et al., 2005c). These values correspond quite well to inferred values given in Aharonian et al. (2005c); Mereghetti et al. (1998); Sidoli et al. (2000); Porquet et al. (2003); Sidoli et al. (2004). The resulting fits (and multiwavelength observations) are shown in Figure 5.5. Note that we obtained different optimum values when we fitted the radio, X-ray, and VHE gamma-ray data individually. From Figure 5.4 we found an optimum fit of initial spin-down luminosity $L_0 \sim 2.5 \times 10^{38}$ ergs/s and a spectral break energy of $E_\mathrm{b} \sim 8 \times 10^{-3}$ ergs (using the rms-total test statistic χ_rms calculated from the individual waveband test statistics).

Eq. (5.21) now implies a value of present-day spin-down power of $L(T) \sim 7.4 \times 10^{36}$ ergs/s, which agrees within $\sim 50\%$ with the inferred value of $L(T) \sim 1.5 \times 10^{37}$ ergs/s from *BeppoSAX* observations (Sidoli et al., 2000). One may then also infer a pulsar polar cap (PC) magnetic field strength of $B_\mathrm{PC} \sim 3.2 \times 10^{19} \sqrt{P_0 \dot{P}_0} \sim 5 \times 10^{12}$ G, which is a typical value for the canonical pulsar population.

5.3.4 Summary

We are, however, not yet satisfied with the quality of the total fit, since it is obvious that the radio data are not fitted very well. This is also the case for an alternative nebular field which is initially larger, and falls exponentially to the present-day assumed value of $B_{\rm n}(T) = 6\mu$G. We wanted to study the effect of relaxing the initial spin period P_0 and age T (keeping them free), and include extra components in the injection spectrum, to see if we could obtain better quality fits for the spectral energy distribution (SED) of G0.9+0.1. However, a similar recent study has been performed (Zhang et al., 2008), based on the model discussed in this section, where a two-component injection spectrum has been applied (with particles coming from the pulsar magnetosphere plus shock acceleration). This updated model has been applied to the Crab Nebula, MSH 15-52, and HESS J1825-137. It is therefore still possible to apply the newer model to G0.9+0.1 to obtain better constraints on its PWN parameters.

5.4 Contributions from Nearby Pulsars to the Local Cosmic Ray Electron Spectrum

This paper has been included in Section B.1 of Appendix B. We were interested in considering whether nearby pulsars could make non-negligible contributions to the local interstellar electron spectrum (LIS). We considered the nearby PSR J0437-4715 as an example of an old MSP with unscreened PC, and Geminga as an example of a canonical pulsar with a screened PC.

The old age of PSR J0437-4715 justifies a steady-state evaluation of the contribution from this pulsar to the LIS. We calculated the electron spectrum (see Figure B.1) at the light cylinder in the framework of the unscreened General Relativistic PC model described in Chapter 2, and used this as an injection spectrum in a steady-state diffusion model (Section B.1.3). The diffusion model was solved using a Green's function (Eq. [B.12] and [B.16]), from which the cosmic ray electron density was calculated numerically. From Figure B.2, it is apparent that the expected flux of cosmic ray electrons from this pulsar is way below the observed flux, and *PSR J0437-4715 is therefore not expected to make a significant contribution to the LIS.*

We next considered the younger Geminga pulsar, for which a steady-state diffusion approach is no longer justified, and we used an impulsive injection model. We calculated the electron injection spectrum using a similar framework than for G0.9+0.1 (Section 5.3.2). We furthermore introduced a multiplicity factor M' describing the enhancement of the number of electrons in a screened pulsar magnetosphere due to pair production. Time-dependent diffusion of the emerging cosmic ray elec-

trons were performed (Section B.1.4) using a different Green's function (Eq. [B.28]). Figures B.4 through B.6 indicate that, *depending on the magnitude of the diffusion coefficient, Geminga might contribute between a fraction of a percent and almost 100% of the locally observed cosmic ray electron flux below 1 TeV.*

5.5 Constraints on the Lepton Content of PWN from the Local Cosmic Ray Positron Spectrum

This paper has been included in Section B.2 of Appendix B. In this paper, *we studied the two middle-aged pulsars Geminga and B0656+14 as sources of leptonic cosmic rays.* The winds of these pulsars had most probably powered PWN that broke up less than about 100 kyr after the birth of these pulsars. Assuming that leptonic particles accelerated by the pulsars were confined in the PWN and were released into the interstellar medium on breakup of the PWN, we calculated the contribution of these particles to the locally observed cosmic ray electron and positron spectra. As mentioned in Section 1.4, lepton SR and IC losses are very high, so that measuring high-energy leptons will imply that they come from nearby sources. Furthermore, at high energies (above a few GeV), positrons and electrons are not expected to be modulated by the solar wind, so that transport calculations are simplified. Also, since the positron component of the LIS is about 10% of that of the electron component at these energies, one should expect to find better constraints on pulsar parameters using positron spectra data.

We used a framework similar to that described in Sections 5.4 and B.1, and calculated the positron injection spectrum coming from the screened magnetospheres of Geminga and B0656+14. The diffusion equation was once again solved using a Green's function (Eq. [B.45]). Upon comparison with the positron LIS in Figure B.8, *we saw that Geminga's birth period* $P_0 > 35$ *ms.* In the framework of the model, $P_0 k_0$*-space may be constrained,* with k_0 the normalisation of the diffusion coefficient (Figure B.9). *We found that birth periods* $P_0 <\approx 20$ *ms may be excluded,* as these imply too high lepton numbers in the PWN. *Assuming that each pulsar contributes 50% to the cosmic ray positron flux, we excluded some range of* $P_0 k_0$*-space, which may roughly be summarised as* $k_0 \gtrsim 0.001 P_0^{-1.7}$ *for Geminga, and* $k_0 \gtrsim 0.004 P^{-1.9}$ *for B0656+14.* Lastly, we noted that since both pulsars are located at almost the same position in the sky, we expected an anisotropy in the local cosmic ray positron flux.

5.6 A Cosmic Ray Positron Anisotropy due to Two Middle-Aged, Nearby Pulsars?

This paper has been included in Section B.3 of Appendix B. As mentioned in Section 5.5, the cosmic ray positron component of the LIS is about 10% of that of the electron component above a few GeV. One should therefore expect to find better constraints on pulsar parameters as sources of leptonic cosmic rays when using positron data, rather than electron data.

Within this context of nearby pulsars producing relativistic leptons which may contribute to the locally measured cosmic-ray spectra, we noted that Geminga and B0656+14 are the closest pulsars with characteristic ages in the range of 100 kyr to 1 Myr, and that the winds of these pulsars had most probably powered PWN that broke up less than about 100 kyr after the birth of the pulsars. By assuming that leptonic particles accelerated by the pulsars were confined in the PWN and were released into the interstellar medium on breakup of the PWN, we were able to show that, *depending on the pulsar parameters, both pulsars make a non-negligible contribution to the local cosmic ray positron spectrum.* Indeed, these two pulsars may be the main contributors above several GeV. *The relatively small angular distance between Geminga and B0656+14 thus implies an anisotropy in the local cosmic ray positron flux at these energies.*

As in Section 5.5, we calculated the positron injection spectra, this time using a time-dependent σ-parameter and nebular field. As before, the diffusion equation was solved, and the energy-dependent anisotropy δ in the cosmic-ray flux was calculated (Eq. [B.66]). This anisotropy formally reduced to the energy-independent value when $E \rightarrow 0$. Figures B.10 and B.11 indicate that one can expect a non-negligible cosmic ray positron component in the LIS from nearby pulsars that may become dominant above several GeV. In the context of our model, we were furthermore able to constrain the permissible pulsar birth period P_0, depending on the magnitude of the interstellar diffusion coefficient k_0, as noted in Section 5.5. *Also, for B0656+14, in the absence of a background flux, we found a predicted anisotropy in the positron LIS of up to almost 3%, significantly larger than the expected value of $\approx$0.25% for Geminga. Conversely, a measured anisotropy larger than the $\approx$3% we obtained for B0656+14 would be an indication of the existence of an even younger, nearby source, e.g. a longer lifetime T of the PWN.* As the predicted flux from PSR B0656+14 appears to overpredict the observed flux above 10 GeV, more severe constraints on this pulsar's output is implied, whereas Geminga's parameters are not that severely constrained by cosmic ray positron observations.

We lastly remarked that cosmic ray electrons and positrons at 1 GeV at earth may exhibit a heliospheric anisotropy of up to a few percent, assuming that they enter the heliosphere isotropically

(Potgieter & Langner, 2004). However, the anisotropy that we have predicted in Buesching et al. (2008a) is the largest above 10 GeV, an energy range at which only the *PAMELA* mission (Boezio et al., 2004) may be able to gather sufficient statistics to find an anisotropy of the predicted magnitude.

5.7 Conclusion

In this chapter, we discussed results involving relativistic particles escaping from the magnetospheres of pulsars. In Section 5.2, we calculated the unpulsed ICS and SR fluxes due to particles escaping from an ensemble of MSPs in a GC, which is complementary to the calculation of pulsed curvature radiation expected from the GC 47 Tucanae (Section 4.5). We found that the SR component occurs in the optical / X-ray waveband, and the ICS, consisting of a starlight and CMBR component, in the gamma-ray waveband. The ICS flux will probably not be visible for *H.E.S.S.*, while telescopes such as *Chandra* and *Hubble* may find it difficult to test the SR component prediction of diffuse radiation when there are many unresolved sources in the field of view. We noted that upper limits may however be derived for the SR component.

In Section 5.3, we went on to model the Galactic Centre composite SNR G0.9+0.1. Using multi-wavelength data, we found an optimum fit of initial spin-down luminosity $L_0 \sim 2.5 \times 10^{38}$ ergs/s and a spectral break energy of $E_b \sim 8 \times 10^{-3}$ ergs, with the predicted X-ray and gamma-ray fluxes corresponding quite well to the observed values. A value of present-day spin-down power of $L(T) \sim 7.4 \times 10^{36}$ ergs/s was obtained, which agrees within $\sim 50\%$ with the inferred value of $L(T) \sim 1.5 \times 10^{37}$ ergs/s from *BeppoSAX* observations. Lastly, a typical PC magnetic field strength of $B_{PC} \sim 5 \times 10^{12}$ G was inferred. We noted that it is possible to apply a newer model (Zhang et al., 2008) to G0.9+0.1 to obtain better constraints on its PWN parameters.

In Section 5.4 through 5.6, we summarised results from ongoing collaborative research on the contribution of nearby pulsars to the local interstellar cosmic ray lepton spectrum. Relevant papers on this subject are included in Appendix B. Our conclusions were the following:

1. The MSP PSR J0437-4715 is not expected to make a significant contribution to the LIS.

2. Depending on the magnitude of the diffusion coefficient, Geminga might contribute between a fraction of a percent and almost 100% of the locally observed cosmic ray electron flux below 1 TeV.

3. We obtained a constraint on Geminga's birth period ($P_0 > 35$ ms).

4. We obtained constraints on $P_0 k_0$-space for Geminga and B0656+14.

5. We showed that, depending on the pulsar parameters, both Geminga and B0656+14 make a non-negligible contribution to the local cosmic ray positron spectrum.

6. For B0656+14, in the absence of a background flux, we found a predicted anisotropy in the positron LIS of up to almost 3%, significantly larger than the expected value of $\approx$0.25% for Geminga. Conversely, a measured anisotropy larger than the $\approx$3% we obtained for B0656+14 would be an indication of the existence of an even younger, nearby source, e.g. a longer lifetime T of the PWN.

7. Our predicted anisotropy is the largest above 10 GeV, an energy range at which only the *PAMELA* mission (Boezio et al., 2004) may be able to gather sufficient statistics to find an anisotropy of the predicted magnitude.

Chapter 6

Model Refinements

In this chapter, we briefly discuss some model refinements that may be taken into account in future studies, such as including a theta-component in the accelerating E-field (Section 6.1), and performing Lorentz transformations to account for the effects of aberration (Section 6.2). We lastly propose a way in which to parametrise the electric potential and charge density, and use data to constrain these fundamental quantities (Section 6.3). A summary is given in Section 6.4.

6.1 Including a Theta-component in the Accelerating E-field

Consider the electric potential in the GR frame-dragging pulsar model derived by Muslimov & Tsygan (1992); Harding & Muslimov (1998) for the distant case (Eq. [2.116] in Section 2.4.3), for an unscreened polar cap (PC):

$$\Phi = \frac{1}{2}\Phi_0 \left(\zeta_0 \Theta_0\right)^2 \left\{ \kappa \left(1 - \frac{1}{\eta^3}\right) \cos\chi \; + \frac{3}{4} \left[\zeta(\eta)\Theta(\eta)H(\eta) - \zeta_0\Theta_0 H(1)\right] \xi \sin\chi \cos\phi \right\} \left(1 - \xi^2\right). \quad (6.1)$$

As noted before, the radial component of the electric field is given by

$$\begin{aligned} E_r &\equiv -\frac{\partial \Phi}{\partial r} && (6.2)\\ &= -\frac{\partial \Phi}{\partial \eta}\frac{d\eta}{dr} && (6.3)\\ &= -E_0 \left(\zeta_0 \Theta_0\right)^2 \left\{ \frac{3}{2}\frac{\kappa}{\eta^4} \cos\chi + \frac{3}{8}\Theta(\eta)H(\eta)\delta(\eta)\xi \sin\chi\cos\phi \right\} \left(1 - \xi^2\right), && (6.4) \end{aligned}$$

with $E_0 \equiv \Phi_0 / R$. In Section 2.4.3, we assumed that $E_{||} \approx E_r$. This is true for low altitudes and small polar angles. However, in the case of millisecond pulsars (MSPs), this approximation breaks down as both $\eta / R_{\rm LC}$ and $\xi\Theta(\eta)$ increase. It is then necessary to also take into account the ϑ-component of the

E-field, which is calculated using

$$E_\vartheta \equiv -\frac{1}{r}\frac{\partial \Phi}{\partial \vartheta} \tag{6.5}$$

$$= -\frac{1}{\eta R}\frac{\partial \Phi}{\partial \xi}\frac{d\xi}{d\vartheta} \tag{6.6}$$

$$= -E_0\left(\zeta_0\Theta_0\right)^2\frac{1}{\Theta(\eta)\eta}\left\{-\kappa\left(1-\frac{1}{\eta^3}\right)\xi\cos\chi + \frac{3}{8}\left[\Theta(\eta)H(\eta)-\Theta_0 H(1)\right]\left(1-3\xi^2\right)\sin\chi\cos\phi\right\}. \tag{6.7}$$

The parallel component of the electric field can now be calculated by observing that

$$E_{||} = \frac{\mathbf{E}\cdot\mathbf{B}}{|\mathbf{B}|} = \frac{E_r B_r + E_\vartheta B_\vartheta}{\sqrt{B_r^2 + B_\vartheta^2}}, \tag{6.8}$$

with

$$B_r = B_0\frac{f(\eta)}{f(1)}\frac{1}{\eta^3}\cos\vartheta \tag{6.9}$$

$$B_\vartheta = \frac{1}{2}B_0\alpha\left[-2\frac{f(\eta)}{f(1)} + \frac{3}{f(1)(1-\epsilon/\eta)}\right]\frac{1}{\eta^3}\sin\vartheta \tag{6.10}$$

as in Muslimov & Tsygan (1992); Muslimov & Harding (1997), and Section 2.3.3.

Figure 6.1 indicates contour plots of $-E_{||}$ in cgs units vs. scaled polar angle ξ (zero at the centre, unity at the rim) and magnetic azimuthal angle ϕ (changing from 0° to 360°). The left column is for $E_\vartheta = 0$, while the right column is for $E_\vartheta \neq 0$. The colour scale is the same for all eight panels of the figure. The scaled radial coordinate η for each row is $\eta = 1.1$, 1.4, 1.7, 2.0 from top to bottom. While a full study of the effect of implementing $E_\vartheta \neq 0$ in the model is beyond the scope of this section, we note the following:

1. We observe that $E_{||}$ is a maximum at the magnetic axis $\xi = 0$, as $E_{||} \approx E_r \propto (1-\xi^2)$ at low altitudes. We furthermore clearly observe the decrease of $E_{||}$ with η, since E_r scales with η^{-4} at low altitudes (Figure 6.1).

2. When $E_\vartheta = 0$ (left column of Figure 6.1), $-E_{||} > 0$ for the first three panels ($\eta = 1.1$, 1.4, 1.7) and only develops a different sign at some regions of the PC for $\eta \gtrsim 2$ (this negative field has only a small magnitude). However, when setting $E_\vartheta \neq 0$, an annulus develops (right column of Figure 6.1) close to the stellar surface with a different sign of $E_{||}$ at the rim ($-E_{||} < 0$ when $\xi \sim 1$) than at the magnetic axis ($-E_{||} > 0$ when $\xi \sim 0$). *It should be considered in future whether this new feature may help to solve the return current problem.*

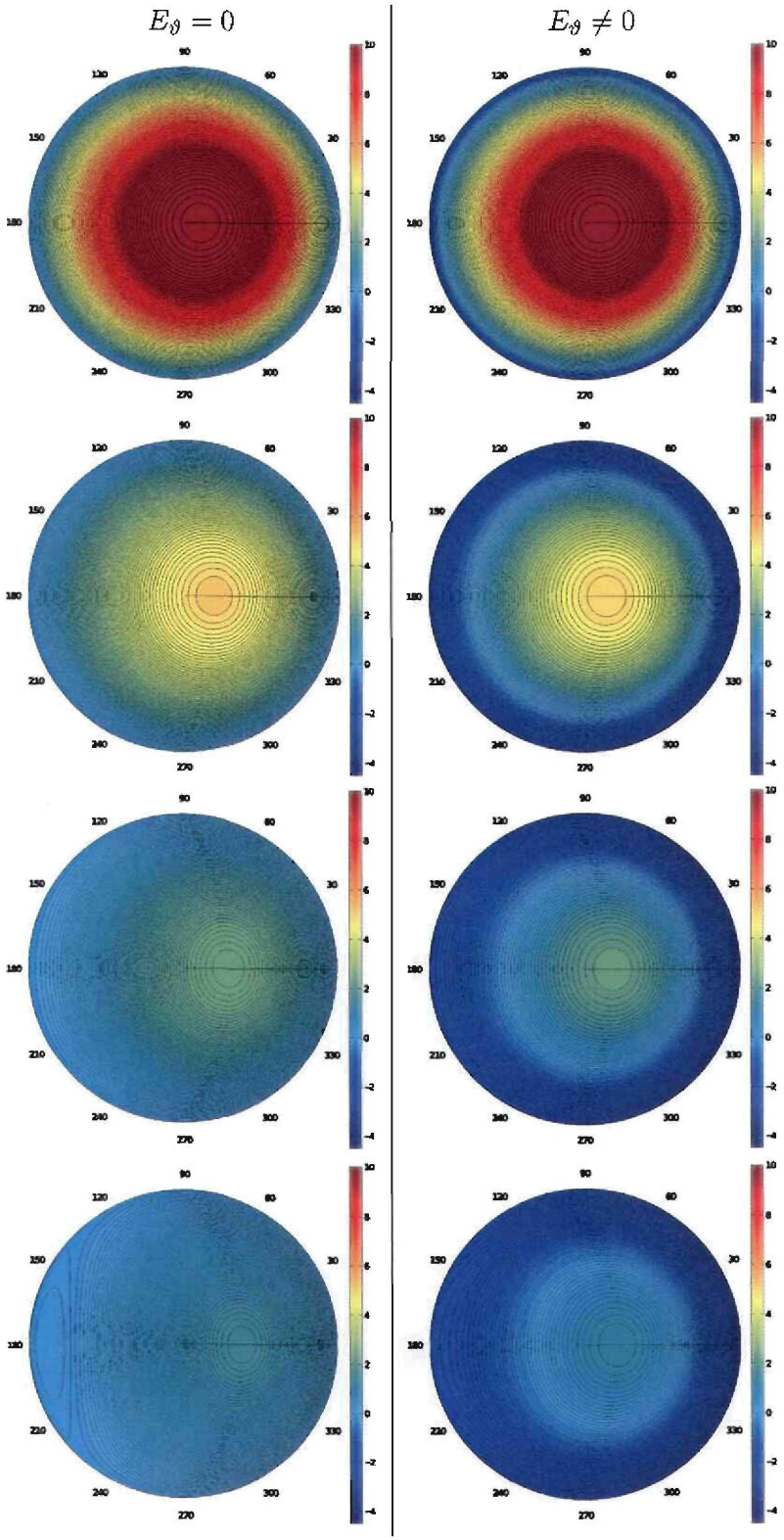

Figure 6.1: Contour graphs of the parallel E-field $-E_{||}$ in cgs units vs. ξ and ϕ, for different radial heights η above the PC. The left column is for $E_\vartheta = 0$ ($E_{||} = E_\tau$), while the right column is for $E_\vartheta \neq 0$. The colour scale is the same for all eight panels (to be multiplied by 10^4). The scaled radial coordinate η for each row is $\eta = 1.1, 1.4, 1.7, 2.0$ from top to bottom. We used the parameters of PSR J0437-4715, as well as $M = 1.4M_\odot$, $R = 10^6$ cm, $I = 0.4MR^2$, and $\chi = 35°$ when computing these graphs.

3. Also, this new E-field's impact on particle oscillation above the PC should be investigated (in combination with the derivation of $E_{||}$ valid for higher altitudes – Section 2.4.6).

6.2 Implementing the Lorentz Transformation Using Spherical Trigonometry

Consider the corotating frame with the magnetic moment $\vec{\mu}$ of a dipolar magnetic field directed along the z-axis:

$$\vec{\mu} = (0,\, 0,\, \mu). \tag{6.11}$$

The magnetic azimuthal angle ϕ is defined zero in the direction of the angular velocity vector $\mathbf{\Omega}$, and the magnetic axis is at an inclination of χ with respect to $\mathbf{\Omega}$. The magnetic colatitude ϑ is measured with respect to $\vec{\mu}$. The position vector is then given by

$$\mathbf{r} = (r\sin\vartheta\cos\phi,\, r\sin\vartheta\sin\phi,\, r\cos\vartheta). \tag{6.12}$$

The angular velocity vector is

$$\mathbf{\Omega} = (\Omega\sin\chi,\, 0,\, \Omega\cos\chi), \tag{6.13}$$

implying a normalised corotation velocity of

$$\vec{\beta}_{\rm cor} = \frac{\mathbf{\Omega}\times\mathbf{r}}{c} \tag{6.14}$$

$$= \frac{\Omega r}{c}(-\sin\vartheta\sin\phi\cos\chi,\, \sin\vartheta\cos\phi\cos\chi - \cos\vartheta\sin\chi,\, \sin\vartheta\sin\phi\sin\chi). \tag{6.15}$$

One may therefore choose the axes so that the corotation speed is

$$|\vec{\beta}_{\rm cor}| = \frac{\Omega r}{c}\sqrt{1-\cos^2\vartheta\cos^2\chi - \sin^2\vartheta\cos^2\phi\sin^2\chi - \frac{1}{2}\sin 2\chi\sin 2\vartheta\cos\phi}, \tag{6.16}$$

which reduces to

$$|\vec{\beta}_{\rm cor}| = \frac{\Omega r}{c}\sin\vartheta \tag{6.17}$$

when $\chi = 0$. As usual, the corotation Lorentz factor may be calculated by

$$\gamma_{\rm cor} = \frac{1}{\sqrt{1-\beta_{\rm cor}^2}}. \tag{6.18}$$

Assuming that the electrons radiate in a direction tangential to the magnetic field line, one may straightforwardly calculate the beam half angle ρ. In the case of a classical dipolar magnetic field for which $r = k_m \sin^2\vartheta$ is valid along a field line designated by a constant k_m, the following relation may be obtained (by calculating the derivative dy/dx):

$$\rho_{\rm classic} = \cos^{-1}\left\{\frac{3\cos^2\vartheta - 1}{\sqrt{3\cos^2\vartheta + 1}}\right\}. \tag{6.19}$$

Since the emission height above the stellar surface is much smaller than the distance of the pulsar from earth ($h \ll d$), one may use the approximation of "parallel emission rays" and transport the unit emission direction vector in the corotating frame ($\hat{\mathbf{k}}'$) from the actual emission point to the origin. It is then clear that

$$\hat{\mathbf{k}}' = (\sin\rho\cos\phi,\ \sin\rho\sin\phi,\ \cos\rho). \tag{6.20}$$

This vector $\hat{\mathbf{k}}'$ is inclined by an angle ζ' with respect to the rotation axis $\mathbf{\Omega}$, which implies that

$$\zeta' = \cos^{-1}\left\{\frac{\mathbf{\Omega}\cdot\hat{\mathbf{k}}'}{|\mathbf{\Omega}|}\right\}. \tag{6.21}$$

The emission direction in the corotating frame is aberrated to a 'new' direction $\hat{\mathbf{k}}$, (towards the inertial observer), inclined at an angle ζ with respect to $\mathbf{\Omega}$. The aberration formula is (Dyks et al., 2004c):

$$\hat{\mathbf{k}} = \frac{\hat{\mathbf{k}}' + \left[\gamma_{\rm cor} + (\gamma_{\rm cor} - 1)\left(\vec{\beta}_{\rm cor}\cdot\hat{\mathbf{k}}'\right)/|\vec{\beta}_{\rm cor}|^2\right]\vec{\beta}_{\rm cor}}{\gamma_{\rm cor}\left(1 + \vec{\beta}_{\rm cor}\cdot\hat{\mathbf{k}}'\right)}. \tag{6.22}$$

For low altitudes, it may be shown (Dyks et al., 2004c) that Eq. (6.22) reduces to

$$\hat{\mathbf{k}} \approx \hat{\mathbf{k}}' + \vec{\beta}_{\rm cor}. \tag{6.23}$$

Similar to Eq. (6.21), the inclination angle of the aberrated direction of emission with respect to $\mathbf{\Omega}$ is

$$\zeta = \cos^{-1}\left\{\frac{\mathbf{\Omega}\cdot\hat{\mathbf{k}}}{|\mathbf{\Omega}|}\right\}. \tag{6.24}$$

The aberration angle is

$$\eta_{\rm ab} = \cos^{-1}\left\{\hat{\mathbf{k}}'\cdot\hat{\mathbf{k}}\right\} \tag{6.25}$$

(with $\eta_{\rm ab} \approx \beta_{\rm cor}$ at low altitudes) and the new (aberrated) beam half angle is then

$$\rho_{\rm ab} = \cos^{-1}\left\{\frac{\vec{\mu}\cdot\hat{\mathbf{k}}}{|\vec{\mu}|}\right\}. \tag{6.26}$$

One may next calculate a new phase angle due to aberration by using spherical trigonometry (using a sphere of unit radius, since we are dealing with unit wave vectors $\hat{\mathbf{k}}'$ and $\hat{\mathbf{k}}$). By carefully considering different cases representing different values of r and ϕ, we obtain the following aberration phase angle which is valid for $0 \leq \phi \leq \pi$:

$$\phi_{\rm ab} = \cos^{-1}\left\{\frac{\cos\eta_{\rm ab} - \cos\zeta\cos\zeta'}{\sin\zeta\sin\zeta'}\right\}. \tag{6.27}$$

The "old" phase angle ϕ_L is calculated by

$$\phi_L = \sin^{-1}\left\{\frac{\sin\rho\sin\phi}{\sin\zeta'}\right\}. \tag{6.28}$$

The "new" (aberrated) phase is then

$$\phi_L^N = \phi_{\rm ab} - \phi_L, \quad 0 \leq \phi \leq \pi. \tag{6.29}$$

This angle is defined zero at the midpoint, i.e. the scale goes from $-\pi$ to π, but this may easily be rescaled if necessary. For $\pi < \phi < 2\pi$, one needs

$$\phi_1 = \cos^{-1}\left\{\frac{\cos\rho - \cos\chi\cos\zeta'}{\sin\chi\sin\zeta'}\right\} \tag{6.30}$$

to give

$$\phi_L^N = \phi_{\rm ab} + \phi_1, \quad \pi < \phi < 2\pi. \tag{6.31}$$

In order to test these results, one may compare these results with those of Dyks et al. (2004c) approximation for low altitudes:

$$\phi_{\rm ab}^{\rm approx} = \frac{\eta_{\rm ab}}{\sin\zeta} \approx \frac{|\vec{\beta}_{\rm cor}|}{\sin\zeta} \approx \frac{\Omega r}{c}, \quad r \ll R_{\rm LC}. \tag{6.32}$$

We find that the correspondence is quite good, except for regions in (r,ϕ)-space where $\zeta \to 0$ and so $\phi_{\rm ab}^{\rm approx} \to \infty$. The approximation also breaks down for large values of r as expected.

6.3 Parametrization of Φ and ρ

As mentioned in Chapter 7, the GR frame-dragging model overpredicts the pulsed integral flux at $\sim$ 1 GeV, violating the *EGRET* upper limits. Also, the predicted cut-off energy is typically of the order of a few tens of GeV for MSPs, and it is evident that this is very sensitive to geometry and individual pulsar parameters. With these model weaknesses in mind, it therefore seems a good idea to retract and use a first-order model to derive constraints on the magnetospheric charge density ρ and potential Φ (although we expect that $\rho \approx \rho_{\rm GJ}$) using experimental data. The value of such a future study is that it may give constraints on the order of magnitude of these very fundamental quantities which should be present in any (future) PC model. We are not concerned about these quantities' detailed functional dependence upon (r, ϕ, ϑ). That is why we choose an exponential decay for the E-field, and only use a simple expression for ρ at the stellar surface (no angular dependencies, only radial). We also include two parameters ϵ_1 and ϵ_2 which allow us to scale the magnitudes of Φ and ρ.

In order to choose sensible expressions for ρ and Φ, we look to some theoretical results used over the years. First, the solution of Deutsch (1955) for the radial component of the E-field outside a perfectly conducting, sharply bounded spherical star rotating rigidly in vacuum, for the region well inside the light-cylinder radius ($r \ll c/\Omega$), is given by (in MKS units):

$$E_r = -\frac{\Omega\mu_0 R R_1(R)}{4\eta^4}\left[\cos\chi\,(3\cos 2\vartheta + 1) + 3\sin\chi\sin 2\vartheta\cos\lambda\right], \tag{6.33}$$

with $\eta = r/R$ the scaled radial coordinate, and R the stellar radius. It is clear from e.g. Deutsch's expression for the energy loss rate due to dipole radiation (MKS units),

$$\frac{dW}{dt} = -\frac{2\pi\Omega^4\mu_0}{3c^3}R^6 R_1^2(R)\sin^2\chi, \tag{6.34}$$

that we should take $R_1(R) = H = B_0/\mu_0$ to conform with common practice of setting the spin-down luminosity equal to dipole radiation losses (in cgs units)

$$\dot{E}_{\rm rot} = -\frac{B_0^2\Omega^4 R^6}{6c^3}\sin^2\chi, \tag{6.35}$$

where B_0 is the magnetic field at the pole. Rewriting in terms of the scaled radial coordinate $\eta = r/R$ and converting to cgs units ($\mu_0 \to 4\pi/c^2$, and $B \to B/c$), the radial E-field becomes

$$E_r = -\left(\frac{\Omega R}{c}\right)\frac{B_0}{4\eta^4}\left[\cos\chi\,(3\cos 2\vartheta + 1) + 3\sin\chi\sin 2\vartheta\cos\lambda\right]. \tag{6.36}$$

To order of magnitude, this becomes (also see Muslimov & Harding (1997))

$$E_{||,D} \sim -\left(\frac{\Omega R}{c}\right)\frac{B_0 \cos\chi}{\eta^4}, \tag{6.37}$$

using the approximation $E_r \approx E_{||}$ when $r \sim R$. Let $\Phi_0 = (\Omega R/c)B_0 R$. Assuming a typical scale length of R, this implies a potential at the stellar surface of roughly

$$\Phi_{\mathrm{D},1} \sim \left(\frac{\Omega R}{c}\right) B_0 R \cos\chi = \Phi_0 \cos\chi. \tag{6.38}$$

However, if one uses a typical scale length of $R_{\mathrm{PC}} = R\sin\Theta_0 \sim R(\Omega R/c)^{1/2}$, one obtains

$$\Phi_{\mathrm{D},2} \sim \left(\frac{\Omega R}{c}\right)^{3/2} B_0 R\cos\chi = \Phi_0\left(\frac{\Omega R}{c}\right)^{1/2}\cos\chi \sim \Phi_0\Theta_0\cos\chi, \tag{6.39}$$

with Θ_0 the PC angle. This potential drop is typically larger than that of Goldreich & Julian (1969), obtained for an aligned rotator ($\chi = 0$) between the pole and PC angle (see Eq. [1.24]):

$$\Phi_{\mathrm{GJ}} = \frac{1}{2}\left(\frac{\Omega R}{c}\right)^2 B_0 R = \frac{1}{2}\Phi_0\left(\frac{\Omega R}{c}\right) \sim \frac{1}{2}\Phi_0\Theta_0^2. \tag{6.40}$$

The latter expression agrees (see Eq. [1.31]) with the result of Sturrock (1971) who solved a one-dimensional Poisson equation and obtained an expression for Φ:

$$\Phi_{\mathrm{S}} = 2\pi j x^2. \tag{6.41}$$

Sturrock assumed $j \approx \rho = \Omega B_0/2\pi c \sim \rho_{\mathrm{GJ}}$ (see Eq. [6.48]). If one sets $x = R_{\mathrm{PC}} \sim R(\Omega R/c)^{1/2}$, it follows that

$$\Phi_{\mathrm{S}} = \left(\frac{\Omega R}{c}\right)^2 B_0 R = 2\Phi_{\mathrm{GJ}}. \tag{6.42}$$

(One may even obtain equality of Φ_{GJ} and Φ_{S} by setting $x = R_{\mathrm{PC}}/\sqrt{2}$). In the GR frame-dragging regime (Harding & Muslimov, 1998), the unscreened electric field rises from zero to a value of (ignoring the oscillating term for the moment, see Eq. [2.117])

$$E_{||} \sim -\frac{3}{2}\frac{\Phi_0}{R}\Theta_0^2\frac{\kappa}{\eta^4}\cos\chi \tag{6.43}$$

near the PC ($\eta \sim 1.1$). This corresponds to a potential of (Harding & Muslimov (1998), see Eq. [2.116])

$$\Phi_{\rm HM} \sim \Phi_{\rm GJ}\kappa\cos\chi\left(1-\frac{1}{\eta^3}\right). \tag{6.44}$$

The charge density applicable for this case is (see Eq. [2.115])

$$\rho_{\rm HM} \sim -\frac{\Omega B_0}{2\pi c\alpha\eta^3}(1-\kappa)\cos\chi. \tag{6.45}$$

Close to the stellar surface, this becomes

$$\rho_{\rm HM} \sim -\frac{\Omega B_0}{2\pi c\sqrt{1-\epsilon}}(1-\kappa)\cos\chi. \tag{6.46}$$

For typical MSP parameters, $\kappa = \epsilon I/MR^2 \sim 0.15$ and $\epsilon = 2GM/c^2R \sim 0.5$, so that $(1-\kappa)/(1-\epsilon)^{1/2} \sim 1$. This leads to

$$\rho_{\rm HM} \sim \rho_{\rm GJ}\cos\chi, \tag{6.47}$$

with

$$\rho_{\rm GJ} = -\frac{\mathbf{\Omega}\cdot\mathbf{B_0}}{2\pi c}\left(\frac{1}{1-(\Omega r/c)^2\sin^2\vartheta}\right) \sim -\frac{\Omega B_0}{2\pi c} \tag{6.48}$$

the well-known Goldreich-Julian charge density.

We are interested in the acceleration of electron primaries coming from the stellar surface and producing curvature radiation as they move along the magnetic field lines. It is useful to suppose that electrons will be coming from the centre of one PC, and that ions from the the rim, or vice versa, to maintain charge neutrality. It seems reasonable to propose the following expressions for $E_{||}$ and ρ (also see Bulik et al., 2000) for the PC region releasing the electron primaries:

$$E_{r,p} = -\frac{\epsilon_1\Phi_{\rm GJ}\cos\chi}{R}\exp(-\eta) \tag{6.49}$$

$$\rho_p(R) = -\frac{\epsilon_2\Omega B_0}{2\pi c}\cos\chi \sim \epsilon_2\rho_{\rm GJ}\cos\chi. \tag{6.50}$$

This implies a potential of

$$\Phi_p(r) = \epsilon_1\Phi_{\rm GJ}\cos\chi\,[\exp(-1)-\exp(-\eta)] \tag{6.51}$$

when the boundary condition $\Phi_p(R) = 0$ is used. For this potential, it follows that $E_\vartheta = E_\phi = 0$, since it is only a function of r and other pulsar parameters. Using the GR magnetic field (see Section 2.3.3

and Section 6.1), the E-field parallel to the B-field may then be calculated using

$$E_{||,p} = \frac{E_{r,p}B_r}{|\mathbf{B}|}. \tag{6.52}$$

One procedure might be to model the total output of pulsed gamma rays due to a population of MSPs in 47 Tucanae (using $E_{||,p}$ and ρ_p in the MSP model), and use experimental upper limits for this object to constrain the magnitudes of $E_{||,p}$ and ρ_p at the stellar surface (i.e constraining the average values of ϵ_1 and ϵ_2 for the population). The aim is to present a plot of ϵ_1 vs. ϵ_2 and exclude regions violating experimental data.

It should also be clear that the gamma-ray efficiency already produces a constraint on the permissible values of ϵ_1 and ϵ_2, in addition to the constraints to be obtained from data. From Eq. (6.50), one can estimate the current leaving one PC (it is customary to set the maximal value of magnetic dipole radiation L_{md} (when the magnetic inclination angle $\chi = \pi/2$) equal to $\dot{E}'_{\rm rot} = I\Omega\dot{\Omega}$ when obtaining a value for B_0)

$$I_p \sim c\rho_p A_{\rm PC} = \epsilon_2 \cos\chi \sqrt{\frac{3c}{2}\dot{E}'_{\rm rot}}. \tag{6.53}$$

Similarly, the potential may be written as

$$\Phi_p(r) = \epsilon_1 \cos\chi \left[\exp(-1) - \exp(-\eta)\right] \sqrt{\frac{3}{2c}\dot{E}'_{\rm rot}}. \tag{6.54}$$

It follows that (for $\eta \to \infty$)

$$L_\gamma \sim \Phi_p I_p = \frac{3\epsilon_1\epsilon_2}{2\exp(-1)} \cos^2\chi \dot{E}'_{\rm rot} = \eta_\gamma I\Omega\dot{\Omega}, \tag{6.55}$$

giving the constraint (using the definition of $\dot{E}'_{\rm rot} = I\Omega\dot{\Omega}$)

$$\eta_\gamma \approx \frac{3\epsilon_1\epsilon_2\cos^2\chi}{2\exp(-1)} \approx 4\epsilon_1\epsilon_2\cos^2\chi. \tag{6.56}$$

Reference	Potential	Charge density
Deutsch (1955)	$\Phi_{\rm D,1} \sim \Phi_0 \cos\chi, \quad \Phi_0 \equiv (\Omega R/c)B_0R$	–
Deutsch (1955)	$\Phi_{\rm D,2} \sim \Phi_0\Theta_0\cos\chi$	–
Goldreich & Julian (1969)	$\Phi_{\rm GJ} \sim \Phi_0\Theta_0^2/2$	$\rho_{\rm GJ} \sim -\Omega B_0/2\pi c$
Sturrock (1971)	$\Phi_{\rm S} = 2\pi j x^2 \sim \Phi_{\rm GJ}$	$\rho_{\rm S} \sim \rho_{\rm GJ}$
Harding & Muslimov (1998)	$\Phi_{\rm HM} \sim \Phi_{\rm GJ}\kappa\cos\chi(1-\eta^{-3})$	$\rho_{\rm HM} \sim \rho_{\rm GJ}\cos\chi$
Section 6.3	$\Phi_p(r) = \epsilon_1\Phi_{\rm GJ}\cos\chi[\exp(-1) - \exp(-\eta)]$	$\rho_p(R) \sim \epsilon_2\rho_{\rm GJ}\cos\chi$

Table 6.1: Comparison of different expressions for the potential and charge density in PC models.

(Generally, one should replace the $\cos^2\chi$ factor in the right hand side by a factor $\cot^2\chi$ when using an arbitrary χ in the expression of $\dot{E}_{\rm rot}$ for dipole radiation and obtaining B_0 from the latter expression).

Probably the best way to implement the approach outlined in this section is to apply this to an MSP population study as follows. Assuming that *GLAST* will discover many new gamma-ray MSPs, it will be possible to stack data from different MSPs. Although the noise resulting from the stacking procedure will be much greater than for a population of MSPs in a globular cluster (GC), there are two advantages: the number of MSPs N in this 'population' is known (with the noise scaling as $N^{-1/2}$), as well their individual spin-down powers. This is not the case for an ensemble of MSPs in a GC, where intrinsic $\dot{P}$-values have to be obtained, and N is a free parameter, or at least not accurately known (see Section 4.5). Also, the distances are known, so that the brightest pulsars may be selected for this new population using $\dot{E}_{\rm rot}/d^2$, improving statistics. Next, one may model the cumulative flux expected for this population with known values of N, P_i, and $\dot{P}_i$, for $i = 1, \cdots, N$:

$$F_{\rm cum}^{\rm slice}(>E) = \sum_{i=1}^{N} F_i^{\rm slice}(>E), \tag{6.57}$$

using the parametrised values of $E_{||,p}$ and ρ_p obtained above. In this way, it may be possible to constrain $\epsilon_1\epsilon_2$-space, giving order of magnitude values for these fundamental pulsar quantities (averaged over the population). The problem of geometry is thus sidestepped, as an average beaming factor Λ is implicitly obtained using Monte Carlo sampling over χ and observer angle ζ. This procedure may be pursued as a guest investigator program for *GLAST*.

6.4 Summary

We noted in Section 6.1 that the behaviour of $E_{||}$ is quite different for the cases when $E_\vartheta = 0$ and $E_\vartheta \neq 0$. In the latter case, an annulus develops close to the stellar surface with a different sign of $E_{||}$ at the rim $\xi \sim 1$ than at the magnetic axis $\xi \sim 0$. It should be considered in future whether this feature may help to solve the return current problem. Also, the new E-field's impact on particle oscillation above the PC should be investigated. As η increases, the E_ϑ-component becomes increasingly more important, as the B-lines significantly deviate from the radial direction. The behaviour of $E_{||}$ therefore differs significantly from that of E_r at high altitudes. One should in future try and solve the Maxwell equations without the small angle approximation if the results will be applied to MSPs.

Section 6.2 described a general implementation of the Lorentz transformation which should in future be implemented when e.g. calculating pulse profiles of MSPs.

Lastly, Section 6.3 described one way of implementing a parametrised unscreened electric potential and charge density, so that these quantities may be constrained using data. This is probably the closest one can come to deriving constraints on fundamental pulsar quantities in a (nearly) model-independent manner, sidestepping the problem of unknown (inaccurately known) geometry which attends single MSPs, and on which the model output sensitively depends. We noted that a procedure involving data stacking of MSPs discovered by *GLAST* may be pursued as a guest investigator program for *GLAST*.

Chapter 7

Conclusion

In their book on pulsars, Manchester & Taylor (1977) wrote the following dedication:

> *"To Jocelyn Bell, without whose perceptiveness and persistence we might not yet have had the pleasure of studying pulsars."*

Since the serendipitous discovery of the very first pulsar by Bell and others (Hewish et al., 1968), there has been four decades of avid theoretical study in order to truly understand how pulsars operate. Although much progress has been made, there are still some important open questions. Harding (2007a) mentions that, while pulsar physicists agree on the basic mechanism of rotation-powered pulsars being rotating, magnetised neutron stars, there are many less confirmed assumptions, notably those of the boundary conditions on the charge flow and electric potential. This is true for both the polar cap (PC) and outer gap (OG) pulsar models.

De Angelis et al. (2007) recently pointed out that one clear goal of very high energy (VHE) Astrophysics is to discriminate between different processes of pulsar magnetospheric emission (e.g. PC vs. OG models), and added that no test of these models has been achieved in the range $10 - 100$ GeV yet (also see Thompson, 2004a). The launch of *Gamma-Ray Large Area Space Telescope (GLAST)* in June of 2008, and construction of second phases of successful ground-based Cherenkov gamma-ray telescopes such as the *High Energy Stereoscopic System (H.E.S.S.)* and *Major Atmospheric Gamma-Ray Imaging Cherenkov (MAGIC)*, to be completed in 2008 – 2009, certainly hold the promise of solving this issue, and yielding a vast amount of new data which will enable further progress to be made.

In this thesis, we opted to work with one of the most sophisticated models in the PC category, which includes the effect of General Relativistic (GR) frame dragging, enhancing the predicted accelerating electric field in the pulsar magnetosphere (e.g. Muslimov & Tsygan, 1992; Muslimov & Harding, 1997;

Harding & Muslimov, 1998; Harding et al., 2002b). Our main aim was to test this model in a variety of ways by implementing it in a numerical code and performing various applications, and to constrain the resulting model predictions using multiwavelength and cosmic-ray data. In addition to millisecond pulsars (MSPs), we also modelled pulsar wind nebulae (PWN) as sources of gamma rays and cosmic rays.

As mentioned in Section 1.5, many favourable circumstances provided unique opportunities for deriving MSP and PWN model constraints. These included the availability of a rigorous derivation of a PC GR pulsar model (e.g Muslimov & Harding, 1997; Harding & Muslimov, 1998); membership of the *H.E.S.S.* Collaboration, simplifying a dialogue between theoretical predictions and gamma-ray data; membership of a Flagship project of the *Centre for High Performance Computing (CHPC)* which guaranteed access to a 640-CPU computing facility; availability of analytical and numerical predictions enabling calibration of our model results; the unique unscreened MSP PSR J0437-4715, with several important parameters accurately measured, presenting a unique laboratory where the naked electric potential may be probed without the complicating effect of pair cascades; availability of approximate values of the screened E-field; justified neglect of Special Relativistic effects such as aberration and time-of-flight delays by using phase-averaged results; circumventing the problem of unknown pulsar geometry by using population studies of MSPs; availability of multiwavelength data which allowed us to constrain the injection spectrum break energy and birth spin-down power of the PWN G0.9+0.1; collaboration with cosmic-ray transport experts which facilitated the constraining of pulsar parameters.

7.1 Main Results And Contributions

Our main results were as follows (a detailed discussion of each of these is given in Section 7.2):

1. We succeeded in implementing a fully 3D GR frame-dragging PC MSP model (Chapter 2), sampling non-thermal curvature radiation (CR) gamma-ray emission and relativistic particles from a range of magnetic field lines above the PC, using the framework of Harding, Muslimov, and Tsygan. This model was subsequently used to investigate single MSPs as well as ensembles of MSPs as sources of gamma rays and cosmic rays (Venter & de Jager, 2005a,b; Venter et al., 2005; de Jager & Venter, 2005; Venter & de Jager, 2006, 2008a).

2. We performed detailed numerical modelling of the unscreened and screened MSPs PSR J0437-4715 and PSR B1821-24 (Chapter 3). We found a maximum CR cut-off energy of $1 - 20$ GeV for PSR J0437-4715, depending on the assumed geometry (χ and ζ) and equation of state

(EOS) (Venter & de Jager, 2005a; de Jager & Venter, 2005), in agreement with the findings of similar studies. This is in contrast with earlier studies which predicted PSR J0437-4715's CR cut-off energy to be in the range $50 - 100$ GeV (Harding et al., 2002b; Bulik et al., 2000), making proposals for ground-based telescopes with imaging thresholds near 100 GeV attractive. Thus *GLAST* and 4^{th} generation Cherenkov telescopes are generally needed in order to observe CR emission from unscreened gamma-ray MSPs. For the screened PSR B1821-24, we found CR energies, highly sensitive to the assumed geometry, of up to ~ 150 GeV, compatible with similar predictions. Given the low spectral cut-offs for both pulsars, even the planned *Cherenkov Telescope Array (CTA)* may have a hard time probing the CR tails of the gamma-ray integral fluxes.

3. We found that the 1 GeV *Energetic Gamma-Ray Experiment Telescope (EGRET)* upper limit for PSR J0437-4715 was violated by model predictions (Venter & de Jager, 2005a, Chapter 3), implying that the gamma-ray efficiency $\eta_\gamma^{\text{beam}} \leq 0.55\%$ (although this constraint depends sensitively on the geometrical beaming factor Λ). For the case of PSR B1821-24, we found that $\Lambda \sim 1\ 500$ (indicative of off-beam radiation), corresponding to a value of $\eta_\gamma^{\text{beam}} = 1.6\%$.

4. We studied the behaviour of the basic MSP model for a mesh of $(P, \dot{P}, \chi, \zeta)$-space (Chapter 4). We found that cut-off energies, efficiencies, energy fluxes, and integral fluxes generally decrease with larger P and smaller $\dot{P}$. Also, we found that maxima of the above-mentioned quantities occur for on-beam radiation ($\chi \sim \zeta$). All pulsar properties are thus sensitive functions of the assumed geometry (as well as P and $\dot{P}$), so that accurate knowledge of pulsar geometry is crucial when making predictions regarding MSP visibility. In addition, screening complicates the matter for high-$\dot{E}_{\text{rot}}$ pulsars, where pair-creation leads to suppression of the E-field.

5. Derivation of sensible constraints on gamma-ray efficiencies $\eta_\gamma^{\text{beam}}$ depend sensitively on beaming correction factors $\Lambda = \epsilon\overline{\Delta\Omega}/\beta^{\text{slice}}$. We found that Λ may be significantly larger than unity, and that actual trends may be concealed when Λ is unknown (Chapter 4). We numerically confirmed the theoretical expectation for the gamma-ray luminosity $L_\gamma^{\text{beam}} \approx 0.07\dot{E}_{\text{rot}}$ for MSPs with unscreened PCs.

6. We found that the approximation $L_\gamma^{\text{beam}}(0) = 0.75\kappa(1-\kappa)\dot{E}_{\text{rot}}$ overpredicts L_γ^{beam}, and that better results follow when using the more general expression $L_\gamma^{\text{beam}}(\chi) = L_\gamma^{\text{beam}}(0)[\cos^2\chi + C\sin^2\chi]$. The latter equation may be approximated by $L_\gamma^{\text{beam}}(\chi) = 0.5\kappa(1-\kappa)\dot{E}_{\text{rot}} \approx 0.07\dot{E}_{\text{rot}}$, indicating that $\eta_\gamma^{\text{beam}} \approx 7\%$ for unscreened MSPs in the context of the GR frame-dragging pulsar

model (Chapter 4).

7. Using a population of 59 MSPs with $-2.7 \leq \log_{10}[P] \leq -2.0$ and $-22 \leq \log_{10}[\dot{P}] \leq -19$, we found that roughly half of the population of 59 MSPs are expected to be visible for *GLAST*, with fluxes $\sim 10^{-8}$ cm^{-2}.s^{-1} (Chapter 4).

8. We performed a population study of MSPs in the globular cluster (GC) 47 Tucanae (Chapter 4), and we sampled randomly from this ensemble. We were therefore able to calculate absolute cumulative fluxes expected from the MSP population, without needing to use approximate spectra, or scale up single MSP predictions or single particle spectra. We found that such a population provides the unique opportunity to sidestep the issue of pulsar geometry (which is crucial when modelling a single MSP) by averaging over numerous spectra and geometries, which results in a "geometry-averaged" spectrum with relatively small uncertainty (Venter & de Jager, 2008a). We found good agreement for the average single pulsar efficiencies for electron and gamma-ray production between our results and those of other authors. However, our average pulsed spectrum, including errors, exceeded the *EGRET* upper limit at 1 GeV, constraining the number of visible GC pulsars to $N = 100/3.76 \approx 27$. Generally, setting $N = 22, 100$, and 200, we found that $\langle F_{\rm obs} \rangle \,/\, \langle F_{\rm model} \rangle \leq 1.3, 0.27, 0.14$ for *EGRET*, thus constraining the integral flux above 1 GeV. This indicates that the *EGRET* limit is obeyed for $N = 22$, but that larger values of N imply a reduction in the model-predicted integral flux (by, e.g., factors of 4 and 8 for $N = 100$ and 200). In the case of a *GLAST LAT* non-detection, we found $\langle F_{\rm obs} \rangle \,/\, \langle F_{\rm model} \rangle \leq 0.03, 0.007, 0.003$ for $N = 22, 100$, and 200.

9. We calculated the unpulsed inverse Compton scattering (ICS) and synchrotron radiation (SR) fluxes due to particles escaping from an ensemble of MSPs in the GC 47 Tucanae (more details in Venter & de Jager, 2008b,c, Chapter 5), and found that the SR component occurs in the optical / X-ray waveband, while the ICS occurs in the gamma-ray waveband. The ICS flux will probably not be visible for *H.E.S.S.*, while telescopes such as *Chandra* and *Hubble* may find it difficult to test the SR component prediction of diffuse radiation when there are many faint unresolved sources in the field of view. We noted that upper limits may however be derived for the SR component.

10. We found that the inclusion of the E_ϑ-component in the expression of the accelerating E-field changes the electrodynamical picture significantly, and should be included in future studies (Chapter 6). Near the PC rim close to the stellar surface, an annulus developed with a different

sign of $E_{||}$ at the rim ($-E_{||} < 0$ when $\xi \sim 1$) than at the magnetic axis ($-E_{||} > 0$ when $\xi \sim 0$). It should be considered in future whether this new feature may provide the means to extract ions from the stellar surface, effectively solving the return current problem by providing charge neutrality. Also, this new E-field's impact on particle oscillation above the PC should be investigated (in combination with the derivation of $E_{||}$ valid for higher altitudes).

11. We modelled the Galactic Centre composite supernova remnant (SNR) G0.9+0.1 (Venter & de Jager, 2006, Chapter 5). Using multiwavelength data, we found an optimum fit of initial spin-down luminosity $L_0 \sim 2.5 \times 10^{38}$ ergs/s and an injection spectral break energy of $E_b \sim 8 \times 10^{-3}$ ergs, with the predicted X-ray and gamma-ray fluxes corresponding quite well to the observed values. We obtained a present-day spin-down power of $L(T) \sim 7.4 \times 10^{36}$ ergs/s, which agrees within $\sim 50\%$ with the value inferred by *BeppoSAX*. Lastly, a typical PC magnetic field strength of $B_{PC} \sim 5 \times 10^{12}$ G was inferred.

12. We participated in ongoing collaborative research involving pulsars and PWN as sources of cosmic rays (Buesching et al., 2007a, 2008b,a, Chapter 5). We concluded that PSR J0437-4715 is not expected to make a significant contribution to the LIS. Also, depending on the magnitude of the diffusion coefficient, Geminga might contribute between a fraction of a percent and almost 100% of the locally observed cosmic ray electron flux below 1 TeV. We constrained Geminga's birth period ($P_0 > 35$ ms), as well as $P_0 k_0$-space for Geminga and B0656+14 (with k_0 the normalisation of the diffusion coefficient). We found that both Geminga and B0656+14 may make a non-negligible contribution to the local cosmic ray positron spectrum. For B0656+14, in the absence of a background flux, we found a predicted anisotropy in the positron LIS of up to almost 3%, and $\approx$0.25% for Geminga. A measured anisotropy larger than $\approx$3% would be an indication of the existence of an even younger, nearby source, e.g. a longer lifetime T of the PWN. The predicted anisotropy will probably only be testable by the *PAMELA* mission (Boezio et al., 2004).

7.2 Detailed Conclusions

We now proceed by discussing conclusions following from each of the aims outlined in Section 1.5 in more detail than in the previous section.

7.2.1 Implementing a PC GR Frame-Dragging Pulsar Model in a Computer Code

In Chapter 2, we gave an overview of the relevant processes, quantities, and other elements needed for constructing a successful MSP model. We also described the synthesis of all the different concepts when implementing the model in a computer code. We firstly gave background to several radiation processes: SR in Section 2.1.1, CR in Section 2.1.2, and ICS in Section 2.1.3. We considered CR as the dominant high-energy mechanism for pulsed radiation from MSPs (Chapters 3 and 4), and performed SR and ICS calculations in Chapter 5 where we considered unpulsed radiation from an ensemble of MSPs in a GC, as well as from PWN.

When high-energy photons traverse a very strong magnetic field, pair production is expected to ensue. We discussed pair production in Section 2.1.4 (also Sections 3.6.1 and 3.7.1), noting that the presence of an E-field is not expected to influence the pair production rate significantly. In Section 2.1.5, we noted that high-temperature PCs are likely to have a free supply of charge, as the binding energies of both electrons and ions may be exceeded, leading to favourable conditions for space-charge limited flow (SCLF) accelerators (e.g. Harding & Muslimov, 1998) to operate.

Turning to the GR effect of frame dragging, we touched on the Lense-Thirring effect, which describes the precession of intertial frames close to a rotating mass (Section 2.2). In the case of a fast-rotating pulsar, this GR effect enhances the induced E-field over that of the classical value. We described the GR framework of Harding, Muslimov, and Tsygan for the pulsar model (Section 2.3), mentioning the basic equations (Section 2.3.1), rewriting them in the corotating frame (Section 2.3.2), and obtaining expressions for the GR-corrected B-field (Section 2.3.3), potential (Section 2.3.4), and parallel electric field for different scenarios (Section 2.4).

We next described some details of our implementation of the pulsar model in a computer code. We reported on the coordinate system we used (Section 2.5.1), choices of the **E**- and **B**-fields (Sections 2.5.2 and 2.5.3), the calculation of the curvature radius of B-field lines as a function of position in the pulsar magnetosphere (Section 2.5.4), surface patches (Section 2.5.5), and path length traversed by primary electrons moving along the B-lines (Section 2.5.6). Next, we wanted to calculate high-energy radiation spectra for different observers, and therefore needed various angles describing photon emission directions (Section 2.5.7). We discussed the Special Relativistic effects of slippage and aberration (Section 2.5.8), and justified why these were not explicitly included in our calculations. We set up and outlined the solution of the transport equation accounting for electron acceleration and losses in Section 2.5.9. From this, we calculated the radiation properties of the CR gamma rays. Lastly, we discussed the calculation of spectra, fluxes, and luminosities involving beaming corrections

(Section 2.5.10). In some cases, such calculations have been performed using a cluster of computers.

7.2.2 Predicting Single MSP Visibility for Screened and Unscreened Pulsars

In Chapter 3 we presented various results from the GR model of single, isolated pulsars (described in detail in Chapter 2). To make definite predictions, we chose PSR J0437-4715 and PSR B1821-24 as examples of pulsars with unscreened and screened E-fields for detailed modelling. These two MSPs are furthermore probably the best candidates for observation by current gamma-ray telescopes, the first due to its proximity, and the latter due to its high spin-down power.

After summarising observations of PSR J0437-4715 and PSR B1821-24 in Sections 3.2.1 and 3.2.2, we offered a preliminary 'first look' analysis, and obtained model-independent constraints on the gamma-ray efficiency $\eta_\gamma^{\rm beam}$ of PSR J0437-4715 and PSR B1821-24 in Section 3.3. We noted that the maximum expected gamma-ray efficiencies for PSR J0437-4715 and PSR B1821-24 were $\lesssim 0.7\Lambda$ % and $\lesssim 1.3\Lambda$ %, assuming the functional form of dN/dE as in Eq. (3.8). The effect of beaming is already evident in this result, and more detailed studies involving Λ followed in Sections 4.3 and 4.4. Assuming non-detection by *GLAST LAT* and *CTA*, we showed that $\eta_\gamma^{\rm beam}$ may be much more severely constrained: $\eta_\gamma^{\rm beam} \lesssim 0.04\Lambda$ % and $\eta_\gamma^{\rm beam} \lesssim 0.07\Lambda$ % for PSR J0437-4715 and PSR B1821-24 respectively.

In Section 3.4 we described the discovery of oscillations in the unscreened accelerating GR electric field due to the reversal of the E-field's sign, and justified why we neglected B-field lines along which E-field reversals occur when performing our model calculations. We then presented some useful theoretical results (Section 3.5; also see Appendix A).

The main sections of Chapter 3 dealt with detailed results obtained from numerical modelling using the Harding-Muslimov-Tsygan GR model, applied to PSR J0437-4715 (Section 3.6) and PSR B1821-24 (Section 3.7). We motivated the unscreened E-field of PSR J0437-4715 in Section 3.6.1, and the screened one of PSR B1821-24 (Section 3.7.1). In addition to flux predictions, the spectral cut-off of a given pulsar gamma-ray spectrum determines whether the pulsar will be visible for a particlular gamma-ray telescope (see e.g. de Jager et al., 2001). Also, the nature of the spectral cut-offs may be a discriminator between the rival PC and OG models. For these reasons, we studied the spectral cut-off energy predictions of PSR J0437-4715 and PSR B1821-24 in Sections 3.6.2 and 3.7.2.

For PSR J0437-4715, we found a maximum CR cut-off energy of $1 - 20$ GeV, depending on the assumed geometry (χ and ζ) and equation of state, in agreement with the findings of similar studies. This is in contrast with earlier studies which predicted PSR J0437-4715's CR cut-off energy to be in the range $50 - 100$ GeV (Harding et al., 2002b; Bulik et al., 2000), making proposals for ground-based telescopes with imaging thresholds near 100 GeV attractive. We found that maximum energy

values are obtained when $\chi \sim \zeta$, and also close to the magnetic axis (small ξ and large $\cos\phi$). We therefore concluded that the low predictions of the maximum CR energy indicate that *GLAST* and 4$^{\text{th}}$ generation Cherenkov telescopes are generally needed in order to observe CR emission from unscreened gamma-ray MSPs. While an ICS component resulting from TeV electrons upscattering the UV / soft X-rays from the surface of PSR J0437-4715 may still be detectable, this prediction by Bulik et al. (2000) should also be re-evaluated within a GR electrodynamical framework. For PSR B1821-24, we found CR energies up to $\sim$ 150 GeV, compatible with similar predictions. We demonstrated that the CR cut-off energy decreases rapidly when the impact angle becomes large, and that the CR cut-off energy as a function of χ and ζ was more symmetrical with respect to the $y = x$ line for the screened case. We also confirmed that the largest energies are obtained for small χ, since the electric field scales with the factor $\cos\chi$, and at $\xi = 0$ (where the E-field approximation attains a maximum). The screened E-field doesn't change sign above the PC. (The fact that the unscreened E-field has only one sign, may cause charge accumulation above the PC, changing the electrodynamics of the steady-state solution). It is unfortunate that PSR B1821-24 is expected to have a large impact angle (from radio polarimetric observations), since low spectral cut-offs are then expected, implying that PSR B1821-24 may also not be visible for current gamma-ray telescopes. Given the low spectral cut-offs for both pulsars, even *CTA* may have a hard time probing the CR tails of the gamma-ray integral fluxes.

PSR J0437-4715's maximum gamma-ray energy was shown to be $\sim$ 10 GeV, while the maximum electron energy was $\sim$ 10 TeV (Section 3.6.3). The position above the PC where the maxima of the energies occured corresponded reasonably well to the position of the maximum of the fractional gamma-ray luminosity, meaning that photons of the maximum CR energy (and electrons having energies close to the maximum energy) were produced abundantly. For PSR B1821-24, the maximum gamma-ray energy was $\sim$ 150 GeV, while the maximum electron energy was $\sim$ 50 TeV (Section 3.7.3). These values are much higher than for PSR J0437-4715, since PSR B1821-24's E-field reaches much higher values (due to its larger spin-down luminosity). In this case, the position of the maxima of the energies also correspond quite well to the position where the maximum of the fractional gamma-ray luminosity occurs.

We calculated a band of possible spectra for PSR J0437-4715, with the uncertainty stemming from unknown geometry and EOS parameters (Section 3.6.4). We found that the 1 GeV *EGRET* upper limit constrained the luminosity of the GR model, and we used this upper limit to constrain the gamma-ray efficiency of PSR J0437-4715 by scaling the flux curves so as not to violate the *EGRET* upper limits and *H.E.S.S.* threshold energy. Our photon spectrum $(dN/dE)^{\text{slice}}$ due to CR was quite hard, resulting in a constant time-averaged integrated photon flux seen by the observer at low energies.

One may try to explain this overprediction in terms of geometry uncertainties, but in Chapter 4 we showed that for an ensemble of the MSPs in the GC 47 Tucanae, the average flux also overshoots the *EGRET* upper limits for that object. Therefore, more serious attempts will have to follow in order to solve this problem (see Section 6.3). More sensitive observations at energies of a few GeV will help to probe the CR spectral tail, and thus limit the accelerating potential. We furthermore modelled the gamma-ray flux expected from PSR B1821-24 (Section 3.7.4). We found that this pulsar is not expected to be visible for *H.E.S.S.* unless the geometry is favourable. Assuming that the inferred angles χ and ζ are correct, this MSP will probably not even be visible for *GLAST LAT*, despite its large spin-down luminosity.

When calculating the particle and gamma-ray efficiencies of PSR J0437-4715, we found that $L_{\gamma}^{\rm beam}/L_{\rm prim,max} \sim 1$ (Section 3.6.5). This means that almost all particle luminosity is converted into photon luminosity as expected for strong radiation reaction. Radiation reaction, combined with further (weak) acceleration towards the light cylinder, resulted in a total residual electron power of $\sim 1 - 2.5\%$ of the spin-down power at the light cylinder. However, since the *EGRET* limits imposed constraints on the GR model, we had to scale the integral flux curve, and found that $\eta_{\gamma}^{\rm beam} \leq 0.55\%$, although it must be borne in mind that the geometrical beaming factor Λ might alter this constraint significantly. Forthcoming *GLAST* observations will possibly be able to directly measure the value of $\eta_{\gamma}^{\rm beam}$. For the case of PSR B1821-24, we found that $\Lambda \sim 1\ 500$ (indicative of off-beam radiation), corresponding to a value of $\eta_{\gamma}^{\rm beam} = 1.6\%$. No scaling of integral flux graphs were necessary, as the predicted curve did not violate experimental limits.

Lastly, the lightcurves of PSR J0437-4715 were briefly studied in Section 3.6.6. We noted that a full treatment would require the correct Lorentz transformation from the corotating to the observer frame (see Section 6.2). We concluded that GR theory predicts a relatively narrow pulse ($\beta^{\rm slice} \sim 0.2$ phase width) centered on the magnetic axis, and found an estimate for the beaming solid angle of ~ 0.5 sr per PC when selecting radiation with energy $\gtrsim 100$ MeV (for $\chi = 35°$). We furthermore calculated lightcurves for PSR J0437-4715 for different observer angles ζ. Maximal heights were obtained when $\zeta \sim \chi$. However, the pulse heights decreased rapidly as the radiation became off-beam. The 'dips' in lightcurves with $\zeta \geq \chi$ near phase $\phi_L/2\pi \sim 0.5$ (where $\phi \sim \pi$) were most probably due to the sign reversal of the electric field. Since the radio and X-ray pulses are in phase, one would expect that the gamma-ray pulse will also be in phase with these, provided all pulses are produced near the magnetic axis. We are hopeful that *GLAST LAT* might measure lightcurves of PSR J0437-4715 around a few GeV.

7.2.3 Studying the MSP Model Behaviour in Pulsar Parameter Space

In Section 4.3 of Chapter 4 we applied the basic MSP model described in Chapter 2 for a mesh of $(P, \dot{P}, \chi, \zeta)$-space. Generally speaking, cut-off energies, efficiencies, energy fluxes, and integral fluxes decrease with larger P and smaller $\dot{P}$. Also, more and more MSPs become invisible as the minimum energy of the integral flux is increased. The effect of geometry is furthermore evident, where maxima of above-mentioned quantities occur for on-beam radiation (with asymmetrical distributions about the $\chi = \zeta$ line for the unscreened pulsars), while the beaming correction is a minimum in this case. The energy ratio is typically $\sim 1 - 2$, so that the cut-off energy is a good approximation for the average energy of the photon spectrum. It therefore emerges that all the pulsar properties are sensitive functions of the assumed geometry (as well as P and $\dot{P}$), so that accurate knowledge of pulsar geometry is crucial when making predictions regarding their visibility. In addition, screening complicates the matter for high-spin-down pulsars, where pair-creation leads to suppression of the E-field.

7.2.4 Obtaining Constraints on the MSP Model by Modelling Single MSP Spectra

From the detailed modelling of single pulsars in Chapter 3, we found that PSR J0437-4715's maximum gamma-ray energy was $\sim$ 10 GeV, while the maximum gamma-ray energy for PSR B1821-24 was $\sim$ 150 GeV. These cut-off energies may be tested by future gamma-ray telescopes, which will constrain the electric potential of the pulsars. More significant constraints are expected in the case of PSR J0437-4715 which has a largely unscreened PC, as the complicating effect of secondary pair production is eliminated in this case.

From gamma-ray integral flux calculations for PSR J0437-4715, we found that the 1 GeV *EGRET* upper limit was not obeyed, indicating that the gamma-ray luminosity is overpredicted by the model. We used this upper limit to constrain the gamma-ray efficiency, after scaling the integral flux curve, to $\eta_\gamma^{\rm beam} \leq 0.55\%$. For the case of PSR B1821-24, we found that $\eta_\gamma^{\rm beam} = 1.6\%$.

7.2.5 Obtaining Constraints on the MSP Model by Modelling MSP Population Cumulative Spectra: Pulsed and Unpulsed Radiation

When considering an ensemble of MSPs, we found that such a population provides the unique opportunity to sidestep the issue of pulsar geometry (which is crucial when modelling a single MSP) by averaging over numerous spectra and geometries, which results in a "geometry-averaged" spectrum with relatively small uncertainty (Venter & de Jager, 2008a). The relative spread of ensemble values for the bolometric gamma-ray and electron luminosities as well as the spin-down power and average

gamma-ray spectra are typically one order smaller than for the same quantities averaged as single MSP quantities. This illustrates the importance of testing pulsar models by observing GCs. (We furthermore found that varying the EOS did not alter conclusions significantly, so that the geometry, along with the values of P and $\dot{P}$, are the main factors determining MSP visibility).

In Chapter 4, we calculated the pulsed gamma-ray flux expected from a population of MSPs in 47 Tucane for $N = 100$ visible members, but the spectra can easily be (linearly) scaled to any other reasonable number (we plan to do this when presenting future work on the pulsed and unpulsed radiation expected from nearby GCs, Venter & de Jager (2008b,c)). We were especially interested in obtaining errors on the pulsed gamma-ray spectrum which would reflect the uncertainty in the geometries, as well as the spread in P and $\dot{P}$, of the individual pulsars. In this way, we wanted to see whether it would be possible to constrain the underlying pulsar model independently of the assumed pulsar geometry. It remains to be shown whether the spread of the 13 selected pulsars represents the true inherent spread of MSPs in 47 Tucanae.

We found good agreement for the average single pulsar efficiencies for electron and gamma-ray production between our results and those of other authors. However, our average pulsed spectrum, including errors, exceeded the *EGRET* upper limit at 1 GeV (for the average integral flux spectrum, by a factor of ~ 3.9). Assuming that this model predicts the gamma-ray flux correctly, this *EGRET* upper limit constrains the number of GC pulsars to $N = 100/3.76 \approx 27$. Generally, setting $N = 22, 100,$ and 200, we found that $\langle F_{\rm obs} \rangle \,/\, \langle F_{\rm model} \rangle \leq 1.3, 0.27, 0.14$ for *EGRET*. This indicates that the *EGRET* limit is obeyed for $N = 22$, but that larger values of N imply a reduction in the model-predicted integral flux (by, e.g., factors of 3.7 and 7.4 for $N = 100$ and 200). In the case of a *GLAST* LAT non-detection, we found $\langle F_{\rm obs} \rangle \,/\, \langle F_{\rm model} \rangle \leq 0.03, 0.007, 0.003$ for $N = 22, 100,$ and 200. We lastly noted that *GLAST* LAT might even constrain the maximum average electric potential per pulsar $\langle \Phi_{\rm max} \rangle$ via the CR cut-off energy.

In Chapter 5, we discussed results involving relativistic particles escaping from the magnetospheres of pulsars. In Section 5.2, we calculated the unpulsed ICS and SR fluxes due to particles escaping from an ensemble of MSPs in the GC 47 Tucanae, which is complementary to the calculation of pulsed CR expected from this GC (Section 4.5). We found that the SR component occurs in the optical / X-ray waveband, and the ICS, as a result of scattering the starlight and CMBR components, in the gamma-ray waveband. The ICS flux will probably not be visible for *H.E.S.S.*, while telescopes such as *Chandra* and *Hubble* may find it difficult to test the SR component prediction of diffuse radiation when there are many strong point sources in the field of view. We noted that upper limits may however be derived for the SR component.

We lastly noted in Section 4.6.4 that since existing radio telescopes will not be able to monitor all pulsars on a regular basis, most faint gamma-ray pulsars discovered by *GLAST LAT* will remain unidentified in the absence of contemporary radio parameters (also see Ransom, 2007). We referred to the fraction of the pulsar population which will be visible to both *meerKAT* and *GLAST LAT*, and underlined the importance of concurrent radio and gamma-ray observations of pulsars.

7.2.6 Obtaining Constraints on the MSP Model by Modelling the Contribution of Nearby Pulsars to the Local Cosmic-Ray Spectrum

In Section 5.4 through 5.6 of Chapter 5, we summarised results from ongoing collaborative research on the contribution of nearby pulsars to the local interstellar cosmic ray lepton spectrum. Relevant papers on this subject are included in Appendix B. Our conclusions were the following:

1. The MSP PSR J0437-4715 is not expected to make a significant contribution to the LIS.

2. Depending on the magnitude of the diffusion coefficient, Geminga might contribute between a fraction of a percent and almost 100% of the locally observed cosmic ray electron flux below 1 TeV.

3. We obtained a constraint on Geminga's birth period ($P_0 > 35$ ms).

4. We obtained constraints on $P_0 k_0$-space for Geminga and B0656+14.

5. We showed that, depending on the pulsar parameters, both Geminga and B0656+14 make a non-negligible contribution to the local cosmic ray positron spectrum.

6. For B0656+14, in the absence of a background flux, we found a predicted anisotropy in the positron LIS of up to almost 3%, significantly larger than the expected value of $\approx$0.25% for Geminga. Conversely, a measured anisotropy larger than the $\approx$3% we obtained for B0656+14 would be an indication of the existence of an even younger, nearby source, e.g. a longer lifetime T of the PWN.

7. Our predicted anisotropy is the largest above 10 GeV, an energy range at which only the *PAMELA* mission (Boezio et al., 2004) may be able to gather sufficient statistics to find an anisotropy of the predicted magnitude.

7.2.7 Studying the Typical Beaming Angles of MSPs

We were interested in estimating typical geometrical beaming corrections, using the basic MSP model to perform a population study. Derivation of sensible future constraints on gamma-ray efficiencies depend sensitively on this factor, where the total luminosity is estimated using the measured energy flux. We found that the beaming correction factors Λ may be significantly larger than unity. Also, we see that actual trends may be concealed when Λ is unknown. It is encouraging to see that the theoretical expectation $L_\gamma^{\rm beam} \approx 0.07\dot{E}_{\rm rot}$ for MSPs with unscreened PCs is borne out by the numerical calculations.

Using the same MSP population, we also found that roughly half of the population of 59 MSPs are expected to be visible for *GLAST*, with integral fluxes $\sim 10^{-8}$ cm^{-2}.s^{-1}. Lastly, we found that, assuming $L_\gamma^{\rm beam} \approx L_{\rm prim,max}$, the approximation $L_\gamma^{\rm beam}(0) = 0.75\kappa(1-\kappa)\dot{E}_{\rm rot}$ overpredicts $L_\gamma^{\rm beam}$, and that better results follow when using the more general expression $L_\gamma^{\rm beam}(\chi) = L_\gamma^{\rm beam}(0)[\cos^2\chi + C\sin^2\chi]$. The latter equation may be approximated by $L_\gamma^{\rm beam}(\chi) = 0.5\kappa(1-\kappa)\dot{E}_{\rm rot} \approx 0.07\dot{E}_{\rm rot}$, indicating that $\eta_\gamma^{\rm beam} \approx 7\%$ for unscreened MSPs in the context of the GR frame-dragging pulsar model.

7.2.8 Investigating Future Model Refinements

We briefly considered future model refinements in Chapter 6. In this chapter, and elsewhere the thesis, we mentioned the transformation from the corotating to the observer frame, GR effects such as light bending, redshift, aberration, and charge pile-up, as well as investigating multipoles instead of a dipolar magnetic field (Navarro et al., 1997; Harding, 2007a), making more appropriate assumptions concerning the primary electrons' initial velocities (Sakai & Shibata, 2003), and treating the field reversals properly. We furthermore noted that the inclusion of the E_ϑ-component in the expression of the accelerating E-field promises to change the electrodynamical picture significantly. Near the PC rim close to the stellar surface, an annulus developed with a different sign of $E_{||}$ at the rim ($-E_{||} < 0$ when $\xi \sim 1$) than at the magnetic axis ($-E_{||} > 0$ when $\xi \sim 0$). It should be considered in future whether this new feature may provide the means to extract ions from the stellar surface, effectively solving the return current problem by providing charge neutrality. This new E-field (in combination with the derivation of $E_{||}$ valid for higher altitudes) also promises to improve the situation regarding particle oscillation above the PC.

7.2.9 PWN Modelling

In Section 5.3, we modelled the Galactic Centre composite SNR G0.9+0.1. Using multiwavelength data, we found an optimum fit of initial spin-down luminosity $L_0 \sim 2.5 \times 10^{38}$ ergs/s and a spectral break energy of $E_b \sim 8 \times 10^{-3}$ ergs, with the predicted X-ray and gamma-ray fluxes corresponding quite well to the observed values. A value of present-day spin-down power of $L(T) \sim 7.4 \times 10^{36}$ ergs/s was obtained, which agrees within $\sim 50\%$ with the inferred value of $L(T) \sim 1.5 \times 10^{37}$ ergs/s from *BeppoSAX* observations. Lastly, a typical PC magnetic field strength of $B_{PC} \sim 5 \times 10^{12}$ G was inferred. We noted that it is possible to apply a newer model (Zhang et al., 2008) to G0.9+0.1 to obtain better constraints on its PWN parameters.

7.3 Future Outlook and Recommendations

One major conclusion which follows from the above is that while the GR pulsar model seems to make reasonable predictions, model refinement is necessary (notably, flux overpredictions should be corrected). With the launch of *GLAST*, and 4th generation Cherenkov telescopes coming online soon, models of ever-increasing complexity and accuracy are needed to explain the probable vast number of new pulsars and PWN to be discovered and re-observed with these much more sensitive instruments. It has been forty years since the discovery of pulsars, and pulsar physicists acknowledge that there are many more challenges to face in our quest for better understanding of the pulsar mechanism (e.g. Michel, 2004; Harding, 2007a). They are also hopeful that the wealth of new data will take the field to the next level. With this in mind, we make the following recommendations:

1. Pair-starved MSPs should be a "clean sample" that may be used to constrain the PC potential (and in a lesser sense the current, which should be close to Goldreich-Julian), without the effect of screening, which introduces many complications. However, as the bulk of the pulsar population are young pulsars, it is unavoidable that screened pulsar magnetospheres should be modelled with the best possible accuracy, to explain the majority of new pulsar discoveries.

2. We noted that gamma-ray and radio telescopes (indeed, also other facilities operating at different wavelengths) should have open communication channels, so that contemporaneous observations of pulsars in these two wavebands may yield the largest possible number of discoveries of pulsed emission (also see Ransom, 2007). It would probably be highly advisable for gamma-ray physicists to talk to the *SKA* demonstrator groups which are currently planning and constructing the most sensitive radio telescopes in the world.

3. In this work, we mainly considered CR as the dominant gamma-ray radiation component. It is however important to redo calculations, considering SR and ICS in pulsar magnetospheres within the full GR framework.

4. In the short-term, it is important to parametrise a pulsar model and "let the data speak for itself" by constraining the model. One may then obtain order of magnitude estimates for fundamental pulsar quantities, before doing any further detailed mathematical work.

5. It may be useful, as a long-term project, to consider rederiving the pulsar model in full GR formalism (involving possible collaboration with GR specialists), and also calculating the photon trajectories using the full rotating metric, so that effects such as redshift, light bending, aberration, time delays, etc. are automatically taken into account, and not added as ad-hoc transformations when e.g. calculating lightcurves. Of course, this depends on the practicality of such an undertaking, and the expected advantages to be derived. Numerical calculations may prove more feasible in this regard, so that analytical approximations are not necessary when solving for the accelerating E-field. This will hopefully lead to stationary solutions which will not give rise to particle oscillations in the magnetosphere.

6. Microscopic modelling, e.g. particle-in-cell (PIC) simulations, may be useful to gain better understanding of the pulsar magnetosphere, and may bring us nearer to a self-consistent solution of pulsar electrodynamics. It may be possible to solve a particular electrodynamical problem with associated boundary conditions, and then iterate until a steady-state solution is obtained. The effect of changing the electrodynamic boundary conditions may thus be studied. The possibility of an extended hybrid PC / OG accelerator may also be considered using numerical tools (its existence seemingly being indicated by wide lightcurves). The longstanding problem of a return current may possibly also be investigated in this way. In keeping with the times, new technology, such as computer clusters, must be utilised to obtain better understanding of the pulsar phenomena.

7. It has been noted that some pulsars exhibit magnetic multipole behaviour (e.g. Navarro et al., 1997). For simplicity, the standard dipolar magnetic field is usually used in pulsar models. Gil and co-workers however propose that multipoles may provide smaller curvature radii, leading to higher-energy CR, which in turn may convert to pairs. This means that 'pair-starved pulsars' may in fact not be pair-starved, providing a mechanism for radio emission observed from MSPs (de Jager 2008, personal communication). It is important to study the effect of changes in the

magnetic field geometry (Harding, 2007a), and to consider whether multipolar pulsar magnetospheres with (newly-induced) screening will allow photons of high enough energy to escape from the pulsar magnetosphere before being converted to electron-positron pairs. In addition, the effects of sweepback and retardation of the magnetic field have to be carefully considered, especially for the case of MSPs.

8. One should try and keep theoretical predictions as practical and testable as possible, and work hard at maintaining close relationships with experimentalists, so that maximum profit may be gained from such interactions. This is the only way to best constrain models and interpret data. This will conversely also provide impetus for more and better quality observations of pulsars and PWN.

9. Many applications of the same basic model should be performed if possible in order to have maximum constraining power by using different sets of data. One example of this may be probing SR from the bow shock of PSR J0437-4715 using the optical telescope *SALT*, which may lead to constraints on the σ-parameter.

10. Future collaboration with transport and MHD experts may lead to significant improvement of PWN modelling.

11. Finally, we noted that deep *GLAST* observations of GCs and stacking of skymaps above 1 GeV for selected MSPs (with known values of the number of pulsars, their periods, and period-derivatives) may be the closest one can come to deriving constraints on fundamental pulsar quantities in a (nearly) model-independent manner, sidestepping the problem of unknown (inaccurately known) geometry which attends single MSPs, and on which the model output sensitively depends (Section 6.3). Such a project may be pursued as a guest investigator program for *GLAST*.

Appendix A

Various Mathematical Results

In this Appendix, various details are collected seperately from the main work in order to facilitate a clear flow of the latter. Some results have been derived or alluded to previously (Venter, 2004).

A.1 Estimation of the Generalised Gamma-Luminosity as Function of Inclination Angle

Harding et al. (2002b) calculate the luminosity of the primary electron beam in the PC pulsar model using

$$L_{\rm prim} = \alpha c \int |\rho_{\rm e}| \Phi \, dS. \tag{A.1}$$

The appropriate electron charge density is (see Eq. [2.115])

$$\rho_{\rm e} = -\frac{\Omega B_0}{2\pi c \alpha \eta^3} \frac{f(\eta)}{f(1)} \left[(1-\kappa)\cos\chi + \frac{3}{2}\zeta_0 \Theta_0 H(1) \xi \sin\chi \cos\phi \right]. \tag{A.2}$$

For an aligned rotator ($\cos\chi = 1$), this becomes

$$|\rho_{\rm e}| = \frac{\Omega B_0}{2\pi c \alpha \eta^3} \frac{f(\eta)}{f(1)} (1-\kappa). \tag{A.3}$$

The element of spherical surface $dS(\eta, \xi, \phi)$ cut by the last open field lines at the radial distance r is given by

$$dS = \frac{\Omega R^3 \eta^3}{c f(\eta)} \xi d\xi d\phi. \tag{A.4}$$

When there is no pair production by CR, the electric potential $\Phi(\eta, \phi, \xi, \chi)$ is given by (Eq. [2.116])

$$\Phi = \frac{1}{2}\Phi_0(\zeta_0\Theta_0)^2 \left\{ \kappa \left(1 - \frac{1}{\eta^3}\right) \cos\chi + \frac{3}{4} \left[\zeta(\eta)\Theta(\eta)H(\eta) - \zeta_0\Theta_0 H(1)\right] \xi \sin\chi\cos\phi \right\} \left(1 - \xi^2\right) \quad \text{(A.5)}$$

(valid when $h > R_{\rm PC}$). If evaluated at $\cos\chi = 1$ this becomes:

$$\Phi\,|_{\cos\chi=1} = \frac{1}{2}\Phi_0(\zeta_0\Theta_0)^2 \left(1 - \xi^2\right) \kappa \left(1 - \frac{1}{\eta^3}\right) \quad \text{(A.6)}$$

$$= \frac{B_0\Omega R^2}{2c} \left[\frac{\Omega R}{cf(1)}\right] \left(1 - \xi^2\right) \kappa \left(1 - \frac{1}{\eta^3}\right). \quad \text{(A.7)}$$

Substituting these expressions into (A.1) and integrating over ξ and ϕ, Harding et al. (2002b) obtain:

$$L_{\rm prim}^{|\chi=0} = \alpha c \int_{\rm PC} |\rho_e| \Phi \, dS \quad \text{(A.8)}$$

$$= \alpha c \left(\frac{\Omega B_0 f(\eta)}{2\pi c \alpha \eta^3 f(1)}\right) \left(\frac{B_0\Omega R^2}{2c}\right) \left(\frac{\Omega R}{f(1)c}\right) \left(\frac{\Omega R^3 \eta^3}{cf(\eta)}\right)$$

$$\times \; \kappa(1-\kappa) \left(1 - \frac{1}{\eta^3}\right) \int_0^{2\pi} \int_0^1 \left(1 - \xi^2\right) \xi d\xi d\phi \quad \text{(A.9)}$$

$$= \left[\frac{\Omega^4 B_0^2 R^6}{4\pi c^3 f^2(1)}\right] \kappa(1-\kappa) \left(1 - \frac{1}{\eta^3}\right) \int_0^{2\pi} d\phi \int_0^1 (\xi - \xi^3) d\xi \quad \text{(A.10)}$$

$$= \frac{3}{4} \left(1 - \frac{1}{\eta^3}\right) \kappa(1-\kappa) \dot{E}_{\rm rot}, \quad \text{(A.11)}$$

with $\dot{E}_{\rm rot} \equiv \Omega^4 B_0^2 R^6 / 6c^3 f^2(1)$. In order to obtain the maximum power in the primary beam, let $\eta \to \infty$ (see Eq. [A.1]):

$$L_{\rm prim,max}^{|\chi=0} = \frac{3}{4}\kappa(1-\kappa)\dot{E}_{\rm rot}. \quad \text{(A.12)}$$

A more detailed analysis (using $\int_0^{2\pi} \cos\phi d\phi = 0$ and $\int_0^{2\pi} \cos^2\phi d\phi = \pi$) yields the general result for an oblique rotator:

$$L_{\rm prim} = \frac{3}{4} \left(1 - \frac{1}{\eta^3}\right) \kappa(1-\kappa) \cos^2\chi \dot{E}_{\rm rot}$$

$$+ \; \frac{9}{64} \Theta_0^c H(1) \sin^2\chi \left[\Theta^c(\eta) H(\eta) - \Theta_0^c H(1)\right] \dot{E}_{\rm rot} \quad \text{(A.13)}$$

$$= L_{\rm prim}^{|\chi=0} \left\{ \cos^2\chi + \frac{3}{16} \frac{\Theta_0^c H(1) \sin^2\chi \left[\Theta^c(\eta) H(\eta) - \Theta_0^c H(1)\right]}{(1 - 1/\eta^3)\,\kappa(1-\kappa)} \right\}. \quad \text{(A.14)}$$

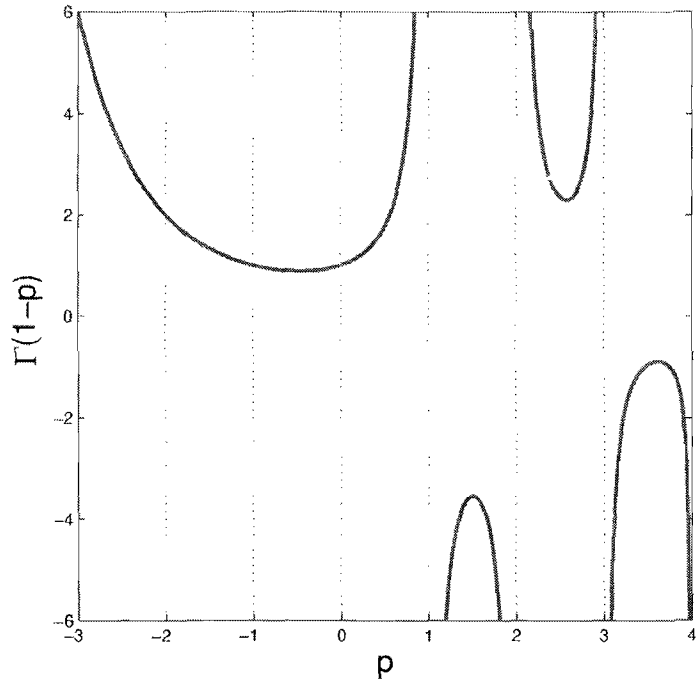

Figure A.1: $\Gamma(1-p)$ vs. p.

However, $\Theta^c(\eta)$'s definition is only valid inside the light cylinder. Adopting a value of $\Theta^c(\eta) = \pi/2$ for distances $\eta > c/(\Omega R)$ and letting $\eta \rightarrow \infty$ as before, we obtain (with $H(\eta) \rightarrow 1$ as $\eta \rightarrow \infty$)

$$L_{\rm prim,max} = L^{|\chi=0}_{\rm prim,max} \left\{ \cos^2\chi + \frac{3}{16} \frac{\Theta^c_0 H(1) \sin^2\chi \left[\pi/2 - \Theta^c_0 H(1)\right]}{\kappa(1-\kappa)} \right\}, \tag{A.15}$$

which reduces back to Eq. (A.12) when $\chi = 0$.

From Eq. (A.12) and (A.15), one reaches the conclusion that the maximum efficiency of conversion of pulsar spin-down power ($\dot{E}_{\rm rot} \equiv I\Omega\dot{\Omega}$) into γ-ray luminosity L_γ is about 10% for typical pulsar parameters (with $\kappa \sim 0.15$) for the GR frame-dragging model when assuming that $L_\gamma \sim L_{\rm prim,max}$ (Harding et al., 2002b, also refer to Sections 3.6.5 and 4.4.)

A.2 Integral of Generic Spectral Form

CR photon spectra have the form of a power law with a spectral index of -2/3 for a mono-energetic beam of particles (see Section 2.1.2), with an exponential (or super-exponential) cut-off occurring at energies greater than E_0 when they are continuously accelerated by a parallel electric field (Harding

et al., 2002b). Integration of a spectrum of the form

$$KE^{-p}\exp\left(-\frac{E}{E_0}\right), \tag{A.16}$$

with K and p constants, may be cast in the form of a Γ-function if the limits of integration are 0 and ∞. The Γ-function is defined as follows (Kreyszig, 1999)

$$\Gamma(\alpha) = \int_0^\infty t^{\alpha-1}e^{-t}dt, \quad \alpha > 0. \tag{A.17}$$

Integration by parts shows that

$$\Gamma(\alpha+1) = \alpha\Gamma(\alpha). \tag{A.18}$$

Since $\Gamma(1) = 1$, the Γ-function may be regarded as the generalisation of the elementary factorial function

$$\Gamma(n+1) = n!, \quad n = 0, 1, \ldots \tag{A.19}$$

In addition to the Γ-function, the upper and lower incomplete Γ-functions are defined by

$$\Gamma(\alpha, x) = \int_x^\infty t^{\alpha-1}e^{-t}dt \tag{A.20}$$

$$\gamma(\alpha, x) = \int_0^x t^{\alpha-1}e^{-t}dt, \tag{A.21}$$

such that

$$\Gamma(\alpha) = \Gamma(\alpha, x) + \gamma(\alpha, x). \tag{A.22}$$

By substituting $t = E/E_0$, it follows that (see Figure A.1)

$$\int_0^\infty KE^{-p}\exp\left(-\frac{E}{E_0}\right)dE = KE_0^{1-p}\Gamma(1-p). \tag{A.23}$$

If the argument $1-p$ is a non-zero, negative value, but not an integer, one may use the relation

$$\Gamma(1-p) = \frac{\Gamma(2-p+n)}{(1-p)(-p)(-p+1)\ldots(1-p+n)}, \quad p \neq 1, 2, \ldots \tag{A.24}$$

with n the smallest integer such that $n > p-2$, to evaluate Γ with a negative argument. Equation (A.23) is an improvement to the approximation

$$\int_0^\infty KE^{-p}\exp\left(-\frac{E}{E_0}\right)dE \approx \int_0^{E_0} KE^{-p}\,dE = \frac{KE_0^{1-p}}{1-p}. \tag{A.25}$$

Using this result, we may obtain the following expression for the integral flux:

$$\overline{F}^{\text{slice}}(>E_1) = \int_{E_1}^{\infty} \left(\frac{dN}{dE}\right)^{\text{slice}} dE \tag{A.26}$$

$$= KE_0^{1-p}\,\Gamma(1-p, E_1/E_0) \tag{A.27}$$

$$\approx \frac{KE_0^{1-p}}{1-p}, \quad E_1 \ll E_0. \tag{A.28}$$

Also, the luminosity may be written as

$$L_\gamma^{\text{beam}} = \frac{\overline{\epsilon\Delta\Omega}^{\text{beam}} d^2}{\beta^{\text{slice}}} \int_0^{\infty} E \left(\frac{dN}{dE}\right)^{\text{slice}} dE \tag{A.29}$$

$$= \Lambda d^2 K E_0^{2-p}\,\Gamma(2-p) \tag{A.30}$$

$$\approx \Lambda d^2 \frac{KE_0^{2-p}}{2-p}. \tag{A.31}$$

A.3 Flat Shape of the Integral Flux at Low Energies

Assume that the photon spectrum may be parametrised according to

$$\frac{dN}{dE} = KE^{-p} \exp\left(-\frac{E}{E_0}\right), \tag{A.32}$$

as in Eq. (A.16). The integral flux above an energy E_1 is derived in Section 3.5.2:

$$F(>E_1) = KE_0^{1-p}\Gamma(1-p,\, E_1/E_0) = KE_0^{1-p}\left[\Gamma(1-p) - \gamma(1-p,\, E_1/E_0)\right]. \tag{A.33}$$

It is clear that $\gamma(1-p, E_1/E_0) \ll \Gamma(1-p)$ for small values of E_1 and when $p < 1$, such that the previous equation reduces to

$$F(>E_1) \approx KE_0^{1-p}\,\Gamma(1-p) = \text{constant}, \quad E_1 \ll E_0. \tag{A.34}$$

This behaviour may for example be seen in Figure 4.3.

A.4 Scaling of Integral Flux

Once again, assume that the differential photon spectrum may be described by

$$\frac{dN}{dE} = KE^{-p} \exp\left(-\frac{E}{E_0}\right) \tag{A.35}$$

with units $\mathrm{erg}^{-1}\,\mathrm{s}^{-1}\,\mathrm{cm}^{-2}$. According to the analytical estimate of Harding et al. (2002b),

$$L_\gamma \sim L_{\mathrm{prim,max}} = \frac{3}{4}\kappa(1-\kappa)\dot{E}_{\mathrm{rot}}. \tag{A.36}$$

If one assumes that L_γ stays constant for two different integral flux spectra with normalisation constants K_a and K_b and cut-off energies E_a and E_b, it follows from (A.30) that

$$\Lambda_a d^2 K_a E_a^{2-p_a}\,\Gamma(2-p_a) = \Lambda_b d^2 K_b E_b^{2-p_b}\,\Gamma(2-p_b) \tag{A.37}$$

$$\frac{K_a}{K_b} = \left(\frac{\Lambda_b}{\Lambda_a}\right)\left(\frac{\Gamma(2-p_b)}{\Gamma(2-p_a)}\right)\left(\frac{E_b^{2-p_b}}{E_a^{2-p_a}}\right) \tag{A.38}$$

$$\frac{K_a}{K_b} \approx \left(\frac{E_b}{E_a}\right)^{2-p}, \tag{A.39}$$

assuming $\Lambda_a \approx \Lambda_b$ and $p_a \approx p_b \approx p$. From (A.27) and (A.39),

$$\frac{\overline{F}_a(>E_1)}{\overline{F}_b(>E_2)} \approx \left(\frac{K_a}{K_b}\right)\left(\frac{E_a}{E_b}\right)^{1-p}\frac{\Gamma(1-p, E_1/E_a)}{\Gamma(1-p, E_2/E_b)} \tag{A.40}$$

$$\approx \left(\frac{E_b}{E_a}\right)\frac{\Gamma(1-p, E_1/E_a)}{\Gamma(1-p, E_2/E_b)}. \tag{A.41}$$

We can write

$$\frac{\overline{F}_a(>E_1)}{\overline{F}_b(>E_2)} \approx \left(\frac{E_b}{E_a}\right) \tag{A.42}$$

when any of the following conditions are met:

- $E_1 \ll E_a$ and $E_2 \ll E_b$
- $E_1 \sim E_a$ and $E_2 \sim E_b$
- $E_1 \sim E_2$ and $E_a \sim E_b$.

If the slope of $\overline{F}_b(>E)$ is very flat (which it typically is: Section A.3), so that $\overline{F}_b(>E_2) \approx \overline{F}_b(>E_3)$, with the value E_3 limited by the flatness of the slope of $\overline{F}_b(>E)$, we can use the above conditions to write

$$\frac{\overline{F}_a(>E_1)}{\overline{F}_b(>E_3)} \approx \left(\frac{E_b}{E_a}\right). \tag{A.43}$$

The above cases may be applied recursively, so that if one scales the cut-off energy of spectrum 'a' with factor $\lambda = E_b/E_a$, the scaled flux $\overline{F}_b(>E_2)$ (spectrum 'b') is (collecting all results for the different energy ranges):

$$\overline{F}_b(>E_2) \approx \frac{\overline{F}_a(>E_1)}{\lambda}. \tag{A.44}$$

This result has been applied in Venter & de Jager (2005a).

A.5 Relating Bolometric and Observer Luminosities

The phase-averaged observer integral flux above an energy E_1 is given by (see Eq. [2.174])

$$\overline{F}^{\rm slice}(>E_1) = \int_{E_1}^{\infty} \left(\frac{dN}{dE}\right)^{\rm slice} dE \tag{A.45}$$

$$= \int_{E_1}^{\infty} \left[\frac{1}{\overline{\Delta\Omega}^{\rm slice} d^2\, dE} \iiint_{\zeta+d\zeta/2}^{\zeta+d\zeta/2} \left(\frac{dL}{d\phi_L dE d\zeta}\right) \frac{I(E,dE)}{E_\gamma^{\rm c}}\, d\phi_L\, dE\, d\zeta\right] dE \tag{A.46}$$

$$= \frac{1}{\overline{\Delta\Omega}^{\rm slice} d^2} \int_{E_1}^{\infty} \left[\frac{1}{E}\left(\frac{dL}{dE}\right)\right] dE \tag{A.47}$$

$$= \frac{L_\gamma^{\rm slice}}{\overline{E}_{\rm L}\, \overline{\Delta\Omega}^{\rm slice} d^2}, \tag{A.48}$$

where

$$\overline{E}_{\rm L} \equiv \frac{\int_{E_1}^{\infty} (dL/dE)\, dE}{\int_{E_1}^{\infty} (1/E)\,(dL/dE)\, dE} \approx \frac{L_\gamma^{\rm slice}}{\overline{\Delta\Omega}^{\rm slice} d^2\, \overline{F}^{\rm slice}(>E_1)} \tag{A.49}$$

for small E_1. Finally, if we assume that $L_\gamma^{\rm beam} \equiv \alpha_{\rm L} L_\gamma^{\rm slice}$, with $\alpha_{\rm L}(\chi,\zeta)$ a geometrical factor, we obtain (using Eq. [A.48])

$$L_\gamma^{\rm beam} \approx x\overline{F}^{\rm slice}(>E_1)\overline{E}_{\rm L} \approx x\overline{F}^{\rm slice}(>E_1)E_0, \tag{A.50}$$

with $x = \alpha_{\rm L} d^2 2\pi \sin\zeta d\zeta$, $E_1 \ll E_0$, and E_0 the spectral cut-off energy. This approach has been used in Venter & de Jager (2005a). We have since formalised this conversion from the slice to the beam luminosity, involving the definition of a geometric beaming factor Λ (Section 2.5.10).

A.6 Logarithmic Binning

This section describes the method of binning (reordering) a quantity $X(r_1, r_2, ...)$ depending e.g. on parameters r_1, r_2,... according to e.g. energy, with the result $X(E)$. By way of example, consider the calculation of the photon spectrum dN/dE by binning (and integrating) the incremental luminosity according to associated energy E (see Section 2.5.10).

First, we decide on an energy interval $[E_\alpha, E_{\rm f}]$, and the number of bins N to be used. Energies are constructed according to

$$E_k = E_\alpha e^{k\delta}, \quad k = 0, 1, ..., N-1. \tag{A.51}$$

It follows that

$$\delta = \frac{\ln\left(E_{\mathrm{f}}/E_{\alpha}\right)}{N-1}. \tag{A.52}$$

Next, a binning index i is calculated as follows

$$i = \lceil \ln\left(E/E_{\alpha}\right)/\delta \rceil, \tag{A.53}$$

for each incremental luminosity dL associated with an energy E. All the values of $(1/E)[dL/(d\phi_L d\zeta dE)]$ are then accumulated in a matrix at index i according to their associated energies. Since $E < E_{\alpha}$ implies $i < 0$, we set $i = 0$ in these cases. This means that all quantities associated with energies smaller than the lower bound of the considered energy range are accumulated in the 0^{th} bin. Afterwards, this bin is ignored when plotting dN/dE. The maximum energy of the range, E_{f}, is chosen so that the energies of the process under consideration will always be less than this, so as not to exceed the maximum matrix size when binning quantities. We also construct an 'average' energy

$$E_{\mathrm{avg},\,k} = \frac{1}{2}\left(E_{k-1} + E_k\right) = \frac{1}{2}E_{\alpha}\left(e^{k\delta} + e^{(k-1)\delta}\right) \tag{A.54}$$

for the energy bin spanning $[E_{k-1}, E_k]$, $k = 1, 2, ..., N-1$. All plots of spectra are made using this average energy as the independent variable. Lastly, each bin of the matrix is divided by the energy bin size

$$dE_k = E_k - E_{k-1} = E_{\alpha}\left(e^{k\delta} - e^{(k-1)\delta}\right), \tag{A.55}$$

as well as the factor $d^2 2\pi \sin\zeta d\zeta$, with d the pulsar distance, and ζ the observer angle with respect to the pulsar spin axis. This yields the proper (cgs) units $\mathrm{erg}^{-1}\mathrm{cm}^{-2}\mathrm{s}^{-1}$. Formally, this may be summarised by the expression

$$\left(\frac{dN}{dE}\right)^{\mathrm{beam}}\left(E_{\mathrm{avg},\,k}, \chi\right) = \frac{1}{2\pi d^2 \sin\zeta\, d\zeta dE_k}\iiint\left[\frac{dL}{d\phi_L dE d\zeta}\right]\frac{I(E_k, dE_k)}{E_{\gamma}^{\mathrm{c}}}\, d\phi_L\, dE\, d\zeta. \tag{A.56}$$

The indicator function $I(E_k, dE_k)$ picks out radiation in the energy range $(E_k, E_k + dE_k)$ (see Section 2.5.10).

The above outlines the calculation of the total beam photon spectrum. If the ζ-integral is evaluated for the interval $(\zeta - d\zeta/2, \zeta + d\zeta/2)$ prior to energy binning, the result is the observer (slice) photon spectrum, denoted by $(dN/dE)^{\mathrm{slice}}$.

A.7 Logarithmic Integration

Consider for example the calculation of the observer integral flux

$$F(>E_1)^{\rm slice} = \int_{E_1}^{\infty} \left(\frac{dN}{dE}\right)^{\rm slice} dE. \tag{A.57}$$

Using the notation of the previous section, and assuming k to be a continuous variable for the moment,

$$\frac{dE_k}{dk} = \delta E_k. \tag{A.58}$$

This can also be derived when k is a discrete value, and $\Delta k = 1$:

$$\begin{aligned}
\frac{\Delta E}{\Delta k} &= E_k - E_{k-1} && \text{(A.59)}\\
&= E_\alpha e^{k\delta}\left(1 - e^{-\delta}\right) && \text{(A.60)}\\
&= E_\alpha e^{k\delta}\left(1 - (1 - \delta - ...)\right) && \text{(A.61)}\\
&\approx \delta E_k. && \text{(A.62)}
\end{aligned}$$

The integral then becomes

$$F(>E_1)^{\rm slice} \approx \sum_{k=m}^{N-1} \left(\frac{dN}{dE}\right)_k^{\rm slice} \delta E_k, \tag{A.63}$$

and E_m is the average energy closest to, but larger than, E_1. Formally, we replaced E_k with $E_{{\rm avg},\,k}$ in the above expression, since the photon spectrum is calculated as a function of the average energy, rather than E_k (The new energy points may be obtained using $E_{{\rm avg},k} = 0.5E_\alpha(1+e^{-\delta})e^{k\delta}$, $k = 1, \cdots, N-1$). The numerical integration is only carried out up to a maximum energy of $E_{\rm f} > E_0$, and the integral will converge, since the integral flux decreases rapidly for energies larger than the cut-off energy E_0. (The value of $E_{\rm f}$ should be chosen to give converging results for the integral).

We have also used exponentially increasing radial steps in some cases when solving for the primary electron's Lorentz factor as function of position, instead of linearly increasing ones. This leads to an increase in computational speed, and the answers (of e.g. total gamma-ray luminosity, and CR cut-off energy) agree within a few percent for these two approaches.

Appendix B

Selected Publications

In this Appendix, we include selected peer-reviewed papers and conference proceedings resulting from collaborative research which were not discussed extensively in the main thesis. These papers deal with the origin and transport of cosmic rays in the context of pulsars and PWN, and references are made to these in the appropriate sections of the main text (Chapter 5).

B.1 Contributions from Nearby Pulsars to the Local Cosmic Ray Electron Spectrum

Reference: Buesching, I., Venter, C., & de Jager, O.C., 2008, *Contributions from Nearby Pulsars to the Local Cosmic Ray Electron Spectrum*, Adv. Space Res., 42, 497-503.

B.1.1 Abstract

PSR J0437-4715 is one of the closest millisecond pulsars (MSPs) to earth, lying at a distance of $\sim$ 140 pc. This pulsar has a characteristic age of 4.9 Gyr and a relatively low spin-down power of $\sim 10^{34}$ ergs/s. During its rather long lifetime, a large fraction of the energy output has been in the form of multi-TeV electrons. In this paper, we investigate the possible contribution of this nearby MSP to the local interstellar electron spectrum (LIS). The old age of the system justifies a steady-state evaluation of the contribution from this pulsar to the LIS. We calculate the electron spectrum at the light cylinder in the framework of a General Relativistic polar cap (PC) model, and use this as an injection spectrum in a diffusion model. The younger Geminga pulsar is also very close to earth and warrants investigation. A steady-state approach is however no longer justified, so we use an impulsive injection model. We will present results of a study of the contribution from these pulsars

to the cosmic-ray LIS. Our calculations show that pulsars like Geminga can make a non-negligible contribution to the LIS.

Subject headings: Millisecond Pulsar — Cosmic Ray Electrons — Geminga — PSR J0437-4715 — Local Interstellar Spectrum

B.1.2 Introduction

A number of studies have been done involving pulsars as sources of cosmic-ray electrons (e.g. Shen, 1970) as well as cosmic-ray protons and iron primaries (Giller & Lipski, 2001; Bednarek & Protheroe, 2002; Bednarek et al., 2005; Bhadra, 2006). In this paper, we investigate the possible contribution of two nearby pulsars to the local cosmic ray electron spectrum: one MSP and one canonical pulsar. PSR J0437-4715 represents the closest known MSP to earth (Johnston et al., 1993), with an estimated distance of 139 ± 3 pc (van Straten et al., 2001). During its long lifetime (it has a characteristic age $\tau = P/2\dot{P}$ of 4.9 Gyr) it has ejected a significant number of particles in the form of multi-TeV electrons, despite its relatively low spin-down power of $\sim 10^{34}$ ergs/s. The second pulsar we investigate is Geminga (PSR J0633+1746). It is also very close, lying at ~ 160 pc, and has a similar spin-down than that of PSR J0437-4715 ($\sim 3.5 \times 10^{34}$ ergs/s), but a much younger characteristic age of $\sim 3.4 \times 10^5$ yr (Caraveo et al., 1996).

(i) Millisecond Pulsars and Canonical Pulsars

The rotation of a pulsar, characterised by the spin-down luminosity $L_{\rm sd} = I\Omega\dot{\Omega}$, with $\Omega = 2\pi/P$ the angular velocity, provides a source of energy which is converted into particle and radiation luminosity with a certain efficiency. We may write (for the pulsar magnetosphere)

$$L_{\rm part} + L_{\rm rad} = (\eta_{\rm part} + \eta_{\rm rad})\, L_{\rm sd}, \tag{B.1}$$

with $\eta_{\rm part}$ and $\eta_{\rm rad}$ the respective efficiencies for converting spin-down luminosity $L_{\rm sd}$ into particle and radiation luminosities ($L_{\rm part}$ and $L_{\rm rad}$).

In the usual polar cap (PC) pulsar model, the pulsar acts as a unipolar inductor, and currents above the PC develop due to the extraction of charges from the stellar surface (Goldreich & Julian, 1969). Extracted electron primaries are accelerated along magnetic field lines by an induced electric field and produce high-energy radiation via curvature and synchrotron radiation, as well as by inverse Compton scattering.

Beyond the light cylinder radius, electron primaries and electron-positron secondaries are injected

into the surrounding pulsar wind nebula (PWN), where they undergo acceleration and further losses. If the system breaks up (and merges with the surrounding interstellar medium), these particles are released and eventually diffuse to earth.

When modelling pulsars, it is important to bear in mind that there are fundamental differences between the canonical (young) and millisecond pulsar (MSP) (old) populations. The most obvious one is the age difference, which implies that different approaches are needed for treating members of different populations. In the case of modelling particle injection by pulsars, it is reasonable to assume that an MSP has reached steady-state, whereas an impulsive injection model is appropriate for a young pulsar due to the rapid decrease of spin-down power.

Another difference between the two pulsar populations may be stated in terms of pair creation and screening of the electric field. Young pulsars are usually capable of producing sufficient electron-positron pairs from high-energy radiation of electron primaries to screen the accelerating electric field over the whole of the PC (Harding et al., 2005b). This means that acceleration of charged particles only occur at low altitudes. High multiplicity numbers, indicating the average number of secondary electron-positron pairs formed in a cascading process due to the radiation of a single electron primary, are thus expected. The opposite is however true for MSPs. Harding & Muslimov (2001, 2002); Harding et al. (2002b) found that the magnetic fields of most MSPs are too low to create significant pairs via curvature radiation, and that the multiplicity of pairs created via inverse Compton scattering is too low to completely screen the accelerating electric field. The implication is that most MSPs continue to accelerate primaries and pairs to high altitudes above the PC.

(ii) Pulsars as Sources of Cosmic Ray Electrons

The observation of several supernova remnants (SNR) in TeV γ-rays have given observational proof that cosmic-ray electrons are accelerated at these sites. Kobayashi et al. (2004) showed that young, nearby SNR can produce distinct features in the LIS at cosmic-ray electron energies above 1 TeV. For a diffusion coefficient proportional to energy to the power δ, we can estimate the minimum energy for cosmic-ray particles from a source with an age T at a distance x as

$$E \leq E_0 \left(\frac{x^2}{2T k_0} \right)^{1/\delta} . \tag{B.2}$$

For Vela with an age of 11 kyr and a distance of 0.3 kpc, Eq. (B.2) yields a minimum energy of $\approx$ 500 GeV for cosmic-ray electrons accelerated by the remnant[1] reaching us now, assuming k_0 =

[1]The particles from the Vela pulsar are still confined in the PWN

$0.1\mathrm{kpc}^2\mathrm{Myr}^{-1}$ (for $E_0 = 1\,\mathrm{GeV}$), whereas particles with energies > 500 GeV from the shell may have reached earth by now, contributing to the diffuse local electron spectrum above this energy. As the pulsars we are considering are rather old, we do not expect them to contribute to the LIS at high energies. Nevertheless, as we show in the subsequent sections, Geminga might make, depending on the pulsar parameters, a non-negligible contribution to the LIS at low energies. Thus if it is possible to experimentally quantify such a contribution one will be able to put constraints on the pulsar parameters.

It is therefore important to consider middle-aged to old pulsars (with ages $> 10^5$ yr), rather than SNR shells, as sources of electrons contributing to the local interstellar cosmic-ray spectrum (LIS) in the GeV to sub-TeV range.

In what follows, we obtain a steady-state electron injection spectrum from a General Relativistic PC model for PSR J0437-4715 , and next parametrise and diffuse it to earth (§ B.1.3). For Geminga, we assume a typical injection spectrum and model the time-dependent propagation of cosmic-ray electrons (§ B.1.4). Finally, we draw conclusions and offer a future outlook (§ B.1.5).

B.1.3 Steady-State Millisecond Pulsar Model: PSR J0437-4715

(i) The Injection Spectrum

In our model, electron primaries are extracted from the stellar surface and accelerated along dipolar magnetic field lines according to

$$\dot{\gamma} \approx \frac{e}{m_e c}\left[E_{||} - \left(\frac{2e}{3\rho_c^2}\right)\gamma^4\right], \tag{B.3}$$

with $\beta = v/c = (1-\gamma^{-2})^{1/2}$ and $E_{||}$ the accelerating electric field parallel to the magnetic field lines. (We only consider curvature radiation producing gamma rays, since this is the dominant radiation process in terms of radiation luminosity L_{rad}).

As in Venter & de Jager (2005a), we use the GR-corrected expressions for a static dipolar magnetic field and curvature radius ρ_c of an oblique pulsar with magnetic moment $\mu = B_0 R^3/2$ inclined at an angle χ relative to the spin axis (Muslimov & Tsygan, 1992). For $E_{||}$, we use the model of Harding et al. (Muslimov & Tsygan, 1992; Muslimov & Harding, 1997; Harding & Muslimov, 1998) for the unscreened case, which includes the effect of GR frame dragging:

$$E_{||}^{\mathrm{near}} = -\frac{\Phi_0}{R}\left\{12\kappa\Theta_0^2 s_1 \cos\chi + 6 s_2 \Theta_0^3 H(1)\delta(1)\sin\chi\cos\phi\right\}, \tag{B.4}$$

with the vacuum potential $\Phi_0 \equiv B_0 \Omega R^2/c$, compactness parameter $\kappa = \epsilon I/MR^2$, $\epsilon = 2GM/Rc^2$, pulsar mass M, polar angle of last closed magnetic field line $\Theta(\eta) \approx [(\Omega R\eta/cf(\eta)]^{1/2}$, $\Theta_0 \equiv \Theta(1)$, and $f(\eta)$ a correction factor of order unity (Harding & Muslimov, 1998). In Eq. (B.4),

$$s_1 = \sum_{i=1}^{\infty} \frac{J_0(k_i\xi)}{k_i^3 J_1(k_i)} \left[1 - e^{-\gamma_i(1)(\eta-1)}\right] \tag{B.5}$$

$$s_2 = \sum_{i=1}^{\infty} \frac{J_1(\tilde{k}_i\xi)}{\tilde{k}_i^3 J_2(\tilde{k}_i)} \left[1 - e^{-\tilde{\gamma}_i(1)(\eta-1)}\right], \tag{B.6}$$

with k_i and $\tilde{k}_i$ the positive roots of the Bessel functions J_0 and J_1, $\xi \equiv \theta/\Theta(\eta)$ the normalised polar angle, ϕ the magnetic azimuthal angle, and $H(1)\delta(1) \approx 1$. Also (see Muslimov & Harding (1997); Harding & Muslimov (1998) for details and definitions of $\tilde{\gamma}_i$,γ_i, $\delta(\eta)$, $H(\eta)$, and $f(\eta)$),

$$E_{||}^{\rm far} \simeq -\frac{\Phi_0}{R}\left(1-\xi^2\right)\Theta_0^2 \left\{\frac{3}{2}\frac{\kappa}{\eta^4}\cos\chi + \frac{3}{8}\Theta(\eta)H(\eta)\delta(\eta)\xi\sin\chi\cos\phi\right\}. \tag{B.7}$$

The 'near' and 'distant' cases for $E_{||}$ correspond to $\eta \simeq 1$ and $\eta \gg 1$, with $\eta = r/R$ the normalised radial coordinate. We next calculate the injection electron spectrum $Q(E)$ at $r_{\rm LC}$ numerically, using

$$Q(E) = I(E, E+dE)\frac{dN(\phi,\theta,r=r_{\rm LC})}{dE}, \tag{B.8}$$

with I the indicator function picking out the energy bin $(E, E+dE)$. Here $dN = -\beta c\rho_e dS/e$ is the rate at which electrons leave a stellar surface patch with area dS, ρ_e being the actual charge density. In the following, we parametrise Q as:

$$Q(E) = K\exp(-\varsigma^2(E-E_{\rm p})^2 - (E/E_0)). \tag{B.9}$$

From this model, we find $\eta_{\rm rad} \sim 0.1$, and $\eta_{\rm part} \sim \eta_{\rm rad}/3$ (evaluated at the light cylinder radius $r_{\rm LC} = c/\Omega$ - similar to Harding et al. (2002b)), and $E_0 \sim 1$ TeV, as can be gathered from Figure B.1, for the parameters of PSR J0437-4715 . By fixing ς and $E_{\rm p}$, we can shift Q both horizontally and vertically by changing E_0 and $\eta_{\rm part}$, and suitably normalising via $\int_0^\infty Q(E)E\,dE = \eta_{\rm part}L_{\rm sd}$.

(ii) Cosmic Ray Electron Propagation

The MSP accelerates cosmic-ray electrons over a time span much larger than the diffusion and loss timescales for cosmic-ray electrons of several GeV. We can therefore describe the propagation in the

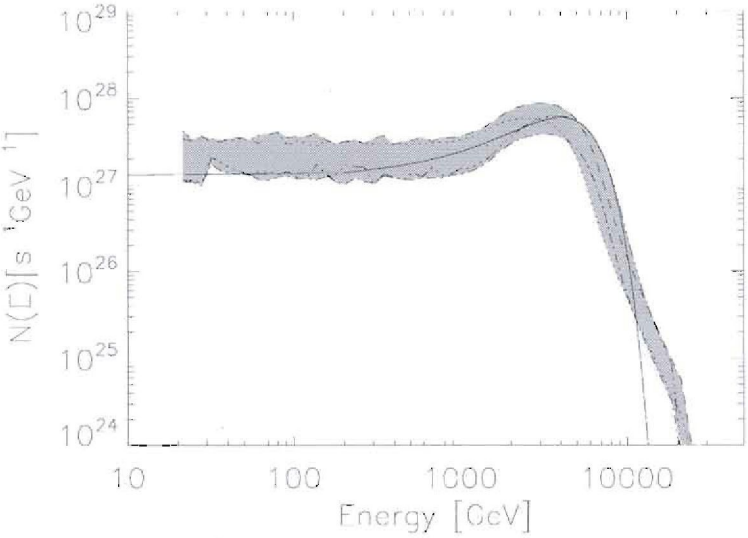

Figure B.1: Electron source spectra for the MSP PSR J0437-4715 at the light cylinder for different source parameters (dashed, dashed-dotted, and dotted lines). The grey region marks the band in which we expect the source spectrum for reasonable source parameters. The solid line marks a fit given by Eq. (B.9).

steady-state diffusion model:

$$-S = \nabla \cdot (k \nabla N) - \frac{\partial}{\partial E}(bN)\,. \tag{B.10}$$

Here, N is the cosmic ray electron density, k the spatial diffusion coefficient, b the rate of continuous losses,

$$S \;=\; Q(E)\delta\left(\vec{r} - \vec{r}_{\rm s}\right) \tag{B.11}$$

the source term, and $\vec{r}_{\rm s}$ the position of the point source. Since no X-ray synchrotron emitting electrons ($E_e > 100\,\mathrm{TeV}$) have been observed as MSP wind nebula, we assume there is no further acceleration of the electrons beyond the light cylinder.

As the source is quite near to earth, boundary effects can be neglected. We thus solve Eq. (B.10) for infinite space using a Green's function, which is given by

$$G(\vec{r}, \vec{r}_0, E, E_0) \;=\; \frac{\exp\left(-\frac{(\vec{r}-\vec{r}_0)^2}{4\int_{E_0}^{E} k/b\, dE}\right)}{b\left(\sqrt{4\pi\left(\int_{E_0}^{E} k/b\, dE\right)}\right)^3}. \tag{B.12}$$

The solution of Eq. (B.10) for an arbitrary source function S is thus given by the convolution

$$N = \int G(\vec{r}, \vec{r_0}, E, E_0) \cdot S(\vec{r_0}, E_0)\, d\vec{r_0} dE_0. \tag{B.13}$$

If we assume losses due to synchrotron radiation and inverse Compton scattering,

$$b = b_0 E^2, \tag{B.14}$$

and use the same form of the spatial diffusion coefficient as inferred from the Boron to Carbon ratio measured at earth,

$$k = k_0 \left(\frac{E}{1\ \mathrm{GeV}}\right)^{0.6}, \tag{B.15}$$

Eq. (B.12) becomes

$$G = \frac{\exp\left(-\frac{(\vec{r}-\vec{r_0})^2}{10(k_0/b_0)\left(-E^{-0.4}+E_0^{-0.4}\right)}\right)}{b_0 E^2 \left(10\pi\,(k_0/b_0)\left(-E^{-0.4}+E_0^{-0.4}\right)\right)^{1.5}}. \tag{B.16}$$

The integral Eq. (B.13) is then solved numerically.

(iii) The Contribution of PSR J0437-4715 to the LIS

We calculated the contribution of electrons from PSR J0437-4715 to the local cosmic ray electron spectrum for a range of Galactic diffusion coefficients. The results are shown in Figure B.2. Our aim was to search in $(E_0, \eta_{\mathrm{part}})$-space for a solution which may, after diffusing to earth, contribute to the LIS for reasonable values of E_0 and η_{part}. However, as is apparent in this plot, the expected flux of cosmic-ray electrons from this pulsar is way below the observed flux, and PSR J0437-4715 is therefore not expected to make a significant contribution to the LIS. Thus not even a very nearby old MSP can give a significant contribution to the local cosmic ray electron spectrum.

B.1.4 Impulsive Injection – Canonical Pulsar Model: Geminga

(i) The Injection Spectrum

Geminga is $\sim 10^4$ times younger than PSR J0437-4715, and its magnetic field is $\sim 10^4$ times higher, implying copious pair production in its magnetosphere. This will significantly modify the injection spectrum $Q(E)$, since one primary electron released from the stellar surface will induce a cascade of

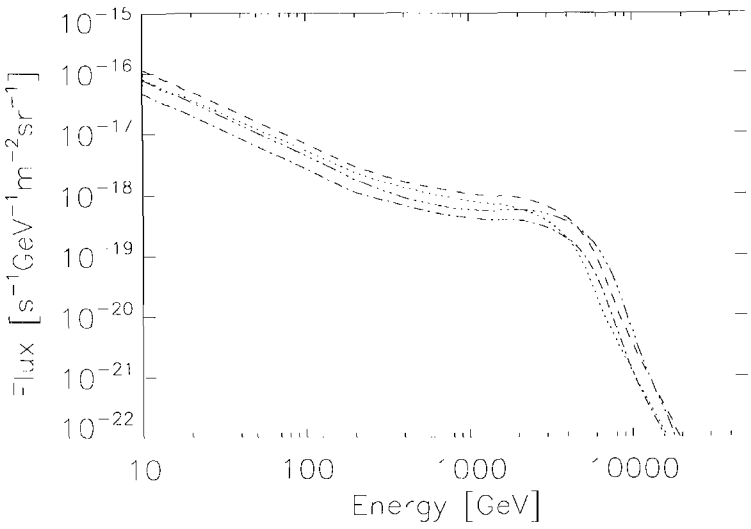

Figure B.2: Propagated spectra at earth from the MSP PSR J0437-4715 .

electron-positron pairs, leading to a significant amplification in the number of injected electrons. This is modelled by introducing a multiplicity M'.

For Geminga, we assume that the electrons from the pulsar were re-accelerated at the pulsar shock, and thus use a power law with spectral index of 2 for the particle spectrum with a maximum energy of

$$E_{\rm max}(t) = \epsilon e C \sqrt{\left(\frac{\sigma}{\sigma+1}\right)\frac{\dot{L}_{\rm sd}(t)}{c}}, \tag{B.17}$$

where C is the compression ratio at the shock. This maximum energy stems from the condition that the ratio of the Lamour radius to the radius of the pulsar shock should be less than a fraction ϵ in order to ensure particle confinement. For our calculations we assume $\epsilon = 0.1$, $C = 3$. We use a magnetisation parameter $\sigma = 0.1$ as given by Sefako & de Jager (2003) for Vela-like pulsars. The fraction of the spin-down power deposited in electrons then is

$$\eta_{\rm part} = \frac{1}{1+\sigma}. \tag{B.18}$$

We further assume that these electrons are confined in the PWN until they are released after a time T (in seconds) from the formation of the PWN. The energy losses of the electrons inside the PWN

are taken into account by introducing a break in the electron spectrum at

$$E_{\rm break} = \frac{422}{B_{\rm PWN}^2 T} \quad [\rm erg], \tag{B.19}$$

where $B_{\rm PWN}$ is the magnetic field inside the PWN measured in units of Gauss (we use here an average value of 6μG). Thus we have for the source function

$$Q(E) = K \begin{cases} (E/E_{\rm break})^{-2} & , \quad \text{for } E < E_{\rm break} \\ (E/E_{\rm break})^{-3} & , \quad \text{for } E \geq E_{\rm break} \end{cases} . \tag{B.20}$$

The curvature of the observed spectrum of the VHE γ-ray source *H.E.S.S.* 1825-137, which is associated with the Vela-like PSR B1823-13, can be explained by a such a broken power law spectrum (Aharonian et al., 2006d).

Rather than attempting to model such a source with unknown evolutionary parameters (see e.g. Bednarek & Bartosik (2003) on the modelling), we infer the leptonic parameters of relatively aged PWN (such as *H.E.S.S.* J1825-137) directly from *H.E.S.S.* observations of the inverse Compton signal (de Jager, 2007), showing that the observed γ-ray spectral break near 1 TeV is consistent with a particle spectral turnover from a E^{-2} to E^{-3} shape for a relatively low field strength of $B_{\rm PWN} \sim 2\mu$G and an age of ~ 20 kyr. This low field strength also explains why this source is less luminous in X-rays compared to VHE γ-rays (de Jager & Djannati-Ataï, 2008). This PWN is also the largest in our galaxy and the low pressure associated with its large size makes it plausible that this source is now starting to merge with the ISM to release leptons. Thus, given the absence of detailed model parameters, we rather assume that *H.E.S.S.* J1825-137 (with an evolved Vela-like pulsar) represents the evolution of a typical canonical pulsar. We therefore assume that the model presented below, describes the final state of such a PWN satisfactorily, so that we can scale the total lepton output in terms of the birth period and spin-down timescale. The birth period also sets the amount of GeV electrons contributing to the LIS, since these electrons do not suffer radiation losses compared to those above the break.

The normalisation K was derived from the condition

$$N_e = \int Q(E) dE = \int^T \int Q'(E,t)\, dE\, dt, \tag{B.21}$$

where N_e is the total number of particles in the PWN before breakup. $Q'(E,t) = K' E^{-2}$ for each

time has to satisfy

$$\int_{E_{\rm min}}^{E_{\rm max}} Q'(E,t)dE = \frac{M' I_{\rm GJ}}{e} \quad \text{(B.22)}$$

$$\int_{E_{\rm min}}^{E_{\rm max}} Q'(E,t)EdE = \eta_{\rm part} L_{\rm sd}(t). \quad \text{(B.23)}$$

Using a value of 100 MeV for $E_{\rm min}$, Eq. (B.22,B.23) also yield the multiplicity M' at a given time. In Eq. (B.22), $I_{\rm GJ}$ represents the Goldreich-Julian current (Sturrock, 1971):

$$I_{\rm GJ} \approx 2c\rho_{\rm GJ} A_{\rm PC} \approx \frac{B_0 \Omega^2 R^3}{c}, \quad \text{(B.24)}$$

with $\rho_{\rm GJ}$ the Goldreich-Julian charge density (Goldreich & Julian, 1969), and $A_{\rm PC} \approx \pi R_{\rm PC}^2$ the PC area.

When assuming that the pulsar magnetic field does not decay (i.e. $\dot{P}P^{n-2} = \dot{P}_0 P_0^{n-2}$), the time-evolution of $L_{\rm sd}$ is given by (Reynolds & Chevalier, 1984)

$$L_{\rm sd}(t) = L_{\rm sd,0}\left(1 + \frac{t}{\tau_0}\right)^{-\frac{n+1}{n-1}}, \quad \text{(B.25)}$$

with $n = 3$ representing a dipolar magnetic field, and $\tau_0 = P_0/((n-1)\dot{P}_0)$, P_0 the birth period, and $\dot{P}_0$ the period's time-derivative at pulsar birth. These quantities are connected to the spin-down luminosity at birth via

$$L_{\rm sd,0} = -\frac{4\pi^2 I \dot{P}_0}{P_0^3}. \quad \text{(B.26)}$$

The variation of $L_{\rm sd}$ with time for an initial period of 40 ms (van der Swaluw & Wu, 2001; Bhadra, 2006) is plotted in Figure B.3.

(ii) Time-Dependent Propagation of Cosmic Ray Electrons

Modelling the propagation of electrons injected during a short period in time, we have to use the time-dependent propagation model. Instead of Eq. (B.10) we thus have

$$\frac{\partial N}{\partial t} - S = k\Delta N - \frac{\partial}{\partial E}(bN), \quad \text{(B.27)}$$

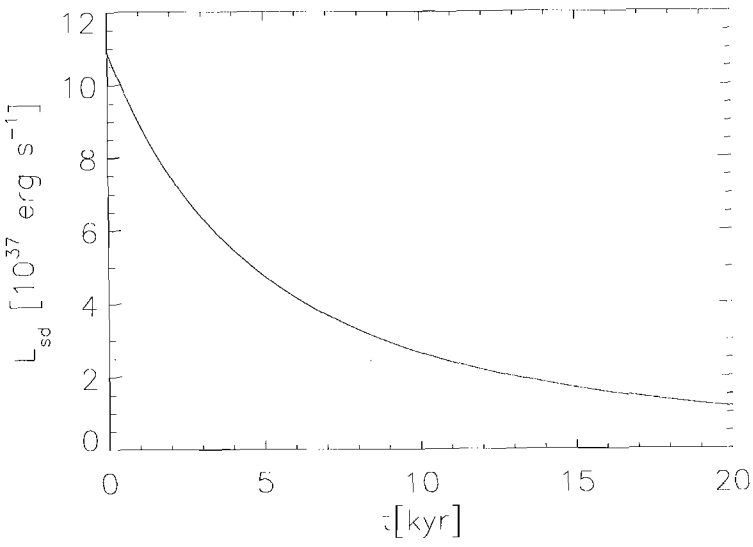

Figure B.3: Spindown power $L_{\rm sd}(t)$ of Geminga, assuming an initial period of 40 ms.

which, by the same argument as for PSR J0437-4715, we solve for infinite space. A Green's function solving Eq. (B.27) in this case can be found in the literature (Berezinskii et al., 1990). It is given by

$$G(\vec{r},\vec{r_0},E,E_0,t,t_0) = \delta\left(t-t_0-\frac{1}{b_0}\left(E_0^{-1}-E^{-1}\right)\right)\frac{\exp\left(-\frac{(\vec{r}-\vec{r_0})^2}{\lambda}\right)}{b(\pi\lambda)^{1.5}}, \tag{B.28}$$

with

$$\lambda = 4\frac{k_0\left(E^{-0.4}\right)-E_0^{-0.4}}{0.4\,b_0}, \tag{B.29}$$

where we have used Eq. (B.14,B.15). In analogy to Eq. (B.13), the solution of Eq. (B.27) is given by

$$N = \int G(\vec{r},\vec{r_0},E,E_0,t,t_0)\cdot S(\vec{r_0},E_0,t_0)d\vec{r_0}dE_0dt_0. \tag{B.30}$$

For a point source at $\vec{r_s}$, with a spectrum $Q(E)$ as given by Eq. (B.20) releasing particles at a time t_s, we have

$$S = \delta\left(\vec{r}-\vec{r_s}\right)\delta\left(t-t_s\right)Q(E), \tag{B.31}$$

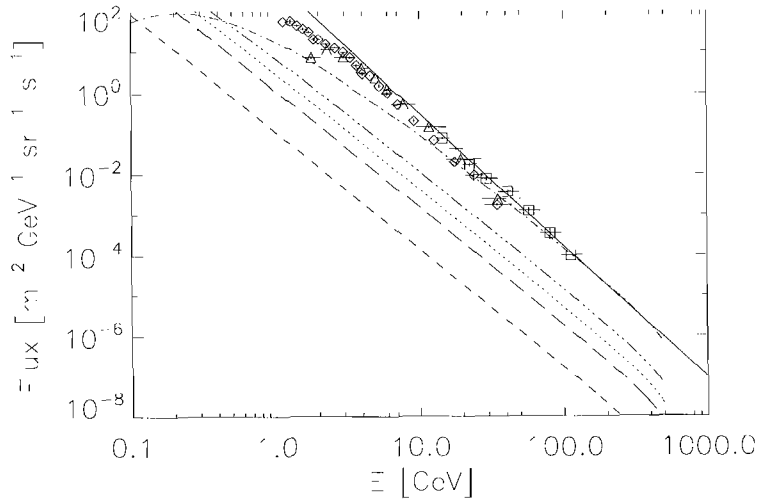

Figure B.4: Contribution to the local (interstellar) cosmic ray electron spectrum for diffusion coefficients of k_0=0.01 kpc^{2}Myr^{-1} (dash-dotted), k_0=0.05 kpc^{2}Myr^{-1} (dash-dot-dotted), k_0=0.1 kpc^{2}Myr^{-1} (dotted), k_0=0.2 kpc^{2}Myr^{-1} (long-dashed) and k_0=1.0 kpc^{2}Myr^{-1} (dashed) for a distance of 157 pc, compared to data from Boezio et al. (2000) (diamonds), Torii et al. (2001) (boxes) and DuVernois et al. (2001) (triangles). The solid line is a power law fit $\propto E^{-3}$ to the data.

and the convolution can be done analytically, thus

$$N = \frac{\exp\left(-\frac{(\vec{r}-\vec{r_0})^2}{\lambda}\right)}{b_0^2 E^2 (\pi\lambda)^{1.5} E_0^2} \left(\left(\Theta\left(E_{\rm break} - E_0\right)\Theta\left(E_0 - E_{\rm min}\right) E_0^{-2}\right) + \left(\Theta\left(E_{\rm max} - E_0\right)\Theta\left(E_0 - E_{\rm break}\right) E_0^{-3}\right)\right), \quad \text{(B.32)}$$

where

$$E_0 = \frac{E}{(t - t_s)\, b_0 E + 1}, \quad \text{(B.33)}$$

and Θ is the Heaviside step function.

(iii) The Contribution of Geminga to the LIS

We calculated the contribution of Geminga to the local cosmic ray electron spectrum where we assumed a distance of 157 pc (Caraveo et al., 1996) and a typical birth period of $P_0 \sim 40$ ms as suggested by van der Swaluw & Wu (2001); Bhadra (2006). A release time of $T = 10$ kyr was chosen. The results of our calculations are plotted in Figure B.4, where we compare the obtained cosmic ray electron flux for different values for the cosmic ray electron diffusion coefficient with data from from Boezio

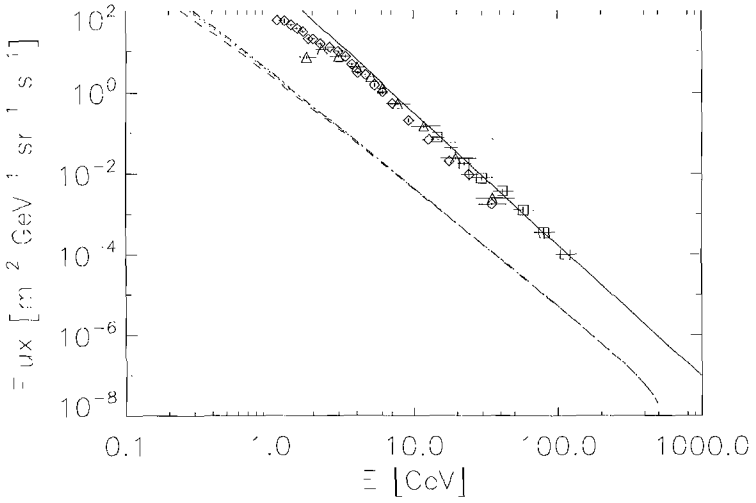

Figure B.5: Same as Figure B.4, for k_0=0.1 kpc^{2}Myr^{-1} and different source distances of 123 pc (dash-dotted), 157 pc (dotted), and 216 pc (dashed).

et al. (2000) (diamonds), Torii et al. (2001) (boxes), and DuVernois et al. (2001) (triangles) for the local electron flux. We inferred the local interstellar electron spectrum using the force field model of solar modulation, assuming a modulation parameter of 600 MV. As can be seen, for a typical diffusion coefficient with k_0=0.1 kpc^{2}Myr^{-1}, we expect a contribution from Geminga to the LIS of the order of some percent. If we decrease k_0 by a factor of 10 however, Geminga might even account for almost all of the cosmic-ray electrons below 1 TeV. On the other hand, as shown in Figure B.5, the uncertainties in distance, as given in Caraveo et al. (1996), seem to affect the results of our calculation only marginally. As there is only little knowledge on the magnitude of the release time T for the particles in the PWN, we also performed calculations for $T = 5$ kyr and $T = 20$ kyr. The results are given in Figure B.6. As can be seen there, the variation of T results only in minor changes of the model output.

A full parameter study is beyond the scope of this article and will be given elsewhere.

B.1.5 Conclusion

We performed a study on the possible contribution of nearby pulsars to the local cosmic ray electron spectrum. In particular, we investigated the contributions from the MSP PSR J0437-4715, a rather old object, and the canonical pulsar Geminga.Our calculations show that the contribution of PSR J0437-4715 to the cosmic-ray electrons observed locally is negligible, in agreement with the finding of Shen (1970) that the continuous production of cosmic-ray electrons from old pulsars is not sufficient to produce the local cosmic ray electron spectrum.

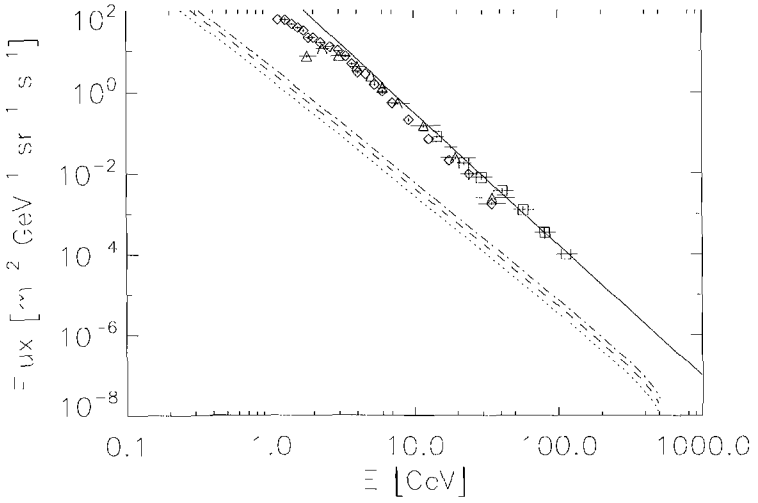

Figure B.6: Same as Figure B.4, for k_0=0.1 kpc^{2}Myr^{-1} and different release times T =5 kyr (dotted), 10 kyr (dashed), and 20 kyr (dash-dotted).

Geminga, depending on the magnitude of the diffusion coefficient, might contribute between a fraction of a percent and almost 100% of the locally observed cosmic ray electron flux below 1 TeV. We further showed that for Geminga, the uncertainties of the distance as given by Caraveo et al. (1996) do not lead to significant changes in the cosmic-ray spectrum expected locally. Also, a change in the release time T does not yield large changes in our model output.

B.1.6 Acknowledgments

This publication is based on work supported by the South African National Research Foundation under grant 2053475.

B.2 Constraints on the Lepton Content of PWN from the Local Cosmic Ray Positron Spectrum

Reference: Buesching, I., de Jager, O.C., Potgieter, M.S., & Venter, C., 2007, *Constraints on the Lepton Content of PWN from the Local Cosmic Ray Positron Spectrum*, Conf. Proc. of the 30th ICRC Conference in Mérida, Mexico.

B.2.1 Abstract

Geminga is a nearby pulsar with an age of 3.42×10^5 yr and a spin-down power of 3.2×10^{34} erg/s at present. B0656+14 has comparable spin-down power, with an age of 1.11×10^5 yr and a distance of 290 pc. The winds of these pulsars had most probably powered PWN that broke up less than about 100 kyr after the birth of these pulsars. Assuming that leptonic particles accelerated by the pulsars were confined in the PWN and got released into the interstellar medium on breakup of the PWN, we calculate the contribution of these particles to the locally observed cosmic ray electron and positron spectra. Our calculations show that within the framework of our model, the local cosmic ray positron spectrum imposes constraints on pulsar parameters for Geminga and B0656+14, e.g. the pulsar period at birth, and also the local interstellar diffusion coefficient for cosmic-ray leptons. Further, as both pulsars are located at almost the same position in the sky, we expect an anisotropy in the local cosmic ray positron flux.

B.2.2 Introduction

Geminga and B0656+14 are the closest pulsars with intrinsic ages in the range of 100 kyr to 1Myr Manchester et al. (2005). They both have spin-down powers of the order 3×10^{34} erg/s at present. The winds of these pulsars had most probably powered pulsar wind nebulae (PWN) that broke up less than about 100 kyr after the births of the pulsars.

Assuming that leptonic particles accelerated by the pulsars were confined in the PWN and got released into the interstellar medium on breakup of the PWN, we calculate the contribution of these particles to the locally observed cosmic ray electron and positron spectra.

Our calculations show that within the framework of our model, the local cosmic ray positron spectrum imposes constraints on pulsar parameters for Geminga and B0656+14, e.g. the pulsar period at birth, and also the local interstellar diffusion coefficient for cosmic-ray leptons.

B.2.3 The Positron LIS

The cosmic ray positron spectrum has been measured by several groups in the last decades Aguilara et al. (2002); Boezio et al. (2000); DuVernois et al. (2001). In Figure B.7 we show some recent measurements at the top of the atmosphere and also the local interstellar spectrum (LIS) as derived from modulation studies.

The heliospheric modulation of cosmic-ray electrons and positrons is primarily caused by four mechanisms: convection by the solar wind, diffusion because of turbulence in the heliospheric magnetic

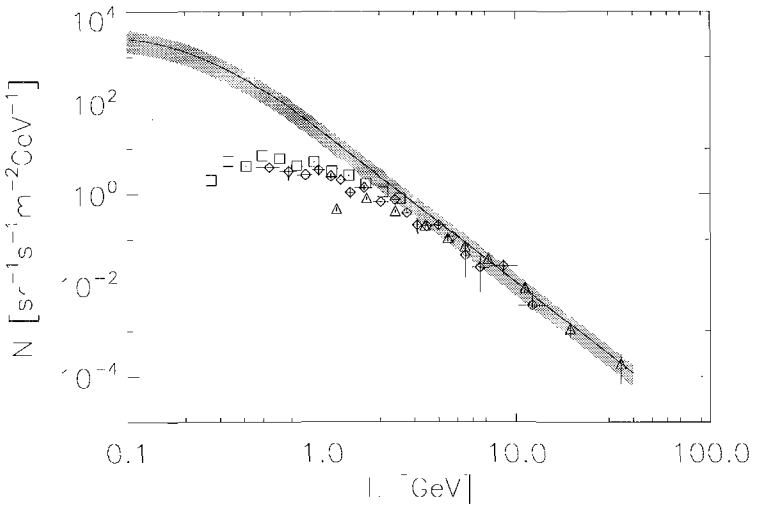

Figure B.7: Positron flux at earth from Aguilara et al. (2002) (boxes), Boezio et al. (2000) (diamonds) and DuVernois et al. (2001) (triangles) and the local interstellar positron spectrum as inferred from solar modulation studies (solid line). The grey band marks the possible range of the LIS Potgieter & Langner (2004).

field (HMF), gradient and curvature drifts caused by the global structure of the HMF, and adiabatic energy losses. The latter is large for cosmic-ray nuclei and causes characteristically shaped modulated spectra at earth below kinetic energy $E <\approx 200$ MeV, with the differential intensity proportional to E^{+1}.

This process is so effective that irrespective of the spectral slope of the LIS of cosmic-ray nuclei with $E <\approx 200$ MeV, the modulated spectra at earth will have a E^{+1} form at these energies (e.g. Moraal & Potgieter (1982)). LISs for cosmic-ray nuclei at these low energies will therefore only be observed when spacecraft crosses the heliopause into the interstellar medium (Ferreira & Potgieter, 2002). However, for electrons and positrons the energy losses are significantly less because they spend much less time in the expanding solar wind as relativistic particles before reaching earth than e.g. galactic protons. The result is that at $E <\approx 200$ MeV, modulated electron and positron spectra at earth will already exhibit spectral slopes closely resembling that of the LIS.

B.2.4 Positrons from PWN

The relatively high surface magnetic fields of 1.63×10^{12} G and 4.66×10^{12} G for Geminga and B0656+14 respectively, imply copious pair production in the magnetospheres of these pulsars, even more when they were young, leading to a significant amplification in the number of injected electrons

and thus also to a number of positrons comparable to that of the electrons. Within the framework of polar cap (PC) pulsar models, a single primary electron released from the stellar surface will induce a cascade of electron-positron pairs, and we model this amplification by introducing a multiplicity M'. We assume that the electrons and positrons from the pulsar are re-accelerated at the pulsar shock, and model the particle spectrum by a power law with spectral index of 2, and with a maximum energy of

$$E_{\rm max} = \epsilon e \kappa \sqrt{\left(\frac{\sigma}{\sigma+1}\right)\frac{L_{\rm sd}}{c}}, \tag{B.34}$$

where κ is the compression ratio at the shock, $L_{\rm sd}$ the spin-down power, and σ the magnetization parameter. This maximum energy stems from a condition on particle confinement: we require that the ratio between the Lamour radius and the radius of the pulsar shock should be less than a fraction ϵ. We assume that $\epsilon = 0.01 - 1$, $\kappa = 3$, and use σ =0.01 – 1 (Sefako & de Jager (2003) propose a value of $\sigma = 0.1$ for Vela-like pulsars).

The fraction of the spin-down power deposited in particles is

$$\eta_{\rm part} = \frac{1}{1+\sigma}. \tag{B.35}$$

We assume that these particles are confined in the PWN for a time T [sec], after which they are released into the surrounding interstellar medium. A break in the leptonic spectrum is enforced to take the maximum energy losses in the PWN into account:

$$E_{\rm b} = \frac{422}{B_{\rm PWN}^2 T} \quad [\rm erg], \tag{B.36}$$

where $B_{\rm PWN}$ is the magnetic field inside the PWN measured in units of Gauss. Thus we have for the source function (at the PWN radius)

$$Q(E) = K \begin{cases} (E/E_{\rm b})^{-2} & , \text{for } E < E_{\rm b} \\ (E/E_{\rm b})^{-3} & , \text{for } E > E_{\rm b} \end{cases}.$$

One might expect that Q describes electrons and positrons occurring in equal abundances, and that the eventual positron spectrum would be $Q/2$. However, simulations of ultrarelativistic shockwaves in proton-electron-positron plasmas by Amato & Arons (2006) showed that the energy of positrons might dominate that of electrons when they are non-thermally accelerated, depending on the upstream flow energy of the ions. Helfand et al. (2001) observed a significant increase in the flux of the Vela PWN's

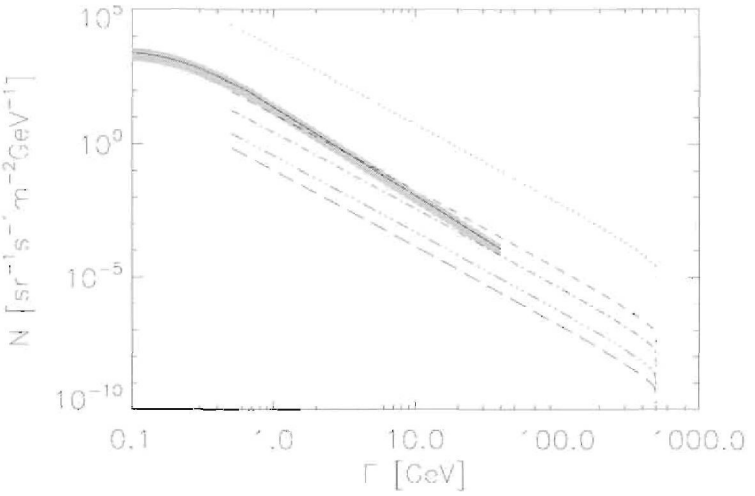

Figure B.8: Expected cosmic ray positron spectra for $k_0 = 0.13\,\mathrm{kpc^2 Myr^{-1}}$, $\sigma = 0.1$, $T = 12\,\mathrm{kyr}$ and for birth periods of P_0=1 ms (dotted), 14 ms (dashed), 35 ms (dash-dotted), 70 ms (dash-trippledotted) and 100 ms (long-dashed) compared to the positron LIS (solid line).

outer arc, similar to the brightening of the Crab's wisps. If this brightening is due to ion cyclotron waves, we might plausibly expect that the presence of ions in PWN might be universal, so that ions will also be found in Geminga. Thus, Q might in some cases be regarded as the full positron spectrum.

We normalize Q by using the condition that the following equations have to be valid at any time

$$\int_{E_{\rm min}}^{E_{\rm max}} Q'(E,t)dE = \frac{M' I_{\rm GJ}}{e} \tag{B.37}$$

$$\int_{E_{\rm min}}^{E_{\rm max}} Q'(E,t)EdE = \eta_{\rm part} L_{\rm sd}(t), \tag{B.38}$$

with $Q'(E,t) = K'E^{-2}$ the particle spectrum at the pulsar wind shock. Conservation of particles relates Q' and Q:

$$\int_0^T \int_{E_{\rm min}}^{E_{\rm max}} Q'(E,t)\,dE\,dt = \int_{E_{\rm min}}^{E_{\rm max}} Q(E)dE. \tag{B.39}$$

We estimate the lower energy $E_{\rm min}$ by assuming that it should be similar to the inferred value of the Crab. Using a value of 500 MeV for $E_{\rm min}$, Eq. (B.37,B.38) also yield the multiplicity M' at a given time. The choice for $E_{\rm min}$ stems from the fact that this is also the energy at which the positron LIS starts to bend over. In Eq. (B.37), $I_{\rm GJ}$ represents the Goldreich-Julian current:

$$I_{\rm GJ} \approx 2c\rho_{\rm GJ}A_{\rm PC} \approx \frac{B_{\rm s}\Omega^2 R^3}{c} = \sqrt{6cL_{\rm sd}}, \tag{B.40}$$

with B_s the pulsar dipolar field strength at the pole, ρ_{GJ} the Goldreich-Julian charge density (Goldreich & Julian (1969)), and $A_{PC} \approx \pi R_{PC}^2$ the PC area.

For a pulsar magnetic field that does not decay (i.e. $\dot{P}P^{n-2} = \dot{P}_0 P_0^{n-2}$), the time-evolution of L_{sd} is given by Rees & Gunn (1974)

$$L_{sd}(t) = L_{sd,0}\left(1 + \frac{t}{\tau_0}\right)^{-\frac{n+1}{n-1}}, \tag{B.41}$$

with $n = 3$ representing a dipolar magnetic field, and $\tau_0 = P_0/((n-1)\dot{P}_0)$, P_0 the birth period, and $\dot{P}_0$ the period's time-derivative at pulsar birth (the subscript '0' denotes quantities at pulsar birth). These quantities are connected to the spin-down luminosity at birth via

$$L_{sd,0} = -\frac{4\pi^2 I \dot{P}_0}{P_0^3}. \tag{B.42}$$

The total number of particles in the PWN before breakup, is then

$$N_e = \iint Q'(E,t)\, dE\, dt. \tag{B.43}$$

The propagation of cosmic-ray electrons and positrons in case of the diffusion coefficient k being spatially constant, is described by

$$\frac{\partial N}{\partial t} - S = k\Delta N - \frac{\partial}{\partial p}(b\,N), \tag{B.44}$$

where N is the differential number density, S the source term and b the rate of energy losses. A Green's function solving Eq. (B.44) can be found in the literature (e.g. Ginzburg & Syrovatskii (1964)). For a functional form of the diffusion coefficient $k = k_0 p^{3/5}$ and the energy losses $b = b_0 p^2$ (i.e. synchrotron and inverse Compton losses) the Greens's function is

$$G = \delta\left(t - t_0 - \frac{E_0^{-1} - E^{-1}}{b_0}\right) \times \frac{\exp\left(-\frac{(\vec{r}-\vec{r_0})^2}{\lambda}\right)}{b_0 E^2 (\pi\lambda)^{1.5}}, \tag{B.45}$$

and $\lambda = 10\left(k_0\left(E^{-0.4}\right) - E_0^{-0.4}\right)/b_0$. For a point source at $\vec{r_s}$, with a spectrum $Q(E)$ as given by

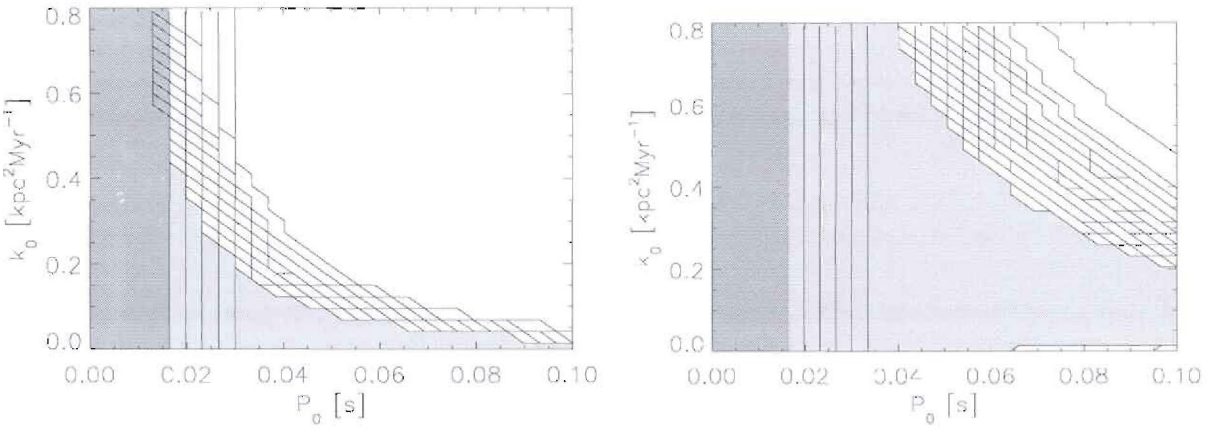

Figure B.9: Tolerable magnitude k_0 of the interstellar diffusion coefficient against the pulsar birth period P_0 (white region) for different model parameters (T =20 kyr, 0.001< ϵ <0.1, 0.01< σ < 1), for Geminga (left) and B0656+14 (right) assuming the contribution of each pulsar is 50% to the cosmic ray positron flux as shown in Figure B.7. Note that we can exclude pulsar birth periods $<\approx$ 20 ms (dark grey region), as these produce lepton numbers in the PWN in excess of $N_e = 10^{52}$ which have not been observed.

Eq. (B.2.4) releasing particles at a time t_s, the convolution can be done analytically, thus

$$\begin{aligned} N &= \frac{\exp\left(-\frac{(\vec{r}-\vec{r}_0)^2}{\lambda}\right)}{b_0^2\, E^2 (\pi\lambda)^{1.5} E_0^2} \\ &\times \left(\left(\Theta\left(E_\mathrm{b} - E_0\right) - \Theta\left(E_0 - E_\mathrm{min}\right) E_0^{-2}\right)\right. \\ &+ \left.\left(\Theta\left(E_\mathrm{max} - E_0\right) - \Theta\left(E_0 - E_\mathrm{b}\right) E_0^{-3}\right)\right) \end{aligned} \tag{B.46}$$

where $E_0 = E/\left(\left(t - t_s\right) b_0 E + 1\right)$. We calculated the contribution from Geminga and B0656+14 to the positron LIS for distances of 157 pc Caraveo et al. (1996) and 290 pc Manchester et al. (2005) respectively. The results for different birth periods of Geminga are plotted in Figure B.8, where we compare our calculation with the positron LIS discussed earlier. From Figure B.8 one can see that for the chosen set of parameters, we can rule out $P_0 < 35$ ms for Geminga.

B.2.5 Conclusions

We have shown that one can expect a non-neglible cosmic ray lepton component in the LIS from nearby pulsars. In the context of our model we are able to constrain the permissible P_0-k_0-space (Figure B.9). This opens a new way to obtain information on the properties of young, nearby pulsars and will therefore help to refine the models for pulsars and PWN. In this study we did not discuss the magnitude of the contribution of secondary positrons to the LIS. Reliable estimates of the contribution

from a prominent, nearby point source may be obtained from measurements of spatial anisotropies stemming from a local gradient in the cosmic ray positron distribution.

B.2.6 Acknowledgements

This work is supported by the SA National Research Foundation and the SA Centre for High Performance Computing.

B.3 A Cosmic Ray Positron Anisotropy due to Two Middle-Aged, Nearby Pulsars?

Reference: Buesching, I., de Jager, O.C., Potgieter, M.S., & Venter, C., 2008, Astrophys. J. Lett., 678, L39-L42.

B.3.1 Abstract

Geminga and B0656+14 are the closest pulsars with characteristic ages in the range of 100 kyr to 1 Myr. They both have spin-down powers of the order 3×10^{34} erg/s at present. The winds of these pulsars had most probably powered pulsar wind nebulae (PWNe) that broke up less than about 100 kyr after the birth of the pulsars. Assuming that leptonic particles accelerated by the pulsars were confined in the PWNe and were released into the interstellar medium (ISM) on breakup of the PWNe, we show that, depending on the pulsar parameters, both pulsars make a non-negligible contribution to the local cosmic ray positron spectrum, and they may be the main contributors above several GeV. The relatively small angular distance between Geminga and B0656+14 thus implies an anisotropy in the local cosmic ray positron flux at these energies. We calculate the contribution of these pulsars to the locally observed cosmic ray electron and positron spectra depending on the pulsar birth period and the magnitude of the local cosmic ray diffusion coefficient. We further give an estimate of the expected anisotropy in the local cosmic ray positron flux. Our calculations show that within the framework of our model, the local cosmic ray positron spectrum imposes constraints on pulsar parameters for Geminga and B0656+14, notably the pulsar period at birth, and also the local interstellar diffusion coefficient for cosmic-ray leptons.

Subject headings: pulsars: individual (Geminga, B0656+14) — acceleration of particles — cosmic rays — diffusion

B.3.2 Introduction

Geminga and B0656+14 are the closest pulsars with characteristic ages in the range of 100 kyr to 1 Myr (Manchester et al., 2005). They both have spin-down powers of the order 3×10^{34} erg/s at present. The winds of these pulsars had most probably powered pulsar wind nebulae (PWNe) that broke up less than about 100 kyr after the birth of the pulsars. The reason for this statement is that we do not observe PWNe associated with pulsars older than 100 kyr.

Assuming that leptonic particles accelerated by the pulsars prior to breakup were confined in the PWNe and were released into the interstellar medium (ISM) on breakup of the PWNe (i.e. when the pressure of the ambient ISM exceeds the magnetic pressure $B^2/(8\pi)$ in the PWN), we calculate the contribution of these particles to the locally observed cosmic ray electron and positron spectra. We further calculate the expected anisotropy in the positron local interstellar spectrum (LIS) in the case of energy-dependent diffusion.

B.3.3 Positrons from PWNe

We discuss the acceleration of particles by pulsars in the framework of the polar cap (PC) model (see e.g. the review of Baring, 2004). Given the relatively high surface magnetic fields of $B_s = 1.6\text{e}12$ G and $B_s = 4.7\text{e}12$ G for Geminga and B0656+14 respectively, a single primary electron released from the stellar surface will induce a cascade of electron-positron pairs in the magnetospheres of these pulsars. This amplification is modeled by introducing a multiplicity M'. The flux of primary electrons from the pulsar PC is given by the Goldreich-Julian current:

$$I_{\rm GJ} \approx 2c\rho_{\rm GJ}A_{\rm PC} \approx \frac{B_{\rm s}\Omega^2 R^3}{c} = \sqrt{6cL_{\rm sd}}, \tag{B.47}$$

with $\rho_{\rm GJ}$ the Goldreich-Julian charge density (Goldreich & Julian, 1969), and $A_{\rm PC} \approx \pi R_{\rm PC}^2$ the PC area.

We assume that the electrons and positrons from the pulsar are re-accelerated at the pulsar shock, and model the particle spectrum by a power law with spectral index of 2, and with a maximum energy of (Venter & de Jager, 2006)

$$E_{\rm max} = \epsilon e \kappa \sqrt{\left(\frac{\sigma}{\sigma+1}\right)\frac{L_{\rm sd}}{c}}, \tag{B.48}$$

where κ is the compression ratio at the shock, $L_{\rm sd}$ the spin-down power, and σ the magnetization parameter (Kennel & Coroniti, 1984). This maximum energy stems from a condition on particle

confinement: we require that the ratio between the Lamor radius r_L and the radius r_S of the pulsar shock should be less than unity. We assume a maximum ratio $\epsilon = r_L/r_S = 0.1$ and that for larger Lamor radii, the curvature of the shock results in particle losses. For the calculations presented in this paper, we assume $\kappa = 3$. As observations suggest that σ depends on the age of the pulsar ($\sigma = 0.003$ is found for the Crab pulsar (Kennel & Coroniti, 1984), which has an age of 1 kyr, but $\sigma = 0.1$ for 11 kyr Vela (Sefako & de Jager, 2003)), we thus assume

$$\sigma(t) = \sigma_0 \left(\frac{t}{1\,\mathrm{kyr}}\right)^{3/2}, \tag{B.49}$$

with $\sigma_0 = 0.003$. The fraction of the spin-down power deposited in particles can be written in terms of the magnetization parameter σ (Buesching et al., 2008b):

$$\eta_{\mathrm{part}} = f\frac{1}{1+\sigma}. \tag{B.50}$$

Here, we introduce a geometry factor $f = \Omega_{\mathrm{acc}}/(4\pi)$, as σ is supposed to be significantly less than unity (Kennel & Coroniti, 1984), implying a large η_{part}. Without f, from Eq. (B.50) η_{part} is of the order unity for $\sigma \ll 1$. This however is in contradiction with observations, indicating $\eta_{\mathrm{part}} \ll 1$, as found e.g. for the Vela PWN (Sefako & de Jager, 2003). We adopt $f = 1/2$.

At any time the conditions

$$\int_{E_{\mathrm{min}}}^{E_{\mathrm{max}}} Q'(E,t)dE = \frac{M' I_{\mathrm{GJ}}}{e} \tag{B.51}$$

$$\int_{E_{\mathrm{min}}}^{E_{\mathrm{max}}} Q'(E,t)EdE = \eta_{\mathrm{part}} L_{\mathrm{sd}}(t) \tag{B.52}$$

have to hold (Sefako & de Jager, 2003), where $Q'(E,t) = K'E^{-2}$ is the assumed particle spectrum at the pulsar wind shock. E_{min} is assumed to be similar to the inferred value of the Crab. A value of 100 MeV is adopted.

For a non-decaying pulsar magnetic field (i.e. $\dot{P}P^{n-2} = \dot{P}_0 P_0^{n-2}$), the time-evolution of L_{sd} is given by Rees & Gunn (1974)

$$L_{\mathrm{sd}}(t) = L_{\mathrm{sd},0}\left(1+\frac{t}{\tau_0}\right)^{-\frac{n+1}{n-1}}, \tag{B.53}$$

with $n = 3$ representing a dipolar magnetic field, and $\tau_0 = P_0/((n-1)\dot{P}_0)$, P_0 the birth period, and $\dot{P}_0$ the period's time-derivative at pulsar birth. (The subscript '0' denotes quantities at pulsar birth).

These quantities are connected to the spin-down luminosity at birth via

$$L_{\rm sd,0} = \left| -\frac{4\pi^2 I \dot{P}_0}{P_0^3} \right| . \tag{B.54}$$

We assume that the particles are confined in the PWN for a time T, after which the PWN breaks up and releases them into the surrounding ISM. The time evolution of the particle spectrum $Q(E,t)$ inside the PWN is described by

$$\frac{\partial Q(E,t)}{\partial t} - Q'(E,t) = \frac{\partial}{\partial E}\left(B_{\rm PWN}(t)^2 E^2 Q(E,t) \right), \tag{B.55}$$

where we assumed a decaying magnetic field in the PWN

$$B_{\rm PWN}(t) \;=\; \frac{1200}{(1+t/{\rm kyr})^2}\ [\mu{\rm G}]. \tag{B.56}$$

This parametrization for B is justified as follows. After 10 to 20 kyr, the PWN field strength is already of the order of 5 μG as observed by *H.E.S.S.* from a number of PWN (see e.g. de Jager, 2008) and after $\sim$ 100 kyr we expect that the ISM pressure will randomize the PWN field structure, leading to relatively fast diffusive escape of charged particles from the nebula. Although the actual age for breakup is difficult to estimate, we assume to a first order a number of less than 100 kyr. *GLAST* observations of a limiting age for mature PWN may shed more light on this epoch of breakup (de Jager, 2008).

Eq. (B.55) can be solved using the Green's function formalism. The particle spectrum at time T is given by

$$Q(E,T) \;=\; \int_0^T Q'(E_0,t_0) E_0^2 E^{-2} \Theta\left(E_0 - E_{\rm min}\right) \Theta\left(E_{\rm max} - E_0\right) dt_0, \tag{B.57}$$

where Θ is the Heaviside step function and

$$E_0 \;=\; \frac{E}{E\int_t^{t_0} B_{\rm PWN}(t')^2 dt' + 1}. \tag{B.58}$$

Our model predicts $\approx$equal numbers of positrons and electrons to be accelerated by pulsars, thus Eq. (B.57) also describes the source function for cosmic-ray electrons.

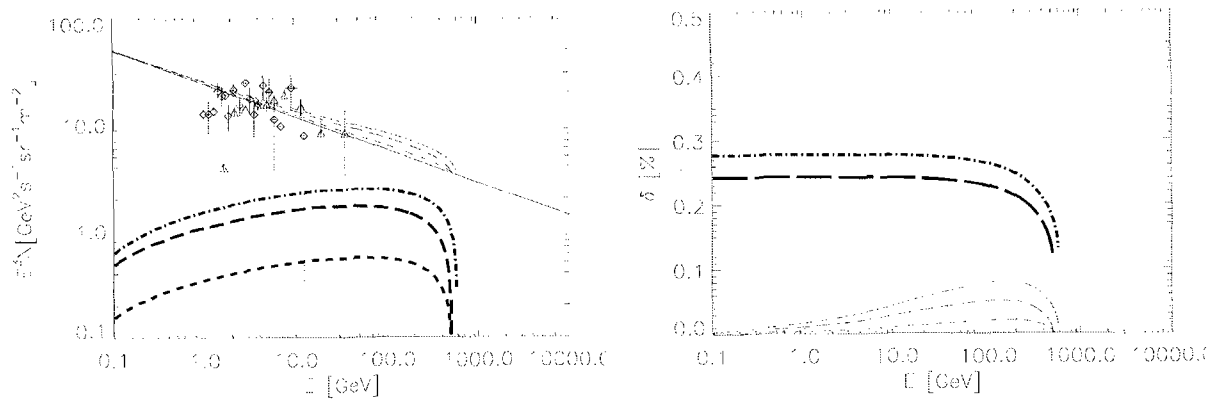

Figure B.10: Left panel: Contribution of Geminga to the positron LIS for $k_0 = 0.1\,\mathrm{kpc}^2\,\mathrm{Myr}^{-1}$ and $P_0 = 40\,\mathrm{ms}$, $T = 20\,\mathrm{kyr}$ (long dashed line), $P_0 = 40\,\mathrm{ms}$, $T = 60\,\mathrm{kyr}$ (dot-dashed line), and $P_0 = 60\,\mathrm{ms}$, $T = 20\,\mathrm{kyr}$ (dashed) on top of an isotropic background (solid line). The thin lines mark the combined spectra (pulsar contribution plus background), whereas the thick lines give the contribution of the pulsar alone. Also shown are data from Boezio et al. (2000) (diamonds) and DuVernois et al. (2001) (triangles). Right panel: the expected local anisotropy in case only Geminga contributes to the LIS (thick lines), and in case Geminga contributes on top of an isotropic background positron flux (thin lines) as given by Barwick et al. (1998) (solid line in left panel). The line styles correspond to the cases as given for the left panel. The thick dashed and long dashed lines coincide.

B.3.4 Propagation of Cosmic Ray Positrons and Local Anisotropy

The propagation of cosmic-ray electrons and positrons in case of the diffusion coefficient k being spatially constant, is described by

$$\frac{\partial N}{\partial t} - S = k\Delta N - \frac{\partial}{\partial E}(bN), \tag{B.59}$$

where N is the differential number density, S the source term, Δ the Lapace operator, and b the rate of energy losses. For a functional form of the diffusion coefficient $k = k_0 E^\alpha$, with $\alpha = 3/5$ and the energy losses $b = b_0 E^2$ (i.e. synchrotron and inverse Compton losses) one can find a Green's function solving Eq. (B.59) in the literature (Berezinskii et al., 1990). It is given by

$$G(\vec{r}, \vec{r_0}, E, E_0, t, t_0) = \delta\left(t - t_0 - \frac{1}{b_0}\left(E_0^{-1} - E^{-1}\right)\right) \frac{\exp\left(-\frac{(\vec{r}-\vec{r_0})^2}{\lambda}\right)}{b(\pi\lambda)^{1.5}}, \tag{B.60}$$

with

$$\lambda = 4\frac{k_0\left(E^{\alpha-1} - E_0^{\alpha-1}\right)}{(1-\alpha)\,b_0}. \tag{B.61}$$

Thus, the solution of Eq. (B.59) is given by

$$N = \int\int\int G(\vec{r}, \vec{r_0}, E, E_0, t, t_0) Q(E_0) \delta(t_0 - t_i)\, \delta(\vec{r_0} - \vec{r_i})\, dE_0 dt_0 d\vec{r_0}, \tag{B.62}$$

where $Q(E_0)$ is given by Eq. (B.57), $\vec{r_i}$ and t_i are the place and time of injection, repectively. We note, that the energy E of a particle at time t is linked to its energy E_0 at injection by

$$E_0 = E/\left((t - t_i)\, b_0 E + 1\right). \tag{B.63}$$

The anisotropy in the cosmic-ray flux can be calculated in the context of diffusion as (Ginzburg & Syrovatskii, 1964)

$$\delta = \frac{I_{\max} - I_{\min}}{I_{\max} + I_{\min}} = \frac{3\, k\, |\nabla N|}{c\, N}, \tag{B.64}$$

where ∇N denotes the gradient of N. The expected anisotropy in the positron LIS was calculated assuming the contribution of a nearby source, as given by Eq. (B.62), on top of an isotropic background. For the background we assumed a power law fit given by Barwick et al. (1998). The calculated anisotropies are given in the right panels of Figures B.10 and B.11 (thin lines).

To get an estimate of the maximum expected anisotropy, we also calculate the anisotropy assuming that the whole cosmic ray positron flux originates from a point source (thick lines in the right panels of Figures B.10 and B.11). For energy-independent diffusion, Mao & Shen (1972) derived the simple relation

$$\delta = \frac{3}{2c} \frac{r_i}{t_i}. \tag{B.65}$$

Allowing for energy-dependent diffusion, we get, inserting Eq. (B.62) into Eq. (B.64),

$$\delta = \frac{3}{2\,c} r_i\, b_0\, (\alpha - 1)\, E^{\alpha} \left(E^{\alpha-1} - E_0^{\alpha-1}\right)^{-1}. \tag{B.66}$$

As in the case of Eq. (B.65), Eq. (B.66) also does not depend on the magnitude of the diffusion coefficient, only on the distance r_i to the source, and via Eq. (B.63), on the time since the injection of the particles into the ISM. In the limit of $E \rightarrow 0$, Eq. (B.66) reduces to Eq. (B.65).

We calculated the contribution from Geminga and B0656+14 to the positron LIS for distances of 157 pc (Caraveo et al., 1996) and 290 pc (Manchester et al., 2005) respectively (assuming $T = 20$ kyr and $T = 60$ kyr), in addition to the expected anisotropies in the positron LIS. The results for birth

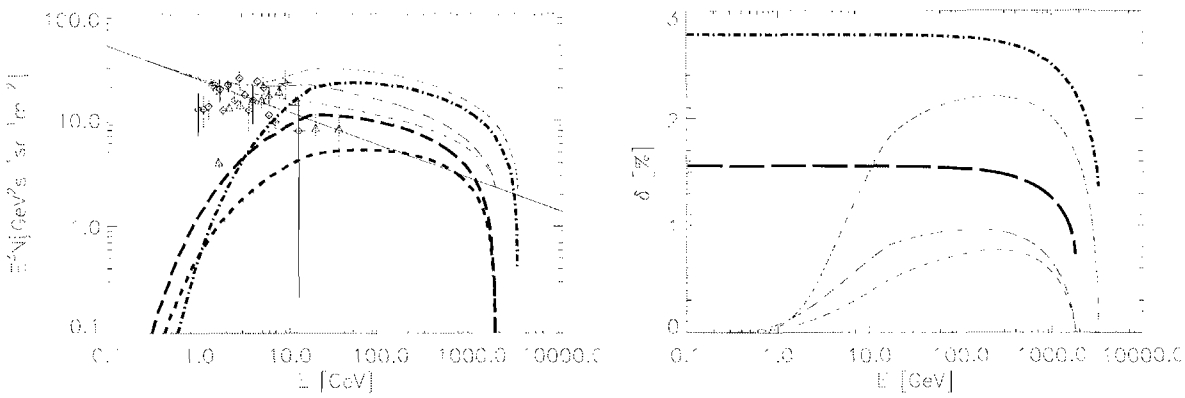

Figure B.11: Same as Figure B.10 but for B0656+14.

periods of 40 ms and 60 ms are plotted in the left panels of Figures B.10 and B.11, where we compare our calculations with the measurements from Boezio et al. (2000) and DuVernois et al. (2001).

B.3.5 Conclusions

We have shown that one can expect a non-negligible cosmic ray positron component in the LIS from nearby pulsars that may become dominant above several GeV, in agreement with Atoyan et al. (1995) who showed that the high-energy positron LIS may be explained by a young, nearby source. In the context of our model, we are able to constrain the permissible pulsar birth period P_0, depending on the magnitude of the interstellar diffusion coefficient. For the two nearest pulsars with characteristic ages in the range 1×10^5 yr to 1×10^6 yr, Geminga and B0656+14, we show that in particular for B0656+14 one can expect, in the absence of a background flux, an anisotropy in the positron LIS of up to almost 3%, significantly larger than the expected value of $\approx$0.25% for Geminga. As shown in Figures B.10 and B.11, the observed anisotropy also gives an estimate of the contribution of the pulsar to the positron LIS. On the other hand, a measured anisotropy larger than the $\approx$3% we obtained for B0656+14 would be, from Eq. (B.65) and Eq. (B.66), an indication of the existence of an even younger, nearby source, e.g. a longer lifetime T of the PWN. We also note that the predicted flux from PSR B0656+14 appears to overpredict the observed flux above 10 GeV. This implies more severe constraints on the pulsar output, whereas Geminga's parameters are not that severely constrained by cosmic ray positron observations.

We remark that Galactic cosmic rays, including electrons and positrons, are subjected to solar modulation at energies below $\approx$10 GeV. The encounter of these particles with the solar wind and imbedded magnetic field causes a heliospheric anisotropy that is primarily determined by the combined

modulation effects of convection, diffusion, and drifts - all solar cycle dependent. Drifts will cause this anisotropy to have a 22-year cycle. Cosmic ray electrons and positrons at 1 GeV at earth may therefore exhibit a heliospheric anisotropy of up to a few percent, assuming that they enter the heliosphere isotropically (Potgieter & Langner, 2004).

It will be an interesting exercise to determine how this anisotropy will change if the LIS is anisotropic. However, the anisotropy that we predict here is the largest above 10 GeV, an energy range at which only the *PAMELA* mission (Boezio et al., 2004) may be able to gather sufficient statistics to find an anisotropy of the predicted magnitude.

B.3.6 Acknowledgments

This work is supported by the SA National Research Foundation and the SA Centre for High Performance Computing.

Bibliography

Aguilara, M. et al. 2002, Phys. Rep., 366, 331

Aharonian, F. et al. 2004a, Nature, 432, 75

—. 2004b, A&A, 425, L13

—. 2005a, Science, 307, 1938

—. 2005b, A&A, 435, L17

—. 2005c, A&A, 432, L25

—. 2006a, A&A, 460, 743

—. 2006b, Nature, 440, 1018

—. 2006c, Nature, 439, 695

—. 2006d, A&A, 460, 365

—. 2006e, Science, 314, 1424

—. 2006f, ApJ, 636, 777

—. 2007, A&A, 466, 543

—. 2008, in preparation

Aharonian, F. A. et al. 2002, A&A, 395, 803

Albert, J. et al. 2006, ApJL, 638, L101

Alpar, M. A., Cheng, A. F., Ruderman, M. A., & Shaham, J. 1982, Nature, 300, 728

Amato, E. 2003, Chinese Journal of Astron. Astrophys. Suppl., 3, 316

Amato, E. & Arons, J. 2006, ApJ, 653, 325

Arendt, Jr., P. N. & Eilek, J. A. 2002, ApJ, 581, 451

Armitage, P. J. & Natarajan, P. 1999, ApJ, 525, 909

Arons, J. 1981, ApJ, 248, 1099

—. 1983, ApJ, 266, 215

—. 1996, A&A Suppl., 120, C49

Arons, J. & Scharlemann, E. T. 1979, ApJ, 231, 854

Atoyan, A. M., Aharonian, F. A., & Völk, H. J. 1995, Phys. Rev. D, 52, 3265

Atwood, W. B. 2006, Adv. Space Res., 37, 1862

Baade, W. 1942, ApJ, 96, 188

Baade, W. & Zwicky, F. 1934, Proc. Nat. Acad. Sci. 20, 254

Backer, D. C., Kulkarni, S. R., Heiles, C., Davis, M. M., & Goss, W. M. 1982, Nature, 300, 615

Backer, D. C. & Sallmen, S. T. 1997, Astron. J., 114, 1539

Backus, P. R., Taylor, J. H., & Damashek, M. 1982, ApJL, 255, L63

Bailes, M. & Lorimer, D. 1995, in ASP Conf. Ser., Vol. 72, Millisecond Pulsars. A Decade of Surprise, ed. A. S. Fruchter, M. Tavani, & D. C. Backer, 17

Bailyn, C. D. 1993, ApJL, 411, L83

Baring, M. G. 2000, in AIP Conf. Ser., Vol. 516, Proc. 26th Int. Cosmic Ray Conf., ed. B. L. Dingus, D. B. Kieda, & M. H. Salamon, 153

Baring, M. G. 2004, Adv. Space Res., 33, 552

Baring, M. G. & Harding, A. K. 2001, ApJ, 547, 929

Barret, D. et al. 1994, A&A, 288, 472

Barwick, S. W. et al. 1998, ApJ, 498, 779

Beatty, J. J. et al. 2004, Phys. Rev. Lett., 93, 241102

Becker, W. & Pavlov, G. G. 2002, The Century of Space Science, ed. J. Bleeker et al. (Dordrecht: Kluwer, astro-ph/0208356)

Becker, W. & Trümper, J. 1993, Nature, 365, 528

—. 1997, A&A, 326, 682

—. 1999, A&A, 341, 803

Becker, W., Trümper, J., Brazier, K. T. S., & Belloni, T. 1993, IAU Circ., 5701, 2

Becker, W. et al. 2003, ApJ, 594, 798

Bednarek, W. & Bartosik, M. 2003, A&A, 405, 689

Bednarek, W. & Protheroe, R. J. 2002, Astropart. Phys., 16, 397

Bednarek, W. & Sitarek, J. 2007, MNRAS, 377, 920

Bednarek, W. et al. 2005, in Proc. 29th Int. Cosmic Ray Conf., Vol. 6, 349

Bélanger, G. et al. 2006, ApJ, 636, 275

Bell, J. F., Bailes, M., & Bessell, M. S. 1993, Nature, 364, 603

Bell, J. F., Bailes, M., Manchester, R. N., Lyne, A. G., Camilo, F., & Sandhu, J. S. 1997, MNRAS, 286, 463

Bell, J. F., Bailes, M., Manchester, R. N., Weisberg, J. M., & Lyne, A. G. 1995, ApJL, 440, L81

Berezinskii, V. S., Bulanov, S. V., Dogiel, V. A., & Ptuskin, V. S. 1990, Astrophysics of Cosmic Rays (Amsterdam: North-Holland, edited by Ginzburg, V.L.)

Beskin, V. S. 1990, Soviet Astron. Lett., 16, 286

Beskin, V. S. & Malyshkin, L. M. 1998, MNRAS, 298, 847

Bhadra, A. 2006, Astropart. Phys., 25, 226

Bhattacharya, D. & van den Heuvel, E. P. J. 1991, Phys. Rep., 203, 1

Blandford, R. D., Romani, R. W., & Applegate, J. H. 1987, MNRAS, 225, 51P

Blondin, J. M., Chevalier, R. A., & Frierson, D. M. 2001, ApJ, 563, 806

Blumenthal, G. R. & Gould, R. J. 1970, Rev. Mod. Phys., 42, 237

Boezio, M. et al. 2000, ApJ, 532, 653

—. 2004, Nuclear Phys. B Proc. Suppl., 134, 39

Bogdanov, S., Grindlay, J. E., Heinke, C. O., Camilo, F., Freire, P. C. C., & Becker, W. 2006a, ApJ, 646, 1104

Bogdanov, S., Grindlay, J. E., & Rybicki, G. B. 2006b, ApJL, 648, L55

Bogdanov, S., Rybicki, G. B., & Grindlay, J. E. 2007, ApJ, 670, 668

Bowers, R. L. & Deeming, T. 1984, Astrophysics I - Stars (Boston: Jones & Bartlett Publishers, Inc.)

Bowyer, S., Byram, E. T., Chubb, T. A., & Friedman, H. 1964, Nature, 201, 1307

Bucciantini, N. 2002a, A&A, 387, 1066

—. 2002b, A&A, 393, 629

—. 2008a, Adv. Space Res., 41, 491

Bucciantini, N. 2008b, in AIP Conf. Ser., Vol. 983, 186

Bucciantini, N., Amato, E., & Del Zanna, L. 2005, A&A, 434, 189

Bucciantini, N. & Bandiera, R. 2001, A&A, 375, 1032

Bucciantini, N., Blondin, J. M., Del Zanna, L., & Amato, E. 2003, A&A, 405, 617

Buesching, I., de Jager, O. C., Potgieter, M. S., & Venter, C. 2007a, in Proc. 30th Int. Cosmic Ray Conf. (in press)

Buesching, I., de Jager, O. C., Potgieter, M. S., & Venter, C. 2008a, ApJL, 678, L39

Buesching, I., de Jager, O. C., & Snyman, J. 2007b, ApJ, 656, 841

Buesching, I., Venter, C., & de Jager, O. C. 2008b, Adv. Space Res., 42, 497

Bulik, T. & Rudak, B. 1999, Astrophys. Lett. Comm., 38, 37

Bulik, T., Rudak, B., & Dyks, J. 2000, MNRAS, 317, 97

Burgay, M. et al. 2003, Nature, 426, 531

Burns, M. L. & Harding, A. K. 1984, ApJ, 285, 747

Cameron, P. B., Rutledge, R. E., Camilo, F., Bildsten, L., Ransom, S. M., & Kulkarni, S. R. 2007, ApJ, 660, 587

Camilo, F., Lorimer, D. R., Freire, P., Lyne, A. G., & Manchester, R. N. 2000, ApJ, 535, 975

Camilo, F. & Rasio, F. A. 2005, in ASP Conf. Ser., Vol. 328, Binary Radio Pulsars, ed. F. A. Rasio & I. H. Stairs (San Francisco: ASP), 147

Camilo, F., Thorsett, S. E., & Kulkarni, S. R. 1994, ApJL, 421, L15

Caraveo, P. A. 2006, in ESA Special Publication, Vol. 604, The X-ray Universe 2005, ed. A. Wilson, 131

Caraveo, P. A., Bignami, G. F., Mignani, R., & Taff, L. G. 1996, ApJL, 461, L91

Carroll, B. W. & Ostlie, D. A. 1996, An Introduction to Modern Astrophysics (Addison Wesley Publishing Co., Inc.)

Carson, J. E. 2006, ArXiv Astrophysics e-prints (astro-ph/0610960)

Catanese, M. & Weekes, T. C. 1999, Proc. Astron. Soc. Pac., 111, 1193

Chen, K., Ruderman, M., & Zhu, T. 1998, ApJ, 493, 397

Chen, W. C. & Li, X. D. 2006, A&A, 450, L1

Cheng, K. S., Ho, C., & Ruderman, M. 1986a, ApJ, 300, 500

—. 1986b, ApJ, 300, 522

Cheng, K. S., Ruderman, M., & Zhang, L. 2000, ApJ, 537, 964

Cheng, K. S. & Taam, R. E. 2003, ApJ, 598, 1207

Cheng, K. S., Taam, R. E., & Wang, W. 2006, ApJ, 641, 427

Chevalier, R. A. 2004, Adv. Space Res., 33, 456

Chiang, J. & Romani, R. W. 1992, ApJ, 400, 629

—. 1994, ApJ, 436, 754

Chiu, H. Y. & Salpeter, E. E. 1964, Phys. Rev. Lett., 12, 413

Cocke, W. J., Disney, M. J., & Taylor, D. J. 1969, Nature, 221, 525

Cognard, I. & Backer, D. C. 2004, ApJL, 612, L125

Cognard, I., Bourgois, G., Lestrade, J.-F., & Biraud, F. 1995, in ASP Conf. Ser., Vol. 72, Millisecond Pulsars. A Decade of Surprise, ed. A. S. Fruchter, M. Tavani, & D. C. Backer, 369

Cognard, I., Bourgois, G., Lestrade, J.-F., Biraud, F., Aubry, D., Darchy, B., & Drouhin, J.-P. 1996, A&A, 311, 179

Cognard, I. & Lestrade, J.-F. 1997, A&A, 323, 211

Danner, R., Kulkarni, S. R., Saito, Y., & Kawai, N. 1997, Nature, 388, 751

Danner, R., Kulkarni, S. R., & Thorsett, S. E. 1994, ApJL, 436, L153

Danziger, I. J., Baade, D., & della Valle, M. 1993, A&A, 276, 382

Daugherty, J. K. & Harding, A. K. 1982, ApJ, 252, 337

—. 1983, ApJ, 273, 761

—. 1994, ApJ, 429, 325

—. 1996, ApJ, 458, 278

Daugherty, J. K. & Lerche, I. 1975, Astrophys. Space Sci., 38, 437

—. 1976, Phys. Rev. D, 14, 340

Daum, A. 2001, in Towards a Major Atmospheric Čerenkov Detector - V, ed. O. C. de Jager, 178

De Angelis, A., Mansutti, O., & Persic, M. 2007, ArXiv Astrophysics e-prints (astro-ph/0712.0315)

de Jager, O. & Venter, C. 2005, in Towards a Network of Atmospheric Cherenkov Detectors VII, ed. B. Degrange & G. Fontaine (astro-ph/0511098)

de Jager, O. C. 2005, in Astrophysical Sources of High Energy Particles and Radiation, AIP Conf. Ser., ed. T. Bulik, B. Rudak, & G. Madejski, Vol. 801, 298

de Jager, O. C. 2007, ApJ, 658, 1177

—. 2008, ApJL, 678, L113

de Jager, O. C. & Djannati-Ataï, A. 2008, to appear in Lecture Notes in Physics, ArXiv Astrophysics e-prints (astro-ph/0803.0116)

de Jager, O. C., Harding, A. K., Sreekumar, P., & Strickman, M. 1996, A&A Suppl., 120, C441

de Jager, O. C., Konopelko, A., Raubenheimer, B. C., & Visser, B. 2001, Proc. 27th Int. Cosmic Ray Conf., 613

de Naurois, M. et al. 2005, in Proc. 29th Int. Cosmic Ray Conf., Vol. 4, 101

Del Zanna, L., Bucciantini, N., & Londrillo, P. 2003, A&A, 400, 397

Del Zanna, L., Volpi, D., Amato, E., & Bucciantini, N. 2006, A&A, 453, 621

Del Zanna, L., Zanotti, O., Bucciantini, N., & Londrillo, P. 2007, A&A, 473, 11

Deutsch, A. J. 1955, Annales d'Astrophysique, 18, 1

Djannati-Atai, A., de Jager, O. C., Terrier, R., Gallant, Y. A., & Hoppe, S. 2007, in Proc. 30th Int. Cosmic Ray Conf. (in press)

DuVernois, M. A. et al. 2001, ApJ, 559, 296

Duyvendak, J. J. L. 1942, Proc. Astron. Soc. Pac., 54, 91

Dyks, J., Frąckowiak, M., Słowikowska, A., Rudak, B., & Zhang, B. 2005, ApJ, 633, 1101

Dyks, J., Harding, A. K., & Rudak, B. 2004a, ArXiv Astrophysics e-prints (astro-ph/0403428)

—. 2004b, ApJ, 606, 1125

Dyks, J. & Rudak, B. 2000, A&A, 362, 1004

—. 2002, A&A, 393, 511

—. 2003, ApJ, 598, 1201

Dyks, J., Rudak, B., & Bulik, T. 2001, in ESA Special Publication, Vol. 459, Exploring the Gamma-Ray Universe, ed. A. Gimenez, V. Reglero, & C. Winkler, 191

Dyks, J., Rudak, B., & Harding, A. K. 2004c, ApJ, 607, 939

Dyks, J., Rudak, B., & Rankin, J. M. 2007, A&A, 465, 981

Edelstein, J., Foster, R. S., & Bowyer, S. 1995, ApJ, 454, 442

Eifert, T. 2005, Diploma thesis, Humboldt-Universität zu Berlin

Enomoto, R. et al. 2002, Astropart. Phys., 16, 235

Erber, T. 1966, Rev. Mod. Phys., 38, 626

Erickson, W. C., Mahoney, M. J., Becker, R. H., & Helfand, D. J. 1987, ApJL, 314, L45

Fawley, W. M., Arons, J., & Scharlemann, E. T. 1977, ApJ, 217, 227

Fernández, R. & Reisenegger, A. 2005, ApJ, 625, 291

Ferraro, F. R., Possenti, A., D'Amico, N., & Sabbi, E. 2001, ApJL, 561, L93

Ferreira, S. E. S. & Potgieter, M. S. 2002, J. Geophys. Res. (Space Phys.), 107, 1221

Fichtel, C. E., Hartman, R. C., Kniffen, D. A., Thompson, D. J., Ogelman, H., Ozel, M. E., Tumer, T., & Bignami, G. F. 1975, ApJ, 198, 163

Fierro, J. M. et al. 1995, ApJ, 447, 807

Flowers, E. G., Ruderman, M. A., Lee, J.-F., Sutherland, P. G., Hillebrandt, W., & Mueller, E. 1977, ApJ, 215, 291

Forman, W., Jones, C., Cominsky, L., Julien, P., Murray, S., Peters, G., Tananbaum, H., & Giacconi, R. 1978, ApJS, 38, 357

Foster, R. S., Backer, D. C., Taylor, J. H., & Goss, W. M. 1988, ApJL, 326, L13

Foster, R. S., Fairhead, L., & Backer, D. C. 1991, ApJ, 378, 687

Frail, D. A. & Moffett, D. A. 1993, ApJ, 408, 637

Frąckowiak, M. & Rudak, B. 2005a, Advances in Space Research, 35, 1152

—. 2005b, Memorie della Societa Astronomica Italiana, 76, 523

Freire, P. C., Camilo, F., Kramer, M., Lorimer, D. R., Lyne, A. G., Manchester, R. N., & D'Amico, N. 2003, MNRAS, 340, 1359

Friedman, R. A. & Kaufmann, III, W. J. 2002, Universe (6^{th} ed.; New York: W.H. Freeman and Co.)

Fritz, G., Henry, R. C., Meekins, J. F., Chubb, T. A., & Friedman, H. 1969, Science, 164, 709

Fruchter, A. S., Stinebring, D. R., & Taylor, J. H. 1988, Nature, 333, 237

Funk, S. 2007, in AIP Conf. Ser., ed. S. Ritz, P. Michelson, & C. A. Meegan, Vol. 921, 393

Funk, S., Carson, J. E., Giebels, B., Longo, F., McEnery, J. E., Paneque, D., Reimer, O., & Reyes, L. C. 2007, in AIP Conf. Ser., ed. S. Ritz, P. Michelson, & C. A. Meegan, Vol. 921, 379

Funk, S., LAT Collab. Pulsars, G., SNR, & Plerions group. 2006, in Bull. Am. Astron. Soc., Vol. 38, 1107

Gaensler, B. M. 2001, in AIP Conf. Ser., Vol. 565, Young Supernova Remnants, ed. S. S. Holt & U. Hwang, 295

Gaensler, B. M. 2005, Adv. Space Res., 35, 1116

Gaensler, B. M., Pivovaroff, M. J., & Garmire, G. P. 2001, ApJL, 556, L107

Gaensler, B. M. & Slane, P. O. 2006, Ann. Rev. Astron. Astrophys., 44, 17

Gallant, Y. A. 2007, Astrophys. Space Sci., 309, 197

Gallant, Y. A. et al. 2008, in 40 Years of Pulsars: Millisecond Pulsars, Magnetars and More, AIP Conf. Ser., Vol. 983, 195

Giacconi, R., Gursky, H., Paolini, F. R., & Rossi, B. B. 1962, Phys. Rev. Lett., 9, 439

Gil, J. & Krawczyk, A. 1996, in ASP Conf. Ser., Vol. 105, IAU Colloq. 160: Pulsars: Problems and Progress, ed. S. Johnston, M. A. Walker, & M. Bailes, 213

Gil, J. & Krawczyk, A. 1997, MNRAS, 285, 561

Giller, M. & Lipski, M. 2001, in Proc. 27th Int. Cosmic Ray Conf., Vol. 6, 2092

Ginzburg, V. L. & Syrovatskii, S. I. 1964, The Origin of Cosmic Rays (New York: Macmillan)

—. 1965, Ann. Rev. Astron. Astrophys., 3, 297

—. 1969, Ann. Rev. Astron. Astrophys., 7, 375

Gold, T. 1968, Nature, 218, 731

—. 1969, Nature, 221, 25

Golden, A., Butler, R. F., & Shearer, A. 2001, A&A, 371, 198

Goldreich, P. & Julian, W. H. 1969, ApJ, 157, 869

Gonthier, P. L. & Harding, A. K. 1994, ApJ, 425, 767

Gonthier, P. L., Ouellette, M. S., Berrier, J., O'Brien, S., & Harding, A. K. 2002, ApJ, 565, 482

Gonthier, P. L., Story, S. A., Clow, B. D., & Harding, A. K. 2007, Astrophys. Space Sci., 309, 245

Gonthier, P. L., Van Guilder, R., & Harding, A. K. 2004, ApJ, 604, 775

Gothoskar, P. & Gupta, Y. 2000, ApJ, 531, 345

Gotthelf, E. V. 2004, in IAU Symposium, Vol. 218, Young Neutron Stars and Their Environments, ed. F. Camilo & B. M. Gaensler, 225

Gratton, R. G., Bragaglia, A., Carretta, E., Clementini, G., Desidera, S., Grundahl, F., & Lucatello, S. 2003, A&A, 408, 529

Gray, A. D. 1994, MNRAS, 270, 835

Green, D. A. 1984, MNRAS, 209, 449

Griffiths, D. J. 1999, Introduction to Electrodynamics (3^{rd} ed.; New Jersey: Prentice-Hall, Inc.)

Grindlay, J. E., Camilo, F., Heinke, C. O., Edmonds, P. D., Cohn, H., & Lugger, P. 2002, ApJ, 581, 470

Haas, M. R. & Ross, D. K. 1975, Astrophys. Space Sci., 32, 3

Halliday, D., Resnick, R., & Walker, J. 1997, Fundamentals of Physics, Extended (5^{th} ed.; New York: John Wiley & Sons, Inc.)

Halpern, J. P. & Holt, S. S. 1992, Nature, 357, 222

Halpern, J. P., Martin, C., & Marshall, H. L. 1996, ApJ, 462, 908

Hamilton, T. T., Helfand, D. J., & Becker, R. H. 1985, Astron. J., 90, 606

Hansen, B. M. S. & Phinney, E. S. 1998, MNRAS, 294, 569

Harding, A. & Muslimov, A. 2005, Astrophys. Space Sci., 297, 63

Harding, A. K. 1981, ApJ, 245, 267

Harding, A. K. 1995, in Millisecond Pulsars. A Decade of Surprise, ed. A. S. Fruchter, M. Tavani, & D. C. Backer, Vol. 72, 322

—. 2005, ArXiv Astrophysics e-prints (astro-ph/0503300)

—. 2007a, ArXiv Astrophysics e-prints (astro-ph/0710.3517)

Harding, A. K. 2007b, in AIP Conf. Ser., Vol. 921, The First GLAST Symposium, ed. S. Ritz, P. Michelson, & C. A. Meegan, 49

Harding, A. K., Gonthier, P. L., Ouellette, M. S., O'Brien, S., & Berrier, J. 2002a, in ASP Conf. Ser., Vol. 271, Neutron Stars in Supernova Remnants, ed. P. O. Slane & B. M. Gaensler, 335

Harding, A. K. & Muslimov, A. G. 1998, ApJ, 508, 328

—. 2001, ApJ, 556, 987

—. 2002, ApJ, 568, 862

Harding, A. K., Muslimov, A. G., & Zhang, B. 2002b, ApJ, 576, 366

Harding, A. K. & Preece, R. 1987, ApJ, 319, 939

Harding, A. K., Stern, J. V., Dyks, J., & Frackowiak, M. 2008, ArXiv e-prints, 803

Harding, A. K., Tademaru, E., & Esposito, L. W. 1978, ApJ, 225, 226

Harding, A. K., Usov, V. V., & Muslimov, A. G. 2005a, in Towards a Network of Atmospheric Cherenkov Detectors VII, ed. B. Degrange & G. Fontaine (astro-ph/0511098)

Harding, A. K., Usov, V. V., & Muslimov, A. G. 2005b, ApJ, 622, 531

Hartle, J. B. 2003, Gravity: An Introduction to Einstein's General Relativity (San Francisco: Pearson Education, Inc., publishing as Addison Wesley)

Hartman, R. C. et al. 1999, ApJS, 123, 79

Heinke, C. O., Grindlay, J. E., Edmonds, P. D., Cohn, H. N., Lugger, P. M., Camilo, F., Bogdanov, S., & Freire, P. C. 2005, ApJ, 625, 796

Helfand, D. J. & Becker, R. H. 1987, ApJ, 314, 203

Helfand, D. J., Gotthelf, E. V., & Halpern, J. P. 2001, ApJ, 556, 380

Hermann, G., Hofmann, W., Schweizer, T., & Teshima, M. 2007, ArXiv e-prints, (astro-ph/0709.2048v1), 709

Hewish, A., Bell, S. J., Pilkington, J. D., Scott, P. F., & Collins, R. A. 1968, Nature, 217, 709

Hibschman, J. A. & Arons, J. 2001, ApJ, 546, 382

Hillas, A. M. 1985, in Proc. 19th Int. Cosmic Ray Conf., ed. F. C. Jones, Vol. 3, 445

Hillier, R. R., Jackson, W. R., Murray, A., Redfern, R. M., & Sale, R. G. 1970, ApJL, 162, L177

Hinton, J. A. 2004, New Astron. Rev., 48, 331

Hinton, J. A., Funk, S., Hofmann, W., Rolland, L., & de Naurois, M. 2005, in Proc. 29th Int. Cosmic Ray Conf., Vol. 4, 21

Hirotani, K. 2005, Advances in Space Research, 35, 1085

—. 2007, ArXiv Astrophysics e-prints (astro-ph/0701243)

Hirotani, K., Harding, A. K., & Shibata, S. 2003, ApJ, 591, 334

Hirotani, K. & Shibata, S. 1999a, Publ. Astronom. Soc. Japan, 51, 683

—. 1999b, MNRAS, 308, 54

—. 1999c, MNRAS, 308, 67

—. 2001a, ApJ, 558, 216

—. 2001b, MNRAS, 325, 1228

Ho, C. 1990, in Bull. Am. Astron. Soc., Vol. 22, 747

Hofmann, W. 1997, in Towards a Major Atmospheric Čerenkov Detector - V, ed. O. C. de Jager (Potchefstroom: Wesprint), 405

Hofmann, W. 1999, in Towards a Major Atmospheric Čerenkov Detector - VI, ed. B. L. Dingus, M. H. Salomon, & D. B. Kieda, 500

Hofmann, W. 2001, in Proc. 27th Int. Cosmic Ray Conf., Vol. 7, 2785

Hofmann, W. 2002, in The Universe Viewed in Gamma-Rays, ed. R. Enomoto, M. Mori, & S. Yanagita (Tokyo: Univ. Academy Press), 357

Hofmann, W. 2003, in Proc. 28th Int. Cosmic Ray Conf., Vol. 5, 2811

Hofmann, W. 2005, in Towards a Network of Atmospheric Cherenkov Detectors VII, ed. B. Degrange & G. Fontaine, 43

Huang, Z.-K. & Wu, X.-J. 2003, Chinese J. of Astron. Astrophys., 3, 166

Hulse, R. A. & Taylor, H. J. 1974, in Bull. Am. Astron. Soc., Vol. 6, 453

Ivanova, N., Fregeau, J. M., & Rasio, F. A. 2005, in ASP Conf. Ser., Vol. 328, Binary Radio Pulsars, ed. F. A. Rasio & I. H. Stairs (San Francisco: ASP), 231

Jackson, J. D. 1975, Classical Electrodynamics (2^{nd} ed.; New York: John Wiley & Sons, Inc.)

Jacoby, B. A., Hotan, A., Bailes, M., Ord, S., & Kulkarni, S. R. 2005, ApJL, 629, L113

Janssen, G. H. & Stappers, B. W. 2006, A&A, 457, 611

Jenet, F. A., Anderson, S. B., Kaspi, V. M., Prince, T. A., & Unwin, S. C. 1998, ApJ, 498, 365

Johnston, S. & Bailes, M. 1991, MNRAS, 252, 277

Johnston, S., Manchester, R. N., Lyne, A. G., Bailes, M., Kaspi, V. M., Qiao, G., & D'Amico, N. 1992, ApJL, 387, L37

Johnston, S. et al. 1993, Nature, 361, 613

Kanbach, G. 2001, in The Universe in Gamma Rays, ed. V. Shönvelder, A&A Library, 127

Kanbach, G. 2002, in Neutron Stars, Pulsars, and Supernova Remnants, ed. W. Becker, H. Lesch, & J. Trümper, 91

Kanbach, G. et al. 1980, A&A, 90, 163

Kargaltsev, O. & Pavlov, G. G. 2008, in AIP Conf. Ser., Vol. 983, 171

Kargaltsev, O., Pavlov, G. G., & Romani, R. W. 2004, ApJ, 602, 327

Kawai, N., Tamura, K., & Saito, Y. 1998, Advances in Space Research, 21, 213

Kennel, C. F. & Coroniti, F. V. 1984, ApJ, 283, 694

Kniffen, D. A. 1990, in Astrophysics and Space Science Library, Vol. 166, IAU Colloq. 123: Observatories in Earth Orbit and Beyond, ed. Y. Kondo, 63

Kniffen, D. A., Hartman, R. C., Thompson, D. J., Bignami, G. K., Fichtel, C. E., Tumer, T., & Ogelman, H. 1974, Nature, 251, 397

Kobayashi, T., Komori, Y., Yoshida, K., & Nishimura, J. 2004, ApJ, 601, 340

Konopelko, A. 2005, Astropart. Phys., 24, 191

—. 2007, Proc. 30th Int. Cosmic Ray Conf. (in press)

Konopelko, A., Finley, J. P., & Urbanski, G. 2007, Proc. 30th Int. Cosmic Ray Conf. (in press)

Korpela, E. J. & Bowyer, S. 1998, Astron. J., 115, 2551

Kramer, M. 2008a, in ASP Conf. Ser., ed. A. H. Bridle, J. J. Condon, & G. C. Hunt, Vol. 395, 249

Kramer, M. 2008b, in Relativistic Astrophysics and Cosmology - Einstein's Legacy, ed. B. Aschenbach, V. Burwitz, G. Hasinger, & B. Leibundgut, 87

Kramer, M., Lange, C., Lorimer, D. R., Backer, D. C., Xilouris, K. M., Jessner, A., & Wielebinski, R. 1999, ApJ, 526, 957

Kramer, M., Lyne, A. G., O'Brien, J. T., Jordan, C. A., & Lorimer, D. R. 2006a, Science, 312, 549

Kramer, M., Xilouris, K. M., Lorimer, D. R., Doroshenko, O., Jessner, A., Wielebinski, R., Wolszczan, A., & Camilo, F. 1998, ApJ, 501, 270

Kramer, M. et al. 2003, MNRAS, 342, 1299

—. 2006b, Science, 314, 97

Kreyszig, E. 1999, Advanced Engineering Mathematics (8^{th} ed.; Singapore: John Wiley & Sons, Inc.)

Kuiper, L., Hermsen, W., Verbunt, F., Thompson, D. J., Stairs, I. H., Lyne, A. G., Strickman, M. S., & Cusumano, G. 2000, A&A, 359, 615

Kulkarni, S. R. 1995, in ASP Conf. Ser., Vol. 72, Millisecond Pulsars. A Decade of Surprise, ed. A. S. Fruchter, M. Tavani, & D. C. Backer, 79

Kulkarni, S. R., Lyne, A. G., Brinklow, A., Middleditch, J., Backer, D. C., & Clifton, T. R. 1987, in Bull. Am. Astron. Soc., Vol. 19, 949

Landau, L. D. & Lifshitz, E. M. 1975, The Classical Theory of Fields (4^{th} Revised English ed.; Oxford: Pergamon Press)

Langer, U. W. 2004, Ph.D. Thesis, Potchefstroomse Universiteit vir Christelike Hoër Onderwys

Large, M. I. 1971, in IAU Symposium, Vol. 46, The Crab Nebula, ed. R. D. Davies & F. Graham-Smith, 165

Large, M. I., Vaughan, A. E., & Mills, B. Y. 1968, Nature, 220, 340

LaRosa, T. N., Kassim, N. E., Lazio, T. J. W., & Hyman, S. D. 2000, Astron. J., 119, 207

Levinson, A., Melrose, D., Judge, A., & Luo, Q. 2005, ApJ, 631, 456

Li, X. H., Qi, S., & Han, J. L. 2003, Acta Astronomica Sinica, 44, 258

Lipunov, V. M. 1992, Astrophysics of Neutron Stars (Berlin: Springer-Verlag)

Longair, M. S. 1994, High Energy Astrophysics, Volume 2: Stars, the Galaxy and the Interstellar Medium (2^{nd} ed.; Cambridge: Cambridge Univ. Press)

Lorimer, D. R. 2005, Living Reviews in Relativity, 8 (http://www.livingreviews.org/lrr-2005-7)

Lorimer, D. R., Camilo, F., Freire, P., Kramer, M., Lyne, A. G., Manchester, R. N., & D'Amico, N. 2003, in ASP Conf. Ser., Vol. 302, Radio Pulsars, ed. M. Bailes, D. J. Nice, & S. E. Thorsett, 363

Luo, Q. 1996, ApJ, 468, 338

Luo, Q., Shibata, S., & Melrose, D. B. 2000, MNRAS, 318, 943

Lyne, A. G. 2006, Chinese J. of Astron. Astrophys. Suppl., 6, 162

Lyne, A. G., Brinklow, A., Middleditch, J., Kulkarni, S. R., & Backer, D. C. 1987, Nature, 328, 399

Lyne, A. G. & Graham-Smith, F. 1990, Pulsar Astronomy (Cambridge, England and New York: Cambridge University Press (Cambridge Astrophys. Ser., No. 16))

Lyne, A. G. & Manchester, R. N. 1988, MNRAS, 234, 477

Lyne, A. G. et al. 1998, MNRAS, 295, 743

—. 2004, Science, 303, 1153

Mahoney, M. J. & Erickson, W. C. 1985, Nature, 317, 154

Malov, I. F. & Machabeli, G. Z. 2001, ApJ, 554, 587

Manchester, R. N. 1995, in ASP Conf. Ser., Vol. 72, Millisecond Pulsars. A Decade of Surprise, ed. A. S. Fruchter, M. Tavani, & D. C. Backer, 3

Manchester, R. N. 2001, Publ. of the Astron. Soc. of Australia, 18, 1

Manchester, R. N., Hobbs, G. B., Teoh, A., & Hobbs, M. 2005, Astron. J., 129, 1993

Manchester, R. N. & Johnston, S. 1995, ApJL, 441, L65

Manchester, R. N. & Taylor, J. H. 1977, Pulsars (San Francisco: W.H. Freeman and Co.)

Manchester, R. N. et al. 2001, MNRAS, 328, 17

Mao, C. Y. & Shen, C. S. 1972, Chinese J. of Phys., 10, 16

Mayall, N. U. & Oort, J. H. 1942, Proc. Astron. Soc. Pac., 54, 95

Mayer-Hasselwander, H. A. et al. 1982, A&A, 105, 164

McConnell, D., Ables, J. G., Bailes, M., & Erickson, W. C. 1996, MNRAS, 280, 331

McEnery, J. E. 2006, in Bull. Am. Astron. Soc., Vol. 38, 1154

McLaughlin, M. A. & Cordes, J. M. 2000, ApJ, 538, 818

McLaughlin, M. A. et al. 2006, Nature, 439, 817

Mereghetti, S., Sidoli, L., & Israel, G. L. 1998, A&A, 331, L77

Mészáros, P. 1992, High-Energy Radiation from Magnetized Neutron Stars (Chicago: The Univ. of Chicago Press)

Michel, F. C. 1974, ApJ, 192, 713

—. 1982, Rev. Mod. Phys., 54, 1

—. 1987, Nature, 329, 310

—. 2004, Advances in Space Research, 33, 542

Middleditch, J., Lyne, A. G., Brinklow, A., Backer, D. C., Clifton, T. R., & Kulkarni, S. R. 1987, IAU Circ., 4401, 1

Middleditch, J. H., Imamura, J. N., & Steiman-Cameron, T. Y. 1988, ApJ, 335, 753

Mineo, T., Cusumano, G., Massaro, E., Becker, W., & Nicastro, L. 2004, A&A, 423, 1045

Minkowski, R. 1942, ApJ, 96, 199

Misner, C. W., Thorne, K. S., & Wheeler, J. A. 1973, Gravitation (San Francisco: W.H. Freeman and Co., 1973)

Moraal, H. & Potgieter, M. S. 1982, Astrophys. Space Sci., 84, 519

Muslimov, A. G. & Harding, A. K. 1997, ApJ, 485, 735

—. 2003, ApJ, 588, 430

—. 2004a, ApJ, 606, 1143

—. 2004b, ApJ, 617, 471

Muslimov, A. G. & Tsygan, A. I. 1992, MNRAS, 255, 61

Navarro, J. & Manchester, R. N. 1996, in Astronomical Society of the Pacific Conference Series, Vol. 105, IAU Colloq. 160: Pulsars: Problems and Progress, ed. S. Johnston, M. A. Walker, & M. Bailes, 249

Navarro, J., Manchester, R. N., Sandhu, J. S., Kulkarni, S. R., & Bailes, M. 1997, ApJ, 486, 1019

Nel, H. I., Raubenheimer, B. C., de Jager, O. C., Brink, C., Meimtjes, P. J., North, A. R., & van Urk, G. 1992, ApJ, 398, 602

Ng, C.-Y. & Romani, R. W. 2004, ApJ, 601, 479

Oppenheimer, J. R. & Volkoff, G. M. 1939, Phys. Rev., 55, 374

Ostriker, J. P. & Gunn, J. E. 1969, ApJ, 157, 1395

Pacini, F. 1967, Nature, 216, 567

—. 1968, Nature, 219, 145

Padmanabhan, T. 2000, Theoretical Astrophysics, Volume I: Astrophysical Processes (Cambridge University Press)

—. 2001, Theoretical Astrophysics, Volume II: Stars and Stellar Systems (Cambridge University Press)

Pavlov, G. G. & Zavlin, V. E. 1997, ApJL, 490, L91

—. 2000, ApJ, 529, 1011

Porquet, D., Decourchelle, A., & Warwick, R. S. 2003, A&A, 401, 197

Possenti, A., Colpi, M., D'Amico, N., & Burderi, L. 1998, ApJL, 497, L97

Potgieter, M. S. & Langner, U. W. 2004, ApJ, 602, 993

Punch, M. 2005, in Towards a Network of Atmospheric Cherenkov Detectors VII, ed. B. Degrange & G. Fontaine, 379

Qiao, G.-J., Wang, X.-D., Wang, H.-G., & Xu, R.-X. 2002, Chinese J. of Astron. Astrophys., 2, 361

Rajagopal, M. & Romani, R. W. 1996, ApJ, 461, 327

Ramanamurthy, P. V. & Wolfendale, A. W. 1986, Gamma-ray Astronomy (Cambridge Univ. Press)

Ransom, S. M. 2007, in AIP Conf. Ser., Vol. 921, The First GLAST Symposium, ed. S. Ritz, P. Michelson, & C. A. Meegan, 54

Ransom, S. M. 2008, in AIP Conf. Ser., Vol. 983, 415

Rees, M. J. & Gunn, J. E. 1974, MNRAS, 167, 1

Reimer, O., Hinton, J. Hofmann, W., Hoppe, S., Masterson, C., & Raue, M. 2007, in Proc. 30th Int. Cosmic Ray Conf. (in press)

Revnivtsev, M. G. et al. 2004, A&A, 425, L49

Reynolds, S. P. & Chevalier, R. A. 1984, ApJ, 278, 630

Richards, D. W. & Comella, J. M. 1969, Nature, 222, 551

Ritz, S. 2007, in AIP Conf. Ser., Vol. 921, The First GLAST Symposium, ed. S. Ritz, P. Michelson, & C. A. Meegan, 3

Rohlfs, T. 2000, Tools of Radio Astronomy (Springer-Verlag)

Romani, R. W. 1996, in Astronomical Society of the Pacific Conference Series, Vol. 105, IAU Colloq. 160: Pulsars: Problems and Progress, ed. S. Johnston, M. A. Walker, & M. Bailes, 331

Romani, R. W. & Johnston, S. 2001, ApJL, 557, L93

Romani, R. W., Kulkarni, S. R., & Blandford, R. D. 1987, Nature, 329, 309

Romani, R. W. & Yadigaroglu, I.-A. 1995, ApJ, 438, 314

Rots, A. H. et al. 1998, ApJ, 501, 749

Rudak, B. & Dyks, J. 1999, MNRAS, 303, 477

Rudak, B., Dyks, J., & Bulik, T. 2002, in Neutron Stars, Pulsars, and Supernova Remnants, ed. W. Becker, H. Lesch, & J. Trümper, 142

Ruderman, M. 2003, ArXiv Astrophysics e-prints (astro-ph/0311228)

Ruderman, M. A. & Sutherland, P. G. 1975, ApJ, 196, 51

Rutledge, R. E., Fox, D. W., Kulkarni, S. R., Jacoby, B. A., Cognard, I., Backer, D. C., & Murray, S. S. 2004, ApJ, 613, 522

Rybicki, G. B. & Lightman, A. P. 1979, Radiative Processes in Astrophysics (John Wiley & Sons)

Saito, Y., Kawai, N., Kamae, T., Shibata, S., Dotani, T., & Kulkarni, S. R. 1997, ApJL, 477, L37

Saito, Y., Kawai, N., Rots, A., Kamae, T., & Shibata, S. 2001, in Astronomical Society of the Pacific Conference Series, Vol. 251, New Century of X-ray Astronomy, ed. H. Inoue & H. Kunieda, 404

Sakai, N. & Shibata, S. 2003, ApJ, 584, 427

Sakano, M., Koyama, K., Murakami, H., Maeda, Y., & Yamauchi, S. 2002, ApJS, 138, 19

Sakano, M., Warwick, R. S., & Decourchelle, A. 2003, in Workshop on Galaxies and Clusters of Galaxies, 9

Sakano, M., Warwick, R. S., Hands, A., & Decourchelle, A. 2004, Memorie della Societa Astronomica Italiana, 75, 498

Sakano, M., Yokogawa, J., & Murakami, H. 1999, in Japanese-German Workshop on High Energy Astrophysics, ed. W. Becker & M. Itoh, 113

Sandhu, J. S., Bailes, M., Manchester, R. N., Navarro, J., Kulkarni, S. R., & Anderson, S. B. 1997, ApJL, 478, L95

Scharlemann, E. T., Arons, J., & Fawley, W. M. 1978, ApJ, 222, 297

Schlickeiser, R. 2002, Cosmic Ray Astrophysics (Berlin: Springer-Verlag)

Schönfelder, V. 2001, in The Universe in Gamma Rays, ed. V. Shönvelder, A&A Library, 1

Schroeder, P. C. et al. 1995, ApJ, 450, 784

Sefako, R. R. & de Jager, O. C. 2003, ApJ, 593, 1013

Sengupta, S. 1995, ApJ, 449, 224

Shen, C. S. 1970, ApJL, 162, L181

Sidoli, L., Belloni, T., & Mereghetti, S. 2001, A&A, 368, 835

Sidoli, L., Bocchino, F., Mereghetti, S., & Bandiera, R. 2004, Memorie della Societa Astronomica Italiana, 75, 507

Sidoli, L., Mereghetti, S., Israel, G. L., & Bocchino, F. 2000, A&A, 361, 719

Sidoli, L., Mereghetti, S., Israel, G. L., Chiappetti, L., Treves, A., & Orlandini, M. 1999a, ApJ, 525, 215

Sidoli, L. et al. 1998, in The Active X-ray Sky: Results from BeppoSAX and RXTE (Nucl. Phys. B Proc. Suppl. 69), ed. L. Scarsi, H. Bradt, P. Giommi, & F. Fiore (Amsterdam: Elsevier), 88

Sidoli, L. et al. 1999b, Astrophys. Lett. Comm. 38, 309

Simpson, J. A. 2001, in The Century of Space Science, ed. J. A. M. Bleeker, J. Geiss, & M. Huber (Kluwer Academic Publishers), 117

Slane, P. 2005, Adv. Space Res., 35, 1092

Slane, P. 2008, in AIP Conf. Ser., ed. Y.-F. Yuan, X.-D. Li, & D. Lai, Vol. 968, 143

Smith, D. A. 2008, in AIP Conf. Ser., Vol. 983, 40 Years of Pulsars: Millisecond Pulsars, Magnetars and More, 624

Smith, I. A., Michel, F. C., & Thacker, P. D. 2001, MNRAS, 322, 209

Spitkovsky, A. 2006, ApJL, 648, L51

Staelin, D. H. & Reifenstein, E. C. 1968, Science, 162, 1481

Stage, M. D., Allen, G. E., Houck, J. C., & Davis, J. E. 2006, Nature Physics, 2, 614

Stella, L. & Vietri, M. 1998, ApJL, 492, L59

Stewart, J. 1999a, Multivariable Calculus (4^{th} ed.; Pacific Grove: Brooks/Cole Publishing Co.)

—. 1999b, Single Variable Calculus (4^{th} ed.; Pacific Grove: Brooks/Cole Publishing Co.)

Story, S. A., Gonthier, P. L., & Harding, A. K. 2007, ApJ, 671, 713

Sturrock, P. A. 1971, ApJ, 164, 529

Sturrock, P. A., Harding, A. K., & Daugherty, J. K. 1989, ApJ, 346, 950

Tademaru, E. 1974, Astrophys. Space Sci., 30, 179

Takata, J., Chang, H.-K., & Shibata, S. 2008, MNRAS, 386, 748

Takata, J., Shibata, S., & Hirotani, K. 2004, MNRAS, 354, 1120

Takata, J., Shibata, S., Hirotani, K., & Chang, H.-K. 2006, MNRAS, 366, 1310

Tananbaum, H., Gursky, H., Kellogg, E. M., Levinson, R., Schreier, E., & Giacconi, R. 1972, ApJL, 174, L143

Tauris, T. M. et al. 1994, ApJL, 428, L53

Tayler, R. J. 1994, The Stars: Their Structure and Evolution, Second Edition (Cambridge University Press)

Taylor, J. H. & Stinebring, D. R. 1986, Ann. Rev. Astron. Astrophys., 24, 285

Taylor, J. H. & Weisberg, J. M. 1989, ApJ, 345, 434

Testa, V. et al. 2004, Memorie della Societa Astronomica Italiana, 75, 50

Thacker, P. D., Michel, F. C., & Smith, I. A. 1998, in Revista Mexicana de Astronomia y Astrofisica Conf. Ser., ed. R. J. Dufour & S. Torres-Peimbert, Vol. 7, 211

Thomas, R. M. C. & Gangadhara, R. T. 2007, A&A, 467, 911

Thompson, D. J. 2001, in AIP Conf. Ser., ed. F. A. Aharonian & H. J. Völk, Vol. 558, 103

Thompson, D. J. 2004a, in IAU Symposium, Vol. 218, Young Neutron Stars and Their Environments, ed. F. Camilo & B. M. Gaensler, 399

Thompson, D. J. 2004b, New Astron. Rev., 48, 543

—. 2007, ArXiv Astrophysics e-prints (astro-ph/0711.4278v1), 711

Thompson, D. J., Fichtel, C. E., Kniffen, D. A., & Ogelman, H. B. 1975, ApJL, 200, L79

Torii, S. et al. 2001, ApJ, 559, 973

Torres, D. F. 2007, in AIP Conf. Ser., Vol. 921, The First GLAST Symposium, ed. S. Ritz, P. Michelson, & C. A. Meegan, 37

Toscano, M., Sandhu, J. S., Bailes, M., Manchester, R. N., Britton, M. C., Kulkarni, S. R., Anderson, S. B., & Stappers, B. W. 1999, MNRAS, 307, 925

Trümper, J., Pietsch, W., Reppin, C., Voges, W., Staubert, R., & Kendziorra, E. 1978, ApJL, 219, L105

Usov, V. V. 1983, Nature, 305, 409

Usov, V. V. & Melrose, D. B. 1996, ApJ, 464, 306

van der Swaluw, E., Achterberg, A., Gallant, Y. A., & Tóth, G. 2001, A&A, 380, 309

van der Swaluw, E., Downes, T. P., & Keegan, R. 2004, A&A, 420, 937

van der Swaluw, E. & Wu, Y. 2001, ApJL, 555, L49

van Straten, W., Bailes, M., Britton, M., Kulkarni, S. R., Anderson, S. B., Manchester, R. N., & Sarkissian, J. 2001, Nature, 412, 158

Vargas, M. et al. 1997, in ESA Special Publication, Vol. 382, The Transparent Universe, ed. C. Winkler, T. J.-L. Courvoisier, & P. Durouchoux, 129

Venter, C. 2004, M.Sc. Thesis, Potchefstroomse Universiteit vir Christelike Hoër Onderwys (Unpublished)

Venter, C. & de Jager, O. C. 2005a, ApJL, 619, L167

—. 2005b, Astrophys. Space Sci., 297, 399

Venter, C. & de Jager, O. C. 2006, in MPE Report 291, Vol. 801, Proc. of the 363 WE-Heraeus Seminar on: Neutron Stars and Pulsars (Posters and contributed talks), ed. W. Becker & H. Huang, 40

—. 2008a, ApJL, 680, L125

—. 2008b, to appear in the Proceedings of COSPAR 2008

—. 2008c, to appear in the Proceedings of the Heidelberg Gamma-ray Symposium 2008

Venter, C., de Jager, O. C., & Tiplady, A. 2005, in Astrophysical Sources of High Energy Particles and Radiation, AIP Conf. Ser., ed. T. Bulik, B. Rudak, & G. Madejski, Vol. 801, 278

Verbunt, F. 2001, A&A, 368, 137

Verbunt, F., Hartman, J. W., Bhattacharya, D., Wijers, R. A. M. J., & Nelemans, G. 1999, in Pulsar Timing, General Relativity and the Internal Structure of Neutron Stars, ed. Z. Arzoumanian, F. Van der Hooft, & E. P. J. van den Heuvel, 215

Verbunt, F., van den Heuvel, E. P. J., van Paradijs, J., & Rappaport, S. A. 1987, Nature, 329, 312

Vincent, P. 2005, in Proc. 29th Int. Cosmic Ray Conf., Vol. 5, 163

Vivekanand, M. 2000, ApJ, 543, 979

—. 2001, MNRAS, 326, L33

Vivekanand, M., Ables, J. G., & McConnell, D. 1998, ApJ, 501, 823

Wada, T. & Shibata, S. 2007, MNRAS, 376, 1460

Wang, W. 2006, Chinese J. of Astron. Astrophys. Suppl., 6, 268

Weekes, T. C. et al. 1989, ApJ, 342, 379

Weiler, K. W. & Panagia, N. 1978, A&A, 70, 419

Weisskopf, M. C. et al. 2004, Nuclear Physics B Proceedings Supplements, 132, 566

Wheeler, J. A. 1966, Ann. Rev. Astron. Astrophys., 4, 393

White, N. E. & Stella, L. 1988, Nature, 332, 416

Willems, B. & Kolb, U. 2002, MNRAS, 337, 1004

Wolszczan, A. 1990, IAU Circ., 5073, 1

Wolszczan, A. & Frail, D. A. 1992, Nature, 355, 145

Wright, G. A. E. 2004, MNRAS, 351, 813

Yakovlev, D. G., Gnedin, O. Y., Gusakov, M. E., Kaminker, A. D., Levenfish, K. P., & Potekhin, A. Y. 2005, Nuclear Physics A, 752, 590

Zavlin, V. E. 2006, ApJ, 638, 951

—. 2007, to appear in Lecture Notes in Physics, ArXiv Astrophysics e-prints (astro-ph/0702426)

Zavlin, V. E. & Pavlov, G. G. 1998, A&A, 329, 583

Zavlin, V. E. & Pavlov, G. G. 2002, in Neutron Stars, Pulsars, and Supernova Remnants, ed. W. Becker, H. Lesch, & J. Trümper, 263

Zavlin, V. E., Pavlov, G. G., Sanwal, D., Manchester, R. N., Trümper, J., Halpern, J. P., & Becker, W. 2002, ApJ, 569, 894

Zhang, B. & Harding, A. K. 2000, ApJ, 532, 1150

Zhang, L., Chen, S. B., & Fang, J. 2008, ApJ, 676, 1210

Zhang, L., Cheng, K. S., Jiang, Z. J., & Leung, P. 2004, ApJ, 604, 317

Zheng, Z., Zhang, B., & Qiao, G. J. 1998, A&A, 334, L49